CHEMICAL REVIEWS

Review

Cite This: *Chem. Rev.* 2019, 119, 2752–2875

pubs.acs.org/CR

Electro- and Solar-Driven Fuel Synthesis with First Row Transition Metal Complexes

Kristian E. Dalle,[†] Julien Warnan,[†] Jane J. Leung, Bertrand Reuillard, Isabell S. Karmel, and Erwin Reisner*

Christian Doppler Laboratory for Sustainable SynGas Chemistry, Department of Chemistry, University of Cambridge, Lensfield Road, Cambridge CB2 1EW, United Kingdom

ABSTRACT: The synthesis of renewable fuels from abundant water or the greenhouse gas CO_2 is a major step toward creating sustainable and scalable energy storage technologies. In the last few decades, much attention has focused on the development of nonprecious metal-based catalysts and, in more recent years, their integration in solid-state support materials and devices that operate in water. This review surveys the literature on 3d metal-based molecular catalysts and focuses on their immobilization on heterogeneous solid-state supports for electro-, photo-, and photoelectrocatalytic synthesis of fuels in aqueous media. The first sections highlight benchmark homogeneous systems using proton and CO_2 reducing 3d transition metal catalysts as well as commonly employed methods for catalyst immobilization, including a discussion of supporting materials and anchoring groups. The subsequent sections elaborate on productive associations between molecular catalysts and a wide range of substrates based on carbon, quantum dots, metal oxide surfaces, and semiconductors. The molecule−material hybrid systems are organized as "dark" cathodes, colloidal photocatalysts, and photocathodes, and their figures of merit are discussed alongside system stability and catalyst integrity. The final section extends the scope of this review to prospects and challenges in targeting catalysis beyond "classical" H_2 evolution and CO_2 reduction to C_1 products, by summarizing cases for higher-value products from N_2 reduction, $C_{x>1}$ products from CO_2 utilization, and other reductive organic transformations.

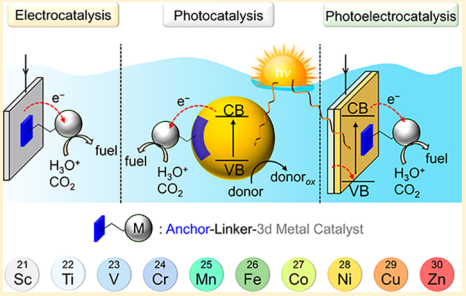

CONTENTS

Special Issue: First Row Metals and Catalysis

Received: June 21, 2018
Published: February 15, 2019

DOI: 10.1021/acs.chemrev.8b00392
Chem. Rev. 2019, 119, 2752–2875

1. INTRODUCTION

1.1. Motivation and Strategy

The worldwide reliance on fossil fuels as energy carriers and raw materials for industrial products presents several challenges for the coming decades. Reserves are finite, and their combustion for power generation and use by the petrochemical industry has substantially contributed to rising atmospheric CO_2 levels,[1−3] which has recently been emphasized by the 2015 United Nations Climate Change Conference in Paris.[4] Worldwide energy demand is steadily increasing, and fossil fuels made up more than 80% of global energy consumption in 2017.[5,6] Alternatives such as wind, hydro, and solar power are rapidly growing sources of sustainable electricity, but their intermittency makes energy storage a contemporary challenge. Renewable electricity also does not provide combustible fuels for use in the transport sector, in particular aviation and heavy freight over long-distances, nor feedstock chemicals for making plastics, rubbers, fertilizers, and pharmaceuticals. New approaches are therefore needed to provide sustainable resources for fuels and commodity production.

CO_2 is the thermodynamically stable end product of numerous chemical and biological oxidation reactions,[2,7] and the reverse processes that form chemicals from CO_2 thus require energy input.[7,8] The Sun continuously supplies approximately 100 000−120 000 TW to Earth, more than 5000 times the current global primary energy consumption of 18 TW, making it the most sustainable energy source available to humanity.[5,9−11] Nature harnesses this energy through photosynthesis, using sunlight to drive fixation of atmospheric CO_2 under mild conditions on an estimated scale of 100−120 gigatonnes per annum.[12,13] This biological process provides a strategy for employing light to capture CO_2 and convert it into a chemical energy vector, thereby closing the carbon cycle and simultaneously alleviating global warming.[2] Mimicry of the natural pathways through artificial photosynthetic design can provide us with a route to solar fuels (Figure 1).

'Solar fuels' describes any concentrated chemical energy carrier with long-term storage capacity that contains chemical bonds in which solar energy has been stored.[14,15] This review primarily focuses on pathways to these fuels that have been among the most intensely researched in the last decades: those employing molecular catalysts with the ability to use sunlight directly (photoresponsive systems) or indirectly (by photosensitizer-coupling) to generate H_2 and products from CO_2 reduction. Photocatalytic processes that produce these products are collectively described as artificial photosynthesis,[16] as they take inspiration from the first step of natural photosynthesis where water is photocatalytically split into dioxygen and "hydrogen".[9] "Hydrogen" refers here to the combination of protons and low potential electrons extracted from H_2O, which in Nature are then used along with CO_2 to form organic compounds. These chemicals are the basis of our global energy economy, providing us with "fuels" to sustain life, whether sugars for metabolism or fossil fuels for generating electricity and powering transportation. Combining the "hydrogen" bound in

DOI: 10.1021/acs.chemrev.8b00392
Chem. Rev. 2019, 119, 2752−2875

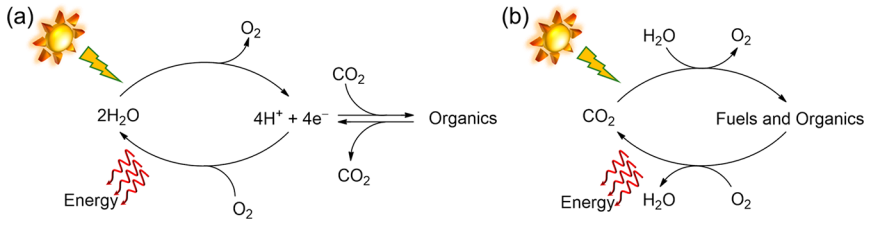

Figure 1. Schematic representation of (a) natural and (b) artificial photosynthesis.

these fuels with O_2 releases energy, reversing the process and thereby liberating H_2O and CO_2 (Figure 1).[9] In this regard, photocatalytic production of H_2 through water splitting can be seen as the most basic form of artificial photosynthesis, providing molecular hydrogen as a solar fuel, albeit without the advantage of carbon fixation for producing valuable organic compounds.[1]

Nature has evolved enzymes for reducing protons and CO_2 with excellent performance under mild biological conditions and has thereby provided a blueprint for effectively achieving the catalytic reactions central to generating solar fuels. These archetypal biological systems are therefore vital to advancing our understanding of the fundamental aspects of small molecule activation, which may allow for improved design of catalysts and catalytic processes for fuel production and manufacture of commodities.[1,17] However, while fuel-producing enzymes can reach high turnover rates with excellent selectivity for specific transformations, they are typically sensitive to operational conditions such as pH, temperature, and the presence of O_2, and are restrictively expensive to isolate for large-scale applications.[11,16−19] Solid-state material catalysts are often stable but may exhibit low product selectivity, giving mixtures of carbon-based products from CO_2 reduction.[20,21] In contrast, synthetic coordination complex catalysts can achieve excellent product selectivity with acceptable long-term stability and tolerance to experimental conditions.[21−23] They are also amenable to mechanistic investigation through in situ spectroscopy, and their catalytic properties can be tailored through variation of the metal, and through rational ligand design.[21,24] Immobilizing molecular catalysts on solid-state supports can thus provide a system displaying single-site catalysis, enhancing selectivity and simplifying identification of the active species, while also facilitating product isolation and catalyst recycling.[21,24,25] Furthermore, use of a suitable semiconductor (SC) support can supply the energy required for substrate transformation directly through absorption of solar light.[20,25]

1.2. Biological Templates for Artificial Photosynthesis

Whether considering H_2 evolution by hydrogenases (H_2ases), reversible reduction of CO_2 to CO by carbon monoxide dehydrogenases (CODHs), or extraction of protons and electrons from H_2O by the oxygen evolving complex (OEC) in Photosystem II, these inspirational biocatalysts generally possess one (or more) Earth-abundant 3d transition metal element in their active sites.[17,26] The metal centers typically cycle between different oxidation states, reversibly storing electrons and protons that can be added to or extracted from the relevant substrates, while also providing a binding site at which transformation of these molecules can be carefully controlled.[17,26] The identity of these metal sites in Nature has been influenced by their bioavailability, but noteworthy differences also exist in the chemistry of 3d transition metals compared to heavier analogues. For example, while iron(II) and nickel(II) complexes rapidly undergo ligand exchange, the corresponding ruthenium/osmium(II) and palladium/platinum(II) complexes tend to be kinetically inert.[27] This greater lability results in kinetically controlled chemistry for the lighter elements, imparting unique reactivity profiles. In combination with their vastly greater availability (elemental abundance in Earth's crust in mg kg^{-1} = Fe: 5.63×10^4, Ni: 8.4×10^1, Ru: 1×10^{-3}, Os: 1.5×10^{-3}, Pd: 1.5×10^{-2}, Pt: 5×10^{-3}), these properties make the 3d transition metals the most promising candidates for appreciating and reproducing subtle aspects of metalloenzyme reactivity.[28] In-depth studies of the natural systems have revealed recurring characteristics that help shape reactivity, and the following overview highlights selected examples with features that have been, or have the potential to be, applied for enhancing the activity of synthetic systems.

Two types of metalloenzyme with particular relevance to catalytic H_2 generation are the [FeFe]- and [NiFe]-H_2ases, both of which reversibly interconvert two electrons and two protons into molecular hydrogen.[29,30] Although the [FeFe]-H_2ases are generally more sensitive to irreversible O_2 inactivation, they show greater activity for H_2 production, competing with metallic platinum in terms of performance and reaching rates of up to 10 000 s^{-1}.[16,31−33] The names of these enzymes reflect the composition of their bimetallic active sites: the [NiFe]-H_2ases possess one nickel and one iron atom, whereas the [FeFe]-H_2ases utilize two iron centers (Figure 2a,b). Both feature biologically unusual organometallic CO and CN^- ligation at the Fe atoms, with thiolates as the remaining donors in both terminal and bridging (μ) positions. A subclass of the [NiFe]-H_2ases also exists in which one of the terminally coordinating amino acids has been substituted for a selenocysteine residue, with these enzymes being known as [NiFeSe]-H_2ases.[19,29,30] Each H_2ase typically contains several iron-sulfur clusters that facilitate electron transport to and from the protein surface, with the [FeFe]-H_2ase active site being directly wired to one such [4Fe4S] cluster through a bridging cysteine residue at the "proximal" iron (Fe_p) center.

Precise mechanistic details for each type are still under debate, but both are thought to operate through reversible heterolytic dissociation of the H−H bond into a metal-hydride and a proton. The hydride coordinates as a bridging ligand between the two metal atoms in [NiFe]-H_2ases, whereas it occupies a terminal position on the "distal" iron (Fe_d) in [FeFe]-H_2ases. In

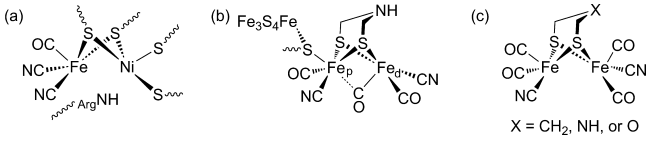

Figure 2. Structures of (a) [NiFe]-H_2ase active site, (b) [FeFe]-H_2ase active site (Fe_p = "proximal" iron, Fe_d = "distal" iron), and (c) synthetic cofactors used to reconstitute [FeFe]-H_2ases.

DOI: 10.1021/acs.chemrev.8b00392
Chem. Rev. 2019, 119, 2752−2875

the former, the proton is thought to be initially accepted by an arginine residue close to the active site.[34] In contrast, [FeFe]-H_2ases possess a unique azadithiolate cofactor, $HN(CH_2S)_2^{2-}$, which provides a neighboring amine group that acts as the proton acceptor.[29] The contribution of this basic nitrogen to reactivity is emphasized by a pair of studies that introduced dithiolate cofactors with differing central functionalities $(X(CH_2S)_2^{2-}$, where X = CH_2, NH, or O) into an apo-[FeFe]-H_2ase (Figure 2c).[35,36] Activity similar to the wild-type was only observed for the holo-enzymes reconstituted with the N-containing cofactor.[35,36] The presence of a proximal proton acceptor site thus plays a vital role in the mechanism of H_2ases, and is a feature especially applicable to the activity of molecular complexes.

CODHs are metalloenzymes that convert CO to CO_2. Despite the existence of two types of these biocatalysts, namely the [CuMo]-CODHs and [NiFe]-CODHs, only the latter are known to act as bidirectional catalysts and perform the reverse reaction of reducing CO_2 to CO at the thermodynamic potential.[37,38] The active site in [NiFe]-CODHs is formed by one nickel and one iron center, further supported by a Fe_3S_4 cluster that provides two μ-sulfido ligands to the nickel and one to the iron (Figure 3).[39,40] Crystals incubated under reducing conditions show a structure with the nickel additionally ligated by a cysteine residue in an unusual three-coordinate T-shaped geometry, which may hint at a fourth hydride ligand.[40,41] The iron coordination sphere is completed by a cysteine, a histidine, and a fourth water-derived ligand oriented toward the nickel site, with a lysine providing an H-bonding contact and thought to promote reversible conversion of the Fe-bound aqua ligand from water into hydroxide.[40,42,43] Crystal treatment with the same reducing conditions in the presence of $NaHCO_3$ resulted in a structure consistent with binding of CO_2, featuring a two atom bridge with Ni−C and Fe−O bonds.[40] Both CO_2-derived O-atoms are also closely associated with two nearby protein residues (Figure 3b).[40] These observations imply that H-bonding interactions may contribute to stabilizing a metallo-carboxylate intermediate, which has also been detected by in situ infrared (IR) spectroscopic studies.[42,44] Site-directed substitution of either amino acid for alanine shows diminished activity, whereas double mutants are entirely inactive.[39,45] Details of the catalytic cycle are still under debate, particularly the involvement of a nickel-hydride species, but there is strong evidence that H-bonding and proton shuttling functionality are essential for activity, as in the case of the H_2ases discussed above.[42]

An additional factor that can contribute to catalysis is the presence of redox noninnocent ligands. Reversible storage of redox equivalents is typically assigned to changes in metal center oxidation states, but the supporting organic scaffold can also participate, thereby lowering reorganization energy by delocalizing charge density and making electron transfer (ET) more facile.[17,46] Nature uses such noninnocence in photosynthesis, for instance when light absorption in Photosystem I causes an electron to be temporarily stored in the porphyrin-like macrocyclic ligand of a Mg-containing chlorophyll complex.[46,47] A further example can be found in the tyrosine/tyrosyl redox pair, which accepts electrons extracted from water by the Mn-containing OEC in Photosystem II, and acts in concert with a copper ion in galactose oxidase for the two-electron oxidation of primary alcohols into aldehydes (Figure 4).[17,46,48] Although the tyrosine residue does not directly coordinate to the $[CaMn_4]$-cluster in the OEC, in both scenarios proton-coupled electron transfer (PCET) occurs.[17,46,48] This coupling is vital for optimal activity, especially for processes going beyond single-electron transformations, as it can avoid the formation of high-energy intermediates.[16,49] This is particularly important for the multielectron reduction reactions of CO_2 (eqs 1−7 below), which can thermodynamically proceed at relatively modest potentials.[1,22]

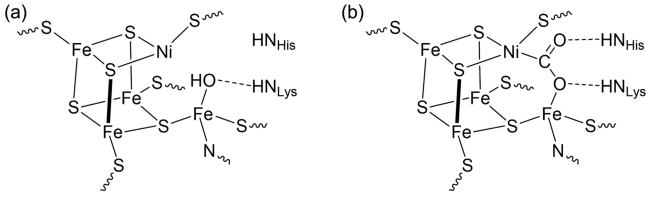

Figure 3. Structure of [NiFe]-CODH active site with (a) reduced nickel center in the absence of substrate and (b) bound CO_2 after incubation with $NaHCO_3$.

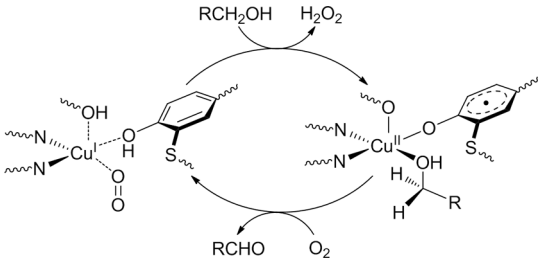

Figure 4. Catalytic cycle of galactose oxidase showing a noninnocent tyrosine ligand that cooperates with a copper ion to achieve a two-electron substrate transformation.

1.3. Structure and Activation of CO_2

CO_2 is a nonpolar linear molecule with a pair of short bonds of 1.16 Å.[7,28] The individual bonds are polarized due to the electronegativity of the constituent elements, resulting in an electrophilic C-atom and nucleophilic O-atoms.[7,23] Nevertheless, the electrons in CO_2 are tightly bound, with a first ionization potential of 13.8 eV, imparting nonbasic character to the O-atoms and a limited affinity for Brønsted and Lewis acids.[1,23,50] ET into the antibonding lowest unoccupied molecular orbitals (LUMOs) of CO_2 increases the C−O bond lengths and simultaneously induces geometric distortion away from linearity.[7,51] Bending of the molecule is associated with a significant cost in terms of reorganization energy, as reflected by the very negative potential required to achieve uncoupled outer-sphere reduction of CO_2 by one electron.[1,7,23] Coupling reduction with energetically favorable bond formation can partially offset this penalty.[22,52,53] CO_2 activation is thus often achieved by inner-sphere ET to the C-atom coupled with interaction of Lewis acids at the O-atoms, as illustrated by the CO_2-bound CODH structure (Figure 3b).[1,7,23,40] This bifunctional activation analogous to frustrated Lewis pairs is also reminiscent of the mechanism used by H_2ases and highlights the importance of functionality that can simultaneously provide electrons and protons to facilitate PCET.[1,22]

$$2H^+ + 2e^- \rightarrow H_2 \quad E^{\circ\prime} = -0.41\ \text{V} \tag{1}$$

$$CO_2 + e^- \rightarrow CO_2^{\bullet -} \quad E^{\circ\prime} = -1.93\ \text{V} \tag{2}$$

$$CO_2 + 2H^+ + 2e^- \rightarrow CO + H_2O \quad E^{\circ\prime} = -0.53\ \text{V} \tag{3}$$

DOI: 10.1021/acs.chemrev.8b00392
Chem. Rev. 2019, 119, 2752−2875

$$CO_2 + H^+ + 2e^- \rightarrow HCO_2^- \quad E^{\circ\prime} = -0.39\ V \tag{4}$$

$$CO_2 + 4H^+ + 4e^- \rightarrow HCHO + H_2O \quad E^{\circ\prime} = -0.48\ V \tag{5}$$

$$CO_2 + 6H^+ + 6e^- \rightarrow CH_3OH + H_2O \quad E^{\circ\prime} = -0.38\ V \tag{6}$$

$$CO_2 + 8H^+ + 8e^- \rightarrow CH_4 + 2H_2O \quad E^{\circ\prime} = -0.24\ V \tag{7}$$

All values are repoted vs normal hydrogen electrode (NHE) at pH 7.

The multielectron reduction of CO_2 can yield a variety of products with relevance to catalytic fuel synthesis, shown in eqs 1−7.[22,54−56] As emphasized above, these reactions are usually proton coupled, and therefore functionality with appropriate proton donor−acceptor properties in suitable proximity to the catalytic site can be expected to assist in such multielectron substrate transformations.[1,8,22] However, as these reactions occur at similar thermodynamic potentials ($E^{\circ\prime}$) different mechanistic pathways can compete, giving product mixtures and thus resulting in poor selectivity. This is particularly problematic when operating in aqueous media, as the generally more facile proton reduction reaction will become a significant competing process.[21,22,57,58] The relative concentrations of CO_2 (0.033 M at 298 K under 1 atm CO_2)[1,28] and H_2O/H^+ substrates in an aqueous environment therefore provide a challenge but can be influenced by changes in pH and can even lead to direct production of industrially useful syngas (CO + H_2).[2,21,59,60] Selectivity for a particular product can be tuned by using molecular catalysts, with the most frequently observed products synthesized from aqueous CO_2 to date being H_2, CO, and HCO_2H.[21−23,58] These compounds are produced through two-electron reduction reactions and are thought to form largely as a result of a number of distinct mechanisms.

1.4. Mechanistic Pathways

Extensive experimental and theoretical studies have revealed several mechanistic processes which contribute to H_2 formation when mediated by transition metal-containing molecular catalysts. A generalized scheme depicting possible homolytic and heterolytic pathways is shown in Figure 5.[22,61] Catalytic H_2 production by molecular complexes is generally thought to proceed through metal-hydride intermediates, which are formed by reduction and protonation of a transition metal center.[22,61−63] The hydrides produced can subsequently form H_2 by two possible routes. In the homolytic mechanism, two metal hydride complexes react with each other via reductive elimination, both donating a proton and an electron to yield H_2. Alternatively, a further reduced metal hydride species can be protonated and release H_2 through a heterolytic mechanism.[22,61] Both pathways can also function simultaneously, and in some cases the dominant route in operation depends upon the experimental conditions employed, such as pH, catalyst concentration, or proton source.[22] It should be noted that although these labels are widely used to refer to the two pathways, the descriptors homolytic and heterolytic actually describe the reverse bond cleavage reactions.

Metal-hydride intermediate formation is also believed to influence the products of CO_2 reduction.[22,64,65] Reaction of CO_2 with molecular complexes usually occurs in one of two ways, either by insertion into a metal-hydride bond or by binding to a vacant coordination site at the metal center (Figure 6).[22,23] The usual pathway by which CO_2 inserts into a metal-hydride is

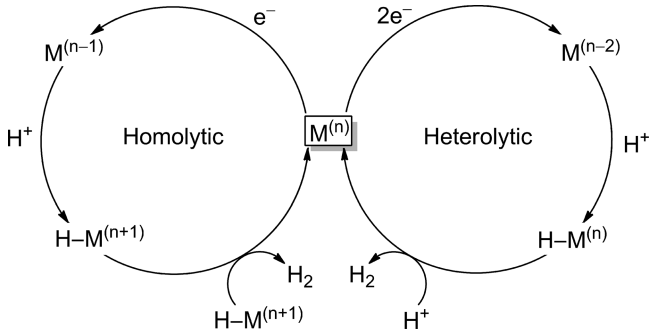

Figure 5. Simplified mechanistic pathways for H_2 evolution by a molecular catalyst (M) with oxidation state n ($M^{(n)}$).[61]

referred to as "normal" and is thought to be promoted by electrostatic attractions between the polarized O−C and M−H bonds, positioning the electrophilic carbon-atom in close proximity to the nucleophilic hydride moiety.[23,66,67] In contrast, electron-rich metals possessing free binding sites favor CO_2 activation through monodentate C-coordination, leading to a metallo-carboxylate species with O-atoms sterically exposed and available for protonation.[23,51] Though both insertion and coordination can proceed through different routes that vary in the mode of CO_2 interaction with the metal center, the former process typically affords HCO_2H as a product, whereas the latter has a greater tendency to yield CO.[22,65,68] O-coordinated CO_2-adducts have been implicated in exceptions to this general trend, but the above reactivity profiles are the most commonly observed.[69−71] The much greater availability of protons in aqueous solution in comparison to CO_2 thus means thorough experimental analysis is required in order to accurately assess product distribution.

1.5. Figures of Merit and Practical Considerations

Several key parameters are typically used to evaluate the performance of a catalytic system.[61,72−74] Selectivity describes the tendency of a catalyst to produce a particular reaction product and is usually reported as a molar percentage of total conversion (eq 8).

$$\text{selectivity}(\%) = 100 \times \frac{n_{prod}}{n_{total}} \tag{8}$$

where n_{prod} is the product of interest (mol) and n_{total} is the sum of total products formed (mol).

Turnover number (TON) and turnover frequency (TOF) are used to quantify catalyst performance and reflect the stability of the system and the rate at which product is generated.[61,73,74] TON_{prod} represents the overall number of moles of a specific product generated per mole of catalyst (eq 9), either during the course of bulk controlled potential electrolysis (CPE) or upon irradiation of a photocatalytic system. TOF_{prod} is defined as the TON_{prod} per unit of time (eq 10).

$$TON_{prod} = \frac{n_{prod}}{n_{cat}} \tag{9}$$

$$TOF_{prod} = \frac{TON_{prod}}{t} \tag{10}$$

where n_{cat} is the amount of catalyst present in the system (mol) and t is time (s).

More elaborate methods that can grant insights from the interpretation of electrochemical data alone have been

DOI: 10.1021/acs.chemrev.8b00392
Chem. Rev. 2019, 119, 2752−2875

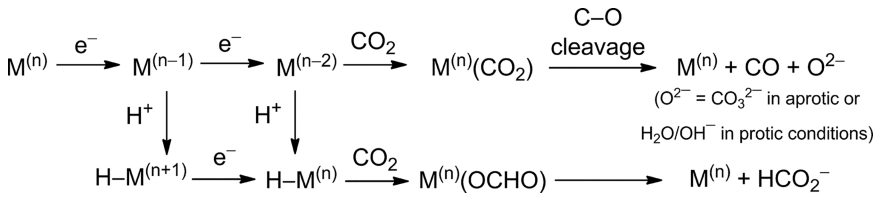

Figure 6. Competing pathways for CO and HCO_2H formation from CO_2, showing the pivotal role of the metal-hydride in determining product distribution. Either of the two hydrides shown can undergo side reactions to form H_2 as in Figure 5. Oxide (O^{2-}, above right) is produced as either CO_3^{2-} or H_2O/OH^-.

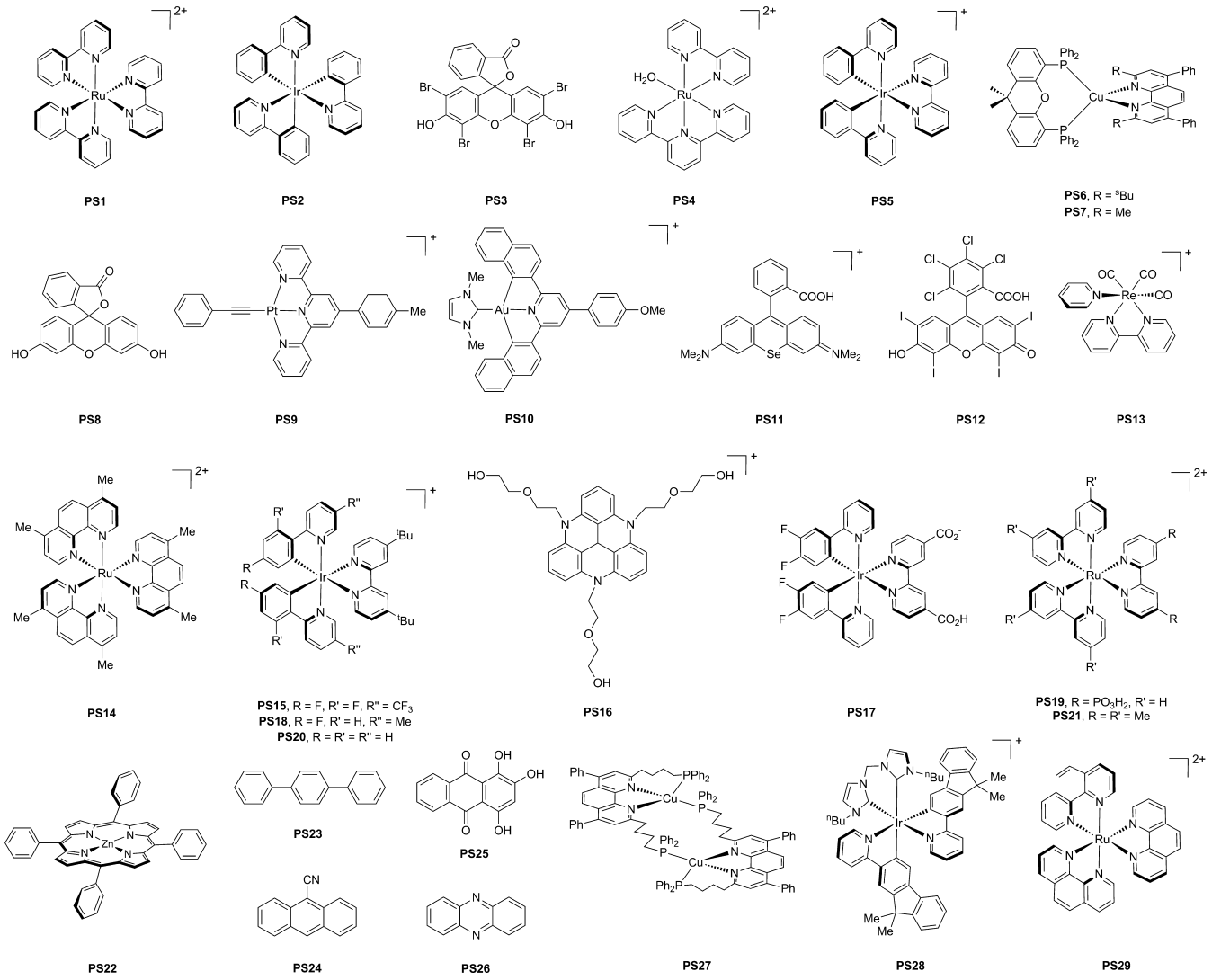

Figure 7. Photosensitizers used in photocatalytic fuel synthesis (counterions have been omitted for clarity).

published elsewhere.[61,75−77] For example, the observed rate constant can be used to estimate TOF and is obtained directly from cyclic voltammetry (CV) by numerical treatment of changes in current.[61,77] While TOF values derived in such a way are a useful parameter for benchmarking catalytic activity, they do not always give results that accurately reflect experimental findings and provide little information about stability and performance under operational conditions.[23,75,78] It should be noted that the electrocatalytic metrics discussed in this review are primarily based on the results of product quantification (gas chromatography, ion chromatography, etc.), which can furthermore allow determination of Faradaic efficiency (FE). This metric gives the conversion efficiency between electricity and products and can reveal if electron flow is being redirected to parasitic reactions (e.g., solvent, electrode, and/or catalyst decomposition).[21] FE_{prod} is determined by comparing quantified product with charge passed during electrolysis (eq 11).

$$FE_{prod}(\%) = 100 \times \frac{zFn_{prod}}{Q} \tag{11}$$

where z is the number of electrons required for the reduction reaction, F is the Faraday constant (96 485 C mol^{-1}), and Q is the total charge (C) passed.

DOI: 10.1021/acs.chemrev.8b00392
Chem. Rev. 2019, 119, 2752−2875

Onset potential (E_{onset}) and overpotential (η) are also important electrocatalytic parameters. The former indicates the minimum electrochemical potential that must be applied for a catalytic reaction to commence with a particular catalyst (usually determined by CV), although a greater applied potential (E_{appl}) is often used to achieve faster reaction rates (up to the maximum rate of the catalyst) and measurable quantities of product (in CPE experiments).[21,72,74] The overpotential is obtained by the difference between E_{onset} or E_{appl} and the thermodynamic potential under the experimental conditions ($E^{\circ\prime}$) and represents the driving force required to start the reduction reaction or achieve a particular rate with the catalyst of interest (eq 12).[21,61,72]

$$\eta = \left|E_{onset} - E^{\circ\prime}\right| \text{ (in CV) and } \left|E_{appl} - E^{\circ\prime}\right| \text{ (in CPE)} \quad (12)$$

Meaningful comparison of this parameter between systems is challenging, as different criteria are used for defining which E_{appl} value is relevant, and a variety of methods are employed for determining $E^{\circ\prime}$ under nonstandard conditions.[72,73] For organic media containing proton donors, converting reference electrode potentials and calculating $E^{\circ\prime}$ both rely on a number of assumptions about pK_a values and contributions from ion-pairing and homoassociation, which can greatly differ from aqueous conditions.[72,74] Experimental determination of $E^{\circ\prime}$ in such media is possible, and standardized methods for defining η have been suggested, but neither approach is widely employed in the literature.[72,73] Due to these uncertainties, the values herein are given versus their reported reference electrodes when measured in nonaqueous media, and η is largely used conceptually to facilitate discussion rather than as an absolute property. The E_{onset} is instead reported and taken as the value at the base of the catalytic wave for simplicity, but an accurate comparison between systems requires that all of the features of a catalyst are considered.

In comparison with electrocatalysis, photocatalytic systems employ additional components. A dye or photosensitizer (PS) is usually required, and while photoreduction coupled to water oxidation can be achieved in a Z-scheme similar to oxygenic photosynthesis, most experiments with molecular catalysts are carried out with a sacrificial electron donor (SED).[22,79] The PSs can be metal complexes, organic dyes, or inorganic SCs, and their corresponding absorption wavelengths, excited state lifetimes, photostabilities, and redox properties greatly affect the catalytic performance of the light-driven system.[79] The PSs used in the homogeneous systems outlined in section 2 and in several heterogeneous constructs discussed later in this manuscript are depicted in Figure 7. A great variety of SEDs are known, with triethanolamine (TEOA) and ascorbic acid (AA) being among the most commonly employed under aqueous conditions.[79,80] Quantum yield (QY), which is dependent on the above factors and reflects the conversion of photons to products formed, is also used as a measure of system efficiency.[80,81] It can be determined by comparing quantified product (mol) with the molar quantity of monochromatic photons incident on the sample during photocatalysis (eq 13).

$$\mathrm{QY}_{prod}(\%) = 100 \times \frac{z n_{prod}}{n_{photons}} \quad (13)$$

The irradiation wavelength (λ) used is important as it determines whether a system can operate using the solar spectrum. When assessing a catalyst for photocatalytic performance, the TON, QY, and durability of the system are important parameters. Although there are frequently similarities between catalyst performance under electrocatalytic and photocatalytic conditions, a substantial number of factors contribute to activity in each case and thus results from the two types of experiments do not always correlate seamlessly. Nevertheless, when applied in combination the complementary nature of the two approaches often allows for deeper insights and a greater understanding of the system under investigation.

In addition, sources of both the reaction products and catalytic activity should be closely examined. Isotopic labeling studies are crucial for establishing the origin of reaction products, especially when using CO_2 as a substrate to produce carbon-containing compounds.[55] Molecular integrity should be investigated, as a number of first row transition metal complexes can decompose into active nanoparticles under catalytic conditions, and metallic impurities in supporting electrolyte solution may act in a similar manner.[21,82−85] Ruling out such scenarios is vital to correctly assigning the catalytically active species, and entire articles dedicated to the topic are available.[86,87] Procedures should furthermore be reported in sufficient detail to assess the validity of the results. For example, one widely used test involves adding Hg^0 to poison metallic particles by amalgamation or surface adsorption. It must be conducted with a large excess and strong stirring, such that the Hg^0 contacts the entire reaction solution, but lack of experimental details often makes it difficult to determine if this was the case. The working electrode (WE) material can also have a significant influence on the apparent catalytic activity through direct reaction with the substrate or by altering the properties of the molecular catalyst under investigation.[23,88−90] The above factors should be considered when comparing transition metal-containing molecular complexes, particularly if meaningful structure−activity relationships for improving catalysts are to be revealed.

2. HOMOGENEOUS CATALYSIS

This section outlines homogeneous examples of H_2 evolution catalysts (HECs) and CO_2 reduction catalysts (CRCs) that use H_2O as a proton source, cosolvent, or reaction medium.

2.1. Aqueous Conditions for Catalysis

The abundance, elemental composition, and nontoxicity of H_2O make it an attractive "green" medium for sustainable energy storage processes,[61] and water oxidation can potentially be coupled with the relevant reduction reaction to provide both protons and electrons for fuel synthesis. An important consideration for future development also arises from the ubiquity of water in the atmosphere; practical application of molecular catalysts is greatly facilitated if they can use or at least tolerate H_2O. A selection of the most promising molecular catalysts is detailed here, organized first by differentiating between HECs and CRCs and then subdividing each section by metal center. As a large proportion of catalysts are insoluble in aqueous media, some examples employing purely organic solvents are also included, particularly those where the catalyst has an immobilized counterpart or the study illustrates a concept generally applicable to catalysis. It is worth noting that the properties of the organic solvent or coadded proton source may considerably influence activity, especially when PCET is involved. To emphasize this point pH values that have been measured under nonaqueous conditions are therefore reported in this review as pH′. Moreover, the solvent may be noninnocent

DOI: 10.1021/acs.chemrev.8b00392
Chem. Rev. 2019, 119, 2752−2875

in catalytic mechanisms, which introduces additional complexity when comparing systems that operate in different reaction media.[91]

2.2. Hydrogen Evolution Catalysts

2.2.1. Scandium, Titanium, Vanadium, and Chromium.

As a result of their oxophilicity limiting compatibility with water, and the stability of their higher oxidation states requiring large negative potentials for reduction, scandium, titanium, vanadium, and chromium have not been the subject of intensive research for catalytic fuel synthesis. CV experiments with **Ti1** and **V1** exhibit increases in current at negative potentials when water is introduced to Ar-saturated acetonitrile (MeCN) electrolyte solutions, but product identification was not reported.[92] The pair of related titanocene complexes **Ti2** and **Ti3** have been more thoroughly investigated. Addition of water to a toluene solution of decamethyltitanocene(III) triflate, **Ti2** (OTf = triflate = $CF_3SO_3^-$), induces evolution of H_2.[93] In situ IR spectroscopy, electron paramagnetic resonance (EPR) spectroscopy, single crystal X-ray diffraction analysis, and density functional theory (DFT) calculations suggest that two H_2O molecules initially coordinate to **Ti2**, displacing the triflate counterion. Two of these diaqua complexes then interact and each donates a hydrogen atom, giving H_2 and hydroxide-coordinated Ti^{4+} products. The triflate remains closely associated during the reaction, and may assist by stabilizing the Ti-coordinated aqua ligands through hydrogen bonding.[94] While H_2 results from stoichiometric reactivity in this case, contributions from H-bond stabilization and the interaction of two metal centers are aspects that are frequently associated with highly active molecular catalysts, as well as with their corresponding enzymatic counterparts. To the best of our knowledge, Sc- or Cr-based HECs have not yet been reported.

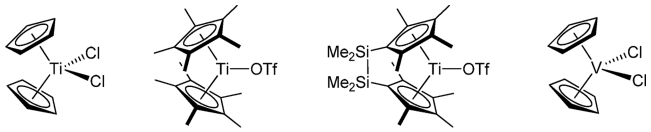

Ti1 Ti2 Ti3 V1

2.2.2. Manganese.

Manganese is the third most abundant transition metal in the Earth's crust (9.50×10^2 mg kg^{-1})[28] and is present in the oxygen-evolving Mn_4CaO_5 cluster found in all photosynthetic organisms, making it ubiquitous in Nature.[17,26] Most applications so far have targeted CO evolution with complexes such as **Mn1**, where manganese is a promising alternative to the heavier element rhenium.[95,96]

The majority of studies with Mn-based HECs have been conducted in organic solvents using strong acids, with only a few reports employing H_2O as a proton source. The organometallic half-sandwich complexes, **Mn2** and **Mn3**, contain a vinylidene or allenylidene unit, respectively.[97] In dichloromethane (DCM) or MeCN solutions containing HBF_4, these complexes are protonated and convert into metal-carbyne species. One-electron reduction then triggers H_2 formation, thought to occur through a homolytic pathway. CPE with **Mn2** in DCM over a Hg pool WE at E_{appl} = −1.75 V vs the ferrocenium/ferrocene redox couple (Fc^+/Fc) resulted in gas evolution and a TON_{H2} of 5 after 1 h (assuming quantitative FE_{H2}). Catalytic currents observed in CV using **Mn3** were up to 50% greater, but E_{onset} occurred at potentials roughly 0.7 V more negative than with **Mn2**. CPE for **Mn3** was not reported.[97]

Examples that employ bimetallic Mn-complexes reminiscent of H_2ase active sites have also been reported.[98,99] Photolysis of

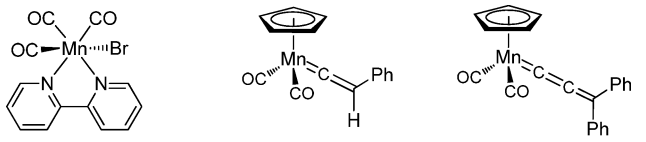

Mn1 Mn2 Mn3

$[Mn_2(CO)_{10}]$ with diphenyl disulfide and 2,2'-bipyridine (bpy) generates thiophenolate-bridged $\mathbf{Mn_2 1}$, which possesses $[Mn(bpy)_3]^+$ as a counterion. CV scans in MeCN revealed two reductive features at −1.90 and −1.50 V vs Fc^+/Fc, both showing current enhancements upon introduction of trifluoroacetic acid (TFA).[99] A TOF_{H2} of 44 600 s^{-1} (using 300 equivalents TFA) was calculated based on CV analysis, which is among the highest reported for molecular HECs. CPE at E_{appl} = −1.50 V vs Fc^+/Fc in MeCN with TFA consistently gave FE_{H2} > 75%, although decomposition to a tetranuclear $Mn_4(CO)_{12}(SPh)_4$ cluster was observed. Rearrangment and H_2 generation may be initiated by a thiophenolate shift to a terminal position, along with protonation of the S-atom, which could then be transferred to produce a Mn-hydride species.[99] The related selenophenolate-bridged Mn_2 complex is also an active HEC, but shows significantly different electrochemical behavior.[98]

Manganese complexes with both a *fac*-tricarbonyl motif and an unsaturated bidentate ligand, typically a bpy or related derivative, also function as HECs.[95,100,101] Their octahedral geometry is usually completed by an anion which dissociates upon reduction, ultimately giving a five-coordinate complex with a vacant site for substrate binding.[100,102] While these complexes have mainly been studied as CRCs (section 2.3.4), they often produce H_2 as a byproduct, and examples where this attribute is especially pronounced are highlighted here.

CPE using **Mn1** with a glassy carbon (GC) WE in CO_2-saturated H_2O:MeCN (5:95) at E_{appl} = −1.70 V vs Ag/$AgNO_3$ for 22 h revealed a FE_{H2} = 15% (in addition to CO production).[95] In the same media using a GC WE at E_{appl} = −1.63 V vs a saturated calomel electrode (SCE), N-heterocyclic carbene (NHC) complex **Mn4** yielded a FE_{H2} = 53% after 4 h.[100] **Mn4** also features an atypical isothiocyanate ligand, and the bromido-ligated analogue produced no H_2 under almost identical conditions. This has been tentatively attributed to a lack of SCN^- dissociation upon **Mn4** reduction, which would result in a coordinately saturated metal-center.[100] Later studies spectroscopically identified a Mn-hydride species, proposed as an intermediate for H_2 evolution by these catalysts, and as such the mechanism through which **Mn4** achieves selectivity for proton reduction merits more detailed investigation.[64,65]

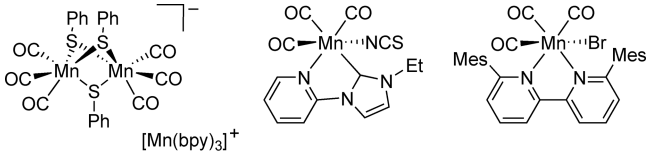

$Mn_2 1$ Mn4 Mn5

Mn5 contains the bulky 6,6′-dimesityl-2,2′-bipyridine ligand, which allows for generation of a catalytically active species at more positive potentials (section 2.3.4).[101] CV in MeCN (under N_2, no H_2O added) in the presence of TFA displayed an E_{onset} = −1.45 V vs Fc^+/Fc, and a TOF_{H2} of 5500 s^{-1} was determined. CPE under these conditions using a GC WE at E_{appl} = −1.50 V vs Fc^+/Fc gave quantitative FE_{H2} over 21 h, with a TON_{H2} of 75.[101,102]

DOI: 10.1021/acs.chemrev.8b00392
Chem. Rev. 2019, 119, 2752−2875

Progress has been made with Mn-based HECs under semiaqueous conditions, but the activity of these catalysts is still relatively underexplored in comparison with their later 3d transition metal counterparts. Studying more structurally diverse complexes may prove to be a promising strategy, especially for their use in photocatalytic schemes, as manganese(I)-tricarbonyl complexes are photosensitive to ultraviolet−visible (UV−vis) irradiation.[103−108]

2.2.3. Iron. *2.2.3.1. Electrocatalysis.* Iron is the most abundant transition metal in the Earth's crust (5.63×10^4 mg kg^{-1}) and is present in the active site of [FeFe]-H_2ases, which operate with a TOF_{H2} up to 10 000 s^{-1}.[11,31,33] Molecular systems that mimic these enzymes have allowed for improved understanding of their remarkable reactivity.[109−112] This biomimetic or bioinspired line of research forms a field of its own, and exhaustive reviews on synthetic H_2ase model complexes are available.[109−112] In-depth discussion of this topic is beyond the scope of this review, but some highlights with general conceptual relevance for achieving proton reduction are summarized here.

Although synthetic models provide useful insights, there are key differences between the natural and artificial systems. Biomimetics frequently achieve catalysis through [Fe^0Fe^+] intermediates, whereas the lowest oxidation state accessed by the parent enzymes is [Fe^+Fe^+].[111−113] Moreover, protonation of synthetic analogues often gives bridging hydrides, rather than the more reactive terminal species formed in [FeFe]-H_2ases.[110,111,113] These structural changes influence reactivity and are likely significant contributors to the relatively large overpotential requirements and low catalytic rates shown by artificial systems.[111−113]

An early example of proton reduction with a bimetallic species used diferrocene **$Fe_2$1**.[114] Dissolution in $BF_3{\cdot}H_2O$ yielded one equivalent of H_2, resulting from one-electron oxidation of each iron center.[114] No H_2 evolution occurred with diluted $BF_3{\cdot}H_2O$ solutions or with other aqueous acids, owing to the weak basicity of the ferrocene units.[115] This limitation could be partially offset by grafting an analogue of **$Fe_2$1** onto a polystyrene polymer to construct a hybrid photocathode (section 7.2.6).[115] However, no product quantification was reported, and evidence confirming the molecular nature of the active species is limited.

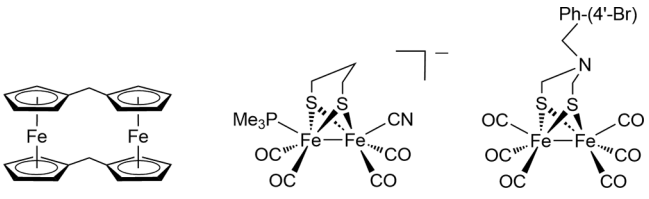

$Fe_2$1 **$Fe_2$2** **$Fe_2$3**

Electrocatalytic activity with a biomimetic complex was first shown using **$Fe_2$2**.[116] This bimetallic Fe^+ species yields a neutral μ-hydride in acidified MeCN, which reacts further in the presence of H_2SO_4, HCl, or tosylic acid (TsOH), to form a cation protonated at the cyano-ligand N-atom. Subsequent reduction was reported to trigger H_2 evolution. CV analysis revealed a catalytic wave at E_{onset} = −1.03 V vs Ag/AgCl, and CPE conducted at E_{appl} = −1.20 V vs Ag/AgCl using a Hg pool WE in MeCN containing H_2SO_4 gave a TON_{H2} of 6 with a quantitative FE_{H2} over 15 min.[116] A later study used a bioinspired dithiolate with a tertiary amine bridgehead moiety, giving **$Fe_2$3**.[117] Addition of acid to MeCN solutions of **$Fe_2$3** caused spectroscopic changes consistent with protonation of this HEC. CV showed a pH-dependent catalytic feature at E_{onset} = −1.40 V vs Fc^+/Fc, and CPE with a graphite WE at E_{appl} = −1.48 vs Fc^+/Fc in MeCN containing $HClO_4$ gave a TON_{H2} of 25 after 10 min. Catalysis is believed to involve a hydride-bridged species formed by alternating protonation and reduction steps, with the amine acting as a proton shuttle in a manner reminiscent of [FeFe]-H_2ases.[117]

Exposure of the asymmetric complex **$Fe_2$4** to a strong acid produces a terminal hydride at low temperature, which converts into a μ-hydride at room temperature (RT).[118] **$Fe_2$5** and **$Fe_2$6** display analogous behavior despite having symmetric ligand frameworks.[119] Although the terminal hydride of **$Fe_2$5** isomerizes to a μ-hydride within minutes at −20 °C, that of **$Fe_2$6** has a half-life of about 10 min at RT. CV studies at 0 °C in DCM showed that the terminal hydride is reduced at a potential 200 mV more positive than the μ-hydride, and that catalytic onset occurs at this more anodic potential when excess acid is present.[119] These findings highlight the electrochemical changes that can result from different substrate binding modes.

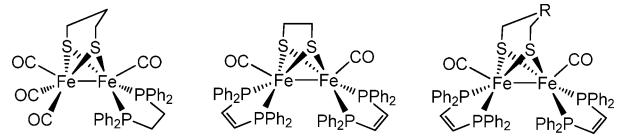

$Fe_2$4 **$Fe_2$5** **$Fe_2$6**, R = CH_2
$Fe_2$7, R = NH

Inclusion of an amine at the bridgehead position of **$Fe_2$6** affords **$Fe_2$7**, which has the same azadithiolate cofactor present in [FeFe]-H_2ases.[120] Addition of weak acid to DCM solutions of **$Fe_2$7** favors formation of the terminal hydride at low temperature, whereas stronger acids can donate a second proton to give the corresponding ammonium dication.[120] The crystal structure of the latter displays an N−H···H−Fe distance of only 1.88(7) Å, indicative of dihydrogen-bonding, which may reflect the mechanism employed by [FeFe]-H_2ases.[120,121] CV studies at 0 °C in DCM containing weak acid show E_{onset} at −1.25 V vs Fc^+/Fc (TOF_{H2} = 5000 s^{-1}), whereas E_{onset} occurs at −0.80 V vs Fc^+/Fc (TOF_{H2} = 58 000 s^{-1}) with strong acid.[120] This system illustrates how proton shuttling functionality can dramatically influence catalysis. CPE at 0 °C in DCM containing weak acid with a GC WE held at −1.80 V vs Fc^+/Fc gave a FE_{H2} of 99%, and a TON_{H2} of 2 after 1 h. While the TOF_{H2} for **$Fe_2$7** is among the highest known, the η of 0.5 V is relatively high, and the system uses purely organic media.[120]

Various approaches have been used to impart water-solubility to biomimetic iron HECs. Coordination of amino-functionalized phosphines gives **$Fe_2$8** and **$Fe_2$9**.[122] Both show a reductive feature in aqueous KCl, and catalytic onset when acetic acid (AcOH) is added, but no CPE or product analysis was reported.[122] Solubility can also be improved by appending quaternary ammonium groups to coordinating terminal phosphine ligands or by introducing carbohydrate moieties into the disulfide bridge, though no electrochemical studies were reported for purely aqueous media.[123,124] Adding sulfonate groups to the bridging disulfide yields **$Fe_2$10**, **$Fe_2$11**, and **$Fe_2$12**.[125−127] While exhibiting promising electrochemical properties in aqueous solutions, catalytic H_2 generation has only been shown photochemically.[125−128] Protein scaffolds[129−132] and hosts like cyclodextrin[128] or chitosan[133] were also used to solubilize related HECs in photocatalytic systems (sections 2.2.3.2 and 5.2). Micelle-forming surfactants such as

DOI: 10.1021/acs.chemrev.8b00392
Chem. Rev. 2019, 119, 2752−2875

sodium dodecyl sulfate (SDS) have also shown promise with **$Fe_2$13** and **$Fe_2$14**.[134−136] CPE of **$Fe_2$13** using a Hg pool WE at E_{appl} = −0.66 V vs NHE in aqueous SDS/NaCl with AcOH (pH 3.0) displays close to 100% FE_{H2} with a TON_{H2} of 52 after 1 h.[135]

The tetranuclear iron cluster **$Fe_4$1** catalyzes H_2 evolution in aqueous solution (pH 5−9), with E_{onset} = −1.10 V vs SCE and greater currents at lower pH values.[137,138] The dianion $[Fe_4N(CO)_{12}]^{2-}$ is thought to be the catalytically active species. CPE conducted in acetate buffer (pH 5.0) with a GC WE at E_{appl} = −1.25 V vs SCE gave a FE_{H2} of 98% with a TON_{H2} of 34 over 2.5 h.[137] **$Fe_4$1** also shows activity toward CO_2, selectively producing HCO_2H in neutral aqueous solutions, but substitution of CO by $PPh_2CH_2CH_2OH$ to give **$Fe_4$2** suppresses this reactivity in favor of H_2 formation.[139] **$Fe_4$2** thus shows a FE_{H2} of 97% and TON_{H2} of 40 over 50 min when electrolyzed under CO_2 in H_2O:MeCN (5:95) with a GC WE at E_{appl} = −1.4 V vs SCE.[139] The hydroxy-phosphine ligand in **$Fe_4$2** likely acts as a proton shuttling moiety, though performance in purely aqueous media is yet to be reported.

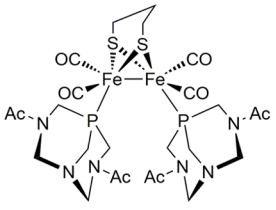

$Fe_2$8

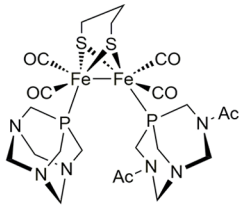

$Fe_2$9

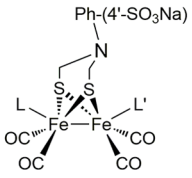

$Fe_2$10, L = L' = PMe_3
$Fe_2$11, L = PPh_3, L' = CO
$Fe_2$12, L = $P(OMe)_3$, L' = CO

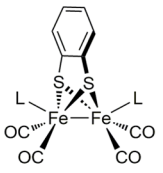

$Fe_2$13, L = CO
$Fe_2$14, L = $P(OMe)_3$

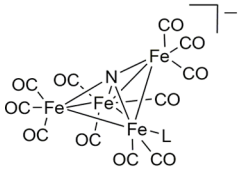

$Fe_4$1, L = CO
$Fe_4$2, L = $PPh_2CH_2CH_2OH$

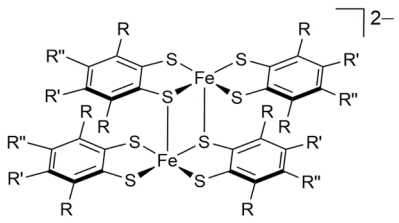

$Fe_2$15, R = R' = R'' = H
$Fe_2$16, R = R' = H, R'' = Me
$Fe_2$17, R = Cl, R' = R'' = H
$Fe_2$18, R = R' = R'' = Cl

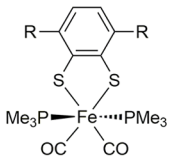

Fe1, R = H
Fe2, R = Cl

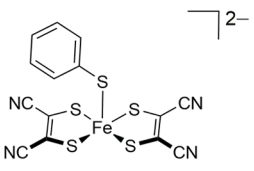

Fe3

Several studies use bioinspired sulfur-rich donor sets such as those present in dithiolene scaffolds. These ligands are resistant to hydrogenation and show noninnocence, facilitating reversible electron and proton transfer events.[140,141] An early study revealed that methanol (MeOH) solutions of the bis(*o*-benzenedithiolate)-iron(II) dianion evolve H_2 stoichiometrically upon HCl addition.[142] The initial reaction step likely involves protonation of a thiolate donor, followed by formation of a dimer that liberates H_2 upon one-electron oxidation of each iron center.[142] The solid-state structure of the corresponding Fe^{3+} species **$Fe_2$15** is consistent with this proposal, showing a bimetallic adduct.[142,143] CV studies in MeCN containing H_2O (1 M) with **$Fe_2$15** and the related Fe^{3+} complexes **$Fe_2$16**, **$Fe_2$17** and **$Fe_2$18** indicate reversible formation of corresponding Fe^{2+} species in all cases.[140] The reversible redox waves range from −0.72 to −0.93 V vs SCE and overlay with E_{onset} in the presence of TFA, indicating that the Fe^{2+} states are the active species.[140,142] Photocatalysis with these compounds and quantum dot (QD) PSs in H_2O:EtOH (1:1) revealed a correlation between H_2 production and HEC reduction potential, with more negative E_{onset} giving greater activity.[140]

Fe1 and **Fe2** are chelated by *o*-benzenedithiolates, with IR and nuclear magnetic resonance (NMR) spectra of MeCN solutions showing protonation of the dithiolate when $HClO_4$ is added (deprotonation occurs with pyridine).[113,144] CV of **Fe2** in MeCN shows two irreversible one-electron reduction waves at potentials more negative than −2.0 V vs Fc^+/Fc. TFA addition causes two new waves to appear at −1.2 and −1.7 V vs Fc^+/Fc, which increase upon introduction of further acid. CPE with a carbon rod WE at E_{appl} = −1.3 V (TON_{H2} = 4) and −1.7 V vs Fc^+/Fc (TON_{H2} = 14) show H_2 production at both potentials over 80 min. DFT supports a mechanism involving protonation of an iron-hydride intermediate, where the dithiolate unit serves as a proton shuttle.[113] Maleonitrile dithiolate-coordinated complex **Fe3** provides an additional example where the S-atoms are thought to act as proton shuttles.[145]

Porphyrins and related tertrapyrrole-macrocyclic derivatives are a versatile ligand class, with the corresponding iron complexes catalyzing CO_2 reduction and various reactions of relevance to water splitting.[146,147] These ligands often feature aryl groups in their *meso*-positions, which adopt an orientation roughly perpendicular to the equatorial plane of the metal-binding cavity. Moieties appended to these *meso*-groups can thus interact with substrates approaching or bound to the axial coordination site of the corresponding metal complexes, and as such these scaffolds have proven useful for studying the effects of hydrogen-bonding and proton-donating peripheral functionality. Fe^{2+} porphyrins are oxidized to the Fe^{3+} state under aerobic conditions, and are often handled as chlorido-coordinated square-pyramidal ferric complexes. Electrochemical studies thus typically show three sequential one-electron reduction events to generate a formal Fe^0 state. While this terminology is used in the following, the exact electronic configuration of these species likely differs, with spectroscopic and computational evidence consistent with an Fe^{2+} porphyrin diradical structure,[148,149] despite these CRCs displaying metal-centered reactivity.[150,151]

An early demonstration of proton reduction with these HECs used the *meso*-tetraphenylporphyrin (TPP) complex, **Fe4**.[152] CV conducted in *N*,*N*-dimethylformamide (DMF) revealed a catalytic wave upon addition of triethylammonium chloride at E_{onset} = −1.35 V vs SCE, which corresponds to the Fe^+/Fe^0 couple. CPE with a Hg pool WE at E_{appl} = −1.60 V vs SCE results in a FE_{H2} of 100% after 1 h (TON_{H2} = 22). The formal Fe^0 state was therefore assigned as the catalytically active species.[152] Reactivity toward various substrates can be influenced by integration of peripheral functionality, as detailed below.

DOI: 10.1021/acs.chemrev.8b00392
Chem. Rev. 2019, 119, 2752−2875

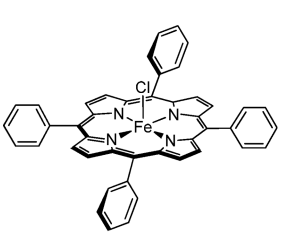

Fe4

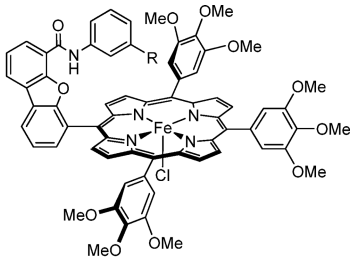

Fe5, R = H
Fe6, R = NMe_2
Fe7, R = SO_3H

The iron hangman porphyrins **Fe5**, **Fe6**, and **Fe7** contain acidic or basic residues appended in the *meso*-positions.[153] CV in MeCN with an organic acid and triphenylphosphine (PPh_3) revealed that catalysis already occurs in all cases at the Fe^{2+}/Fe^{+} couple, attributed to PPh_3 coordination increasing the reactivity of the Fe^{+} species and resulting metal-hydride.[153,154] Numerical analysis of CV data indicated that the differing substituents influence catalytic rate, but CPE showed a constant FE_{H2} of ~65% in all cases at a GC WE with $E_{appl} = E_{onset}$ (~−1.50 V vs Fc^{+}/Fc). The changes in rate for **Fe5**-**Fe7** are thought to result from differences in proton shuttling ability, and steric restriction of substrate access to the iron active center.

A similar proton-shuttling strategy was used with iron-porphyrins bearing 1,2,3-triazole groups, **Fe8**, **Fe9**, and **Fe10**.[154] CV studies in MeCN showed three reversible, one-electron redox couples, with E_{onset} at the Fe^{2+}/Fe^{+} potential in the presence of TsOH. Adding PPh_3 had a minimal influence on catalytic behavior, whereas substituting TsOH for phenol caused a shift in E_{onset} to the Fe^{+}/Fe^{0} potential. UV−vis spectra of **Fe8** showed changes in the presence of TsOH which can be reversed by triethylamine (TEA) addition, but no such process was observed using phenol. These findings result from reversible protonation of **Fe8** at the triazole moieties, provided a sufficiently strong acid is used. DFT calculations indicate that the protonated triazoles can interact with a vacant axial iron coordination site or putative iron-bound hydride species. While no bulk CPE was conducted under homogeneous conditions, **Fe8** dropcast onto graphitic electrodes produced H_2 with a FE_{H2} of 86% over 1 h at E_{appl} = −0.70 V vs Ag/AgCl in aqueous H_2SO_4 (pH 1.0). This example further shows that suitably positioned proton donors can have a significant influence on the mechanistic pathways accessible to a catalyst and thereby drastically alter the resulting activity.

Iron complexes containing ligands related to the tris(2-pyridylmethyl)amine (TPA) framework, **Fe11**-**Fe13**, show promising activity under aqueous conditions.[155−157] CV of **Fe11** in H_2O:MeCN (1:1) with TFA displayed an E_{onset} at −1.15 V vs SCE (η of ~0.8 V), significantly more cathodic than the Fe^{3+}/Fe^{2+} couple.[156] **Fe11** also showed similar behavior indicative of catalytic activity in purely aqueous solutions. CPE in citrate-phosphate solution (pH 5.0) with a GC WE at E_{appl} = −1.20 V vs SCE gave a FE_{H2} of 98% after 1 h (TON_{H2} of 23). The Fe^{3+}/Fe^{2+} couple was shown to be pH-dependent, shifting to more positive potentials upon introduction of greater amounts of acid. This shift is thought to result from protonation of the phenolic residue in **Fe11**, a process more thoroughly investigated by synthetic modification of the aromatic group. **Fe12** and **Fe13** have thus also been established as HECs in organic solvents, but both showed limited solubility in water.[155−157]

Chelation with related tetradentate tripodal ligands gives **Fe14** and **Fe15**, which are also active in aqueous media.[158,159] CV of **Fe14** in DMF shows two features assigned as sequential one-electron reductions of the iron center, and addition of AcOH leads to an E_{onset} that coincides with the Fe^{2+}/Fe^{+} redox wave.[159] CPE in aqueous phosphate solution (pH 7.0) with a GC WE at E_{onset} = −1.50 V vs $Ag/AgNO_3$ produced a FE_{H2} of 93% over 1 h (TON_{H2} = 141). Longer CPE experiments showed that the current remains stable for at least 40 h.[159] In contrast, complex **Fe15** has an additional reductive feature in CV scans and is thought to be catalytically active as an Fe^{0} species.[158] Despite this, E_{onset} occurs at a similar value to **Fe14**. CPE at E_{appl} = −1.45 V vs Ag/AgCl with **Fe15** in the same aqueous media gave a FE_{H2} of 96% after 2 h (TON_{H2} = 568). In this case the HEC was active for at least 72 h.[158]

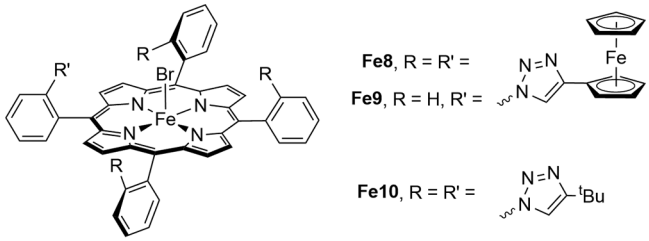

Fe8, R = R' =
Fe9, R = H, R' =
Fe10, R = R' =

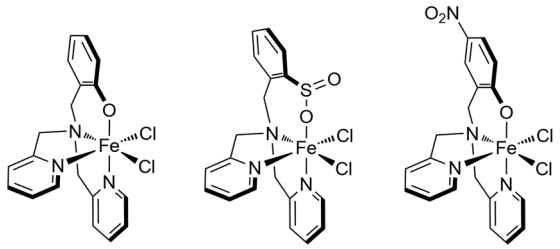

Fe11 Fe12 Fe13

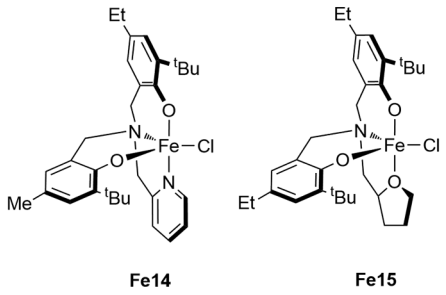

Fe14 Fe15

2.2.3.2. Photocatalysis. Photocatalytic studies initially employed Fe_2**19**-Fe_2**21**, which all possess a dithiolate bridge with a tertiary amine.[160] Exchange of the CO units for poorly σ-donating tris(*N*-pyrrolyl)-phosphine groups was investigated to improve photostability without a large negative shift in reduction potentials. Singly substituted Fe_2**20** displayed the best performance, with a TON_{H2} of 4.3 after 3 h irradiation (λ > 400 nm) using **PS1** in H_2O:MeCN (1:1) solution containing AA.[160] In contrast, illumination (λ > 400 nm) of Fe_2**20** with **PS2** in H_2O:acetone (1:9) with TEA (pH′ 11.0) resulted in a TON_{H2} of 466 after 8 h.[161] Under acidic conditions (λ = 455−850 nm) with dithiolene-ligated Fe_2**22** and **PS1** in H_2O:DMF (1:1) containing AA (pH′ 5.5), a TON_{H2} of ~200 resulted after 2.5 h, with a QY_{H2} of 1%.[162]

Using precious-metal-free **PS3**, Fe_2**23** reaches a TON_{H2} of 226 after 15 h (λ > 450 nm) in H_2O:EtOH (1:1) with 10% TEA

DOI: 10.1021/acs.chemrev.8b00392
Chem. Rev. 2019, 119, 2752−2875

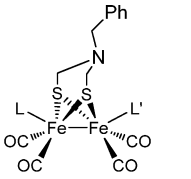

$Fe_2$19, L = L' = CO
$Fe_2$20, L = CO, L' = $P(Pyr)_3$
$Fe_2$21, L = L' = $P(Pyr)_3$

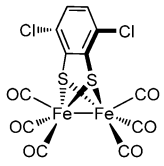

$Fe_2$22

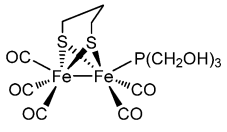

$Fe_2$23

(pH′ 10.0), giving a QY_{H2} of 5.6% (λ = 520 nm).[163] A faster rate is observed for binaphthalene-dithiol bridged **$Fe_2$24** under comparable conditions, achieving a TON_{H2} of 224 after 2 h when irradiated (λ > 420 nm) with **PS3** in H_2O:MeCN (1:1) containing TEA (pH′ 10.0).[164] CV of **$Fe_2$24** in MeCN shows two features, assigned as metal-centered one-electron reductions. In H_2O:MeCN (1:1) with increasing amounts of AcOH, the first wave at −0.95 V vs SCE is largely pH-independent, whereas catalytic current emerges at the second wave at −1.25 V vs SCE, the onset of which thereby being correlated with the $[Fe^0Fe^0]$ state.[164] Interestingly, photoexcited **PS3** has insufficient driving force to generate the catalytically active forms of either **$Fe_2$23** or **$Fe_2$24**, with one mechanistic proposal also involving direct ET to the catalyst from photogenerated TEA radicals.[163,164]

Synthetic modification of iron-based HECs has led to fully aqueous photocatalytic systems. The use of a 1,2-ethanedithiolate bridge with an appended sulfonate group affords water-soluble **$Fe_2$25**.[125] Irradiation (λ > 400 nm) with **PS1** in aqueous AA buffer (pH 4.0) gave a TON_{H2} of 88 after 4 h. Replacement of the chelating bridge by two analogous 2-mercaptoethanesulfonates affords **$Fe_2$26**. Upon 450 nm illumination, aqueous AA solutions (pH 4.0) containing **PS1** and either **$Fe_2$25** or **$Fe_2$26** reach respective TON_{H2} values of 114 and 178 after 6 h. In contrast, when metal chalcogenide QDs are used as PSs under otherwise identical conditions **$Fe_2$25** and **$Fe_2$26** reach respective TON_{H2} values of 18 800 and 26 500 over 12 h, with both exceeding 15 000 in the first 6 h.[126]

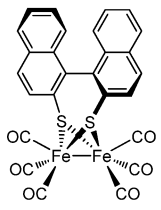

$Fe_2$24

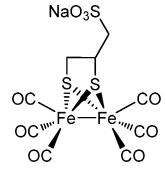

$Fe_2$25

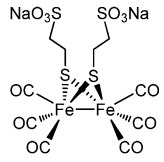

$Fe_2$26

Hybrid systems made from protein-bound HECs have also been investigated. Reaction of $[Fe_2(CO)_9]$ with a polypeptide possessing two cysteine residues close in sequence yields **$Fe_2$27**.[131] Irradiation (λ = 410−770 nm) with **PS1** in aqueous AA (pH 4.7) gave a TON_{H2} of 82 after 3 h.[131] Simultaneously binding **PS4** through a histidine residue in a related system resulted in a TON_{H2} of only 9 after 2 h.[132] A comparable approach uses a polypeptide with a synthetic amino acid featuring a 1,3-propanedithiol moiety.[130] Reaction of $[Fe_3(CO)_{12}]$ with this side-chain provided the desired bimetallic iron site, and 410−700 nm illumination with **PS1** present in AA/citrate solution (pH 4.5) reached a TON_{H2} of 84 after 2.5 h.[130] **$Fe_2$28** has a tethered maleimide, which enables covalent binding to a cysteine residue in the β-barrel protein known as nitrobindin.[129] Using 410−700 nm light with **PS1** in AA solution (pH 4.0), this adduct produced a TON_{H2} of 130 after 6 h.[129] Despite showing activity in aqueous environments, the performance of these peptide-hybrid systems has not significantly exceeded those of HECs solubilized by addition of sulfonate groups.

Dendrimer-based thiolate bridges were employed in **$Fe_2$29**, with a TON_{H2} of 21 500 resulting after 8 h of irradiation (λ = 400−800 nm) with **PS5** in H_2O:acetone (1:9) containing TEA (QY_{H2} = 28% at λ = 440 nm).[165] It was suggested that vectorial ET is promoted by the dendrimer; the hydrophobicity of the poly(arylalkyl ether)-based shell may favor close association of the reduced charge-neutral **PS5**, with electron donation to the catalytic core then producing a cation with a higher affinity for bulk solution.[165] This performance is among the highest reported for homogeneous Fe-based HECs, and exploration of functionalized dendrites may thus be a promising avenue for further development.

A substantial number of systems that integrate PSs and bimetallic dithiolate-bridged HECs into a single molecule have been investigated. However, the performance of such dyads has been low, with typical TON_{H2} values less than 2.[166−168] Exceptions employ tethered organic dyes such as **$Fe_2$30** and **$Fe_2$31**, which both gave maximum TON_{H2} values of ∼30 under UV irradiation (λ = 254 and 355 nm, respectively) in MeCN containing organic acids.[169,170] Reinvestigation of **$Fe_2$30** under slightly altered conditions reported a TON_{H2} of 539 after 7 h of irradiation (λ = 254 nm) in an MeCN solution containing TEA and TFA.[171] Using the ionic surfactant cetyltrimethylammonium bromide (CTAB) allowed for the same catalyst to operate in purely aqueous media, but the TON_{H2} was significantly reduced.[171]

Several systems using iron complexes less closely related to the H_2ase active site show water tolerance, while also producing H_2 under visible light irradiation. Mono-, di-, and tri-iron carbonyl complexes are active HECs in H_2O:TEA:tetrahydrofuran (THF) (1:1:4) solutions with **PS5**.[172] $[Fe_3(CO)_{12}]$ performed best, giving a TON_{H2} of 400 after 3 h (λ > 420 nm).[172] Iron-hydride $[HFe_3(CO)_{11}]^-$ was identified as the major compound present irrespective of the starting complex, and is thought to be the active species.[173] Screening of phosphine additives showed that tris(4-trifluoromethylphenyl)- or tris[3,5-bis(trifluoromethyl)phenyl]-phosphine gave enhanced performance, with TON_{H2} for the latter reaching 1450 over 24 h when a H_2O:TEA:THF (1:2:3) solution was irradiated (λ > 420 nm).[173] Addition of an *iso*-propyl group at the *ortho*-position of the bpy unit in **PS5** gave a TON_{H2} of 2770 after 24 h using 440 nm light and H_2O:TEA:THF (1:2:3) containing the latter phosphine (QY_{H2} = 16.4% at 440 nm).[174]

Copper-based PSs were also studied employing the same HEC. A TON_{H2} of 931 was obtained over 60 h with $[Fe_3(CO)_{12}]$ and **PS6** in H_2O:TEA:THF (1:3:4) using unfiltered Xe-light.[175,176] DFT studies in combination with NMR and in situ Fourier-transform-infrared (FT-IR) spectroscopic analysis revealed that the $[HFe_3(CO)_{11}]^-$ intermediate is transformed through reaction with the phosphine-functionalized PS, giving a bimetallic diphenylphosphine-bridged iron species.[177] Correlating H_2 evolution with species formed in situ shows the latter is also catalytically active, granting insight into the improvements observed above upon addition of fluorinated phosphines.[177]

A variety of iron-cyclopentadienone catalysts also function with the related dye **PS7**.[178] The carbonyl O-atom in these HECs can act as a reversible proton acceptor, reminiscent of the

DOI: 10.1021/acs.chemrev.8b00392
Chem. Rev. 2019, 119, 2752−2875

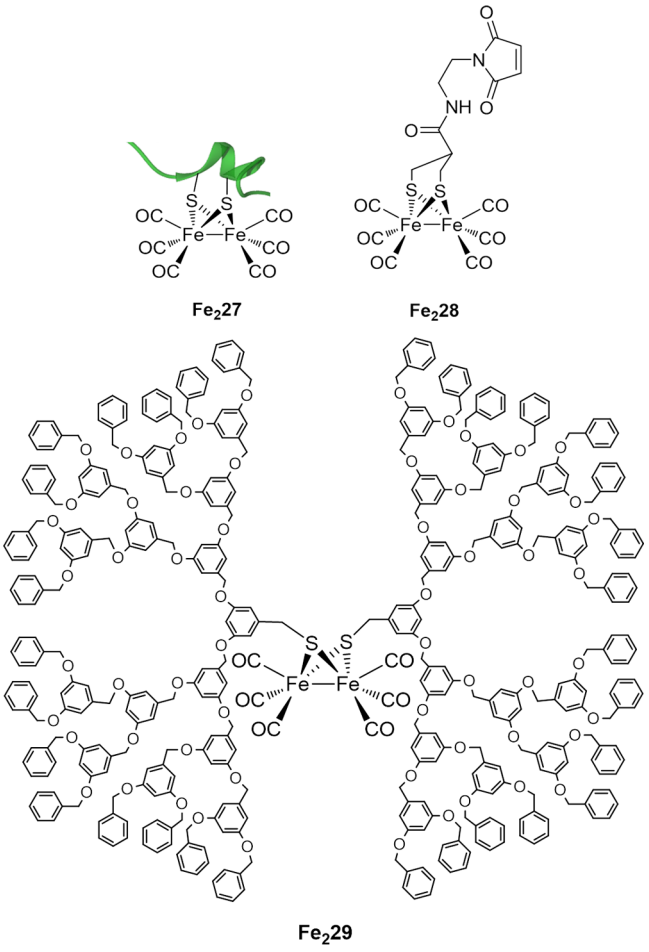

azadithiolate bridges in [FeFe]-H_2ase models.[179] The greatest activity was observed for **Fe16**, reaching a TON_{H2} of 131 after 7 h upon unfiltered Xe-light irradiation in H_2O:TEA:THF (1:3:4).[178] Use of λ > 400 nm light or an air mass 1.5 global (AM1.5G) filter still produced H_2, but led to diminished performance. No photoactivity was observed unless an external base is introduced, which is thought to be needed for opening a free coordination site on **Fe16** by liberating a bound CO through the water-gas shift reaction.[178] In contrast, $[Fe_3(CO)_{12}]$ shows no activity in the presence of an external base but otherwise reached a TON_{H2} of 90 over an ∼4-fold longer time frame.[178]

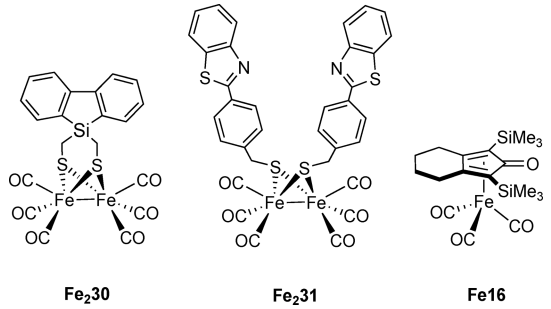

Using organic dye **PS8**, HECs **Fe11**-**Fe13** gave respective TON_{H2} values of 2100, 740, and 1000 over 24 h upon 520 nm light-emitting diode (LED) illumination in H_2O:EtOH (1:1) containing 5% TEA (pH′ 12.5).[180] This contrasts with electrocatalytic results, where **Fe12** showed the greatest activity. H_2 evolution with the latter began to level off after 6 h, which is thought to result from the less stable 7-membered chelate ring in **Fe12**. Conversely, rates for **Fe11** and **Fe13** continued in an almost linear fashion, indicative of good HEC stability. This was supported by readdition of **PS8,** which restored activity for **Fe11** and allowed for a total TON_{H2} of ∼2800 after 38 h. Dynamic light scattering (DLS) experiments after 12 h irradiation provide further evidence for a molecular active species. Respective QY_{H2} values of 3.1%, 1.9%, and 3.4% were determined for **Fe11**-**Fe13** at λ = 520 nm. Notably, lake water was also tested as a reaction medium following gravity filtration, and after addition of **Fe11** along with **PS8**, TEA, and EtOH, a TON_{H2} of ∼1000 was obtained after 24 h.[180]

2.2.4. Cobalt. Cobalt sites play no role in biological H_2 production but are among the most prevalent in synthetic HECs.[181,182] These catalysts commonly feature Co^{3+} or Co^{2+} resting states with planar (pseudo)macrocyclic chelating ligands.[183] A simplified mechanism for H_2 evolution mediated by cobalt-based HECs is depicted below (Figure 8).[184]

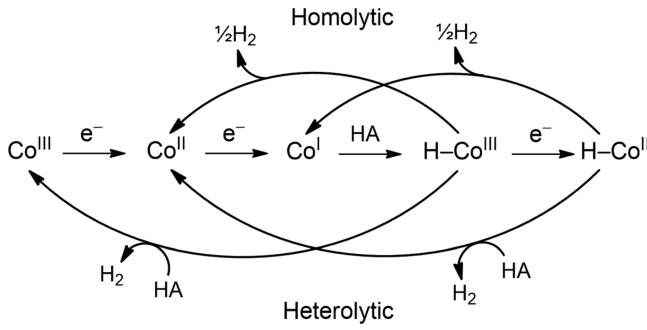

Figure 8. General mechanism of H_2 generation by Co-based molecular catalysts (HA = acid).[184]

2.2.4.1. Electrocatalysis. In 1971, a stable cobalt-hydride species, **Co1**, was shown to evolve H_2 upon thermolysis at 150 °C.[185] An early study of **Co2** reports CPE with a Hg pool WE at E_{appl} = −1.60 V vs NHE in H_2O:MeCN (2:1), giving a TON_{H2} of ∼80 with a FE_{H2} of 80% after 19 h.[186] Subsequently, (pseudo)macrocyclic cobalt complexes such as those containing diglyoximes (cobaloximes) were identified as HECs in non-aqueous photocatalytic conditions,[187,188] or by using divalent metal salts as reducing agents in aqueous HCl.[189] CPE with **Co3** in 1,2-dichloroethane containing Et_3N·HCl using a graphite WE at E_{appl} = −0.90 V vs Ag/AgCl gave a FE_{H2} of 85−100%, with a TON_{H2} of 100 in 2.5 h.[188,190] Cobaloximes were later shown to operate in neutral aqueous media.[191−193] Owing to their high FEs, low overpotential requirements, and simple syntheses, these HECs are some of the most studied in the field, and dedicated reviews are available.[183,184,194] They are also among the few HECs that show operational O_2-tolerance, an important consideration for their use in full water-splitting systems.[191,192,195]

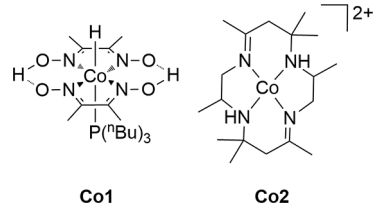

Cobaloximes are synthesized as octahedral Co^{3+} or Co^{2+} complexes with two singly deprotonated glyoxime units,

DOI: 10.1021/acs.chemrev.8b00392
Chem. Rev. 2019, 119, 2752−2875

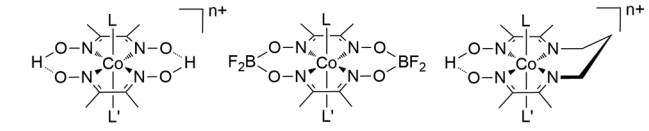

Co3, L = Cl, L' = Pyridine, n = 0
Co4, L = L' = H_2O, n = 1

Co5, L = L' = MeCN
Co6, L = L' = H_2O

Co7, L = L' = Br, n = 0
Co8, L = L' = H_2O, n = 2
Co9, L = L' = Cl, n = 0

typically the dimethylglyoximato anion (dmgH), which form a pseudomacrocycle in the equatorial plane through mutual O−H···O bridges.[196] Substitution with electron-withdrawing groups at the glyoxime C-atoms can lower the driving force required for reduction, but this diminishes the basicity of the metal center, thus decreasing activity.[183] Conversely, axial pyridine ligation in **Co3** increases the metal nucleophilicity and activity compared to the aqua analogue **Co4** without detrimental effects on reduction potential, and use of differently substituted pyridines can further tune catalytic performance.[188,193] While cobaloximes are unstable in acidic conditions, this can be improved by exchanging the bridging H-atoms for -BF_2 groups, affording (difluoroboryl)dimethylglyoximato anionic ligands ($dmgBF_2$), as in **Co5** and **Co6**.[188,190,196] Replacing one oxime bridge with a propane tether also enhances stability, and the diimine-dioxime HECs **Co7**-**Co9** are also well-studied.[197,198] CPE with **Co5** and **Co8** in aqueous phosphate solution (pH 2.2) using a GC WE at E_{appl} = −0.93 V vs SCE gave respective TON_{H2} values of 16 and 23 after 2 h, with FE_{H2} of around 80% in both cases.[199] DFT provides some insight into the greater activity of **Co8**, suggesting that the dioxime moiety may be involved in facilitating catalysis through proton transfer.[200,201]

Several computational studies have addressed the mechanism by which cobaloximes and related diimine-dioximes achieve H_2 evolution.[200−202] Generally, reduction to the Co^+ state is followed by protonation to produce a metal-hydride, Co^{3+}−H.[181,184] Theoretical evidence suggests reduction to the corresponding Co^{2+}−H is needed before H_2 is evolved, though this may occur at more positive potentials than those required to generate the Co^+ species, or directly with protonation of the latter in a PCET process.[200−202] While direct protonation of a Co^0 intermediate is an alternative,[181,184] strongly reducing electrolytic conditions can produce catalytically active nanoparticles, as shown with cobaloximes and closely related complexes, **Co6**, **Co9**, **Co10**, and **Co11**.[203−206] Limited stability of these HECs is also observed in photocatalytic systems (section 2.2.4.2).[166] Though Hg^0 can be used to amalgamate nanoparticles and offset their contribution to activity, care must be taken in assigning active species, particularly when electrodes can act as nucleation sites.[86,206]

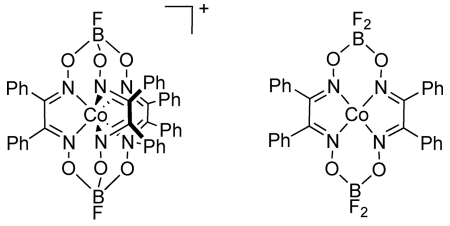

Co10

Co11

Cobalt-based porphyrins and related macrocycles are also well-studied as HECs.[146,147] Early reports using **Co12** show an E_{onset} of −0.75 V vs SCE at the Co^{2+}/Co^+ couple when H_2O is added to dimethyl sulfoxide (DMSO) solutions.[207] Both **Co12** and **Co13** also display E_{onset} = −0.70 V vs SCE in acidic aqueous solution (pH 2.9−3.4). Quantitative FE_{H2} at E_{appl} = −0.95 V vs SCE in aqueous TFA solutions was observed in both cases over 20 min, although full analysis was complicated by adsorption of the complexes at the Hg pool WE.[207] The cobalt analogue of acetylated microperoxidase-11, **Co14**, contains a porphyrin ring linked to an 11-residue peptide, providing water solubility.[208] CPE with **Co14** in aqueous phosphate solution (pH 7.0) using a Hg pool WE at E_{appl} = −1.50 V vs Ag/AgCl gave a FE_{H2} of 98% over 4 h with a TON_{H2} of 25 000, but currents drop significantly and solutions visibly bleach after the first 15 min.[208] CPE of water soluble **Co15** in phosphate solution (pH 7.0) with a GC WE at E_{appl} = −1.29 V vs NHE gave quantitative FE_{H2} with a TON_{H2} of 19 000 over 73 h.[209] While this system performed for much longer than **Co14**, UV−vis spectra of **Co15** still show bleaching indicative of loss of aromaticity, reflecting gradual hydrogenation of the ligand.[209] When the sulfonate groups were exchanged for chlorine atoms to give **Co16**, approximately 3-fold improvements in catalytic rate over **Co15** were observed under identical conditions.[210] CPE with **Co17** showed comparable activity to **Co15**, but no substantial current losses were observed over 72 h, indicating that perfluorination may enhance stability.[211] These promising properties have led to many reports of immobilized porphyrins and related HECs.[146,147]

The catalytic mechanism for **Co12** was initially thought to involve protonation of Co^+ to form the corresponding Co^{3+}−H intermediate.[207] However, a later study provided evidence that H_2 evolution only occurs upon reduction of Co^+ to Co^0, likely in a PCET process which affords a Co^{2+}−H species.[212] Related studies of Co-porphyrins also reach this conclusion when weak proton sources such as H_2O are used, or electron deficient *meso*-substituents are present. Nevertheless, the use of strong acids or electron-rich porphyrins may allow for protonation of the Co^+ state.[209,211,213] Regardless of the oxidation state that initially produces the metal-hydride, both computational and experimental results indicate that a Co^{2+}−H intermediate is necessary for H_2 production.[201,213] These findings are in agreement with the mechanism proposed for cobaloxime and the related diimine-dioxime HECs.[200−202]

Polypyridyl-cobalt complexes are a diverse family of HECs, featuring pyridine- and bpy-derived tetra- and penta-dentate ligands.[181] While cobalt tris-bpy was among the earliest HECs studied photocatalytically, electrocatalytic activity was only established much later with bpy-derived **Co18**.[214] CV in MeCN showed an E_{onset} at the Co^{2+}/Co^+ couple after adding TFA, and CPE with a GC WE gave a FE_{H2} of 99% at E_{appl} = −1.0 V vs SCE. Similar behavior resulted in H_2O:MeCN (1:1) solutions, though no CPE data was reported.[214] Exchange of the methoxy residue in **Co18** for a methyl group yields **Co19**, which displays an E_{onset} of −0.90 V vs NHE in AA solution (pH 4.0) that coincides with Co^+ species formation.[215] E_{onset} was shifted positively by installing -CF_3 groups to give **Co20**, but activity was decreased with respect to **Co19**, similarly to an analogous pair of polypyridyl cobalt HECs.[215,216] CPE in H_2O was not reported in either case, but aqueous photocatalytic experiments revealed activity trends consistent with the electrochemical findings (section 2.2.4.2).[215,216]

CV of **Co21**-**Co23** in aqueous AA solution (pH 7.0) revealed E_{onset} = −0.80 V vs NHE for **Co23**, and E_{onset} = −1.00 V vs NHE for **Co21** and **Co22**. CPE in the same solution with a GC WE at E_{appl} = −1.20 V vs NHE gave only trace amounts of H_2 for **Co23**, whereas **Co21** and **Co22** reached respective TON_{H2} values of 60

DOI: 10.1021/acs.chemrev.8b00392
Chem. Rev. 2019, 119, 2752−2875

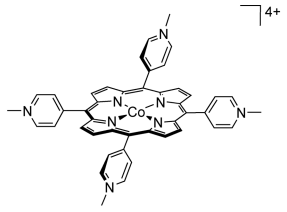
Co12

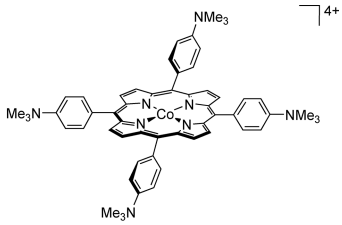
Co13

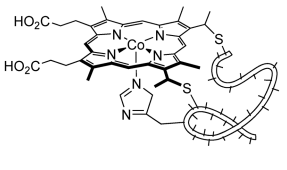
Co14

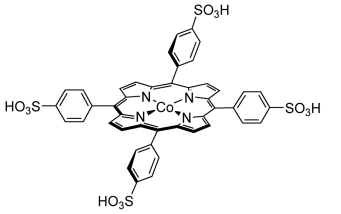
Co15

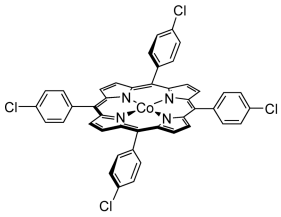
Co16

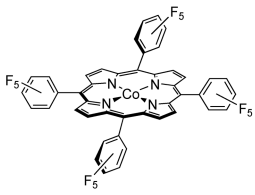
Co17

and 44 over 3 h (FE_{H2} = 100%).[215] In comparison with complexes **Co21**-**Co23**, **Co24** possesses one additional pyridine moiety. It shows an E_{onset} of −1.20 V vs NHE in phosphate solution (pH 7.0), which is slightly more negative than the Co^{2+}/Co^{+} couple.[217] CPE in the same solution with a Hg pool WE at E_{appl} = −1.30 V vs NHE gave a TON_{H2} of 55 000 after 60 h. Charge passed over this time was almost linear, indicating excellent stability. The E_{onset} could be further tuned by substitution of the central pyridine with electron-donating or -withdrawing groups, giving **Co25** and **Co26** (no CPE data reported for these derivatives).[217] Systematic exchange of the pyridine groups for pyrazine residues gives **Co27**-**Co29**, with replacement of the central unit resulting in an E_{onset} that is associated with formation of a ligand-based radical. CPE with **Co27**-**Co29** in aqueous phosphate solution (pH 7.0) using a Hg pool WE at E_{appl} = −1.20 V vs NHE displayed a quantitative FE_{H2} and almost linear passage of charge over 12 h, with **Co28** and **Co29** showing more than 4-fold greater activity than **Co27** (TON not reported).[218]

Bis(iminopyridine) complex **Co30** is an active HEC in aqueous solution (pH 2.0−8.0).[219] CV shows two catalytically relevant features, assigned as a Co^{2+}/Co^{+} couple at −0.90 V vs SCE and formation of a $Co^{+}(L^{\bullet-})$ ligand radical at −1.20 V vs SCE. Greater activity was observed by CV and CPE at potentials corresponding to generation of the radical species, suggesting ligand noninnocence likely contributes to the activity of this system.[219] Related CRC **Co31** is known to undergo ligand-based reduction,[220] but CV experiments showed catalytic onset at a potential associated with the Co^{2+}/Co^{+} couple upon addition of AcOH to MeCN or aqueous solutions. CPE in aqueous AcOH with a GC WE at E_{appl} = −0.95 V vs SCE produced a FE_{H2} > 90% and a TON_{H2} > 50.[220] Notably, the ligand-based radical $Co^{+}(L^{\bullet-})$ is associated with catalytic onset in **Co31**-mediated CO_2 reduction, and the N−H group is thought to assist in the mechanism (section 2.3.6.1).

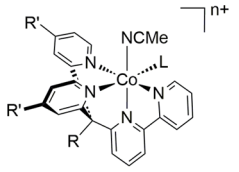
Co18, R = OMe, R' = H, L = MeCN, n = 2
Co19, R = Me, R' = H, L = OTf, n = 1
Co20, R = Me, R' = CF_3, L = MeCN, n = 2

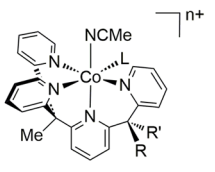
Co21, R = R' = H, L = OTf, n = 1
Co22, R = H, R' = Me, L = OTf, n = 1
Co23, R = R' = Me, no L, n = 2

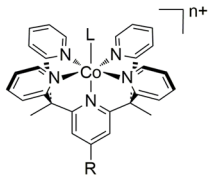
Co24, R = H, L = H_2O, n = 2
Co25, R = CF_3, L = H_2O, n = 2
Co26, R = NMe_2, L = OTf, n = 1

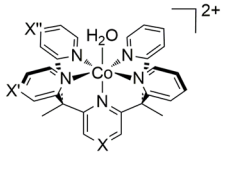
Co27, X = N, X' = X'' = CH
Co28, X' = N, X = X'' = CH
Co29, X' = X'' = N, X = CH

Another class of Co HECs is supported by dithiolenes, which aid catalysis by reversibly transferring electrons and protons from strong acids.[140,141,221] CV of **Co32** showed a reversible couple consistent with single ET in H_2O:MeCN (1:1), and TsOH triggered catalytic onset at the reductive wave of this feature.[222] CPE at E_{appl} = − 1.00 V vs SCE with a GC WE in the same media gave a FE_{H2} > 99% over 1 h (no TON_{H2} reported).[222] Related HECs **Co33**, **Co34**, and **$Co_2$1** were later studied, with **$Co_2$1** becoming monomeric upon reduction.[221] Although **$Co_2$1** features electron-withdrawing nitrile moieties and showed the best photocatalytic performance of this HEC group (section 2.2.4.2), it required the largest electrochemical potential for catalytic onset.[221] A DFT study where the redox potentials and pK_a values of the whole series were assessed revealed that **$Co_2$1** operates through a different mechanism compared to **Co32**-**Co34**.[223] The latter undergo dual protonation at the S-atoms following one-electron reduction, giving neutral species which enter the catalytic cycle after receiving a further electron at similar potentials to the first reduction. In contrast, **$Co_2$1** is less basic and accepts only one proton upon initial reduction, giving an anionic intermediate for which injection of an extra electron is less favorable. Formation of a Co^{3+}−H active species is then believed to proceed by intramolecular proton transfer in all cases.[223]

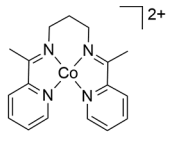
Co30

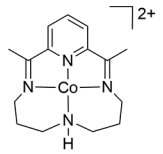
Co31

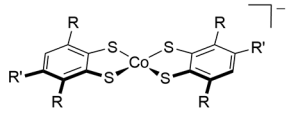
Co32, R = R' = H
Co33, R = H, R' = Me
Co34, R = Cl, R' = H

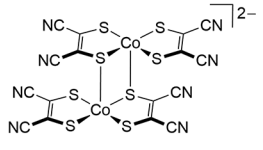
$Co_2$1

2.2.4.2. Photocatalysis. Following initial reports on cobaloxime activity when sensitized with **PS1**, these HECs were subject to further photocatalytic investigation.[166,187,194] Preincubation of **Co3** with Photosystem I gave a semisynthetic hybrid assembly

DOI: 10.1021/acs.chemrev.8b00392
Chem. Rev. 2019, 119, 2752−2875

containing 2.5 catalyst units per protein monomer and produced H_2 upon illumination ($\lambda > 500$ nm) in an aqueous MES solution (pH 6.3) with AA as a SED and cytochrome c_6 as a mediator (cobalt-based TON_{H2} of 2080 after 1.5 h).[224] A semiaqueous study used **Co3** and platinum dye **PS9** in H_2O:MeCN (1:24) with TEOA (pH′ 8.5), giving a TON_{H2} of ∼2150 after 10 h illumination ($\lambda > 410$ nm).[225,226] Hg^0 addition caused a neglible difference in activity, supporting the molecular nature of the HEC.[86,226] Catalytic rate also correlated linearly with HEC concentration, which further suggests a heterolytic pathway.[226] Higher H_2O content led to reduced activity (TON_{H2} of ∼1000 after 10 h in H_2O:MeCN (2:3; pH′ 8.5)), with BF_2-modified **Co6** giving substoichiometric activity under the latter conditions.[226] In contrast, gold dye **PS10** and **Co3** in H_2O:MeCN (1:4) with TEOA reached a TON_{H2} of 375 after 4 h ($\lambda > 385$ nm).[227] Activity has also been shown with precious-metal-free dyes, as outlined below.

The instability of cobaloximes is emphasized by several studies that observe sustained activity upon addition of excess dioxime.[228−230] When **PS3** is irradiated ($\lambda > 450$ nm) in H_2O:MeCN (1:1) containing 5% TEOA (pH′ 7.0), **Co3** achieved a TON_{H2} of 72 (QY_{H2} = 4% at λ = 520 nm).[229] However, if experiments are carried out with 12 additional equivalents of $dmgH_2$ ligand the rate is not greatly affected, but the lifetime increases to reach a Co-based TON_{H2} of 180 over 12 h. Similar results were obtained using **PS11** in H_2O:MeCN (1:1) with 5% TEOA (pH′ 7.0) during 24 h illumination ($\lambda >$ 455 nm), giving a TON_{H2} = 51 with isolated **Co3**, and TON_{H2} = 127 with excess $dmgH_2$.[230] A QY_{H2} = 32.8% at λ = 520 nm was obtained with **Co3** alone. Isolated **Co35** outperforms **Co3** when irradiated ($\lambda > 400$ nm) in H_2O:MeCN (1:1) containing 4% TEOA (pH′ 7.5) with **PS3**, giving a TON_{H2} of 111 after 5 h. DFT indicates that the carboxylic acid-substituted pyridine H-bonds with an O-atom of the dioxime units, which may suppress dioxime dissociation and enhance activity through proton shuttling.[231]

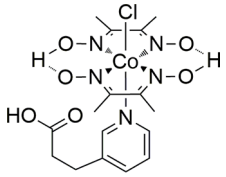

Co35

Difluoroborylated HEC **Co6** gave a TON_{H2} of 327 in H_2O:MeCN (2:1) with 10% TEA (pH′ 10) after 5 h illumination ($\lambda > 400$ nm) with **PS12**.[232] Gradual bleaching of the UV−vis signal of **PS12** suggests system deactivation results from dye degradation.[232] Related dioxime-diimine **Co7** yielded a TON_{H2} of 307 after 4 h irradiation ($\lambda > 400$ nm) with **PS2** in H_2O:MeCN (1:1) containing 10% TEA (pH′ 10).[233] Activity plateaus after 2 h, with addition of fresh **PS2** or **Co7** showing much greater recovery in activity for the latter. Experiments repeated with two equivalents of PPh_3 show slower initial rates but the system remains active for longer, giving a TON_{H2} of 696 in 10 h.[233] Spectroscopy and electrochemistry revealed that PPh_3 binds to the Co^+ intermediate, and it is believed that this adduct then becomes the resting state in the catalytic cycle.[233] **Co7** can also function in purely aqueous media, with 380 nm LED illumination of AA solutions (pH 4.1) containing **PS13** giving a TON_{H2} of 90 after 30 h (QY_{H2} = 20% at λ = 380 nm).[234] This reduced activity may arise from a "short-circuit" pathway where oxidation of the AA SED produces dehydroascorbic acid (DHA), which in turn competes with the HEC for reducing equivalents generated by the PS, and thereby limits catalysis.[234]

Many cobaloxime-based dyads have been studied, usually made up of a HEC unit bound axially to a pyridine-functionalized PS. Most systems use purely organic media, but a few exceptions exist. Zn-porphyrin dyad **Co36** gave a TON_{H2} of 22 after 5 h irradiation ($\lambda > 400$ nm) in H_2O:THF (1:4) with TEA.[235] HEC and Mg- or apo-porphyrin reached respective TON_{H2} values of 3 and <1, whereas no H_2 was detected when the Zn-porphyrin and **Co3** were added separately.[235] Post-catalytic **Co36** solutions showed UV−vis spectra consistent with the two dissociated components.[235] Using a boron dipyrromethene pyridine-derivative gives **Co37**.[236] A TON_{H2} of 85 resulted after 5 h illumination ($\lambda > 420$ nm) in H_2O:MeCN (1:4) with 5% TEOA (pH′ 8.5).[236,237] Studies on related systems have shown that, while pyridine dissociation from inert Co^{3+} is slow, it is accelerated by irradiation or reduction, explaining the instability of such dyads.[228] It was also found that the glyoximate ligands dissociate during photocatalysis, in part rationalizing the limited stability reported for cobaloximes.[228]

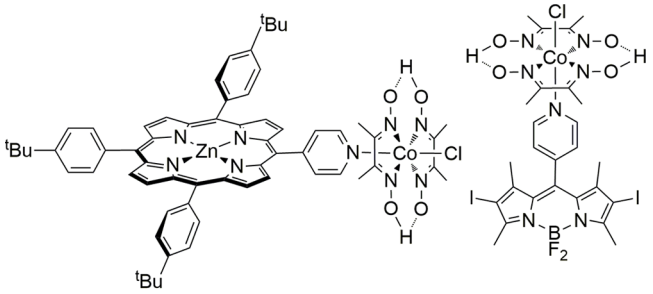

Co36 **Co37**

Cobalt heteroaromatic HECs generally outperform cobaloximes and their derivatives under photocatalytic conditions. Irradiation ($\lambda > 400$ nm) of **PS1** in phosphate solution (pH 7.0) with AA and porphyrin **Co12** gave a TON_{H2} of 725 after 4 h.[212] UV−vis analysis showed loss of the **Co12** signal over this time. Phthalocyanine (Pc) **Co38** displayed even greater stability with **PS1** in H_2O:EtOH (1:4) containing TEA (pH′ 10), reaching a TON_{H2} of 2400 after 10 h ($\lambda > 420$ nm; QY_{H2} = 4.2% at λ = 420 nm).[238] Using **Co38** and **PS8** affords a precious-metal-free system, with a TON_{H2} of 2650 after 10 h irradiation ($\lambda >$ 420 nm) in H_2O:EtOH (1:4) containing TEA (pH′ 12; QY_{H2} = 6.1% at λ = 420 nm).[239] **Co38** activity was retained in the presence of Hg^0 in both cases.[238,239] The **PS8** system yields no H_2 when **Co38** is replaced with an analogous Co-porphyrin that only undergoes metal-based reduction.[239] In contrast, two-electron reduction of **Co38** yields a cobalt(I)-ligand radical, suggesting ligand noninnocence may contribute to activity.[240] This example also shows that precious-metal systems can be matched in performance by those using entirely Earth-abundant elements.

Early studies reported H_2 evolution from aqueous SED solutions (pH 7.5−10.0; TEOA or AA as SEDs) of bpy and $CoCl_2$ when irradiated with visible light ($\lambda > 400$ nm).[241,242] In situ formation of $[Co(bpy)_3]^+$ was proposed based on UV−vis analysis.[241,242] Later reports with isolated **Co39** and Ru dye **PS14** gave a TON_{H2} of 74 over 30−60 min in H_2O:MeCN (1:1) containing TEOA upon LED illumination (λ = 465 nm).[243] Using organic dye **PS12** instead gave a TON_{H2} of 631 over 2 h irradiation ($\lambda > 450$ nm) in H_2O:MeCN (1:1; pH′ 10) with 10%

DOI: 10.1021/acs.chemrev.8b00392
Chem. Rev. 2019, 119, 2752−2875

TEA.[244] Under these conditions cobaloximes **Co3** and **Co6** gave respective TON_{H2} values of 54 and 212. The basic pH likely disfavors metal-hydride protonation and a homolytic mechanism was therefore suggested.[244]

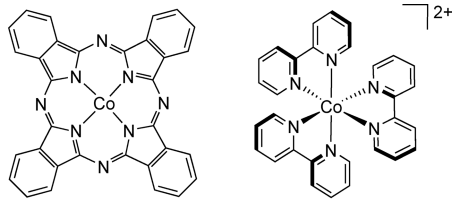

Co38 **Co39**

2,2′:6′,2″:6″,2‴-Quaterpyridine (qtpy) complex **Co40** reaches a TON_{H2} of 1150 after 20 h illumination (λ > 420 nm) using **PS15** in H_2O:MeCN (5:95) with TEOA as a SED and *p*-cyanoanilinium as a proton source.[245] Readdition of the PS after H_2 evolution had ceased led to a recovery of activity, indicating good HEC stability.[245] LED irradiation (λ = 469 nm) of related **Co41** and **PS1** in AA buffer (pH 4.0) yielded a TON_{H2} of 333 over 3 h,[246] whereas **Co42** gave a TON_{H2} of 745 after 12 h under almost identical conditions.[247] DFT indicates **Co42** is first reduced at the ligand, but catalytic onset requires a further reduction step.[247]

Related nonplanar polypyridyl HECs reach high photocatalytic TON_{H2} values. Pyridine-bpy hybrid **Co43** and **PS13** achieve a TON_{H2} of ∼9000 after 20 h in aqueous AA solution (pH 4.1) using LED irradiation (λ = 385 nm).[248] Hg^0 presence did not result in changes in activity. Liquid chromatography and mass spectrometry (MS) revealed that >90% of the PS and HEC were intact postcatalysis. Further investigation showed that DHA resulting from AA oxidation limits HEC activity by competing for the reducing equivalents generated by the PS. When **Co43** is bound to a styrene-based resin, and the photocatalysis solution exchanged every 15 h, no substantial activity loss occurs after 6 cycles, showing that this HEC is stable for over 105 h.[248] **Co19**, with a methyl group in place of the hydroxyl, gave a TON_{H2} > 10 000 under 452 nm LED illumination with **PS1** in AA solution (pH 4.0), though only at HEC concentrations < 1 μM.[215] At ∼3-fold higher amounts of **Co19** using AM1.5G simulated solar light, the TON_{H2} stabilized at 4200 after 2.5 h (QY_{H2} = 7.5% at λ = 452 nm). Activity resumed after readding **PS1**, consistent with the high stability of these HECs demonstrated above.[215]

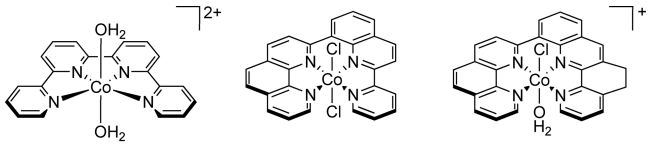

Co40 **Co41** **Co42**

Co44 features a TPA-derived ligand with a bpy instead of one pyridine and yielded a TON_{H2} of 4400 after 2 h with **PS1** under 450 nm LED illumination in aqueous AA (pH 4.0).[249] Reactivation required both fresh **PS1** and **Co44** and gave only partial recovery, representing an exception to the usually robust behavior of these HECs.[249] **Co45** has two bpy units tethered by a methyl-pyridyl fragment and produced a TON_{H2} of 1630 after 13 h with **PS1** in aqueous AA buffer (pH 4.0) under 452 nm LED irradiation (QY_{H2} = 3.6% at λ = 452 nm).[216] Fluorinated analogue **Co46** afforded a TON_{H2} of 1390 under similar conditions (QY_{H2} = 2.7% at λ = 452 nm). DFT studies suggest that the electron withdrawing $-CF_3$ groups stabilize the Co^+ state, lowering reactivity, in agreement with a similar trend seen for cobaloximes.[183,216] H_2 evolution slowed with both HECs after 3−4 h but addition of fresh PS restored activity.[216] **Co45** methyl-group exchange to a hydroxy-moiety affords **Co47**, which gives a TON_{H2} of 1380 after 13 h using 385 nm LED illumination with **PS13** in aqueous AA (pH 4.1). Hg^0 presence caused negligible changes in activity.[250] Under identical conditions related penta-pyridyl **Co48** gave a TON_{H2} of 1180 after 42 h, reflecting a much faster rate for **Co47**.[250]

The catalysis-limiting back-reaction of DHA photogenerated from AA can be overcome by coupling with another SED that is less prone to back ET, thus regenerating AA from the DHA and avoiding build-up of this competing reversible electron acceptor.[251] Tris(2-carboxyethyl) phosphine (TCEP) can convert DHA to AA and acts as an oxide acceptor in the process.[252,253] Photocatalysis in aqueous AA/TCEP solution (pH 5.0) with **Co47** gave great improvements compared with either SED alone, in terms of both evolution rate and total H_2 formed, yielding a benchmark TON_{H2} of 33 300 after 11 h using 470 nm LED irradiation with **PS1**.[251] Planar macrocyclic **Co49** reached a TON_{H2} of 21 900 after 41 h with **PS1** in aqueous AA/TCEP during 453 nm LED illumination. Though Hg^0 had no significant effect on performance, **Co49** shows limited stability in aerobic aqueous solution, even in the dark.[254]

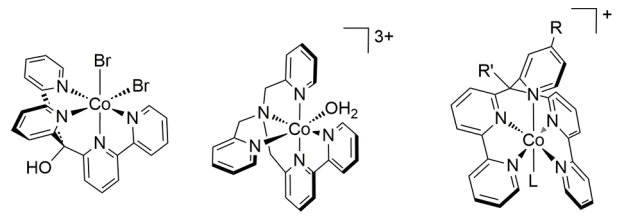

Co43 **Co44** **Co45**, R = H, R' = Me, L = OTf
Co46, R = CF_3, R' = Me, L = OTf
Co47, R = H, R' = OH, L = Br

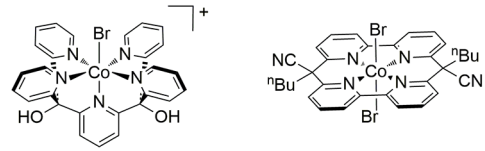

Co48 **Co49**

In an early study, "daylight lamp" irradiation (λ = unspecified) of **Co31** and **PS1** in AA solution (pH 4.0) achieved a TON_{H2} of ∼300 over 18 h.[255] Using **PS5**, a **Co31** TON_{H2} of 180 resulted after 6 h irradiation (λ > 390 nm) in H_2O:MeCN (2:3) with TEOA and AcOH (pH′ 7.1; QY_{H2} = 47% at λ = 468 nm).[220] **Co31** was later used to compare **PS1** with the organic triazatriangulenium dye **PS16**.[256] Illumination (λ = 400−700 nm) of aqueous acetate solutions containing AA (pH 4.5) yielded similar TON_{H2} values of ∼900 after 22 h. Lowering **Co31** concentration from 50 μM to 5 μM gave a TON_{H2} of 2034 and 5914 for **PS1** and **PS16**, respectively.[256] Further decrease to 1 μM achieved a TON_{H2} of 8952 over 22 h for **Co31**, demonstrating activity and longevity comparable to polypyridyl HECs in aqueous media.

HEC **Co50** functions with **PS3** in semiaqueous H_2O:MeCN (1:1) solution with 10% TEA (pH′ 10), giving a TON_{H2} of 495 after 4 h irradiation (λ > 420 nm).[257] Performance plateaus after this time, though readding PS allows ∼80% recovery of activity,

DOI: 10.1021/acs.chemrev.8b00392
Chem. Rev. 2019, 119, 2752−2875

indicating deactivation is largely due to dye decomposition.[257] Thiosemicarbazide **Co51** reached a TON_{H2} of ~900 with **PS8** in aqueous TEA (pH 11.5) over 16 h illumination (λ > 420 nm).[258] Hg^0 had a neglible influence on performance.

LED illumination (λ = 520 nm) of dithiolene HECs **Co32**-**Co34** and **$Co_2$1** with **PS1** in H_2O:MeCN (1:1) AA solution (pH′ 4.0) gave respective TON_{H2} values of 2700, 2300, 6000, and 9000 after 12 h.[221,222] Although TON_{H2} appears to reflect the electron-withdrawing nature of the ligands, DFT analysis suggests that the two types of complex (**Co32**-**Co34** vs **$Co_2$1**) evolve H_2 by distinct mechanistic pathways.[223] Intramolecular proton transfer from the coordinated S-atoms has been proposed to be involved in all cases.[223] Considerable progress has been made with cobalt-based HECs under purely homogeneous conditions. Even more inspiring performance has been reported using HECs such as **Co32**-**Co34** with QD PSs, achieving TON_{H2} values in excess of 300 000 over 60 h.[259]

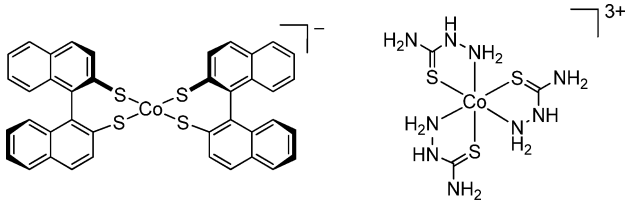

Co50 **Co51**

2.2.5. Nickel. Nickel is a potentially inexpensive alternative to palladium and platinum for designing HECs, and is more abundant and biologically relevant than cobalt.[28,58] Interestingly, only the nickel center changes oxidation state in the generally accepted mechanism of [NiFe]-H_2ases, whereas the iron remains redox inactive, hinting at the catalytic potential of the former metal.[29,30] Proton or CO_2 transformations mediated by molecular nickel catalysts typically involve reduction of a square-planar Ni^{2+} state to a tetrahedral Ni^+ intermediate, and as such tetradentate ligation features prominently in the HECs outlined below.[58]

2.2.5.1. Electrocatalysis. The earliest nickel HECs were supported by cyclam (1,4,8,11-tetraazacyclotetradecane) and related derivatives, such as in **Ni1** and **Ni2**.[70,186] Initially studied as a CRC, **Ni2** also produced H_2 from H_2O:MeCN (2:1) solutions with a FE_{H2} of ~33% using a Hg pool WE at E_{appl} = −1.60 V vs SCE (no TON_{H2} reported).[186] In aqueous solution (pH 7.4) **Ni1** showed catalytic onset correlated with reduction to nickel(I), and CPE gave a TON_{H2} > 100 over an unspecified time with a Hg pool WE operating at E_{appl} = −1.50 V vs SCE.[70] The bimetallic analogue **$Ni_2$1** showed a similar E_{onset} and reached comparable TONs under identical conditions, but with up to 10-fold faster rates, likely due to the proximity of the two adjacent nickel sites.[70] The effect of pH value has also been studied in aqueous media using a Hg pool WE at E_{appl} = −0.96 V vs NHE, revealing that while **Ni1** and the more active **Ni3** and **Ni4** reduce CO_2 almost exclusively at pH 5.0, H_2 evolution is favored by all of these catalysts at pH < 2.[59]

Related complexes with N4-ligation such as nickel glyoximes and imine-oximes have also been studied, but only in the absence of water. BF_2-substituted glyoximes **Ni5** and **Ni6** display a catalytic wave in CV upon addition of $HClO_4$ to DMF electrolyte solutions, but no CPE or product identification was reported.[260] CPE experiments with imine-oximes **Ni7**-**Ni9** all show catalytic activity, with TON_{H2} > 4.[197] **Ni9** reached a TON_{H2} of 20 after 3 h with a FE_{H2} of 70% using a GC WE at E_{appl} = −1.10 V vs Fc^+/Fc in MeCN containing *p*-cyanoanilinium tetrafluoroborate, although obvious decomposition of the catalyst was observed.[197]

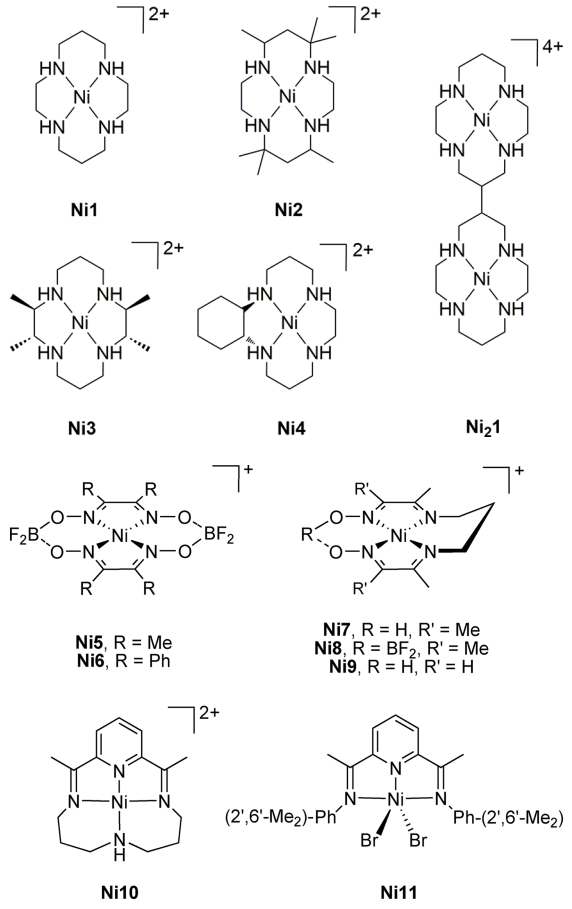

Ni1 **Ni2** **Ni3** **Ni4** **$Ni_2$1**

Ni5, R = Me
Ni6, R = Ph

Ni7, R = H, R' = Me
Ni8, R = BF_2, R' = Me
Ni9, R = H, R' = H

Ni10 **Ni11**

Pyridine-containing **Ni10** is an active HEC under purely aqueous conditions.[261] Using a GC WE at E_{appl} = −1.10 V vs Ag/AgCl in aqueous solution (pH 2.0) gave a TON_{H2} of 12.7 after 12 h, with a FE_{H2} > 95%.[261] A catalytic wave is observed after one-electron reduction of **Ni10**, giving an isolable species characterized as a $Ni^{2+}(L^{\bullet-})$ complex.[261,262] Pincer complex **Ni11** is thought to operate through an analogous intermediate.[263] CPE at E_{appl} = −1.10 V vs NHE with a GC WE in aqueous KCl/HCl (pH 1.0) gave a TON_{H2} of 65 after 1 h with a FE_{H2} of 95%.[263] One-electron reduction of **Ni11** forms a $Ni^{2+}(L^{\bullet-})$ radical, evidenced by both spectroscopic and computational results.[263,264] The latter further indicate that a metal-hydride is subsequently formed by PCET, with protonation then closing the catalytic cycle.[263]

Nickel porphyrins and related macrocycles appear in several studies, with ligand noninnocence commonly being observed. Carboxylic acid functionalized **Ni12** shows catalytic onset at potentials ~100 mV more positive than the bromide-substituted **Ni13**.[265] Both undergo one-electron reduction to a Ni^+ species, with intramolecular proton transfer in **Ni12** thought to be responsible for the more positive E_{onset}, which occurs after a second reduction.[265] Spectroelectrochemical (SEC) and DFT results indicate that this further ET occurs at the ligand.[265] A later DFT study revealed that initial protonation of the reduced species takes place at the porphyrin *meso*-carbon, thereby implicating a phlorin intermediate.[266] Proton relays and ligand

DOI: 10.1021/acs.chemrev.8b00392
Chem. Rev. 2019, 119, 2752−2875

noninnocence can greatly influence HEC mechanistic pathways, as further emphasized below.

Porphyrin **Ni14** shows two reversible redox couples at negative potentials in CV, the first nickel-centered, and the second ligand-based.[267] Adding TFA induces catalytic onset after one-electron reduction, whereas AcOH triggers catalysis only after two-electron reduction. CPE with a GC WE in MeCN with TFA or AcOH at respective E_{appl} = −1.49 or −1.82 V vs Fc^+/Fc established catalytic reactions with TON_{H2} values > 1 and FE_{H2} > 95% over 0.5 h for both pathways.[267] While a heterolytic mechanism is likely with AcOH, stopped-flow and DFT analyses are consistent with a homolytic reaction when TFA is used as the proton source.[267] Porphyrin **Ni14** has also been compared with the corresponding hydrogenated chlorin **Ni15**.[268] CV showed analogous behavior for **Ni15**, with catalytic onset after one-electron reduction in the presence of TFA. Based on catalytic currents, **Ni15** shows a 5-fold higher activity than **Ni14**. CPE in MeCN containing TFA with a GC WE held at an unspecified potential gave a FE_{H2} of > 89% over 6 h, with TON_{H2} > 10 000 for both HECs, being ∼3-fold greater for **Ni15**. DFT studies show that a metal-hydride is formed with **Ni15**, whereas the corresponding intermediate in the case of **Ni14** has a proton located at a pyrrolic nitrogen.

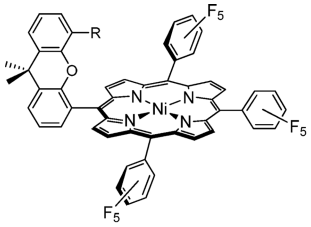

Ni12, R = CO_2H
Ni13, R = Br

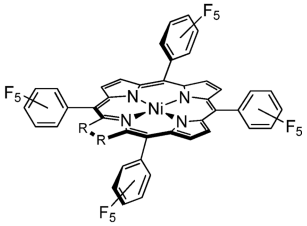

Ni14, R = CH
Ni15, R = CH_2

Polypyridyl ligands stabilize low oxidation states, are often water-compatible, and can serve as redox-active scaffolds to aid PCET during catalysis.[181,218,269] The first study of such Ni-HECs screened various N5-ligands.[270] CV in aqueous media revealed that **Ni16** was most active, undergoing two reductions before entering the catalytic cycle. Comparison with the analogous iron and cobalt complexes suggests reduction is metal-centered. CPE using **Ni16** in aqueous solution (pH 7.0) with a Hg pool WE at E_{appl} = −1.25 V vs NHE gave a TON_{H2} of 308 000 with a FE_{H2} of 91% over 60 h, with no considerable loss in activity observed.[270]

CV scans of **Ni17** in MeCN show two sequential reductions, giving a $Ni^+(L^{\bullet-})$ radical correlated with the catalytic onset upon addition of acid.[271] While CPE in MeCN showed limited activity, using a Hg pool WE at E_{appl} = −1.70 V vs Ag/AgCl in phosphate solution (pH 7.0) gave a TON_{H2} of 1050 with FE_{H2} of 96% after 3 h. Activity plateaued after longer CPE times, whereas photocatalysis gave 3-fold higher TON_{H2} values (section 2.2.5.2).[271] Two pyridine derivatives give Ni-based HECs that operate in neutral aqueous media.[272,273] MeCN solutions of **Ni18** and **Ni19** both show metal-centered one-electron reduction waves in CV, with catalytic onset overlaying these events upon addition of AcOH. CPE using **Ni18** and **Ni19** formed H_2, with a GC WE at E_{appl} = −1.45 V vs Ag/AgCl in aqueous phosphate solution (pH 7.0) giving respective FE_{H2} values of 91% and 88% over 1 h (no TON_{H2} reported).[272,273]

Owing to their ubiquity in H_2ases and redox-active properties, thiolate ligands have been widely applied in HECs.[58,140,141,221] Bis(dithiolene) ligation gives **Ni20**, with a ligand-radical

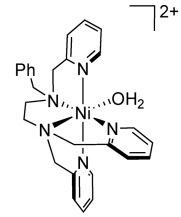

Ni16

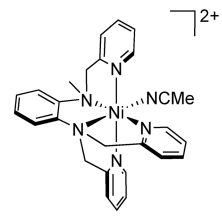

Ni17

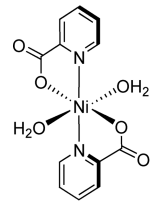

Ni18

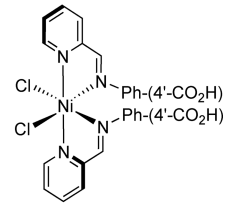

Ni19

structure.[274] When TsOH is added to MeCN solutions of **Ni20**, onset occurs at potentials ∼0.5 V more positive than those of the nonradical complex, **Ni21**. While CPE with **Ni20** confirmed H_2 evolution, it was substoichiometric.[274] Catalytic activity was shown for **Ni22** in DMF containing TFA, with CPE using a GC WE at E_{appl} = −1.67 V vs Fc^+/Fc giving a TON_{H2} of 25 with 83% FE_{H2} after 3 h.[275] Prior studies indicate that reduction largely takes place at the ligands.[276] Notably, DFT revealed that reduced **Ni22** interacts with protons solely through the thiolate S-atoms, without formation of a metal-hydride.[275] A similar mechanism is thought to enable the promising activity of HEC **Ni23**.[277] Using a GC WE in aqueous acetate solution (pH 5.0) at E_{appl} = −0.95 V vs SCE, **Ni23** reached a TON_{H2} of 20 000 with >99% FE_{H2} over 24 h. DFT showed that only ligand-based reductions occur, along with pyrazine protonation through PCET, resulting in metal-hydride formation without low-valent Ni^+ or Ni^0 species.[277]

Ni24 has two radical ligands in the isolated neutral complex, whereas the chelates in **Ni25** are redox innocent.[278−280] Reduction is thus thought to occur at the ligand sites in **Ni24**, while it is nickel-centered in **Ni25**.[279] This may impart the differences in E_{onset} under neutral aqueous conditions for **Ni24** and **Ni25**, which occur at −0.91 and −0.76 V vs NHE, respectively. CPE in phosphate solution (pH 7.0) under air with a GC WE at E_{appl} = −1.21 V vs NHE gave respective TON_{H2} values of 62 000 and 80 000 with FE_{H2} close to 80% after 40 h. Using water from the Genesee River or Gulf of Mexico with dissolved phosphate buffer gave almost identical results after 0.5 h of CPE with **Ni24** or **Ni25**, illustrating the robust nature of these HECs, which also show notable photocatalytic activity (section 2.2.5.2).[279]

Among the most developed Ni-based HECs are those commonly referred to as "DuBois-type" complexes, which feature bis(diphosphine) ligation.[58] Similarly to H_2ases these HECs possess pendant amine proton relays and can operate close to thermodynamic potentials, as shown by their ability to catalyze H_2 oxidation under certain conditions.[58,281,282] They show a CV-derived TOF_{H2} > 10^5 s^{-1}, in the presence of strong acids.[99,120,283,284] Phosphorus and nitrogen functionalities further allow modulation of ligand design and tuning of activity and solubility. Due to water insolubility, these HECs have largely been studied in nonaqueous solvents with organic acids, though H_2O addition improves activity in many cases.[58,285,286]

Initial studies employed **Ni26** and **Ni27**.[286] CV with either complex in MeCN displayed a reversible and a variable feature at

DOI: 10.1021/acs.chemrev.8b00392
Chem. Rev. 2019, 119, 2752−2875

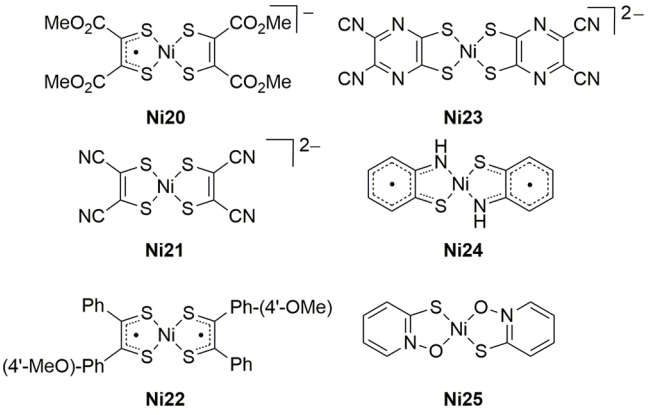

negative potentials, assigned as a Ni^{2+}/Ni^{+} couple and formation of a Ni^{0} species (which may precipitate on the WE). Adding triflic acid to MeCN solutions of **Ni26** induces catalysis associated with the Ni^{2+}/Ni^{+} couple, and CPE using a GC WE at $E_{appl} = -0.94$ V vs Fc^{+}/Fc gave a TON_{H2} of 6.5 with 99% FE_{H2} over an unspecified time. In the presence of TEA and H_2, **Ni27** exhibits an oxidative catalytic wave at potentials slightly positive of the Ni^{2+}/Ni^{+} couple.[286] This H_2ase-like reversible behavior has also been shown using the related **Ni28**, which displays both reductive and oxidative catalytic waves in a single CV cycle.[287] In-depth analysis in MeCN with **Ni26** and acids of different strengths revealed two competing mechanistic pathways for H_2 evolution, with reaction of the Ni^{+} species only occurring if the proton source is sufficiently strong, as depicted in Figure 9.[288]

Another factor influencing the activity of these HECs is the isomeric state of the protonated species.[288−292] Each ring segment linking adjacent P-atoms in the cyclic ligands can adopt an orientation with the proton at the bridgehead nitrogen positioned toward (*endo*) or away from (*exo*) the nickel axial sites, with stabilization of the latter via intramolecular N−H···N hydrogen bonding also possible (pinched-*exo*, Figure 9).[283,289,292,293] While both isomers are similar in energy and thus in equilibrium, experimental and computational evidence indicates that H_2 formation is promoted by intramolecular proton donation from the pendant amines to the nickel center, which requires the *endo*-configuration.[288−292] Favoring *endo*-protonation and facilitating conformer interconversion are thus two desirable attributes for optimizing the performance of these HECs.[283−285,294]

Ni29-**Ni35** possess different substituents at their pendant amine phenyl-groups.[284,285,295] The presence of H_2O improves activity in almost all cases, with the water thought to act as an unencumbered proton shuttle, assisting conformer interconversion and readily protonating the less sterically accessible *endo*-species.[283−285] Hydroxy-modified **Ni34** is a notable example that exhibits a TOF_{H2} of just 35 s^{-1} in anhydrous MeCN containing $[(DMF)H]^{+}$, but shows a dramatically enhanced value of 170 000 s^{-1} in H_2O:MeCN (≈1:1) solutions containing $HClO_4$.[284] CPE in the latter medium using a GC WE with $E_{appl} = -1.23$ V vs Fc^{+}/Fc gave a TON_{H2} of 262 with a FE_{H2} of 94% over 1 h. While these metrics show promise, **Ni34** is nonetheless still insoluble in solutions containing less than 25% MeCN.[284]

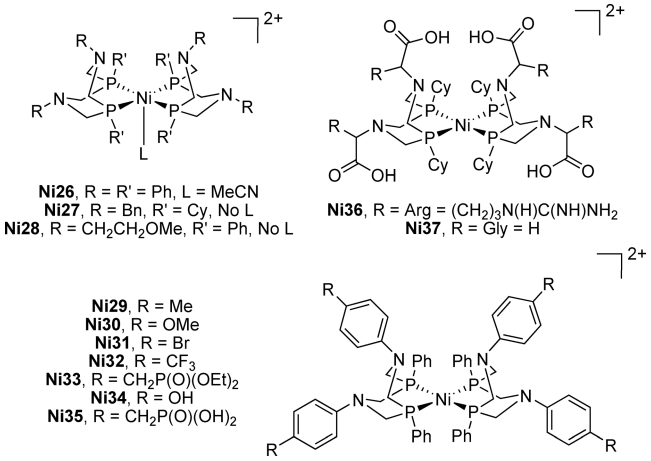

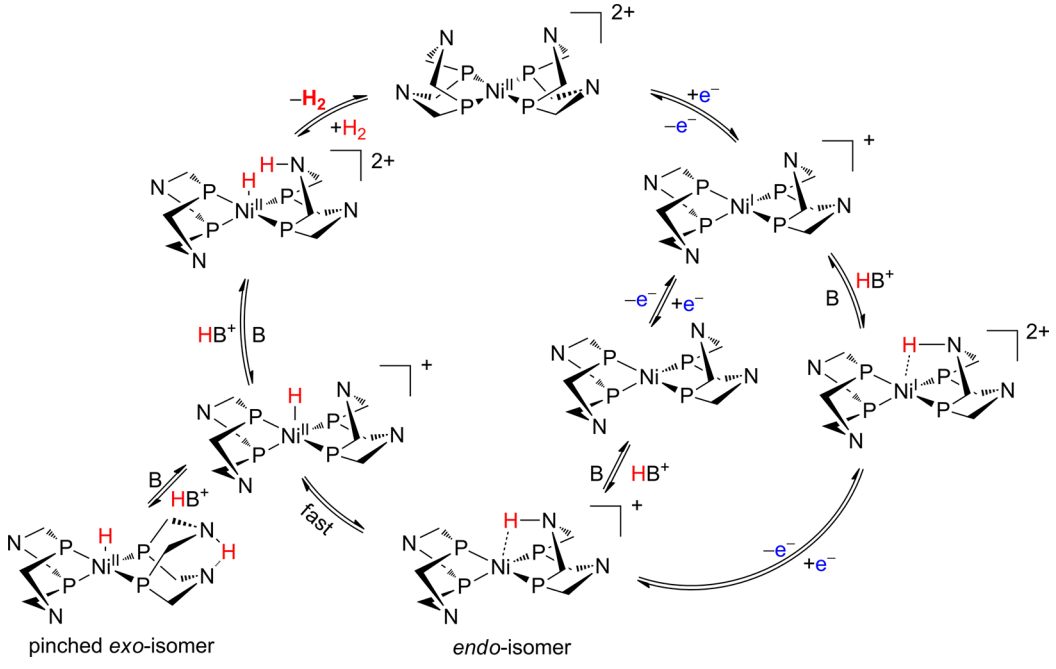

Figure 9. H_2 evolution mechanism for DuBois-type HECs.[288] P and N substituents omitted for clarity (B = base). Weak Brønsted acids promote the center route, whereas stronger ones favor the right pathway.

DOI: 10.1021/acs.chemrev.8b00392
Chem. Rev. 2019, 119, 2752−2875

Functionalization with phosphonic acid, arginine, or glycine residues gives **Ni35**-**Ni37**, all of which are soluble in fully aqueous solutions.[295,296] The phosphonic acids in **Ni35** also allow anchoring to metal oxides, and this HEC has largely been studied in homogeneous and heterogeneous photocatalytic systems (sections 2.2.5.2, 5.2, 6.3, and 7.2.6). Both **Ni36** and **Ni37** show reversible H_2 production/oxidation in aqueous solutions (pH 1.0) under 1 atm 25% H_2/Ar at 348 K.[296] A TOF_{H2} of 300 s^{-1} resulted for **Ni36**, 100-fold greater than that for **Ni37**, and this has been attributed to arginine-arginine interactions which favor positioning of the pendant-amine groups in close proximity to the nickel center (no CPE data given).[296,297] Incorporation of **Ni26** into the protein scaffold of Photosystem I is an alternative strategy which has been used to impart water solubility, though the resulting hybrid was studied under photocatalytic conditions (section 2.2.5.2).[298]

Avoiding inactive pinched-*exo* isomers by removing a pendant amine from the chelate rings of DuBois-type HECs has also been thoroughly explored.[283,293,294,299−301] **Ni38**-**Ni43** are coordinated by two 7-membered cyclic diphosphines featuring a single N-atom, with **Ni38** and **Ni39** showing CV-derived H_2 evolution rates of 100 000 s^{-1} in MeCN containing H_2O and $[(DMF)H]^+$.[283,294] These TOF_{H2} values are ∼100-fold greater than those achieved under comparable conditions with 8-membered analogues having two pendant-amines.[283,285,294] They also exceed the benchmark values of H_2ases, though the enzymes operate in aqueous solution and without an η of 500 mV.[283,294] CPE with **Ni38** and **Ni39** in MeCN containing $[(DMF)H]^+$ using a GC WE held at E_{appl} = −1.4 V vs Fc^+/Fc gave a TON_{H2} of 11 with a FE_{H2} of 99% over an unspecified time frame for both HECs. Rate increases of 3-fold upon addition of H_2O were again attributed to the ability of water to shuttle protons between the *exo*- and *endo*-isomers.[283,294] In support of this proposal, **Ni44** showed no change in activity upon H_2O addition.[299] Conversely to the above examples, which all involve tertiary amines, **Ni44** has secondary N-atoms. As such, it features both an *endo*- and *exo*-proton in the corresponding catalytic intermediate, and thus shows activity that is not influenced by external bases.[299]

Contracted 7-membered rings have also been modified with amino acids.[300,301] **Ni45** features two β-hairpin peptides, with CV in H_2O:MeCN (1:9) containing $[(DMF)H]^+$ revealing a TOF_{H2} = 106 000 s^{-1}, similar to that for **Ni38** and **Ni39**.[294,300] In contrast to the parent HECs which begin to decompose after 30 min in acidic MeCN, **Ni45** is stable over 48 h under comparable conditions.[294,300] CPE using **Ni45** in H_2O:MeCN (1:9) containing $[(DMF)H]^+$ with a GC WE at E_{appl} = −1.35 V vs Fc^+/Fc gave a TON_{H2} of 265 with 92% FE_{H2} over 30 min.[294,300] Related derivatives show increased aqueous solubility but no improvements in activity.[301]

A few other nickel-phosphines have been studied electrochemically but rarely with H_2O present.[302−304] One exception is **Ni46**, which shows catalytic currents in CV under aqueous conditions upon two-electron reduction of the complex.[305,306] CPE in aqueous H_2SO_4 (pH 1.0) using a GC foam WE at E_{appl} = −0.60 V vs NHE gave 92−105% FE_{H2} with a TON_{H2} of 7−9 after 18 h.[306] The charge passed over this time remains linear and a TOF_{H2} of 1850 s^{-1} resulted from CV analysis.[306] Despite showing good stability, the metrics of **Ni46** are modest when compared with DuBois-type complexes. The latter HECs are indeed much more developed, and have been used in several photocatalytic and hetereogeneous systems.

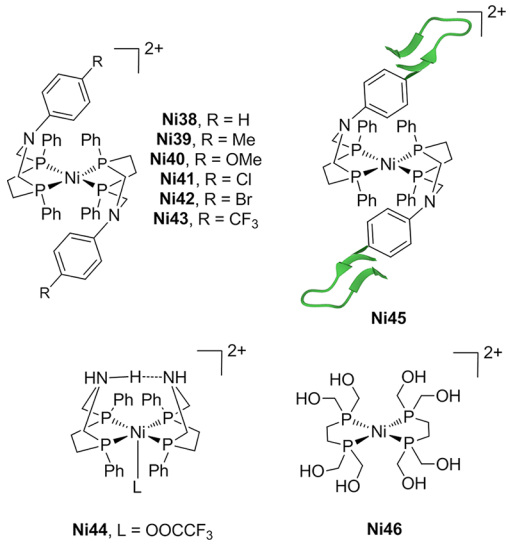

2.2.5.2. Photocatalysis. The first reports of photocatalytic H_2 formation with nickel complexes used dithiolenes **Ni47** and **Ni48**.[307,308] Irradiation (λ > 254 nm) of **Ni47** in H_2O:THF (9:1) gave a TON_{H2} of 36 after 22 h. Isotopic labeling showed that some of the H_2 originates from THF, which may also act as a SED.[307] **Ni48** gave a similar TON_{H2} of ∼30 when illuminated (λ > 350 nm) for 5 h in H_2O:acetone (3:7), though with 10-fold excess ethylenediaminetetraacetic acid (EDTA) as a SED and 100-fold excess methyl viologen (MV).[308] The role of MV remains unclear as no H_2 evolution was observed in its absence. The H_2 evolution reaction is thought to proceed via in situ photoreduction of MV, which further reacts with **Ni48**, **Ni48**$^-$ and H^+. These examples are exceptions as they do not require an additional PS, which is usually the case for the more recently reported systems below that employ a range of molecular dyes such as **PS1**, **PS2**, **PS8**, **PS17**, **PS18**, and **PS19**.

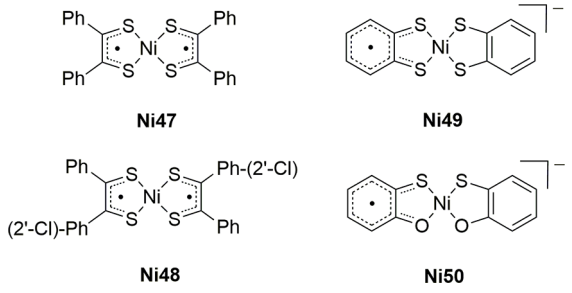

DuBois-type HEC **Ni26** showed linear activity over 150 h, displaying excellent stability, but requires readdition of fresh PS and SED at various intervals.[309] Illumination (λ > 410 nm) of **PS1** in H_2O:MeCN (1:1) containing AA (pH′ 2.25) thereby gave a TON_{H2} of 2700 for **Ni26** over 150 h.[309] In contrast, **Ni26** pre-incubated with Photosystem I to give a hybrid with a single catalyst per protein monomer plateaued at a TON_{H2} of 1870 when irradiated (λ > 500 nm) for 3 h in aqueous MES solution (pH 6.3) containing AA as a SED and cytochrome c_6 as a mediator.[298] Phosphonated analogue **Ni35** achieves comparable activity under completely aqueous conditions.[295] Using **PS19**, irradiation (λ > 420 nm) of AA solutions (pH 4.5) gave a TON_{H2} of 723 for **Ni35** after 2 h (QY_{H2} = 9.7% at λ = 460 nm). Higher HEC concentration gave a lower rate, with the system remaining active for 30 h, but H_2 production still leveled off at a TON_{H2} value of 651. This suggests system performance is

DOI: 10.1021/acs.chemrev.8b00392
Chem. Rev. 2019, 119, 2752−2875

limited by the HEC lifetime, a proposal further supported by partial reactivation upon addition of fresh **Ni35**.[295]

Dithiolene **Ni49** has been studied in aqueous media together with similar HECs featuring a variety of heteroatoms, including **Ni24**, **Ni25**, and **Ni50**.[279] **Ni24** performed best, reaching a TON_{H2} of 6190 after 96 h of LED illumination (λ = 520 nm) in H_2O containing TEOA (pH 9.8) and **PS8**, with **Ni25** and **Ni50** giving respective TON_{H2} values of 5900 and 5600. **Ni24** showed a neglible change in activity with Hg^0 present, providing evidence for a molecular active species.[279] **Ni49** was inactive with **PS8**, though when CdSe QDs were used as PSs with AA (pH 4.5) a TON_{H2} of 105 300 resulted over 168 h.[279] However, when QD solutions with $Ni(NO_3)_2$ instead of **Ni49** were irradiated under almost identical conditions a signficant amount of H_2 was evolved, implying that the activity of molecular **Ni49** is minimal at best.[259]

Ni51-**Ni56** feature similar donor sets to that in **Ni24**.[310] Irradiation (λ > 400 nm) together with **PS2** in H_2O:THF (1:3) containing TEOA gave the highest respective TON_{H2} values of 414 and 416 for **Ni53** and **Ni55**, though a TON_{H2} of 234 also resulted with equimolar $Ni(OAc)_2$. Hg^0 presence led to severely diminished activity, implicating a heterogeneous active catalyst.[310] **Ni57** has an analogous coordination sphere, though features a more flexible ligand that grants water solubility.[311] After 24 h irradiation (λ > 420 nm) of aqueous **PS8** solutions with 5% TEA (pH 11.6) **Ni57** reaches a TON_{H2} of 1510. Hg^0 had a negligible effect on activity, and no H_2 was observed when **Ni57** was exchanged with $Ni(OAc)_2$, both in agreement with a molecular active species. DFT studies show that one of the HEC S-atoms reversibly accepts a proton during catalysis, acting as a relay to aid H_2 formation.[311]

Related chelation is found in **Ni58**.[312] LED illumination (λ = 520 nm) of **PS8** in H_2O:EtOH (1:1) with 5% TEA (pH′ 13) gave a TON_{H2} of 3300 over 70 h, with almost linear H_2 evolution during this time. Hg^0 did not alter performance. Kinetic analysis indicates that the PS and HEC likely form an adduct through π-stacking or dye coordination to the metal center, which may contribute to the system stability.[312] Remarkably high activity has been reported for **Ni59**, which features two thiosemicarbazone ligands.[313] When irradiated (λ > 400 nm) with **PS8** in H_2O:EtOH (1:1) containing 5% TEA (pH′ 12.5) **Ni59** reached a TON_{H2} of 8000 over 24 h.[313] Crystallographic analysis of **Ni59** revealed a short intramolecular distance of 2.82(5) Å between the nickel center and one of the ligand N−H protons, with enhanced acidity of the latter likely due to resonance stabilization.[313]

Ni60 features S4-ligation, and with **PS3** in H_2O:MeCN (1:1) containing 10% TEA (pH′ 10.0) gives a TON_{H2} of 676 after 4 h irradiation (λ > 420 nm).[257] One of the ligand S-atoms is believed to act as a relay, supplying a proton to the presumed metal-hydride intermediate.[257] A similar role is proposed for an N-atom in the mechanism of pyridine-thiolate **Ni61**.[314,315] Together with **PS8**, LED illumination (λ = 520 nm) of **Ni61** in H_2O:EtOH (1:1) containing 5% TEA (pH′ 12.2) gave a TON_{H2} of 5500 after 40 h.[314] Recovery of activity required both PS and HEC readdition, suggesting degradation of both components limits system lifetime. Performance was not affected by Hg^0. Mechanistic studies indicate that **Ni61** must be protonated to become catalytically active, with dissociation of a pyridine N-donor thought to provide a site for this to occur, reminiscent of the proton shuttling which occurs in H_2ases.[314]

Ni61 was later studied in more detail, along with a series of derivatives.[315] Over 30 h using LED illumination (λ = 520 nm)

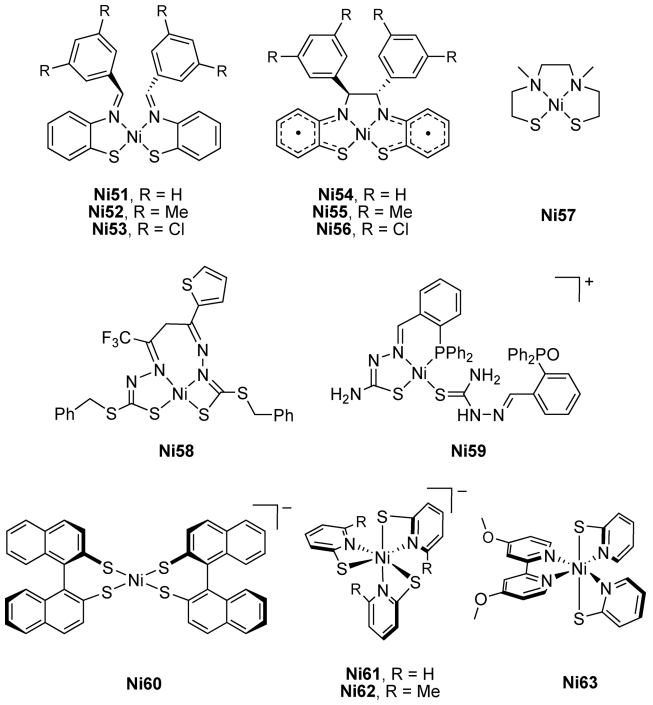

of H_2O:EtOH (1:1) solutions containing TEA (pH′ 11.6) and **PS8**, the HECs **Ni62** and **Ni63** showed the best performance with respective TON_{H2} metrics of 5020 and 7335, whereas **Ni61** gave a TON_{H2} of 3750. The improved activity was correlated with increasing ligand electron density, resulting in a more reactive metal-hydride intermediate.[315] Methylation adjacent to the N-atom is thought to promote dissociation of the latter, allowing it to more readily act as a proton relay, in agreement with the mechanism proposed above.[314,315] Contribution of the bpy to activity was not specifically addressed, though a later study reports moderate performance for the tris(bpy) complex, **Ni64**.[315,316]

Using Ir dye **PS17** in H_2O:MeCN (1:4) containing TEOA (pH′ 9.0), **Ni64** reached a TON_{H2} of 520 after 12 h of LED illumination (λ > 420 nm).[316] In contrast, dioxime **Ni65** gave a TON_{H2} of 42 under the same conditions. Two-electron reduction of **Ni64** causes loss of a bpy ligand, giving the 4-coordinate active species.[316] **Ni66** is related to the latter but features an extra N-heterocyclic unit, which likely serves as a proton relay.[317] Under irradiation (λ > 450 nm) with **PS8** in H_2O:EtOH (1:1) with 5% TEA (pH′ 10.5) **Ni66** gave a TON_{H2} of 3230 in 24 h. H_2 evolution then ceased but could be restored by addition of fresh HEC, consistent with a molecular active catalyst, and Hg^0 also had a negligible effect on activity. DFT results suggest that a Ni^{2+}−H species forms after reduction to a Ni^0 state. The noncoordinated N-donor then brings a proton into close proximity, facilitating H_2 bond formation.[317]

Polypyridyl HEC **Ni17** shows results comparable to **Ni66** using similar conditions but features a redox-active ligand.[271] LED illumination (λ = 520 nm) of **PS8** in H_2O:EtOH (1:1) with 5% TEA (pH′ 12.0) gave a TON_{H2} of 3500 over 24 h. Hg^0 had no effect on activity. DFT indicates that, after metal-centered reduction, a pyridine unit accepts an electron to give a $Ni^+(L^{\bullet-})$ radical. While this species can form an active Ni^{2+}−H state without a Ni^0 intermediate, it may contribute to deactivation by ligand degradation.[271] NiPc HEC **Ni67** also features an intermediate ligand radical species.[318,319] Irradiation (λ > 420 nm) with **PS17** in H_2O:acetone (8:2) containing TEOA (pH′

DOI: 10.1021/acs.chemrev.8b00392
Chem. Rev. 2019, 119, 2752−2875

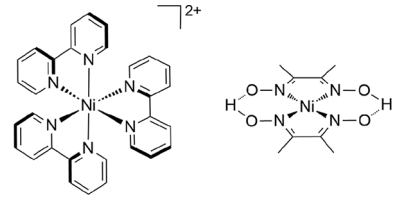

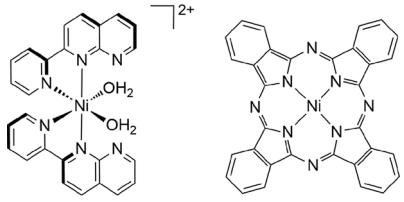

10.0) gave a TON_{H2} of 680 over 8 h (QY_{H2} = 0.82% at λ = 420 nm).[320] Adding PS reactivates the system, implying that **Ni67** remains stable.[320]

A few multinuclear nickel-HECs function in semiaqueous media. The two nickel centers in $\mathbf{Ni_2 2}$ feature different donor sets whereas related $\mathbf{Ni_2 3}$ has equivalent metal sites, despite both possessing identical ligands.[321] Irradiation (λ > 400 nm) of **PS8** in H_2O:MeCN (1:1) with 5% TEOA (pH′ 10.5) gave a TON_{H2} of 320 for $\mathbf{Ni_2 2}$ after 11 h, whereas $\mathbf{Ni_2 3}$ reached a TON_{H2} of 115. Higher activity for $\mathbf{Ni_2 2}$ was ascribed to the more sterically accessible sulfur-ligated nickel center, which is the initial site of reduction based on DFT results.[321]

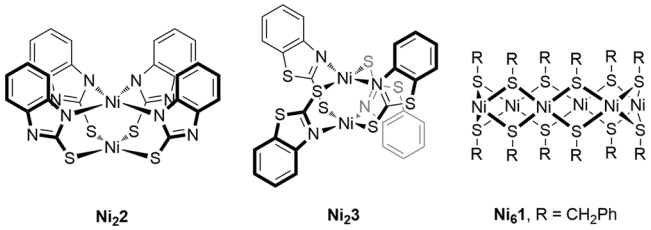

A remarkable QY_{H2} of 24.5% at λ = 460 nm has been reported using aqueous TEOA solutions containing $Ni(OAc)_2$, 2-mercaptoethanol, and an organic PS.[322] A cyclic $[Ni(SCH_2CH_2OH)_2]_6$ hexamer formed in situ was proposed as the active species on the basis of MS findings.[322] A later study investigated $\mathbf{Ni_6 1}$.[323] LED illumination (λ = 460 nm) with **PS18** in H_2O:THF (1:8) containing 10% TEA resulted in a TON_{H2} per cluster of 3750 over 25 h. Importantly, Hg^0 had a minimal effect on performance, supporting the molecular nature of the active species.[323]

2.2.6. Copper. Molecular copper HECs that operate in the presence of H_2O have only started to be explored in the past decade and examples are still limited. A considerable number undergo electrodeposition, forming heterogeneous copper-containing products which may be more active than their molecular precursors.[324−328] Indeed, Cu^+ disproportionates under aqueous conditions, readily giving metallic Cu^0 and Cu^{2+} at RT.[329,330] These factors make assignment of the true catalytic species particularly important in the case of copper.

2.2.6.1. Electrocatalysis. Polypyridine complex **Cu1** illustrates the challenges associated with identifying the active catalyst.[328,331] CPE with **Cu1** using a GC WE at E_{appl} = −0.90 V vs NHE in aqueous phosphate solution (pH 2.5) gave a FE_{H2} of 96% after 0.5 h, with a TON_{H2} of 14 000 over 2 h.[331] Two PCET reduction events were identifed, with spectroscopic data showing that **Cu1** initially forms a pyridine-protonated Cu^+ state. PCET at the metal center then gives a Cu^{2+}−H species which reacts with the pyridinium unit to form H_2.[331] Repeating CPE in fresh buffer after rinsing a GC WE operated with **Cu1** for 2 h showed ∼7% relative activity, and traces of Cu-containing particles were found by scanning electron microscopy (SEM) and energy-dispersive X-ray (EDX) spectroscopy.[331] A later study used similar conditions (−0.90 V vs NHE, pH 1.5) to show that **Cu1** decomposed with Pt leached from the counter electrode, forming nanoparticle films that rival Pt-electrodes in terms of catalytic current densities.[328]

Cu2 is thought to form a $Cu^+(L^{\bullet-})$ pyridine-radical active species.[332] CPE using a Hg pool WE at E_{appl} = −1.70 V vs Ag/AgCl in aqueous phosphate solution (pH 7.0) gave a TON_{H2} of 1670 over 3 h, reaching a TON_{H2} of 3060 after 18 h, but with the FE_{H2} dropping from 90% to 45% over this time. UV−vis spectra show significant changes after 3 h CPE, and to further assess system deactivation a graphite foil WE was then used. Postelectrolysis SEM and X-ray photoelectron spectroscopy (XPS) analysis showed no evidence of electrodeposition, suggesting that the HEC is molecular in nature despite structural similarity to **Cu1**.[332]

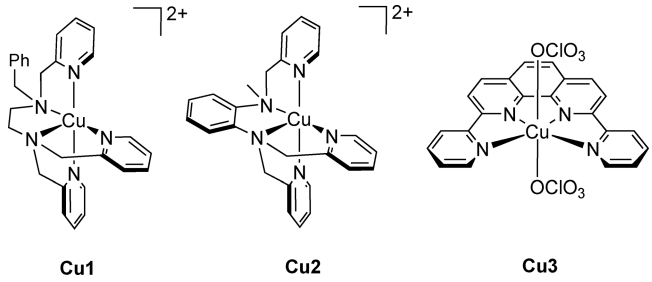

Cu3 shows two irreversible reduction events in MeCN, assigned as copper-centered by comparison with free ligand.[333] Similar behavior occurs in aqueous phosphate buffer (pH 7.0), with catalytic onset at more negative potentials (−0.90 V vs NHE), indicative of a Cu^0 active species. CPE under these conditions using a GC WE at E_{appl} = −1.40 V vs NHE gave a FE_{H2} of 95% with a TON_{H2} of ∼700 after 2 h. Postelectrolysis analysis using DLS, SEM, and EDX spectroscopy showed no evidence of heterogeneous species, and solution UV−vis spectra were almost identical before and after catalysis.[333]

Cu4 shows two quasi-reversible redox couples in DMF, both ascribed to one-electron copper-centered processes.[334] Adding AcOH to DMF solutions triggered catalytic onset that overlaps with the Cu^+/Cu^0 reduction wave.[334] In contrast, the parent complex **Cu5** deposited metallic copper on GC electrodes when reduced to the Cu^0 state in DMF and showed changes at the Cu^{2+}/Cu^+ couple upon addition of AcOH.[335] Catalysis is also observed with **Cu4** in H_2O:MeCN (3:2) phosphate solution (pH′ 7.3) at E_{onset} = −1.20 V vs Ag/AgCl, with CPE in the same media (pH′ 7.0) using a GC WE at E_{appl} = −1.43 V vs Ag/AgCl giving a FE_{H2} of 91% with a TON_{H2} of ∼3600 over 1 h.[334] The charge passed was almost linear over 72 h, though no postelectrolysis analysis was reported.[334] **Cu6** features a related donor set but is water soluble.[336] CPE in aqueous solution (pH 7.0) at E_{appl} = −1.45 V vs Ag/AgCl using a GC WE gives a FE_{H2} of 96% with a TON_{H2} of ∼2300. Electrodes rinsed after CPE and operated again in blank buffer solution gave similar results to freshly polished electrodes.[336]

A group of copper-triazenido complexes show promising HEC activity, though further investigation is required to

DOI: 10.1021/acs.chemrev.8b00392
Chem. Rev. 2019, 119, 2752−2875

establish the identity of the catalytically active species. CV of **$Cu_2$1** in DMF showed two reductive features, assigned as sequential Cu^{2+}/Cu^{+} and Cu^{+}/Cu^{0} metal-based reductions.[337] Adding AcOH triggers catalysis at potentials slightly positive of the proposed Cu^{+}/Cu^{0} couple. In aqueous phosphate solution (pH 6.0) an E_{onset} of ~−1.25 V vs Ag/AgCl was observed, and H_2 was identified after CPE in the same media with a GC WE at E_{appl} = −1.47 V vs Ag/AgCl. Charge passed over 72 h was relatively linear, but no FE_{H2} was reported.[337] **$Cu_2$2** exhibited two reductive waves which were also interpreted as sequential Cu^{2+}/Cu^{+} and Cu^{+}/Cu^{0} events, with onset of catalysis at potentials slightly positive of the latter reduction.[338] CPE in H_2O:MeCN (3:2) phosphate solution (pH′ 7.0) with a GC WE at E_{appl} = −1.45 V vs Ag/AgCl gave a FE_{H2} of 97% with a TON_{H2} of ~4600 over 1 h.[338] **$Cu_3$1** also features a triazenido ligand and shows 94% FE_{H2} with a TON_{H2} of ~6200 after 1 h CPE with a GC WE at −1.40 V vs Ag/AgCl in H_2O:MeCN (3:2) phosphate solution (pH′ 7.0).[339] While electrodes remained colorless after CPE, limited further analysis was conducted, and the current passed over a 72 h experiment appears nonlinear.[339]

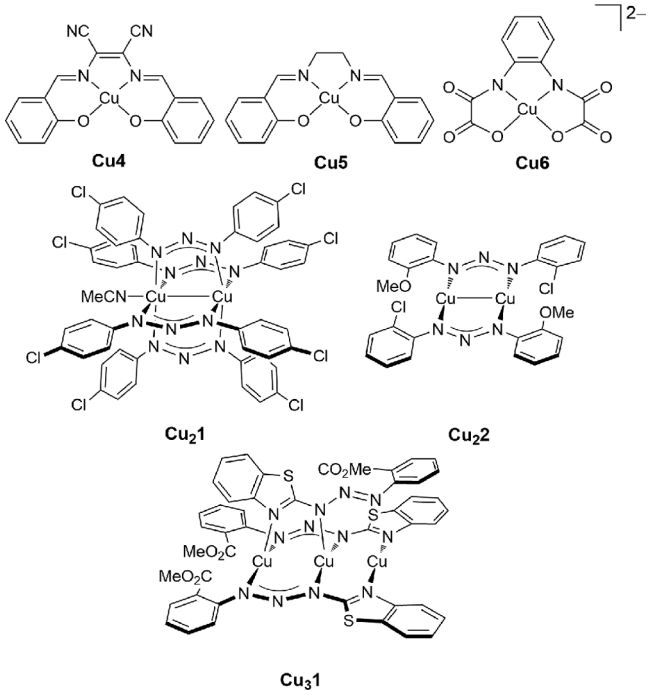

2.2.6.2. Photocatalysis. Light-driven systems with copper HECs are rare. TPA-complexes **Cu7** and **Cu8** reached respective TON_{H2} values of 6108 and 10014 after 6 h when irradiated (λ > 400 nm) in H_2O:MeCN (1:9) with TEA and **PS20** (QY_{H2} = 3.4 and 5.6%, respectively).[340] Ligand non-innocence may enable the greater activity of **Cu8**, as shown by electrochemical comparison with the analogous Zn-complex. However, CPE at E_{appl} = −1.8 V vs SCE (details not specified) showed little difference between the HECs, giving a FE_{H2} of ~95% over 2 h in both cases. Assessment of heterogeneous degradation products was not reported.[340] **Cu3** was also studied under semiaqueous conditions, but irradiation (λ > 400 nm) with **PS3** in H_2O:MeOH (1:2) yields a very low TON_{H2} of only 6 over an unspecified time.[333] In contrast, **$Cu_2$3** gave a TON_{H2} of 2135 over 20 h in H_2O:DMF (1:4) with TEA and **PS8** using visible LED light.[341] While **$Cu_2$3** was stable over 12 h under irradiation in H_2O:DMF (1:4), reactivation of photocatalysis after 22 h required addition of HEC, rather than PS.[341]

The development of copper-based molecular systems for H_2 evolution under aqueous conditions has clearly received significantly less attention than efforts using other 3d transition metals. Complexes related to those discussed above have begun to show promise with respect to catalytic CO_2 reduction, and as such these molecules remain interesting targets for further investigation as HECs.

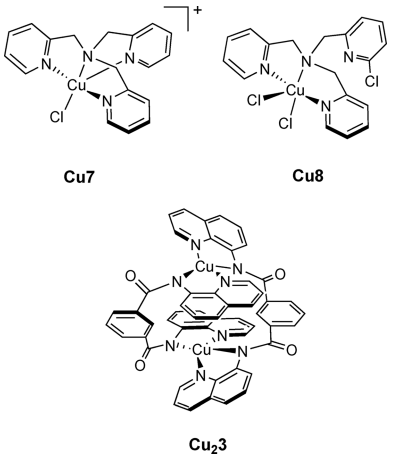

2.2.7. Zinc. To the best of our knowledge, no zinc-based HECs have been reported.

2.2.8. Heterometallic Catalysts. A number of mixed-metal complexes have been investigated as HECs. Taking inspiration from [NiFe]-H_2ases the majority of these systems contain at least one nickel center, though it is often redox inactive, and no studies have been conducted in the presence of water. Trinuclear complexes **Fe_2Ni1** and **FeNi$_2$1** both showed electrochemical features consistent with H_2 formation when analyzed in acidic DCM solutions, but product quantification is lacking for the former, and the latter achieved a TON_{H2} of only 1.5 after 2 h.[342,343] The biomimetic complexes **FeNi1**-**FeNi4** displayed current increases when TFA was introduced to DCM solutions during CV.[344,345] Although no CPE experiments were conducted, complex **FeNi4** showed the earliest onset potential and largest current enhancements, which was attributed to the peripheral pyridine residue acting as a proton shuttle.[344,345]

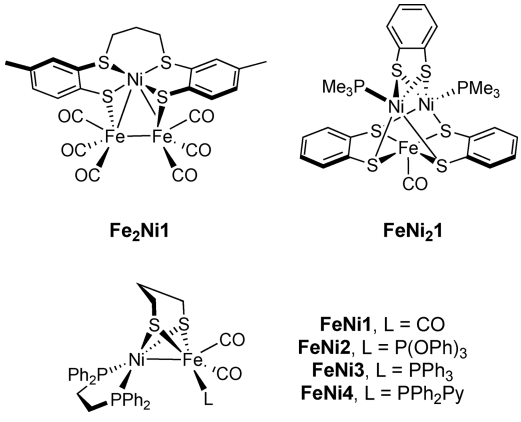

Several heterobimetallic studies employ complexes with cyclopentadienyl-coordinated iron centers. CV scans of **FeNi5** displayed catalytic currents when TFA was added to DMF solutions, with onset occurring at a potential associated with one-electron reduction. CPE at E_{appl} = −1.83 V vs Fc^{+}/Fc using a Hg Pool WE gave a FE_{H2} of 72% with a TON_{H2} of 20 after 4 h.[346]

DOI: 10.1021/acs.chemrev.8b00392
Chem. Rev. 2019, 119, 2752−2875

DFT calculations indicate that **FeNi5** is reduced at the iron-site, inducing loss of a CO unit and formation of a hydride-bridged active intermediate.[346] Despite possessing an almost identical iron coordination sphere, computational analysis of the related **FeNi6** suggests that the bridging thiolate donors act as shuttles which transfer a proton to an intermediate iron-hydride species.[347] Although CPE using a GC WE held at E_{appl} = −1.56 V vs Fc^+/Fc revealed H_2 production with FE_{H2} = 96% after 0.5 h, **FeNi6** gave a substoichiometric TON_{H2} of only 0.26 in MeCN containing TFA.[347]

In contrast to the above cases, the complexes **FeNi7** and **FeNi8** are thought to mediate H_2 production through nickel-centered reactivity. **FeNi7** undergoes reversible single-electron reduction in THF solutions, with onset of a catalytic process overlapping with this feature upon addition of AcOH.[348] DFT studies indicate that initial reduction occurs at the nickel-site, after which formation of a nickel-hydride species is favored over the corresponding protonated thiolate. CPE with a GC WE produced H_2 with FE_{H2} >99% but further experimental details were not reported.[348] CV of **FeNi8** in MeCN displayed two reversible redox couples, each consistent with single-electron transfer.[349] Computational and spectroscopic results support sequential nickel- and bpy-centered reductions to give a $Ni^+(L^{\bullet-})$ radical species, with onset of catalysis correlating with formation of this intermediate upon addition of $[Et_3NH][BF_4]$. CPE at E_{appl} = −1.85 V vs Fc^+/Fc with a Hg pool WE in MeCN containing $[Et_3NH][BF_4]$ gave a FE_{H2} of 70% after 100 min, reaching a TON_{H2} of 16.[349]

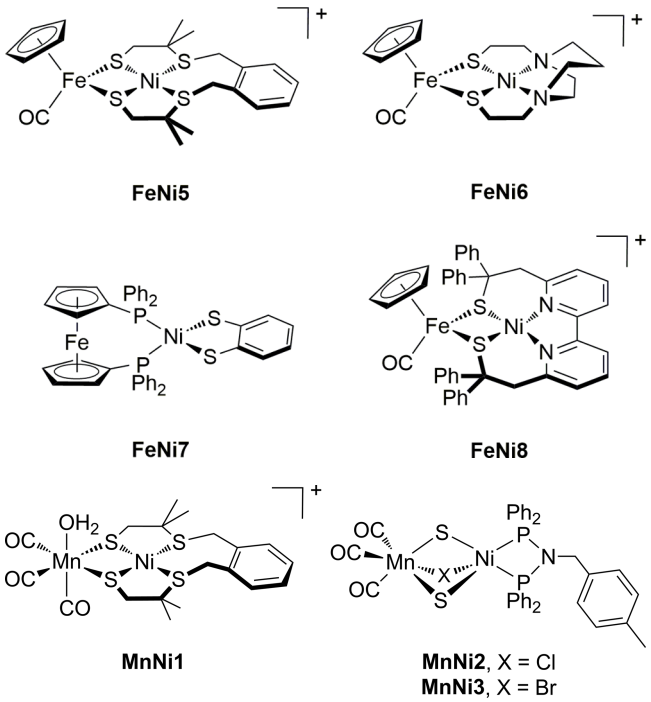

Manganese-nickel heterobimetallic complexes **MnNi1**-**MnNi3** also act as HECs, though again in the absence of water. **MnNi1** shows two irreversible reduction events in CV experiments, with onset of a catalytic wave overlaying the more negative feature when TFA is introduced.[350] DFT modeling suggests that single-electron reduction of both metal ions occurs, after which a hydride-bridged species forms which ultimately liberates H_2 following protonation. CPE with a Hg pool WE held at E_{appl} = −1.6 V vs Ag/AgCl in DMF containing TFA resulted in a TON_{H2} of 15.8 with FE_{H2} = 94% after 4 h.[350] CV analysis of **MnNi2** and **MnNi3** reveals two sequential reductions in each case, with AcOH addition inducing onset of a catalytic current at a potential more negative than both features.[351] No further mechanistic investigation was reported, but catalysis was shown through CPE conducted at E_{appl} = −1.85 V vs Fc^+/Fc with a GC WE. In MeCN containing AcOH, **MnNi2** and **MnNi3** gave respective TON_{H2} values of 10.5 and 9.1, both with FE_{H2} of ∼90% after 0.5 h.[351]

2.2.9. Future Directions. The enzymatic mechanisms for achieving interconversion of protons and molecular hydrogen both proceed by heterolytic pathways, which rely on asymmetric bimetallic active sites. This characteristic is most obviously apparent in the [NiFe]-H_2ases but is also provided to a large extent by the surrounding proten architecture, particularly in the [FeFe]-H_2ases. This proximal functionality also assists in proton and electron transfer, aids in substrate activation and intermediate stabilization, and can facilitate atypical metal geometries and coordinatively unsaturated metal centers. Engineering complexes that faithfully recreate these functional properties is synthetically demanding, and given the inverse correlation between stability and reactivity such species are likely to be intrinsically fragile. Immobilization of molecular catalysts can provide asymmetry as a feature inherent to interfaces and impart a greater degree of control over the local environment by spatially confining system components (e.g., HEC and PS). Such localization can help avoid unwanted side-reactions, improving selectivity and making a system more robust, and may be further accentuated through the use of polymer matrices (see sections 4−7). Combining the above approaches is a promising strategy for creating improved catalytic systems, and a detailed understanding of how each contributes to the overall performance is vital to utilizing them in a productive fashion for achieving solar fuel generation.

2.3. Carbon Dioxide Reduction Catalysts

2.3.1. Scandium and Titanium. To the best of our knowledge, only a couple of reports exist detailing reduction of CO_2 by early 3d transition metal complexes containing scandium or titanium. These examples show stoichiometric reactions in nonpolar solvents, giving metal-bound oxalate products, likely as a result of their oxophilic nature and the high stability of their oxidized states.[352,353]

2.3.2. Vanadium. Although no synthetic vanadium complexes have yet achieved CO_2 reduction, this metal ion is present as a component of a large FeS cluster in the active site of some nitrogenases (N_2ases).[354−356] Several studies demonstrate that these biological sites reduce CO_2 into a range of carbon-containing products including CO and CH_4, as well as higher C_2-C_4 hydrocarbons.[354,355] Molecular vanadium complexes or clusters may thus represent an unexplored avenue for CRCs able to achieve CO_2 reduction directly into liquid fuels.

2.3.3. Chromium. Molecular chromium complexes have received little attention as CRCs. An exception is $[Cr(CO)_6]$, owing to the minor presence of chromium in some catalysts used industrially in the water-gas shift reaction ($CO + H_2O \rightarrow CO_2 + H_2$).[357−359] Two-electron reduction of $[Cr(CO)_6]$ affords $[Cr(CO)_5]^{2-}$, which can react with a proton source such as H_2O to generate $[HCr(CO)_5]^-$. Whereas CO_2 inserts into this hydride to give an O-bound formate adduct, $[(HCO_2)Cr(CO)_5]^-$, reaction with H_2O liberates H_2 and produces the stable hydride-bridged dimer, $\{(\mu\text{-}H)[Cr(CO)_5]_2\}^-$.[358] Conversely, under aprotic conditions, $[Cr(CO)_5]^{2-}$ mediates CO_2 cleavage to give the neutral hexacarbonyl along with an

DOI: 10.1021/acs.chemrev.8b00392
Chem. Rev. 2019, 119, 2752−2875

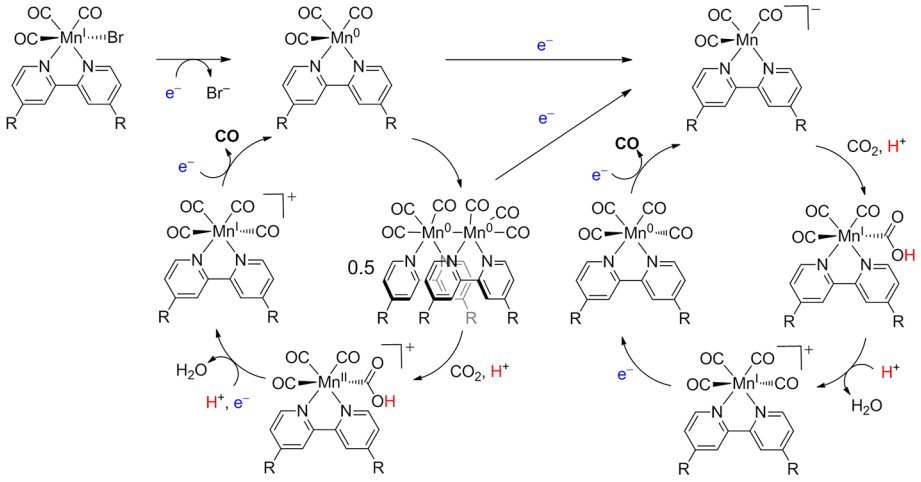

Figure 10. Reaction pathways for $[MnBr(bpy\text{-}R)(CO)_3]$-type CRCs. Different substituents (R-groups) and experimental conditions influence the mechanistic details.

equivalent of carbonate ($[M(CO)_5]^{2-} + 2CO_2 \rightarrow [M(CO)_6] + CO_3^{2-}$).[360] CV of $[Cr(CO)_6]$ under Ar in MeCN or DMF shows an irreversible reduction wave for the formation of $[Cr(CO)_5]^{2-}$ at ∼−2.5 V vs Fc^+/Fc, which becomes catalytic under CO_2. Adding varying amounts of H_2O (up to ∼5%) increasingly suppresses this catalytic current, most likely due to hydride formation.[361] This exemplifies just one of the many challenges associated with CO_2 reduction when moving from aprotic to aqueous media.

2.3.4. Manganese. *2.3.4.1. Electrocatalysis.* A report revealing that Mn-analogues of *fac*-$[ReCl(bpy)(CO)_3]$ function as CRCs has led to a considerable volume of literature exploring closely related systems.[95,362−364] In contrast to the rhenium CRC, the manganese system shows significant activity only in the presence of a proton source such as water, where high selectivity for CO_2 reduction over the competing H_2 evolution is typically observed.[95,96] CPE with nonsubstituted **Mn1** in H_2O:MeCN (5:95) using a GC WE at E_{appl} = −1.70 V vs $Ag/AgNO_3$ gave a TON_{CO} of 13 with quantitative FE_{CO} after 4 h. FE_{CO} for **Mn1** drops to 85% (along with 15% cogeneration of H_2) after 22 h, whereas methyl-functionalized **Mn6** retains quantitative FE_{CO} with a TON_{CO} of 34 after 18 h.[95]

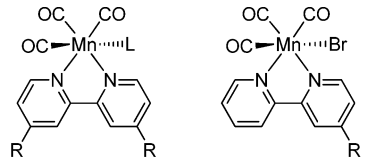

Mn6, R = Me, L = Br
Mn7, R = ^{t}Bu, L = Br
Mn8, R = H, L = CN

Mn9, R = Ph-(4'-NH_2)

Many other *fac*-$[MnBr(bpy\text{-}R)(CO)_3]$ CRCs have been studied by varying the bpy R-group, giving insights into how sterics, electronics, and secondary sphere interactions influence catalysis. One-electron reduction of $[MnBr(bpy\text{-}R)(CO)_3]$ leads to loss of the halido ligand, affording a charge-neutral complex (Figure 10).[96,102] With sterically unrestricted bpy ligands two of these units can undergo Mn−Mn bond formation, producing a dimer with UV−vis absorptions at ∼630 (metal-to-ligand CT) and 810 nm (Mn−Mn $\sigma \rightarrow \sigma^*$).[95,365,366] Further reduction of this homodimer can cleave the metal-metal bond, giving the $[Mn(bpy\text{-}R)(CO)_3]^-$ anion, such as with **Mn1**, **Mn6**, and *tert*-butyl analogue **Mn7**.[95,96] Exposure to CO_2 with a proton donor present typically causes catalytic onset at the potential associated with formation of this anion.[95,96] However, EPR evidence shows that the dimer can also bind and transfer two electrons to CO_2.[367] Regardless of the species which intially reacts, theoretical and experimental studies indicate that a proton is required to stabilize the resulting metallo-carboxylate, accounting for the catalytic dependence on an external proton source.[368,369]

Dimerization is thought to cathodically shift the potential for anion formation, and several studies have explored the effect of inhibiting this process.[102,369] Exchange of the bromido ligand for a more strongly bonding cyanide suppresses anion dissociation and dimerization upon one-electron reduction of **Mn8**.[370] While this initial reduction requires more negative potentials compared to **Mn1**, catalytic current already appears after the transfer of this first electron. This is due to a change in mechanism whereby disproportionation occurs between two of the singly reduced species, regenerating the original **Mn8**, while also producing the catalytically active anion.[370] Subtle changes in the mechanism of these CRCs often greatly impacts upon their activity, which has implications for immobilization. For example, while **Mn9** shows activity comparable to **Mn1** under similar homogeneous conditions, anchoring on a GC WE allows for a 30−40-fold higher TON_{CO}, likely by influencing the mechanism.[64,371]

One notable feature of these Mn-CRCs is the redox-active role played by the bpy unit. While many catalysts cycle between oxidation states largely centered on the metal, both DFT and crystallographic results indicate that the anionic intermediate possesses a reduced bpy ligand.[96,102,372] Indirect evidence for this noninnocence can also be found by comparison with $[Mn(CO)_5]^-$, which shows no catalytic activity toward CO_2 in the presence or absence of water, even at very negative E_{appl}.[361,373] The noninnocent bpy may also impart the selectivity shown by these systems. DFT suggests that electron density on the bpy unit in the highest occupied molecular orbital (HOMO) of the active anion allows for complementary σ- and π-interactions with CO_2. The latter cannot contribute when these CRCs interact with protons, thereby disfavoring hydride formation and suppressing H_2 and HCO_2H production.[102,369] Variation of the bpy unit is thus a powerful strategy for tuning the properties of these CRCs.

DOI: 10.1021/acs.chemrev.8b00392
Chem. Rev. 2019, 119, 2752−2875

Mn5 contains the bulky 6,6′-dimesityl-2,2′-bipyridine ligand, which completely suppresses reduction-induced dimer formation.[102] Instead, **Mn5** accepts two electrons simultaneously to form the corresponding anion at a potential 300 mV more positive than that of unmodified **Mn1**. CV in the presence of H_2O indicates that the anion then undergoes proton-dependent oxidative addition of CO_2 to form a metallo-carboxylic acid adduct. However, significant catalysis is not observed until an additional 400 mV is applied (E_{onset} = −1.90 V vs Fc^+/Fc). IR-SEC results revealed that the metallo-carboxylic acid intermediate must be reduced by an additional electron before C−O bond scission occurs, justifying the extra driving force required to initiate turnover. CPE at E_{appl} = −2.20 V vs Fc^+/Fc with a GC WE in MeCN containing 2,2,2-trifluoroethanol (TFE) gave a TON_{CO} of 4 over 70 min (FE_{CO} of 98%).[102]

Tuning of the electronic properties in these systems has been achieved in the pyridine-(benz)imidazolylidene CRCs **Mn10**, **Mn11**, and **Mn12**, which operate in H_2O:MeCN (5:95).[78,100] Initial reduction occurs at more negative potentials due to the stronger σ-character of the NHC-donors but involves dual ET to give the respective anions in a single step, similarly to **Mn5**.[78,100,374] CPE with **Mn10** and **Mn11** using a GC WE at ∼−1.5 V vs SCE gave CO as the sole gaseous product with a FE_{CO} < 70% after 4 h, revealing losses compared to parent **Mn1**.[78,100] NHC-chelated **Mn13** behaves analogously, but retains a FE_{CO} of 98% over 5 h, giving a TON_{CO} of 14 with a GC WE held at −2.32 V vs Fc^+/Fc.[375]

α-Diimino complexes with various N-substituents, **Mn14**−**Mn19**,[315,316] and mixed pyridine-imine CRCs, **Mn20**−**Mn24**, have also been explored.[376] The steric properties of the ligand influence catalyst speciation upon reduction, with more hindered groups being most effective at impeding dimerization. While electrocatalysis occurred in the presence of CO_2 and H_2O in all cases, catalytic currents were much less pronounced than for **Mn1** and required increased η. A Mn−OCO_2H adduct was identified by IR-SEC studies, suggesting that these CRCs use a different mechanism to the bpy systems, despite sharing other intermediates.[376,377] The Mn−OCO_2H species is proposed to form by CO_2 cleavage, with a second molecule of CO_2 acting as an oxide acceptor to break a C−O bond in the common metallo-carboxylic acid intermediate.[376,377] Further reduction is thought to be required for carbonate dissociation from the product-inhibited state, leading to the high overpotentials needed to drive catalysis.[376,377]

Weak Brønsted acids like H_2O, phenol, and TFE have often been shown to improve the activity of molecular CRCs. Lewis acids such as Mg^{2+} cations can produce similar effects.[150] While the anion formed by **Mn5** reduction reacts with CO_2 and a proton to give a metallo-carboxylic acid, further reduction at higher η is required to achieve C−O bond cleavage. In contrast, CV using **Mn5** in anhydrous CO_2-saturated MeCN with Mg^{2+} cations shows catalytic onset upon anion formation.[378] CV, $^{13}CO_2$ labeling, and IR-SEC studies revealed that a second CO_2 can achieve C−O bond cleavage in the metallo-carboxylic acid, by acting as an oxide acceptor in a magnesium-assisted mechanism. Insoluble $MgCO_3$ forms as a byproduct, rather than a carbonate-inhibited adduct. CPE with a Mg-anode (to replenish precipitated $MgCO_3$) gave a FE_{CO} of 98% over 6 h, with a TON_{CO} of 36 at E_{appl} = −1.60 V vs Fc^+/Fc using a GC WE.[378] This approach utilizes the energetic gains achieved by dimer suppression, but catalytic currents are much less than those obtained without Mg^{2+} cations at higher η.

Mn10, R = Me, NHC = Im
Mn11, R = Et, NHC = Im
Mn12, R = Me, NHC = BzIm

Mn13

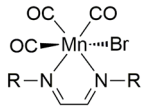

Mn14, R = ^{i}Pr
Mn15, R = Ph-(4'-Me)
Mn16, R = Ph-(2',4',6'-Me_3)
Mn17, R = Ph-(2',6'-^{i}Pr)
Mn18, R = Ph-(4'-Br)
Mn19, R = Ph-(2'-CF_3)

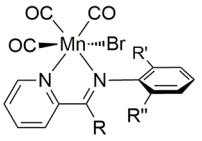

Mn20, R = R' = R'' = H
Mn21, R = R'' = H, R' = ^{i}Pr
Mn22, R = H, R' = R'' = ^{i}Pr
Mn23, R = R'' = H, R' = ^{t}Bu
Mn24, R = Me, R' = ^{t}Bu R'' = H

Covalently tethering proton-donating phenol units to the bpy heterocycle also improves catalysis.[65,100,379] **Mn25** contains a single phenolic functional group,[100] and dimerization, anion formation, and catalytic onset under CO_2 occur by a similar route and at comparable potentials to the unmodified **Mn1** system. However, ∼5-fold greater catalytic currents were achieved for **Mn25**. Methoxy-protected **Mn26** performed similarly to **Mn1**, and linear sweep voltammetry (LSV) with the latter in the presence of 10 equivalents of phenol showed an inhibitory effect on catalysis.[100] These results indicate that the intramolecular proton-donating ability of **Mn25** is responsible for the increase in activity, with computational evidence highlighting the entropic benefits of covalent phenol attachment. CPE with a GC WE at E_{appl} = −1.50 V vs SCE gave a TON_{CO} of 2.7 with a FE_{CO} of 76% over 4 h. Notably, a third catalytic process is observed in CV with **Mn25** at much more negative potentials (E_{onset} = −1.76 V vs SCE). This has been attributed to reduction of phenolic protons in close proximity to the Mn site, hinting at the possibility of a metal-hydride intermediate which may account for the diminished FE_{CO}.[100]

Mn27 features a resorcinol unit linked to the bpy. This CRC shows catalytic currents under CO_2 even without an external proton source, producing traces of H_2 along with CO and HCO_2H (TON_{CO} = 19, FE_{CO} = 70%; TON_{HCO2H} = 6, FE_{HCO2H} = 22%) over 4 h with a GC WE held at E_{appl} = −1.8 V vs SCE.[379] Three cathodic features are observed under Ar, with IR- and UV−vis-SEC studies showing at least five species. This is ascribed to the phenol groups enabling new reaction pathways, such as dimer suppression by chelation of the deprotonated phenoxide moiety and hydride generation through intramolecular proton transfer. The latter of these species is correlated with both H_2 and HCO_2H formation. CPE over 2 h in H_2O:MeCN (5:95) at E_{appl} = −1.5 V vs SCE produces CO, HCO_2H, and H_2 (TON_{CO} = 28, FE_{CO} = 90%; TON_{HCO2H} = 1.4; FE_{HCO2H} = 4%; TON_{H2} = 0.7; FE_{H2} = 2%). Selectivity can be biased toward formate by adding Brønsted acids such as TFE or phenol, giving ∼60% with the latter, albeit with a lower FE (total FE for all products = 60%).[65] A similar system with proximal methoxy groups has also been shown to enable an alternate reaction pathway.[380]

Related complexes have also been studied but often give lower performances than the parent **Mn1**. 2,2′:6′,2″-Terpyridine (tpy)

DOI: 10.1021/acs.chemrev.8b00392
Chem. Rev. 2019, 119, 2752−2875

Mn25, R = H
Mn26, R = Me

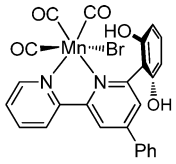

Mn27

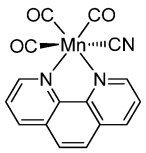

Mn28

CRCs are less stable during catalysis,[381] whereas various pyridine-phosphine ligands result in poor selectivity for CO_2 reduction.[382,383]

2.3.4.2. Photocatalysis. Manganese(I)-tricarbonyl CRCs have also been studied photocatalytically, despite their tendency to release CO upon irradiation.[100,103−108] **Mn1** has two charge-transfer transitions with partial visible absorption, the most intense appearing at 416 nm in MeCN, with minor tailing until ∼550 nm.[95,384] The *fac*-tricarbonyl loses CO when illuminated, but reassociation from solution can form a *mer*-species.[365] In contrast, this *mer*-isomer undergoes homolytic halide loss upon irradiation, giving a radical that reacts further to the Mn-dimer, which absorbs across the entire visible spectrum.[365,367,384] Time-resolved experiments have shown that the latter process occurs very rapidly, approaching the diffusion-controlled limit.[385] The reverse homolytic cleavage of the Mn−Mn bond to give two highly reactive radicals can also occur photochemically, and may contribute in the cases outlined below.[366,386,387]

Monochromatic irradiation (λ = 480 nm) of **PS21** and **Mn1** in DMF:TEOA (4:1) with benzyldihydronicotinamide as a proton source and SED gave a TON_{HCO2H} = 149, TON_{CO} = 12, and TON_{H2} = 14 over 12 h.[388] Absorption of the PS dominates at 480 nm, but UV−vis monitoring revealed an initial build-up of the dimeric species, which rapidly decayed within the first 10−20 min. This correlates with the small amount of CO produced early in the experiment. Similar TONs resulted whether the photoexcited PS potential was matched with (**PS21**) or less than (**PS1**) that of the Mn-dimer, and evidence for paramagnetic species was observed by NMR spectroscopy following photocatalysis.[388] These results suggest that the Mn-dimer produced after initial PS-mediated reduction of **Mn1** undergoes direct photolysis to a radical species, which then reacts with CO_2 to selectively give HCO_2H. Reactivity of such Mn-radicals has seldom been emphasized in electrocatalysis, likely due to their rapid dimerization, but this study highlights that they may yet play a role in photocatalytic systems.

Further support for the reactivity of these radicals is provided by nitrile-bound **Mn8**.[389] Monochromatic irradiation (λ = 470 nm) over 15 h with **PS21** in DMF:TEOA (4:1) solutions of benzyldihydronicotinamide gave TON_{HCO2H} = 130, TON_{CO} = 7, and TON_{H2} = 2, with QY_{HCO2H} = 3.2%. Using MeCN instead of DMF under otherwise identical conditions gave TON_{HCO2H} = 9, TON_{CO} = 21, and TON_{H2} = 1 with QY_{CO} = 0.5%. As described above, CRC **Mn8** retains the axial cyano ligand after reduction and thus does not dimerize. Instead, two of the singly reduced species disproportionate, giving the starting complex and the doubly reduced five-coordinate anion. Comparison between DMF and MeCN using *operando* IR-SEC studies revealed that disproportionation occurs more rapidly in the latter solvent, generating the CO-producing anionic species. Conversely, the singly reduced radical is much longer-lived in DMF, again implying that it may promote HCO_2H production. This study highlights a viable pathway, proposing hydride formation by H-atom abstraction from the SEDs present.[389]

Increases in both photocatalytic performance and CO selectivity were reported for a system using organic dye **PS22**.[390] 1,10-Phenanthroline (phen) CRC **Mn28** was shown to mediate CO_2 reduction in H_2O:MeCN (5:95) with TEA as a SED. Irradiation with a Xe lamp for 3 h resulted in TON_{CO} = 119 and TON_{HCO2H} = 19. A mechanism invoking dimer formation and subsequent reduction to an active anion was proposed, in analogy to **Mn1**. Although HCO_2H production was attributed to a hydride intermediate, no H_2 was detected. Overall, these results demonstrate the wealth of mechanistic pathways and tunability of Mn CRCs.

2.3.5. Iron. *2.3.5.1. Electrocatalysis.* Iron CRCs are among the most prevalent, with porphyrin complexes forming a large subset. TPP is an adaptable platform for appending functionality that can impact on electronic properties, solubility, substrate binding, and transition states, as highlighted in section 2.2.3.1. Most iron porphyrin systems have been studied in polar aprotic organic solvents such as DMF and MeCN, with weak Brønsted acids such as H_2O, TFE, and phenol,[391−394] or Lewis acids like Mg^{2+} and Ca^{2+} improving performance.[150] The air-stable iron(III) state of these CRCs undergoes three sequential reductions to give an iron(0) species, though spectroscopic and computational findings support an iron(II) ligand-diradical structure.[148,149] Nevertheless, the reduced states still display metal-centered reactivity.[150,151]

Catalytic onset for CO_2 reduction with parent TPP CRC **Fe4** occurs at a potential correlated with the Fe^+/Fe^0 redox couple (−1.67 V vs SCE in DMF).[150,151,391,394] While CO_2 reduction to CO requires two electrons, experimental and DFT results suggest that the initial adduct is an $Fe^+-CO_2^{\bullet-}$ species (the dianionic charge contribution from the porphyrin is omitted, both here and in the following discussion).[395−397] Electrochemical analysis employing **Fe4** allowed a detailed mechanism to be derived from reaction rate dependence on added Brønsted acids (Figure 11). The rate-determining step entails a second ET from the iron site in a concerted manner with both proton transfer and C−O bond cleavage.[395] The resulting product-inhibited $Fe^{2+}-CO$ adduct is thought to react with a second Fe^0 species, closing the catalytic cycle by liberating CO and regenerating the coordinatively unsaturated Fe^+ porphyrin.[392,393]

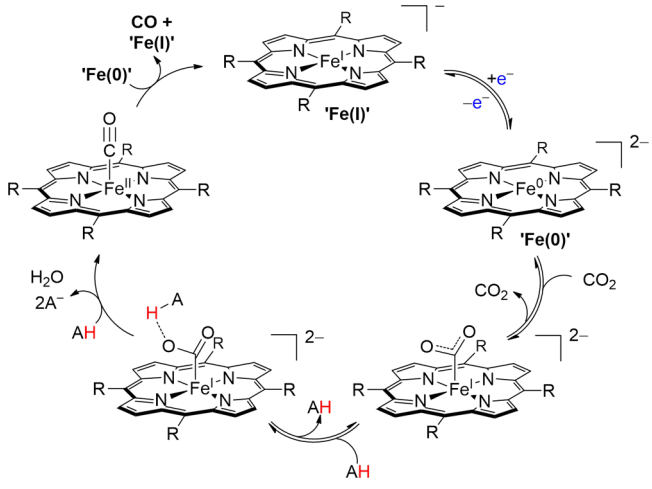

Figure 11. General mechanism for iron porphyrin CRCs. Porphyrin charge state shown as a dianion. R = substituents that do not intramolecularly interact with bound substrate (e.g., phenyl groups).[395]

DOI: 10.1021/acs.chemrev.8b00392
Chem. Rev. 2019, 119, 2752−2875

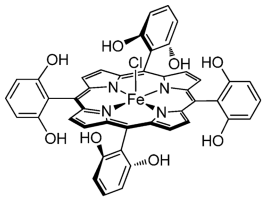

Fe17

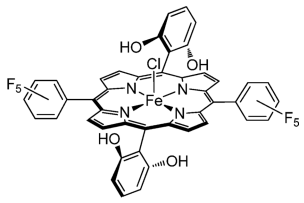

Fe18

Hydroxylation of the *meso*-substituents in **Fe4** to give **Fe17** vastly increases catalytic rates.[394] The resorcinol groups may play a dual role, altering the mechanism by acting as both intramolecular hydrogen-bond donors to stabilize the initial $Fe^{+}-CO_2^{\bullet-}$ adduct, and as internal relays that subsequently transfer protons. In contrast to **Fe4**, a metallo-carboxylic acid intermediate is proposed on the basis of CV analysis. These show a prewave before E_{onset} at −1.57 V vs SCE in DMF, indicating that an extra electron must be injected into the system before catalysis begins.[396] As E_{onset} occurs at a similar potential to the prewave, it was reasoned that charge build-up is avoided, and thus the initial $Fe^{+}-CO_2^{\bullet-}$ adduct must be protonated to give a $Fe^{+}-CO_2H^{\bullet}$ species.[396] Formation of this intermediate is supported by resonance Raman studies on a related system with 1,2,3-triazole residues, though in that case an $Fe^{2+}-CO_2H$ species is proposed based on breathing modes of the porphyrin skeleton being almost identical to the corresponding $Fe^{2+}-CO$ adduct.[398] Electrochemical studies of **Fe17** revealed that the additional reduction takes place simultaneously with intramolecular proton transfer and C−O bond scission, which is furthermore concerted with reprotonation of the internal resorcinol residue provided the external phenol concentration is sufficiently high.[396] Extending this strategy by incorporating two electron-withdrawing penta-fluoro-phenyl-rings in **Fe18** gives an E_{onset} at 60 mV lower overpotential than for **Fe17**, while still displaying the rate acceleration imparted by the two remaining resorcinol groups.[399]

Further modification with *p*-trimethylammonium-groups gives water-soluble **Fe19**. This CRC shows high stability and activity in aqueous KCl solution (pH 6.7), with CPE at E_{appl} = −0.86 V vs NHE using a GC WE giving FE_{CO} = 98−100% over 72 h (no TON_{CO} reported).[400] The positively charged residues in **Fe19** caused an anodic shift of the Fe^{+}/Fe^{0} couple, resulting in a more positive E_{onset} than with related derivatives (ΔE_{onset} = 200, 100, and 40 mV vs **Fe4**, **Fe17**, and **Fe18**, respectively). **Fe20** continues this trend, where the $-NMe_3$ groups occupy *ortho*- rather than *para*-positions, showing that through-space interactions reinforce those occurring through-structure.[401] **Fe20** exhibits the most positive E_{onset} for CO_2 reduction by iron-porphyrins (−1.19 V vs SCE in DMF). In addition, catalytic currents are at least 3-fold greater than for **Fe19**, ascribed to Coulombic stabilization of the initial negatively charged CO_2-adduct by the ammonium residues. Although CPE of **Fe20** exhibited a FE_{CO} = 100% with no apparent degradation over 84 h in DMF containing phenol (3.0 M) and H_2O (0.1 M), there is no data reported for purely aqueous electrocatalysis.[401]

The functionality used in the examples above to aid catalysis is reminiscent of peptide residues surrounding the active sites in many metalloenzymes[34,40] and has also been employed in related iron porphyrin CRCs.[402] An alternative approach to emulating natural systems, with particular relevance to CODH, is to employ a second metal ion. This has been achieved to some extent by a ligand featuring two covalently linked cofacial porphyrin macrocycles.[403] **$Fe_2$32** has an estimated intermetallic distance of 3.4−4.0 Å. CV in DMF under Ar shows at least 3 quasi-reversible features, arising from overlapping reduction of the two Fe^{3+} ions to ultimately give a species assigned as $[Fe^{0}Fe^{0}]$. CV under CO_2 shows a new wave after reduction to the $[Fe^{2+}Fe^{2+}]$ state, possibly due to preassociation of CO_2. E_{onset} occurs at a potential associated with reduction to the $[Fe^{0}Fe^{+}]$ state (∼−1.25 V vs NHE in DMF), which is ∼100 mV more positive than for **Fe4**. Catalytic currents increase by adding H_2O, reaching a maximum at 10% water content. Currents are ∼6-fold greater than for **Fe4** in the same solvent with equivalent iron concentrations. CPE conducted in H_2O:DMF (1:9) for 10 h using a GC WE at E_{appl} = −1.55 V vs Ag/AgCl gave a FE_{CO} = 88% and a FE_{H2} = 12%. Control experiments without catalyst produce similar amounts of H_2, suggesting that the selectivity of **$Fe_2$32** for CO reduction is close to quantitative.

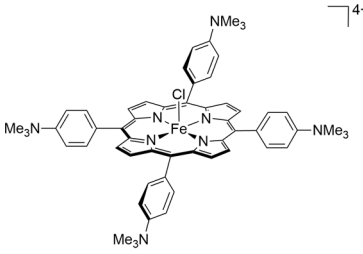

Fe19

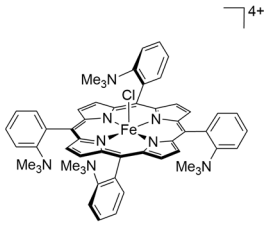

Fe20

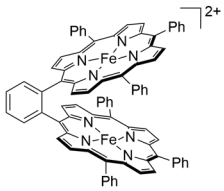

$Fe_2$32

Tafel plots derived from numerical treatment of the above data suggest that **$Fe_2$32** performs comparably to resorcinol-modified CRC **Fe17**.[394,403] Similar analysis of derivatives made with various electron-withdrawing or -donating residues on the phenyl rings indicate that activities exceeding those of **Fe17** are achieved, using purely inductive effects.[404] Incorporation of functional groups capable of interacting directly with the CO_2 substrate, such as trimethylammonium- or hydroxy-substituents, is thus an attractive target for future studies. Using combinations of different 3d transition metal ions to more effectively mimic the CODH active site would also be a promising research direction in the future.

Other aromatic iron-based CRCs have also been studied. Using a qtpy scaffold gives **Fe21**, which exhibited 100% selectivity for CO in CPE with a GC WE at E_{appl} = −1.4 V vs SCE, but with FE_{CO} = 37% over 2 h in MeCN containing phenol. Only traces of HCO_2H and $C_2O_4^{2-}$ were detected.[405] It was later shown that irradiation (λ > 420 nm) during CPE under otherwise equivalent conditions aids in CO release from **Fe21**, avoiding product inhibition and boosting FE_{CO} to 70%.[406] Using the phen-derivative **Fe22** in CPE over 1 h under various conditions in DMF or DMSO gave low selectivities. Mixtures of CO, HCO_2H, $C_2O_4^{2-}$, and H_2 were obtained, with a limited but discernible bias toward HCO_2H.[407] Pyridine-imine **Fe23** is also selective for HCO_2H.[69] Catalytic onset was observed under CO_2 at the Fe^{2+}/Fe^{+} couple, with CPE at E_{appl} = −1.25 V vs SCE using a GC WE for 3 h in DMF giving FE_{HCO2H} = 75−80% and no detectable H_2 or CO. DFT suggests that, while initial binding occurs at the C-atom, limited Fe^{3+}-π-back bonding into the CO_2

DOI: 10.1021/acs.chemrev.8b00392
Chem. Rev. 2019, 119, 2752−2875

π^*-orbitals is inadequate for C−O cleavage, allowing isomerization to an O-bound state which then forms HCO_2H. Formate production by molecular CRCs generally occurs by CO_2 insertion into a metal-hydride bond, but proton donors such as H_2O or phenol had no effect on the catalytic performance of **Fe23**.[69]

CO_2 reduction to HCO_2H has been shown with iron-carbonyl cluster $\mathbf{Fe_41}$.[138] Activity was first established in CO_2-saturated MeCN. Selectivity for HCO_2H or H_2 can be tuned by the pK_a of organic acid additives, with stronger acids favoring H_2. The catalytic onset occurs at a potential corresponding to one-electron reduction of the cluster, suggesting that $[Fe_4N(CO)_{12}]^{2-}$ is the active species. This is further supported by IR-SEC and crystallographic findings after selective one-electron chemical reduction of $\mathbf{Fe_41}$, which have identified $[Fe_4N(CO)_{12}]^{2-}$ and the hydride $[HFe_4N(CO)_{12}]^-$, believed to result from protonation of the dianion.[408] CPE in aqueous solution gives H_2, but under CO_2 the $[Fe_4N(CO)_{12}]^{2-}$ species produces HCO_2H over a broad pH range from 5−13, showing a minimum of 85% selectivity with no CO detected over 50 min at E_{appl} = −1.20 V vs SCE using a GC WE. The highest activity was observed at pH 7, giving FE_{HCO2H} = 95% and TON_{HCO2H} = 88 over 50 min, with current and selectivity maintained for 24 h.[408] Substituting one CO for PPh_3 resulted in lower selectivity, but HCO_2H remained the major product.[139] In contrast, exchanging CO for the proton-shuttling $PPh_2CH_2CH_2OH$ in $\mathbf{Fe_42}$ entirely suppresses CO_2 reduction in favor of H_2 evolution.[139]

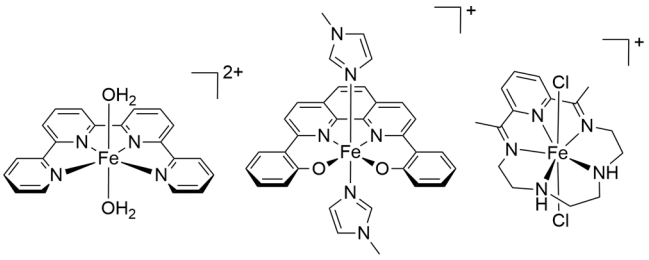

2.3.5.2. Photocatalysis. The promising activity of Fe-CRCs has led to numerous studies of their photocatalytic performance. The intense UV−vis absorption features of Fe-porphyrins allow them to act as both light absorbers and catalysts. Related Pc and corrole complexes show similar properties, and display comparable activities for photocatalytic CO_2 reduction.[409,410] Upon irradiation (λ > 280 nm), **Fe4** undergoes photoinduced reductions in MeCN with a suitable SED such as TEA, forming the catalytically active Fe^0 species.[411] A selectivity for CO of 31% was observed after 10 h in MeCN:TEA (95:5), with TON_{CO} = 17 and TON_{H2} = 37. After 10 h under the same conditions **Fe17** and **Fe18** showed TON_{CO} = 28 and 23, and TON_{H2} = 10 and 15, respectively.[411] An earlier study with **Fe4** in DMF:TEA (95:5) gave a TON_{CO} = 40 over 170 h but included a correction for degradation of DMF to CO.[412] Water soluble **Fe24** gave similar CO yields in aqueous $NaHCO_3$ with 5% TEA (pH 8.8).[412] More recent results indicate that 280−300 nm irradiation is required for photocatalytic CO_2 reduction to CO with **Fe4** in MeCN:TEA (95:5) solution.[411] Notably, these wavelengths are associated with degradation of the porphyrin through hydrogenation of the aromatic scaffold, indicating that performance may be improved by the use of PSs responsive to lower-energy photons.[411]

When the *p*-terphenyl dye **PS23** is present, irradiating (λ > 300 nm) **Fe4** in DMF:TEA (95:5) resulted in 6-fold greater amounts of CO at a 10-fold faster rate.[412,413] This sensitization method has also proven effective for related FePc, **Fe25**, which yielded a 20-fold faster rate and 10-fold more CO compared to analogous experiments without **PS23**.[409] The corroles **Fe27** and **Fe28** displayed similar activity to the tetramethylporphyrin **Fe26**, despite the former two showing catalytic onset already at the Fe^{2+}/Fe^+ couple. All three CRCs reached a TON_{CO} of ∼45 with ∼40% selectivity for CO over 8 h irradiation (λ > 310 nm) with **PS23** in MeCN:TEA (95:5).[410]

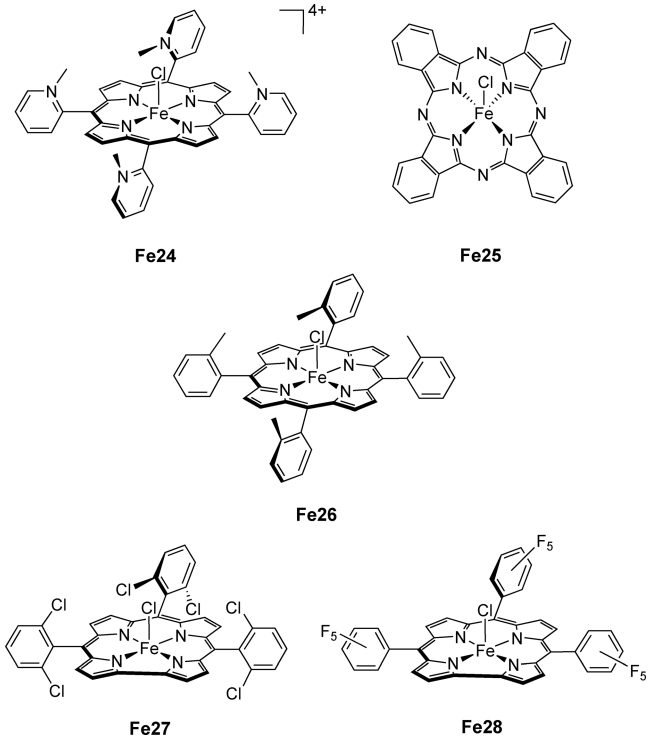

Employing **PS5** in combination with CRC **Fe17** in MeCN:TEA (95:5) gave a TON_{CO} of 140 with only trace H_2 evolved over 55 h irradiation (λ > 420 nm).[414] Substituting the iridium PS for organic dye **PS24** showed a TON_{CO} of 45 with no detectable H_2 upon irradiation (λ > 400 nm) in the same medium. Decreasing TEA to < 1% under otherwise identical conditions gave a TON_{CO} of 60, without sacrificing selectivity. Very modest respective QY_{CO} values of 0.0013 and 0.0008% were determined for the **PS5** and **PS24** systems, likely due to the six bimolecular reactions needed to generate the active Fe^0 species, but linear correlation between TON_{CO} and time in both cases suggests that no CRC degradation occurred.[414]

Together with organic dye **PS25**, **Fe19** displayed TON_{CO} = 60 and TON_{H2} = 3 after 47 h irradiation (λ > 420 nm) in $NaHCO_3$ buffered H_2O:MeCN (9:1) containing TEA (pH′ 6.7).[415] Addition of fresh PS allowed for continued catalysis, reaching a TON_{CO} of 120 (selectivity of 95%) after 94 h. Conversly to the above examples where visible-light-driven activity required addition of a dye, complex **Fe19** is also active under irradiation (λ > 420 nm) without an extra PS. In MeCN with TEA, **Fe19** yields a TON_{CO} of 33 after 47 h without detectable H_2. Using 1,3-dimethyl-2-phenyl-2,3-dihydro-1*H*-benzo[*d*]imidazole (BIH) instead of TEA enhances activity, with **Fe19** then reaching a TON_{CO} of 63 with 100% selectivity over 47 h. Adding TFE does not compromise the system

DOI: 10.1021/acs.chemrev.8b00392
Chem. Rev. 2019, 119, 2752−2875

stability, suggesting that hydrogenation of the porphyrin through hydride formation can be avoided in this case.[416] Taken together, the above results are encouraging with respect to precious-metal-free aqueous CO_2 reduction with visible light.

Irradiation (λ > 400 nm) of **PS1** and **Fe29**, in *N*-methyl-2-pyrrolidone:TEOA (5:1) yielded a TON_{CO} of 129 and TON_{H2} of 162 over 5 h (combined QY = 15% at λ = 440 nm).[417] The cyclopentadienone unit in **Fe16** may be noninnocent in facilitating CO_2 reduction by this CRC, undergoing reversible reduction to the aromatic cyclopentadienyl anion. Using **PS15** in *N*-methyl-2-pyrrolidone:TEOA (5:1), **Fe16** showed only trace H_2 after 5 h of irradiation (λ > 400 nm), with a TON_{CO} = 596 and $TON_{HCO2H} \leq 40$ (QY_{CO} = 58% at λ = 440 nm).[418] Using the copper dye **PS27**, Me_2-phen-ligated CRC **Fe30** gave a TON_{CO} = 273 and TON_{H2} = 75 after 12 h irradiation (λ = 436 nm) in MeCN:TEOA (5:1) containing BIH (QY_{CO} = 6.7% over 2 h).[419]

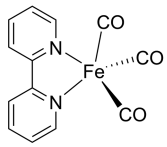

Fe29

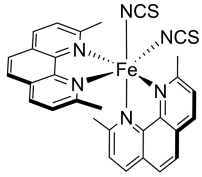

Fe30

Qtpy CRC **Fe21** exhibited a TON_{CO} = 1879, TON_{HCO2H} = 48, and TON_{H2} = 15 using **PS1** and LED excitation (λ = 460 nm) in MeCN:TEOA (4:1) with BIH. Decreasing **Fe21** concentration from 50 μM to 5 μM gave a drop in CO selectivity from 97% to 85%, but higher values of TON_{CO} = 3844, TON_{HCO2H} = 534, and TON_{H2} = 118. Using organic dye **PS25** instead of **PS1** required a shift to DMF (with BIH) to dissolve the PS. LED irradiation (λ = 460 nm) with **Fe21** (5 μM) gave TON_{CO} = 1365 and TON_{HCO2H} = 115 (no H_2 detected). Similar HCO_2H amounts were also formed in the absence of CO_2 or catalyst, most likely from DMF, suggesting that **Fe21** selectivity for CO production is close to quantitative. The Ru-sensitized conditions led to a QY_{CO} of 8.8% over 12 h, whereas the system using **PS25** gave a QY_{CO} of 1.1% over 24 h (both at λ = 458 nm).[405] Appreciable photocatalytic activity for CO_2 reduction with homogeneous systems can thus be accomplished under precious-metal-free conditions.

The potential of Fe-CRCs for reducing CO_2 beyond two-electron products has also been shown. As outlined above, irradiation (λ > 420 nm) of **Fe19** alone in MeCN with TEA reduces CO_2 to CO with 100% selectivity and a TON_{CO} of 33 after 47 h.[420] However, using **PS2** with **Fe19** under otherwise identical conditions yields CH_4, with TON_{CO} = 198, TON_{H2} = 24, and TON_{CH4} = 31. **Fe17** gave a comparable selectivity for CH_4, but with lower overall performance (TON_{CO} = 139, TON_{H2} = 15, and TON_{CH4} = 26). CH_4 evolution only begins after CO build-up in these systems, suggesting a multistep pathway with a common Fe^{2+}−CO intermediate. Experiments under CO showed ∼3-fold increased activity, with TON_{H2} = 28 and TON_{CH4} = 140 after 102 h. Production improved slightly by adding TFE, with TON_{H2} = 34 and TON_{CH4} = 159 after 102 h (QY_{CH4} = 0.18% from the latter data). Using **PS1** instead of **PS2** gave only CO and H_2, suggesting that the high driving force of the latter Ir-dye is required to produce CH_4.[420] In agreement, a later study reports similar **Fe19** activity to that under CO_2 above, but with Ir-dye **PS5** in H_2O:MeCN (7:3).[421] These results hold promise for photocatalytic recycling of CO_2 directly into highly reduced hydrocarbons.

2.3.6. Cobalt. *2.3.6.1. Electrocatalysis.* Molecular Co-CRCs predominantly contain N4-donor sets, often featuring a redox-active ligand scaffold, with the catalytically active species typically in the Co^+ oxidation state. Early reports studied water-soluble Pc **Co52**, as well as TPPs **Co15** and **Co53**. CV in aqueous solution showed enhanced currents under CO_2, with evidence of HCO_2H formation, but products were not quantified.[422,423] An electrostatic binuclear assembly of **Co12** paired with deprotonated **Co15** gave E_{onset} = −1.80 V vs Ag/AgX (X = not reported) for CO_2 reduction in DMSO:H_2O (9:1), with CO, H_2, and formaldehyde (HCHO) identified after CPE.[424] Activity was correlated with cationic **Co12** by CV, and substitution of **Co15** for a copper analogue gave a mixed Co-Cu species yielding even greater currents under CO_2.[424] CV of **Co54** showed enhanced currents in organic solvent under CO_2, but no CPE was conducted or products identified.[425]

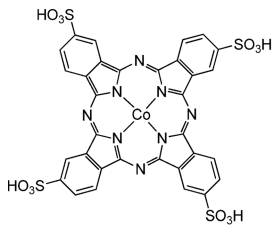

Co52

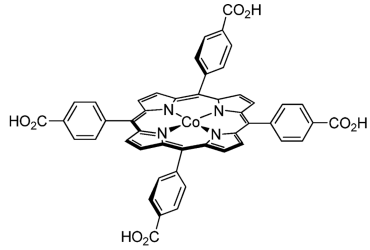

Co53

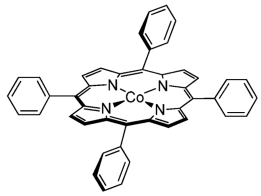

Co54

In addition to those already highlighted as HECs (**Co2** and **Co31**), a number of other tetraaza-macrocycles related to cobalt-cyclam (**Co55**), such as **Co56** and **Co57**, have shown promise as water-tolerant CRCs.[186,255] Early studies reported that CO production was aided by H_2O, and preliminary CPE experiments in aqueous KNO_3 with **Co56** at a Hg pool WE with E_{appl} = −1.60 V vs SCE produced a FE_{CO} = 46.5% and FE_{H2} = 46.5%,[186] or FE_{CO} = 24.4% and FE_{H2} = 38.0%.[255] Both studies quantitatively demonstrated catalytic turnover for **Co56**, and this CRC has since been the focus of in-depth mechanistic investigations.

Following reduction of **Co56** to the square-planar Co^+ state, CO_2 binds at an axial site, giving a Co^+−CO_2 adduct that shows thermochroism in solution.[426−428] This color variation is due to temperature-dependent solvent binding at the remaining axial site and occurs in both MeCN and H_2O.[426,428,429] UV−vis, NMR, FT-IR, and X-ray absorption near edge (XANES) spectroscopic studies have revealed that solvent binding triggers ET from the Co^+ ion, forming a Co^{3+}−CO_2^{2-} species.[429−431] FT-IR shows that H-bonding between the macrocycle N−H groups and O-atoms of the CO_2 fragment stabilizes both the five- and six-coordinate forms of the adduct.[429] No decomposition occurs in MeCN after a day at RT under CO_2 in the absence of proton sources, indicating that neither CO_2 nor a second Co−CO_2 adduct act as an oxide acceptor to facilitate C−

DOI: 10.1021/acs.chemrev.8b00392
Chem. Rev. 2019, 119, 2752−2875

O cleavage.[431] The Co^{3+}–CO_2^{2-} species is also stable with a proton donor such as MeOH present, suggesting further ET is required to initiate catalysis.

Of the tetraaza-macrocycles, pyridine-containing **Co31** performs well.[186,255] **Co31** shows good selectivity for CO in CPE (FE_{CO} = 41.5%, FE_{H2} = 5.3%), compared to **Co56** (FE_{CO} = 56.2%, FE_{H2} = 25.0%), **Co57** (FE_{CO} = 13.3%, FE_{H2} = 58.8%), Pc **Co38** (FE_{CO} = 22.9%, FE_{H2} = 4.3%), and TPP **Co54** (FE_{CO} = 10.5%, FE_{H2} = 19.5%), all operating at a Hg pool WE with E_{appl} = −1.6 V vs SCE in H_2O:DMF (5:95).[255] The activity of **Co31** further improved at E_{appl} = −1.3 V vs SCE (FE_{CO} = 66.4%, FE_{H2} = 5.3%).[255] CV showed catalytic onset after two one-electron reductions of **Co31**, and comparison with the free macrocycle revealed ligand noninnocence, hinting at a $Co^+(L^{\bullet-})$ ligand radical active species.[432] More recent crystallographic and computational findings support this result.[433] DFT shows that CO_2 binds strongly to the $Co^+(L^{\bullet-})$ species, yielding a metallocarboxylate with a bent geometry (O–C–O = 133–134°). Partial ET from the macrocycle gives spin density over the resulting $CO_2^{\bullet-}$, Co^+ ion, and ligand orbitals.[434] H-bonding was also identified between the CO_2 fragment and ligand N–H group, positioning the CO_2 such that it interacts with the π-system on the opposite side of the macrocycle. These results highlight the potential of ligand functionality for activating CO_2.

Related CRC **Co58** contains an N5-macrocycle and shows similar behavior.[69] CPE in DMF with a GC WE at E_{appl} = −1.5 V vs SCE gave exclusively CO with a FE_{CO} of 82% over 1 h. Current was sustained for 3 h, but the charge passed began to plateau, revealing that **Co58** is deactivated. CV was similar to **Co31** and showed two one-electron reductions required to reach catalytic onset for **Co58**, with the second occurring at the ligand to give a $Co^+(L^{\bullet-})$ species. This is further supported by DFT studies, which also reveal an interaction of the macrocycle N–H groups with an O-atom of CO_2. Back-bonding between the CO_2 π^* and Co^{2+} orbitals is thought to weaken and help cleave the C–O bond, thus avoiding rearrangement to the O-bound state which forms HCO_2H in the case of iron analogue **Fe23** (section 2.3.5.1).[69] Bis(iminopyridine) CRC **Co59** also shows catalytic onset when reduced to a $Co^+(L^{\bullet-})$ state, with H_2O presence improving performance. CPE in H_2O:MeCN (1:4) with a GC WE at E_{appl} = −1.95 V vs Fc^+/Fc gave a TON_{CO} ~11 with FE_{CO} = 88% after 1 h.[435]

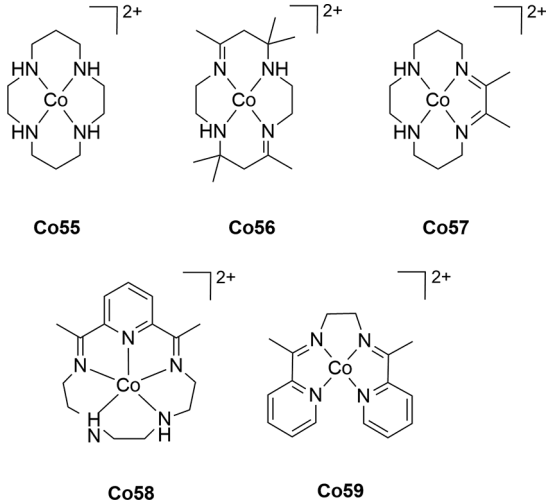

Co60 features two tpy units and has been studied in H_2O:DMF (5:95), with a mechanism thought to involve a ligand-based radical.[436] This CRC shows two reductions in CV, the latter of which is responsible for the catalytic onset under CO_2 and is assigned to formation of a cobalt(I)-ligand radical. CPE with a GC WE at E_{appl} = −1.93 V vs Fc^+/Fc gave a FE_{CO} = 20% and FE_{H2} = 1% (no HCHO, CH_4, CH_3OH, or $H_2C_2O_4$ was detected, and only traces of HCO_2H found from DMF degradation). This limited activity was attributed to side-reactions of the radical species, with NMR analysis showing loss of tpy aromaticity.[436] Using qtpy-supported **Co40** in CO_2-saturated MeCN at E_{appl} = −1.7 V vs SCE with a carbon cloth WE gave FE_{CO} = 80% over 1 h (no HCO_2H or $H_2C_2O_4$ were detected).[89] Deposition of an electroactive film on GC or Pt WEs was observed, and a carbon cloth WE pretreated with **Co40** under reducing conditions maintained CO_2 reduction activity in fresh MeCN (E_{appl} = −1.7 V vs SCE, FE_{CO} = ~35%) or aqueous solution (E_{appl} = −1.3 V vs SCE, FE_{CO} = 36%, and FE_{H2} = 64%).[89] More recently, **Co40** in MeCN with 1.0 M phenol and a GC WE at E_{appl} = −1.4 V vs SCE showed almost linear charge passed over 3 h, resulting in FE_{CO} = 94%.[405] Using 3 M phenol in MeCN gave FE_{CO} = 87% and TON_{CO} = 64 after 8 h with a GC WE at E_{appl} = −1.3 V vs SCE.[406]

Tetra(aminopyridyl) macrocycle **Co61** requires a proton-donor such as MeOH present before showing appreciable catalytic currents for CO formation.[437] CPE using a GC WE at E_{appl} = −2.80 V vs Fc^+/Fc in CO_2-saturated DMF with MeOH gave FE_{CO} = 98% over 2 h (only traces of H_2 detected). In contrast to previous examples, **Co61** is thought to undergo two metal-based reductions, making it a rare case where Co^0 is the proposed active species. Comparison with **Co61** analogues *N*-alkylated at the aliphatic amines indicates that the ring N–H units contribute to activity.[437] A later study revealed that these groups faciliate proton transfer from the reaction medium by H-bonding with suitable donors present in solution.[438]

Featuring a bis(pyridine-pyrrolidine) chelate and two chlorido ligands, **Co62** yielded a FE_{CO} of 85% after 4 h CPE with a GC WE at E_{appl} = −1.7 V vs SCE in MeCN (no H_2 detected).[439] CV showed two reductive features at −1.61 and −1.80 V vs SCE, with the former displaying limited reversibility, indicating loss of one Cl^- ligand. This singly reduced monochlorido complex has significant electron density on the pyridine units according to DFT, resulting in unusual side-on CO_2 binding to this formal cobalt(I) state, with partial ET giving a nonlinear adduct (O–C–O = 150°). Protonation and reduction yielded a further bent metallo-carboxylic acid (O–C–O = 119°), the proton of which forms an H-bond with the Cl^- ligand. DFT predicts this protonation to be energetically favorable only in the presence of the Cl^- ligand,[439] illustrating how the environment around the metal site can assist in substrate transformation.

Cobalt half-sandwich CRCs featuring various cyclic diphosphine ligands with pendant amines in the second coordination sphere selectively reduce CO_2 to HCO_2H in the presence of H_2O.[440] **Co63** performed best, giving FE_{HCO2H} = 98% with a TON_{HCO2H} of 23 over 1 h using a Hg pool WE at E_{appl} = −2.25 V vs Fc^+/Fc in DMF containing H_2O (1.1 M). The amine-free analogue showed much smaller catalytic currents under CO_2. The active state of **Co63** was identified by DFT as a Co^{2+}–H, formed by three reductions, with the pendant amines acting as internal proton relays.[441] Proton shuttling likely occurs in a coupled manner with two of the three ET events. Rather than typical CO_2 insertion, the metal-hydride may initiate nucleophilic attack, aided by an H-bonded water bridge between one pendant amine and a substrate O-atom. HCO_2H is then released

DOI: 10.1021/acs.chemrev.8b00392
Chem. Rev. 2019, 119, 2752–2875

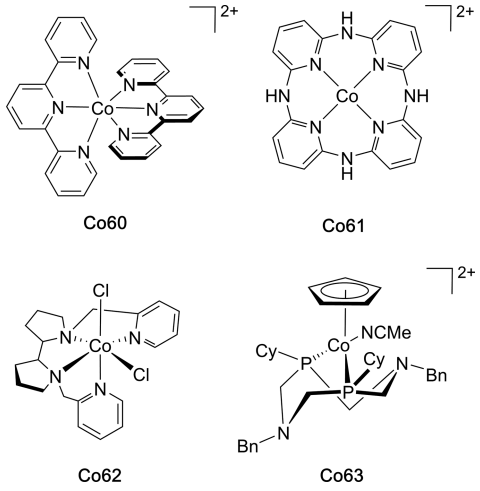

from the Co^{2+} center, closing the catalytic cycle. This mechanism is supported by kinetic isotope effect studies and explains the variation in activity of the different N-derivatives used.[440] These CRCs are an attractive target for immobilization, especially given the success of related nickel-bis(diphosphine) HECs when anchored onto carbon- and metal-oxide-based substrates (see sections 4.2.1 and 4.2.2).

2.3.6.2. Photocatalysis. Early studies reported photocatalytic CO_2 reduction to CO upon irradiation ($\lambda > 400$ nm) of **PS1** and $CoCl_2$, using SEDs such as TEA and TEOA in 20% aqueous MeCN or DMF.[187,442,443] Addition of N-heterocycles such as bpy, phen, and their derivatives altered activity, with 2,9-dimethyl-1,10-phenanthroline giving the highest TON_{CO} = 8 and TON_{H2} = 17 (QY_{CO} of 6.5% at λ = 450 nm) in DMF:TEOA (2:1).[443] Using **PS1** with **Co56**, **Co57**, or **Co31** in aqueous AA solution (pH 4.0) showed low selectivity for CO, with H_2 the major product in all cases.[255] Under irradiation from "daylight lamps" for 18 h, **Co56**, **Co57**, and **Co31** gave respective TON_{CO} values of 22, 10, and ~1, with 22%, 32%, and 0.4% selectivity (derived from $CO:H_2$ ratios, though some HCO_2H was also detected in CPE).[255] Photocatalytic CO_2 reduction was also shown using organic dye **PS23** with **Co56** in MeCN:MeOH:-TEA (4:1:1), giving a TON_{CO} = 2.0, TON_{HCO2H} = 0.3, and TON_{H2} = 1.5 after 1 h irradiation ($\lambda > 290$ nm).[444]

Unmodified cyclam **Co55** reduces CO_2 when paired with organic PSs.[444,445] After 1 h irradiation ($\lambda > 290$ nm) of **PS23** in MeCN:MeOH:TEA (4:1:1), **Co55** yielded a TON_{CO} = 4.7, TON_{HCO2H} = 2.4, and TON_{H2} = 0.7. Replacing MeOH with H_2O lowers activity, whereas exchanging TEA for TEOA yields TON_{CO} = 10.2, TON_{HCO2H} = 6.7, and TON_{H2} = 0.7. (QY_{CO} = 15% and QY_{HCO2H} = 10% at λ = 313 nm).[445] Conversely, when irradiated ($\lambda > 290$ nm) with **PS26** instead of **PS23** in MeCN:MeOH:TEA (2:1:1), **Co55** yields almost exclusively HCO_2H, showing TON_{HCO2H} = 4.4, TON_{CO} = 0.3, and TON_{H2} < 0.1 (QY_{HCO2H} of 7% at λ = 313 nm).[431] In contrast to photoreduced $[\mathbf{PS23}]^{\bullet-}$, $[\mathbf{PS26}]^{\bullet-}$ has insufficient driving force to reduce **Co55** to the Co^+ state. Instead, donation of an H-atom from protonated $[H(\mathbf{PS26})]^{\bullet}$ to the resting Co^{2+} is proposed to directly generate a Co^{3+}–H species.[431] Similar hydride formation was observed with **Co56** in aqueous pulse radiolysis experiments, where $H^{\bullet}$ reacts directly with the Co^{2+} complex.[446] The hydride formed from **Co55** then undergoes CO_2 insertion, yielding HCO_2H without passing through the 4-coordinate Co^+ state necessary for producing CO.[447] These results provide compelling evidence for metal-hydrides as transient species in HCO_2H production and illustrate the role of catalytic intermediates in determining product selectivity.

Cobalt TPPs,[413,425] Pcs,[409] corroles,[410] and corrins[448] can reduce CO_2 photocatalytically. Under irradiation ($\lambda > 320$ nm) in MeCN:TEA (95:5), **Co54** gave TON_{CO} = 80 and TON_{HCO2H} > 220 after 200 h.[425] Irradiation ($\lambda > 300$ nm) with **PS23** increased both the rate and yield of CO evolution due to more efficient generation of the active species (quantitative data not reported),[413] which is best described as a Co^0 state based on photochemical, electrochemical, and spectroscopic analyses.[425] The related Pc **Co64** achieved a TON_{CO} of ~50 after 6 h irradiation ($\lambda > 310$ nm) with **PS23** in MeCN:TEA (95:5), but is thought to feature a cobalt(I) ligand-radical active state.[409] TPP **Co65** and corrole **Co66** yielded respective TON_{CO} values of ~60 and ~80 over 6 h under identical conditions with **PS23**, despite evidence that **Co65** requires a Co^0 state before entering the catalytic cycle, whereas **Co66** is active already after reduction to Co^+.[410] In contrast, while vitamin B_{12a} corrin **Co67** shares a Co^0 active state with the porphyrins, it outperformed **Co65** in both initial CO_2 reduction rate and stability, giving ~6-fold higher yields of both CO and HCO_2H when both are irradiated ($\lambda > 300$ nm) in MeCN:MeOH (9:1) with TEA and **PS23**.[448] These results show that relatively minor structural changes in the ligand can have a profound mechanistic effect and can lead to considerable differences in activity. Such changes can also result from operational conditions, for example by deposition onto an electronically active surface (see section 4).

In contrast to electrocatalysis, photocatalysis using **Co31** and **PS1** in aqueous AA solution (pH 4.0) gave low selectivity for CO (TON_{CO} of ~1 with 0.4% selectivity after 18 h "daylight lamp" irradiation).[255] This may result from photoreduced **PS1** having insufficient driving force to generate the $Co^+(L^{\bullet-})$ active state.[434] IR and DFT studies have identified an adduct between the singly reduced Co^+ state and CO_2, with a relatively weak interaction causing only minor CO_2 distortion (O–C–O = 174–176°).[434,449] In addition, evidence suggests that this adduct can form upon reduction of a **Co31** cobalt(II)-hydrogencarbonate precursor present in wet CO_2-saturated MeCN, and that both species are stabilized by H-bonding between the N-H of the macrocycle and substrate O-atom.[449] While neither adduct achieves catalytic turnover to produce CO, substrate preassociation may prevent competing hydride formation, again emphasizing how ligand functionality can facilitate catalyst selectivity.[433,449]

Analogous H-bonding has also been shown for ring-expanded N5-macrocycle **Co58**, which outperforms **Co31** when both are assayed with the more reducing dye **PS2**.[69] After 22 h LED irradiation (λ = 460 nm) with **PS2** in MeCN:TEA (4:1), **Co31** gave a TON_{CO} of ~55 (minor H_2), whereas **Co58** displayed a TON_{CO} of 270 with a selectivity of 97%. No alcohols, oxalate, or formate were detected. Almost linear CO formation for the first 8 h, Hg^0 addition, and DLS experiments all suggest **Co58** is the active CRC. Under identical conditions TPA-supported **Co68** gave a TON_{CO} of ~160 over 22 h (negligible H_2).[69] A TON_{CO} of 953 resulted after 70 h (~600 after 22 h) with 85% selectivity at a larger **PS2**:**Co68** ratio.[450] In contrast, using the more photostable iridium dye **PS28** with **Co68** under almost identical conditions achieved a TON_{CO} > 2400 with 95% selectivity over 72 h.[451]

Electrochemical and theoretical studies of **Co68** indicate that the cobalt(I) monochlorido species can interact with CO_2.[439,450] DFT showed a relatively minor association with CO_2 (O–C–O = 178°), but protonation of this adduct may trigger ET, causing

DOI: 10.1021/acs.chemrev.8b00392
Chem. Rev. 2019, 119, 2752–2875

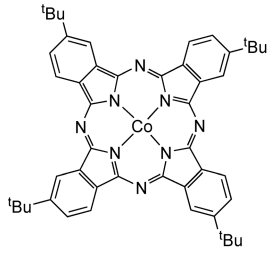

Co64

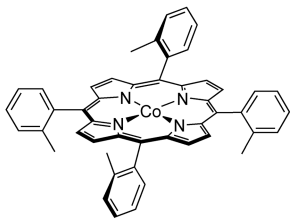

Co65

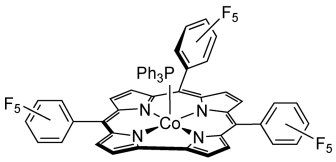

Co66

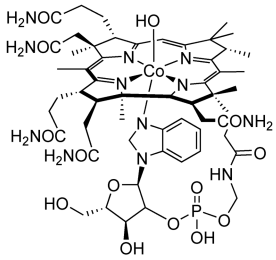

Co67

significant distortion (O−C−O = 121°).[439] The resulting metallo-carboxylic acid proton forms an intramolecular H-bond with the proximal chlorido ligand, and a later study showed that the energetics of protonation can be influenced by the identity of the neighboring anion.[452] This effect was found to impact on photocatalytic activity for both **Co68** and related bis(amino-pyridine) CRC **Co69**.[452,453] **Co68** activity in the presence of H_2O has been directly compared with **Co70**, which features a tris(2- benzimidazylmethyl)amine ligand. In contrast to **Co68**, **Co70** was studied as a halide-free perchlorate salt. In H_2O:MeCN (1:4) with TEOA and **PS29** under LED irradiation (λ = 450 nm), **Co70** gave a TON_{CO} of 1179 over 10 h, with only trace HCO_2H and H_2. While both CRCs display a selectivity of 97%, **Co68** yielded a TON_{CO} of only 686.[454] Respective QY_{CO} values of 0.22% and 0.13% offer some insight into the differing activities, but the influence of coordinated anionic coligand was not further explored.

Several CRCs have been studied which build on the early results shown by combining $CoCl_2$ with bpy- and phen-type ligands. Tris(bpy) complex **Co39** gave a TON_{CO} of 6.2 with a selectivity of 28% over 213 h using **PS1** in DMF:TEOA (4:1) with Xe lamp irradiation.[455] Dyad systems employing a bis(phen) tether to link a ruthenium PS-fragment to a cobalt catalytic center afford bimetallic **Co71** and **Co72**. While selectivity increased after 29 h irradiation (λ = 400−750 nm) in DMF:H_2O:TEOA (3:1:1), neither **Co71** (TON_{CO} = 3, TON_{H2} = 1, and TON_{HCO2H} = 31) nor **Co72** (TON_{CO} = 5, TON_{H2} = 1, and TON_{HCO2H} = 34) exceeded the activity of **PS1** and **Co39** under the same conditions (TON_{CO} = 9, TON_{H2} = 16, and TON_{HCO2H} = 28).[456] HCO_2H formed was attributed to adventitious $[Ru(bpy)_2]^{2+}$ that results from photodecomposition of the PS moiety. A more recent study adopts a similar approach, although uses aromatic linkers between the phen units, with various polypyridyl ligands completing the PS and CRC coordination spheres.[457] Observation of a lag phase before production of HCO_2H led to a similar conclusion regarding PS-unit decomposition, while also revealing enhanced stability of the dyads over the corresponding multicomponent system containing **PS1** and $[Co(phen)_3]^{2+}$. The latter pair thus showed relatively rapid deactivation under irradiation (λ = 415 nm) in MeCN:TEOA (5:1) containing BIH, with activity plateauing in 4−5 h to give TON_{CO} = 30, TON_{H2} = 35, and TON_{HCO2H} = 8, whereas after 8 h **Co73**, **Co74**, and **Co75** reached respective values of TON_{CO} = 51, TON_{H2} = 13, and TON_{HCO2H} = 4−6; TON_{CO} = 54, TON_{H2} = 8, and TON_{HCO2H} = 4−6; and TON_{CO} = 46, TON_{H2} = 23, and TON_{HCO2H} = 3.[457]

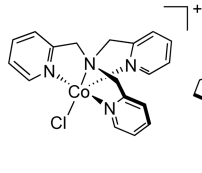

Co68

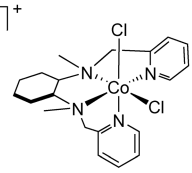

Co69

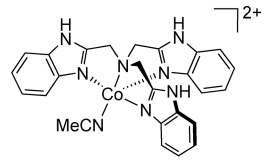

Co70

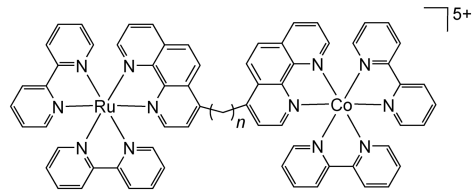

Co71, n = 2
Co72, n = 5

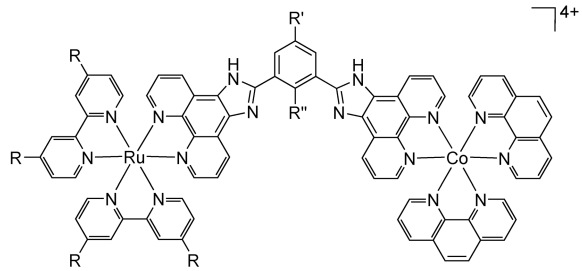

Co73, R = R' = R'' = H
Co74, R = Me, R' = R'' = H,
Co75, R = H, R' = ^{t}Bu, R'' = OH

Qtpy complex **Co40** and **PS1** in MeCN:TEOA (4:1) with BIH gave a TON_{CO} = 497, TON_{H2} = 3, and TON_{HCO2H} = 5 over 80 min under LED irradiation (λ = 460 nm).[405] Decreasing the concentration of **Co40** from 50 μM to 5 μM retains 98% selectivity for CO, but with improved activity per catalytic site (TON_{CO} = 2660, TON_{H2} = 23, and TON_{HCO2H} = 35). Hg^0 addition and DLS experiments suggest the active CRC is **Co40**. Exchanging **PS1** for **PS25** in DMF with BIH and 5 μM **Co40** yielded TON_{CO} = 790, TON_{H2} = 11, and TON_{HCO2H} = 78. Adjusting for HCO_2H formation in the absence of CO_2 or CRC, likely arising from DMF degradation, **Co40** selectivity for CO production is close to quantitative. QY_{CO} = 2.8% was determined for the Ru-sensitized **PS1** system over 12 h at λ = 458 nm, whereas the **PS25** system gave QY_{CO} = 0.8% over 24 h.[405] Despite decreased activity using **PS25**, these findings demonstrate that a considerable TON_{CO} can be achieved under precious-metal-free conditions.

CRC **$Co_2$2** features a cryptand-type ligand with two tripodal tris(2-aminoethyl)amine coordination sites linked by *m*-xylyl spacers.[458] Using **PS29** with LED irradiation (λ = 450 nm) in MeCN:H_2O (4:1), **$Co_2$2** reached a Co-based (i.e., per metal ion) TON_{CO} of 8448 over 10 h with 98% selectivity. Addition of fresh PS after 10 h recovered activity, and DLS experiments excluded nanoparticle formation. A QY_{CO} of only 0.04% was determined (λ = 450 nm), possibly due to the PS concentration being 10 000-fold greater than that of **$Co_2$2**. The mononuclear analogue, **Co76**, gave a TON_{CO} of 1600 over 10 h, with a selectivity of 85% and a QY_{CO} of 0.007% under equivalent conditions (double CRC concentration). These results suggest

DOI: 10.1021/acs.chemrev.8b00392
Chem. Rev. 2019, 119, 2752−2875

that the cobalt sites in Co_2**2** act cooperatively, a proposal supported by the crystal structure of a Co_2**2** carbonate adduct which shows CO_3^{2-} bridging between the two metals. Further computational results identify a transition state in which CO_2 occupies the cavity in Co_2**2** and interacts with both metal centers.[458] This example shows the potential for two metal sites to work together in a manner reminiscent of CO_2-activation in CODH, thereby producing significant improvements in performance over their monometallic counterparts.

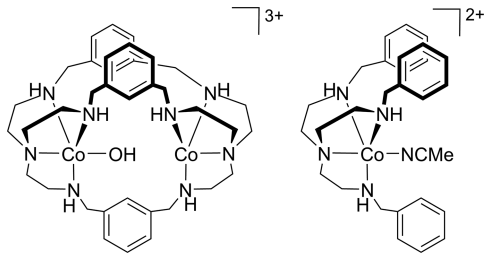

Co_2**2** **Co76**

2.3.7. Nickel. *2.3.7.1. Electrocatalysis.* Early electrocatalytic CO_2 reduction with nickel complexes was largely investigated in parallel with those of cobalt and also commonly featured macrocyclic N4-donor ligands. Water-soluble Pc **Ni68** showed enhanced currents in aqueous solution under CO_2 (products were not analyzed).[422] Subsequently, 14-membered macrocycles related to cyclam were studied in H_2O:MeCN (2:1), with **Ni2** and **Ni10** giving a FE_{CO} = 65.3% (FE_{H2} = 32.7%) and FE_{CO} = 44.0% (no H_2 detected), respectively.[186] The parent cyclam **Ni1** showed high efficiency and selectivity for CO production in purely aqueous solutions,[459] yielding a TON_{CO} of 8000 (no H_2 detected) after CPE at E_{appl} = −1.00 V vs NHE for 8 h with a Hg pool WE in $KClO_4$ solution (pH 4.1).[88] This performance is a benchmark for CRCs, and **Ni1** has been the focus of substantial literature attenion.[59,460,461] A number of factors have been identified that influence the activity of **Ni1**, with the nature of the WE, ligand-substrate H-bonding, and molecular catalyst conformation all being of considerable relevance, as detailed below.

Besides setting an encouraging precedent, seminal studies of **Ni1** also revealed that reduction to the Ni^+ state causes adsorption at Hg WE surfaces, and the bound CRC is responsible for catalytic activity. Formation of a Ni^+−CO species under catalytic conditions was shown by UV−vis and EPR spectroscopy, and loss of CO from this adduct is recognized as vital for avoiding product inhibition.[88] **Ni1** also showed some selectivity and efficiency when using a GC WE; in aqueous KCl

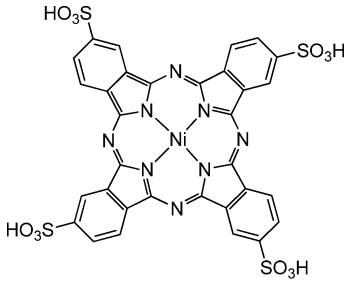

Ni68

it yielded a TON_{CO} = 4 after 3 h of CPE at E_{appl} = −1.20 V vs NHE, whereas 1 h of CPE at E_{appl} = −1.30 V vs NHE gave a FE_{CO} = 90% (no H_2 detected).[462] In contrast, using a Hg pool WE at E_{appl} = −1.40 V vs SCE in wet DMF (∼0.1 M H_2O) under CO_2 generated mainly HCO_2H, with a FE_{HCO2H} = 75% and TON_{HCO2H} = 3.2.[70] Consistent with the lack of H_2 produced, the HCO_2H may form via an O-bound species rather than by CO_2 insertion into a nickel-hydride bond.[70] This mechanism aligns with experimental results that reveal the Ni^+ active species has a greater affinity for CO_2 over protons, even in pure H_2O at acidic pH values > 2.[463] However, a more recent DFT study based on an MeCN:H_2O (4:1) solvent-model predicts that a Ni−OCO adduct is much less stable than a Ni−CO_2 species.[71] While these results provide limited insight with respect to the production of HCO_2H in DMF, they help to rationalize the excellent selectivity of **Ni1** for CO production in aqueous media.

Computational studies further support the proposed Ni^+ active state of **Ni1** and indicate that CO_2 binding alone is not associated with significant ET.[71,461] A second reduction step is thought to occur, coupled with proton donation from H_3O^+ or H_2CO_3, with a low barrier for further protonation of the Ni^{2+}−CO_2H intermediate implying that C−O cleavage may proceed together with PCET in an all-concerted mechanism (Figure 12).[71] While this aspect of CO_2 activation is similar to the iron porphyrins discussed earlier, C−O cleavage does not represent the rate-limiting process in the **Ni1** system, as shown by experiments in MeCN:H_2O (4:1). Using a GC WE a 10-fold increase in the catalytic current under CO_2 was achieved by adding a CO scavenger, indicating that CO inhibits catalysis.[464] Formation of a Ni^+−CO state prevents further CO_2 binding and may lead to deactivation through reduction to a Ni^0−CO species, followed by demetalation. As such CO dissociation from

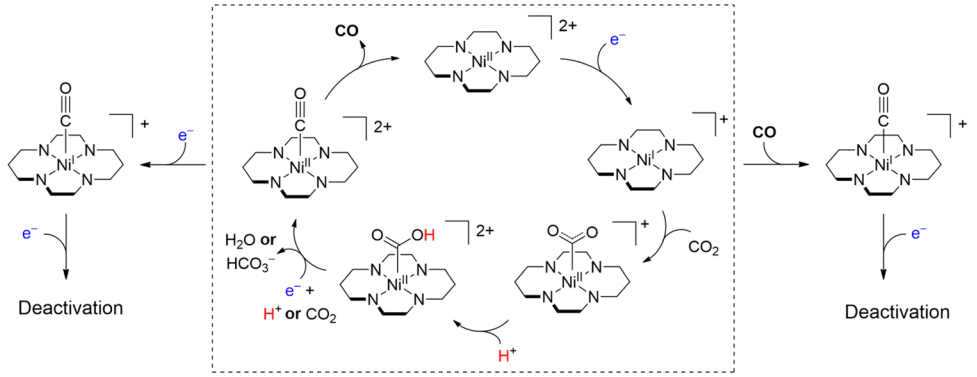

Figure 12. CO_2 reduction to CO mediated by **Ni1**. Hg electrodes are thought to destabilize the product-inhibited Ni^+-CO species, avoiding CRC deactivation.[90] N-bound H atoms omitted for clarity.

DOI: 10.1021/acs.chemrev.8b00392
Chem. Rev. 2019, 119, 2752−2875

the Ni^{+}−CO adduct is rate-determining under homogeneous aqueous conditions.[464]

Several studies have further explored the adsorption process and observed enhanced affinity of the Ni^{+} state for the Hg WE surface.[465,466] Improved activity of bound **Ni1** has also been addressed, and been suggested to result from a range of effects, such as electronic interaction of the Ni-center with the Hg WE surface.[465,467,468] An alternative explanation arises from evidence indicating that adsorption and conformational state of **Ni1** may be linked.[465,469] In aqueous solution at RT **Ni1** exists as a 15:85 mix of *trans*-I and *trans*-III isomers, where the former has all four N-H groups oriented toward the same axial coordination site and the latter adopts a chairlike conformation with two N-H groups pointing in each direction.[90,470] As these conformers and their adducts vary in relative stability, each exhibits a different affinity for CO_2 and CO.[71,461,462,464] For example, conformation will determine the extent of CRC H-bonding with the O-atoms of CO_2, and thus the *trans*-I isomer will form the most stable CO_2 adduct.[71,461,462] While enhanced CO_2 binding can promote selectivity and lower transition state energy, strong association of CO is undesirable, as product-inhibited Ni^{+}−CO leads to deactivation upon reduction to a Ni^{0}−CO species.[90,464,471] DFT indicates that the *trans*-III isomer adsorbs most strongly on Hg surfaces and forms a higher energy Ni^{+}−CO adduct which is further destabilized by interaction with the Hg^{0}.[90,464] This combination of electronic effects and conformational selectivity speeds up the rate-determining step and avoids CRC deactivation, highlighting the importance of both product clearance and surface interaction.

Many derivatives of **Ni1** have been studied for electrocatalytic CO_2 reduction.[59,462,469,472] Increasing alkylation at the N-atoms results in diminishing performance, with loss of H-bond donors and an anodic shift in the Ni^{2+}/Ni^{+} couple both lowering reactivity toward CO_2.[462,469] The two C-alkylated CRCs **Ni3** and **Ni4** show greater activity than the parent **Ni1**. CPE with **Ni1**, **Ni3**, or **Ni4** in aqueous $NaClO_4$ (pH 5.0) for 1 h with a Hg pool WE at E_{appl} = −0.96 V vs NHE gave 6-fold and 4-fold greater charge passed for **Ni3** and **Ni4**, respectively, with an increase in FE_{CO} from 84% for **Ni1** to 88% in the derivatives (only trace H_2 detected).[59] These improvements were attributed to enhanced Ni-Hg and catalyst-CO_2 interactions, the latter including H-bond stabilization and nickel electron donation in the corresponding CO_2 adducts. Interestingly, the Ni^{+} species of both **Ni3** (8.7 M^{-1}) and **Ni4** (13 M^{-1}) show smaller CO_2 association constants when compared to **Ni1** (16 M^{-1}), though whether these values also reflect CO-binding affinity has not been determined. It was further shown that selectivity can be tuned for H_2 by lowering the pH value to 2, though this was more pronounced for **Ni1** than for **Ni3** and **Ni4**, with respective CO:H_2 ratios of 0.4, 0.8, and 0.6.[59]

Improved selectivity under acidic conditions (pH 2.0) is also shown by a carboxylic acid functionalized cyclam, **Ni69**.[460] CPE in aqueous $NaClO_4$ with a Hg pool WE at E_{appl} = −0.99 V vs NHE achieved a CO:H_2 ratio of 0.8 with a total FE of 81% over 1 h (TON_{CO} = 591). Under the same conditions, **Ni1** gives a total FE of 86%, but a CO:H_2 ratio of 0.17 (TON_{CO} = 45). Similar adsorption to the Hg WE surface occurred with both CRCs, but greater catalytic currents for **Ni69** were correlated with protonation at the carboxylate. The improved activity was thus tentatively assigned to the proton shuttling ability of the acidic residue in **Ni69**.[460]

C-substituted cyclams with aryl groups of differing electronic properties have also been explored.[473] CPE with **Ni70** in MeCN:H_2O (4:1) using a GC WE at E_{appl} = −1.7 V vs Fc^{+}/Fc gave a TON_{CO} of 4.5 with FE_{CO} = 80% and FE_{H2} = 7% after 0.5 h. This performance considerably exceeds that of **Ni1** using the same experimental conditions.[462,473] Surprisingly, methylation of the phenyl groups in **Ni70** to give **Ni71** had a profound effect on catalytic performance. After 0.5 h CPE under the same conditions, **Ni71** passed ∼10% of the charge, and reached a TON_{CO} of only 0.25 (FE_{CO} = 29%, FE_{H2} = 44%). Single crystal X-ray analysis revealed that **Ni70** adopts a *trans*-III conformation, axially coordinating two solvent molecules to give an octahedral species which persists in MeCN:H_2O (4:1). Conversely, **Ni71** exists as a boat-like *trans*-I species in the solid-state, with UV−vis spectra confirming that it retains square-planar geometry in solution. While these configurations may change upon reduction of **Ni70** and **Ni71** to their Ni^{+} active species, this example shows how minor changes in ligand structure can have a dramatic effect on catalytic activity.[473]

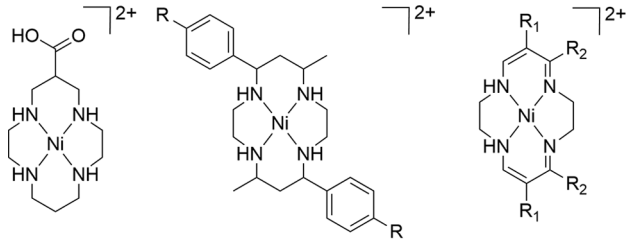

A handful of cyclam derivatives that reduce CO_2 to products other than CO have been identified, but this generally occurs only in nonaqueous solvents, as with **Ni1**.[70] Linking two nickel-cyclam units provided dimeric $\mathbf{Ni_2 1}$, which was explored with the hope of reducing CO_2 to C−C coupled products.[70] Using a Hg pool WE, $\mathbf{Ni_2 1}$ showed significantly decreased formation of CO compared to the aqueous performance of **Ni1**, though $\mathbf{Ni_2 1}$ displayed much greater H_2 evolution. HCO_2H became the major product when measurements were carried out in wet DMF (∼0.1 M H_2O).[70] CPE at E_{appl} = −1.4 V vs SCE with **Ni1** or $\mathbf{Ni_2 1}$ showed better HCO_2H selectivity of 81% for the latter but slightly worse FE_{HCO2H} of 68% after 5 h (no oxalate was detected with either CRC).[70] More promising results were obtained in a separate study with the unsaturated tetraaza-macrocycles, **Ni72**, **Ni73**, and **Ni74**.[474] CPE at a Hg pool WE at E_{appl} ≈ −2.15 V vs Fc^{+}/Fc in anhydrous MeCN showed CO_2 coupling to oxalate in all cases, with **Ni72** achieving the highest TON of 750 for all products combined with a FE_{C2O4H2} of 90%. CRCs lacking RCO_2Et or RCO_2Me substituents displayed lower activity due to instability, resulting from side reactions with CO_2 when this position was unfunctionalized.[474]

Polypyridine Ni-complexes function as CRCs. CV of qtpy complex **Ni75** showed an E_{onset} = −1.6 V vs SCE under CO_2 in MeCN, but CPE using a GC WE at E_{appl} = −1.7 V vs SCE gave small currents and only trace CO.[89] Ni tpy complexes display better activity.[57,436] CV of **Ni76** in H_2O:DMF (5:95) revealed two redox features, both being ligand-centered based on comparison with the analogous Zn-complex.[436] CPE with a Hg pool WE at E_{appl} = −1.72 to −2.14 V vs Fc^{+}/Fc showed 100% selectivity for CO over 3 h. Although no other CO_2 reduction products or H_2 were detected, FE_{CO} did not exceed 18%.

DOI: 10.1021/acs.chemrev.8b00392
Chem. Rev. 2019, 119, 2752−2875

Evidence that this low FE results from loss of ligand aromaticity was obtained from NMR experiments.[436] An additional study assessed the activity of **Ni76** along with related 4′-functionalized derivatives, **Ni77**-**Ni79**. CPE of **Ni76** in MeCN:H_2O (3:1) at E_{appl} = −1.83 V vs Fc^+/Fc using a GC WE gave a selectivity of 98% for CO over 1 h, but this declined to 24% after 12 h, with a final TON_{CO} of 6.5. UV−vis- and FT-IR-SEC results indicate that **Ni76** reacts with CO_2 following one-electron reduction, and vibrational bands corresponding to both Ni−CO_2 and Ni−CO species could be observed.[57] Dissociation of one tpy unit is thought to free a coordination site, in agreement with predictions made by the prior study outlined above.[57,436]

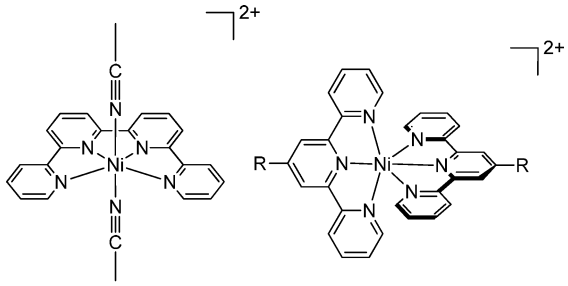

Ni75

Ni76, R = H
Ni77, R = CO_2H
Ni78, R = PO_3H_2
Ni79, R = SH

Electrochemical CO_2 reduction has also been demonstrated with Ni-carbenes.[182,475−477] Bis(pyridine-imidazolyidene-NHC) CRCs **Ni80**, **Ni81**, and **Ni82** all showed activity under CO_2 at the second of two metal-centered one-electron reduction events.[477] **Ni82** showed the most positive E_{onset} at −1.40 V vs SCE, and CPE using a GC WE at E_{appl} = −1.50 V vs SCE in "wet" MeCN revealed a TON_{CO} of ∼12 over 2 h (negligible H_2 detected, FE not reported). The longer linker in **Ni82** was proposed to impart greater flexibility, allowing easier ligand rearrangement upon reduction.[477] Building further upon this scaffold, it was found that E_{onset} can be shifted even more positively to −1.20 V vs SCE by substituting the pyridines in **Ni82** for isoquinoline groups, giving **Ni83**.[182] CPE in water-free MeCN with a GC WE at E_{appl} = −1.80 V vs SCE showed a FE_{CO} of 90% for the first 0.5 h, dropping to 22% over 8 h to give a TON_{CO} = 35. The loss in FE_{CO} was ascribed to reoxidation of CO at the counter electrode.[182]

Several tridentate NHC-ligands have also been studied. **Ni84** displayed three irreversible reduction waves, with the first two assigned as nickel-centered, and the third as ligand-based by comparison with the free NHC.[476] Under CO_2 in MeCN, catalysis occurs slightly before the third reductive feature, with greater currents upon H_2O addition (up to 0.8 mM). CPE with a GC WE at E_{appl} = −1.77 V vs Fc^+/Fc in MeCN with H_2O (0.4 mM) produced CO with no detectable H_2 over 2 h (no FE or TON reported).[476] Exchange of the pyridine in **Ni84** for a more donating aryl group in **Ni85** gave negative shifts of all redox features.[475] In MeCN, **Ni85** undergoes an irreversible reduction at −2.4 V vs Fc^+/Fc, displaying E_{onset} for CO_2 reduction at ∼−2.2 V vs Fc^+/Fc. H_2O addition shifts E_{onset} to −2.1 V vs Fc^+/Fc, but a catalytic wave occurs in the presence and absence of CO_2. Nevertheless, CPE with a GC WE at E_{appl} = −2.30 V vs Fc^+/Fc under CO_2 in MeCN with H_2O (2.0 M) gave a FE_{CO} = 34% and FE_{HCO2H} = 47% (TON of ∼1 for each) with no H_2 being detected over 2 h. While no improvement was observed for CO, TON_{HCO2H} increased to 5 after 9 h of CPE but at the

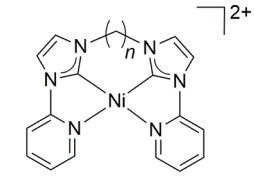

Ni80, *n* = 1
Ni81, *n* = 2
Ni82, *n* = 3

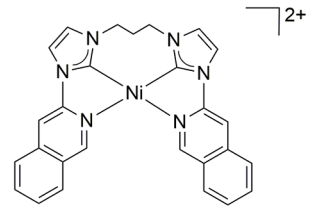

Ni83

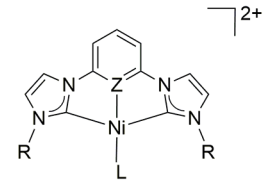

Ni84, Z = N, R = Me, L = MeCN
Ni85, Z = C, R = ^{n}Bu, L = Cl

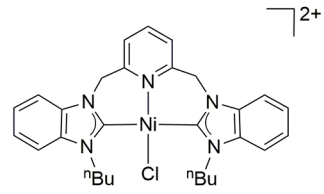

Ni86

cost of a lower overall FE of 16%.[475] **Ni86** features two benzimidazole-derived NHC units linked by a pyridine spacer, but CPE in DMF with TFA shows a maximum FE_{CO} = 4%, with a FE_{H2} = 91%.[478]

Multinuclear Ni_3**1** and Ni_2**4** mediate electrocatalytic CO_2 reduction.[479,480] Ni_3**1** features three bis(diphenylphosphino)-methane chelates in a planar arrangement with opposing methyl isocyanide and iodide groups capping the triangular core. It displays a reversible one-electron reduction in MeCN, giving a neutral radical.[479] The stretching mode of the isocyanide CN bond shows a 270 cm^{-1} shift to lower frequency upon reduction, indicative of noninnocent behavior. Under CO_2, Ni_3**1** mediates reductive CO_2 cleavage to give CO and CO_3^{2-}, reaching a TON_{CO} of 7 after 3 h CPE at E_{appl} = −1.09 V vs Ag/AgCl with a Pt WE, with product origin confirmed by $^{13}CO_2$ labeling. Water vapor presence gives HCO_2H as the dominant product. The neutral radical species is thought to activate CO_2 and give a cluster-bound $CO_2^{\bullet-}$ intermediate. This can react with a proton or second CO_2 to respectively give either HCO_2H or CO and CO_3^{2-}, after further single ET from a second reduced Ni_3**1**.[479] In depth IR-SEC results with related cluster Ni_2**4** support such a mechanism, and EPR and computational findings confirm the involvement of a ligand-based reduction.[480]

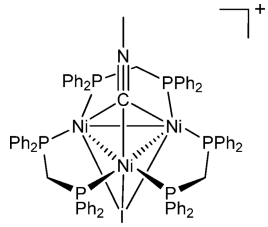

Ni_3**1**

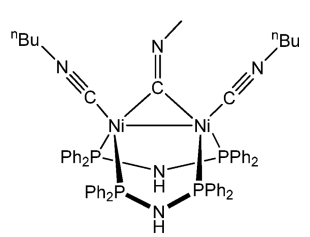

Ni_2**4**

2.3.7.2. Photocatalysis. The promising activity of **Ni1** has led to several photocatalytic studies of this CRC. An early report used irradiation (λ = 340−600 nm) of **PS1** in aqueous AA (pH 4.0), giving a TON_{CO} of 4.8, but only with repeated PS addition.[481] More basic media (pH 6.0) yielded CO selectivity of 78%, but large losses in activity (TON_{CO} = 0.02). Irradiation (λ = 440 nm) of **PS1** in aqueous AA (pH 5.0) with **Ni1** or **Ni87** yielded CO from CO_2 (confirmed by $^{14}CO_2$ radio-labeling

DOI: 10.1021/acs.chemrev.8b00392
Chem. Rev. 2019, 119, 2752−2875

studies), also producing HCO_2H with **Ni87**.[482] The smaller ring in **Ni87** is thought to give nonplanar coordination, freeing two cis sites and allowing for bidentate CO_2 binding. A QY_{CO} = 0.06% resulted for **Ni1**, whereas **Ni87** gave QY_{CO} = 0.05% and QY_{HCO2H} < 0.01%.[482]

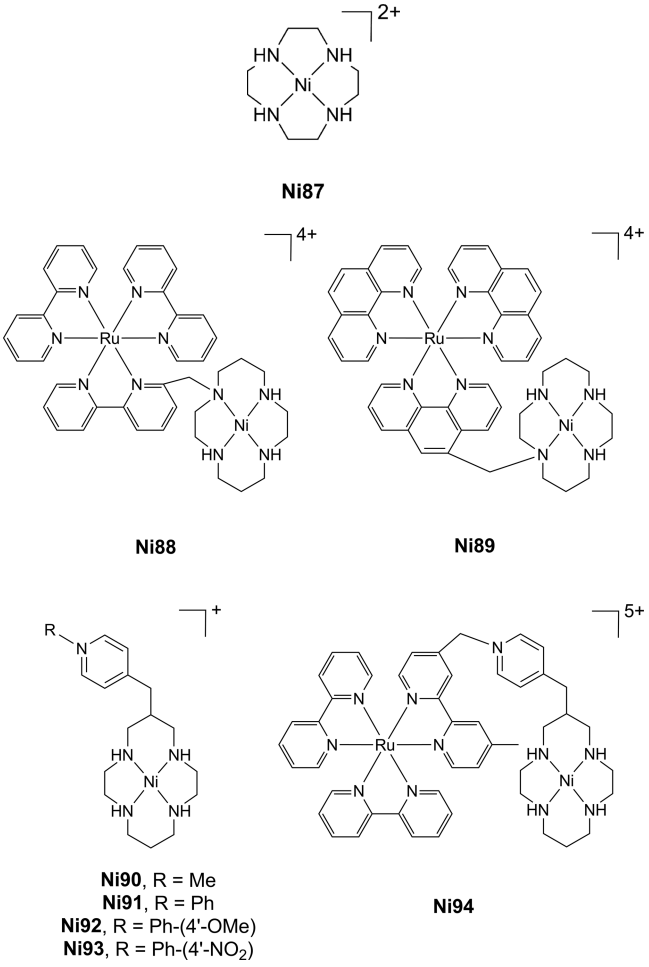

A number of dyads have been explored with a PS linked to a catalytic Ni-cyclam unit. Irradiation (λ = 350−600 nm) of **Ni88** and **Ni89** in aqueous AA (pH 4.0) did not outperform mixtures of **PS1** or **PS29** and **Ni1** after 1 h, but **Ni89** remained active for much longer.[483,484] After a total of 44 h, **Ni89** exceeded the two-component system in terms of selectivity for CO over H_2 (72% for **Ni89** vs 36% for **Ni1**) and gave ∼2.5-fold more CO, though the absolute amount was still below one turnover. **Ni88** was not stable when irradiated, due to Ru-subunit dissociation, likely from the steric strain imposed by the bpy-alkylation site. The low activity of both systems was in part attributed to N-substitution of the cyclam units.[483] To avoid this detrimental effect, linkage at one of the C-atoms in the cyclam ring was used to yield **Ni90**−**Ni94**. With **PS1** as a dye for **Ni90**−**Ni93**, irradiation (λ = 350−600 nm) over 2 h in aqueous AA (pH 5.1) gave improvements over **Ni1** in both CO selectivity (up to 16-fold) and CO production (up to 4.5-fold). Dyad **Ni94** showed lower increases compared to **Ni90**−**Ni93**, which was attributed to elimination of the Ru-subunit by photoinduced cleavage. The enhanced activity of **Ni90**−**Ni93** is believed to result from the pyridinium units reversibly storing electrons, as evidenced by CV measurements.[485] This example underscores the improved activity which can result from combining a transition metal center and a redox-active supporting ligand.

Binuclear analogues with two covalently linked cyclam units have also been studied photocatalytically. Irradiation (λ > 390 nm) of **PS1** in aqueous AA (pH 4) with Ni_2**1**, **Ni95**, or Ni_2**5** showed that Ni_2**1** produced less CO than **Ni1** over 1 h, but both **Ni95** and Ni_2**5** exceeded **Ni1**. Ni_2**5** yielded at least 6-fold more CO than **Ni95** to give a TON_{CO} of 2.0 per nickel center and a selectivity of 94% over H_2 evolution.[486]

Under simulated solar irradiation (AM 1.5 filter) of **PS2** in MeCN with TEA, **Ni83** gave a TON_{CO} = 1500 during 7 h using 200 nM solutions, which further increases to 98 000 upon lowering CRC concentration to 2 nM.[182] No H_2 was detected, but traces of CH_4 and C_2H_4 were observed. CO production plateaued after 13 h, but fresh PS resulted in reactivation, indicating good CRC stability. Assuming average irradiation of λ = 500 nm, a QY_{CO} of 0.01% was determined. Significantly higher efficiencies were exhibited by a system with **Ni96**, which is chelated by a dithioether featuring two terminal pyridine groups.[487] Using **PS1** in H_2O:*N*,*N*-dimethylacetamide (1:9) with BIH, **Ni96** gave a TON_{CO} = 712 over 55 h LED irradiation (λ = 450 nm), forming traces of HCO_2H and negligible H_2. Isotopic labeling with $^{13}CO_2$ confirmed the origin of the CO, and a QY_{CO} of 1.4% at λ = 450 nm was determined.[487] Despite differences in TON, taking into account the different reaction scales (40 mL for **Ni83** vs 4 mL for **Ni96**) the reported values reflect a ∼100-fold greater absolute CO amount (3 μmol for **Ni83** vs 30 μmol for **Ni96**) generated by the latter system over the same ∼7 h time frame. The two examples described above represent significant advances in light-driven CO_2 reduction mediated by homogeneous nickel complexes, though both rely still on precious-metal dyes.

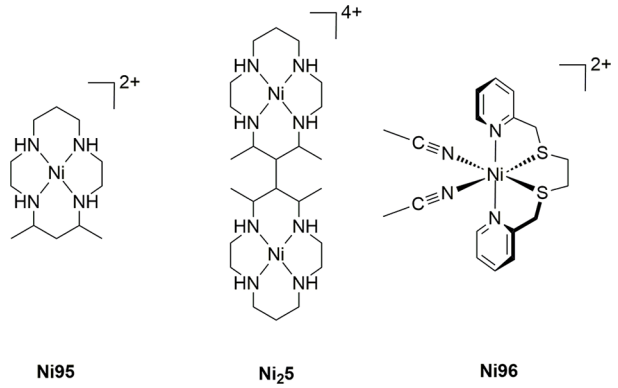

2.3.8. Copper. *2.3.8.1. Electrocatalysis.* An early example of Cu-based CO_2 reduction used a carbonate adduct with two PPh_3 units, **Cu9**.[488] CV in MeCN gave current increases under CO_2, whereas no enhancement was observed in the absence of complex or under N_2. CPE at E_{appl} = −2.0 V vs SCE using a Pt WE with a 1:5 ratio of $CuCl_2$ to PPh_3 in MeCN gave a total FE of 73%, producing HCO_2H, $C_2O_4H_2$, and CO. Further study would be required to ensure the complex is the active catalyst, as metallic copper deposition was observed, which can lead to formation of catalytically active films (section 2.2.6). Copper cyclam and derivatives have also been investigated as CRCs. Parent complex **Cu10** shows catalytic currents under both N_2 and CO_2 using a GC WE in aqueous solution (pH 8.45). While greater enhancements and a more positive E_{onset} are observed under CO_2, no product analysis was reported.[489] A substantial stripping peak is also observed following scan reversal in the anodic direction in both aqueous and organic media, suggesting the deposition of metallic copper.[489−491] This may result from

DOI: 10.1021/acs.chemrev.8b00392
Chem. Rev. 2019, 119, 2752−2875

the inability of the square-planar cyclam to accommodate low copper oxidation states.[489−491] **Cu11** and **Cu12** were designed to provide a more suitable geometry for the reduced metal ion. Although CV showed that this strategy largely suppresses demetalation, catalytic activity was substantially diminished.[489]

Cu13 and **Cu14** are chelated by naphthalene units that feature a hydroxy- and an imino-group in an *ortho*-arrangement.[492] CV showed current enhancements under CO_2 using a GC WE in DMF, but no product characterization was reported.[492] A system studied in more detail uses phosphine substituted bpy ligands, giving $\mathbf{Cu_2}$**4**.[493] Electrochemistry in MeCN showed two one-electron reductions, with catalytic onset at the second reduction under a CO_2 atmosphere. While both events are tentatively assigned as ligand-based, solvent dissociation from the metal center is thought to be required before catalysis commences. CPE at $E_{appl} = -1.7$ V vs Ag/AgCl with a Pt foil WE gave CO as the sole gaseous product, with a $TON_{CO} > 48$ over 24 h. IR-SEC results show formation of a copper-carbonate adduct, further supported by isotopic labeling.[493] CV of the three derivatives, $\mathbf{Cu_2}$**5**, $\mathbf{Cu_2}$**6**, and $\mathbf{Cu_2}$**7**, in MeCN with a GC WE showed similar currents at E_{onset} ∼100 mV more negative than $\mathbf{Cu_2}$**4**.[494] $\mathbf{Cu_2}$**8** displayed no activity, owing to strong coordination of the isonitrile in this species, leading to a lack of CO_2 binding sites upon reduction.[494] These examples highlight the potential of redox noninnocent ligand functionality, and the synergy which can result when proximal metal sites are present.

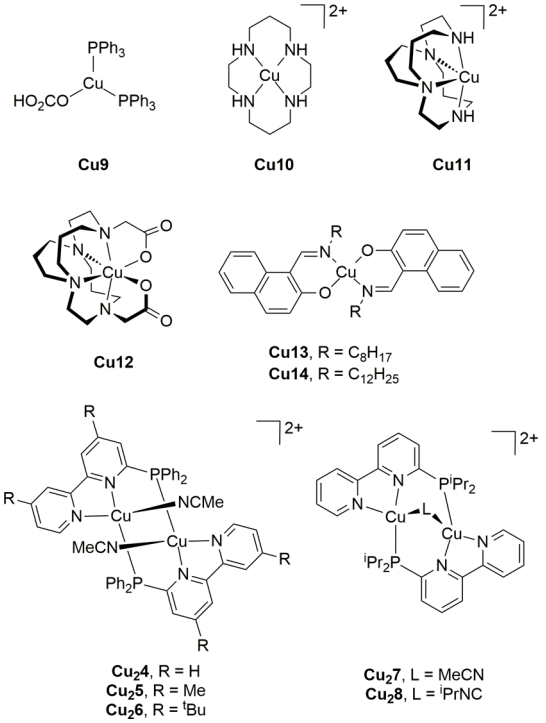

$\mathbf{Cu_2}$**9** possesses two tripodal TPA-like moieties, with an alkyldisulfide linker replacing one pyridine unit at each metal site.[495] In MeCN solution $\mathbf{Cu_2}$**9** sequesters CO_2 directly from the air and couples it selectively to form $C_2O_4^{2-}$. Charge consumption, UV−vis spectroscopy, and MS experiments all support a di-Cu^+ active species, and the source of oxalate was confirmed using isotopic labeling with $^{13}CO_2$. CPE with a GC WE at $E_{appl} = 0.03$ V vs NHE was conducted in MeCN containing $LiClO_4$ as an electrolyte to precipitate $Li_2C_2O_4$, preventing product inhibition by the oxalate product. The $Li_2C_2O_4$ was quantified, revealing a FE_{C2O4H2} of 96% and a TON_{C2O4H2} of 6 after 7 h. While build-up of $Li_2C_2O_4$ on the electrode surface ultimately limits system efficiency, capture of highly dilute CO_2 directly from air is a milestone for achieving practical recycling of this greenhouse gas from the atmosphere.[495]

A related study employs $\mathbf{Cu_2}$**10**.[496] Following reduction with AA in DMF solution, the corresponding di-Cu^+ state of $\mathbf{Cu_2}$**10** gradually reacts with atmospheric CO_2 in 96% yield over several days, giving a species in which oxalate bridges the two copper centers. The origin of the $C_2O_4^{2-}$ was verified by $^{13}CO_2$ labeling, and it was shown that this dianion could be displaced in MeOH by treatment with either HCl or HNO_3. Although only stoichiometric reactivity of $\mathbf{Cu_2}$**10** was reported, these results illustrate the promising reactivity which can result from cooperative interactions between two proximal metal centers, allowing for direct coupling of CO_2 units to give higher molecular weight products containing C−C bonds.[496]

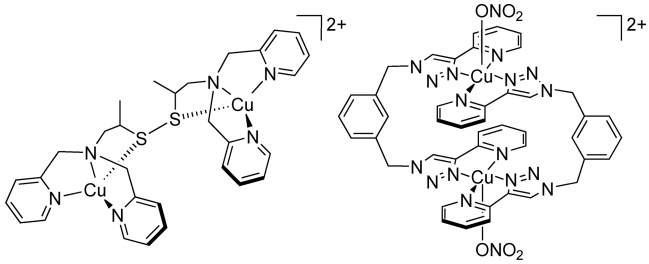

2.3.8.2. Photocatalysis. Carbonate-bridged $\mathbf{Cu_2}$**11** (bridging mode unspecified) is supported by a pair of 1,3-bis(diphenylphosphino)propane ligands, and reduces carbonate stoichiometrically when irradiated ($\lambda > 231$ nm) in MeCN, liberating CO with a yield of 85−93%.[497] Monitoring of the reaction by UV−vis absorption and emission revealed that evolution of CO is concurrent with ligand phosphine-monoxide formation. While quantification of this byproduct allowed a QY_{CO} of 0.01% to be determined at $\lambda = 313$ nm, the role of the ligand as an oxide acceptor in this reaction limits the potential of the system to be employed catalytically.[497]

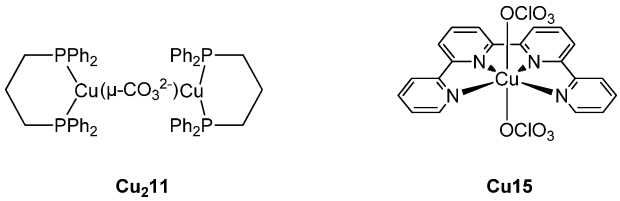

Together with **PS1** in MeCN:TEOA (85:15) containing BIH, qtpy-supported CRC **Cu15** reached a TON_{CO} = 2425, TON_{HCO2H} = 8, and TON_{H2} = 623 after 3.5 h irradiation ($\lambda >$ 420 nm).[498] The activity could be enhanced by adding water, resulting in a TON_{CO} of 12 400 (selectivity of 97%) with 3% v/v H_2O. Isotopic labeling confirmed $^{13}CO_2$ to ^{13}CO conversion, and a QY_{CO} of 1.2% was determined at $\lambda = 460$ nm. The molecular nature of the active CRC is supported by DLS and Hg^0 addition experiments, and measurements with $Cu(ClO_4)_2$ in place of **Cu15**. Mechanistic investigations revealed that one-electron reduction of **Cu15** is followed by dimerization to give a $[Cu_2L_2]^{2+}$ intermediate, a process previously reported with related Cu qtpy complexes.[499] Whether the active species retains this dimeric form is unclear, as further ET to the catalyst is needed to enter the catalytic cycle. Despite this uncertainty,

DOI: 10.1021/acs.chemrev.8b00392
Chem. Rev. 2019, 119, 2752−2875

observation of a bimetallic intermediate is noteworthy, especially given the high proportion of copper complexes that employ two metal centers to achieve CO_2 reduction.[498]

2.3.9. Zinc. Metal-based reduction does not typically occur with Zn^{2+} complexes under conditions desirable for efficient CO_2 reduction, but a few Zn-based CRCs have been reported.

Zn1 and **Zn2** feature phosphine-functionalized pyridine ligands.[500] Following exposure to CO_2 in THF solution, IR spectroscopy of the two complexes revealed changes only for **Zn2**, showing a new carbonyl feature consistent with formation of a CO_2-adduct. CV of **Zn2** in THF under Ar showed an irreversible one-electron reduction at −2.03 V vs Fc^+/Fc. When repeated under CO_2, current enhancement occurred at a potential ∼800 mV more positive, at E_{onset} = −1.20 V vs Fc^+/Fc. CPE in THF with a GC WE at E_{appl} = −1.8 V vs Fc^+/Fc led to CO formation (no quantification reported). A mechanism was proposed in which a phosphorus in **Zn2** initiates nucleophilic attack at the carbon of CO_2, forming an adduct that liberates CO upon reduction, with the Zn-atom behaving solely as a Lewis acid. The lack of CO_2 interaction for **Zn1** was attributed to the greater rigidity of the complex, with the less flexible chelating ligand hindering substrate access to the lone pair of the phosphorus atom.[500]

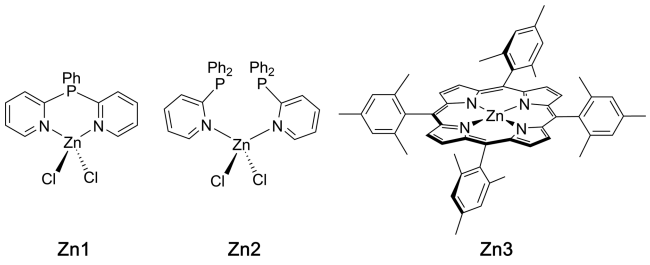

One of the few other examples outlines the use of a porphyrin, **Zn3**.[501] While this system exhibited promising activity in H_2O:DMF (1:9), the CRC was noncovalently deposited on polytetrafluoroethylene-treated carbon fiber paper and thus is discussed in more detail in section 4.3.1.1. While this study reports that the Zn cation is crucial for activity, it highlights that the oxidation state of the metal remains fixed throughout the catalytic cycle.[501] These results further emphasize the potential reactivity that noninnocent redox-active ligands can impart, reversibly storing reducing equivalents and facilitating catalytic conversion of CO_2.

2.3.10. Future Directions. The archetypal system for reduction of CO_2 to CO using 3d transition metal centers is the heterobimetallic active site of the [NiFe]-CODH enzyme. Despite this blueprint, there is a distinct lack of molecular complexes that utilize a combination of two different 3d metal ions for achieving catalytic CO_2 reduction to CO. In addition, catalysts employing functional residues in the second coordination sphere, whether for redox shuttling, proton relay, or electrostatic modulation, have been applied effectively in only a handful of cases. In the corresponding natural systems these features often act in concert, exerting a synergistic effect that dramatically enhances catalytic activity. Integrating comparable functionality into artificial systems is a challenging task but may help to achieve more efficient recycling of CO_2 into fuels and chemicals. Combining highly active molecular catalysts with the anchoring strategies outlined in the following sections is a viable approach toward this goal, and although these features have only just begun to be applied in the case of immobilized molecular catalysts they represent a promising future direction for the field.

3. IMMOBILIZATION STRATEGIES FOR MOLECULAR CATALYSTS

The immobilization of molecular catalysts onto surfaces provides a variety of advantages over homogeneous systems (see section 2). It requires, in the large majority of cases, chemical modification of the ligand structure with an appropriate anchoring unit.[196,502] The choice of anchor depends on the surface chemistry of the material[503] and type of targeted application such as an electrochemical, photochemical, or photoelectrochemical process. Properties of the material such as conductivity, morphology, and stability under experimental conditions (e.g., nature of the solvent, acidity, UV and visible light irradiation, electrochemical potentials, etc.) need to be carefully considered when looking at the elaboration of a molecule-driven, catalytically active device. The molecular catalyst is required to be robust and active under the same experimental conditions as the solid-state material. Conductive scaffolds can generally be used as an electrode material for catalyst immobilization, whereas semiconducting materials do not allow efficient electronic conduction within their bandgap ("forbidden zone") and are therefore usually used as light-absorbers and charge separators in photodriven redox transformations.[504] The morphology of the material surface is also important, with greater effective surface areas providing more

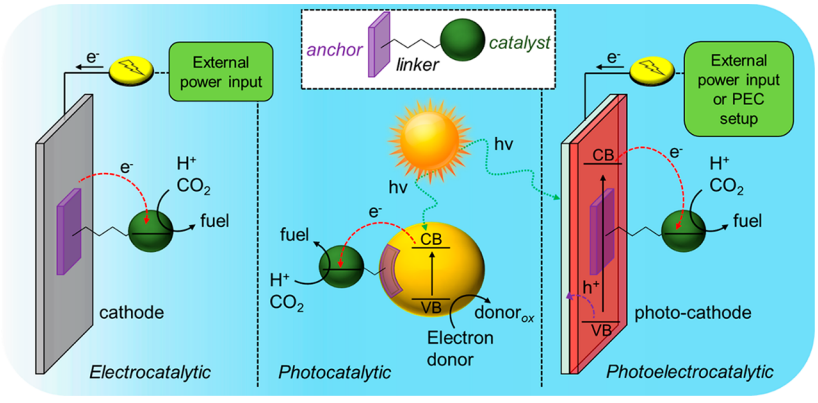

Figure 13. Schematic representation of three different configurations for the production of solar fuels. Left, electrocatalysis: electrode surface modified with a molecular electrocatalyst. Center, photocatalysis: molecular electrocatalyst anchored onto a light-harvesting colloidal material. Right, photoelectrocatalysis: light-harvesting SC-based photocathode modified with a molecular catalyst.

DOI: 10.1021/acs.chemrev.8b00392
Chem. Rev. 2019, 119, 2752−2875

available sites for the catalyst to be anchored, leading to higher loading and generally to higher catalytic performance per geometric surface area. For instance, 3D, mesoporous, and hierarchically organized surfaces often allow loading several orders of magnitude higher than flat surfaces, leading to much larger (photo)current densities and greater amounts of products formed.[505−508]

3.1. Approaches and Configurations

When aiming at immobilizing molecular catalysts for the production of solar fuels, there are currently three main strategies commonly employed (Figure 13). First, the catalyst can be immobilized onto a conducting electrode surface from which it will directly receive electrons for the electrogeneration of fuels. Second, the catalyst can be grafted onto a photoactive colloid that will drive the catalyst to generate fuel upon irradiation. The photogenerated positive charges are quenched by an electron donor. Lastly, the catalyst can be immobilized onto a light-harvesting material affording a photocathode on which photoelectrochemical (PEC) production of fuels will occur upon solar irradiation.

Considering the immobilization of molecular catalysts onto such (photo)electrode or particle surfaces, many different aspects should be considered to maximize the activity, stability, and selectivity of the system. Although often summarized under the vague tag of "anchor-bearing catalyst" or simply "catalyst", the chemical structure of the molecule-to-anchor compound is multifaceted and can be broken down into three different parts of almost equal importance: a coordination complex (that catalyzes the reaction upon reduction), the anchoring group (that permits the chemisorption of the molecular structure), and a linker (ensuring connection and also playing a vital role in ET dynamics; Figures 13 and 14). Compatibility for each of these moieties, the surface of immobilization, and experimental conditions must be achieved in order to afford a stable and efficient (photo)electrocatalytic setup. The catalysts (section 2) and anchors (section 3.3) are described in detail elsewhere in this review, whereas linker attributes are briefly addressed below.

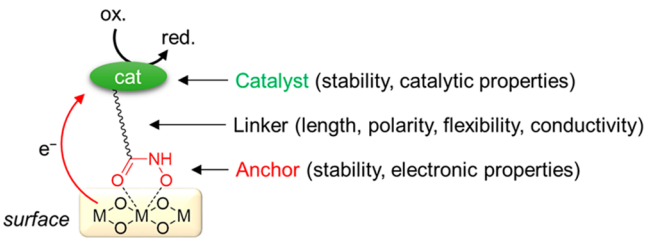

Figure 14. Schematic representation of a heterogenized molecular catalyst on a metal oxide surface, highlighting the main features contributing to efficient electronic interaction between the catalyst and the surface.

The derivatization of the catalyst with a linker moiety in order to introduce an anchoring group is usually carried out by means of covalent bonds through the modification of at least one of its ligands.[509] Care should be taken in the choice of the linker-ligand bonding group as any ligand modification can potentially induce changes in the steric and electronic properties of the catalyst, depending on the size and nature (electron-donating or -withdrawing) of the chemical function employed. This can possibly trigger dramatic changes in the overpotential required to carry out the reductive transformation or in the catalytic activity. The ligand flexibility can also be affected and consequently change its ability to generate catalysis-favorable conformations. Ultimately, as the ET between the surface and the catalyst proceeds either "through-bond" (via the linker orbitals) or "through space" (via direct orbital overlap or superexchange), the length, the chemical nature, and the orientation of the linker have a direct impact on the catalytic properties of the assembly by affecting ET kinetics.[510] For instance, a long, nonconductive, rigid linker will, in most cases, drastically hamper the rate of ET between the surface and the catalyst in both charge separation and recombination processes. Likewise, although the choice of anchor is crucial to establish a stable bond between the surface and the linker/catalyst, the importance of the electronic connection provided to the surface by the nature of the anchoring group should not underestimated.

3.2. Materials

3.2.1. Electrode Materials for Electrocatalysis. Supported electrocatalysis relies on the immobilization of a catalyst on an electrode. Applied toward fuel synthesis, the electrons flow from the electrode to the anchored catalyst to drive the catalysis, through the application of an E_{appl} more negative (cathodic process) than E_{onset} of the catalyst. The choice of cathode can minimize unwanted features such as high capacitive currents, resistive ET toward the catalyst, unwanted catalytic activity (side-reactions), and instability under catalysis conditions.

3.2.1.1. Carbon-Based Electrodes. Carbon-based electrodes are widely used for the fabrication of molecular catalyst-modified electrodes and include a large variety of carbon allotropes such as graphite/reduced graphene oxide (RGO), carbon nanotubes (CNTs), and boron-doped diamond.[511,512] These materials generally exhibit high conductivity and good mechanical stability and offer a wide operational electrochemical window. Another advantage of using RGO- and CNT-based nano-objects as electrode materials is the very high electroactive surface area that they can provide, allowing for high catalyst loading.[511,513] In addition, unless doped or modified with heteroatoms (N, B, and S), these nanomaterials show only low electrocatalytic background currents for proton or CO_2 reduction.[514−516] Thus, they allow for a precise study of the reductive transformations carried out by molecular catalysts either in solution (homogeneous system) or at their surface (heterogenized system).

3.2.1.2. Metal- and Metal Oxide-Based Electrodes. Many metallic electrodes (e.g., Pt, Cu, Au, Ag, etc.) exhibit catalytic activity toward proton- and/or CO_2-reduction and therefore produce products that are not generated by an attached molecular catalyst. This background activity can therefore decrease product selectivity of the modified electrode and prevent accurate characterization of the performance of an immobilized catalyst.[517−520] Metal electrodes also often present flat surfaces that prevent high loading of the catalyst, and their lack of transparency sometimes hinders investigations by spectroelectrochemistry. Metal oxide (MO_x) and SC-based electrodes may also be noninnocent during electrocatalytic experiments and display active catalytic surfaces (e.g., SnO_x).[521−523] Electrochemical studies are often hampered by SC electrodes, as their forbidden zone usually prevents observation of redox waves. On the other hand, the transparent nature of many MO_x electrodes is attractive for SEC studies and for use as protection layers in PEC systems.[524,525]

3.2.2. Colloidal Materials for Photocatalysis. As an alternative to electrocatalysis, another strategy consists of

DOI: 10.1021/acs.chemrev.8b00392
Chem. Rev. 2019, 119, 2752−2875

directly using sunlight as an energy input together with light-absorbing colloidal particles onto, or into, which a molecular catalyst is grafted.[526] The colloidal particle can either be used as a scaffold to associate a visible light-absorbing PS and the molecular catalyst as in dye-sensitized photocatalysis (DSP) schemes,[527] or can also act itself as the light harvester as in QD systems.[528,529] A range of materials with some general characteristics have been identified for colloidal photocatalysis. These characteristics usually consist of high surface area, simple functionalization pathways, good light-harvesting and charge separation ability, as well as energy levels to drive the catalysis and react with the electron donor. As a result, carbon-based colloids/particles, metal chalcogenide QDs, MO_x particles, and micellar aggregates have all been recognized as suitable materials and their respective attributes are discussed below.

3.2.2.1. Carbon-Based Particle Colloids. In analogy to carbon-based electrode materials, metal-free colloidal carbon materials are often based on sp^2 carbon and heteroatoms ordered in a planar organization to generate conjugation. Such colloids are often described as nontoxic, inexpensive, and scalable, and typically do not produce H_2 or CO_2-reduction products under irradiation in the absence of an additional fuel-forming catalyst. Carbon-based materials are used in photocatalytic systems as light-harvesters including carbon nitrides,[530] carbon nanodots,[531] and organic polymers,[532,533] but also as scaffold structures such as graphene oxide (GO)[534] or CNTs

3.2.2.2. Quantum Dot-Based Colloids. Chalcogen-based quantum dots such as cadmium sulfide, selenide, or telluride (CdS, CdSe, or CdTe) absorb visible light and can be used as photosensitizers in direct combination with a molecular catalyst to perform a redox transformation.[528,536] Such semiconducting nanocrystals usually display high extinction coefficients, with both a broad spectral range of absorption and the positions of their conduction band (CB) and valence band (VB) controlled by particle size. Moreover, QDs can continuously absorb multiple photons even after electrons or holes are accumulated, a great advantage for multielectron reactions. QDs can undergo direct surface interaction with catalysts that bear appropriate anchoring groups. Common methods for functionalizing QD surfaces with molecular catalysts primarily rely on electrostatic and covalent interactions by means of carboxylic acid, phosphonic acid, thiol, and dithiocarbamate groups via exchange with the capping ligands in place.[537−539] Such (capping) ligands are often used as surfactants during nanocrystal growth and for solubilizing QDs in various media, and can be tuned to participate productively in photophysical processes or to stabilize the QDs by preventing aggregation. On the other hand, QDs often rely on toxic or rare elements and are also known to suffer from photodegradation and surface defects that lead to charge recombination. Depending on the nature of the capping ligand QDs also exhibit background activity toward H_2 evolution that can limit their use, for instance when employed toward selective CO_2-reduction.

3.2.2.3. Metal Oxide-Based Colloids. MO_x-based colloid systems commonly rely on inexpensive, wide-bandgap, metal-oxide SCs that can only absorb a small fraction of the solar spectrum. However, this disadvantage can be overcome by combining them with a visible-light responsive PS to form a DSP system;[527] an adaptation of dye-sensitized solar cells (DSSCs) for fuel production.[505,540] In a typical DSP setup, photoexcited dyes inject electrons into a titanium dioxide (TiO_2)-based particle, which passes these low-potential electrons on to a coanchored catalyst for fuel synthesis while the holes are collected by a SED.[541] In addition to providing a potential charge-separating junction, nanoparticulate MO_x materials also deliver a polar scaffold with high surface area to receive both anchor-bearing photosensitizer and catalyst. Even for MO_x materials with an inaccessible CB such as Al_2O_3, ZrO_2, or SiO_2, the colloids may allow for direct and nondiffusional ET between coanchored PS and the nearby catalyst.[460,542] The success of these MO_x particles is due to their simple functionalization via polar groups such as carboxylic acids or phosphonic acids, in addition to their good dispersibility in aqueous media and stability under catalytic conditions. The choice of dye furthermore allows for easy tuning of the light absorption in a DSP system, and the colloid substrates usually display little background photoactivity in the absence of a catalyst, preventing unwanted side-reactions.[543]

3.2.2.4. Micelle- and Vesicle-Based Colloids. Micelles (5 nm) and vesicles (20−1000 nm) are aggregates of amphiphilic molecules that can form spontaneously in water or upon input of energy (Figure 15).[81] These transparent aggregates can be combined with molecular catalysts and photosensitizers to generate surface or embedded assemblies, bringing dyes and catalysts into close proximity and thus allowing intermolecular electronic communication.[544−546] In addition to their size difference, it should be noted that vesicles are closed objects made of a bilayer of surfactant that encapsulate a volume of solvent, whereas micelles represent a spherical organization of a surfactant. This discrepancy between vesicles and micelles can result in different scaffolding behavior by promoting encapsulation, embedment, or entrapment effects. Nonetheless, both vesicles and micelles can facilitate photoinduced charge transfer and suppress back ET without the need for an additional anchoring group. They can also permit organic molecules, usually insoluble in water, to be employed in aqueous media without precipitation. Although less reported than the other strategies, encouraging results have been achieved using vesicular and micellar colloids, with their unique nature constituting an alternative to metal-oxide or graphitic materials.[547−549]

3.2.3. Semiconductor Electrodes for Photoelectrocatalysis. Combining electrochemical and photocatalytic systems, a photocathode is capable of injecting electrons into an immobilized molecular catalyst to generate fuel during irradiation.[550−552] In order to carry out reductive transformations, most of the scaffolding materials used to build

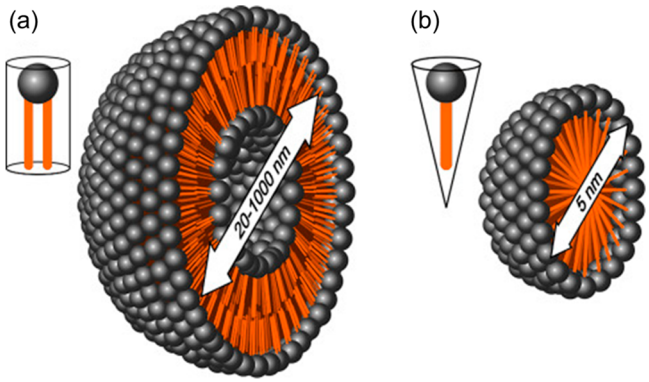

Figure 15. Schematic diagram of (a) a vesicle formed from cylindrically shaped amphiphiles and (b) a micelle formed from conical surfactants (Reprinted with permission from ref 546. Copyright 2015 John Wiley and Sons).

DOI: 10.1021/acs.chemrev.8b00392
Chem. Rev. 2019, 119, 2752−2875

photocathodes are p-type SCs (p-SCs), where holes (the majority carriers) are conducted in the VB and extracted toward a conductive support.[553] Depending on the bandgap of the SC, wide or narrow, two different strategies have been developed.

3.2.3.1. Wide-Bandgap Dye-Sensitized Photoelectrodes. In the case of wide-bandgap SCs, an additional coanchored PS is required to achieve efficient harvesting of solar light and to promote the photoinduced reduction of the catalyst. Further requirements of the p-SC are (i) an ability to enable the robust grafting of a photosensitizing unit and/or molecular catalyst on the surface, (ii) efficient hole extraction from the PS and hole transport kinetics, and (iii) stability under aqueous operating conditions for solar fuel generation in water. This array of prerequisites for the p-SC in dye-sensitized photocathode systems has rendered the search for such SCs extremely challenging, resulting in a lack of suitable material options. Wide-bandgap p-SCs such as nickel oxide (NiO)[554] or some ternary oxides (delafossites) with the general formula ABO_2,[555] commonly used in p-type DSSCs, have been envisioned as suitable cathodic materials for both proton and CO_2 reduction.[556,557] Beside the need for an additional PS, the main limitations of this type of architecture are currently the low charge mobility within the material, limited diversity of suitable p-SCs, rapid charge recombination, and surface states (defects) that all hamper the performances of the dye-sensitized photocathode.[558,559]

3.2.3.2. Narrow-Bandgap Photoelectrodes. P-type SCs with a narrow-bandgap such as p-silicon (Si), gallium phosphide (GaP), or cuprous oxide (Cu_2O) allow direct absorption of visible light and therefore do not require the presence of an additional dye. As a result, they can be directly coupled with a catalyst, provided that the energy level of the CB of the material is more reducing than the E_{onset} of the catalyst. A suitable VB potential (E_{VB}) to transport holes allows current to flow in the desired direction, with the electrons being injected into the immobilized catalyst and the holes into the conductive support. However, the majority of SCs with suitable bandgaps show limited stability in aqueous conditions, leading to the use of stabilizing covering layers often based on MO_x materials.[560] Molecular catalysts bearing conventional oxide-targeting anchors have been used to functionalize such layers.

As outlined, a variety of materials with distinct surface chemistry can be employed for the electro- and photosynthesis of renewable fuels. Thus, a range of different techniques have been developed to anchor molecular catalysts at the surface of nanoparticles or (photo)electrodes.

3.3. Anchoring Strategies

The conditions for grafting a catalyst onto a surface should at first be compatible with the catalyst stability. Covalent linkages usually lead to more stable anchoring but can also involve slightly harsher conditions than noncovalent attachment strategies. As mentioned above, the nature of the anchor can have a particularly important role in the electronic communication between the catalyst and the surface. It also affects the electronic properties of the material itself by generating a dipole at the surface, breaking orbital overlap, releasing protons, or blocking the surface from the solvent, with all of these processes changing the electronic properties.

3.3.1. Anchoring to Carbon-Based Materials. Carbon-based electrodes have been used extensively to immobilize molecular redox species for electroanalysis or electrocatalysis,[511,512] using several different anchoring strategies to modify the surface chemistry of graphite, glassy carbon, carbon nanotubes, graphene, and even diamond.[561−563] Surface modification of CNTs has received particular attention,[564−567] and they are now widely used as electrode materials with high effective surface area combined with excellent conductivity (especially multiwalled CNTs (MWCNTs)) and mechanical stability.[568] Recently, many different techniques have been developed for the chemical functionalization of graphene.[569] Generally, most reactions reported for the modification of sp^2 carbon in CNTs and graphene can potentially be adapted to other types of π-conjugated carbon surfaces. The following section is divided into two sub categories addressing covalent and noncovalent anchoring strategies.

3.3.1.1. Covalent Strategies. A covalent linkage of the molecular catalyst to a carbon surface is typically realized through a first step of derivatization of the sp^2 carbon surface, followed by a chemical reaction between the surface modifiers and a specific function at the molecular catalyst. Reactive functional groups on an sp^2 carbon surface can be generated by applying strongly oxidizing conditions, chemically or electrochemically, to create ketones, quinones, or carboxylic acid groups.[570−573] The presence of a carboxylic acid, for example, allows for grafting of compounds onto the carbon surface through formation of ester or amide bonds (Figure 16a).[574−577] However, this oxidizing strategy can be difficult to control and may lead to degradation of the physical properties of the substrate (conductivity and mechanical stability) through the production of defects within the carbon network.[578]

The reduction of aryl diazonium compounds on sp^2 carbon provides a less damaging means to modify glassy carbon, carbon fibers, or highly oriented pyrolytic graphite (Figure 16b).[578,579] This reaction is achieved by the generation, possibly in situ, of a diazonium salt from an aromatic amine residue, followed by a

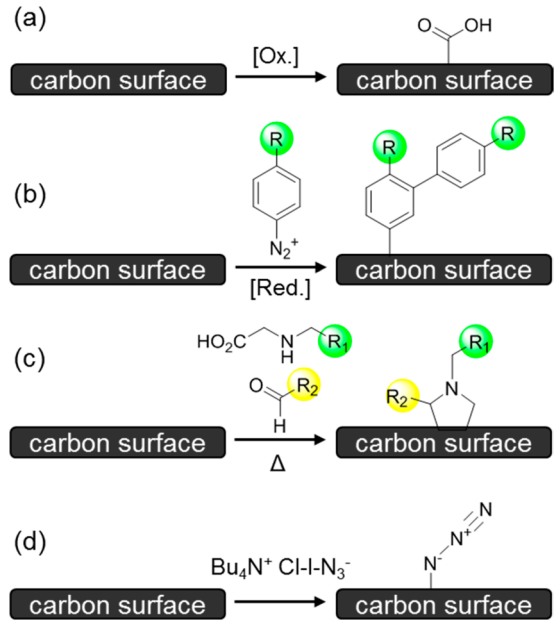

Figure 16. Selected examples of commonly used methods to covalently introduce functional groups onto π-conjugated carbon surfaces that subsequently enable functionalization with a catalyst: (a) chemical or electrochemical surface oxidation, (b) chemical or electrochemical reduction of in situ generated diazonium salts, (c) 1,3-dipolar cycloaddition of azomethine ylides, and (d) direct grafting of azide groups.

DOI: 10.1021/acs.chemrev.8b00392
Chem. Rev. 2019, 119, 2752−2875

reduction step leading to the formation of a radical species able to react with the π-conjugated carbon surface.[562,580] The reduction step can be carried out either electrochemically, directly at the carbon electrode surface, or chemically (e.g., Sandmeyer's reaction[581]) in solution.[582] This strategy allows for a high surface coverage of the modifier and has been employed to incorporate other functional groups such as amines, carboxylic acids, azides, or alkynes.[582−586]

The 1,3-dipolar cycloaddition of azomethine ylides, sometimes called Prato's reaction, has been widely applied to carbon surfaces such as CNTs, carbon nanohorns, and ordered mesoporous carbon surfaces.[587−590] The reaction relies on the condensation between an α-amino acid and an aldehyde, followed by a cycloaddition step leading to the formation of a pyrrolidine unit at the surface of the π-conjugated material (Figure 16c). This method provides the possibility to introduce two different chemical functions (R_1 and R_2).

Azide groups can be introduced at reactive graphitic edges through a Hassner-type addition of IN_3 generated in situ, followed by surface rearomatization through elimination of HI (Figure 16d).[591] The azide-functionalized surface can subsequently react with alkyne derivatives via 1,3-dipolar cycloaddition "click" chemistry to link a molecular catalyst.[592−594] In addition to the approaches listed above, there have also been reports of other methods involving the addition of carbenes[595,596] or nitrenes,[597] cyclopropanation,[598] and Diels−Alder addition,[599] which can functionalize a variety of carbon material surfaces.

3.3.1.2. Noncovalent Strategies. Noncovalent strategies have also been employed to modify carbon-based particles or electrodes without damaging their intrinsic properties (such as disruption of π-conjugation as a result of the grafting procedure). Polyaromatic and saturated compounds are commonly used to smoothly modify the surface of carbon-based materials by means of π-stacking and hydrophobic interactions (Figure 17).[600,601]

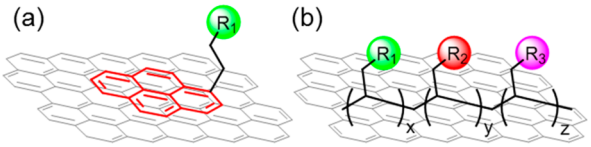

Figure 17. Schematic representation of noncovalent modification of carbon π-conjugated surfaces with (a) compounds bearing polyaromatic moieties enabling π-π interactions or (b) hydrophobic polymeric chains.

Derivatization of π-conjugated carbon surfaces with polyaromatic compounds via supramolecular $\pi-\pi$ interactions has been extensively employed.[600−605] Among polycyclic aromatic derivatives, the pyrene moiety has been particularly popular to anchor new functionalities to carbon surfaces, such as CNTs and graphene (Figure 17a). Pyrene groups interact more strongly with π-conjugated surfaces than smaller aromatic moieties such as anthracene or naphthalene.[603,606−614] Introduction of a pyrene anchor to a molecule of interest has been shown to allow immobilization of a wide range of hybrid structures, including redox probes,[614−617] molecular catalysts,[64,606−609] proteins,[618−621] and polyoxometalates.[622−624] Pyrene derivatization of a carbon surface provides stable anchorage, while also offering excellent control over the surface loading of the targeted molecular species by controlling the concentration of the pyrene-bearing compound in solution during the loading process.[606−611] Pyrene anchoring abilities may also extend to heteroatom-containing carbon surfaces.[612]

Polymers have also shown promise for the functionalization of carbon surfaces, the fabrication of new carbon-based composites, and direct immobilization of redox active species onto surfaces.[564,625,626] The polymer typically carries anchoring functionality for immobilization, and adsorption leads to composite materials with the desired chemical or electrochemical properties. Different strategies have been employed to immobilize polymeric structures on carbon surfaces. For example, they can be adsorbed through hydrophobic interactions or electro-grafted through oxidation/reduction of monomeric synthons containing pyrrole, thiophene, aniline, or vinyl groups.[627−629] Polymeric structures have allowed for robust adsorption of many different types of molecular catalysts for a great number of redox transformations.[630−633] One of the advantages of polymeric structures is their ability to carry several chemical functional groups (Figure 17b). This has been exploited to entrap redox enzymes within redox active films on electrodes.[634−637] A similar strategy has been applied with molecular catalysts to immobilize them on electrode surfaces, enhancing activity and/or tuning selectivity as a result of the polymer matrix environment.[638−640]

3.3.2. Anchoring to Metal Oxide Materials. Metal oxides are an attractive platform for the immobilization of molecular catalysts for photo/electro-catalysis, and the development of DSSCs has spurred substantial efforts toward the chemical modification of MO_x surfaces with metal complexes.[641] Several types of MO_x have been used in DSSCs,[642,643] and a large number of chemical functions have been described for grafting of dyes or catalysts via formation of chemical bonds to the metal of the MO_x surface.[644] Requirements for stability, surface coverage, and electronic properties, as well as synthetic effort need to be balanced in the selection of the anchoring group. Specifically, phosphonates, carboxylates, organosilanes/silatranes, hydroxamates, and acetylacetonates have been extensively used to immobilize molecular catalysts and dyes on MO_x surfaces for aqueous (photo)(electro)chemical fuel synthesis (Figure 18).[509,527,645−647] Although being an anchor-dependent process (footprint, acidity, etc.), the film coverage, quality, and purity also inherently rely on the chemistry of the MO_x surface (hydroxyl concentration, Lewis acidity/basicity) and the functionalization protocol used.

Carboxylate residues can easily be introduced into molecular complexes and are widely used as anchors for MO_x materials, in particular for nonaqueous DSSCs.[540] Carboxylates are believed to undergo a condensation reaction with the hydroxy groups at the surface of the MO_x, forming an ester-type linkage with the metal.[645] Studies have also suggested the possibility of a chelating or bridging binding mode with the metal, and bidentate modes have been shown to be preferred (Figure 18a).[649,650] Despite the facile functionalization of MO_x surfaces with carboxylate derivatives, the stability of the anchoring in aqueous media remains relatively low, especially at neutral and basic pH.[651] Nevertheless, many proteins display a significant number of surface-exposed carboxylates (glutamates and aspartates) that provide high affinity sites for adsorption onto MO_x surfaces such as TiO_2.[652−654]

Phosphonate groups chelate strongly to MO_x surfaces through a variety of binding modes (Figure 18b).[648,655−658] Similarly to carboxylic residues, condensation reactions with terminal hydroxy groups present at the surface of the material

DOI: 10.1021/acs.chemrev.8b00392
Chem. Rev. 2019, 119, 2752−2875

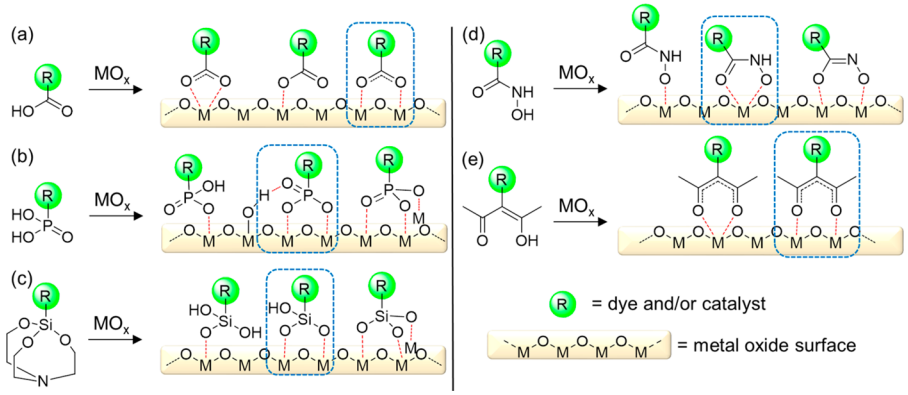

Figure 18. Surface binding motifs of different anchors used for grafting of dyes and catalysts onto MO_x materials: (a) carboxylate moieties through a chelating, unidentate, or bridging binding mode; (b) phosphonate anchors through mono-, bi-, and tridentate motifs; (c) silane functions through a mono-, bi-, or tridentate binding mode; (d) hydroxamates in unidentate, chelating, or bridging binding modes; and (e) acetylacetonate chelating or bridging binding modes. The potentially dominant binding modes are highlighted by a blue frame.[509,648]

allow efficient binding.[655] The tendency of phosphonates to bind more strongly than carboxylates may be due to the dianionic nature of the phosphonate ions, and the possibility of tridentate or a combination of bidentate and hydrogen bonding, rather than solely bidentate coordination to the surface. While limited at basic pH due the hydrolysis of the P−O bonds, the stability of phosphonate-metal bonds in neutral to acidic solutions allows for a broader pH window than many other functions. Integration of phosphonate anchors onto the molecular structure typically uses the Michaelis−Arbuzov reaction of an alkyl phosphite moiety with an alkyl halide derivative, or Hirao coupling between a trialkyl phosphite derivative and an aryl halide.[659−661]

Organosilanes are alternatives to carboxylate and phosphonate anchoring groups, and the resulting silyl ether-metal bonding shows high stability over a broad range of pH values, sometimes superior to phosphonic acids.[645,662−664] The chemical inertness of the Si−O bond, even superior to an ether bond, is usually attributed to a model involving hyperconjugative interactions.[665] Organosilatranes were introduced as a more practical and stable substitute for silanes or halogenosilanes, granting simplified synthetic routes prior to the grafting step of the dye or catalyst.[666−669] As for the phosphonate anchors, the organosilanes/silatranes bind to the surface through mono-, bi-, or tridentate interactions with the metal (bidentate being the preferred option; Figure 18c). The reaction of the organosilane/organosilatrane following a nucleophilic attack from the hydroxy group of the MO_x surface leads to the formation of a strong silyl ether-type surface bonding. In addition, in the case of bidentate binding, the remaining free −OH group can potentially react with neighboring Si anchors.[645] Although this effect can be beneficial toward increasing the stability of the anchoring by generating homocondensation products containing Si−O−Si bonds, it can also result in the formation of a potentially thick and insulating layer that impedes ET.

Hydroxamates have recently emerged as anchoring groups,[646,670,671] because they can form more stable surface adducts than carboxylates through unidentate, chelating, or bridging bidentate binding modes with the MO_x surface (Figure 18d).[672] Another advantage is their capability to allow faster interfacial ET between the dye/catalyst and the metal surface compared to other anchors such as phosphonates.[673] Furthermore, the small footprint of a hydroxamic acid can allow for the formation of densely packed monolayers.

Acetylacetonate groups also allow the formation of strong surface adducts stable in aqueous conditions.[674−677] This is due to their ability to form stable coordination complexes with metal cations.[678] These anchors preferentially bind to the MO_x surface through bidentate or bridging modes (Figure 18e).[675,679] Introduction of this functional group into molecular complexes relies on deprotonation and substitution of the 3-position in the 2,4-pentandione moiety, giving a covalent bond. Integration into aromatic compounds was also demonstrated using Ullmann type coupling,[680] or by reductive opening of isoxazole groups.[681,682]

Other strategies involve polymeric structures containing nitrogen heterocycles such as pyridine or imidazole groups that can physisorb through hydrogen bonding or metal coordination. These functional groups present a low individual affinity for MO_x materials that limits their potential as an anchor. Nonetheless, cooperative effects induced by the polymeric structure can make such anchoring stable and suitable for electrocatalytic purposes in aqueous conditions.[508] Similarly to the modification of carbon electrodes, polymers can also be used to adsorb molecules on MO_x surfaces. Recent examples have used redox or thermally polymerized vinyl-containing structures to adsorb dyes and/or molecular catalysts.[683−687]

3.3.3. Anchoring to Nonoxide Semiconductors. In addition to carbon and MO_x surfaces, molecular catalysts can also be immobilized on nonoxide SC surfaces to carry out catalytic conversions. These nonoxide SCs mostly feature narrow bandgaps and therefore can absorb visible light without an additional PS. There are a broad variety of nonoxide SCs with various chemical properties that have been described either for photocatalytic (colloidal systems) or (photo)electrocatalytic schemes. Such systems frequently rely on metal chalcogenide nanoparticles based on the association of Cd, Zn, In, or Ga with diverse chalcogenides (S, Se, and Te).[259,688−691] The surface modification of such types of particles by a molecule or an enzyme mostly involves the use of thiol, carboxylate, amine, and phosphonate groups (Figure 19a).[692−697] Importantly, the nature of such anchorage as well as the structure of the immobilized species strongly influences the electronic properties of the surface.[528,698] Despite several anchoring strategies being put forward, examples of molecular catalysts directly

DOI: 10.1021/acs.chemrev.8b00392
Chem. Rev. 2019, 119, 2752−2875

immobilized onto such particles remain limited, especially on electrodes.[57,128,699]

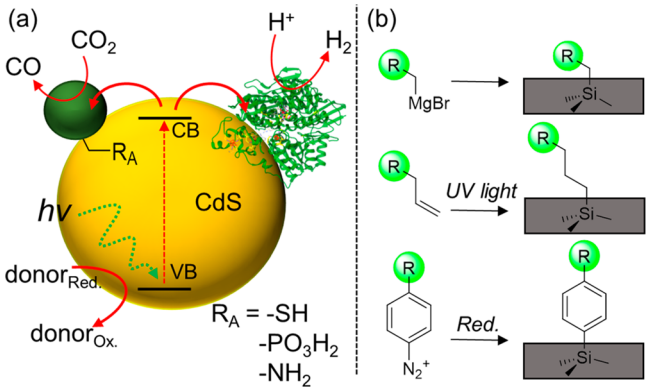

Figure 19. (a) Schematic representation of a semiconducting CdS nanoparticle modified with a molecular catalyst through the anchoring group R_A (left) or an enzyme (right). (b) Molecular modification of p-silicon surfaces using Grignard reagents, UV-induced grafting of alkenes, or reduction of diazonium salts.

Two of the most widely used nonoxide SCs for the fabrication of photocathodes are p-Si and GaP.[700,701] Both are narrow-bandgap SCs and are also notorious for their instability in aqueous or aerobic conditions, readily forming an insulating oxide layer at their surfaces.[560,702] In order to prevent the formation of these oxides direct surface modification has been employed using a variety of synthetic procedures, including Grignard reactions, UV-induced grafting of alkenes and polymers, or diazonium chemistry (Figure 19b).[703−707] Only a few examples have shown the integration of molecular catalysts directly at the surface of these SCs, mostly for proton reduction.[708−710] Another disadvantage of these narrow-bandgap SCs is their low surface area. Without specific design they remain flat and therefore do not permit high catalyst loading at their surfaces. Recent studies have focused on protecting the surface of the SC, while in some cases also increasing the available surface area, for instance by using a TiO_2 coating.[525,711−714] This protecting strategy allows functionalization of the SC with catalysts using the same anchoring functions described above for MO_x materials.

In addition to these nonoxide material photoelectrodes, the development of organic solar cells has recently led to the fabrication of organic polymer-based photocathodes for solar fuel production.[715] Several examples of such organic photocathodes are based on a poly(3-hexylthiophene) (P3HT)-C_{60} blend, generating a p−n junction within the electrode structure.[716,717] Other composites have also been reported to generate enough driving force for light-driven proton reduction.[718,719] To date, there are very few cases of such photocathodes combined with molecular catalysts.[720] The addition of chemically defined interfaces between the polymer blend and the electrolyte solution could potentially enable the use of the methods described above to immobilize molecular catalysts on these organic photocathodes.[721]

4. IMMOBILIZED CATALYSTS FOR ELECTROCATALYSIS

4.1. General Remarks

Grafting of molecular catalysts onto conducting or semiconducting electrodes allows their thorough investigation by electrochemical (and SEC) methods, delivering a deeper understanding of the mechanisms and redox events involved in the catalytic process (Figure 20a). Immobilization of the catalyst can also provide other benefits, such as stabilization over time and the ability to function in solvents in which the isolated catalyst would otherwise be insoluble. In some cases this strategy can increase the catalytic efficiency and/or selectivity toward the desired product. The grafting of molecular catalysts also gives the opportunity to generate a new synthetic environment directly around the catalytic site in order to modify the properties of the latter. Lastly, immobilization of the catalyst also implies that only the substrate and products are then freely diffusing, which improves practicality for potential future applications.

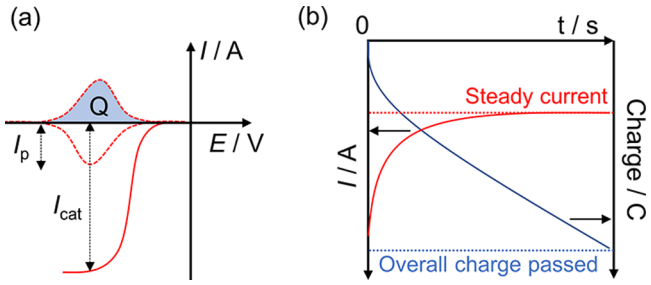

Figure 20. (a) Schematic representation of a CV experiment for an electrode modified with a molecular catalyst showing nonturnover redox waves (red dashed trace) and a catalytic wave (red trace) in the presence of substrate. (b) Schematic representation of chronoamperometry (or CPE) at E_{appl} showing the current value (red trace) and the corresponding charge passed (blue trace).

Nonturnover signals (in the absence of catalysis) in CV scans allow the estimation of surface loading of the electroactive catalyst (Γ, mol cm^{-2}; eq 14).

$$\Gamma = \frac{Q}{zFA} \tag{14}$$

where Q is the charge (C) obtained from integration of the nonturnover redox signal (Figure 20a) and A is the geometrical electrode surface area (cm^2). CPE (Figure 20b) with product quantification enables the determination of the TON and FE for a specific reaction and product (eqs 9 and 11, section 1.5). This section will focus on the main strategies that have been employed to immobilize molecular (and enzymatic) catalysts on "dark" (photoinactive) electrode surfaces for proton and CO_2 reduction in aqueous media or at the minimum using water as the primary proton source.

4.2. Electrocatalytic H_2 Evolution

4.2.1. Carbon Electrodes. *4.2.1.1. Covalent Grafting.* Many of the covalent strategies described in section 3 have been utilized to graft molecular HECs and CRCs onto carbon surfaces to allow for stable anchorage. Modification through electrochemical reduction of an in situ generated 4-aminoethylbenzenediazonium salt at a GC electrode has been employed to form an amide bond upon coupling with activated ester- or carboxylic acid-functionalized [FeFe]-H_2ase mimics (Figure 21a).[722−724]

DOI: 10.1021/acs.chemrev.8b00392
Chem. Rev. 2019, 119, 2752−2875

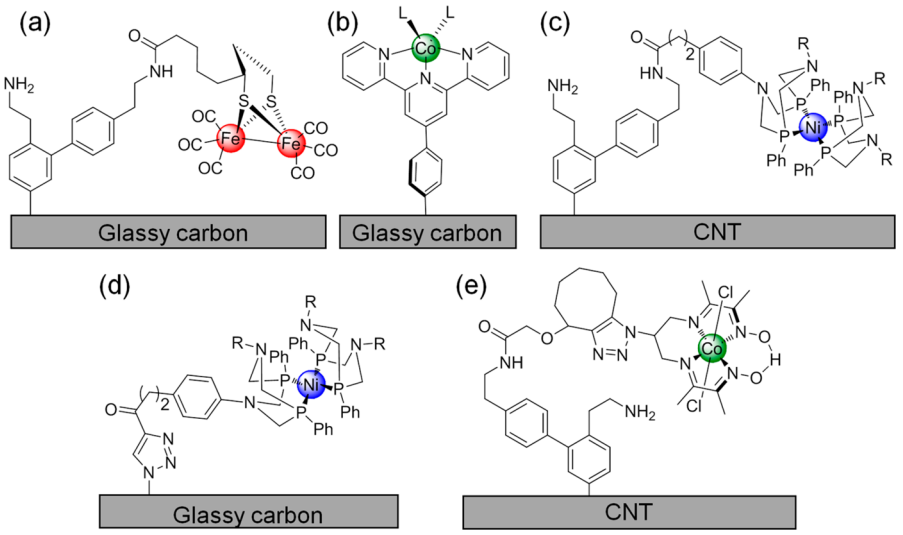

Figure 21. (a) [FeFe]-H_2ase mimic immobilized on an amine modified GC electrode through peptide coupling,[724] (b) Co(tpy)L_2 complex immobilized on a GC electrode through electrochemical reduction of the tpy diazonium salt, followed by metalation,[24] (c) Ni DuBois-type catalyst **Ni97** immobilized onto an amine-functionalized CNT electrode through peptide coupling,[726] (d) Succinamide analogue of **Ni97** immobilized onto GC initially modified with an azide group,[727] and (e) cobalt diimine-dioxime catalyst **Co77** covalently grafted onto an amine functionalized CNT surface through an amide linker.[728]

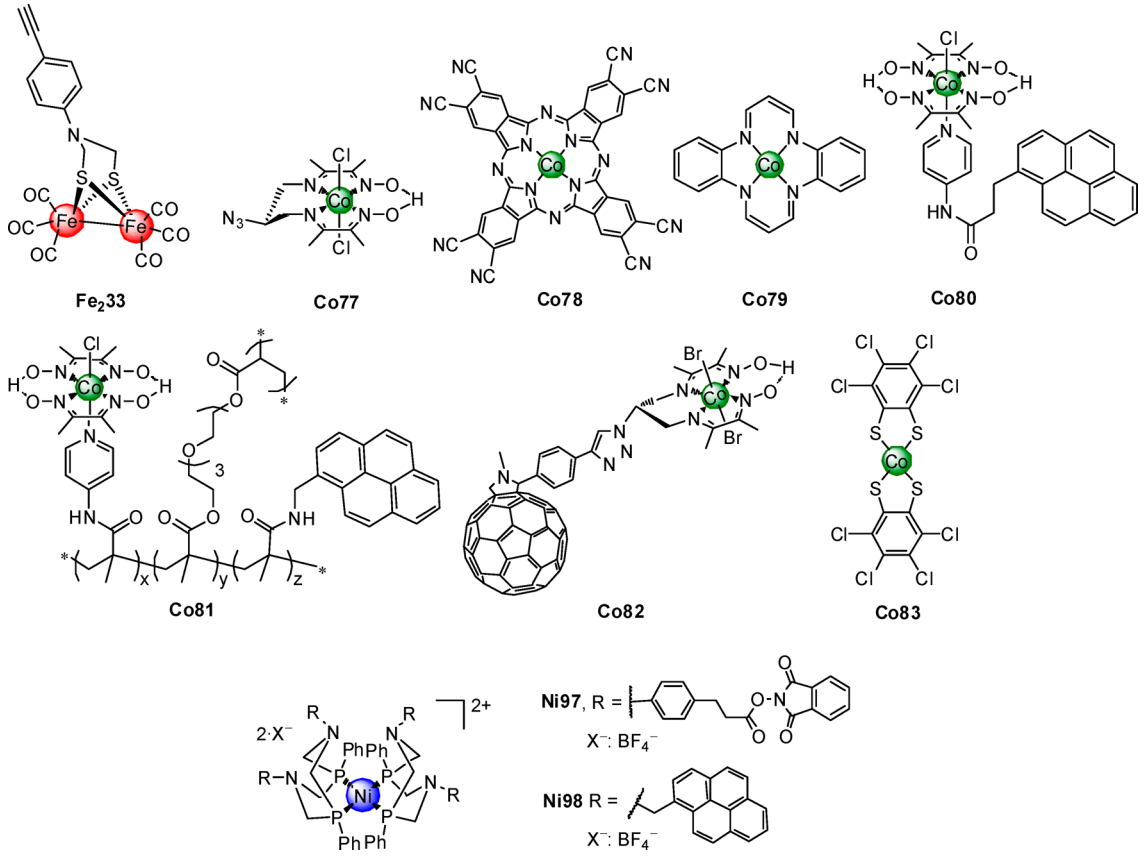

Figure 22. Molecular structure of HECs immobilized on carbon-based electrodes.

However, the immobilized [FeFe]-H_2ase mimic was unstable upon reduction, even in organic solution in the absence of acids, and it was shown that this deactivation was due to loss of the carbonyl ligands rather than leaching of the catalyst into solution through hydrolysis of the amide linkage.[724] A related [FeFe]-H_2ase mimic featuring a *p*-alkynylbenzeneazadithiolate bridging moiety (**$Fe_2$33**, Figure 22) was covalently grafted onto edge-plane graphite (EPG) electrodes using "click" chemistry, and an E_{onset} of −0.5 V vs the reversible hydrogen electrode (RHE) could be observed in LSV in strongly acidic aqueous conditions. CPE at E_{appl} = −0.7 V vs RHE for 20 min (Table 1, entry 1) revealed increased stability for this azadithiolate-grafted [FeFe]-H_2ase model, which could result from the decreased steric hindrance or the proton-shuttling ability of the linker.[725]

DOI: 10.1021/acs.chemrev.8b00392
Chem. Rev. 2019, 119, 2752−2875

Table 1. Electrocatalyic Proton Reduction under Aqueous Conditions Using Electrodes Modified with 3d Transition Metal HECs[a]

entry	electrode	HEC	E_{onset}[b] (V)	$\|j\|$ at E_{appl}[b] (mA cm^{-2} at V)	CPE duration at E_{appl}[c] (h at V)	TON_{H_2}[c]	FE_{H_2}[c]	conditions	ref
1	EPG	**$Fe_2$33**	−0.5	n/a	0.33 at −0.7	n/a	91%	H_2SO_4 pH 0.0	725
2	CNT	**Ni97**	−0.02	4 at −0.31	10 at −0.31	1×10^5	quantitative	H_2SO_4 pH 0 to 1	726
3	CNT	**Co77**	−0.35	1 at −0.59	7 at −0.59	5.5×10^4	97%	acetate pH 4.5	728
4	GC/Nafion	**Co13**	−0.14 (pH 7.0)	n/a	1.5 at −0.65	26	n/a	TFA, pH 1.0	737
5	BPG/ Nafion	**Co54**	n/a	n/a	1 at −0.44	70	n/a	phosphate pH 1.0	738
6	BPG	**Co38**	−0.34	n/a	1 at −0.64	2×10^5	n/a	phosphate pH 1.0	739
7	BPG	**Co52**	−0.34	n/a	1 at −0.64	1×10^3	n/a	phosphate pH 1.0	739
8	BPG	**Co78**	−0.34	n/a	1 at −0.64	5×10^4	n/a	phosphate pH 1.0	739
9	GC	**Co79**	−0.43	∼0.8 at −0.69	1 at −0.69	n/a	90%	NaCl, acetate pH 4.6	740
10	CNT	**Ni98**	−0.02	4 at −0.3	6 at −0.3	8.5×10^4	Quantitative	H_2SO_4 pH 0	606
11	CNT	**Co80**	−0.1	0.2 at −0.31	5 at −0.31	80	70%	phosphate pH 6.5	640
12	CNT	**Co81**	−0.1	0.3 at −0.31	>10 at −0.31	420	90%	phosphate pH 6.5	640
13	carbon cloth	**Co82**	−0.23	2.7 at −0.53	1 at −0.53	190	97%	acetate pH 4.5	720
14	graphite	**Co83**	∼−0.40	n/a	8 at −0.50	4.02×10^6	97%	pH 0.3	743
15	GC	**Co84**	∼−0.15	n/a	2 at −0.65	n/a	97%	$NaClO_4$ pH 2.6	745
16	GC	**Ni99**	∼−0.35	3.0 at −0.72	1 at −0.72	n/a	85%	$NaClO_4$ pH 1.3	748
17	GC	**Co85**	∼−0.45	n/a	2 at −0.72	n/a	97%	$NaClO_4$ pH 1.3	749
18	GC	**Co86**	∼−0.17	n/a	1 at −0.36	n/a	98%	$NaClO_4$ pH 1.3	746
19	GC	**Ni100**	∼−0.25	n/a	1 at −0.72	n/a	97%	$NaClO_4$ pH 1.3	746
				n/a	1 at −0.47		70%		
20	mesoITO	**Co90**	n/a	∼0.1 at −0.18	0.08 at −0.18	n/a	50%	phosphate pH 7.0	756
21	mesoTiO$_2$	**Ni35**	∼−0.1	∼0.6 at −0.25	8 at −0.25	600	88%	Na_2SO_4 pH 3.0	757
22	IO-ITO	[NiFeSe]-H_2ase	∼ 0	1.5 at −0.24	5 at −0.24	n/a	96%	MES pH 6.0	782

[a]All potentials are reported against RHE unless otherwise specified (n/a = not available). [b]Extracted from LSV measurements, unless otherwise stated. [c]Extracted from CPE measurements.

Direct modification of GC electrode surfaces with metal-coordinating ligands has also been investigated. A tpy ligand could be grafted directly onto the electrode surface via electrochemical reduction of a tpy-diazonium salt (Figure 21b).[24] Metalation of the covalently bound ligand gives a straightforward route to the mono-tpy Co-complex, which is thought to be the active species in analogous homogeneous systems using **Co60** (section 2.3.6.1).[436] CPE at E_{appl} = −1.5 V vs Ag/AgCl in DMF containing AcOH showed vastly improved H_2 evolution activity, producing apparent TON_{H2} values of 24 000 at a FE_{H2} of 90% after 3 h.[24]

Similar modification of a CNT-based electrode with 4-(2-aminoethyl)phenyl groups through electroreduction of the corresponding diazonium salt has allowed covalent attachment of a Ni DuBois-type catalyst (section 2.2.5.1) via peptide coupling between the amine modified surface and an activated ester implemented on the P_2N_2 ligand (**Ni97**, Figure 22). This surface engineering resulted in relatively low catalyst loading (Γ = 1.5 nmol cm^{-2}; Figure 21c), most likely due to a low coupling reaction yield, but displayed proton reduction activity in organic solvent.[726] Grafting of **Ni97** to a membrane-electrode assembly led to similar surface loading but allowed high activity for H_2 evolution in acidic media (0.5 M H_2SO_4), giving quantitative FE_{H2} with a TON_{H2} of 100 000 after 10 h of CPE at E_{appl} = −0.31 V vs RHE (Table 1, entry 2).[726] Remarkably, this hybrid electrode displayed reversible conversion of protons/H_2 at the thermodynamic potential, which is usually only observed with immobilized H_2ases or Pt.[726] Thanks to these very specific features, several CNT-Ni DuBois electrode architectures were also employed as precious-metal free molecular anodes in H_2/O_2 fuel cells.[729−732] Ni DuBois-type HECs have also been covalently grafted onto azide prefunctionalized GC electrodes. This method led to very low surface loading when the succinimide analogue of **Ni97** was anchored through reaction with a lithiated 1,2,3-triazolate functionalized GC surface (Γ ≈ 0.1 nmol cm^{-2}), and a TOF_{H2} of 28 s^{-1} could be calculated from CV analysis in anhydrous MeCN with [(DMF)H](SO_3CF_3) as a proton source (Figure 21d).[727] 1,2,3-Triazole immobilization was also achieved through cyclization between an azido group at the surface and an alkyne-bearing diphosphine ligand, followed by Ni metalation and addition of more diphosphine to reconstitute the complex on the electrode (no catalytic activity observed).[733] The above examples of DuBois-type HEC covalent immobilization illustrate the versatility of this "P_2N_2" ligand scaffold, as highlighted in section 2.2.5.1. The straightforward synthesis of these ligands from easily accessible amine starting materials allows the incorporation of a broad range of potential anchoring groups for covalent attachment on electrode surfaces.

DOI: 10.1021/acs.chemrev.8b00392
Chem. Rev. 2019, 119, 2752−2875

In addition to Ni DuBois catalysts, cobaloximes and cobalt diimine-dioximes have also been investigated on carbon surfaces. Immobilization of a cobalt diimine-dioxime moiety on CNTs was achieved by modifying the surface using a diazonium precursor, followed by esterification of the resulting primary amine with a functionalized cyclooctyne moiety (Figure 21e).[728] Azide-modified **Co77** (Figure 22) was grafted to the CNT surface through a copper-free 1,3-dipolar cycloaddition with the cyclooctyne, leading to Γ = 4.5 nmol cm^{-2}. The covalently modified hybrid electrode exhibited high activity in aqueous acetate solution (pH 4.5) with a TON_{H2} of 55 000 after 7 h CPE at E_{appl} = −0.59 V vs RHE (FE_{H2} = 97%; Table 1, entry 3).[728] The activity and stability of the Co diimine-dioxime moiety was thus greatly enhanced in comparison with homogeneous conditions, where a TON_{H2} of only ∼20 was obtained (section 2.2.4.1).[199] Immobilization may lead to isolation of the cobalt centers and therefore prevent degradation into other heterogeneous species, as has been seen in homogeneous organic or acidic conditions.[203−205,734] Moreover, diffusion-free systems may increase ET rates, thereby limiting side reactions such as hydrogenation of the glyoxime ligand.[735] However, thorough characterization of molecular integrity precatalysis, in operando, and postelectrolysis is important for an accurate interpretation of results with immobilized catalysts.[86,206] Interestingly, cobaloximes and Co diimine-dioximes display O_2 tolerance during catalysis in homogeneous solution and when immobilized on carbon electrodes, acting as oxygen reduction catalysts that co-produce a mixture of H_2O and H_2O_2.[191−193,195,640,736] This ability to operate under O_2 is a great advantage, as few catalysts remain active under these conditions.[195]

4.2.1.2. Noncovalent Grafting. Many early examples of noncovalent grafting used polymer matrices to bind molecular catalysts to carbon electrode surfaces. Immobilization of a tetracationic porphyrin (**Co13**, section 2.2.4.1) was achieved using this technique, by drop-casting a mixture of the HEC and a Nafion solution onto a GC electrode surface. The resulting modified electrode yielded a TON_{H2} = 26 at E_{appl} = ∼−0.65 V vs RHE (Table 1, entry 4; Figure 23a).[737] Subsequently, a similar strategy employing a basal-plane graphite (BPG) electrode with unmodified CoTPP (**Co54**, section 2.3.6.1) trapped in a Nafion film showed a TON_{H2} = 70 at E_{appl} = −0.44 V vs RHE (Table 1, entry 5).[738] Similarly, the use of a polyvinylpyridine (PVP) polymer as a matrix to immobilize different cobalt phthalocyanines (CoPc, **Co38**, section 2.2.4.2, $CoPc(SO_3H)_4$, **Co52**, section 2.3.6.1, and $CoPc(CN)_8$, **Co78**, Figure 22) gave a TON_{H2} of up to 200 000 after 1 h CPE at E_{appl} = −0.64 V vs RHE at pH 1 (Table 1, entries 6−8). Although the molecular integrity of the HECs was not verified after CPE, the polymer matrix may play a critical role in the high activity observed, as outlined below (section 4.3.1.1).[739]

Following these early studies on the entrapment or coadsorption of HECs in polymeric structures, several strategies used more defined polymeric matrices to immobilize catalysts on carbon-based electrodes. A DuBois Ni catalyst (not depicted) and [FeFe]-H_2ase mimic were both immobilized on carbon electrode surfaces through the respective formation of polythiophene or polypyrrole films. The HECs were grafted onto the GC surfaces through either electro-oxidation of the thiophene directly on the P_2N_2 ligand framework of the Ni-based catalyst or after postmodification of a polypyrrole film-functionalized electrode surface in the case of the Fe-catalyst (Figure 23b).[77,631] Both catalysts remained active upon

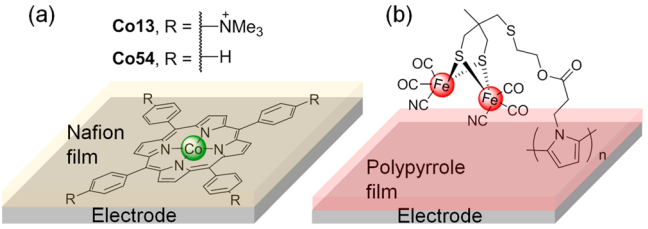

Figure 23. (a) Entrapment of Co porphyrins **Co13** or **Co54** in Nafion films deposited onto a glassy carbon electrode[737,738] (b) [Fe-Fe]-H_2ase mimic immobilized onto a pyrrole modified glassy carbon electrode.[631]

immobilization and demonstrated activity in organic solvent, as opposed to previously described examples of similar HECs when covalently immobilized. This shows the benefit of polymeric matrices for stabilizing the grafted catalytic core. In a related example, a cobalt dibenzotetraaza[14]annulene (**Co79**, Figure 22) catalyst immobilized onto a GC electrode surface through oxidative electropolymerization of the ligand framework showed moderate activity for proton reduction at E_{appl} = −0.69 V vs RHE at pH 4.6 (Table 1, entry 9).[740]

Over the past few years, modification of CNT electrodes with molecular catalysts through noncovalent π-stacking interactions has been widely employed due to its simplicity. An initial example used tetrapyrene modified catalyst **Ni98** (Figure 22), resulting in Γ of up to 11 nmol cm^{-2}, and highlighting the benefit of this anchoring strategy (Figure 24a) by giving a 7-fold increase compared to covalently bound DuBois catalyst **Ni97**.[606] At lower loadings of Γ = 2 nmol cm^{-2}, **Ni98** showed high TON_{H2} of 85 000 at E_{appl} = −0.3 V vs RHE. At higher loadings of Γ = 11 nmol cm^{-2}, a current density (J) of up to 4 mA cm^{-2} could be obtained (Table 1, entry 10).[606] Nevertheless, lower TONs were obtained compared with the **Ni97** system and could potentially result from the bulky pyrene-modified P_2N_2 framework, which may limit ligand flexibility and hinder the required proton shuttling (section 2.2.5.1).

Cobaloxime derivatives modified with pyrene anchoring groups were also immobilized onto CNT-based freestanding "buckypaper" electrodes via $\pi-\pi$ interactions.[640] A "monomeric" cobaloxime (**Co80**) and a cobaloxime integrated within a multifunctional polymeric chain (**Co81**) were compared, with the highly porous morphology of the "buckypaper" electrode allowing immobilization of high amounts of catalyst (Γ up to 200 nmol cm^{-2}; Figure 24b,c). The polymer-cobaloxime cathode delivered a TON_{H2} = 420 after 24 h at E_{appl} = −0.31 V vs RHE at pH 6.5, which is more than five times higher than for the "monomeric" counterpart **Co80** (TON_{H2} = 80; Table 1, entries 11 and 12).[640] This enhancement was attributed to the multifunctional polymeric matrix, which may facilitate proton diffusion and increase catalyst stability by entrapping the cobaloxime units in the polymer during turnover. This strategy of combining multifunctional polymer matrices and nanostructured electrodes is of great interest to increase the activity and/or stability of molecular catalysts on electrode surfaces.

Carbon cloth was employed as a conductive scaffold for H_2 evolution after modification with an alkyne-bearing fullerene (C_{60}) that was "clicked" with an azide-bearing cobalt diimine-dioxime catalyst (**Co82**, Figure 22).[720] $\pi-\pi$ interactions between the fullerene moiety and surface of the electrode resulted in high Co loading (Γ > up to 260 nmol cm^{-2}), with the cathodes achieving a TON_{H2} = 190 after CPE for 1 h at E_{appl} = −0.53 V vs RHE (Table 1, entry 13). It is however difficult to assess the real potential of such electrodes, as a large amount of

DOI: 10.1021/acs.chemrev.8b00392
Chem. Rev. 2019, 119, 2752−2875

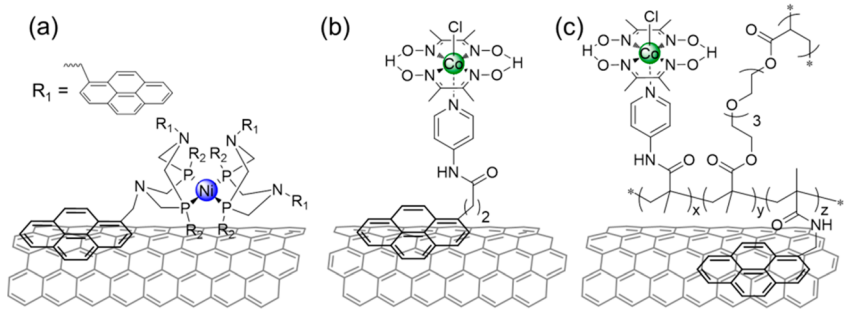

Figure 24. Immobilization of molecular catalysts onto CNT surfaces through π- π-stacking: (a) Ni DuBois catalyst **Ni98**,[606] (b) cobaloxime with an axial pyridine linked to a pyrene anchor, **Co80**,[640] and (c) cobaloxime ligated via axial pyridine units within a polymer matrix, **Co81**.[640]

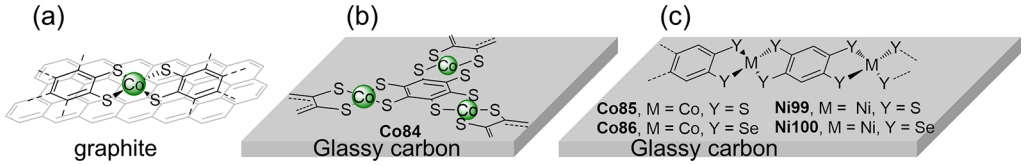

Figure 25. (a) Co dithiolate derivatives adsorbed onto a graphite surface.[742] (b) 2D Co coordination polymer **Co84** immobilized onto glassy carbon.[745] (c) Ni or Co 1D coordination polymer immobilized onto glassy carbon.[746]

the HEC remains inactive due to the poor wettability of the assembly and the packed organization of the C_{60}-based catalyst within the electrode matrix. It is worth noting that "click" syntheses often use copper-catalyzed cycloaddition, which can result in replacement of Co by Cu in the diimine-dioxime ligand.[728,741] Furthermore, as Cu-based complexes are often converted into active H_2 evolving materials during CPE (section 2.2.6), residual traces of Cu should be thoroughly removed and quantified prior to studying an immobilized molecular catalyst.

Several Co bis(benzenedithiolate) derivatives were studied on graphene and highly oriented pyrolytic graphite electrodes by taking advantage of noncovalent hydrophobic interactions (Figure 25a).[742−744] In comparison to the nonsubstituted benzene dithiolate, extended aromaticity in the naphthalene dithiolate derivative allowed adsorption of higher amounts of catalyst onto the graphitic surface and decreased η for proton reduction. Other derivatives were also shown to produce H_2 when immobilized on graphite, and a $TON_{H2} = 4.02 \times 10^6$ was determined for the most active cobalt tetrachlorobenzene dithiolate derivative (**Co83**, Figure 22) in acidic conditions (CPE performed at $E_{appl} = -0.5$ V vs RHE at pH 0.3), despite requiring a relatively high η ($E_{onset} \approx -0.4$ V vs RHE) (Table 1, entry 14).

Two-dimensional molecular films based on cobalt dithiolate derivatives with different aromatic structures were also deposited onto carbon electrode surfaces. The resulting metal organic surface (MOS) films enabled similar Γ of up to 4000 nmol cm^{-2} through hydrophobic interactions.[745] A similar MOS film consisting of Co benzenehexathiolate (**Co84**, Figure 25b) on a GC plate displayed proton reduction with a FE_{H2} of 97% after 2 h CPE at $E_{appl} = -0.65$ V vs RHE (Table 1, entry 15).[745] CPE for 10 h at less negative potentials ($E_{appl} = -0.4$ and -0.5 V vs RHE) showed moderate stability for this hybrid material.

Coordination of Ni to the same benzenehexathiolate ligand also led to formation of two-dimensional films, and LSV scans with a rotating disk electrode in H_2SO_4 (0.5 M) displayed an early E_{onset} for proton reduction at -0.11 V vs RHE (product analysis not reported).[747] One-dimensional coordination polymers generated from Co, Ni, Fe, and Zn with benzene-1,2,4,5-tetrathiol immobilized onto carbon electrodes were also studied.[748,749] The Ni-based complex (**Ni99**, Figure 25c) showed the most promising activity, followed by the Co counterpart (**Co85**, Figure 25c), with respective E_{onset} at ~ -0.35 and -0.45 V vs RHE. CPE showed steady catalytic current for **Ni99** ($\sim$3 mA cm^{-2} for 1 h), with a FE_{H2} of 85% at $E_{appl} = -0.72$ V vs RHE in aqueous conditions (pH 1.3; Table 1, entries 16 and 17).[748,749] A lower FE resulted for the Ni compared to the Co catalyst film and may be due to degradation under acidic conditions, as observed with films of the parent monomeric Ni compound.[750]

Analogous 1D coordination polymers were also synthesized based on coordination of Co or Ni by the Se-containing ligand benzene-1,2,4,5-tetraselenolate (**Co86** and **Ni100**, Figure 25c).[746] Both films were deposited onto GC electrode surfaces and shown to be active for proton reduction in acidic conditions. **Co86** showed two successive catalytic waves, attributed to different mechanisms, with the earlier $E_{onset} = -0.17$ V vs RHE (pH 1.3). CPE at $E_{appl} = -0.36$ V vs RHE gave a FE_{H2} of 98% (Table 1, entry 18, see entry 19 for **Ni100**).[746] The selenium within the [NiFeSe]-H_2ase-inspired ligand framework[19,751,752] was proposed to be responsible for the increased activity, enabling complementary catalytic mechanisms.[223,275,753]

4.2.2. Metal Oxide Electrodes. Metal oxide electrodes provide another means to immobilize molecular catalysts through the use of different surface chemistry (section 3.3.2). Although "dark" electrocatalysis does not require transparent electrodes, this property of many MO_x materials facilitates SEC characterization of the immobilized molecular species to unravel the catalytic mechanism.[524] Moreover, catalyst-MO_x architectures can easily be directly transposed onto photoelectrodes (sections 6 and 7).

Grafting of a Co diimine-dioxime catalyst (**Co87**, Figure 26) onto a mesoporous indium tin oxide (mesoITO) electrode was achieved via two phosphonic acid groups on the bridge of the diimine-dioxime ligand (Γ = 150 nmol cm^{-2}; Figure 27a).[754] Although a catalytic wave from the Co complex could be observed with the modified electrode, degradation of ITO in aqueous conditions at negative potentials prevented long-term CPE experiments. The strong coloration of the yellow Co^{3+}, red Co^{2+}, and blue Co^{+} oxidation states in the ITO-Co diimine-

DOI: 10.1021/acs.chemrev.8b00392
Chem. Rev. 2019, 119, 2752−2875

dioxime assembly allowed for SEC characterization and also inspired the assembly of a tricolored electrochromic device.[755] Several cobaloxime and Co diimine-dioxime catalysts (all bearing phosphonic acid moieties as anchoring groups) were synthesized, and their activity for proton reduction compared in a colloidal dye-sensitized system (section 5.2.3).[194,527,541,543,754] As highlighted already in section 2.2.4.2, the axially coordinated pyridine becomes labile upon irradiation or reduction. This led to loss of **Co88** from the electrode surface during turnover, whereas the diimine-dioximes **Co87** and **Co89** showed enhanced stability, thus underlining the importance of robust linking of the catalytic core to the anchoring group in order to prevent leaching of the grafted catalyst.

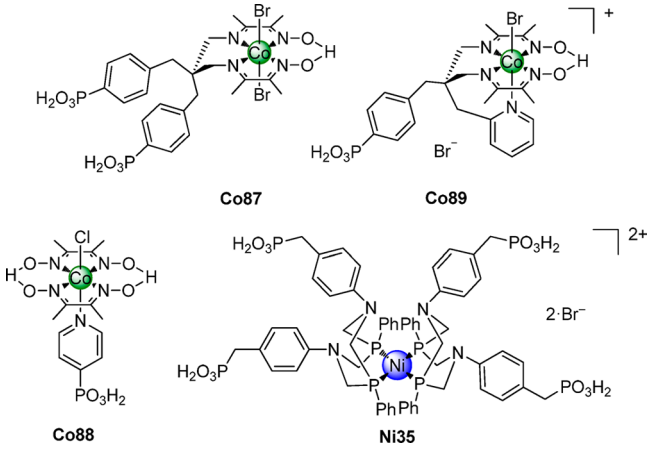

Figure 26. Molecular structures of HECs immobilized on metal oxide electrodes.

Photopolymerization of 4-vinylpyridine onto mesoITO has been described, providing an anchoring ligand for a cobaloxime derivative and enabling SEC characterization (**Co90**, Figure 27b).[756] Despite the instability of ITO at negative potentials, CPE at E_{appl} = −0.18 V vs RHE produced a moderate FE_{H2} of 50% (Table 1, entry 20).

A cathode employing a mesoporous TiO_2 ($mesoTiO_2$) surface with a Ni DuBois catalyst bearing four phosphonate anchoring units was assembled for proton reduction (**Ni35**, Figure 27c).[757] In contrast to ITO, semiconducting TiO_2 hampers electrochemical characterization of the adsorbed catalyst within the "forbidden zone" but provides a conducing scaffold at potentials more negative than the potential of its CB (E_{CB}). CV with a TiO_2 electrode in the absence of adsorbed catalyst displays a "trumpet plot" from charging/discharging of the CB of TiO_2. CV with the immobilized phosphonated Ni DuBois catalyst (Γ up to 15 nmol cm^{-2}) resulted in an increase of the cathodic process (at an onset close to 0 V vs RHE) and the disappearance of the anodic wave upon scan reversal. This observation confirms discharging of the CB of TiO_2 due to charge transfer to the immobilized catalyst and is further evidenced by spectroelectrochemistry of the "blue" TiO_2 CB electrons that can easily be observed upon charging the CB of TiO_2 at reducing potentials. CPE at E_{appl} = −0.25 V vs RHE resulted in a TON_{H2} for **Ni35** of 600 and a FE_{H2} of almost 90% (Table 1, entry 21).[757]

As illustrated above, porous ITO and TiO_2 provide complementary electrode materials that allow the study of immobilized catalysts at a high loading. The degenerate SC ITO gives a conductive scaffold that is ideally suited for electrochemical characterization coupled with spectroelectrochemistry.[524] However, instability at negative potentials prevents its use in electrocatalysis with heterogenized catalysts requiring substantial η. TiO_2 is insulating in the "normal" potential window but becomes conducting at potentials where ITO degrades. The charging of the TiO_2 CB can be followed spectroscopically and provides valuable information about ET kinetics to an immobilized species. The robust nature of TiO_2 makes it a suitable material for electrocatalytic fuel synthesis.

4.2.3. Hydrogenase-Based Electrocatalysis. Despite their limitations (common O_2 sensitivity, cost of purification, and limited stability), isolated H_2ases are model systems for the development of efficient catalysts for proton reduction, as they operate at the thermodynamic potential and thereby catalyze proton reduction at remarkable rates at a small η.[29,758−761] Since the demonstration of direct ET and electrocatalysis by immobilized H_2ases on carbon black, GC, and EPG electrodes,[762−765] many of the properties of different H_2ase enzymes could be unraveled through the use of protein film electrochemistry (PFE).[760,761] Because H_2ases are sensitive macromolecules, several strategies have emerged to stabilize H_2ase protein films on carbon electrodes. The use of coadsorbents such as polymyxin,[765] redox polymers to entrap the protein,[634,766,767] modified electrodes with higher surface area,[768,769] or electrostatics and covalent linkages[770−772] has allowed for improvements in protein loading, interfacial electronic communication, and stability for H_2 oxidation and proton reduction.[619,769,773−776] Porous MO_x electrodes are emerging as versatile platforms that enable high loading of electroactive protein, with excellent stability in defined electrochemical windows and prospects for SEC investigations.[777,778]

H_2ases have been immobilized onto porous MO_x electrodes such as TiO_2 and ITO,[713,779−781] and reversible electro-

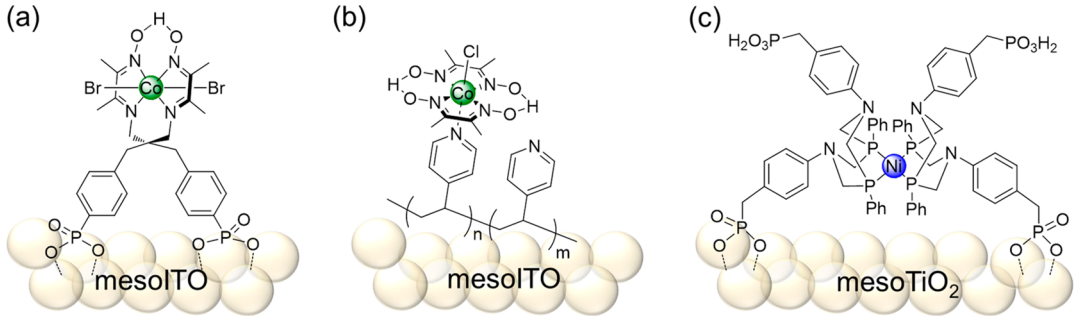

Figure 27. Immobilization of (a) phosphonated Co diimine-dioxime **Co87** onto mesoITO,[754] (b) a cobaloxime derivative through coordination to a polymerized polypyridine (**Co90**) deposited on mesoITO,[756] and (c) a Ni DuBois catalyst onto $mesoTiO_2$ using phosphonate anchoring **Ni35**.[757]

DOI: 10.1021/acs.chemrev.8b00392
Chem. Rev. 2019, 119, 2752−2875

chemistry similar to that observed on carbon electrodes has been demonstrated when the H_2ase active site sits close enough to the conductive substrate (e.g., ITO). Using a hierarchical mesoporous inverse opal (IO) ITO electrode allowed a high loading of a [NiFeSe]-H_2ase from *Desulfomicrobium baculatum*,[782] and absolute current densities of up to 1.5 mA cm^{-2} (stable over 5 h) were observed for proton reduction with FE_{H2} = 96% at E_{appl} = −0.24 V vs RHE (Table 1, entry 22; Figure 28). As the H_2ase only requires a small η for proton reduction, porous ITO could be employed as a robust and stable electrode material in CPE, giving high TONs with almost quantitative FE, which is yet to be achieved with a synthetic first row transition metal catalyst.

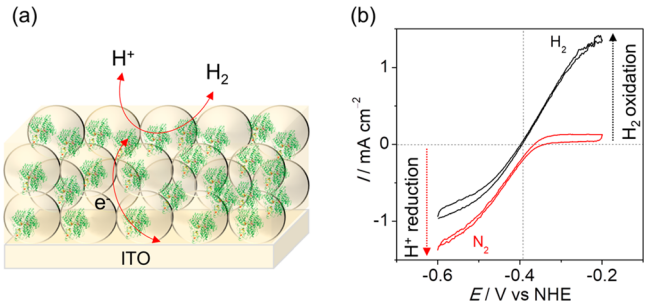

Figure 28. (a) [NiFeSe]-H_2ase immobilized within an IO-ITO electrode. (b) Protein film voltammetry (pH 6.0) of a [NiFeSe]-H_2ase immobilized within an IO-ITO electrode showing reversible electrocatalytic H_2 conversion (proton reduction and H_2 oxidation at the thermodynamic potential).[782]

4.3. Electrocatalytic CO_2 Reduction

4.3.1. Carbon Electrodes. *4.3.1.1. Noncovalent Grafting.* Early studies described the integration of Co or Fe macrocycles (in particular phthalocyanins or porphyrins) on carbon surfaces for the electro-reduction of CO_2.[783−787] The first reports involved the "functionalization" of pyrolytic graphite or carbon cloth electrodes via hydrophobic interactions, through drop casting or "impregnation" from solutions containing metallomacrocycle catalysts with no defined linker for immobilization. Using this method, a CoPc (**Co38**, section 2.2.4.2) adsorbed on carbon cloth showed high activity for CO_2 reduction at pH 5 with TON_{CO} = 370 000 (Table 2, entry 1), but the FE_{CO} remained at 55% due to competing H_2 evolution (Figure 29a).[784]

Other Pcs (Ni, Cu, Fe, and Mn) or Co macrocycles adsorbed onto graphite or GC electrodes gave CO and various other products such as formate and CH_4 at large overpotentials in acidic conditions with low FEs.[788−790] A related approach employing a Zn-porphyrin (**Zn3**, section 2.3.9) deposited on commercial polytetrafluoroethylene-treated carbon fiber paper reduces CO_2 to CO with $|J|$ = 2.1 mA cm^{-2} at E_{appl} = −1.70 V vs NHE, giving in a FE_{CO} of 95% over 4 h in H_2O:DMF (1:9). Blank experiments in the absence of the complex resulted in only H_2 production, and SEM, XPS, and XANES analyses provided evidence for the stability of **Zn3** during electrolysis.[501]

Immobilization of CoTPP or CoPc onto carbon electrodes was also carried out through coordination of the Co centers to pyridine units, enhancing CO_2 reduction to CO compared with the anchor-free systems above. Pyridine bound **Co91** (Figure 29b) displayed a TON_{CO} of 10^7 and a FE_{CO} > 90% at E_{appl} = −0.5 V vs RHE (Table 2, entry 2).[791] As an alternative strategy, PVP polymers were used as an encapsulating matrix for immobilization of CoPc on graphite electrodes,[630,792] thus providing relatively stable anchorage of the new catalyst through polymer entrapment (**Co92**, Figure 29c). It was proposed that axial coordination of the pyridine to the cobalt makes the Co^+ active species more nucleophilic, thereby explaining the high activity for CO_2 reduction.[638] In addition, the polymer matrix provides a secondary coordination sphere of pyridine units that can assist with proton transfer during catalytic turnover (Figure 29c).[638] CPE gave TON_{CO} = 34 000 with FE_{CO} = 89% (Table 2, entry 3), revealing improved performance of the polypyridine entrapped CRC when directly compared to analogous pyridine- and polymer-free systems. These studies highlight how integration of unmodified catalysts within functional electrode surfaces and/or polymeric matrices can alter the first and second coordination spheres, enhancing the activity of the hybrid molecular system.

Several other polymeric matrices, such as Nafion membrane or polyvinyl films, were used to incorporate CRCs onto electrode surfaces. Nafion was used to immobilize a cobalt bis-tpy (**Co60**, section 2.3.6.1) complex onto a BPG electrode,[793] and the resulting assembly was shown to reduce CO_2 to formate in aqueous conditions with a TON_{HCO2H} = 11 and FE_{HCO2H} = 51% at E_{appl} = −0.68 V vs RHE after 4.8 h CPE (Table 2, entry 4). **Co93** (Figure 30) and various other metal tpy complexes were electropolymerized onto a GC electrode via a vinyl group on the tpy ligand.[794−796] The polymer-modified electrodes produced formaldehyde as the main CO_2 reduction product (Table 2, entry 5). A cobalt chlorin was successfully immobilized in MWCNT films on GC electrodes using Nafion, and CO_2 reduction to CO with TON_{CO} ∼1100 and FE_{CO} ∼89% at E_{appl} = −0.62 V vs RHE in aqueous solution (pH 4.6) was reported (**Co94**, Figure 31a).[797] An analogous RGO-modified electrode showed lower activity (Table 2, entries 6 and 7), and this was attributed to the higher specific surface generated with the porous MWCNT matrix over RGO. The **Co94**-MWCNT electrode design was later coupled with a $BiVO_4$ based photoanode, allowing for a 1.5 V decrease in the overall bias voltage necessary to oxidize H_2O and reduce CO_2 through irradiation with visible light.[798]

The same Nafion strategy was also used to entrap qtpy **Co95** (Figure 30) in MWCNT films, using Nafion as a binder.[799] Immobilized **Co95** was shown to be very active for CO_2 reduction to CO in aqueous solution, with a quantitative FE_{CO} at low η (E_{appl} = −0.48 V vs RHE) for 3.5 h, and a TON_{CO} up to 89 000 after 4.5 h (Table 2, entry 8). This is far superior to the TON reported with the same CRC under homogeneous conditions in MeCN containing phenol as a proton source, once again highlighting the benefits of immobilization.[406] Similar encapsulation of [MnBr(bpy)$(CO)_3$] (**Mn1**, section 2.2.2) on GC surfaces also allowed the use of this catalyst in aqueous solution (Figure 31b).[60] CPE at E_{appl} = −0.88 V vs RHE gave a TON_{CO} up to 471 with a maximum FE_{CO} = 51% after 4 h (Table 2, entry 9). Immobilization increased activity by an order of magnitude. Additionally, Mn-bpy derivatives bearing *tert*-butyl, hydroxy, or carboxylic acid substituents in the 4,4′-positions were encapsulated within a Nafion/MWCNT composite on GC electrodes.[800] Although drastic differences in the electrocatalytic performance of the catalysts were observed in homogeneous organic solution, once immobilized within the Nafion film the hydroxy- and carboxylic acid-containing derivatives produced solely H_2. Only the di-*tert*-butyl Mn complex showed activity for CO production, with TON_{CO} = 46 and FE_{CO} = 23% in CPE at E_{appl} = −0.84 V vs RHE.

DOI: 10.1021/acs.chemrev.8b00392
Chem. Rev. 2019, 119, 2752−2875

Table 2. Electrocatalytic CO_2 Reduction under Aqueous Conditions Using Electrodes Modified with 3d Transition Metal CRCs[a]

entry	electrode	CRC	E_{onset}[b] (V)	$\|j\|$ at E_{appl}[b] (mA cm^{-2} at V)	CPE duration at E_{appl}[c] (h at V)	TON[c]	FE[c]	conditions	ref
1	carbon cloth	**Co38**	~−0.4	0.98 at −0.6	n/a at −0.6	3.7×10^5 (CO)	~55%	citrate pH 5.0	784
2	GC	**Co91**	~−0.4	n/a at −0.5	n/a at −0.5	1×10^7 (CO)	~92%	phosphate pH 6.0	791
3	EPG	**Co92**	~−0.45	2.5 at −0.72	2 at −0.72	3.4×10^4 (CO)	~89%	phosphate pH 4.7	638
4	BPG/ Nafion	**Co60**	~−0.63	n/a	4.8 at −0.68	11 (formate)	~51%	phosphate pH 7.0	793
5	GC	**Co93**	n/a	n/a	n/a	1.1×10^4 (H_2CO)	39%	$NaClO_4$ pH n/a	796
6	CNT	**Co94**	~−0.5	n/a	n/a at −0.62	1100 (CO)	89%	Na_2SO_4 pH 4.6	797
7	RGO	**Co94**	~−0.5	n/a	n/a at −0.62	350 (CO)	n/a	Na_2SO_4 pH 4.6	797
8	CNT/ Nafion	**Co95**	~−0.3	~9 at −0.48	4.5 at −0.48	8.9×10^4 (CO)	~100%	$NaHCO_3$ pH 7.3	799
9	GC/Nafion	**Mn1**	~−0.5	n/a	4 at −0.88	471 (CO)	51%	phosphate pH 7.0	60
10	GC	**Co96**	~−0.4	~0.05 at −0.55	4 at −0.55	n/a (CO)	~84%	K_2SO_4 pH 6.5	639
11	carbon disk	**Co97**	~−0.4	~1 at −0.7	7 at −0.7	1400 (CO)	~76%	$KHCO_3$ pH ~7.0	803
12	carbon disk	**Co98**	~−0.4	n/a	24 at −0.67	3.4×10^4 (CO)	90%	$KHCO_3$ pH 7.3	804
13	carbon disk	**Co99**	~−0.4	n/a	24 at −0.67	4.8×10^4 (CO)	91%	$KHCO_3$ pH 7.3	804
14	GC	**Fe31**	~0.5	~0.5 at −0.63	~24 at −0.63	5.5×10^4 (CO)	85%	$KHCO_3$ pH 7.3	806
15	CNT	**Co38**	~−0.4	10 at −0.63	10 at −0.63	9.7×10^4 (CO)	~90%	$KHCO_3$ pH 6.8	807
16	CNT	**Co78**	~−0.4	15 at −0.63	1 at −0.63	n/a (CO)	98%	$KHCO_3$ pH 6.8	807
17	CNT	**Co78**	~−0.4	~12 at −0.54	24 at −0.54	7.7×10^5 (CO)	90%	$NaHCO_3$ pH 7.4	808
18	carbon cloth	**Co100**	~−0.45	~4 at −0.8	10 at −0.8	n/a (CO)	93%	$NaHCO_3$ pH 7.2	810
19	CNT	**Co54**	~−0.43	~3 at −0.67	4 at −0.67	1118 (CO)	91%	$KHCO_3$ pH 7.3	811
20	CNT	**Fe32**	~−0.55	~0.2 at −0.6	12 at −0.6	813 (CO)	97%	$NaHCO_3$ pH 7.3	812
21	CNT	**Mn29** (high loading)	~−0.45	~1 at −0.65	8 at −0.65	1400 (CO)	25%	$KHCO_3$ pH 7.4	64
22	CNT	**Mn29** (low loading)	~−0.45	~1 at −0.65	8 at −0.65	3900 (formate)	15%	$KHCO_3$ pH 7.4	64
23	CNT	**Mn30**	~−0.25	~2.4 at −0.39	24 at −0.39	722 (CO)	87%	$K_2B_4O_7$ K_2SO_4 pH 6.9	813
24	CNT	**Fe33**	~−0.41	~0.16 at −0.62	3 at −0.62	750 (CO)	80%	$NaHCO_3$ pH 7.3	815
25	SnO_2	**$Fe_2$34**	~−0.45	~1.5 at −0.53	5 at −0.53	n/a (CO)	70%	borate pH 7.0	817
26	EPG	Ni-CODH	~−0.4	n/a	n/a	n/a	n/a	MES pH 7.0	821

[a]All potentials are reported against RHE unless otherwise specified (n/a = not available). [b]Extracted from LSV measurements, unless otherwise stated. [c]Extracted from CPE measurements.

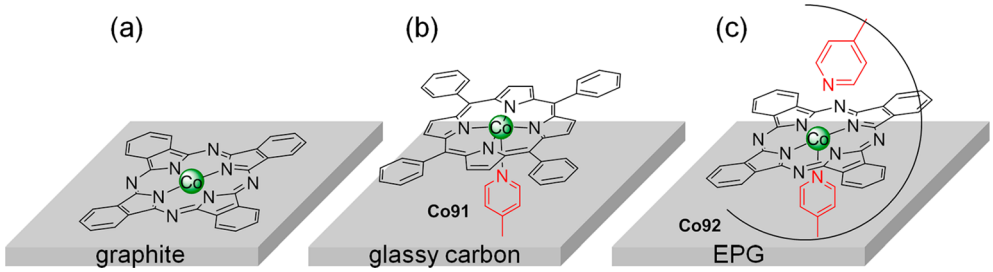

Figure 29. (a) Immobilization of **Co38** onto graphite electrodes through impregnation or drop-casting.[784] (b) Attachment of **Co91** through coordination to a pyridine moiety grafted onto a glassy carbon electrode.[791] (c) Encapsulation of a CoPc within a polypyridine polymer (**Co92**) acting as an immobilization matrix as well as first and secondary coordination spheres.[638]

Using a different strategy, cobalt protoporphyrin **Co96** (Figure 31c) could be immobilized at the surface of a GC electrode through electro-oxidation of a vinyl group on the porphyrin ring, leading to formation of a film at the electrode surface.[639,801] The resulting films ($\Gamma \approx 14$ nmol cm^{-2}) catalytically reduced CO_2 in aqueous conditions with a FE_{CO} up to 84% at $E_{appl} = -0.55$ V vs RHE (Table 2, entry 10). A similar strategy allowed the immobilization of an Fe-porphyrin derivative through electro-oxidation of carbazole substituents.[802] Although this method provided good control over catalyst loading onto the electrode and electrochemical reduction of CO_2 was achieved in MeCN, the film displayed limited stability.

Noncovalent CRC immobilization at carbon electrode surfaces has also involved the use of metal organic framework (MOF) and covalent organic framework (COF) approaches. Successful integration of a Co porphyrin for CO_2 reduction within 3D porous MOF or COF scaffolds at electrode surfaces has been reported (Figure 32).[803,804] The CRC-modified electrode was assembled by reacting a tetracarboxylated CoTPP (**Co53**, section 2.3.6.1) with Al_2O_3 deposited on a carbon electrode via atomic layer deposition (ALD), giving a

DOI: 10.1021/acs.chemrev.8b00392
Chem. Rev. 2019, 119, 2752−2875

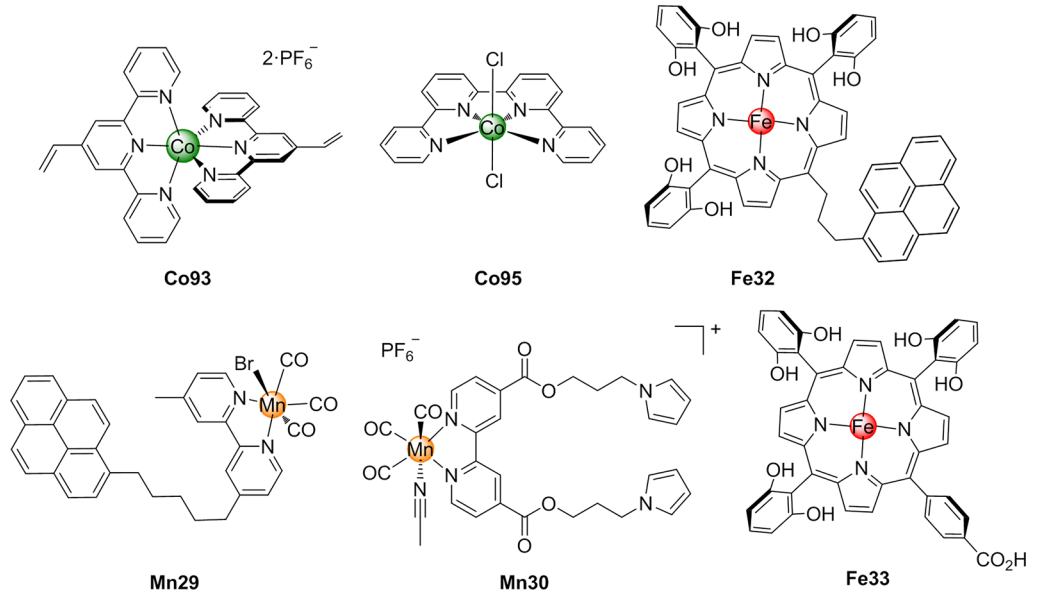

Figure 30. Structures of CRCs immobilized on carbon-based electrodes.

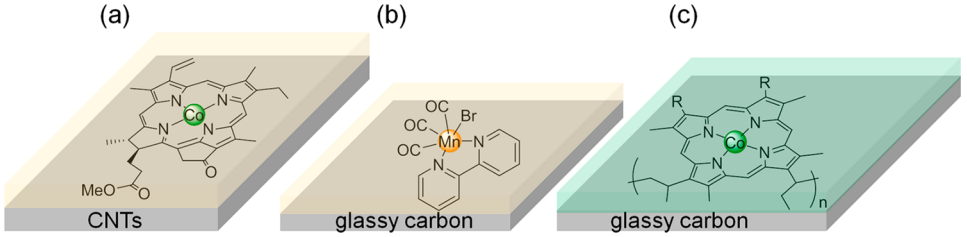

Figure 31. (a) Co chlorin **Co94** encapsulated in a Nafion membrane on CNTs.[797] (b) Mn-bpy catalyst **Mn1** entrapped in a Nafion matrix on glassy carbon.[60] (c) Co protoporphyrin IX polymer **Co96** electropolymerized onto a glassy carbon electrode.[639]

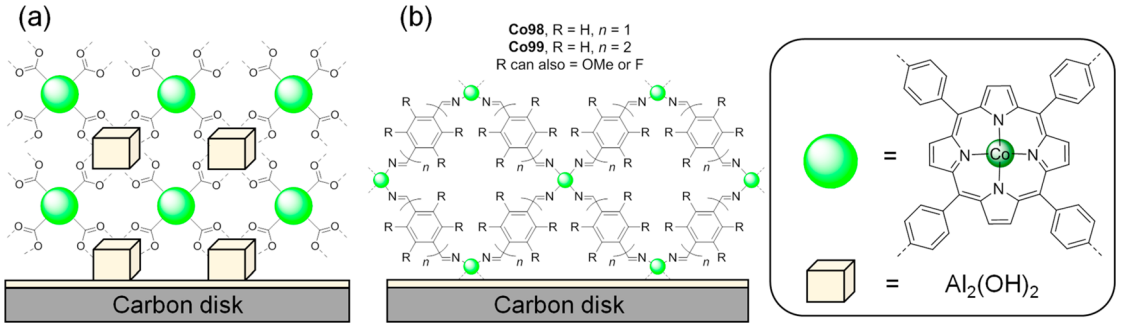

Figure 32. (a) Co porphyrin MOF (**Co97**) based on **Co53**[803] and (b) Co porphyrin based COFs (**Co98** and **Co99**)[804,805] immobilized onto a thin ALD layer of alumina on a carbon disk electrode.

MOF. A stable electrode with a 50 nm thick MOF-film (**Co97**, Figure 32a) showed activity in CPE for 7 h, giving a TON_{CO} of 1400 with a FE_{CO} of 76% at E_{appl} = −0.7 V vs RHE (Table 2, entry 11).[803] Spectroelectrochemisty on the MOF-modified electrode supported that most Co centers were active during catalysis.

A Co porphyrin-based COF-modified electrode, obtained through imine condensation of a tetraamino CoTPP derivative and 1,4-benzenedicarboxaldehyde, showed even higher activity and stability (**Co98**, Figure 32b, Table 2, entry 12).[804] Activity could be enhanced even further through fabrication of a more porous COF structure by using biphenyl-4,4′-dicarboxaldehyde, thus allowing better substrate access to the catalytic site and giving a Co-based TON_{CO} = 48 000 with a FE_{CO} of 91% after 24 h CPE at E_{appl} = −0.67 V vs RHE (**Co99**, Figure 32b, Table 2, entry 13). Decreasing the Co loading in the COF structure resulted in an optimized Co-based TON_{CO} of almost 300 000. In addition, this COF strategy was further investigated, and the electronic density at the Co porphyrin core could be tuned by substituting the 2,3,5,6-positions of the 1,4-benzenedicarboxaldehyde linker with fluorine or methoxy moieties.[805] These functional groups also induced different hydrophobicity within the COFs, which was linked to changes in selectivity and activity.

An immobilized Fe porphyrin-based porous organic cage has also been described for CO_2 reduction.[806] Increased activity could be obtained with the porous organic cage (**Fe31**, not shown) on CNT-coated GC electrodes when compared with parent FeTPP (**Fe4**, section 2.2.3.1) modified electrodes at

DOI: 10.1021/acs.chemrev.8b00392
Chem. Rev. 2019, 119, 2752−2875

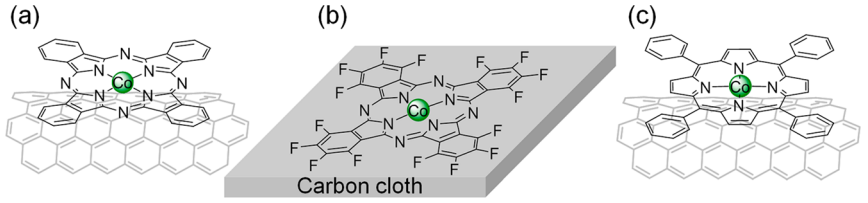

Figure 33. Different Co macrocycles immobilized on π-conjugated surfaces: (a) **Co38** onto a CNT,[807] (b) **Co100** onto carbon cloth,[810] and (c) **Co54** onto a CNT.[811]

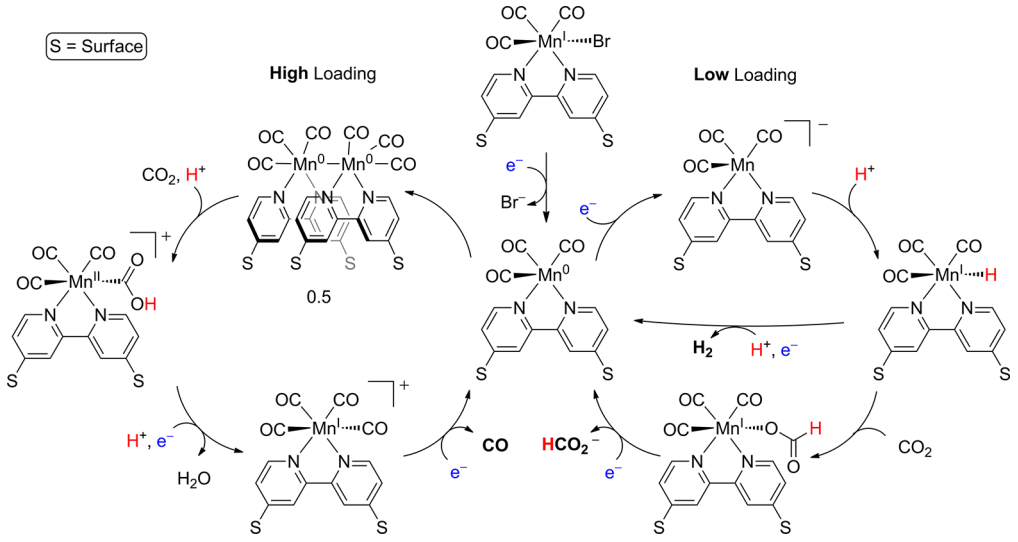

Figure 34. Schematic representation of concentration-dependent mechanism toward CO, HCO_2^-, and H_2 with [Mn(bpy)(CO)$_3$]-type CRC immobilized on a MWCNT-electrode.[64]

identical catalyst loadings (Γ = 6.78 nmol cm^{-2}). **Fe31** gave almost twice the TONs for CO (TON$_{CO}$ = 55 000), with improved FE$_{CO}$ of 85% after 24 h CPE at E_{appl} = −0.63 V vs RHE (Table 2, entry 14). The enhanced activity of the porous organic cage-based catalyst was attributed to the more porous nature of the molecular network, allowing better substrate access to the catalytic centers within the film.[806] Strategies utilizing MOF and COF structures to integrate molecular catalysts on surfaces show great promise. They allow control over the architecture of the resulting films in terms of both steric and electronic features, and can thereby directly impact on the activity of the grafted catalyst.

As another noncovalent immobilization strategy, the relatively stable film formation of metalloporphyrins or phthalocyanins on extended sp^2 carbon surfaces through π−π interactions was exploited with high surface area CNTs. Co phthalocyanin **Co38** was immobilized onto the sidewalls of CNTs (in addition to carbon black and graphene) and a TON$_{CO}$ of 97 000 could be obtained with FE$_{CO}$ of ∼90% at E_{appl} = −0.63 V vs RHE for 10 h (Figure 33a; Table 2, entry 15).[807] Modification of the CRC with electron-withdrawing cyano groups (**Co78**, Figure 22) resulted in a high FE$_{CO}$ of 98% at E_{appl} = −0.63 V vs RHE, demonstrating the possibility of catalyst tuning through modification of electronic properties (Table 2, entry 16).[807] Activity of **Co78** for longer than one day with a stable FE$_{CO}$ of 90% has also been shown (Table 2, entry 17).[808] A later study further investigated the effect of carbon paper surface loading of **Co38** on the catalytic properties of the hybrid material.[809] Lower loading yielded higher TONs and TOFs for CO, as catalyst aggregation on the surface was prevented. However, improved CO selectivity could be reached at higher loading, where proton reduction at the carbon surface is prevented by the high catalyst surface concentration. Perfluorinated Co phthalocyanin **Co100** (Figure 33b) has similarly been immobilized on a carbon cloth electrode, and achieved a FE$_{CO}$ of 93% at E_{appl} = −0.8 V vs RHE at pH 7.2 (Table 2, entry 18).[810] The same **Co100**-carbon electrode also performs water oxidation and was used as both a cathode and anode in a two-electrode CO_2 electrolysis cell to produce CO and O_2 at an applied voltage of 2.5 V (η = 1.15 V) for ∼3 h. Similar noncovalent immobilization of TPP **Co54** on CNTs (Figure 33c) reduces CO_2 to CO with $|j|$ = ∼3 mA cm^{-2} at E_{appl} = −0.67 V vs RHE, resulting in a FE$_{CO}$ of 91% over ∼4 h in aqueous conditions at pH 7.3 (Table 2, entry 19).[811]

Noncovalent immobilization of these TPP and Pc catalysts onto π-conjugated surfaces through π-π interactions relies on their planar structures. It was shown that the introduction of hydroxyl groups as proton relays into an Fe porphyrin (**Fe17**) decreases the overpotential and enhances the activity for CO_2 reduction (section 2.3.5.1).[394] Modification of **Fe17** with an additional pyrene unit as an anchoring group (**Fe32**, Figure 30) allowed efficient attachment onto a CNT electrode (Γ = 24 nmol cm^{-2}) and evaluation of performance in water.[812] The **Fe32**-modified electrode produced stable currents of $|j|$ = 0.2 mA cm^{-2} for 12 h at E_{appl} = −0.6 V vs RHE, reaching a TON$_{CO}$ of 813 with a maximum FE$_{CO}$ of 97% (Table 2, entry 20). Importantly, **Fe32** showed better activity and higher selectivity for CO when compared to similarly immobilized **Fe17** lacking the pyrene anchoring group, emphasizing the importance of the immobilization strategy for performance optimization.

A similar method was utilized in order to immobilize a [Mn(bpy)(CO)$_3$]-type catalyst onto MWCNTs through the introduction of a pyrene anchoring group as a substituent of the

DOI: 10.1021/acs.chemrev.8b00392
Chem. Rev. 2019, 119, 2752−2875

bpy ligand (**Mn29**, Figure 30). This strategy allowed excellent control over the catalyst loading on the electrode surface, and different loadings led to the formation of different CO and formate product ratios.[64] CO was preferentially obtained at high catalyst loadings (Γ > 30 nmol cm^{-2}; TON_{CO} > 1000 with CPE at E_{appl} = −0.65 V vs RHE), whereas formate and H_2 were the main products at lower surface concentrations (Γ < 20 nmol cm^{-2}; TON_{HCO2H} > 3000; Table 2, entries 21 and 22). UV−vis- and IR-SEC characterizations demonstrated that a dimer intermediate is involved in the reduction of CO_2 to CO at higher loading, whereas a mononuclear hydride intermediate is involved in the catalytic cycle at lower loadings (Figure 34). This work highlights the possibility of tuning catalyst selectivity and stability through manipulation of the catalytic cycle by immobilizing a molecular catalyst.[64] A [Mn(bpy)(CO)$_3$]-catalyst featuring a bpy modified with pyrrole groups (**Mn30**, Figure 30) was also electrodeposited onto a CNT electrode, and showed a TON_{CO} of 722 after 24 h CPE at E_{appl} = −0.39 V vs RHE in aqueous electrolyte, with FE_{CO} up to 87% (Table 2, entry 23).[813] A beneficial effect of K^+ cations on lowering the overpotential was also identified in this system.

4.3.1.2. Covalent Grafting. In addition to noncovalent immobilization, several of the covalent strategies described above were utilized in order to anchor CRCs at carbon surfaces. Covalent grafting of a tpy ligand onto a GC surface through reduction of a diazonium salt gave a CRC-functionalized electrode (Figure 21b).[24] After metalation of the immobilized tpy with Co, the modified electrode was shown not only to reduce protons (section 4.2.1.1) but also CO_2 to CO (TON_{CO} = 70) in DMF. Using a similar method, immobilization of bpy units on a GC electrode via reduction of a diazonium salt and addition of Mn (and Re) allowed for CO_2 reduction catalysis (Γ ≈ 1 nmol cm^{-2}, TON_{CO} > 200) in MeCN/MeOH.[371]

Through "click" 1,3-dipolar cycloaddition, a CoTPP substituted with alkyne groups was anchored on an azide-modified boron doped diamond electrode (Figure 35a).[814] The covalent immobilization provided stable production of CO from CO_2 in MeCN (confirmed by isotopic labeling experiments), with a TOF_{CO} of 0.8 s^{-1} (calculated from 16 h CPE).

The modification of CNT sidewalls through diazonium salt reduction of a protected amine also allowed peptide coupling of a carboxylic acid-modified Fe porphyrin (**Fe33**, Figure 30) after N-deprotection (Figure 35b).[815] The Fe porphyrin-modified CNTs were subsequently deposited onto GC electrodes, and a lower loading (Γ = 6.4 nmol cm^{-2}) was obtained compared to the analogous catalyst immobilized via a pyrene anchor (**Fe32**). The covalently bound hydroxy-functionalized Fe porphyrin reduces CO_2 to CO in aqueous electrolyte solution. Currents ($|J|$ = 0.16 mA cm^{-2}) were sustained during 3 h of CPE, with a TON_{CO} of 750 and a FE_{CO} of 80% at E_{appl} = −0.62 V vs RHE (Table 2, entry 24). This performance is comparable to the pyrene modified **Fe32** catalyst described above, and the slight drop in FE for CO could be attributed to the lower surface loading obtained with covalent grafting, enabling background proton reduction at the CNT electrode surface. Covalent linkage of the parent **Fe17** porphyrin lacking hydroxyl groups also gave activity for CO_2 reduction but with a lower selectivity (51% after 3 h).

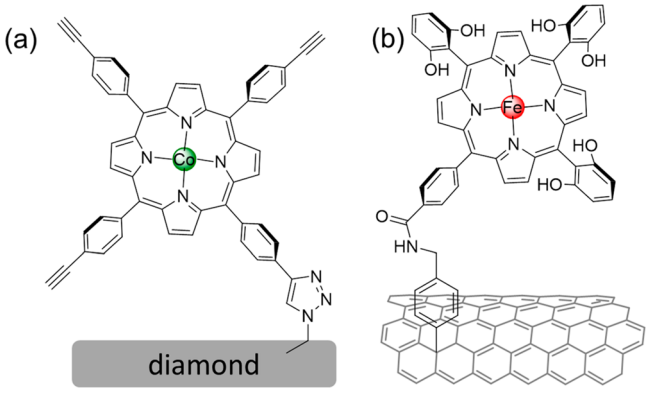

Figure 35. Covalent grafting of (a) a Co porphyrin onto an azide-modified diamond electrode surface using "click" chemistry,[814] and (b) **Fe33** onto an amine-modified CNT using peptide coupling.[815]

4.3.2. Metal Oxide Electrodes. Most anchoring strategies for CO_2 reducing molecular catalysts have been developed for carbon-based electrodes, but the immobilization of CRCs on MO_x materials is emerging as a popular alternative approach. Electrophoretic deposition of an Fe porphyrin-based MOF onto fluorine-doped tin oxide (FTO)-coated glass substrates has been described, and reduction of CO_2 in MeCN containing TFE gave a TON_{CO} up to 1500 with FE_{CO} of 40% at E_{appl} = −1.3 V vs NHE.[816]

Using a phosphonate anchoring group, an Fe porphyrin dimer could be immobilized onto an FTO-coated glass electrode for CO_2 reduction in fully aqueous conditions (**$Fe_2$34**, Figure 36a).[817] Limitations arising from low surface coverage (Γ = 0.0046 nmol cm^{-2}) could be overcome by depositing an additional SnO_2 layer, thus increasing the electrode porosity, to reach Γ = 0.26 nmol cm^{-2}. This strategy allowed a stable current ($|J|$ = 1.5 mA cm^{-2}) at E_{appl} = −0.53 V vs RHE with FE_{CO} = 70% (Table 2, entry 25).

A phosphonate-substituted [MnBr(bpy(PO_3H_2)$_2$)(CO)$_3$] complex has been grafted at high loadings (Γ = 34 nmol cm^{-2}) onto a mesoTiO$_2$ film on an FTO-coated glass electrode (Figure 36b).[818] CV in the presence of CO_2 showed a catalytic wave in H_2O:MeCN (5:95). CPE resulted in a TON_{CO} of 112 with a FE_{CO} of 85%. Interestingly, the transparency of the TiO$_2$|ITO|glass electrode architecture enabled in situ SEC measurements, which supported the dynamic formation of a catalytically active Mn dimer at the electrode surface (or at least within the porous scaffold) upon electrochemical reduction.[818] This assignment was confirmed in a related study with a carboxylic acid-bearing Mn-bpy complex immobilized on TiO_2.[819] Anchoring of a Ni-cyclam (**Ni69**, section 2.3.7.1) via its carboxylate group onto porous TiO_2 was also demonstrated, but no electrocatalytic reduction of CO_2 was reported in this case (Figure 36c).[820]

4.3.3. CO_2 Reductase-Based Electrocatalysis. The two-electron reduction of CO_2 is carried out in Nature by different types of redox active metalloenzymes. Ni-based CODHs are able to carry out the conversion of CO_2 to CO or the oxidation of CO to CO_2 at a marginal η without soluble redox mediators.[42,821,822] In addition, Mo- and W-based formate dehydrogenases (FDHs; note that 4d and 5d transition metals are beyond the scope of this review) allow the reduction of CO_2 to formate and the oxidation of formate to CO_2, reversibly and with direct ET from the electrode surface to the enzyme active site.[54,56,823,824] There are also several FDHs that rely on reduced nicotinamide adenine dinucleotide (NADH) as a reducing reagent.[825−827]

PFE has been used to characterize different [NiFe]-CODHs, as well as [W]- and [Mo]-FDHs, when adsorbed onto electrode surfaces.[54,56,824,828] [NiFe]-CODH from *Carboxydothermus*

DOI: 10.1021/acs.chemrev.8b00392
Chem. Rev. 2019, 119, 2752−2875

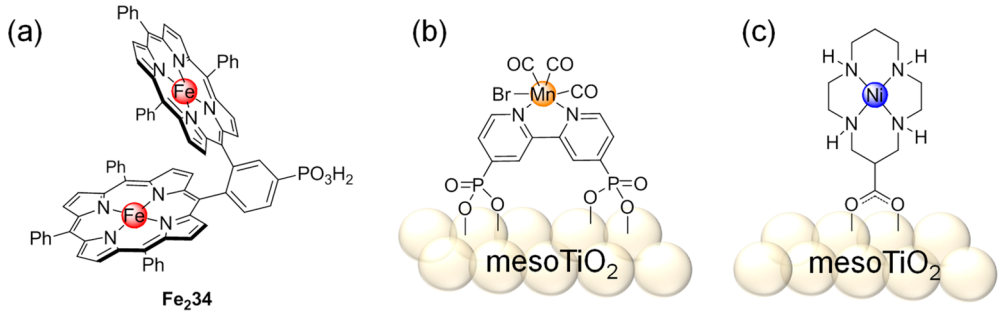

Figure 36. (a) Structure of Fe porphyrin **$Fe_2$34** bearing a phosphonate anchor.[817] Immobilization of (b) a Mn bpy catalyst modified with phosphonate groups (**Mn29**) onto mesoTiO$_2$[818] and (c) a carboxylic acid modified Ni cyclam (**Ni69**) onto a mesoTiO$_2$ electrode.[820]

hydrogenoformans immobilized onto a EPG electrode in the presence of CO and CO_2 displays reversible electrocatalysis, with a cathodic reduction of CO_2 to CO and an anodic oxidation of CO to CO_2 at the thermodynamic potential.[822] K_M values for CO and CO_2 at different E_{appl} have also been established, and TOFs as high as 40 000 s^{-1} were reported (Table 2, entry 26).[42,821,822] PFE of W-containing FDH from *Syntrophobacter fumaroxidans* and Mo-containing FDH from *Escherichia coli* showed the reversible interconversion of CO_2 and formate when immobilized on graphite electrodes.[54,56,824] For the [W]-FDH, a TON of 42 000 was estimated for a densely packed monolayer of the protein at E_{appl} = −0.35 V vs RHE, with FE_{HCO2H} of almost 100%. The [Mo]-FDH was shown to display a stronger bias toward CO_2 reduction on a graphite-epoxy electrode compared to the solution assay, and a FE_{HCO2H} of 100% was obtained after 1 h CPE at E_{appl} = −0.2 V vs RHE.[54]

As for H_2ases, PFE of such CO_2 reductases has allowed information to be gathered concerning the mechanisms involved in the reversible catalytic conversion of CO_2 to CO or formate achieved by these metalloenzymes. However, there are still no examples of molecular complexes able to reproduce this reversible catalysis. Surface modification with CRCs combining the different strategies listed above may be the way forward to developing molecularly engineered electrodes capable of CO_2 reduction, as well as CO or formate oxidation, using elaborate electrode environments inspired by CO_2 reductases.

5. COLLOIDAL PHOTOCATALYSIS

5.1. General Remarks

Colloidal photocatalysis relies on a nanoparticulate assembly involving a light harvester paired with a molecular catalyst placed in solution to achieve a specific substrate conversion. Electrons for fuel synthesis are usually provided by a SED, which regenerates an oxidized light-absorbing SC colloid or a light-harvesting molecule that is immobilized on a colloid. "Colloidal" refers to particles dispersed in a medium that have a dimension in at least one direction between approximately 1 nm and 1 μm or where discontinuities in the system are found at distances of that order.[81] Supported colloidal photocatalysis implies the existence of electronic communication between the light harvester and the catalyst by means of immobilization. This architecture combines the advantages of homogeneous (e.g., selective chemistry) and heterogeneous catalysis (e.g., stability) and provides a wireless and potentially scalable platform for solar fuel synthesis.[829]

Colloidal materials can be used in two ways, either as a light harvester (e.g., QDs; Figure 37a) or as a scaffolding agent (e.g., MO_x, micelles; Figure 37b). The former employs the colloid to both capture light and inject electrons into a surface-anchored molecular catalyst, whereas the latter only indirectly participates in the photoinduced process, by improving the transfer of charge from an additional PS to the catalyst. In both cases, efficient solar light absorption and the generation of long-lived electrons that are sufficiently reducing to sustain catalysis are required.

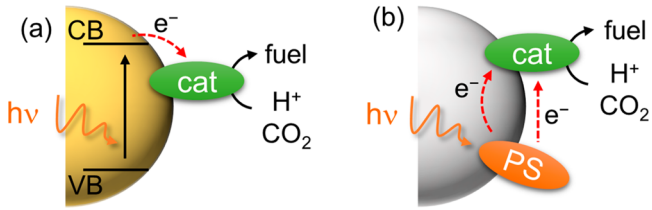

Figure 37. Schematic representation of two classes of supported colloidal photocatalysis, where the colloidal material is used either as (a) a light absober or (b) a scaffolding agent.

Many colloidal photocatalytic systems have been employed for fuel synthesis (in particular proton reduction) by using deposited metal catalysts such as Pt, Co, and Ni at the surface of a colloidal SC.[829,830] The development of more efficient, robust, and selective molecular catalysts paired with a better understanding of grafting molecules on surfaces has given momentum to the development of molecule-supported colloidal photocatalysis for fuel synthesis.[25,527] Over the past decade, studies addressing catalyst immobilization on/in carbon-, MO_x-, quantum dot-, or micelle-based colloids have been reported, and this section will summarize examples where a defined immobilization strategy has been employed to link the colloid to a molecular HEC or CRC.

5.2. Photocatalytic H_2 Evolution

5.2.1. Carbon-Based Colloids. Among carbon-based materials, graphitic carbon nitride (g-C_3N_4) is a visible light-absorbing class of scalable material (Figure 38). g-C_3N_4 is an amorphous polymeric material based on a graphitic carbon-nitrogen assembly with SC-like properties and excellent thermal and chemical stability during irradiation.[530,831,832] It can be synthesized by condensation of cyanamide, dicyandiamide, or melamine at elevated temperatures.[833,834] g-C_3N_4 has a medium-sized bandgap potential (E_g ≈ 2.7 eV), enabling solar absorption with an CB energy appropriate for fuel synthesis (E_{CB} ≈ −1.4 V vs NHE, pH 7).[833,835] Assemblies of g-C_3N_4 with precious metal,[836] non-precious metal,[837,838] and in situ deposited solid-state catalysts[839,840] have been reported, but few examples exist with defined molecular catalysts.[612,841,842]

DOI: 10.1021/acs.chemrev.8b00392
Chem. Rev. 2019, 119, 2752−2875

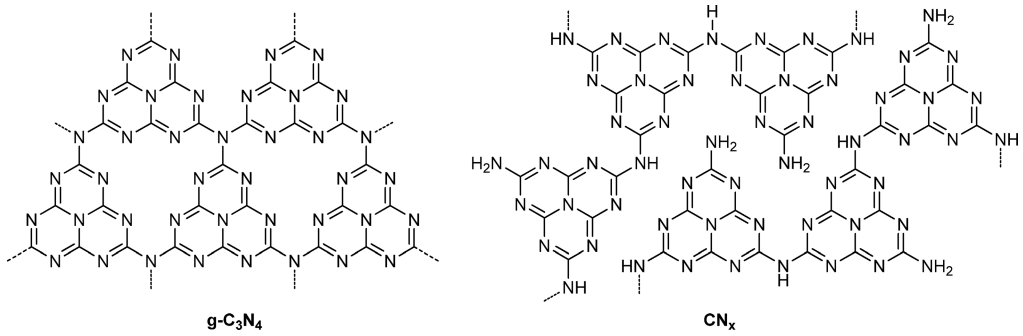

Figure 38. Carbon nitride-based architectures.

Visible light irradiation (λ = 420−740 nm) of a cobaloxime [$Co^{3+}Cl(dmgH)_2$(pyridine)], **Co3** (section 2.2.4.1), with g-C_3N_4 in alkaline aqueous TEOA solution (15% vol) produces H_2 and removal of the UV filter increases the performance by an order of magnitude.[841] Weak interactions between the cobaloxime and g-C_3N_4 were reported ($\Gamma \approx 5$ nmol $mg_{C_3N_4}^{-1}$) and the catalyst decomposes into cobalt oxide after 8 h irradiation (Table 3, entry 1).[612,841] Carboxylic acid functionalized **Co101** and pyrene substituted **Co102** both show a higher affinity for g-C_3N_4, with Γ values of 13 and 18 nmol mg_{C3N4}^{-1}, respectively (Figure 39; Table 3, entries 2 and 3). Irradiation (λ > 400 nm) of **Co3**, **Co101**, or **Co102** with g-C_3N_4 in MeCN:H_2O (9:1) with TEOA gave respective TON_{H2} values of 195, 234, and 281.[612]

A common issue in supported catalysis is detachment of the anchored catalyst from the particle surface, making the distinction between activity arising from immobilized and solubilized catalyst challenging. For **Co3**, **Co101**, and **Co102** with g-C_3N_4, H_2 evolution was found to originate from both homogeneous and heterogenized cobaloximes. The different photoactivity was assigned to different modes of catalyst adsorption, with possible π-π-stacking interactions provided by the pyrene anchor affording a more effective interaction between g-C_3N_4 and cobaloxime.[612]

The H_2ase-inspired Ni DuBois catalyst, **Ni35**[295] (section 2.2.5.1), was successfully combined with melon carbon nitride (CN_x, Figure 38), a 1D poly(aminoimino)heptazine material that is less condensed than g-C_3N_4.[842] Under simulated solar irradiation (AM1.5G, 1 Sun) in EDTA solution, the water-soluble tetraphosphonic acid-bearing **Ni35** (η = 200 mV at pH 4.5) photogenerated a TOF_{H2} of 109 mol_{H2} mol_{cat}^{-1} h^{-1} with a TON_{H2} > 160 after 4 h (Table 3, entry 4). Despite most of the catalyst remaining in solution, weak interactions between **Ni35** and CN_x were suggested to occur via H-bonding (Γ = 2 $nmol_{Ni35}$ mg_{CNx}^{-1}). The short lifetime of the photocatalytic system was attributed to the decomposition of the catalyst as the activity was restored upon readdition of **Ni35**. Increase of the catalyst lifetime was also demonstrated by replacing EDTA with 4-methylbenzyl alcohol as a clean electron donor that does not decompose into reactive radicals.[843]

Addition of RGO as a scaffolding agent in the latter system also resulted in superior performance by interaction with both the catalyst and CN_x, as well as by promoting ET toward the catalyst.[844] Likewise, GO was shown to act as an "electron-relaying" scaffold to anchor both a porphyrin and the molecular [FeFe]-H_2ase mimic Fe_3**1** (Figures 39 and 40),[534] which also bears a ferrocene moiety to mimic the iron cluster found in natural H_2ase.[845] CV conducted on Fe_3**1** in MeCN solution revealed an E_{onset} at −2.12 V vs Fc^+/Fc in the presence of acetic acid that follows a mechanism including two successive electrochemical-chemical (EC) steps to reduce protons. The TPP and Fe_3**1** were both covalently bound to the surface of GO via condensation and Prato's reaction, respectively (section 3.3.1.1). A high loading of TPP and Fe_3**1** was obtained (Γ = 290 and 600 nmol mg_{GO}^{-1}, respectively) and rapid quenching of photoexcited TPP was detected by fluorescence experiments, indicating ET from the TPP to GO. Photocatalytic experiments in the presence of cysteine as a SED at pH 1 resulted in low activity (calculated TON_{H2} ~3−4), potentially due to the lack of driving force needed to generate the catalytic state of Fe_3**1** from the excited state of TPP, as well as unproductive, competing processes (Table 3, entry 5). Although the system stability and recyclability were demonstrated via repeated experiments and washings, no evidence of catalyst integrity was provided. Nevertheless, this approach holds promise for future exploration of graphene-like materials with molecular catalysts.

Alongside the carbon-based colloids discussed above, carbon nanodots are a promising family of 0 D carbon-based architecture that have recently emerged as a low-cost, stable, nontoxic, and scalable visible light-harvester toward photocatalytic fuel production.[531,846] These carbon nanoparticles (ranging from 1−10 nm diameter) consist of a nanoscale carbon core stabilized by oxidized surface groups such as carboxylic acids and alcohols, which impart water solubility and potential for further chemical functionalization. Although not yet studied with covalently anchored molecular catalysts for solar fuel synthesis, several studies have already explored their potential as stable light harvesters when combined with enzymes[577] and molecular Ni and Co catalysts.[847,848]

5.2.2. Quantum Dots. To date, the vast majority of systems that have investigated transition metal molecular catalysts with QDs were performed under diffusion-limited conditions, with high photocatalytic activities frequently being achieved.[140,259,689,690,849−853] Examples of QDs combined with 3d transition metal molecular catalysts for H_2 evolution in aqueous conditions are listed below.

Irradiation (λ > 420 nm) of pyridine-bearing cobaloximes [$Co^{3+}Cl(dmgH)_2$Py-R] and CdS nanoparticles (⌀ = 50 nm) under semiaqueous conditions resulted in H_2 evolution.[537] The catalysts **Co3**, **Co103**, and **Co104** feature the respective axial ligands pyridine, 4-dimethylaminopyridine, and 2-mercaptopyridine (Figure 41). These HECs gave respective Γ of 3, 61, and 286 nmol per mg of nanoparticle, suggesting that amine and, more significantly, thiol groups are suitable anchors for Cd^{2+} coordination sites. The E_{CB} of CdS (~−0.90 V vs NHE, pH 7) is more negative than E_{onset} of the catalyst (reduction of [Co^{2+}] to [Co^+] at approximately −0.8 V vs NHE), and irradiation of the CdS-cobaloxime hybrid system in the presence of lactic acid as a

DOI: 10.1021/acs.chemrev.8b00392
Chem. Rev. 2019, 119, 2752−2875

Table 3. Colloidal Systems with Immobilized 3d Metal Complex Electrocatalysts Active for the Reduction of Aqueous Protons

entry	colloidal PS	HEC	loading (interaction)	TON_{H_2} (after t in h)	TOF_{H_2} / h^{-1}	QY_{H2} (λ/nm)	conditions[a]	illumination	ref
1	g-C_3N_4	**Co3**	5 nmol mg^{-1} (n/a)[b]	195 (12)	n/a	n/a	MeCN:H_2O, TEOA, (pH 9)	300 W Xe lamp λ > 400 nm	612
2	g-C_3N_4	**Co101**	13 nmol mg^{-1} (n/a)	234 (12)	n/a	n/a	MeCN:H_2O, TEOA, (pH 9)	300 W Xe lamp λ > 400 nm	612
3	g-C_3N_4	**Co102**	18 nmol mg^{-1} (π interactions)	281 (12)	n/a	n/a	MeCN:H_2O, TEOA, (pH 9)	300 W Xe lamp λ > 400 nm	612
4	CN_x	**Ni35**	2 nmol mg^{-1} (hydrogen bonding)	166 (4)	109	0.37% (365)	H_2O, EDTA, pH 4.5	100 mW cm^{-2} AM 1.5G	842
5	TPP|GO	**$Fe_3$1**	600 nmol mg^{-1} (covalent)	3−4 (5)	n/a	n/a	H_2O, cystine, pH 1	450 W Hg lamp λ > 380 nm	534
6	CdS	**Co3**	3 nmol mg^{-1} (n/a)	171 (15)	20	9.1% (420)	MeCN:H_2O, TEOA	300 W Xe lamp λ > 420 nm	537
7	CdS	**Co103**	61 nmol mg^{-1} (n/a)	n/a	0.077	n/a	DMF:H_2O, lactic acid	300 W Xe lamp λ > 420 nm	537
8	CdS	**Co104**	286 nmol mg^{-1} (n/a)	n/a	0.1	n/a	DMF:H_2O, lactic acid	300 W Xe lamp λ > 420 nm	537
9	CdS	**Co3**	3.5−16.8 nmol mg^{-1} (pH 4−7) (electrostatic)	n/a	39.6−10.8 (pH 4−7)	n/a	MeOH:H_2O	300 W Xe lamp λ > 420 nm	855
10	CdS	**Co105**	~39.0−16.5nmol mg^{-1} (pH 4−7) (electrostatic)	n/a	5.0−3.6 (pH 4−7)	n/a	MeOH:H_2O	300 W Xe lamp λ > 420 nm	855
11	CdTe	**Co106**	0.45% (w/w) (Cd^{2+} coordination)	1.4×10^4 (30) 2.3×10^4 (70)	700	5.3% (400)	H_2O, AA, pH 5.5	300 W Xe lamp λ > 400 nm	538
12	CdTe	**Co107**	trace (n/a)	4990 (30)	n/a	1.5% (400)	H_2O, AA, pH 5.5	300 W Xe lamp λ > 400 nm	538
13	ZnS	**$Fe_2$35**	7.5 nmol mg^{-1} (n/a)	2607 (38)	100	2.5% (325)	DMF:H_2O, AA	300 W Xe lamp	851
14	ZnS	**$Fe_2$37**	0.4% (w/w) (Zn^{2+} coordination)	3400 (30)	151	n/a	DMF:H_2O, TEOA (pH 11)	300 W Xe lamp	860
15	ZnS	**$Fe_2$38**	0.03% (w/w) (Zn^{2+} coordination)	4950 (30)	282	n/a	DMF:H_2O, TEOA (pH 11)	300 W Xe lamp	860
16	CdSe	**$Fe_2$36**	0.78% (w/w) (n/a)	8781 (82)	596	n/a	H_2O, AA, pH 4.0	160 mW cm^{-2} λ = 410 nm LED	859
17	CdSe	**$Fe_2$39**	n/a (Cd^{2+} coordination)	2.7×10^4 (8)	1.3×10^4	3.2% (450)	H_2O, AA, pH 4.0	294 mW cm^{-2} λ = 450 nm LED	539
18	CdSe	**$Fe_2$39**	n/a (Cd^{2+} coordination)	8.4×10^4 (28)	n/a	n/a	PEI, H_2O, AA, pH 4.0	3 W λ = 450 nm LED	861
19	CdSe-β-CD	**$Fe_2$40**	9.7% (w/w) (host−guest)	2370 (28)	150	3.2% (400)	H_2O, AA, pH 4.5	300 W Xe lamp λ > 400 nm	128
20	CdS-DETA	**Ni101**	0.7% (w/w) (covalent bond)	4.4×10^4 (26)	1692	9.9% (420)	EtOH:H_2O, TEA (pH 12.2)	300 W Xe lamp λ > 420 nm	870
21	**PS19**-TiO_2	**Co88**	6.6 nmol mg^{-1} (chemisorption)	108 (10)	15	n/a	H_2O, TEOA, pH 7	100 mW cm^{-2}, AM 1.5G, λ > 420 nm	873
22	**PS19**-TiO_2	**Co88** (excess ligand)	6.6 nmol mg^{-1} (chemisorption)	>300 (24)	15	n/a	H_2O, TEOA $dmgH_2$, pH 7	100 mW cm^{-2}, AM 1.5G, λ > 420 nm	873
23	**PS19**-TiO_2	**Co108**	11.2 nmol mg^{-1} (chemisorption)	99 (15)	12	n/a	H_2O, TEOA, pH 7	100 mW cm^{-2}, AM 1.5G, λ > 420 nm	873
24	**PS19**-TiO_2	**Co87**	n/a (chemisorption)	2 (4)	1	n/a	H_2O, TEOA, pH 7	100 mW cm^{-2}, AM 1.5G, λ > 420 nm	543
25	**PS19**-TiO_2	**Co89**	12 nmol mg^{-1} (chemisorption)	22 (4)	10	0.35% (465)	H_2O, TEOA, pH 7	100 mW cm^{-2}, AM 1.5G, λ > 420 nm	543
26	**PS19**-TiO_2	**Co89**	12 nmol mg^{-1} (chemisorption)	18 (4)	13	n/a	H_2O, AA, pH 4.5	100 mW cm^{-2}, AM 1.5G, λ > 420 nm	543
27	**PS19**-ZrO_2	**Co89**	n/a (chemisorption)	10 (4)	8	n/a	H_2O, AA, pH 4.5	100 mW cm^{-2}, AM 1.5G, λ > 420 nm	543
28	**PS3**, TiO_2	**Co109**	n/a (chemisorption)	9 (6)	n/a	n/a	H_2O, TEA, pH 11	300 W Xe lamp λ > 420 nm	880
29	**PS3**, TiO_2	**Co110**	n/a (chemisorption)	90 (6)	n/a	n/a	H_2O, TEA, pH 11	300 W Xe lamp λ > 420 nm	880
30	**PS3**, TiO_2	**Co111**	n/a (chemisorption)	43 (6)	n/a	n/a	H_2O, TEA, pH 11	300 W Xe lamp λ > 420 nm	880
31	**PS19**-TiO_2	**Ni35**	32 nmol mg^{-1} (chemisorption)	278 (30)	72	n/a	H_2O, AA, pH 4.5	100 mW cm^{-2}, AM 1.5G, λ > 420 nm	295
32	**PS19**-ZrO_2	**Ni35**	20 nmol mg^{-1} (chemisorption)	524 (30)	92.2	n/a	H_2O, AA, pH 4.5	100 mW cm^{-2}, AM 1.5G, λ > 420 nm	295
33	**PS30**-TiO_2	**Ni35**	1 nmol mg^{-1} (chemisorption)	205 (21)	24.5	0.40% (500)	H_2O, AA, pH 4.5	100 mW cm^{-2}, AM 1.5G, λ > 420 nm	877

DOI: 10.1021/acs.chemrev.8b00392
Chem. Rev. 2019, 119, 2752−2875

Table 3. continued

entry	colloidal PS	HEC	loading (interaction)	TON_{H_2} (after t in h)	TOF_{H_2} / h^{-1}	QY_{H2} (λ/nm)	conditions[a]	illumination	ref
						0.15% (550)			
34	**PS31**-TiO_2	**Ni35**	n/a (chemisorption)	27 (3)	n/a	0.09% (420)	H_2O, AA, pH 4.5	100 mW cm^{-2}, AM 1.5G, λ > 420 nm	881
35	**PS32**-(SiO_2-C_{18})	**Co112**	n/a (hydrophobic)	1322 (n/a)	n/a	n/a	H_2O, AA, pH 4.0	85 mW, λ = 453 nm LED	542
36	**PS33**-DOPC	**Co113**	12.6% mol (embedment)	165 (13)	n/a	n/a	H_2O, TEOA, pH 8.3	High power λ = 455 nm LED	885
37	**PS34**-DOPC	**Co113**	n/a (embedment)	13 (18)	n/a	n/a	H_2O, TEOA, pH 7.5	High power λ = 535 nm LED	885
38	**PS5**-CTAB	**Co39**	n/a (embedment)	7.9 (6)	n/a	n/a	MeCN:H_2O, TEOA, acidic	1000 W, λ > 420 nm, IR filter	548
39	**PS35**-SDS	**$Fe_2$41**	n/a (embedment)	~ 0.13 (1)	n/a	n/a	H_2O, AA	500 W, Hg lamp, glass filter	547
40	**PS3**-SDS	**$Fe_2$13**	n/a (embedment)	117 (4.5)	n/a	n/a	H_2O:Et_3N (pH 10.5)	λ = 455 nm LED	134
41	**PS1**-polymer	**$Fe_2$42**	4.6% (w/w) (embedment)	133 (2)	n/a	n/a	H_2O, AA, pH 4.0	λ = 450 nm LED	886
42	**CdSe**-DOPC	**$Fe_2$43**	5.2% mol (embedment)	651 (72)	n/a	n/a	H_2O, AA, pH 4	91 mW cm^2, λ = 455 nm, blue LEDs	549
43	CN_x	[NiFeSe]-H_2ase	n/a (physisorption)	5.0×10^4 (48)	5.5×10^3	7×10^{-2}% (365) 5×10^{-3}% (465)	H_2O, EDTA, pH 6	100 mW cm^{-2}, AM 1.5G, λ > 300 nm	842
44	CdTe	[FeFe]-H_2ase	n/a (electrostatic)	n/a	9.0×10^4	9% (532)	H_2O, AA, pH 4.75	150 W halogen lamp AM 3	688
45	nanorod-CdS	[FeFe]-H_2ase	1 H_2ase per CdS (electrostatic)	1×10^6 (4)	1.4×10^6	20% (405)	H_2O, AA, pH 7.0	800 μmol m^{-2} s^{-1}, λ = 405 nm LED	691
46	**PS19**-TiO_2	[NiFeSe]-H_2ase	1.8×10^{-2} nmol mg^{-1} (chemisorption)	3.4×10^5 (4)	1.8×10^5	n/a	H_2O, TEOA, pH 7.0	250 W, tungsten halogen lamp λ > 420 nm	652
47	CN_x-TiO_2	[NiFeSe]-H_2ase	0.1 H_2ase per CN_x-TiO_2 particle (chemisorption)	5.8×10^5 (72)	2.8×10^4	0.51% (400)	H_2O, EDTA, pH 6.0	100 mW cm^{-2}, AM 1.5G, λ > 420 nm	654
48	**PS30**-TiO_2	[NiFeSe]-H_2ase	n/a (chemisorption)	8.8×10^4 (21)	8.7×10^3	n/a	H_2O, AA-MES, pH 6.0	100 mW cm^{-2}, AM 1.5G, λ > 420 nm	877

[a]In the case of solvent mixtures, apparent pH values (pH′) are indicated in parentheses. [b]n/a = not available.

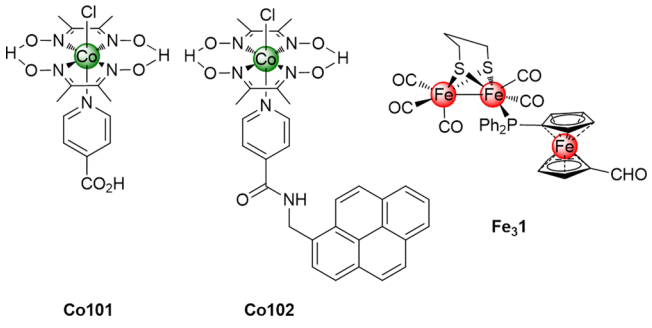

Figure 39. Molecular structures of HEC combined with carbon colloids.

SED resulted in a H_2 evolution rate of 46, 77, and 100 μmol h^{-1} for **Co3**, **Co103**, and **Co104**, respectively (Table 3, entries 6–8). These results highlight the beneficial impact of the thiol group. The system CdS|**Co3** performed for ~15 h, delivering a TON_{H2} of 171, and could be reactivated via addition of fresh catalyst.[537]

A recent study proposed that ET mostly takes place between CdS QDs and adsorbed catalyst (**Co3**), while HECs dissolved in solution contribute little to the photoactivity.[854] Two modes of adsorption were proposed for **Co3** on the surface of CdS, either in place of the capping ligand or on surface defect sites, with the latter being more efficient ET centers for both free and trapped electrons. Electrostatic interaction between the surface of CdS (isoelectric point of ~4.4) and the cobaloxime varies with pH

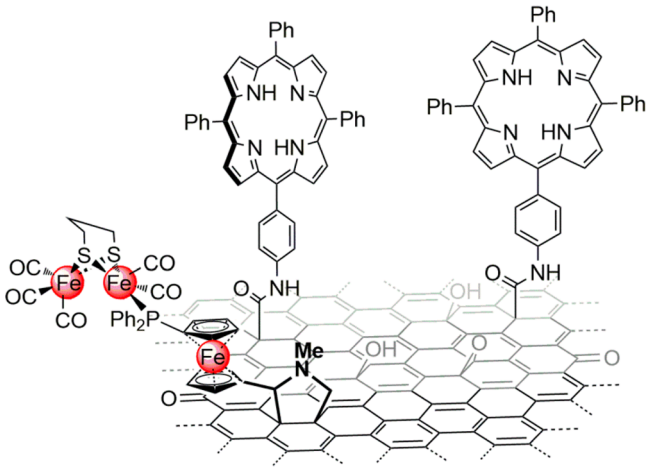

Figure 40. Schematic representation of photocatalytic TPP|GO|**$Fe_3$1** assembly.[534]

and affects photocatalytic activity.[855] The overall charge of **Co3** is essentially zero around neutral and slightly acidic pH, whereas pyridine-free $[Co^{3+}Cl_2(dmgH)(dmgH_2)]$ (**Co105**, Figure 41) is negatively charged. As a result, adsorption experiments revealed a superior **Co3** loading at higher pH, whereas **Co105** loads more efficiently at lower pH. In methanolic aqueous solution, photocatalytic activity (TOF_{H2}) at different pH values for **Co3** followed an opposite trend than expected from loadings, and **Co105** exhibited very little variation (~0.012 mol_{H2} s^{-1}; Table

DOI: 10.1021/acs.chemrev.8b00392
Chem. Rev. 2019, 119, 2752–2875

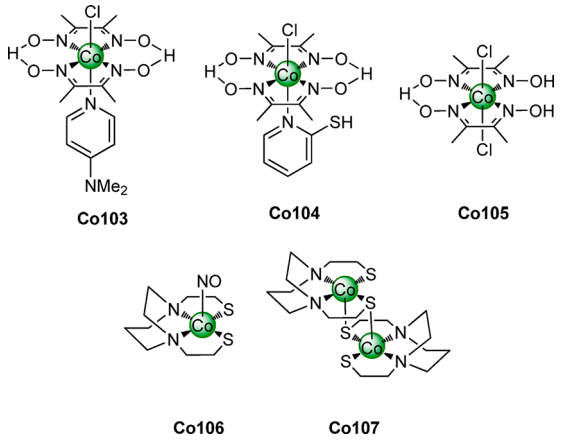

Figure 41. Molecular structure of Co-based catalysts employed with QDs toward H_2 evolution.

3, entries 9 and 10). It was concluded that an electrostatic attraction may actually hinder charge separation efficiency due to acceleration of the backward ET (from the reduced catalyst to the oxidized QD), which ultimately results in lower photocatalytic activity. This highlights that the strength of electrostatic interactions between a catalyst and the surface of the QDs may reach an optimum that ensures sufficiently fast forward paired with slow backward charge transfer. Along the same lines, a recent study demonstrated that stronger alkaline conditions (pH 13.5) can affect the QD-catalyst interface and even unlock a simultaneous two-ET process from the QD to the catalyst, which is energetically favorable compared to two successive one-ET steps.[856]

A phosphonic acid-bearing cobaloxime catalyst **Co88** (Figure 26) was immobilized on CdSe QDs with a protective ZnS shell (66 cobaloximes per QD), and transient absorption spectroscopy (TAS) revealed efficient ET from the CB of the QDs (−0.97 V vs NHE) to the catalyst.[699] The QD|cobaloxime hybrid system displayed a Co-based TON_{H2} > 150 in presence of TEOA as SED in toluene (without H_2O) after 10 h irradiation. Another family of Co catalyst, based on the *N,N'*-bis(2-mercaptoethyl)-1,4-diazacycloheptane ligand, was combined with water-soluble thioglycolic acid-stabilized CdTe QDs (TGA-CdTe, ⌀ ≈ 2.7 nm).[538] In the case of **Co106** (Figure 41), the sulfur-rich ligand provides good attachment to the surface and affords a Co complex with a sufficiently positive reduction potential to accept electrons from the CB of the CdTe dots.[538,857] Centrifugation, luminescence, and IR experiments demonstrated that the attachment of the catalyst reaches ∼0.45% w/w in the isolated QD|**Co106** hybrid assembly. A TON_{H2} of 23 000 was observed during photocatalysis in aqueous AA solution (pH 5.5) after 70 h of irradiation (λ > 400 nm), with a QY of 5.3% at λ = 400 nm (Table 3, entry 11). The gradual decrease in H_2-evolution rate was assigned to aggregation of the QDs, detachment of the grafted complex, and ligand dissociation with the consecutive substitution of the cobalt center in solution generating a less active TGA-Co complex. Transmission electron microscopy showed no metallic deposits, but further experiments to assess the nature of the active catalyst were not conducted. The analogous dimer **Co107** (Figure 41) displayed no anchoring ability and a photocatalytic activity similar to $Co(NO_3)_2$ salt, providing insight into the importance of anchoring (Table 3, entry 12).

Building on previous works combining QDs with [FeFe]-H_2ase in solution,[688,691,858] synthetic H_2ase mimics have also been interfaced with QDs, yielding high photoactivity for H_2 evolution.[128,539,851,859−861] Although generalization is not possible, it is worth noting that the formation of iron colloids from the decomposition of [FeFe]-H_2ase-inspired carbonyl catalysts has often been observed. The resulting Fe particles may catalyze proton reduction, making careful assessment of the active species in such systems essential.[160,172,862−865]

The $[(\mu\text{-SPh-4-NH}_2)_2Fe_2(CO)_6]$ catalyst bearing two amino groups, and unfunctionalized $[(\mu\text{-S})_2Fe_2(CO)_6]$, (**$Fe_2$35** and **$Fe_2$36**, respectively, Figure 42), were compared in combination with zinc sulfide nanoparticles (⌀ = 50 nm).[851] ZnS is an n-type

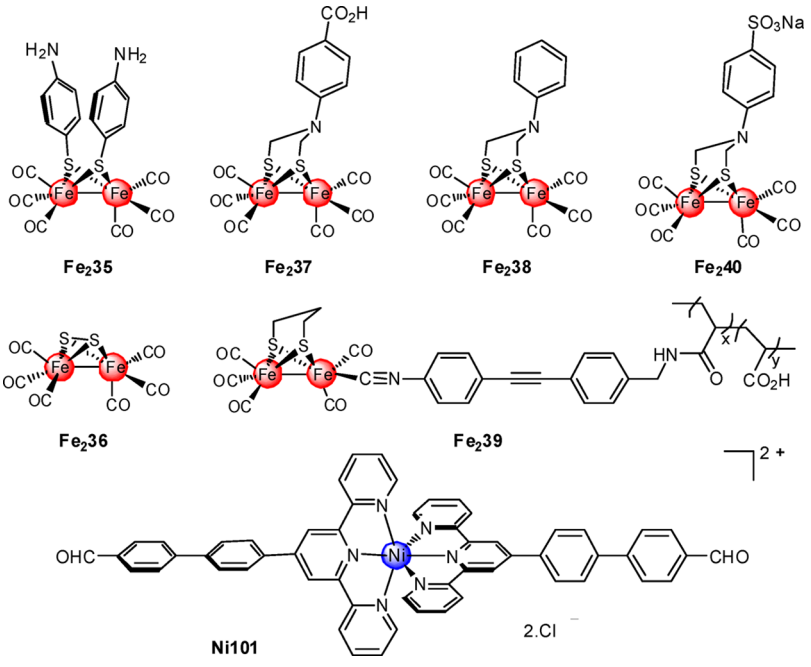

Figure 42. Molecular structure of HECs used with QDs in photocatalysis.

DOI: 10.1021/acs.chemrev.8b00392
Chem. Rev. 2019, 119, 2752−2875

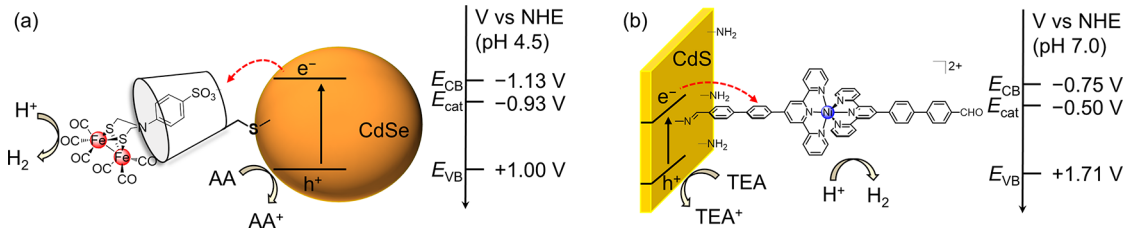

Figure 43. (a) Schematic representation of CdSe/β-CD|**$Fe_2$40** assembly and related potentials.[128] (b) Schematic representation of CdS-DETA|**Ni101** assembly and related potentials.[870] The first reduction potential of each catalyst is shown as E_{cat}.

SC with a wide bandgap of 3.66 eV, which undergoes anodic photocorrosion in purely aqueous solutions, leading to formation of elemental sulfur and/or sulfate ions.[866] In hydro-organic media, an eight times higher adsorption coefficient was obtained for **$Fe_2$35** compared to **$Fe_2$36**, demonstrating a beneficial affect of the amino groups.[851] Estimation of the E_{onset} of the **$Fe_2$35** metal-hydride ($E([HFe^{2+}Fe^{+}]/[HFe^{+}Fe^{+}])$ = −1.75 V vs NHE) revealed that the photoexcited ZnS (E_{CB} = −1.85 V vs NHE, pH 7)[866] is capable of reducing the HEC. Photocatalysis (unfiltered 300 W Xe lamp irradiation) gave a TOF_{H2} of 100 h^{-1} in DMF:H_2O (9:1) with a TON_{H2} of 2600 after 38 h, and a QY_{H2} of 2.5% (λ = 325 nm; Table 3, entry 13). The catalyst integrity after irradiation experiments was not reported.[851]

Although the bandgap of ZnS makes it rather unattractive for solar energy conversion (absorption at λ < 340 nm), it was also employed under similar conditions in combination with [FeFe]-H_2ase mimics **$Fe_2$37** and **$Fe_2$38** (Figure 42), where adsorption of 0.4% (w/w) and 0.03% (w/w) of the assembly was observed, respectively.[860] IR evidence suggests that a carboxy linkage with coordinatively unsaturated Zn ions on the surface of ZnS occurs in the case of **$Fe_2$37**, whereas an exposed sulfur group of the surface may support the adsorption of **$Fe_2$38**. Despite lower loading, **$Fe_2$38** achieved higher catalytic performance than **$Fe_2$37** in DMF:H_2O (9:1) containing TEOA, with respective TON_{H2} values of 4950 and 3400 after 30 h under 300 W irradiation without UV-cutoff filter (Table 3, entries 14 and 15). Although no change in particle size was observed after experiments, IR revealed alteration of the catalyst structure, which may account for the loss of activity after 30 h H_2 evolution.

Replacing ZnS with the water-soluble 3-mercaptopropionic acid-stabilized CdSe QDs (MPA-CdSe, ⌀ = 1.9 nm, E_g = 2.7 eV) resulted in a relatively high loading of **$Fe_2$36** (0.78%, w/w), and IR studies confirmed a strong chemisorption of the hydrophobic catalyst onto the QDs.[859] Although photocatalytic experiments conducted in the absence of catalyst or under homogeneous conditions in hydro-organic media with AA as SED led to some H_2 evolution, attributed to the QDs, results were significantly lower than those achieved in pure water by the CdSe|**$Fe_2$36** assembly, realizing a TON_{H2} of 8800 after 82 h and an initial TOF_{H2} of 596 h^{-1} (Table 3, entry 16). The integrity of the catalyst during experiments was not reported.

An Fe_2S_2 motif anchored on the side chain of a water-soluble poly(acrylic acid) polymer via an amide bond provided the polymeric catalyst **$Fe_2$39** (Figure 42), which is soluble in water and permits anchoring onto the surface of CdSe QDs (⌀ = 1.8 nm, E_g = 3.64 eV) via coordination between the carboxylic acid and Cd^{2+} atoms.[539,689,867,868] Photocatalysis of the MPA-CdSe with the Fe_2S_2-polymer catalyst in aqueous AA solution (pH 4.0) reached a TON_{H2} of ∼27 000 after 8 h of LED irradiation (λ = 450 nm), with an initial H_2 evolution TOF_{H2} of 3.6 s^{-1} (Table 3, entry 17).[539] The catalyst integrity under operating conditions was not reported. Although attachment of the polymer was not quantified, experiments suggest that the poly(acrylic acid) wrapped around the QD. As a result the distance between the PS and the Fe_2S_2 core was reduced, resulting in rapid ET from the photoexcited MPA-CdSe QDs to the Fe_2S_2 unit, three times faster than hole extraction. Additionally, the wrapping of the polymer also reduces QD aggregation, which improves the lifetime of the photocatalytic system. The performance could be further increased by adding an additional polymer, polyethylenimine (PEI), into the colloidal solution. Polyethylenimine promotes the interaction of CdSe QDs with **$Fe_2$39** and AA, with PEI also protecting the cadmium chalcogenide nanocrystals from aggregation.[861,869] Steady-state and time-resolved spectroscopy revealed that PEI enhances the rate of hole transfer up to ∼30-fold, helping the system to achieve a TON_{H2} of ∼84 000 (Table 3, entry 18).[861]

An alternative to the direct anchoring of a catalyst onto the QD surface is employing an additional "binder" to dock the catalyst in solution via a host−guest interaction.[128] Building on the abilities of β-cyclodextrine (β-CD) to form inclusion complexes with hydrophobic molecules (including [FeFe]-H_2ase mimics),[127] it was demonstrated that this strategy can deliver superior photocatalytic performances than nonanchored approaches.[128] Mercaptoacetic acid capped CdSe QDs (MAA-CdSe, ⌀ = 2.2 nm) were functionalized via the coordination of a thiolato group-bearing CD to the Cd^{2+}-rich surface (Figure 43a), with the CD-cavity being accessible for inclusion of the water-soluble diiron catalyst **$Fe_2$40** (Figure 42). A mass fraction of 9.7% (w/w) of **$Fe_2$40** in the CdSe/β-CD assembly was measured by inductively coupled plasma optical emission spectrometry analysis. At pH 4.5, the QDs E_{CB} and the first reduction potential for the **$Fe_2$40** incorporated into the CD were determined at −1.13 and −0.93 V vs NHE, respectively, demonstrating the exergonic nature of ET between the two entities. Photocatalytic H_2 evolution studies in aqueous AA solution demonstrated that inclusion of the catalyst in the β-CD cavity improves catalyst stability during illumination, giving a TON_{H2} of 2370 after 28 h (TON_{H2} of 894 was obtained without β-CD; Table 3, entry 19). In situ IR spectroscopy revealed that the system is limited by aggregation of QDs and degradation of the catalyst.[128]

An inorganic−organic hybrid CdS-diethylenetriamine (DETA) material, composed of multiatomic layers of $(CdS)_n$ and DETA molecules, can be covalently functionalized by the modified nickel bis-tpy catalyst, **Ni101**, to perform light-driven H_2 evolution (Figures 42 and 43b).[870] CdS-DETA nanosheets possess a lateral size distribution of 300−800 nm and a thickness of about 30 nm (the presence of amino groups at its surface is supported by XPS). The E_{VB} maximum of CdS-DETA was

DOI: 10.1021/acs.chemrev.8b00392
Chem. Rev. 2019, 119, 2752−2875

estimated at around 1.71 V vs NHE (pH 7) from its XPS valence band spectrum by comparison with TiO_2 anatase (used as a reference), and E_{CB} was calculated at −0.75 V vs NHE (E_g = 2.46 eV). The first reduction potential of **Ni101** was measured at around −0.50 V vs NHE, allowing for ET from the QD upon irradiation. The aldehyde groups in **Ni101** permits condensation with a terminal amino-group of the CdS-DETA nanosheets, resulting in the imine-anchored catalyst in the CdS-DETA|**Ni101** assembly. Raman and IR spectroscopy and EDX analysis confirm attachment of the catalyst with inductively coupled plasma optical emission spectrometry analysis giving a catalyst loading of 0.7% (w/w). Solar irradiation (λ > 420 nm) in EtOH:H_2O with TEA as SED (alkaline solution) showed a TON_{H2} of ∼44 000 (based on the amount of immobilized complexes), an initial TOF_{H2} of 0.47 s^{-1}, and an apparent QY_{H2} of 9.9% (λ = 420 nm; Table 3, entry 20). Although bare CdS-DETA combined with the aldehyde-free Ni bis-tpy in an homogeneous scheme also photogenerates H_2, a higher activity was reached with the CdS-DETA|**Ni101** assembly.[870]

5.2.3. Dye-Sensitized Semiconductors. Dye-sensitized approaches have been extensively employed in PEC assemblies (discussed in section 7), with colloidal systems using DSP schemes becoming more commonly used in solar fuel synthesis.[527,558] Two distinct systems have emerged that can be differentiated by their predominantly "on particle" or "through particle" ET pathways from the dye to catalyst (Figure 44).[295] The former involves a DSP system that mainly operates via direct reduction of a catalyst by a nearby photoexcited PS on the particle surface; a mechanism enforced by utilizing an inert SC that is thermodynamically unable to receive electrons from the photoexcited dye. Compared to homogeneous multicomponent systems, ET between the dye and catalyst is not diffusion limited in this system, potentially leading to faster ET kinetics. The photocatalytic mechanism of the "on particle" system often proceeds via reductive quenching of the PS excited state (PS*) by the SED, followed by reduction of the catalyst by the reduced PS (PS^-). In the "through particle" system, the PS excited state is typically oxidatively quenched by the CB of the SC, which shuttles the electrons to the catalyst. The oxidized PS (PS^+) is regenerated by the SED. These systems often benefit from ultrafast quenching of the PS* and generation of multiple, low-potential electrons that have a long lifetime for fuel synthesis.[527]

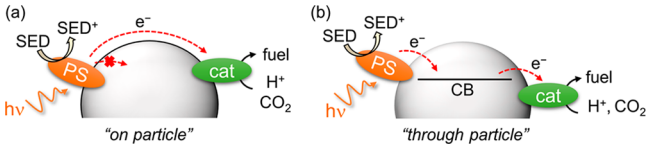

Figure 44. Schematic representation of (a) "on particle" and (b) "through particle" systems in DSP.[295]

The prototype assembly consisted of the HEC **Co88** (Figure 26) and the Ru-based PS, **PS19** (Figure 7), immobilized on TiO_2 nanoparticles via phoshponic acid anchors.[541] This DSP system functions via a "through particle" mechanism and benefits from an efficient PS-TiO_2 interface that also forms a key component in DSSCs. TiO_2 is the most commonly used wide-bandgap SC in DSP constructs, as its phase composition (anatase or anatase/rutile) and tendency to agglomerate have a great impact on the charge separation properties and the photocatalytic activity.[871,872] Phosphonic acid groups are commonly used as anchoring moieties as they provide good stability in acidic and pH-neutral aqueous solution (section 3).[655] As required for a "through particle" mechanism, E_{onset} of **Co88** at −0.60 V vs NHE is less negative than E_{CB} of TiO_2 at ∼−0.70 V vs NHE (pH 7).[873] **PS19** bears two phosphonic acid groups and injects electrons into the CB of TiO_2 with a yield of 97%. Both phosphonated molecules were anchored on TiO_2 (P25, 8/2 anatase/rutile, Brunauer, Emmett, and Teller-surface area of 50 m^2 g^{-1}) in an aqueous solution (pH 7) containing TEOA as a SED. UV-filtered simulated solar irradiation of the **PS19**|TiO_2|**Co88** assembly generated a Co-based TOF_{H2} of 15 h^{-1}, with a TON_{H2} of 108 after 10 h (Table 3, entry 21).[191,873] For comparison, anchor-free **Co3** loaded only marginally onto the surface ($\Gamma \approx 1.0$ $nmol_{Co3}$ mg_{TiO2}^{-1} vs 6.6 $nmol_{Co87}$ mg_{TiO2}^{-1}) and displayed an order of magnitude lower H_2 evolution activity. UV irradiation of TiO_2|**Co88** generates H_2 through bandgap excitation, but photoactivity ceased in the presence of phosphate ions, which displace the catalyst from the SC surface.[873] A homogeneous system consisting of **PS19** and **Co88** in solution without TiO_2 did not photogenerate H_2 under the same experimental conditions.[191,873]

Replacement of TiO_2 by ZnO, $SrTiO_3$, ZrO_2, CeO_2, or ITO in this DSP system resulted in marginal or no H_2 production due to less favorable interactions or mismatching of the CB levels.[874] This highlights the importance of anchoring the dye and catalyst on a suitable SC scaffold and demonstrates the exclusive "through particle" H_2-evolving pathway for this dye|TiO_2| catalyst architecture. Adding more $dmgH_2$ ligand in solution with **PS19**|TiO_2|**Co88** permits the restoration of catalyst activity and consequently an increase of its activity and stability to TON_{H2} > 300 after 24 h (Table 3, entry 22). This observation is in agreement with dissociation of the cobaloxime ligands during photocatalytic turnover (section 2.2.4.2).

Time-resolved spectroscopy on the **PS19**|TiO_2|**Co88** system revealed that visible light absorption at **PS19** generates an almost quantitative and ultrafast charge separation (180 ps) at the dye|TiO_2 interface and ensures the formation of long-lived, low potential electrons.[873] Some inefficiency of the system results from slow $PS19^+$ regeneration by TEOA (∼0.1 ms), which is responsible for some recombination losses with CB electrons (∼1 ms). The ET from TiO_2 to the **Co88** catalyst [$Co^{3+/2+}$] occurs on an ∼4 μs time scale whereas the second reduction [$Co^{2+/+}$] is significantly slower (at least 10 000-fold), which illustrates the need for a faster regenerating system or more efficient two electron reduction.[875] The straightforward synthesis, good activity, and stability of catalyst **Co88** has promoted its use in several other studies aimed at achieving H_2 evolution with immobilized HECs.[543,699,876,877] Replacement of **PS19** by other dyes for systems with improved light harvesting has also been reported.[699,876,877]

Further catalyst structure optimizations have been conducted, with the aim of improving stability and activity. The introduction of an additional phosphonic acid group on the axial pyridine ligand on **Co108** (Figure 45) resulted in increased catalyst loading (Γ = 11.2 $nmol_{Co106}$ mg^{-1}_{TiO2}) without leading to higher activity (TON_{H2} = 99; Table 3, entry 23).[873] Catalysts **Co88** and **Co108** suffer from an axial pyridine ligand that becomes labile after initial reduction and dissociates from the $Co(dmgH)_2$ core. Although the core can readily recoordinate to the anchored ligand in a bulk DSP suspension through a "hop-off, hop-on" mechanism, a more permanent attachment may result in improved performance.[527,878] Thus, **Co87** and **Co89** (Figure 26) were designed, where the phosphonic acid moiety

DOI: 10.1021/acs.chemrev.8b00392
Chem. Rev. 2019, 119, 2752−2875

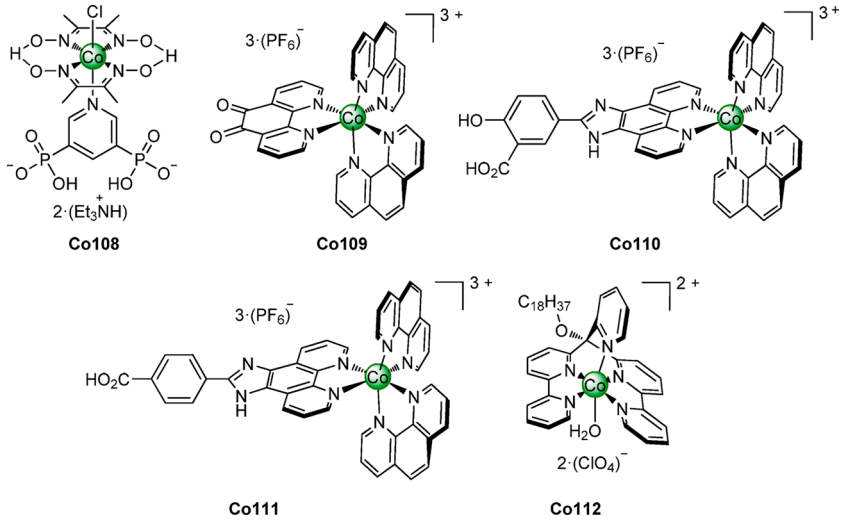

Figure 45. Molecular structure of Co-based HECs employed toward H_2 evolution in DSP systems.

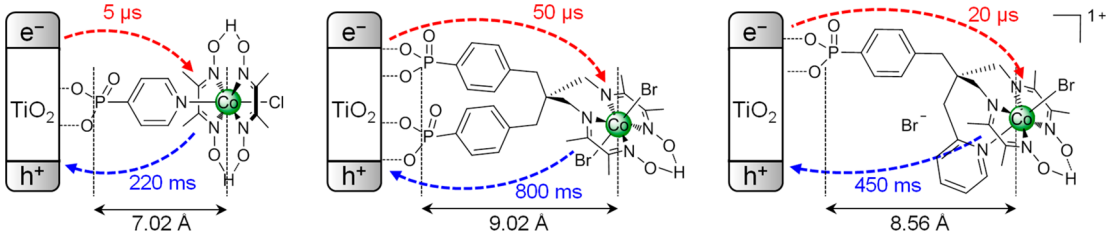

Figure 46. Schematic representation of the anchored catalyst **Co88**, **Co87**, and **Co89** and the corresponding Co-phosphonate distance, as well as charge transfer kinetics of the [$Co^{3+/2+}$] couple.[879]

was introduced in a more robust, pseudomacrocyclic diimine-dioxime ligand framework.[543,754] Although a more robust anchoring was indeed achieved compared to **Co88** and **Co108**, **Co87** evolved smaller amounts of H_2 when immobilized on **PS19**-sensitized TiO_2 nanoparticles (Table 3, entry 24), attributed to its more negative E_{onset} (−0.72 vs NHE at pH 7). Catalyst **Co89** with a covalently tethered phosphonic acid and pyridyl unit was subsequently reported and required a lower overpotential for H_2 evolution. A higher loading capacity was also observed compared to **Co108** and **Co88**, and a TON_{H2} of 22 was obtained in photocatalysis when combined with a **PS19**-TiO_2 assembly in pH neutral TEOA solution (Table 3, entry 25), superior to the TON_{H2} reached with **Co87**. As further evidence of its robust nature, the **Co89** system also maintained activity in aqueous AA solution (pH 4.5), whereas **Co88** and **Co108** were not stable (Table 3, entry 26). Replacing TiO_2 with ZrO_2 prevents the **PS19** photoexcited or reduced state from injecting electrons into the too negative CB energy level of ZrO_2. However, the **PS19**|ZrO_2|**Co89** assembly gave a TON_{H2} of 10 after 4 h of irradiation (Table 3, entry 27), which was attributed to an "on particle" mechanism enabled by reductive dye quenching by AA (pH 4.5).[543]

In a comparative kinetic study of the catalysts **Co88**, **Co87**, and **Co89** immobilized on TiO_2, ET dynamics at the TiO_2-catalyst interface was studied by UV-light excitation of the SC. Rates correlated with the distance of the catalytic core from the SC surface, resulting in slower rates for forward ET and recombination with increasing distance (Figure 46).[879] Thus, an ideal catalyst distance from the surface can be envisioned, which allows for sufficiently rapid forward ET and suitably slow recombination for optimal catalyst turnover.

Photocatalysis (300 W, λ > 420 nm) of the trisphenantroline-based Co catalysts, **Co109**, **Co110**, and **Co111** (Figure 45) with TiO_2 nanoparticles and Eosin-Y (**PS3**, Figure 7) in aqueous TEA solution (pH 11) gave a TON_{H2} of 9, 90, and 43 after 6 h of irradiation, respectively (Table 3, entries 28−30).[880] The low efficiency of **Co109** was attributed to a weak interaction of the 1,2-diketone unit with the surface of TiO_2, whereas the respective salicylic and carboxylic acid groups in **Co110** and **Co111** provide higher affinity to the MO_x.

The only Ni-based catalyst used in a DSP system is **Ni35**, which strongly anchors to TiO_2 thanks to its four phosphonic acid groups.[295] On **PS19**-sensitized TiO_2, a TON_{H2} of 278 and TOF_{H2} of 72 h^{-1} were achieved after 30 h of solar light irradiation (100 mW cm^{-2}, AM 1.5G, λ > 420 nm) at pH 4.5 (Table 3, entry 31). Oxidative quenching of **PS19*** by the CB of TiO_2 was 1000 times faster than reductive quenching by AA (180 ps vs 250 ns), thereby favoring a "through particle" pathway. Replacement of TiO_2 by ZrO_2 also resulted in a high TON_{H2} due to an efficient "on particle" mechanism, accessible via reductive quenching of **PS19*** by AA (Table 3, entry 32).[295]

A series of organic PSs based on the diketopyrrolopyrrole (DPP) chromophore were studied in a precious-metal-free DSP system with **Ni35**.[877] **PS30** was identified as the best performing DPP dye (Figure 47) and displays a strong and broad absorption in the visible part of the solar spectrum (λ = 400 to 575 nm, $\varepsilon_{496\ nm}$ = 26 000 M^{-1} cm^{-1}). It also features an excited state that allows for electron injection into TiO_2, as well as an oxidized state that can be efficiently regenerated (>94%) by AA in employed photocatalytic conditions. When anchored onto TiO_2 together with **Ni35** in aqueous conditions, TON_{H2} values close to that of **PS19** were achieved after 21 h of irradiation (AM1.5G,

DOI: 10.1021/acs.chemrev.8b00392
Chem. Rev. 2019, 119, 2752−2875

1 Sun, λ > 420 nm, Table 3, entry 33). Using Pt instead of **Ni35**, **PS30** outperformed **PS19** (**PS30**-based TON_{H2} = 2660; **PS19**-based TON_{H2} = 431), most likely due to its better light-harvesting properties. No H_2 resulted if TiO_2 was replaced with ZrO_2, indicating that H_2 evolution with **PS30** proceeds only via an oxidative "through particle" mechanism. The advantage of broad light absorption with **PS30** was illustrated by QY_{H2} measurements at λ = 500 (the maximum solar energy emission) and 550 nm, giving a yield of 0.40% and 0.15%, respectively (QY_{H2} = 0.1% at λ = 500 nm and 0.0% at λ = 550 nm with **PS19**).[877]

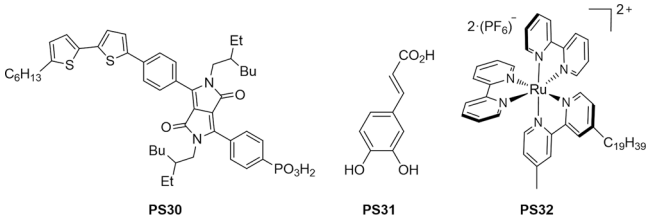

Figure 47. Structures of the PSs used in DSP systems.

While most DSP systems rely on a type I sensitizer (transition based on intramolecular excitation), catechol derivatives such as caffeic acid (**PS31**) have been shown to act as type II sensitizers (transition based on dye-to-SC excitation).[881,882] A **PS31**|TiO_2|**Ni35** assembly generated a TON_{H2} of 27 during AM1.5G irradiation (1 Sun, λ > 420 nm; Table 3, entry 34).

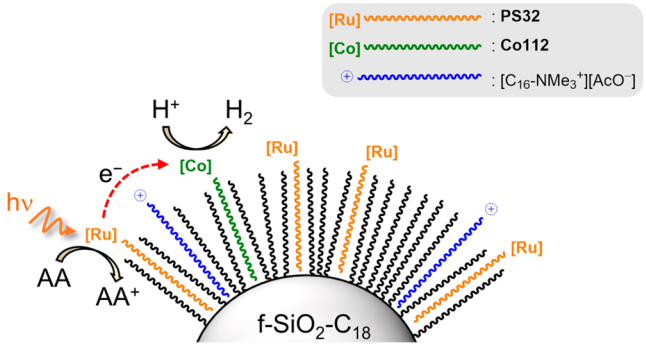

Figure 48. Schematic representation of the **PS32**|f-SiO_2-C_{18}|**Co112** assembly for H_2 evolution.[542]

Hydrophobic interactions have also been shown to produce efficient PS|MO_x|HEC colloidal systems. Such noncovalent anchoring of both catalyst and PS on hydrophobic solids is straightforward, while displacement of the components in aqueous media by protonation or competing (ionic or polar) species is greatly diminished. Photocatalysis can be achieved via 'on particle' ET. C_{18}-functionalized fumed silica nanoparticles (f-SiO_2-C_{18}, Figure 48) were coated with a HEC and PS both bearing lipophilic chains (**Co112**, Figure 45, and **PS32**, Figure 47).[542] The strong adsorption of both the PS and catalyst was confirmed by ^{13}C cross polarization magic angle spinning solid-state NMR spectroscopy and fluorescence experiments. In order to maintain dispersibility, an amphiphilic surfactant (*N*,*N*,*N*-trimethylhexadecyl ammonium acetate, [C_{16}-NMe_3^+][AcO^-]) was also loaded onto the nanoparticles. When exposed to LED irradiation (λ = 453 nm) and suspended in an aqueous AA solution (pH 4.0), the PS/HEC-loaded silica particles achieved a **Co112**-based TON_{H2} of 1322 (Table 3, entry 35). Further experiments conducted after removal of the particles did not produce H_2, supporting that no major amounts of **PS32** and **Co112** leach into solution, and that H_2 evolution occurs at the surface of the silica.

5.2.4. Micelles and Vesicles. Photocatalytic H_2 production across vesicle membranes was early demonstrated with a zinc porphyrin PS embedded in the lipid bilayer, a rhodium HEC in solution, and MV as an electron mediator.[883] Later, a functionalized [Fe-Fe]-H_2ase mimic was also embedded into vesicles at up to 28 mol% of the assembly, but (solar-driven) H_2 evolution was not reported.[884] Photocatalytic H_2 production in aqueous TEOA (pH 8.3) was shown with lipid membrane vesicles (⌀ = 98 nm and a polydispersity index of 0.33) based on 1,2-dioleoyl-*sn*-glycero-3-phosphocholine (DOPC) that contained a cobaloxime catalyst, **Co113**, and a Ru dye, **PS33** (Figures 49 and 50), accounting for 12.6 mol% and 3.15 mol% of the assembly, respectively.[885] Both molecules bear hydrophobic chains to promote embedment into the hydrophobic layer of the vesicles. TON_{H2} values of 165 and 13 were obtained after 13 and 18 h irradiation using Ru-based **PS33** or the lipophilic **PS34** (Figure 50), respectively (Table 3, entries 36 and 37). This highlights the benefits of using long-lived excited state dyes, which increase the probability of ET between the PS and the catalyst at the surface of the membrane.

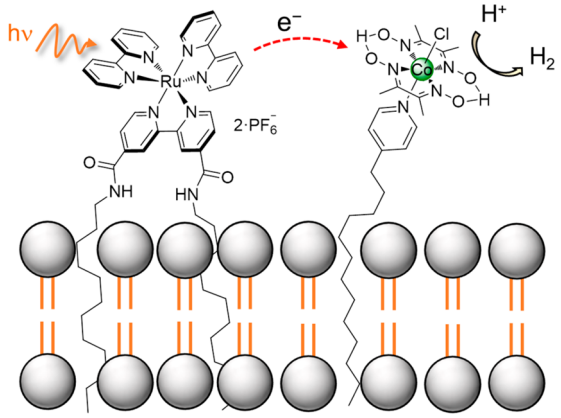

Figure 49. Schematic of **Co113** and **PS33** embedded into a lipid membrane for H_2 evolution (not to scale).[885]

Micelles were also shown to provide an adapted environment for colloidal photocatalysis. An investigation of micelle polarity on photocatalytic performance was provided through the combination of micelles featuring different polarity, with $[Co^{2+}(bpy)_3]Cl_2$ as a catalyst (**Co39**, section 2.2.4.2) and an Ir complex as a light harvester (**PS5**, Figure 7).[548] The cationic CTAB micelles demonstrated the highest activity, achieving a **Co39**-based TON_{H2} of 7.9 in aqueous TEOA after 6 h irradiation (λ = 350 nm, Table 3, entry 38), followed by nonionic micelles and anionic micelles. All micelle-containing systems allowed catalytic performances superior to those obtained under homogeneous conditions in MeCN:H_2O (TON_{H2} = 1.3). Localization of the PS and HEC molecules in the interior or at the interface of the microheterogeneous environment is thought to bring the two components into close proximity, creating a higher effective concentration and thus promoting PS-HEC interaction. Although not directly investigated, it was proposed that the balance of Coulombic and hydrophobic forces within cationic micelles positions the catalytic subunits at the interface, an arrangement that provides

DOI: 10.1021/acs.chemrev.8b00392
Chem. Rev. 2019, 119, 2752−2875

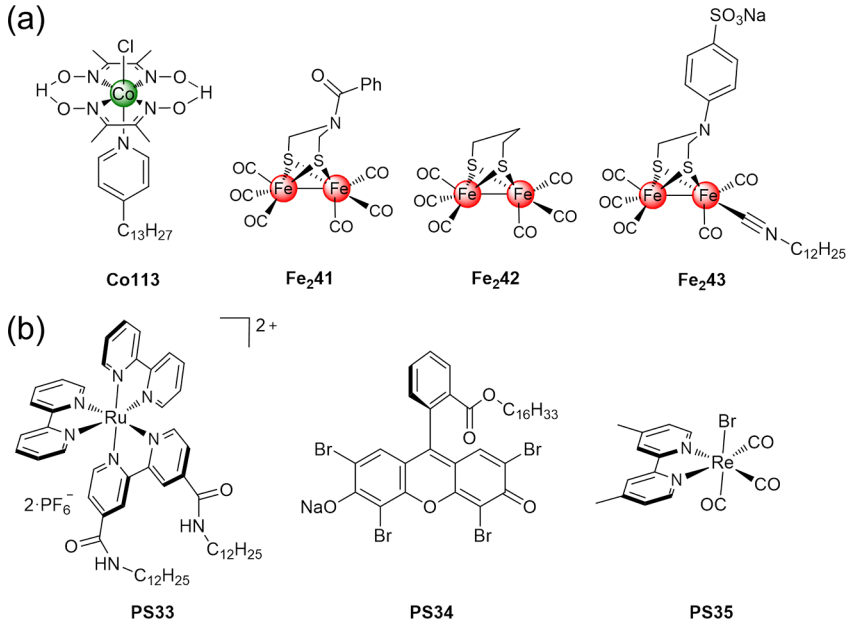

Figure 50. Structure of (a) HECs associated with micelles and vesicles and (b) the accompanying molecular photosentizer.

exposure to TEOA and protons from bulk solution. In contrast, the positively charged PS and HEC units are thought to be deeply buried within the hydrophobic region of the anionic micelles, limiting access of the substrate and SED.

A series of hydrophobic [Fe-Fe]-H_2ase mimics were combined with hydrophobic Re dyes to conduct photocatalytic H_2 evolution in water (Figure 50).[547] The incorporation of the PS and catalyst into the hydrophobic interior of SDS micelles was verified by spectroscopic studies, showing increasing absorbance and emission of a PS-containing aqueous solution upon addition of an SDS micellar solution. Under light irradiation for ∼1 h, only a minimal amount of H_2 evolution was observed with a **$Fe_2$41**-based TON_{H2} of 0.13 using **PS35** (Figure 50) in aqueous AA solution (Table 3, entry 39). Despite the limited H_2 evolution activity, probably due to the small exergonicity of the ET from the dye to the catalyst, this work presents a concept of how to integrate an insoluble catalyst or dye to perform catalysis under aqueous conditions.

Improved performances were obtained upon replacing the PS with **PS3** and HEC with **$Fe_2$13** (Figure 7 and section 2.2.3.1, respectively).[134] Under LED light irradiation (λ = 455 nm, 0.3 W) using TEA as a SED (10% v/v) in water (pH 10.5), the micellar system reached TON_{H2} of 117 after 4.5 h (Table 3, entry 40), which is four times higher than SDS-free experiments. System deactivation was attributed to decompostition of the PS, while catalyst homogeneity was assessed by adding Hg^0. In spite of the presence of SDS micelles, poor solubility of **$Fe_2$13** under the experimantal conditions was also found to be a limiting factor for performance.[134] Another micelle system based on an amphiphilic polymer similarly demonstrated activity of a hydrophobic catalyst **$Fe_2$42** (Figure 50) and **PS1** (Figure 7) in an aqueous environment.[886] **$Fe_2$42** incorporation was monitored via UV−vis and IR experiments, and a saturated loading of 4.6% (w/w) was recorded without noticeable change in the particle size. Under LED irradiation (λ = 450 nm) for 2 h in the presence of AA the system achieved a **$Fe_2$42**-based TON_{H2} of 133 (Table 3, entry 41). A TON_{H2} of only 4.1 was obtained under homogeneous conditions, which highlights the capacity of the micelles to act as "cages" to increase the probability of collision between the catalyst and the PS.

Beside molecular PSs, CdSe QDs have also been incorporated and concentrated into lipid membranes together with the amphiphilic HEC **$Fe_2$43** (Figure 50), which bears a long hydrophobic chain and a sulfonate group.[549] DLS measurements and size exclusion chromatography demonstrated the incorporation of both the QDs and catalysts into the membrane of a DOPC-based vesicle. Such embedment permitted the solubilization of the oleic acid-capped CdSe QDs into an aqueous media without precipitation, allowing the latter to be used as a PS. An **$Fe_2$43**-based TON_{H2} of 651 was achieved in aqueous AA solution (pH 4) under visible light irradiation (Table 3, entry 42).

5.2.5. Hydrogenase-Based Systems. Natural hydrogenases, as the archetypal 3d transition metal HEC operating at high rates close to the thermodynamic potential, represent an ideal platform to evaluate the potential of a light harvesting unit. Alongside electrode-immobilized (detailed in section 4.2.3) and homogeneous photocatalysis examples, colloid-anchored H_2ase-based systems have also been achieved with a broad range of materials (e.g., carbon nitride, quantum dots, and metal oxides) due to the versatile anchoring ability of the H_2ases.[16,19,653,887]

For instance, the [NiFeSe]-H_2ase from *Desulfomicrobium baculatum* was assembled with melon carbon nitride (CN_x, Figure 38).[842] Under simulated solar irradiation (AM1.5G, 1 Sun), the hydrogenase generated a TON_{H2} of 50 000 after 48 h in pH 6 EDTA solution (Table 3, entry 43), demonstrating the biocompatibility of CN_x. Although most of the ET occurs under collisional probability, weak interactions between the H_2ase and melon were observed. These supposedly occur due to the formation of hydrogen bonding with the −NH−, terminal −NH_2, or Lewis basic heptazine edge nitrogens in CN_x and/or electrostatic interactions (zeta-potential = −15 mV at pH 6).[835,888,889]

CdS[691,858,890−892] and CdTe[688,893] were also explored as visible light-harvesting quantum materials that are capable of docking with H_2ases. The interface relies on electrostatic interactions between the positively charged protein surface

DOI: 10.1021/acs.chemrev.8b00392
Chem. Rev. 2019, 119, 2752−2875

surrounding the distal iron-sulfur cluster of the [FeFe]-H_2ase from *Clostridium acetobutylicum* (Hyd^A) and the negatively charged surface of the MPA-capped particles. In the case of CdTe nanodots, the adsorption was monitored by following the decreased mobility of the particles upon the adsorption of the H_2ase. In the presence of AA (pH 4.75) this assembly delivers a QY of 9% at λ = 532 nm (Table 3, entry 44), and a photon-to-hydrogen efficiency of 1.8% under simulated sunlight with an enzyme-based TOF_{H2} of 25 s^{-1}.[688] Using CdS nanorods instead of CdTe QDs under comparable conditions (AA, pH 7) resulted in an order of magnitude enhancement of the performance, reaching a TOF_{H2} of 380 s^{-1} and TON_{H2} of 10^6 (Table 3, entry 45) under monochromatic illumination (λ = 405 nm).[691] The loss of system activity after 4 h was attributed to the progressive oxidation of the MPA capping ligands that is responsible for the docking of the electropositive H_2ase via the electronegative carboxylate groups. Replacement of the C_3-MPA with longer mercaptocarboxylate capping ligands resulted in a lower H_2 evolution performance, whereas C_2 ligand-based systems delivered the best performance. This effect is believed to be the result of faster ET with shorter alkyl chain ligands, highlighting the importance of having a short distance between the CdS surface and the H_2ase.[858]

Following the use of bare UV-absorbing TiO_2 particles,[894,895] H_2ase-anchored colloidal systems progressively evolved toward visible-light harvesting dye-sensitized MO_x particles. *Desulfomicrobium baculatum* [NiFeSe]-H_2ase was successfully combined with Ru complex-,[652,781] CN_x-,[654] and **PS30**[877]-sensitized P25 TiO_2. The enzyme achieved a TOF_{H2} of 50 s^{-1} upon visible light irradiation when attached to a **PS19**-sensitized TiO_2 nanoparticle in aqueous TEOA (pH 7.0). 250 W irradiation with a cutoff filter (λ > 420 nm) was used to avoid direct E_g excitation of TiO_2 (Table 3, entry 46).[652] Replacement of **PS19** by CN_x can generate a direct transition from the dye to the CB of TiO_2 that ultimately permitted a TOF_{H2} of 8 s^{-1} in aqueous EDTA (pH 6.0) under simulated solar light (Table 3, entry 47).[654] Similar catalytic performances were achieved with the dye **PS30**, using 2-(*N*-morpholino)ethanesulphonic acid (MES) buffer and AA as a SED (pH 6.0, Table 3, entry 48).[877]

5.3. Photocatalytic CO_2 Reduction

Although some homogeneous systems have achieved good performances for CO_2 reduction, they still often suffer from drawbacks associated with product isolation, catalyst recovery, limited stability, and low water compatibility of both the light-harvester and the catalyst. Supported catalysis for CO_2 reduction appears as an attractive solution to most of these limitations. Colloidal-reduction of CO_2 with molecular catalysts in the presence of water has been reported, but most cases employ Ru- or Re-based catalysts and/or excess of organic solvent.[896−905] State-of-the-art systems in water-containing media have reached CO_2-reduction TONs > 2000 for Ru-based catalysts on carbon nitride, and TONs of ∼1000 for Re-based catalysts on TiO_2 nanoparticles.[898,903] Only a small number of examples of colloidal systems involving immobilized first row transition 3d metals for CO_2 reduction have been reported.

5.3.1. Carbon-Based Colloids. An iron porphyrin catalyst bearing four carboxylic acid groups (**Fe34**, Figure 51) is able to functionalize carbon nitride nanosheets via both $\pi-\pi$ interactions, observed by X-ray diffraction, and supposedly via H-bonding between the $-CO_2H$ groups and the amino groups or N-containing rings.[906] The g-C_3N_4 nanosheets display a high surface area (135.8 m^2 g^{-1}) and the anchoring of the catalyst is also supported by IR spectrometry, as well as g-C_3N_4 photoluminescence quenching experiments. Under irradiation (220 mW cm^{-2}) in an MeCN:H_2O solution, a TON_{CO} of 5.7 was observed with high selectivity (Table 4, entry 1). The benefit of the carboxylic acid groups was confirmed as the corresponding carboxylic acid-free parent FeTPP (**Fe4**) only achieved a quarter of the activity. This could be due to improved attachment to g-C_3N_4, or a more positive reduction potential due to the electron-withdrawing effect of the $-CO_2H$ that renders the ET more exergonic.

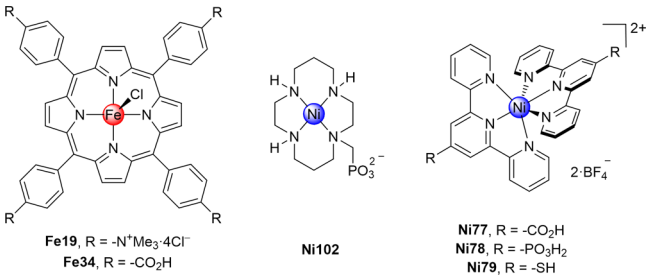

Figure 51. Molecular structure of CRCs employed in colloidal systems.

Another porphyrinoid catalyst, the Co^{2+}-chlorin **Co94** (Figure 31), performs photocatalytic reduction of CO_2 in the presence of MWCNTs and a Ru trisphenantroline-based dye **PS14** (Figure 7) in MeCN:H_2O (95:5) containing TEA.[535,797] No quantification of immobilized **Co94** was reported, but an enhancement of CO and H_2 evolution was observed upon introduction of CNTs. This was assigned to the formation of two reduced [Co^+-chlorin]$^-$ molecules in close proximity to each other to facilitate the two-electron reduction of CO_2 to CO. An additional explanation of this enhancement is the increased local concentration of CO_2 in the vicinity of the catalyst due to the hydrophobicity of the CNTs, which may act as a scaffolding agent promoting catalysis. The photocatalytic mechanism was ascribed to reductive quenching of the excited state of **PS14** by TEA, which generates **PS14**$^-$ for the production of [Co^+-chlorin]$^-$ (E(**Co94**/**Co94**$^-$) = −0.89 V vs SCE) to reduce CO_2 or H^+. After 11 h of irradiation, four times more CO was generated with the system featuring MWCNTs (TON_{CO} ≈ 501, TON_{H2} ≈ 209, QY = 0.1% at λ = 450 nm; Table 4, entry 2) compared to MWCNT-free conditions.

5.3.2. Quantum Dots. Instead of employing a molecular photosensitizer, successful integration of first row transition metal catalysts in aqueous media was also recently demonstrated with QDs.[57,907] CRC **Ni102** (Figure 51) was used for CO evolution in water with QDs (⌀ = 4.5−5 nm) of ZnSe, which is a stable and visible light-absorbing SC (direct E_g = 2.7 eV).[907] Additionally, electron mobility in single crystal ZnSe (610 cm^2 V^{-1} s^{-1}) is significantly higher than in its sulfur analogues, ZnS (200 cm^2 V^{-1} s^{-1}) and CdS (385 cm^2 V^{-1} s^{-1}).[908] ZnSe is a suitable light-harvester to drive CO evolution with **Ni102**, as the E_{CB} at approximately −1.4 V vs NHE (at pH 5.5) is about 400 mV more negative than E_{onset} of **Ni102**. Catalyst immobilization was demonstrated using ZnSe QDs free of capping ligands, permitting a loading of 1.51 mol of **Ni102** per mol of QD. Under 1 Sun irradiation (λ > 400 nm) with AA as a SED (pH 5.5) in aqueous media the integrated system evolved CO, achieving a TON_{CO} of 121 with a selectivity of 8%. A substantial selectivity increase from 8% to 33% toward CO - achieving an ideal syngas ratio - was realized via the addition of a capping ligand, 2-(dimethylamino)ethanethiol (MEDA). Using this additive, a

DOI: 10.1021/acs.chemrev.8b00392
Chem. Rev. 2019, 119, 2752−2875

Table 4. Colloidal Systems with Immobilized 3d Metal Complex Electrocatalysts for Aqueous CO_2 Reduction

entry	colloidal PS	CRC	loading (interaction)	TON_{CO}/ TON_{H_2} (after t in h)	TOF_{CO} / h^{-1}	QY_{CO} (λ/nm)	conditions	illumination	ref
1	g-C_3N_4 (nanosheets)	**Fe34**	n/a[a] (π interactions)	5.7/0 (6)	n/a	n/a	MeCN:H_2O TEOA	220 mW cm^{-2}, 420−780 nm	906
2	**PS14**-MWCNTs	**Co94**	n/a (π interactions)	501/209 (20)	n/a	0.1% (450)	MeCN:H_2O TEA	Xe lamp, λ > 420 nm	535
3	ZnSe	**Ni102**	1.51 mol_{cat} mol_{QD}^{-1} (Zn^{2+} coordination)	283/575 (20)	n/a	3.4% (400)	H_2O, AA pH 5.5	100 mW cm^{-2}, AM 1.5G, λ > 400 nm	907
4	CdS	**Ni77**	3 mol_{cat} mol_{QD}^{-1} (Cd^{2+} coordination)	0.4/39.6 (4)	n/a	n/a	H_2O, TEOA pH 6.7	100 mW cm^{-2}, AM 1.5G, λ > 400 nm	57
5	CdS	**Ni78**	23 mol_{cat} mol_{QD}^{-1} (Cd^{2+} coordination)	1.1/9.9 (4)	n/a	n/a	H_2O, TEOA pH 6.7	100 mW cm^{-2}, AM 1.5G, λ > 400 nm	57
6	CdS	**Ni79**	51 mol_{cat} mol_{QD}^{-1} (Cd^{2+} coordination)	5.1/0.4 (4) 20/12 (22)	n/a	0.28% (400)	H_2O, TEOA pH 6.7	100 mW cm^{-2}, AM 1.5G, λ > 400 nm	57
7	$CuInS_2$/ZnS	**Fe19**	0.03 mol_{cat} mol_{QD}^{-1} (electrostatic interactions)	450/5 (30)	∼16	0.025% (420)	H_2O, TEOA pH 5.7	laser 4.5 mW, λ = 450 nm	910
8	**PS19**-ZrO_2	**Ni102**	3.4 nmol mg^{-1} (chemisorption)	5/20 (7)	n/a	n/a	H_2O, AA pH 4	40 mW cm^{-2}, 375−795 nm	911
9	**PS19**-TiO_2	Ni-CODH	0.48 nmol mg^{-1} (chemisorption)	∼2000 (4)	504	n/a	H_2O, MES pH 6.0	45 mW cm^{-2}, tungsten halogen lamp, λ > 420 nm	916
10	Ag-TiO_2	Ni-CODH	1.0 nmol mg^{-1} (chemisorption)	2.5×10^5 (6)	5.04×10^4	∼1.5% (500)	H_2O, TEOA EDTA pH 6.0	300 W arc lamp, λ > 420 nm	918
11	nanorod-CdS	Ni-CODH	<0.01 nmol mg^{-1} (n/a)	2.3×10^4 (5)	4.4×10^3	n/a	H_2O, MES pH 6.0	23 mW cm^{-2}, tungsten halogen lamp, λ > 420 nm	917

[a]n/a = not available.

TON_{CO} of 283 was obtained after 20 h of irradiation, with a QY toward CO of 3.4% (λ = 400 nm) (Table 4, entry 3).[907]

A series of Ni^{2+} bis-tpy catalysts was used in combination with CdS QDs (⌀ = 5.3 nm) for CO evolution in aqueous media in the presence of TEOA.[57] Catalysts **Ni77**, **Ni78** and **Ni79** (section 2.3.7.1, Figure 51) bearing a carboxylic acid, a phosphonic acid, and a thiol, respectively, were used to study their loading affinity for capping ligand-free CdS QDs,[909] and the resulting photocatalytic activity of such assemblies. While the E_{CB} of the QDs was measured at approximately −0.84 V vs NHE (pH 6.7), the E_{onset} was estimated at around −0.80 V vs NHE, permitting exergonic ET to the catalyst.[57] Major differences between the loading capacity of the catalysts were observed by UV−vis experiments, with an affinity order of **Ni79** (51 mol_{Ni105} mol_{QD}^{-1}), **Ni78** (23 mol_{Ni104} mol_{QD}^{-1}), and **Ni77** (3 mol_{Ni103} mol_{QD}^{-1}), indicating that the soft sulfur-based functional group is the most effective anchor.

The photocatalytic activity followed the same order, affording selectivity toward CO of 93% (for **Ni79**), 10% (for **Ni78**), and 1% (for **Ni77**) after 4 h of irradiation (Table 4, entries 4−6). This result contrasts with the electrocatalytic experiments conducted under homogeneous conditions, but this trend shows that interfacing the molecular catalyst with the nanoparticles is a key to selective photocatalytic activity in aqueous solution. Long-term experiments performed with **Ni79** achieved a TON_{CO} of 20 (24 h) with a lower CO selectivity of 62%, resulting from the slow desorption of the catalyst exposing bare QD surface which performs H_2 evolution. In the case of the CdSl **Ni79** assembly, the average QY toward CO at λ = 400 nm was 0.28%, comparable to results obtained with precious-metal-containing systems. A CO-catalytic mechanism supported by FT-IR spectroscopy was proposed that involves a ligand-based reduction of **Ni79**, which then reacts with CO_2 after the loss of one tpy unit to produce the catalytically active species, stabilized by an additional DMF ligand.[57]

$CuInS_2$/ZnS core/shell QDs (⌀ = 2.5 nm, λ_{max} = 420 nm) were recently associated with a tetra-(trimethylamino)-substituted FeTPP (**Fe19**, Figure 51, section 2.3.5.1) to achieve CO_2-to-CO reduction in water.[910] Electrostatic associations between the two components were promoted by using S-bound MPA as a capping ligand resulting in a carboxylate end in aqueous solution that permits Coulombic interactions with the tetratrimethylamonium functionalized porphyrin. Although no information about the loading was provided, UV−vis and flurorescence experiments demonstrated porphyrin adsorption on the QDs in a "face-on" organization and fast ET from the QD to the CRC. Fine tuning of the size and nature of the assembly through control of electrostatic interactions via the addition of K^+ or Zn^{2+} ions resulted in major differences in the CO_2 reduction ability of the system. Photocatalytic experiments using a 450 nm laser (4.5 mW) and performed in aqueous 5 M KCl containing TEOA (pH ∼5.7) achieved a TON_{CO} of 450, as well as high chemical selectivity of 99% after 30 h (Table 4, entry 7). The low QY (0.025% at 450 nm) of the system was partially ascribed to the 30:1 QD:**Fe19** ratio that results in only 3% of the QDs bearing an adsorbed catalyst.

5.3.3. Dye-Sensitized Semiconductors. DSP systems typically employ TiO_2 particles, but the E_{CB} of this SC provides little driving force for aqueous CO_2 reduction. To employ synthetic catalysts with a significant η, TiO_2 nanoparticles have been used in hydro-organic or organic media[876,903,904] in order to increase the flat-band potential of this SC, or MO_xs with more negative reducing potentials such as tantalum oxynitride have been used instead.[901] To the best of our knowledge, no TiO_2-containing DSP system has yet been reported in pure water with a synthetic molecular catalyst for CO_2 reduction. Nevertheless, a

DOI: 10.1021/acs.chemrev.8b00392
Chem. Rev. 2019, 119, 2752−2875

CO_2-reducing Re-based catalyst, *fac*-[Re(4,4′-$(PO_3H_2$-$CH_2)_2$-2,2′-bpy)$(CO)_3Cl$] (Figure 52), achieved CO evolution with a dye-sensitized TiO_2 particle.[876,903,904] This was enabled by replacing H_2O by MeCN as the solvent to achieve a more reducing E_{CB} (TiO_2) that renders the reduction reaction of the CRC more exergonic. Controlled addition of H_2O to this system together with coanchoring of the HEC **Co88** demonstrated syngas generation with controllable selectivity (Figure 52).[876]

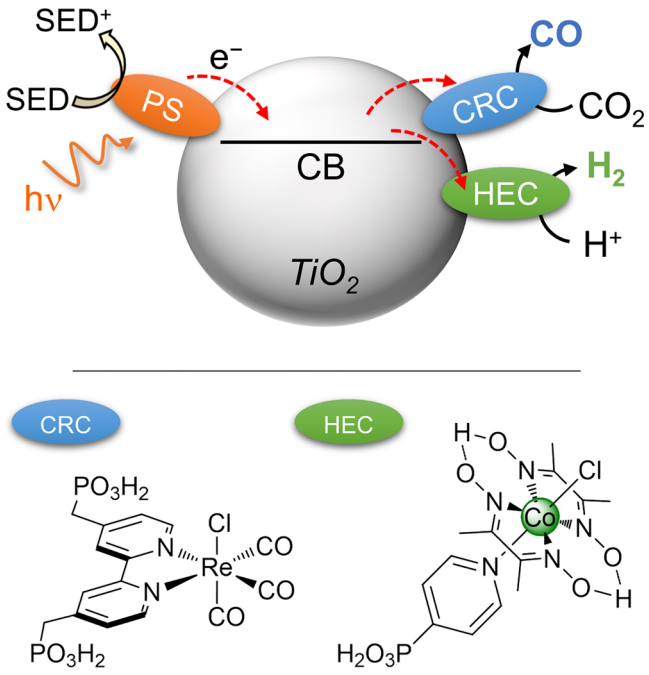

Figure 52. Diagram of a syngas-evolving colloidal DSP system using **Co88** and a CO_2-reducing Re catalyst in MeCN:H_2O with BIH as a SED.[876]

PS19-sensitized ZrO_2 nanoparticles (20−100 nm) with a coanchored phosphonated Ni(cyclam) catalyst, **Ni102** ($E_{onset} \approx -0.95$ V vs NHE, pH 4; Figure 51), in aqueous AA solution (pH 4) produced a Ni-based TON_{CO} of 4.8 (TON_{H2} of 19.9; Table 4, entry 8).[911] The E_{CB} of ZrO_2 is unable to quench the excited states of **PS19** in this **PS19**|ZrO_2|**Ni102** system, and the mechanism therefore proceeds via an "on particle" pathway that involves reductive quenching of **PS19*** followed by ET to proximal **Ni102**. Isotopic labeling confirmed the origin of ^{13}CO from $^{13}CO_2$, and the colloidal system was found to be superior to an analogous ZrO_2-free system (section 2.3.7.2), likely due to the proximity of the immobilized PS and HEC.[481]

The shortfall in the development of aqueous CO_2 reduction using DSP schemes with first row transition metal catalysts can be attributed to limited diversity in such CRCs, their low water tolerance, and restricted availability of light harvesters with suitable energetics and kinetics. Employing organic solvents can circumvent low selectivity and water incompatibility issues but is unlikely to be sustainable for large-scale applications, with the use of aqueous media affording a more realistic indication of system performance under potential operating conditions. In addition, carbon-containing solvents can be a source of questionable results as their degradation under photocatalytic conditions can generate products similar to those of CO_2 reduction, as has been observed with DMF, for example.[912,913] As a result, in such organic or hydro-organic media, clear evidence of CO_2 reduction such as ^{13}C isotopic labeling experiments should be provided.

5.3.4. CO_2 Reductase-Based Systems. Alongside the synthetic CRCs presented above and a few bacteria-based examples,[914,915] isolated enzymes have also been implemented into different immobilized photocatalytic schemes.[16] For instance the Ni-based CODH from *Carboxydothermus hydrogenoformans* performs CO_2 to CO reduction with an E_{onset} of −0.46 V vs NHE (pH 6) and has been used in DSP and QD systems achieving high turnover numbers and turnover frequencies in water.[18,916−918] High enzyme efficiency allowed dye-sensitized TiO_2 to be employed, and the natural binding affinity of CODH toward MO_xs resulted in a TOF_{CO} of 0.14 s^{-1} in a **PS19**|TiO_2|CODH assembly in aqueous MES solution (pH 6.0, Table 4, entry 9).[18,916] Faster selective CO evolution (TOF_{CO} = 14 s^{-1} over 3 h at 25 °C) was recently reported by replacing **PS19** with Ag clusters in a TEOA and EDTA containing solution (pH 6.0), resulting in a TON_{CO} of 250 000 after 6 h (Table 4, entry 10).[918] The high activity of CODH on TiO_2 is remarkable as no synthetic molecular catalyst immobilized on dye-sensitized TiO_2 has yet demonstrated activity in pure water, likely due to the large η required. Replacement of the dye-sensitized TiO_2 with CdS nanorods as a light-harvesting colloid provides more driving force than the CB of TiO_2 and resulted in a CdS|CODH assembly that attained a TOF_{CO} of 1.23 s^{-1} (Table 4, entry 11) under irradiation (23 mW cm^{-2}, λ > 420 nm).[917]

Thus, CO_2 reductases are benchmark CRCs as they have achieved performances in colloidal photocatalytic systems that are as yet difficult to match with synthetic catalysts. Operating selectively with minimal E_{onset} enables them to be associated with a wider range of colloidal SC materials, which inspires the design of synthetic 3d transition metal CRCs with comparable performance.

5.4. Conclusion and Outlook

Solar fuel synthesis through colloidal photocatalysis has been performed through the combination of molecular catalysts and light harvesting scaffolds for several decades. Major advances were achieved in (i) using first row transition metal complexes, (ii) catalyst design and stability in water, (iii) developing a wide range of visible light-harvesting materials, and (iv) interfacing strategies resulting in catalytic performances closer to those of the archetypal natural H_2ases or CO_2 reductases. For instance, the development of carbon-based light-harvesting colloids enables the utilization of hydrophobic interactions to interface nonwater-soluble catalysts, whereas DSP systems allow for the implementation of cheap organic chromophores instead of precious-metal-based complexes. In-depth investigations of ET kinetics, electrochemical behavior of immobilized catalysts, and the nature of catalyst−surface interactions have also revealed key information which may aid in catalyst design that is optimized for a specific surface.

However, in order to achieve superior performance and system stability several significant issues remain to be addressed in catalyst design, light-harvesting colloid development, and interface engineering. Among these issues, the low catalyst loadings, background H_2 evolution activity of QDs, slow electron accumulation and turnover in catalysts leading to charge recombination, general instability of the colloid/catalyst interface, as well as the low driving force of MO_x-based systems toward CO_2 reduction all appear to be of primary importance. To a higher degree, the reliance of the near totality of the

DOI: 10.1021/acs.chemrev.8b00392
Chem. Rev. 2019, 119, 2752−2875

systems on SEDs decreases the sustainability of the colloidal photocatalysis approach, and useful alternatives must therefore be developed to valorize the oxidative reaction. Alongside water oxidation, biomass reformation and organic synthesis of valuable compounds are two other possibilities that have recently been proposed.[843,919] Finally, as illustrated by the limited number of examples reported (Table 3 vs Table 4), numerous difficulties associated with CO_2 reduction in water remain to be addressed. Selectivity toward CO_2-reduction products, catalyst stability in the presence of water, and the lesser availability of light-harvesting colloids with suitable driving force to drive the reaction are another set of challenging issues to be solved by the community.

6. DYE-SENSITIZED PHOTOCATHODES

6.1. General Remarks

Solar-driven fuel generation can be achieved by immobilizing molecular HECs and CRCs onto light-responsive electrodes to afford a photocathode.[553,558,920] An approach toward molecular catalyst-based photocathodes has been the modification of wide-bandgap p-SC electrodes with a light-harvesting component, most often a molecular dye, to photoreduce the coanchored catalyst. Acting as a hole-selective layer, the p-SC gives directionality to ET when E_{VB} is able to accept holes from the excited photosensitizer (see Figure 53 for a general energy scheme of a dye-sensitized photocathode (DSPC)). When paired with a photoanode in a PEC tandem device, the electrons for dye regeneration can be sourced directly from the oxidation half-reaction occurring at the photoanode instead of an applied electrochemical potential.

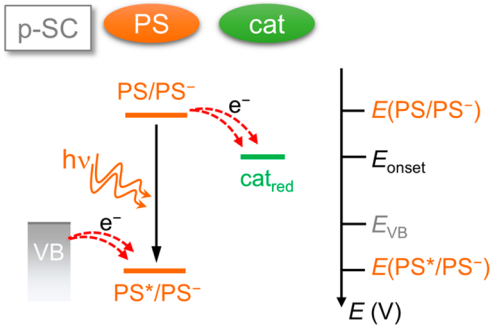

Figure 53. Band diagram depicting energy level requirements for a functional DSPC system.

The concept of dye-sensitized PEC cells has received substantial attention, but examples of dye-sensitized photoanodes for molecular-based water oxidation have far outnumbered those of their DSPC counterparts for fuel-forming transformations.[556,558,921−924] Commonly featuring precious-metal complexes,[557,925−927] the number of DSPC systems is reduced even further when only considering those based on 3d transition metal complexes. Nevertheless, interest in DSPCs has seen continued growth in recent years, with investigations ranging from devising different immobilization strategies, to searching for novel p-type semiconducting materials.

6.2. Component Requirements and Characteristics

6.2.1. p-Type Semiconductor: a NiO Story. In contrast to DSP systems (see section 5), the immobilization of the dye onto a p-SC electrode in DSPCs enables fast dye regeneration by the SC substrate instead of a diffusional chemical SED. It is therefore an attractive strategy toward closed redox catalysis in a PEC architecture. By far the most commonly employed p-SC in DSPCs is NiO.[556] Its p-type semiconductivity arises from nickel vacancies and interstitial oxygen in the lattice, which is promoted by thermal annealing in aerobic conditions.[928,929] Its flat-band potential (an indication of the upper limit of E_{VB}) is around 0.75 V vs RHE.[928,930−932] It is generally assumed that the majority of PS* quenching in NiO-based DSPC systems occurs via a reductive pathway due to fast hole injection.[933] This contrasts with "through particle" DSP systems, where PS* quenching is typically oxidative due to fast electron injection into n-type SCs and a diffusional SED (see section 5).

Mesoporous and, more generally, nanostructed NiO electrodes (required to achieve high loading of both photosensitizer and molecular catalyst) can be prepared by a variety of methods,[554] including electrodeposition,[934] sol−gel deposition,[935,936] hydrothermal synthesis,[937,938] and block copolymer templating.[939,940] The physical and electrochemical properties of NiO electrodes prepared in several different laboratories were recently compared and their PEC performances benchmarked against one another using the same dye and molecular HEC.[941] It was found that the photocurrent densities were all in the same order of magnitude (photocurrent density, $J_{ph} \approx 10\ \mu A\ cm^{-2}$ at E_{appl} = 0.21 V vs RHE). The low photocurrents achieved for NiO-based DSPCs can largely be attributed to the limited hole mobility in the SC. The hole diffusion coefficient of mesoporous NiO in p-DSSCs has been reported to be 10^{-8} to $10^{-7}\ cm^2\ s^{-1}$, which is at least two orders of magnitude lower than the electron diffusion coefficient of TiO_2 often used in dye-sensitized water oxidation photoanodes.[942,943] Moreover, in-depth spectroscopic characterization of NiO showed that surface Ni^{3+} states act as efficient traps for both electrons and holes.[559]

6.2.2. Photosensitizer and Electrocatalyst. In DSPCs, the immobilized photosensitizer is primarily responsible for light absorption and, in most cases, subsequent charge transfer to a molecular catalyst. In order to fulfill these functions, photosensitizers are thermodynamically required to (i) possess an excited state reduction potential (E_{PS^*/PS^-}) more positive than the flat-band potential of the p-type SC on which it has been immobilized and (ii) possess a regeneration potential (E_{PS/PS^-}) that is more negative than the E_{onset} of the electrocatalyst (Figure 53). The former is to ensure that hole quenching by the SC can occur, whereas the latter is mandatory for electrocatalysis.

Fulfilling these thermodynamic prerequisites does not ensure effective ET dynamics. From a kinetic point of view, requirements in DSPCs echo those also needed in colloidal DSP systems. Namely, it is important that the photosensitizer can maintain a relatively long-lived charge-separated state in order for photoinduced charge injection to be able to compete with deactivation processes. How fast the catalyst receives electrons from the reduced dye and subsequently turns over during the catalytic process are also important parameters that can affect overall charge separation efficiency. To date, the vast majority of molecular dyes used in DSPCs with 3d transition metal complex catalysts has been previously studied or belong to classes of compounds also studied in DSSCs, and include organic dyes and Ru polypyridyl photosensitizers. A common approach undertaken in the field of DSSCs to achieve directional charge carrier separation within the photosensitizer itself has also been employed for the same purpose in DSPCs, namely, the use of push−pull architectures.[882] This can be achieved by designing the dye such that it has a donor-π-acceptor structure, in which its HOMO and LUMO are located close to where it is desired for

DOI: 10.1021/acs.chemrev.8b00392
Chem. Rev. 2019, 119, 2752−2875

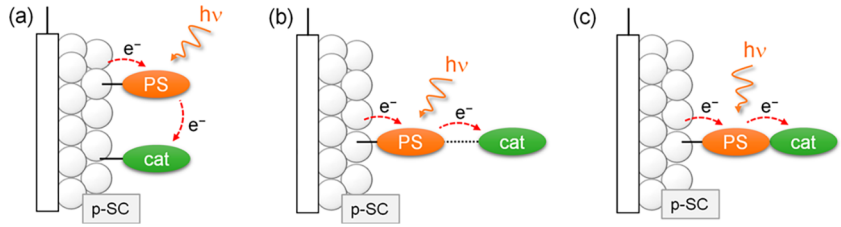

Figure 54. Assembly approaches that have been adopted to construct DSPCs: (a) coimmobilization, (b) layer-by-layer coassembly, and (c) PS-catalyst dyad.

the photoexcited hole or electron to be, respectively, in order to achieve charge "delocalization" within the molecule. In the case where it is desired for holes to be injected into NiO in DSPCs, the HOMO of the dye would ideally be located close to the PS's anchoring group, which would end up in the vicinity of the supporting MO_x upon dye immobilization. This push−pull mechanism can be extended further to the other "end" of the photosensitizer in order to influence electron injection into the catalyst.[944] In the context of H_2 evolution, the push−pull architecture is also instrumental for fostering unilateral ET through direct connection of the dye's acceptor moiety (where the LUMO is located) with the catalyst. For example, a dyad comprising the photosensitizer and the catalyst can be synthesized, which should in theory promote faster intramolecular direct ET from the former to the latter.[945,946]

As with DSP systems, a broad absorption band and high extinction coefficient of the PS helps to maximize light harvesting of the solar spectrum. An additional consideration arises in a tandem PEC cell design, where both the photocathode and the photoanode need to absorb light. In such a setup, any strong overlap in the absorption spectra of the two photosensitizers in the two half-cells should be avoided in order to ensure that the second photoelectrode upon which the solar light is incident still receives light of wavelengths appropriate for exciting its photosensitizer. Reviews for the optimal spectral design of complementary tandem architectures are available elsewhere.[947−949]

A relevant figure of merit is the incident photon-to-current conversion efficiency (IPCE), which describes how many of the incoming photons at a particular wavelength are converted into electrons. Comparing the absorption spectrum of the photosensitizer with the profile of the photocathode's IPCE curve is key to demonstrating whether the DSPC is able to harness wavelengths across the full absorption spectrum of the photosensitizer.

As with the DSP systems discussed in section 5, both the PS and catalyst must be stable and operate under the same aqueous conditions. The robust attachment of both species onto the supporting p-SC is imperative for photocathode stability and performance. In addition, the anchoring moieties should allow for any necessary charge transfer to occur (e.g., between the molecule and the MO_x SC that supports it). As with other oxide SCs, the flat-band potential of NiO exhibits a pH-dependency ($\Delta E = -59$ mV pH^{-1}) that needs to be carefully considered with regards to its capacity to reduce the anchored PS.[551]

This section has been categorized into the following three immobilization strategies: coimmobilization, layer-by-layer coassembly, and dye-catalyst dyad assemblies (Figure 54).

6.3. Photoelectrochemical H_2 Evolution

6.3.1. Coimmobilization. The majority of DSPCs prepared with 3d transition metal complex-based catalysts have used cobaloximes as the HEC, with their low overpotential and synthetic tunability being of advantage. A DSPC for H_2 evolution (albeit with the catalyst lacking a defined anchoring moiety) utilized the organic dye **PS36** (Figure 55) and an H_2-evolving catalyst $[Co(dmgBF_2)_2(H_2O)_2]$ (**Co6**, section 2.2.4.1).[950] The chromophore **PS36** was anchored to a nanostructured NiO substrate via carboxylic acid functional groups, whereas the cobaloxime was subsequently drop-cast onto the NiO|**PS36** electrode from a solution in MeCN. Photocurrents attributed to H_2 evolution decayed within a few minutes and could only be recovered upon addition of fresh catalyst. This suggested that either catalyst decomposition and/or desorption from the surface were the main reasons for loss in PEC activity, with the latter suspected to be more likely due to the lack of any anchoring functionality on the cobaloxime.

A number of subsequent systems anchored both the photosensitizer and the catalyst equipped with suitable functional groups on MO_x electrodes. A common strategy employed for assembling early examples of DSPCs was to coadsorb the components onto the NiO electrode; either one at a time or both simultaneously (Figure 54a). Care must be taken that dye and catalyst bind to the SC and their adsorption ratio also needs to be optimized to enable best performance.

A tandem PEC device was constructed where the dye for both the water-oxidizing TiO_2-based photoanode and the proton-

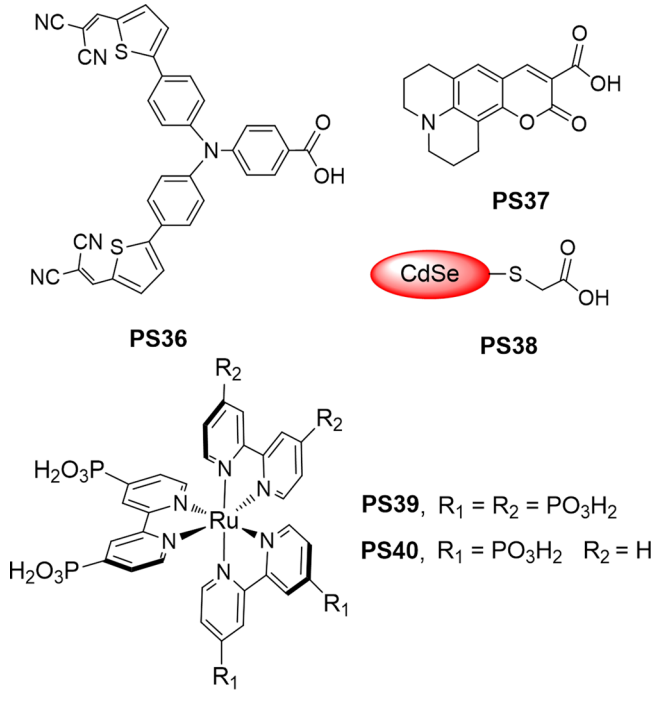

Figure 55. Molecular structures of PSs used in DSPC.

DOI: 10.1021/acs.chemrev.8b00392
Chem. Rev. 2019, 119, 2752−2875

reducing NiO-based photocathode was the same phosphonic acid-containing Ru bipyridyl complex, **PS19** (Figure 7).[951] The anchoring group for the cobaloxime HEC (**Co114**, Figure 56) was an axial pyridine-2,6-dicarboxylic acid moiety. The NiO|**PS19-Co114** photocathode afforded a J_{ph} of −13 μA cm^{-2} at E_{appl} = 0.21 V vs RHE in pH 7 phosphate solution (Table 5, entry 1). The fully assembled tandem PEC cell evidenced that the photocathode was the bottleneck in overall water splitting and the use of the same photosensitizer leads to noncomplementary light absorption. Controlled potential photoelectrolysis (CPPE) measurements beyond 3 min were not reported and production of H_2 gas was not demonstrated.

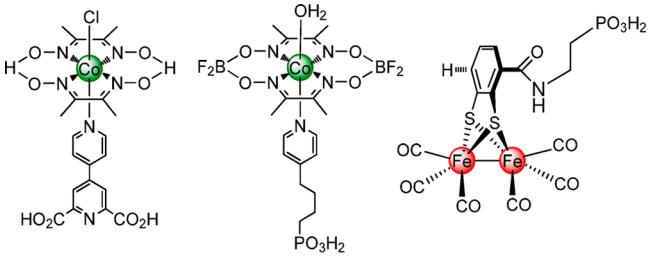

Figure 56. Molecular structures of HECs used in DSPC.

The Ru-dye **PS19** was subsequently replaced by the organic dye **PS36** for the proton-reducing photocathode, and by another organic chromophore at the water-oxidizing photoanode.[952] The cobaloxime HEC **Co115** (Figure 56) anchors to the NiO scaffold via a phosphonic acid-bearing axial pyridine ligand. Operating in pH-neutral phosphate solution, the NiO|**PS36-Co115** photocathode achieved a J_{ph} of ∼−45 μA cm^{-2} in LSV scans, plateauing at E_{appl} < 0.31 V vs RHE. In CPPE measurements, the average J_{ph} was −35 μA cm^{-2}, of which −20 μA cm^{-2} remained after 1.5 h with a FE_{H2} of 68% (Table 5, entry 2). A full water-splitting tandem molecular PEC device operating under pH-neutral aqueous conditions was also demonstrated with precious-metal-free PSs, but using a Ru-based water oxidation catalyst at the photoanode. IPCE analysis revealed that the NiO-based photocathode was again the probable bottleneck to the system. Specifically, the IPCE value at the absorption maximum of **PS36** was found to be much lower than that at the absorption maximum of the photoanode's chromophore (3.9% vs 25.2%). A likely explanation for this observation is the differing thicknesses between the photocathode (1 μm) and the photoanode (8 μm), and therefore the molecular loadings of both PS and catalyst on the former will be lower, leading to a smaller contribution from the photocathode to the overall tandem's photocurrent. The well-known limitations of NiO (e.g., short hole diffusion length) were again suggested to constrain the photocathode performance.[952]

Charge transfer between a coadsorbed molecular dye and catalyst on the SC surface is assumed to rely on electron hopping. This process must be faster than the charge recombination between the photoreduced dye and holes present in NiO. Likewise, the reduced state of the catalyst that is subsequently formed from this intermolecular charge transfer must be relatively long-lived in order to reach a doubly reduced state to carry out proton reduction without recombination. This light-driven electron hopping phenomenon between molecules on the surface of a SC was studied by TAS.[953] The dye

Table 5. PS-Modified Photocathodes with Immobilized 3d Metal HECs and CRCs in Aqueous Systems[a]

entry	electrode	HEC/CRC	E_{onset}[b] (V)	$\lvert J_{ph}\rvert$ at E_{appl}[b] (μA cm^{-2} at V)	CPPE duration at E_{appl}[c] (min at V)	TON[c]	FE[c]	conditions	illumination	ref
1	NiO|**PS19**	**Co114**	n/a	13 at 0.21[c]	2.75 at 0.21	n/a	n/a	phosphate pH 7.0	300 mW cm^{-2}, λ > 400 nm	951
2	NiO|**PS36**	**Co115**	n/a	∼45 at 0.0	90 at 0.41	n/a	68%	phosphate pH 7.0	100 mW cm^{-2}, λ > 400 nm	952
3	NiO|**PS37**	**Fe$_2$44**	n/a	10 at 0.16[c]	21 at 0.16	n/a	∼50%	acetate pH 4.5	LED lamp, white (5000 K)	955
4	NiO|**PS38**	**Co88**	n/a	∼118 at 0.20[c]	210 at 0.07	n/a	81% (at E_{appl} = 0.20 V)	Na_2SO_4 pH 6.8	300 W lamp, λ > 400 nm	957
5	$CuCrO_2$| **PS30**	**Ni35**	0.90	15 at 0.0	120 at 0.0	126	34%	Na_2SO_4 pH 3.0	100 mW cm^{-2}, λ > 420 nm	969
6	NiO| **PS39**-Zr^{4+}	**Ni35**	n/a	∼6.4 at 0.0	120 at 0.30	n/a	9%	Na_2SO_4 pH 3.0	100 mW cm^{-2}, λ > 400 nm	930
7	ITO|**DA**-Zr^{4+}-**PS39**-Zr^{4+}	**Ni35**	n/a	56 at 0.051[c]	240 at 0.051	n/a	53%	MES pH 5.1	5 mW cm^{-2}, λ_{max} = 445 nm	980
8	$NiK_{0.02}O$| $NiCu_{0.02}O$| **PS40**-Zr^{4+}	**Ni35**	n/a	58 at 0.045[c]	120 at 0.045	n/a	86%	MES and KCl pH 5.0	20 mW cm^{-2}, λ > 400 nm	981
9	NiO|Al_xO_y | **Co116**	**Co116**	∼0.87	∼20 at 0.0	150 at 0.51	n/a	∼68%	KH_2PO_4 and Na_2CO_3 pH 7.0	300 W lamp, λ > 420 nm	982
10	NiO|**Co117**	**Co117**	0.93	15 at 0.14[c]	180 at 0.14	n/a	9%	MES and NaCl pH 5.5	65 mW cm^{-2}, λ > 400 nm	945
11	NiO|**Co118**	**Co118**	0.48	20 at 0.48[c]	18 at 0.48	0.05	n/a	acetate pH 4.8	LED lamp, white (5000 K)	946
12	NiO|**Fe$_2$45**	**Fe$_2$45**	0.70	56 at 0.30	5 at 0.30	n/a	52%	Na_2SO_4 pH 6.8	300 W lamp, λ > 400 nm	991
13	NiO|**PS36**	[NiFe]-CODH	∼0.27	25 at 0.0	50 at 0.08	n/a	n/a	MES pH 6.0	white light, 45 mW cm^{-2}, λ > 420 nm	993

[a]All potentials are reported against RHE. In the cases where photocathode-photoanode tandem systems have also been reported, only the performance of the photocathode studied in a three-electrode half-cell set-up has been included in this table (n/a = not available). [b]Extracted from LSV measurements, unless otherwise stated. [c]Extracted from CPPE measurements.

DOI: 10.1021/acs.chemrev.8b00392
Chem. Rev. 2019, 119, 2752−2875

coumarin-343 (**PS37**, Figure 55) and an iron-containing molecular complex were both bound to NiO via a carboxylic acid group, and it was found that the catalyst was stable in its reduced state on the 100 μs time scale. Slow recombination kinetics between the reduced catalyst and holes in the NiO were attributed to the bulky phenyl groups at the phosphorus ligands shielding the iron center from the MO_x surface, as well as to the long electron tunneling distance between the iron center and the NiO surface consisting of five saturated bonds. No H_2 production was reported in this system.

The catalyst was replaced by a bimetallic iron-based complex equipped with a carboxylate anchor, $[Fe_2(bdtc)(CO)_6]$, bdtc = 3-carboxybenzene-1,2-dithiolate, the parent complex of which is a [FeFe]-H_2ase-inspired HEC in solution (**$Fe_2$13**, section 2.2.3.1).[954] TAS measurements showed that ET from the **PS37** to the catalyst was fast ($t_{1/2} \approx 10$ ps), with a transfer yield of 40−80%, suggesting close proximity of the dyes to the catalyst to allow for electron hopping across a short distance. As with the previous work, the reduced Fe catalyst was also found to persist in the μs time scale, but no H_2 evolution was reported.

The carboxylate moiety in $[Fe_2(bdtc)(CO)_6]$ was subsequently replaced by a phosphonic acid anchor in **$Fe_2$44** (Figure 56), which was also accompanied by a longer linker between the catalytic core and the anchor than in $[Fe_2(bdtc)(CO)_6]$ (Table 5, entry 3).[955] The phosphonic acid provides superior binding to MO_x materials in aqueous conditions (see section 3), whereas the longer linker may slow charge recombination between the reduced catalyst and the holes in NiO. Indeed, the lifetime of the reduced catalyst was extended from the μs to the ms time scale, highlighting the importance of the anchoring strategy, not just for immobilization purposes but also for controlling ET kinetics. The NiO|**PS37**-**$Fe_2$44** photocathode was subsequently studied by CPPE in aqueous acetate solution (pH 4.5) and achieved a J_{ph} = −10 μA cm^{-2} under white LED illumination for a few minutes with a FE_{H2} of 50%. The low photocurrent was partially attributed to the low solar light-harvesting ability of **PS37** (λ_{max} ∼400 nm). Catalyst instability under irradiation was confirmed by the release of CO ligands from **$Fe_2$44**. A follow-up kinetic study compared the charge transfer reactions of NiO|**PS37**-**$Fe_2$44** to those of an analogous photocathode where **PS37** had been replaced by an organic push−pull dye and found that key differences in these mechanisms drastically affect the lifetime of the reduced catalyst species on the surface and, by extension, the possibility of any light-induced second reduction step of the catalyst.[956] In addition to highlighting the importance of the dye-catalyst packing on the performance of cosensitized DSPCs, this study also demonstrated the use of femtosecond mid-infrared TAS to monitor catalyst reduction upon dye excitation in cosensitized NiO films.

The remaining example of a photosensitizer-modified NiO photocathode based on coadsorption employs a QD as the light harvester.[957] Owing to their favorable properties, QDs have been employed as light harvesters in solar cells and in photocatalysis (section 5).[958,959] The majority of the latter are homogeneous systems that rely on SEDs to regenerate the QDs.[167,960−962] CdSe QDs (**PS38**, Figure 55) and a cobaloxime catalyst (**Co88**, Figure 26) were coadsorbed onto NiO electrodes via the TGA functionality of the former and the phosphonic acid group of the latter.[963] TGA functions not only as an anchoring group for the CdSe QDs through its carboxylate but also as a capping ligand to prevent QD aggregation. With E_{VB} and E_{CB} of 1.30 and −0.97 V vs NHE,[964] respectively, CdSe QDs can thermodynamically inject holes into the VB of NiO and reduce the cobaloxime for proton reduction (E_{onset} = −0.6 V vs NHE).[191] CPPE of the NiO|**PS38**-**Co88** photoelectrodes in an aqueous Na_2SO_4 solution (pH 6.8) afforded a J_{ph} of ∼−118 μA cm^{-2} at E_{appl} = 0.20 V vs RHE with good stability over several hours and a FE_{H2} of 81% (Table 5, entry 4).[957] An analogous system employing an anchor-free catalyst resulted in a decline in photocurrent over the course of minutes.[963,965] TAS measurements of this system found that the TGA capping ligands on the **PS38** QDs acted as trap sites for photogenerated holes.[966] The majority of holes were trapped by the thiol groups and/or sulphide ions of the linker instead of being productively injected into the VB of NiO, which limited the H_2 evolution efficiency of this photocathode.

Cobaloxime catalysts employed in aqueous DSPC systems rely on anchoring to a NiO electrode via their axial pyridine ligand. As discussed in section 2.2.4.2, an axial pyridine ligand on the low-spin Co^{3+} center of a cobaloxime becomes inherently labile during catalytic turnover and contributes to catalyst instability and loss of activity.[188,228,878] Despite synthetic strategies to anchor Co catalysts robustly,[543,754] such cobaloxime derivatives have not yet been introduced in DSPC systems.

Instead, nickel bis(diphosphine) DuBois-type catalysts, $[Ni(P_2N_2)_2]^{2+}$, possess a robust chelating ligand framework,[967] and are the only other class of 3d transition metal complexes that have been immobilized on DSPCs for H_2 evolution in water. A $[Ni(P_2N_2)_2]^{2+}$ catalyst modified with hydroxamic acid groups was coimmobilized on a NiO electrode alongside a naphthalene diimide organic dye, but this system did not evolve H_2.[968] The lack of PEC activity was attributed to dye aggregation, which would cause fast recombination between the reduced dye and holes in NiO, limiting successful charge transfer to the HEC. Examples for H_2 evolution with anchored $[Ni(P_2N_2)_2]^{2+}$ catalysts through supramolecular assemblies (Figure 54b) are summarized in section 6.3.2.

PEC proton reduction with a Ni DuBois-catalyst using coimmobilization was reported with a $CuCrO_2$ delafossite p-SC instead of NiO.[969] Wide-bandgap Cu^+-based mixed MO_xs such as $Cu^+M^{3+}O_2$ delafossites (M = Co, B, In, Sc, Cr, Al, and Ga) have been employed in p-type DSSCs, but their incorporation into solar fuel devices is limited.[970−972] Coimmobilizing a phosphonic acid-bearing DPP-based organic dye (**PS30**, Figure 47)[877] alongside HEC **Ni35** (section 2.2.5.1) on a $CuCrO_2$ film yields a precious-metal-free DSPC for H_2 production.[969] $CuCrO_2$ is a wide-bandgap p-SC (E_g = 3.16 eV), where its p-type conductivity stems predominantly from Cu^+ vacancies in the crystal lattice.[973−975] Measured at +1.0 V vs RHE, $CuCrO_2$ displays a 250 mV more positive flat-band potential than that of NiO, and its Brunauer, Emmett, and Teller-surface area of 25 m^2 g^{-1} is comparable to that of other mesoporous structures.[941] Upon grafting, **PS30** is quenched reductively by the p-SC affording an $E_{PS30^-/PS30}$ of −0.7 V vs RHE, which provides ∼500 mV for the reduction of **Ni35** (E_{onset} = −0.21 V vs RHE[842]). Initial comparison between $CuCrO_2$|**PS30** and NiO|**PS30** films in the presence of an electron acceptor in solution showed that the photocurrent response is around twice as large for the delafossite electrode. Upon coimmobilization of **Ni35**, $CuCrO_2$|**PS30**-**Ni35** exhibited a photocurrent E_{onset} = 0.75 V vs RHE, making $CuCrO_2$ an attractive choice for dye-sensitized tandem applications. Under CPPE conditions, the photocathode achieved a J_{ph} of −15 μA cm^{-2} at E_{appl} = 0.0 V vs RHE in Na_2SO_4 solution (pH 3; Table 5, entry 5).[969] A **Ni35**-based TON_{H2} of 126 and a FE_{H2} of 34% were reached after 2 h, which outperformed an analogous NiO|**PS30**-**Ni35** electrode by 2−3

DOI: 10.1021/acs.chemrev.8b00392
Chem. Rev. 2019, 119, 2752−2875

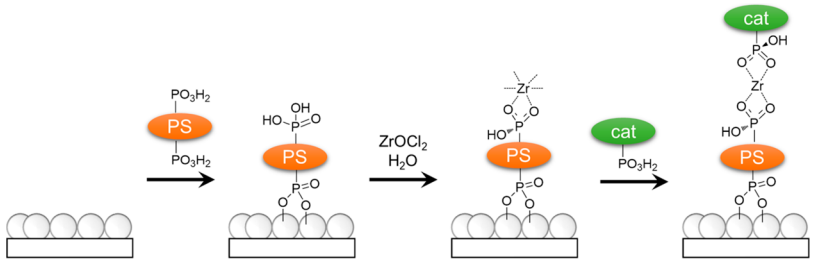

Figure 57. Layer-by-layer coassembly of PS and catalyst via Zr^{4+}-bridge approach on MO_x electrode.

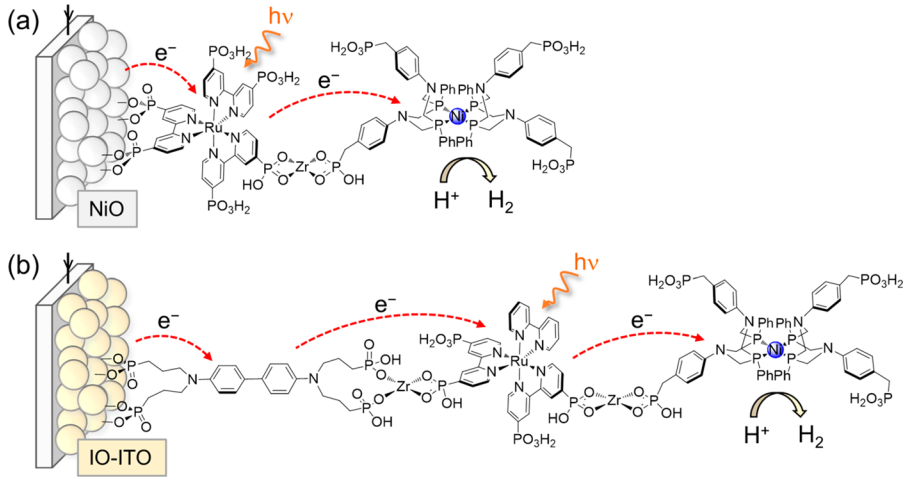

Figure 58. Schematic representation of Zr^{4+} bridge-based photocathodes; (a) NiO|**PS39**-Zr^{4+}-**Ni35**,[930] and (b) IO-ITO|**DA**-Zr^{4+}-**PS40**-Zr^{4+}-**Ni35**.[980]

times. The low FE_{H2} was suspected to originate in part from reduction of Cu^{2+} and oxygen deintercalation within the delafossite,[976] as well as dye decomposition.[969] Nevertheless, this study lays the groundwork toward discovering more p-SC alternatives to NiO.

6.3.2. Layer-by-Layer Coassembly. An alternative to coadsorption was used in a $[Ni(P_2N_2)_2]^{2+}$-based DSPC active toward H_2 evolution (Figure 54b).[930] A layer-by-layer deposition approach to immobilize phosponated PS and HEC with Zr^{4+} bridges was employed (Figure 57), in a similar fashion to those previously utilized to construct multilayered molecular films in DSSCs and dye-sensitized photoanodes for water oxidation.[655,977−979] Zr^{4+} ions bind strongly to the phosphonic acid moieties of the ruthenium bipyridyl dye (**PS39**, Figure 55) and the DuBois catalyst **Ni35** and enable a robust supramolecular assembly (Figure 58a). The NiO|**PS39**-Zr^{4+}-**Ni35** electrode exhibited a J_{ph} of −6.4 μA cm^{-2} at E_{appl} = 0.3 V vs RHE in aqueous Na_2SO_4 (pH 3) solution under simulated solar irradiation (λ > 400 nm) with approximately half of J_{ph} remaining after 2 h of CPPE (FE_{H2} of 9%; Table 5, entry 6). The low activity of NiO|**PS39**-Zr^{4+}-**Ni35** was attributed to inefficient charge transfer dynamics at the NiO|**PS39** interface and between reduced **Ni35** and oxidized **PS39**, as well as the low loading of the former (Γ = 5 nmol cm^{-2}). Nevertheless, photocurrents observed without the Zr^{4+} bridge using the same coadsorded molecular components (NiO|**PS39**-**Ni35**) were six times lower than the layer-by-layer supramolecular assembly, and no H_2 was detected. This highlights the benefits of spatially separating the catalyst from the NiO surface to reduce charge recombination losses.

Subsequently, the construction of a three-layered Zr^{4+}-bridged DSPC consisting of a "donor-dye-catalyst" assembly was reported, where a phosphonic acid containing a dianiline donor was used alongside a tetraphosphonated Ru-bipyridyl chromophore (**PS40**, Figure 56) and **Ni35** (Figure 58b).[980] The presence of the dianiline (**DA**) donor allows the degenerate SC ITO to be used instead of p-type semiconducting NiO for photocathodic fuel synthesis. Zr^{4+}-phosphonate bridges were again utilized as spatial separators to generate long-chain assemblies in which the ET distance could play a significant role in controlling the dynamics of interfacial charge recombination. To enable effective surface immobilization of these supramolecular chains, macro-mesoporous hierarchically ordered "inverse opal"-type ITO electrodes similar to those reported for enzyme and nanoparticle immobilization on MO_x electrodes were employed.[508,782,881] The IO-ITO|**DA**-Zr^{4+}-**PS40**-Zr^{4+}-**Ni35** electrode was tested for PEC performance in MES solution (pH 5.1) at E_{appl} of 0.05 V vs RHE and afforded an initial J_{ph} of −56 μA cm^{-2} that dropped by 50% within 4 h of operation, giving a FE_{H2} of 53% (Table 5, entry 7).[980] In contrast, negligible H_2 production was observed by an analogous electrode using a mesoITO film instead of the inverse opal structures, demonstrating the impact of using large macro-mesopores to ensure sufficient chain assembly coverage.[782]

A similar layer-by-layer immobilization strategy with a visible light-absorbing **PS31**-sensitized (Figure 47) TiO_2 nanoparticles on an IO-ITO electrode showed that the type II dye-TiO_2 moiety can direct the electron flow toward the electrolyte solution and thereby enable photocathodic currents in the presence of a soluble electron acceptor. Although H_2 production was not reported, this system is a first step to transferring DSP colloids from section 5 onto photocathodes.[881]

An improved supramolecular DSPC system employing **PS40** and **Ni35** was recently prepared via a multilayer scaffolding SC

DOI: 10.1021/acs.chemrev.8b00392
Chem. Rev. 2019, 119, 2752−2875

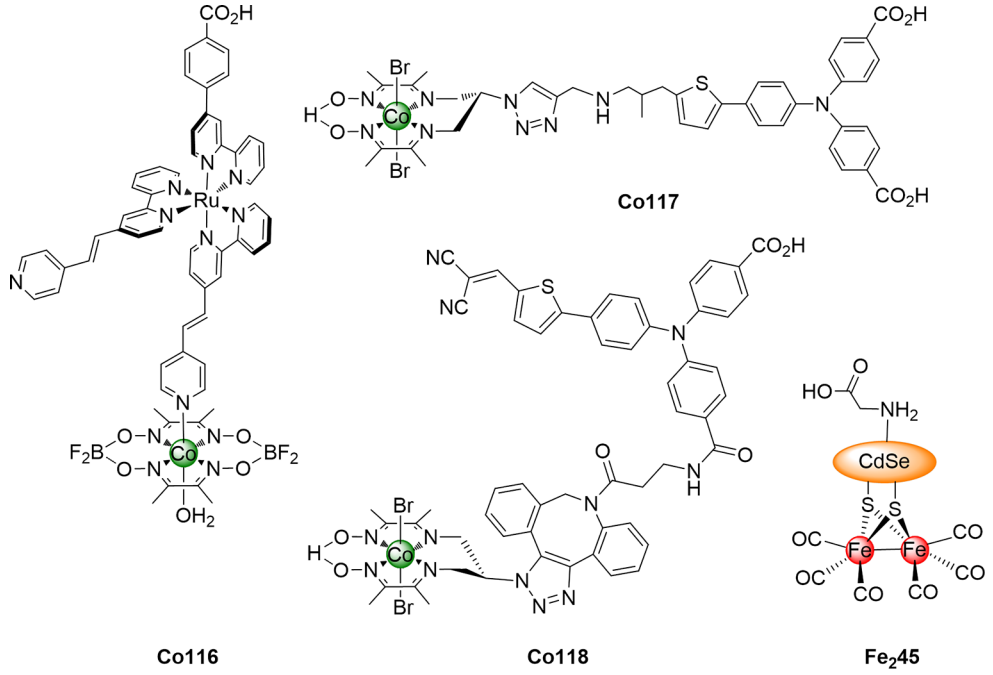

Figure 59. Structures of photosensitizer-molecular catalyst dyads.

composed of two mesoporous doped NiO layers covered with an IO-ITO scaffold.[981] The NiO film was prepared as doped bilayers with different dopants selected to modify E_{VB} edges and establish an internal driving force for hole transport from the surface to the FTO back contact. The dopants giving the least positive (2% K^+) and most positive (2% Cu^{2+}) flat-band potentials were selected, creating 0.2 eV of driving force for interlayer hole transport. The doped bilayer-containing electrode, $NiK_{0.02}O|NiCu_{0.02}O|$IO-ITO|**PS40**-$Zr^{4+}$-**Ni35**, was found to generate twice the photocurrent (∼−58 μA cm^{-2}) of its undoped counterpart with a FE_{H2} of 86% at E_{appl} of 0.05 V vs RHE in a pH 5.0 solution (0.1 M MES + 0.4 M KCl; Table 5, entry 8). Singly doped NiO photocathodes ($NiK_{0.02}O|NiK_{0.02}O$ or $NiCu_{0.02}O|NiCu_{0.02}O$) were shown not to enhance efficiency as much as the doubly doped photocathodes, underlining the impact of creating an internal cascade of driving force that improves hole transport from the outer $NiCu_{0.02}O$ to the inner $NiK_{0.02}O$ layer and therefore reduces interfacial charge recombination.[981]

6.3.3. Photosensitizer-Catalyst Dyads. Most DSPC systems discussed thus far suffer from long-term stability issues, the majority of which have been partially attributed to dye and/or catalyst degradation or desorption from the surface. The final DSPC organization discussed here consists of a dyad assembly in which the chromophore is covalently bound to the catalyst (Figure 54c); this aims to achieve both catalyst stabilization as well as effective charge separation.[882] Although synthetically challenging, several examples of such efforts have emerged in recent years.

The first example of a photosensitizer-3d metal-based HEC dyad performing proton reduction in aqueous solutions was reported on a NiO electrode. It consists of a Ru tris(bipyridine) PS anchored to NiO via a carboxylic acid linkage and axially coordinated to the cobalt metal center of a [Co-$(dmgBF_2)_2(H_2O)$] unit via the vinylpyridyl substituent of one of the bipyridine ligands (**Co116**, Figure 59; Table 5, entry 9).[982,983] **Co116** acts as a H_2-evolving photocatalyst upon immoblization on an ALD-deposited alumina monolayer covering a mesoporous NiO film. The $NiO|Al_xO_y|$**Co116** photocathode exhibited an early photocurrent E_{onset} of 0.87 V vs RHE, with J_{ph} plateauing at ∼0.51 V vs RHE with a maximum value of −20 μA cm^{-2}. It was suggested that the ALD layer enhances the photocurrent density as a result of reduced germinate charge recombination between holes in NiO and electrons in the reduced dye molecules.[984−986] CPPE at E_{appl} of 0.51 V vs RHE in pH 7 phosphate solution resulted in a stable J_{ph} of −8 μA cm^{-2} and a FE_{H2} of 68% over the course of 2.5 h. An analogous approach using ALD-deposited Al_2O_3 was recently used to prepare a NiO-supported DSPC based on a surface-immobilized organic perylene-3,4-dicarboximide chromophore and cobaloxime/DuBois-type HER catalyst in solution.[987]

A photocatalyst composed of a cobaloxime bound to an anchor-bearing push−pull organic dye (**Co117**, Figure 59) obtains a covalent dye-catalyst molecular dyad assembly free of precious metals in both the HEC and the PS.[945] The PS is covalently bound to the cobaloxime via "click-chemistry", providing a binding through the equatorial ligand sphere that is expected to be more robust than a dative bond.[741] Chenodeoxycholic acid was cografted onto the NiO surface to prevent deleterious dye aggregation in a 4:1 ratio alongside the **Co117**.[988,989] The NiO|**Co117** DSPC displayed an early photocurrent onset potential of 0.93 V vs RHE and a J_{ph} of −15 μA cm^{-2} at E_{appl} of 0.14 V vs RHE under simulated solar irradiation in pH 5.5 MES (Table 5, entry 10). This J_{ph} dropped to −6 μA cm^{-2} over the course of 2−3 h of CPPE, and a FE_{H2} of 8−10% was reported. Such low efficiencies were initially attributed to competitive reduction of the bulk NiO electrode and reductive degradation of the dye-catalyst assembly. However, a following study showed that a significant amount of H_2 remained in solution, and quantification using a high-sensitivity micro Clark-type electrode allowed for an amended FE_{H2} of ∼60%, far superior to the originally determined value.[990]

A NiO-based DSPC also consisting of an organic dye covalently linked to a cobaloxime catalyst was subsequently

DOI: 10.1021/acs.chemrev.8b00392
Chem. Rev. 2019, 119, 2752−2875

reported (**Co118**, Figure 59).[946] In this work, a push−pull triphenylamine- and dicyanovinyl-based dye functionalized with a carboxylic acid group for MO_x immobilization was linked to a HEC via the Huisgen reaction with a dibenzylcyclooctyne being introduced on the dye prior to catalyst linkage (section 3). Extensive time-resolved fluorescence and TAS were carried out to gain insight into the kinetics of interfacial and intramolecular charge transfers. A near unity hole injection efficiency from the excited **Co118** to the VB of NiO was concluded, taking place on dual timescales of $\tau \sim 1$ and 30 ps, whereas the rate constant of ET from the reduced dye to the cobaloxime unit was measured to be $\sim 3 \times 10^9$ s^{-1}. PEC testing of the NiO|**Co118** DSPC was conducted in pH 6.8 phosphate solution and pH 4.8 acetate solution, with the latter favoring greater proton reduction activity, yielding an initial J_{ph} of ~ -20 μA cm^{-2} at $E_{appl} = 0.48$ V vs RHE. This value drops rapidly during the first few minutes of CPPE, and an overall TON_{H2} of 0.05 was reported (Table 5, entry 11). This low performance was partially attributed to molecular twisting on the NiO surface and configurations of **Co118** unfavorable for catalyst reduction. Moreover, the linker between the light-harvesting part and the catalyst is not conjugated and relatively distant in space, rendering intramolecular charge transfer more challenging.

A photosensitizer-catalyst dyad with a CdSe QD instead of a molecular dye has also been reported.[991] The construct classifies itself as a dyad because the catalyst, $[Fe_2S_2(CO)_6]$, one of the simplest mimics of natural [FeFe]-H_2ases, was immobilized onto the QDs and this dyad then modified with a glycine anchoring group to form the final construct **$Fe_2$45** (Figure 59). The direct anchoring of the catalyst onto the QD facilitates vectorial ET from the CB of CdSe to the adjoining catalyst. The bifunctional glycine linker afforded anchoring of the QD construct onto NiO; this was thought to be possible without total replacement of the catalyst molecules on the QD surface because of the weaker affinity of the glycine's amino group as compared to the thiol moiety of $Fe_2S_2(CO)_6$. The resulting NiO|**$Fe_2$45** photoelectrode yielded an early onset potential of 0.70 V vs RHE in aqueous conditions (pH 6.8) and a J_{ph} of -0.56 μA cm^{-2} at E_{appl} of 0.30 V vs RHE in CPPE, achieving a FE_{H2} of 52% (Table 5, entry 12).

The modest performances obtained with the dyad approach and to some extent with DSP and DSPC systems is the result of the slow kinetics of multiple-ET to the catalyst. In order to address this issue, strategies toward fast ET kinetics and/or long-lived electron accumulation must be found; for example, via storage in the PS-catalyst bridging moiety.[992]

6.4. Photoelectrochemical CO_2 Reduction

The relative infancy of the approach to modify photocathodes with photosensitizers and couple this with a molecular catalyst for solar fuels generation is particularly apparent in CO_2 conversion. A number of DSPCs for CO_2 reduction exist but the majority of them are based on precious-metal-containing molecular catalysts.[557,925−927] The lack of efficient 3d metal-based molecular CRCs, let alone those that are able to be immobilized, has prevented the burgeoning of this field.

CO_2 reduction can be fundamentally challenging as the simple one-electron reduction to the $CO_2^{\bullet-}$ radical anion is highly unfavorable. However, the proton-coupled two-electron reduction of CO_2 to CO or formate has no such energy-costing restriction. As a result, catalysts that are able to accumulate reductive charges and therefore access this PCET pathway have an advantage. Enzymes such as CODH have a highly efficient active site and additional redox centers to capture the required reducing/oxidizing equivalents and protons needed to complete the catalytic cycle. Immobilization of CODH I from *Carboxydothermus hydrogenoformans* onto a dye-sensitized NiO electrode has been achieved using dye **PS36** (NiO|**PS36**|[NiFe]-CODH; Table 5, entry 13).[993] Photoexcited **PS36** provides sufficient driving force ($\sim$650 mV) to allow CO_2 reduction catalyzed by [NiFe]-CODH, yielding a photocurrent density of ~ -25 μA cm^{-2} when held at 0.08 V vs RHE in aqueous MES buffer solution (pH 6.0), although CO was not directly detected. CO_2 reduction was demonstrated by deliberate introduction of cyanate (NCO^-) into the solution, which is isoelectronic with CO_2 and inhibits catalysis. Interestingly, in the absence of any dye, unidirectionality of the enzymatic activity was studied by measuring currents produced when [NiFe]-CODH was immobilized on p-type NiO or n-type TiO_2. For the former, only CO oxidation was observed, whereas the enzyme performed only CO_2 reduction on the latter, irrespective of the potentials applied to the electrodes. This demonstrates how the nature of the SC on which the enzyme is immobilized has the power to modulate what is originally an efficient and reversible electrocatalyst such that it behaves unidirectionally.

6.5. Conclusion and Outlook

The concept of modifying p-type SCs with photosensitizers and molecular catalysts to construct DSPCs for solar fuel generation has been explored for almost a decade, but only a limited number of successful strategies have emerged. The simplest and earliest-adopted approach is to coadsorb the PS and catalyst side-by-side onto the p-SC surface. Interestingly, ratio considerations between the two species have been rarely discussed, even though one would expect this to be a key parameter for optimization. More recently, supramolecular DSPC systems based on Zr^{4+}-phosphonate bridge constructs have emerged, where the Zr^{4+} ion serves as an inert linkage to connect the dye to a catalyst, which is located at a certain distance from the supporting p-SC substrate to reduce charge recombination kinetics. Finally, the most synthetically challenging approach in immobilizing photosensitizers and catalysts has been to combine them as covalently linked dyads, sometimes deliberately in a push−pull architecture to induce directional charge transfer.

The challenges of this relatively new approach are highlighted by the homogeneity of the types of dye-catalyst systems adopted and the dominant role of NiO as p-SC material. The poor hole mobility in NiO has limited these DSPC devices such that their photocurrent densities rarely exceed the tens of μA cm^{-2}. The lack of alternative options to replace NiO is perhaps the biggest challenge facing the improvement of these photocathodes' performances. However, a number of approaches have been formulated to combat this issue in p-type DSSCs. Specifically, dealing with surface defects has been the focus of some of these strategies, as such imperfections, atomic vacancies or dangling bonds, that are often formed during fabrication of the MO_x film can act as charge carrier trap sites, lowering charge separation yields. Strategies for surface passivation and reducing the density of defects have included improving the crystallinity of the film,[994,995] and depositing a thin overlayer on the surface of NiO either by ALD or solution-phase deposition.[984−986] This approach using ALD, and that of Al_2O_3 in particular, has been adopted for H_2-evolving DSPCs,[982,987] as well as attempts to dope NiO in order to modify its VB edges and therefore

DOI: 10.1021/acs.chemrev.8b00392
Chem. Rev. 2019, 119, 2752−2875

establish an internal driving force for hole transport.[981] Searches are underway by a number of research groups to realize alternative p-SC materials that can outcompete NiO in terms of hole mobility, band edge potentials, nanostructuring and hence molecular loading capacities, while maintaining the ease of fabrication and low cost. Recently, promising work in the development and adoption of a $CuCrO_2$ delafossite in place of NiO as the p-SC in a molecular catalyst-based DSPC has highlighted the importance of this route.[969]

Perhaps the component in DSPCs that displays the widest variety to date is the PS, ranging from coordination complexes and organic dyes to QDs. The latter (CdSe QDs) are employed in the most active and stable 3d transition metal catalyst-based DSPC for H_2 evolution reported to date.[957] This field of research has benefited from the more mature development in p-type DSSCs over DSPCs, wherein immobilized dyes are a common motif that span across both areas. Nevertheless, much work is still needed to develop and realize new and better candidates for all the basic building blocks that make up a DSPC (the p-SC, the PS, the molecular catalyst, and all linkers involved with species immobilization). In doing so, the modular separation of light harvesting, charge transport, and catalysis in DSPCs can be taken advantage of by allowing the separate components to be individually optimized for best performance, where the rates of each transfer step dictate the overall device efficiency. With many components present in a DSPC-based system, the number of potential kinetic bottlenecks in the system is significant and kinetic insights from fast spectroscopies such as TAS are thus greatly valuable. For example, the importance of the linker length and identity have been elucidated in terms of how they can accelerate or decelerate recombination. Salient examples of this have been the improvement of a NiO|**PS37**|[FeFe]-catalyst system upon increasing the length of the catalyst linker,[954,955] as well as identification of hole traps in the thiol group linkers of the aforementioned CdSe-based work.

Looking forward, a possible new approach for DSPC assembly gathers inspiration directly from DSP systems in which the dye and catalyst are interfaced to one another via a SC that ensures the efficient transfer of multiple, low-potential electrons toward a catalyst (Figure 60). Importantly, this differs to supramolecular assemblies (Figure 54b) as the linker in the latter is typically inert and serves only to physically connect the molecular components. A SC bridge with an appropriate E_{CB} energy level allows the p-SC supporting substrate (e.g., NiO) to be replaced with a (degenerately doped) conductive material (e.g., ITO), which could potentially overcome issues such as limited hole mobility that are inherent to conventional p-SCs. A recent example that demonstrated early efforts in this translation of DSP systems onto DSPC adopted a type II sensitization, whereby **PS31** (Figure 47) was employed to bind to TiO_2 nanoparticles via its catechol linker, while the carboxylic acid moiety remained free for further anchoring to a MO_x electrode.[881]

Besides [FeFe] catalysts, other HECs employed in DSPC systems can be categorized as either cobaloximes or Ni DuBois type catalysts. The former class possesses low η and are synthetically easy to derivatize, a major advantage especially in the case where synthetic manipulation must be undertaken to achieve covalently attached dyads. The latter are among the most active and stable 3d transition metal-based catalysts for proton reduction. In the case of CO_2 reduction, no synthetic 3d metal molecular catalysts have yet been successfully coupled with a photosensitizer to construct an operational DSPC, and

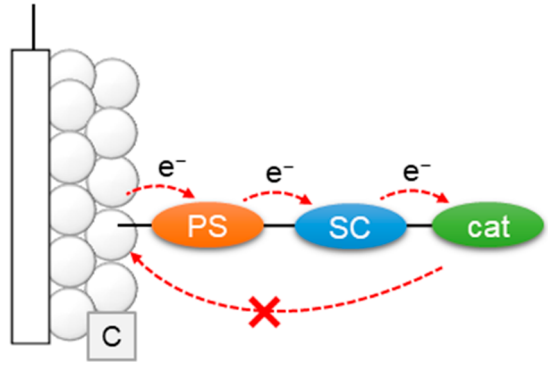

Figure 60. Possible DSPC assembly where ET between the photosensitizer and catalyst is mediated by a SC, and the assembly is attached to a conductive surface (C).[881]

there exists only one example for the enzyme CODH.[993] This illustrates the difficulties of successfully implementing catalyst and light harvesters on the same electrode.

In general, molecule desorption and/or degradation is a common reason for unstable PEC activity, and maintaining the molecular integrity of the catalytic species has been a main challenge for all molecular catalyst-based systems. The lack of standardization in reporting PEC performance of DSPCs is another problem and key indicators of performance are rarely reported under the same conditions (see section 1.5).

7. NARROW-BANDGAP SEMICONDUCTOR PHOTOCATHODES

7.1. General Remarks

An alternative to DSPCs is the construction of photocathodes from narrow-bandgap semiconducting materials that are inherently light-absorbing and their modification with molecular fuel-forming catalysts. Narrow-bandgap p-SCs differ from their dye-sensitized counterparts discussed in the previous section as light absorption, charge carrier generation, separation and mobility are all performed by a single material. The approach of using narrow-bandgap p-SCs to build light-absorbing photocathodes (LAPCs) therefore has the potential advantage over DSPC systems of having a reduced number of components by not requiring an additional PS.

Despite the apparent attractiveness of such an architecture and an early example of a molecular catalyst-based LAPC for PEC H_2 evolution,[115] there has been significant development of such systems only in the past decade. Of these, there remain only a small number of 3d transition metal complexes on LAPCs that also operate under aqueous conditions and no reported examples with proven CO_2 reduction ability without the use of precious-metal based CRCs. The challenge therefore remains to continue the nontrivial task of developing such photocathodes that are active and stable for solar fuel synthesis.

7.2. Component Requirements and Characteristics

7.2.1. Narrow-Bandgap p-Type Semiconductors. Similarly to DSPCs being largely based on materials inspired from and first developed for p-type DSSCs, the narrow-bandgap SCs employed to realize LAPCs for H_2 evolution and CO_2 reduction have also been adapted from the photovoltaics field. Narrow-bandgap p-SCs can be inorganic or organic with examples of LAPCs being based on both types. From a thermodynamic point of view, it is crucial that the E_{CB} of the p-SC is more negative than E_{onset} of the immobilized molecular HEC or CRC (Figure 61).

DOI: 10.1021/acs.chemrev.8b00392
Chem. Rev. 2019, 119, 2752−2875

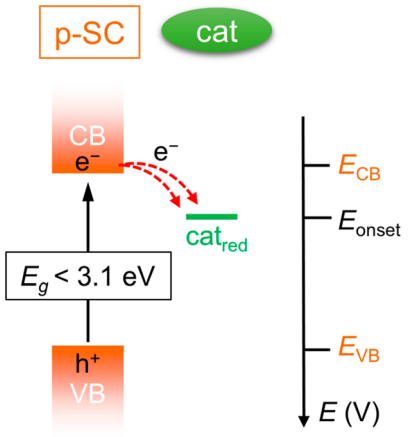

Figure 61. Band diagram depicting energy level requirements for a successful LAPC system.

In addition, E_g of the p-SC determines the maximum proportion of the solar spectrum that can be harvested. Visible and infrared light account for more than 95% of solar irradiation and wide-bandgap SCs with E_g > 3.1 eV can only absorb UV light.[81] Further considerations for E_g must be taken if the assembly of an efficient tandem PEC cell is the final objective. The theoretical upper limit of solar-to-hydrogen efficiency of a tandem PEC cell with a pair of SCs (having bandgaps of 1.0 and 1.6 eV) under 1 Sun irradiation is close to 30%, whereas only 13% are achievable for a single light absorber PEC cell (using a bandgap of 2.2 eV).[947,949,996,997]

Figure 62 depicts the VB and CB edges, as well as the bandgaps, of inorganic p-SC materials that have been used to date to construct LAPCs with 3d transition metal complexes. Of these, p-type silicon has the narrowest bandgap (1.12 eV) and can capture photons from a significant portion of the solar spectrum, even those in the near-infrared.[701] Along with Cu_2O, SCs of the III-V variety, namely, indium phosphide (InP), GaP, and gallium indium phosphide ($GaInP_2$), also have bandgaps appropriate for visible light absorption (2.10,[998] 1.35,[999,1000] 2.26,[1001] and 1.83 eV,[1002,1003] respectively). Furthermore, E_{VB} of GaP is marginally more positive than the potential for the oxygen evolution reaction and may therefore be used as a single light absorber to drive full water splitting with a water oxidation catalyst that requires a minimal overpotential. Nevertheless, solar-to-hydrogen efficiencies usually benefit from a well-designed tandem configuration.

Although the number of p-SC materials that have been successfully used to develop proton- or CO_2-reducing LAPCs is greater than the number of p-SCs used in DSPCs (the majority of which are based on NiO), it is still restricted due to photodegradation of many potential p-type light-absorbing SCs in water and their fragility in acidic media. Conditions that are benign to the SC and immobilized catalyst must therefore be identified to assemble a functional LAPC.

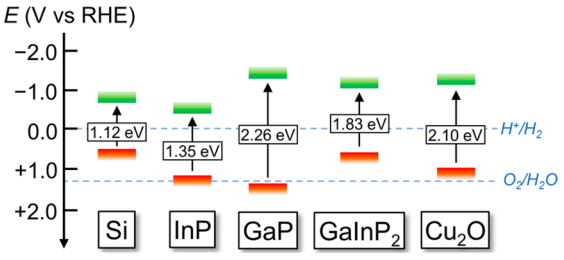

Figure 62. Valence (red) and conduction (green) band positions for inorganic p-type light-absorbing SC materials discussed in this section.

Silicon is inherently unstable in aqueous or aerobic conditions due to the formation of an insulating silica surface layer that passivates the electrode and renders the region inactive for electrochemical reactions. The most commonly used strategy to overcome this problem for H_2-evolving photocathodes has been to decorate the Si with a thermodynamically stable and ultrathin ALD-coating of TiO_2 prior to catalyst immobilization (note that none of these catalysts to date have been synthetic molecular HECs in aqueous environments).[711,1004−1006] Corrosion instability also afflicts Cu_2O and In- and Ga-based light-absorbing SCs and limits their application for PEC solar fuel devices.

In addition to Si, ALD-deposited thin films have therefore also been applied to other unstable SC materials in the context of providing protection against corrosion/passivation under PEC hydrogen-evolving/CO_2-reducing conditions.[702,1007−1009] However, the number of such examples remains scarce when only considering HEC-based photocathodes, especially 3d transition metal complexes.[1007] ALD films are usually transparent to permit light absorption, and sufficiently thin to allow charge transfer, but the intrinsically slow and energy-intensive nature of the deposition method challenges its scalability.[560]

Finally, the p-SC must be able to facilitate some form of anchoring mode in order for catalyst immobilization to be successful. Ideally, this should also allow for a significant amount of molecules to be loaded onto the surface to compensate for the kinetic limitations of molecular catalysts, so some form of nanostructuring to introduce a high surface area-to-volume ratio would be beneficial. A general assembly scheme is presented in Figure 63. The appropriate anchoring modes compatible with different surface types have already been discussed in section 3. In the case of LAPCs with 3d transition metal complexes, the vast majority of the SC surfaces employed have been metallic oxides or III-V type SCs. This has allowed for exploitation of their inherent susceptibilities to the formation of O-metal iono-covalent bonds.

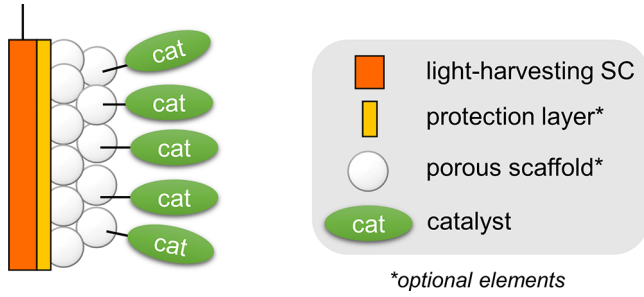

Figure 63. General assembly approach taken to construct LAPCs, where a protection layer and porous scaffold are optional elements.

7.2.2. Molecular Catalyst. The majority of criteria that applied to molecular catalysts in DSPCs also apply when considering appropriate molecular catalysts for LAPCs. For instance, an important prerequisite common to both types of photocathodes is the ability of a catalyst to anchor onto the SC surface and remain stable under catalytic operating conditions. One notable difference is that the anchoring mode must allow for efficient charge transfer to occur between the SC surface and

DOI: 10.1021/acs.chemrev.8b00392
Chem. Rev. 2019, 119, 2752−2875

Table 6. LAPCs with Immobilized 3d Metal Complex Electrocatalysts Active for Proton Reduction in Aqueous Solution[a]

entry	electrode	HEC	E_{onset}[b] (V)	$\|J_{ph}\|$ at E_{appl}[b] (mA cm^{-2} at V)	CPPE duration at E_{appl}[c] (min at V)	TON_{H2}	FE_{H2}	conditions	illumination	ref
1	InP	**$Fe_2$36**	~0.51	~3.8 × 10^{-4} at 0.11	60 at 0.21	n/a	~60%	$NaBF_4$ pH 7.0	395 nm LED	1013
2	GaP	**Co90**	0.76	2.40 at 0.0	5 at 0.17	n/a	n/a	phosphate pH 7.0	100 mW cm^{-2}, Xe lamp	709
3	GaP	**Co90**	0.72	0.92 at 0.0	30 at 0.17	n/a	88%	phosphate pH 7.0	100 mW cm^{-2}, AM1.5G	1015
4	GaP	**Co119**	~0.57	~1.10 at 0.0	15 at −0.12	n/a	97%	acetate pH 4.5	100 mW cm^{-2}, AM1.5G	1020
5	GaP(100)	**Co120**	0.58	1.2 at 0.0	60 at 0.0	n/a	~100%	phosphate pH 7.0	100 mW cm^{-2}, AM1.5G	1021
6	GaP(111)	**Co120**	0.65	0.89 at 0.0	10 at 0.0	n/a	~100%	phosphate pH 7.0	100 mW cm^{-2}, AM1.5G	703
7	GaP	**Co121**	~0.55	1.31 at 0.0	240 at 0.0	n/a	~97%	phosphate pH 7.0	100 mW cm^{-2}, AM1.5G	710
8	GaP	**Fe35**	~0.50	1.29 at 0.0	6 at 0.0	n/a	~45%	phosphate pH 7.0	100 mW cm^{-2}, AM1.5G	710
9	GaP	**Co122**	0.65	1.27 at 0.0	60 at 0.0	n/a	~93%	phosphate pH 7.0	100 mW cm^{-2}, AM1.5G	1026
10	$GaInP_2$|TiO_2|HEC|TiO_2	**Co101**	0.70	11.0 at 0.0	1200 at 0.0	1.4 × 10^5	~100%	NaOH pH 13.0	100 mW cm^{-2}, AM1.5G	1009
11	Si	**$Fe_2$46**	0.25	n/a	n/a	n/a	n/a	$HClO_4$ pH 0.0	870 mW cm^{-2}, Xe lamp	115
12	Si	**Co85**	~0.20	3.80 at 0.0	120 at −0.12	n/a	80%	H_2SO_4 pH 1.3	100 mW cm^{-2}, AM1.5G	749
13	Si|InP	**$Fe_2$36**	~0.20	1.20 at −0.26	50 at −0.26	n/a	n/a	H_2SO_4 pH 1.0	100 mW cm^{-2}, AM1.5G	1029
14	Si|TiO_2	**Ni35**	~0.40	~0.34 at 0.0	1440 at 0.0	646	~80%	acetate pH 4.5	100 mW cm^{-2}, AM1.5G	525
15	Si|TiO_2	**Co89**	~0.35	~0.34 at 0.0	240 at 0.0	11	30%	acetate pH 4.5	100 mW cm^{-2}, AM1.5G	525
16	P3HT	**Co82**	n/a	~0.003 at 0.0	13 at 0.17	n/a	n/a	acetate pH 4.5	100 mW cm^{-2}, AM1.5G	720
17	Si|planar TiO_2	[NiSeFe]-H_2ase	~0.25	~0.004 at 0.0 (~0.003 at 0.0)[c]	60 at 0.0	n/a	95%	MES pH 6.0	10 mW cm^{-2}, LED white light	713
18	Si|mesoporous TiO_2	[NiSeFe]-H_2ase	~0.30	~0.20 at 0.0 (~0.09 at 0.0)[c]	240 at 0.0	n/a	~70%	MES pH 6.0	100 mW cm^{-2}, AM1.5G, λ > 400 nm	525
19	Si|IO-TiO_2	[NiSeFe]-H_2ase	~0.35	~0.550 at 0.0 (~0.69 at 0.0)[c]	300 at 0.0	n/a	86%	MES and KCl pH 6.0	100 mW cm^{-2}, AM1.5G, λ > 420 nm	714
20	black-Si	[FeFe]-H_2ase	~0.38	1.70 at 0.0	300 at 0.1	9.9 × 10^6	33%	phosphate pH 6.8	10 mW cm^{-2}	1037

[a]All potentials are reported against RHE unless otherwise stated (n/a = not available). [b]Extracted from LSV measurements, unless otherwise stated. [c]Extracted from CPPE measurements.

the molecular complex in LAPCs, in contrast to DSPCs where charge transfer between the coadsorbed PS and the catalyst is important. In the latter, charge transfer between the SC surface and the molecular catalyst should be avoided as it leads to undesired charge recombination. Thus, a long spatial separation between the molecular catalyst and the SC may be beneficial in DSPCs in order to reduce recombination, whereas this would slow down forward ET from the light absorber to the catalyst in LAPCs.

The effect of linker length on the kinetics of charge separation and recombination in SC-molecular catalyst hybrid photoelectrodes is important, as demonstrated by an extensive study on the interfacial ET dynamics of a series of mesoporous TiO_2|cobaloxime films.[879] Here, it was revealed that the ET rate from the SC to the attached cobalt catalyst was exponentially dependent on the distance between the TiO_2 and the metal center (see section 5.2.3). Another difference to consider when constructing a LAPC as opposed to a DSPC is the reliance on E_{CB} to reduce the catalyst rather than E_{VB} to quench the holes of the photoexcited PS.

Long-term integrity of the molecule should be verified in postcatalysis experiments in order for performance claims to be substantiated. A difficult and recurring question in molecular catalysis is whether the primary compound is the true catalyst or just a precursor for the true nonmolecular active species (often metals or MO_xs) produced in situ;[86,1010] in particular when operating under highly oxidizing or reducing potentials, strongly acidic or basic media, and in the presence of water. Nevertheless, it should be noted that solution processed single source molecular precursor chemistry has been used as a strategy to intentionally form nonmolecular catalytic layers on p-type SCs in the context of water splitting, but this is beyond the scope of this review.[560,1011,1012]

The remainder of this section will discuss LAPCs that have been prepared with 3d transition metal complex-based catalysts active for proton- and CO_2-reduction in aqueous systems. The literature has been categorized according to the type of light-absorbing SC.

7.2.3. Indium Phosphide. A molecular catalyst-modified LAPC active for H_2 evolution was built from a cross-linked InP

DOI: 10.1021/acs.chemrev.8b00392
Chem. Rev. 2019, 119, 2752−2875

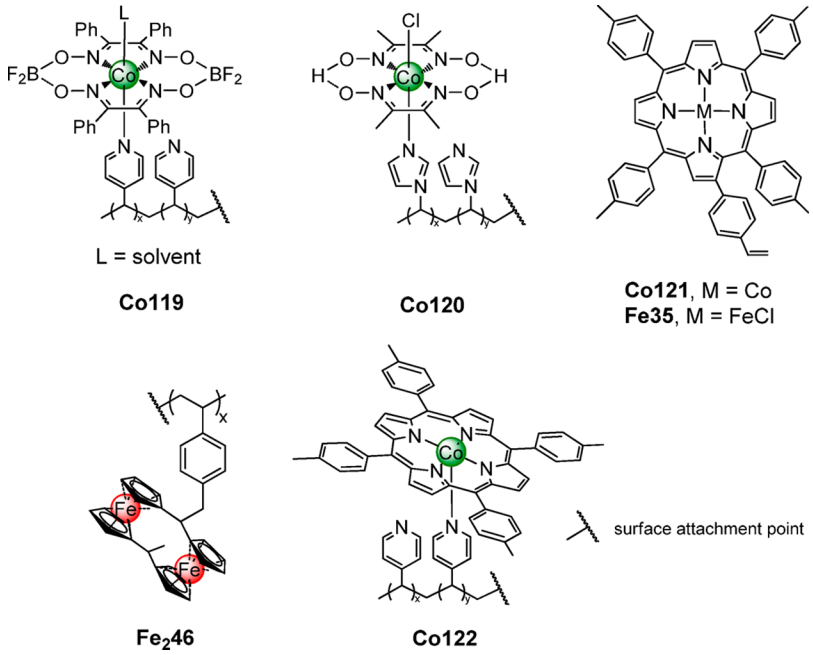

Figure 64. Molecular structures of HEC immobilized on narrow-bandgap photocathodes.

nanoarray as the light-absorbing component with an incorporated iron-sulfur HEC (**$Fe_2$36**, Figure 42), that resembles the subsite of an [FeFe]-H_2ase.[1013] The InP cathode was assembled by first modifying the surface of a gold electrode with a monolayer of 1,4-benzenedithiol, which allowed for subsequent binding of the primary layer of InP nanocrystals. Sequential layer-by-layer build-up of the InP array was achieved by alternating exposure to the dithiol and the nanocrystal solutions. After ten layers of InP nanocrystals were deposited, **$Fe_2$36** was immobilized on the surface by exposure of the electrode to a solution of the iron catalyst. Adsorption of the molecule onto the SC surface was presumed to occur via direct binding of the sulfide bridges to the indium. InP possesses a E_{CB} of −0.39 V vs RHE at pH 7, which provided sufficient driving force for the catalyst to perform proton reduction. In aqueous solution (0.1 M $NaBF_4$, pH 7.0) under 395 nm LED illumination, the InP|**$Fe_2$36** photocathode displayed an E_{onset} = 0.51 V vs RHE but produced only J_{ph} of <1 μA cm^{-2}. Nevertheless, CPPE at E_{appl} = 0.21 V vs RHE for 1 h produced a FE_{H2} of ∼60% (Table 6, entry 1).[1013] This early work inspired the integration of molecular electrocatalysts onto solid-state light-absorbing SCs for solar fuel photocathodes.

7.2.4. Gallium Phosphide. GaP as a visible light-absorbing III-V type SC was employed with molecular HECs by exploiting UV-induced immobilization chemistry of terminal alkenes for surface-initiated photopolymerization[1014] to yield a polymer with attachment points for cobaloxime catalysts. A similar approach had been previously used on GaP and Si surfaces to immobilize a proton reduction Ni bis(diphosphine) catalyst (section 2.2.5.1) via formation of an amide bond, although H_2 evolution was not demonstrated in that case.[708]

The first example of a GaP|polymer-cobaloxime construct employed a vinylpyridine being photochemically grafted onto a GaP(100) surface, followed by coordination of [$CoCl_2$(dmgH)-(dmgH_2)] to pyridyl groups on the surface-attached PVP polymer brushes to yield the final GaP|**Co90** photocathodes (Figure 27).[709,1015] Performing this surface catalyst immobilization in two steps means that not all pyridine units are saturated with cobaloximes, as evidenced by XPS measurements. Nevertheless, it was expected that using a polymer bearing multiple pyridine binding sites would significantly increase the per geometric area loading capacity of the catalysts onto the SC, as compared to approaches using self-assembled monolayers of molecules. A ∼12 nm thick PVP layer was calculated to offer a Γ of 13 nmol cm^{-2}, and extensive grazing angle FT-IR, XPS, and XANES analyses confirmed surface attachment of the cobaloximes.[709]

Under 100 mW cm^{-2} Xe lamp (not AM1.5G) illumination and in aqueous solution (pH 7.0), the GaP|**Co90** photocathode displayed an E_{onset} of 0.76 V vs RHE during irradiation, as compared to 0.69 V vs RHE for a catalyst-free GaP|PVP electrode (Table 6, entry 2).[709] The fill factor for the J−V response of the open circuit voltage improved substantially upon incorporation of the Co catalyst (>200% increase), confirming that the presence of the cobaloxime promotes charge transfer across the surface.[709] CPPE under AM1.5G illumination (different to above) generated a J_{ph} of −0.92 mA cm^{-2} at 0.0 V vs RHE and a FE_{H2} of 88% at E_{appl} of 0.17 V vs RHE (Table 6, entry 3).[1015] Gradual system deactivation was attributed to loss of the cobaloxime species from the surface and is consistent with dissociation of the axial pyridine during redox cycling (discussed in section 2.2.4.1).[202,1016] The photocurrent density of GaP|**Co90** has a linear dependence on the illumination intensity, which indicates that photocarrier transport to the interface was likely a limiting factor for the performance of this photocathode.[1015] The E_{CB} of GaP is located almost 1.0 V more negative than the thermodynamic potential for proton reduction, which, though energy wasteful in some cases, makes it an attractive material choice for photocathodes where the fuel-producing catalyst requires a significant overpotential.[1017−1019]

Exchange of the molecular HEC in **Co90** for a modified cobaloxime (**Co119**, Figure 64) gives a system that reflects results found under homogeneous conditions. Replacing the oxime-linking hydrogen atoms with bridging BF_2 groups imparts slight increases in stability, and substitution of the methyl for the

DOI: 10.1021/acs.chemrev.8b00392
Chem. Rev. 2019, 119, 2752−2875

phenyl moieties at the C-atoms shifts the catalytic onset potential (Table 6, entry 4).[1020] Direct comparison with GaP|**Co90** under identical conditions shows lower activity for GaP|**Co119** at pH 7 in terms of J_{ph} (−1.20 vs −0.56 mA cm^{-2} at 0.0 V vs RHE, respectively). However, the J_{ph} curves become almost identical when the pH is lowered to 4.5 (∼−1.10 mA cm^{-2} at 0.0 V vs RHE). The requirement of acidic conditions to induce higher catalytic activity for **Co119** is most likely due to a correlation between the Co^{2+}/Co^{+} reduction potential and diminished basicity of the Co^{+} state, thereby requiring a lower pH value to form the active cobalt-hydride species during the catalytic cycle (see section 2.2.4.1). Nevertheless, the work on GaP|**Co119** highlights the benefits of the modular approach undertaken to construct these photocathodes in allowing for straightforward catalyst modification.

The versatility of using a polymer graft to interface molecular catalysts with a SC substrate was further demonstrated when the PVP polymer was replaced with a polyvinylimidazole (PVI); the imidazole units of the latter also bind to the cobaloxime in the axial position (**Co120**, Figure 64; Table 6, entry 5).[1021] The GaP|**Co120** photocathodes displayed a slightly thinner film thickness with PVI than with PVP (6 vs 10 nm).[1022] As a result, there is a lower ligand binding site (imidazole/pyridine) density for the PVI film (Γ = 8 vs 11 nmol cm^{-2}), which may partially explain the slightly lower PEC performance. Direct comprison under the same experimental conditions gave an E_{onset} at 0.61 V vs RHE for PVP-based GaP|**Co90**, whereas GaP|**Co120** exhibited an E_{onset} at 0.58 V vs RHE. Similarly, J_{ph} of the former reached −1.3 mA cm^{-2}, whereas the latter reached −1.2 mA cm^{-2} at an applied potential of 0.0 V vs RHE under simulated solar irradiation. CPPE resulted in a near-quantitative FE_{H2} and a loss of ∼30% of J_{ph} after 1 h of operation.[1021]

The polymer grafting approach was further extended to different GaP(111) faces with polymers containing **Co120**, and the GaP(111)|**Co120** photocathodes were found to exhibit similar performance to their GaP(100) counterparts as well as others (111A vs 111B faces; Table 6, entry 6).[703] XPS analysis of these systems provided an estimate of 28−35% for the loading of cobalt centers to all available ligand binding units in the polymer film, thereby illustrating that saturation of all ligand sites on the polymer with cobaloxime catalysts is unlikely when this layer-by-layer electrode fabrication method (polymer deposition first followed by catalyst modification) is employed.

UV-induced polymerization of olefins can be exploited in much the same way for attaching individual molecules to a GaP surface as for inducing surface-initiated polymerization. This approach was employed to immobilize Co- and Fe-centered porphyrins bearing a pendent 4-vinylphenyl surface attachment group at the β-position of the porphyrin ring structure (**Co121** and **Fe35**, Figure 64; Table 6, entries 7 and 8, respectively).[710] Notable differences to previous work on GaP are that the surface-immobilized molecular units here remain discrete from one another, each of them possessing its own attachment point in the absence of polymer. In addition, the catalyst metal centers are already coordinated to their ligand framework prior to surface grafting. Metalloporphyrins are attractive electrocatalysts as they are not only capable of proton reduction but also converting CO_2 into CO. A GaP|**Co121** photocathode outperforms a GaP|**Fe35** photocathode when tested in pH-neutral conditions under simulated solar irradiation, including displaying an earlier E_{onset} (0.55 vs 0.50 V vs RHE), maintaining a more stable J_{ph} at E_{appl} = 0.0 V vs RHE (>90% activity retained after 4 h vs 77% activity retained after 6 min) and achieving a higher FE_{H2} (97% across 30 min vs 45% across 6 min). Possible explanations included the relative instability of iron-porphyrins[1023−1025] and the Co^{2+}/Co^{+} redox couple being positioned at more positive potentials than the Fe^{2+}/Fe^{+} couple of the corresponding complexes.

Metalloporphyrins were also attached to GaP by using the same procedure previously reported for UV-induced polymerization of PVP onto the SC, followed by cobalt-porphyrin attachment to the pyridine units (**Co122**, Figure 64; Table 6, entry 9).[1026] This approach involves two steps to achieve **Co122** surface attachment but does not involve synthetic steps to modify the porphyrin macrocycle with a surface attachment functionality. Performance parameters during CPPE were nearly identical to those of the GaP|**Co121** photocathodes, suggesting that the PVP surface coating does not diminish the performance gains afforded by Co-porphyrin surface modification. J_{ph} was shown to scale linearly with illumination intensity in both systems, suggesting that photocarrier transport to the GaP-catalyst interface remains a limitation to performance. Spectral coverage and photophysical properties of the GaP SC are thought to be limiting factors.

In summary, the series of reports detailed above employ UV-induced attachment of olefin groups to the Ga surface for surface grafting of proton-reducing cobaloximes and metalloporphyrins onto GaP SC substrates. These systems demonstrate that small modifications at the catalyst level (ligand functionalities of cobaloximes, cobaloximes vs metalloporphyrins), polymer level (PVP vs PVI), and GaP level (100 vs 111 faces) can all be investigated and optimized using this versatile approach.

7.2.5. Gallium Indium Phosphide. The majority of LAPCs reported so far are active for proton reduction in pH-neutral or acidic conditions, as the anchored molecular catalyst is stable and can operate under these conditions. An exception is a $GaInP_2|TiO_2|$cobaloxime$|TiO_2$ construct that has been claimed to function under pH 13 conditions (Table 6, entry 10),[1009] which may be beneficial for overall water splitting as water oxidation is usually preferred under strongly basic conditions.[1027] In this photocathode, TiO_2 is deposited as an interlayer and on top of the molecular cobaloxime complex. The 35 nm-thick ALD-TiO_2 layer directly interfaced with $GaInP_2$ provides a conformal layer to protect the III-V SC from corrosion in aqueous solutions,[1028] while also providing oxide sites for surface attachment of the isonicotonic acid-functionalized cobaloxime catalyst (**Co101**, Figure 39). Analogous to dye stabilization on NiO with an ALD-deposited Al_2O_3 overlayer (Section 6),[987] a ∼0.4 nm-thick TiO_2 overlayer deposited on top of the cobaloxime was thought to provide stabilization of the carboxylate linkage under such harsh conditions, although direct comparison of the PEC performances achieved by the $GaInP_2|TiO_2|$**Co101**$|TiO_2$ electrode with an overlayer-free $GaInP_2|TiO_2|$**Co101** photocathode was not discussed.[1009]

Under illumination in aqueous NaOH (pH 13.0) solution, the $GaInP_2|TiO_2|$**Co101**$|TiO_2$ photocathode exhibited an E_{onset} of ∼0.70 V vs RHE and reached J_{ph} of −11 mA cm^{-2} at 0.0 V vs RHE in LSV experiments. J_{ph} drops by only 5% with near-unity FE_{H2} during CPPE within the first 20 min and plateaus at ∼5 mA cm^{-2} after 4 h.[1009] It is worth noting that the molecular integrity of the HEC within this photocathode was not unambiguously verified after operating under the extremely alkaline conditions.[86]

7.2.6. Silicon. Besides III-V SCs, p-type silicon has been adopted for building molecular catalyst-based LAPCs. Several

DOI: 10.1021/acs.chemrev.8b00392
Chem. Rev. 2019, 119, 2752−2875

reports describe the deposition of protection layers to limit the instability of silicon in aqueous solution, but this often requires severe precautions and expensive techniques, most commonly ALD.[702] Most of these reports subsequently deposited non-molecular precious metal heterogeneous catalysts atop the protection layer to complete construction of the H_2-evolving photocathodes. The majority of molecular catalyst-based LAPCs for proton reduction based on Si have been operated under either organic solvents or extremely acidic aqueous solutions, where the Si is more stable.

An early example of a molecular catalyst interfaced with a p-SC to yield a proton-reducing photocathode was the combination of a p-type Si with an incorporated bimetallic metallocene ("ferrocenophane")-type molecular complex and a polystyrene polymer (**$Fe_2$46**, Figure 64, Table 6, entry 11).[115] Although most of the photoelectrochemistry was undertaken in neat HBF_3OH electrolyte solution, the Si|**$Fe_2$46** photocathode was also reported to operate under acidic aqueous conditions, such as 1.0 M $HClO_4$, in which it exhibited an E_{onset} of ∼0.25 V vs RHE when illuminated by a 870 mW cm^{-2} Xe lamp.

A one-dimensional cobalt dithiolene MOS based on the benzene-1,2,4,5-tetrathiolate framework (**Co85**, Figure 25) was deposited as a thin film on a Si electrode (Table 6, entry 12).[749] The surface concentration of **Co85** on top of Si can be easily modified by varying the amount of catalyst dropcast on the electrode. At a Γ of 4000 nmol cm^{-2}, the Si|**Co85** photocathode exhibited an E_{onset} of ∼0.2 V vs RHE during irradiation and reached a J_{ph} of −3.8 mA cm^{-2} at 0.0 V vs RHE in an aqueous H_2SO_4 solution (pH 1.3). CPPE at E_{appl} = −0.12 V vs RHE for Si|**Co85** displayed a stable response for 20 min (FE_{H2} of 80%) with the delamination of the catalyst from the Si surface causing the instability.[749]

Anodized porous p-Si electrodes were interfaced with a QD-catalyst assembly based on the previously demonstrated binding affinity of **$Fe_2$36** for InP (section 7.2.3).[1013,1029] EDX spectroscopy experiments revealed a homogeneous distribution of In and Fe across the porous electrode, attesting to the physisorption of the QD-catalyst assembly, although no quantification of the attachment was provided. Under AM1.5G 100 mW cm^{-2} irradiation the photocathode displayed an E_{onset} of ∼0.2 V vs RHE when placed in 0.1 M H_2SO_4 solution (Table 6, entry 13). CPPE at $E_{appl} \approx$ −0.26 V vs RHE of Si|InP|**$Fe_2$36** revealed a photocurrent of ∼−1.20 mA cm^{-2} after 10 min and H_2 was detected via gas chromatography, although no FE or assessment of the catalyst stability was provided.[1029]

A molecular DuBois Ni catalyst immobilized with a variety of anchoring methods on Si for H_2 evolution was operated in organic solvents with acids as the proton source.[1030,1031] In these systems, the DuBois catalysts were not isolated prior to attachment but assembled layer-by-layer on the electrode surface, where ligand immobilization was followed by metalation and capping with a second equivalent of the ligand to complete the coordination environment. The catalyst was either covalently attached directly to a Cl-terminated Si substrate via a series of coupling steps,[1030] or through a phosphonic acid group directly onto ALD-deposited thin films of TiO_2.[1031] An additional ALD-deposited aluminum-doped zinc oxide layer was used in between the Si and TiO_2 in the latter system to induce a band-edge modulation for a higher p-type barrier height resulting in earlier E_{onset} of the J_{ph}. The transparent and conductive nature of the ultrathin aluminum-doped zinc oxide layer ensured that it was an effective conduit for both photon and electron transmission, respectively. An organic linker (3,5-dimethoxyphenyl) present between the Si and the aluminum-doped zinc oxide layer was shown to further shift the band-edge and resulting onset to more positive potentials. Catalytic investigation under aqueous conditions has yet to be reported for either system.[1030,1031]

A precious-metal-free Si-based photocathode coupled with discrete, surface-immobilized molecular catalyst units for H_2 evolution in water has been reported, without the use of ALD. This system relied on the engineering of a Si|TiO_2 interface that concurrently allowed protection of Si against corrosion in aqueous conditions and provided a mesoporous MO_x surface on which a high loading of the phosphonic acid-bearing Ni-centered DuBois catalyst (**Ni35**, Figure 26) was permitted (Table 6, entry 14).[525] As a result, when placed in pH 4.5 aqueous solution and operated under 1 Sun illumination, the Si|TiO_2|**Ni35** electrode displayed a photocurrent E_{onset} of ∼0.4 V vs RHE and reached a TON_{H2} of 646. The photocathode was shown to be stable for >24 h and the molecular integrity of the surface-immobilized molecular species was verified by XPS and attenuated total reflectance IR measurements.[525]

The phosphonic acid-bearing molecular Co diiminedioxime **Co89** (Figure 26) was also immobilized on the same Si|TiO_2 and achieved a TON_{H2} (11 after 4 h) that matched those reported for this catalyst in colloidal DSP systems, thereby demonstrating the transferal of these catalysts' solution-based performance onto a photocathode architecture (Table 6, entry 15).[525,543] The range of other catalysts (metallic Pt and a H_2ase enzyme) immobilized on the same Si|TiO_2 scaffold are further testament to the versatility offered by this approach in evaluating a wide array of existing and future catalysts.[525]

7.2.7. Organic Bulk Heterojunction Semiconductors.

In addition to inorganic p-SC materials, organic bulk heterojunction (BHJ) solar cells[1032] have been adopted as the light-absorbing component for hydrogen-evolving photocathodes. Such organic SC-based systems typically rely on the charge separation between a p-type fullerene derivative (electron acceptor) and an n-type light-absorbing polymer or small organic molecule. By adding a catalyst layer on top of the photoactive BHJ blend, the kinetics for proton reduction at the photocathode surface can be much enhanced. The low cost and solution processability of organic SCs account for their advantages over more expensive inorganic solid-state SCs.[1033] LAPCs based on organic heterojunctions and active for proton reduction have utilized mostly Pt or MoS_x-type materials as the proton reduction catalysts; investigated a variety of interlayers (fullerenes, TiO_x) between the BHJ and the catalyst; and studied the impact of the material choice for the hole transport layer that interfaces the BHJ with the supporting conductive substrate.[716,717,721,1034−1036]

An example where a molecular catalyst has been immobilized on a "dark" (carbon cloth) electrode (**Co82**, Figure 22) and a BHJ blend photoelectrode for proton reduction is based on an azide-modified Co diimine-dioxime catalyst that was attached to an alkyne-containing fullerene component via "click" chemistry (Table 6, entry 16).[720] The alkyne-containing fullerene derivative is first blended with the light-absorbing polymer P3HT, and this mixture is deposited on an ITO electrode before a final surface functionalization with a cobalt diimine-dioxime HEC (P3HT:**Co82**) via a copper(I)-catalyzed cycloaddition reaction. In aqueous solution (pH 4.5), P3HT:**Co82** achieved a J_{ph} plateauing at ∼−3 μA cm^{-2} under illumination and E_{appl} of 0.17 V vs RHE. One possible reason for the low performance of the photocathode, especially when considering the much higher

DOI: 10.1021/acs.chemrev.8b00392
Chem. Rev. 2019, 119, 2752−2875

currents achieved with its dark carbon cloth counterpart (Table 1, entry 13), could be the small ET driving force (0.1 eV) that exists between the LUMO of the fullerene and the potential required to reduce the HEC to its catalytically active Co^+ oxidation state.

7.2.8. Hydrogenase-Based Systems. Contrasting with the DSPC systems where no example of coimmobilized H_2ase and dyes has yet been reported for H_2 evolution, there are a few studies demonstrating the immobilization of H_2ase on narrow-bandgap semiconductor photocathodes.[525,713,714,1037]

[NiFeSe]-H_2ase isolated from *Desulfomicrobium baculatum* was successfully interfaced on different Si|TiO_2 photoelectrodes, where titania acts as an immobilization scaffold and shuttles electrons from the Si to the H_2ases. These examples differ in the kind of TiO_2 architecture employed, varying between planar,[713] mesoporous,[525] and hierarchical IO scaffolds.[714] The increases in effective surface area resulted in progressively superior loading of H_2ase accompanied by improved photocatalytic performances. In the case of planar TiO_2, deposited on Si from a $TiCl_4$ solution, the E_{onset} of J_{ph} was found to be around 0.25 V vs RHE and a FE_{H2} of 95% after 1 h of CPPE in aqueous MES solution was obtained (pH 6.0, Table 6, entry 17). Although limited ($J_{ph} \approx 4\ \mu A\ cm^{-2}$), the activity of H_2ase was clearly demonstrated by adding the enzyme inhibitor CO into the media of experiment, which resulted in a lower activity from the photocathode due to the inhibition of the H_2ase.[822] Replacing the planar TiO_2 by a mesoporous layer resulted in a Si|mesoTiO_2|H_2ase photocathode displaying higher photocurrents ($\sim -90\ \mu A\ cm^{-2}$) under CPPE at 0.0 V vs RHE and a FE_{H2} around 70% (Table 6, entry 18).[525] The lower FE_{H2} was attributed to a nonoptimal coverage from the H_2ase due to an inefficient penetration depth of the (large footprint) enzyme and the presence of trapped O_2 in the pores. Subsequent replacement of the mesoporous layer of TiO_2 by a high porosity IO-TiO_2 layer deposited on ALD-TiO_2-coated Si electrodes afforded Si|IO-TiO_2|H_2ase photocathodes. These electrodes allowed a loading of H_2ase 3-fold greater than those based on mesoporous TiO_2, and delivered high J_{ph} ($\sim -690\ \mu A\ cm^{-2}$) during CPPE experiments conducted at 0.0 V vs RHE at pH 6.0 (Table 6, entry 19).[714] These results highlight the importance of ALD coating to stabilize Si from passivation, and of porous IO-TiO_2 to increase the loading of the large enzymatic catalyst on the electrode.

[FeFe]-H_2ase isolated from *Clostridium acetobutylicum* has also been used in combination with nanoporous "black" silicon electrodes. Black silicon permits a superior entrapment of enzymes compared to planar Si electrodes thanks to its 250 nm pore size structure.[1037] The black-Si|[FeFe]-H_2ase photocathode achieved a TON_{H2} of $\sim 10^7$ after 5 h of CPPE at 0.1 V vs RHE (pH 6.8) under 0.1 Sun irradiation (Table 6, entry 20). The low irradiation level was found to be necessary in order to maintain the electrode stability, while the low FE_{H2} of 33% was accounted for by the enzyme migration out of the pores, highlighting the limitation of the physisorbtion strategy to attach catalysts.

7.3. CO_2 Reduction

Progress in the assembly of LAPCs with immobilized 3d transition metal complexes for CO_2 reduction lags far behind that of proton-reducing photocathodes. The most efficient and well-studied molecular CRCs are based on precious metals such as Re and Rh, and only a handful of examples where such precious metal complexes have been coupled with p-SCs (Cu_2O, GaP, InP) to construct photocathodes operating in a variety of organic or purely aqueous conditions exist.[1007,1038−1042] Although previous works had coupled 3d transition metal CRCs to Si photoelectrodes in homogeneous solution, to the best of our knowledge no successful immobilized example where CO_2 reduction products are detected has yet been reported.[1043−1045]

7.4. Conclusion and Outlook

As for the DSPC systems described in section 6, the number of examples of 3d transition metal catalysts immobilized on light-absorbing semiconductors to construct LAPCs for solar fuel generation under aqueous conditions remains sparse. Perhaps the biggest hurdle facing development is the search for light-absorbing p-type semiconductors that are stable in water. Indeed, none of the LAPCs utilized to date are inherently stable and have therefore either been operated under extreme pH conditions where corrosion is less likely or have been decorated with a protection layer to prevent direct exposure to the electrolyte solution. Protection layer strategies included ALD-layering of MO_x, the deposition of mesoporous TiO_2 films, and integration of polymer scaffolds. Nevertheless, most reports do not discuss the stability of the photocathodes beyond 1 h (Table 6), rendering a fair assessment of the true stability of the semiconductor and any overlaying protection layer difficult. Inspiration from successful low-cost photovoltaic materials can be considered, with a few reports demonstrating photocatalytic H_2 evolution with BHJ[716,1034] or lead-halide perovskite[1046,1047] systems, although these technologies still require encapsulation or protection layers to isolate water-sensitive components (e.g., poly(3,4-ethylenedioxythiophene) polystyrene sulfonate or perovskite).

In contrast to DSPCs, where the majority of molecular species (photosensitizers and catalysts alike) were immobilized on the semiconducting substrate by acidic moieties (usually phosphonic or carboxylic), polymeric architectures have been more commonly exploited to immobilize catalysts in constructing LAPCs. Immobilized cobaloximes and DuBois Ni catalysts have again been the preferred choice for most systems, and analogous anchoring strategies could be employed to couple other HECs. There remains a need to report photocathode performances with more rigor and standardization, especially in terms of long-term capabilities, as well as more explicit discussion of molecular integrity during catalysis.

8. BEYOND H_2 AND C_1 CHEMISTRY

The use of alternative and sustainable energy sources, as well as the design of more energy efficient processes, is crucial for the future development of the chemical industry, and an attractive option is the use of abundant sunlight for promoting chemical transformations. The application of light-induced chemical reactions in an industrial setup was introduced in the late 1940s, with the use of light-promoted free radical chain reactions for photochlorinations of organic molecules.[1048] This work was followed by a variety of large-scale light-driven industrial applications, such as the sulfochlorination of paraffins, and bleaching of textiles and paper.[1049] Preparative photochemistry has also found use in industry by the synthesis of vitamin D, caprolactam, and lauryl lactam (monomer for the preparation of Nylon 12), among others.[1050] More recently, a strategy for using sunlight to remediate environmental pollution has been developed. Pesticides are a major source of water contamination and have been treated by light-induced catalytic oxidation reactions.[1051]

DOI: 10.1021/acs.chemrev.8b00392
Chem. Rev. 2019, 119, 2752−2875

Nevertheless, the focus remains on photopolymerization reactions, e.g., in coatings and paints in the automative industry, textile printing, photocuring of inks, and 3D printing technologies.[1052] Despite the variety of light-induced reactions used in industrial environments, they are usually not catalytic. Thus, these processes often lead to the formation of large quantities of chemical waste, which is a major cause of environmental pollution. More research will therefore be required to achieve commercial, large-scale photocatalytic processes. This would allow for the preparation of large amounts of indispensable commodities such as bulk and fine chemicals, in addition to fuel synthesis using sunlight as an energy source without the formation of vast amounts of waste. Molecular-based reductive chemical transformations with potential for industrial applications beyond H_2 evolution and the two-electron reduction of CO_2 are reviewed and discussed in this section.

8.1. Reduction of CO_2 to Hydrocarbon Fuels

Hydrocarbon fuels are considered the most important energy source of the last century, which can be ascribed to their abundance, high energy density, and ease of transportation. Current research efforts focus on the synthesis of renewable hydrocarbons from the greenhouse gas CO_2 to replace fossil-derived liquid fuels.[1053] In recent years, extensive research has been carried out in investigating novel CO_2 reduction catalysts, especially in finding systems capable of reducing CO_2 beyond CO and formate to higher hydrocarbons or oxygenates. Only a few catalysts have been shown to catalyze such conversions and are briefly discussed here.

A cobalt tetrahydroxyphenyl porphyrin (**Co123**, Figure 65) was used together with graphene as a charge transfer mediator, giving a photocatalyst with an outstanding photostability. This hybrid system was applied in the reduction of CO_2 to acetylene (C_2H_2) and CH_4 with rates of 113 and 57 μmol m^{-2} h^{-1}, respectively (calculated per surface area of the composite).[1054] Similarly, a cobalt protoporphyrin catalyst (**Co124**, Figure 65) was immobilized on pyrolytic graphite electrodes for electroreduction of CO_2 in aqueous media. Despite screening various different conditions, CO remained the main product, whereas CH_4 and CH_3OH were obtained only as byproducts.[790] When heterogenized on commercially available polytetrafluoroethylene-treated carbon fiber paper, a copper porphyrin (**Cu16**, Figure 65) electroreduces CO_2 at E_{appl} = −0.98 V vs RHE in water to yield methane and ethylene as major reduction products with TOFs of 4.3 and 1.8 molecules $site^{-1}$ s^{-1} for CH_4 and C_2H_4, respectively (FE of 44% for hydrocarbon formation). In addition to the redox cycling of the copper center, the hydroxyl groups in the periphery of the porphyrin ligand play a major role in selective formation of hydrocarbons.[1055]

More recently, an iron TPP complex (**Fe19**, section 2.3.5.1) functionalized with tetramethylammonium groups was demonstrated to photocatalytically reduce CO_2 to CH_4 with an Ir-dye (**PS2**, Figure 7) and TEA as a SED. The highest TONs were achieved when TFE was added as a proton source to give TON_{CO} = 367 (selectivity = 78%), TON_{CH4} = 79 (selectivity = 17%), and TON_{H2} = 26 (selectivity = 5%) after 102 h of irradiation. In this system, CH_4 is formed via a multistep reaction. CO_2 is first reduced to CO, and subsequently the CO formed is further reduced to yield CH_4.[420]

Recent studies have elucidated the great potential of transition metal catalysts in photo- and electrochemical reduction of the greenhouse gas CO_2 to useful multielectron reduction products.

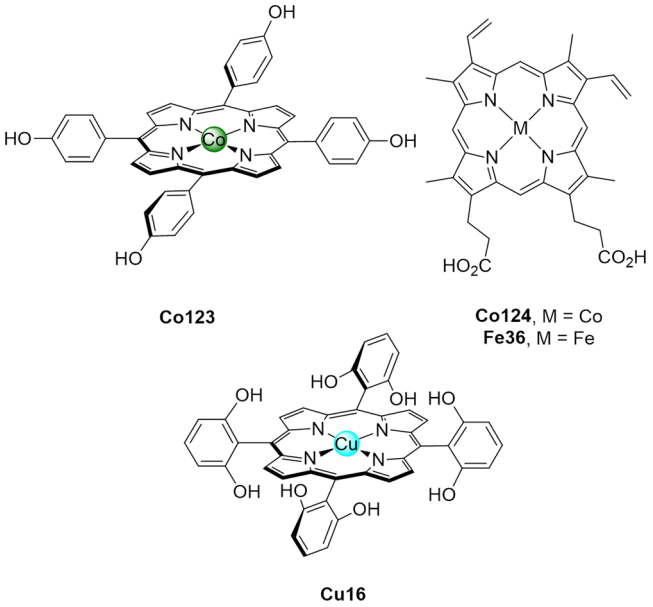

Figure 65. Molecular catalysts that transform CO_2 to highly reduced hydrocarbon products.

Despite the milestones achieved by transition metal porphyrin complexes above, little insight remains into mechanistic details, and there appears to be substantial scope for the development of novel catalysts.

8.2. Reductive Organic Transformations

The use of sunlight and renewable electricity for driving organic reactions, and thus obtaining value-added molecules, is desirable in the context of sustainable synthesis. Artificial photosynthetic systems are of special interest, as they can perform a variety of reductive organic transformations by using sunlight as an energy source. However, most studies focus on H_2 formation or CO_2 reduction. While limited progress has been made in the application of these systems to reductive chemistry for synthesis, recent literature illustrates the use of photocatalytic hybrid systems for reductive organic transformations.[922,1056−1058]

8.2.1. Reduction of Alkenes. The reduction of C═C double bonds presents a possibility to "store" hydrogen in organic molecules, and therefore resembles enzymatic hydrogen fixation in NADH. The reduction of double bonds in organic molecules has been achieved using enzyme-SC hybrid systems.[577,1059] Enzymes are highly selective catalysts, and a variety of such biocatalysts are commercially available and have already been used for industrial applications.[1060]

A hybrid system consisting of the enzyme fumarate reductase (FccA) and Ru-dye (**PS19**) sensitized TiO_2 nanoparticles reduced fumarate to succinate (Scheme 1a) with MES as a SED, giving a TON of 5800 and TOF of 0.4 s^{-1} after 4 h irradiation.[1059] A photosynthetic cycle was realized with a PEC cell consisting of a water-oxidizing $BiVO_4$ photoanode wired to a mesoITO cathode modified with FccA, which gave a solar-to-succinate efficiency of 0.03% with a TOF of 0.01 s^{-1}.[1059] A photocatalytic system using carbon nanodots as PSs and FccA photoproduced succinate (Scheme 1a) in an aqueous EDTA solution, with a TOF of ∼1700 mol succinate (mol FccA) $^{-1}$ h^{-1} and a TON of ∼6000.[577] A further example of an enzymatic hybrid used the MoFe-protein subunit of N_2ase (see section 8.3.1). The latter was modified with a $[Ru(bpy)_2(phen\text{-}R)]^{2+}$ derivative as a PS to photoreduce acetylene to ethylene (Scheme

DOI: 10.1021/acs.chemrev.8b00392
Chem. Rev. 2019, 119, 2752−2875

1b) without hydrolysis of adenosine triphosphate (ATP) (the native energy source for N_2ase activity), displaying a QY < 1%.[1061]

Scheme 1. Catalytic Reactions Leading to the Reduction of Carbon−Carbon Multiple Bonds

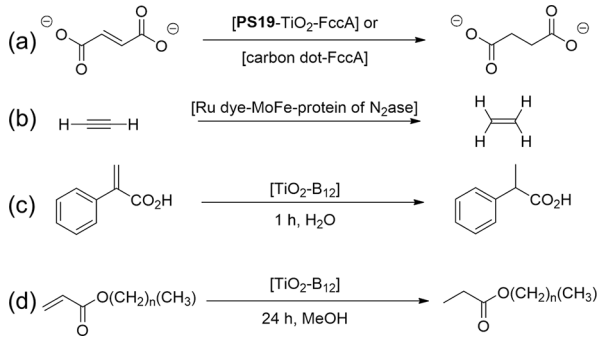

In addition to enzymatic systems, a photocatalytic hybrid with the vitamin B_{12} analogue cyanoaquacobyrinic acid (**Co125**, Figure 66) immobilized on TiO_2 reduces styrene derivates and alkylacrylates (Scheme 1c,d). UV bandgap excitation of TiO_2 induces the reduction of Co^{3+} to Co^{+}, which reacts to form a cobalt(III)-hydride with radical character. Mechanistic studies suggest that this cobalt(III)-hydride species acts as the active catalyst for the reduction of C═C double bonds in the reactions presented in Figure 66, with a TOF up to 100 h^{-1}.[1062]

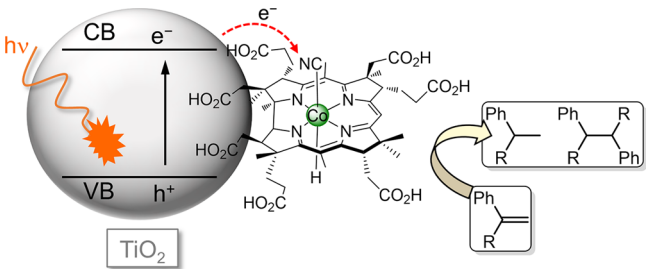

Figure 66. Photoreduction of styrene derivatives (via metal-hydride formation) with TiO_2-**Co125**.

8.2.2. Reductive Dehalogenation. Organohalides are a widespread class of compounds being used in a large variety of industrial processes. This can be attributed to the versatility of these molecules, which find their main applications as solvents for large-scale industrial processes, agrochemicals, and pesticides. Large amounts of these compounds are produced and to some extent released as waste products into the environment.[1063] In order to remediate groundwater and soils contaminated with toxic organohalides, cost- and energy-efficient dehalogenation reactions are under development. The photo- and electrocatalytic reduction of organohalides is a challenging catalytic reaction to achieve, due to the high potentials required for dehalogenation, especially of organochlorides.[1064]

The hybrid system consisting of **Co125** immobilized onto TiO_2 discussed above (Figure 66) has also been studied as a photocatalyst for the reduction of a variety of organohalides. Dehalogenation reactions promoted by **Co125** proceed under mild conditions, via nucleophilic attack of a reactive cobalt(I) intermediate on the organohalide species. This can be attributed to the lower potential required for the formation of the reactive Co^{+} intermediate as compared to the potential required for a direct dehalogenation.[1065] The TiO_2-**Co125** hybrid is capable of reducing organobromides and organochlorides (e.g., the pesticide DDT; Scheme 2). Mechanistic studies have supported a nucleophilic attack of the photogenerated Co^{+} species on the respective organohalide, leading to the desired dehalogenation reaction.

Different reactivity and selectivity have been described when using different crystal phases of TiO_2 for the reduction of bromoethylbenzene. Anatase displayed a higher reactivity (presumably due to ∼0.2 eV more driving force for photogeneration of Co^{+}), whereas rutile led to a more selective product formation assigned to more stable immobilization of **Co125**.[1066] To facilitate workup, the TiO_2-**Co125** hybrid system was immobilized on a glass plate, which allows for a possible use in wastewater purification systems.[1067] The Fe^{3+} protoporphyrin hemin (**Fe36**, Figure 65) and a Co^{3+} porphyrin (**Co53**, Section 2.3.6.1) were also immobilized on mesoTiO_2 films for the reductive dehalogenation of CCl_4 and $CHCl_3$.[1068]

8.2.3. Reduction of Carbonyl Derivatives. The reduction of carbonyl derivatives such as amides, imines, ketones, aldehydes, or esters plays an important role in the chemical industry as well as in research laboratories. Classical methods use stoichiometric amounts of reducing agents, such as $NaBH_4$, $LiAlH_4$, or SmI_2, resulting in a large volume of chemical waste. Catalytic hydrogenation reactions would be more atom-economic and sustainable, in particular if the hydrogen is sourced from water. Despite the benefits of using a catalytic process, most homogeneous hydrogenation catalysts are based

Scheme 2. Product Distribution of Dehalogenation Reactions with Co125 (B12)

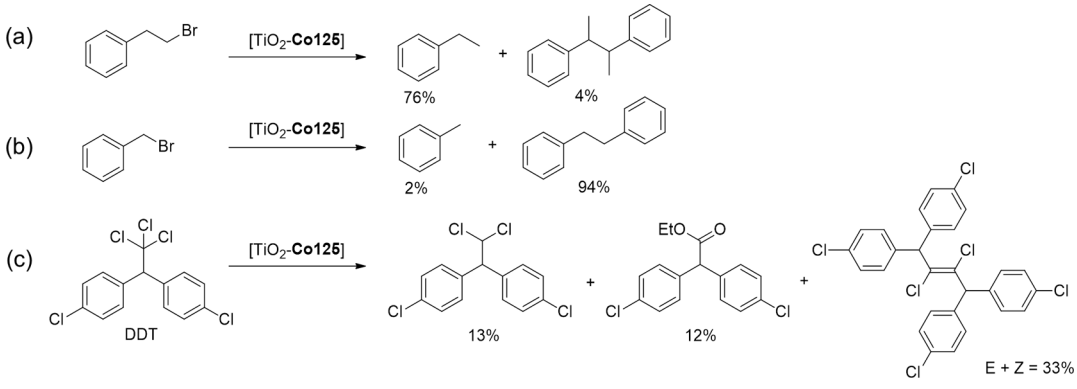

DOI: 10.1021/acs.chemrev.8b00392
Chem. Rev. 2019, 119, 2752−2875

Scheme 3. Possible Products in the Reduction of Amides with H_2

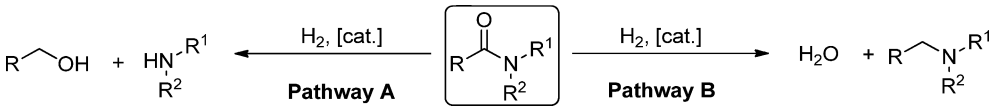

on precious metal compounds, especially in industrial processes. Thus, the development of inexpensive transition metal catalysts for hydrogenation reactions is a requirement for cheaper and less wasteful processes.[1069−1072]

Hydrogenation of amides to the respective amines can proceed via two different pathways. In pathway A (Scheme 3) the C−N bond is broken to yield an alcohol and amine, whereas in pathway B the C═O bond is broken to generate a higher amine and water (Scheme 3).[1073] Fe-PNP and Mn-NNP pincer complexes (**Fe37** and **Mn31**, Figure 67) have been shown to reduce amides under high pressure of H_2 via pathway A (Scheme 4a), in conversion yields up to 99%.[1074−1077]

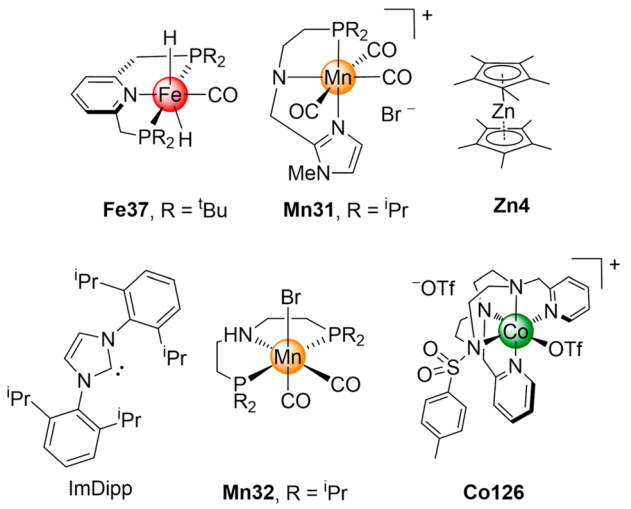

Figure 67. Structures of catalysts used for the hydrogenation of amides or aldehydes/ketones.

Scheme 4. Reaction Conditions for the Catalytic Reduction of Amides and Imines

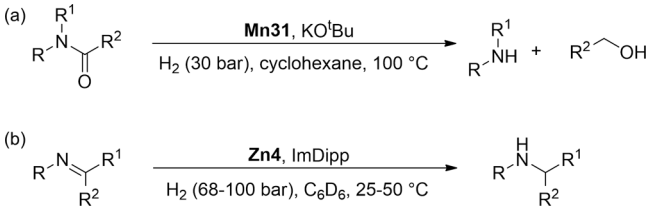

Hydrogenation of imines to the respective amines (Scheme 4b) was demonstrated using decamethyl zincocene and different NHCs, presumably forming frustrated Lewis pairs as the active catalysts. The most reactive combination used 1,3-bis(2,6-diisopropylphenyl)-imidazol-2-ylidene (ImDipp, together with **Zn4**, Figure 67), identified via NMR spectroscopic screening.[1078] Examples based on Co and Fe PNP pincer complexes that efficiently perform this reaction and closely related reductive transformations have also been reported.[1079,1080]

The reduction of activated esters using Fe-PNP catalysts such as **Fe37** affords the respective primary alcohols in high yields (Scheme 5).[1081] A variety of related Mn-,[1082,1083] Fe-,[1084,1085] and Co-PNP[1086,1087] catalysts can also perform reduction of esters to alcohols.

Scheme 5. Reduction of Esters by Iron Catalyst Fe37

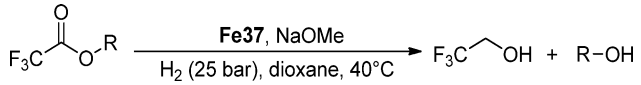

The selective reduction of aldehydes to primary alcohols using H_2 has been achieved with a variety of iron and manganese PNP catalysts, such as with **Mn32** (Figure 67, Scheme 6), which displays TOFs up to 20 000 h^{-1}.[1088] Moreover, these catalysts showed good functional-group tolerance, and selective reduction of aldehydes and ketones was achieved despite the presence of other reducible groups, such as esters, alkynes, and olefins.[1088−1092]

Scheme 6. Reduction of Aldehydes and Ketones by Complex Mn32

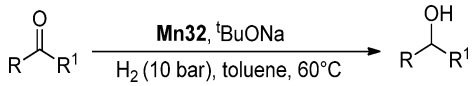

This section has shown a selection of 3d transition metal catalysts for the reduction of a variety of carbonyl derivatives, such as amides, imines, esters, aldehydes, and ketones, which yield commercially valuable chemicals. Nevertheless, H_2 is used as a reducing reagent in all these cases, which is usually sourced from steam reforming and requires operation under high pressures. The development of electrocatalytic, photocatalytic, or PEC processes that use electricity and/or sunlight to hydrogenate organic substrates directly from water would be a safer and more sustainable approach to organic synthesis. In this regard, photocatalytic reduction of aldehydes and aromatic ketones has been demonstrated using visible light with a copper dye (**PS7**, Figure 7) and a cobalt-based molecular catalyst (**Co126**, Figure 67) in predominantly aqueous media (Scheme 7).[1058]

Scheme 7. Photocatalytic Aldehyde and Ketone Reduction Mediated by PS7 and Co126

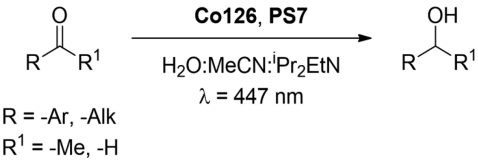

8.2.4. NADH-Mediated Reduction Reactions. Molecular hydrogenation catalysts often display low chemo- and stereoselectivity, which is a limitation for applications in the pharmaceutical and chemical industry.[1093] However, enzymes are known for their notoriously high chemo- and stereoselectivities and have been increasingly applied as biocatalysts for industrial processes. Oxidoreductases are an enzyme class

DOI: 10.1021/acs.chemrev.8b00392
Chem. Rev. 2019, 119, 2752−2875

capable of reducing a variety of carboxylic acid derivatives, such as ketones, aldehydes, and imines, without using molecular hydrogen as a reducing reagent.[1094] Instead of molecular hydrogen, oxidoreductases use hydride transfer reagents such as nicotinamide adenine dinucleotide (NAD^+) cofactors to achieve high conversions. The drawback of using these cofactors as stoichiometric reductants is their expense, leading to very costly processes when oxidoreductases are applied as biocatalysts. Coupling reduction processes catalyzed by oxidoreductases with an NAD^+/NADH (Figure 68) recycling system is thus desirable, as it may allow for application of these procedures.

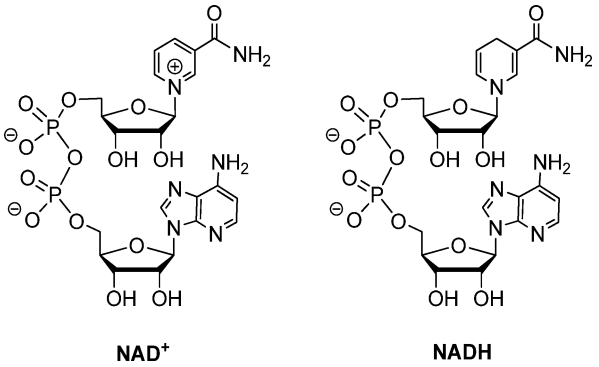

Figure 68. Structures of NAD^+ and NADH cofactors.

An enzymatic system for the reduction of acetophenone to phenylalcohol coupled with the recycling of NADH has been developed, with an alcohol dehydrogenase and NAD^+-reductase coimmobilized on carbon beads (Figure 69).[1095] In order to obtain the electrons required for NADH recycling from H_2, a H_2ase was coimmobilized on the carbon particle. The role of the H_2ase is the oxidation of H_2 and the transfer of electrons to the enzyme NAD^+-reductase, leading to reduction of NAD^+ to NADH. The NADH can be used in a subsequent reduction by the coimmobilized NADH-dependent alcohol dehydrogenase to reduce acetophenone to phenylalcohol (Figure 69). The mild conditions and high TONs (>130 000 per NAD^+) of this system make it attractive for commercial development.[1095]

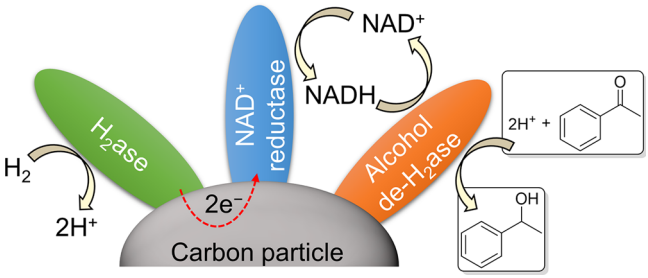

Figure 69. Reaction cascade through coimmobilized enzymes.

A similar approach has been used for the reduction of prochiral pyruvate to (*S*)-lactate. In this study, the NAD^+ reducing subunit (HoxFU) from *Ralstonia eutropha* and a H_2ase were coimmobilized on pyrolytic graphite particles. A lactate dehydrogenase was then introduced into the medium, resulting in a cascade reaction that couples H_2-driven NADH-regeneration with the reduction of the organic substrate.[1096]

Light-induced regeneration of NADH coupled with the enzymatic reduction of α-ketoglutarate to L-glutamate was shown with Eosin Y (**PS3**, Figure 7). **PS3** transfers electrons to an organometallic mediator $[Cp^*Rh(bpy)(H_2O)]^{2+}$ ($Cp^* = C_5Me_5$) upon irradiation and is regenerated by using TEOA as a SED (Figure 70).[1097]

This section has shown examples for reductive organic transformations mediated by molecular catalysts and enzymes. These organic transformations are of importance for a variety of commercial processes, in the chemical, agrochemical, and pharmaceutical industries. Hence, establishing photo- and especially PEC systems that can achieve these reactions is a great challenge for the future of chemical research in an academic and industrial environment. Achieving the large-scale preparation of important synthons and fine chemicals by using abundant sunlight as an energy source will allow a reduction of the energy costs for these processes, and avoid the use of fossil fuels.

8.3. Reduction of Molecular Nitrogen

The Earth's atmosphere consists of 78% N_2, rendering it a vastly abundant and universally available feedstock for the synthesis of chemicals, fertilizers, and fuels. Biosynthetic processes fix the stable and inert N_2 (bond enthalpy of −945 kJ mol^{-1}) to produce NH_3 with N_2ases that require 16 equivalents of ATP to produce two molecules of NH_3 and one of H_2 (Scheme 8).[1098]

Nowadays, 50% of worldwide N_2 conversion into NH_3 occurs by the Haber−Bosch process (Scheme 8), which accounts for about 2% of world energy consumption and contributes 1.5% to anthropogenic global CO_2 emissions.[1099] This process utilizes N_2 and H_2 over Fe or Ru catalysts, with the large energy demand resulting from the high temperatures (~450 °C) and pressures (150−300 bar) required to overcome the kinetic barriers of this exothermic reaction.[1100,1101] Thus, the Haber−Bosch process remains energy intensive but immensely important for securing nutrition for the growing world population through fertilizer production.[1102−1104] Sustainable N_2 fixation, in particular in a decentralized and off-grid setup, has massive potential to transform agriculture in developing countries.

8.3.1. N_2 Fixation by Nitrogenases. N_2ases can be subdivided into three different categories depending on their cofactor composition. These enzymes possess either a Mo-dependent cofactor (FeMo-co), a V-dependent cofactor (VFe-co), or an all-iron cofactor (FeFe-co).[1098] Of these, the Mo-dependent N_2ase has been most intensely studied and consists of a reducing (Fe protein) and a catalytic domain (MoFe protein). Due to the high price of ATP, it is desirable to find a substitute energy source or a recycling system for ATP, which would allow for the rational design of N_2ase-based N_2 reduction systems with lower energy demands.[1105,1106]

Semiartificial N_2 reduction systems have been constructed. These systems use heterogenized N_2ase enzymes, under either electro- or photocatalytic conditions. Sacrificial photocatalytic N_2 reduction was attained with the MoFe protein (the catalytic domain of the Mo dependent N_2ase) adsorbed on CdS nanorods, leading to ATP-free, light-driven N_2 reduction with a TOF_{NH3} of 75 min^{-1} and QY_{NH3} of 3.3% (Figure 71). This performance corresponds to 63% of the efficiency achieved by the ATP-coupled biological process, and the QD-protein hybrid system continues to fix N_2 even after an illumination time of 5 h.[1107]

A bioelectrochemical ammonia fuel cell consisting of a N_2ase cathodic compartment and a H_2ase anodic compartment

DOI: 10.1021/acs.chemrev.8b00392
Chem. Rev. 2019, 119, 2752−2875

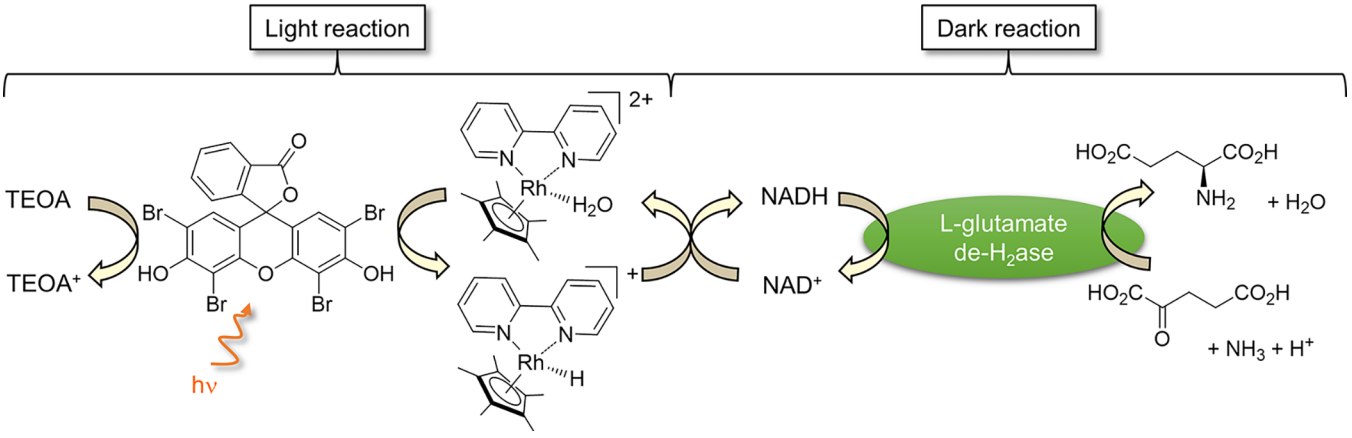

Figure 70. Artificial photosynthetic system for the enzyme-free light-induced regeneration of NADH coupled to enzymatic reduction of glutamate to α-ketoglutarate.

Scheme 8. Reduction of N_2, via Haber–Bosch Process and Natural Process

N_2 (g) + 6H$^+$ ⟶ 2NH_3 (aq) $E°$ = +0.09 V (vs NHE)

Haber-Bosch process:

$N_2 + 3H_2 \xrightarrow{[Fe/Ru]} 2NH_3$

Natural process:

$N_2 + 10H^+ + 8e^- + 16ATP \xrightarrow{[N_2ase]} 2NH_4^+ + 2H_2 + 16ADP + 16P_i$

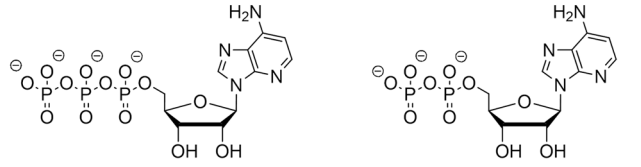

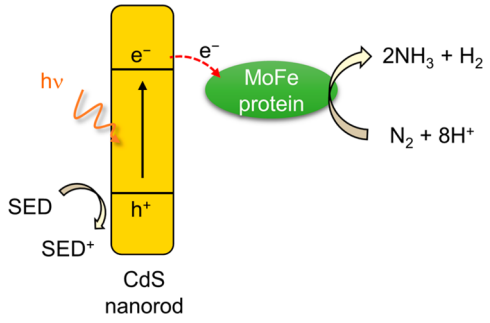

Figure 71. Reduction of N_2 by CdS-MoFe protein hybrid system.

separated by a proton exchange membrane (PEM) with MV acting as an electron shuttle achieves Haber–Bosch chemistry (Figure 72). It was first demonstrated that the use of electrochemically generated $MV^{\bullet+}$ could drive N_2 reduction by the N_2ase, with a FE_{NH3} of 59%. The full system operates at ambient temperature and pressure, and can produce electric current and ammonia simultaneously but still requires ATP hydrolysis for the successful N_2 reduction process.[1108,1109]

These enzymatic hybrid systems show the potential of using sustainable conditions for the reduction of N_2 but still require fragile enzyme constructs, toxic materials such as CdS, stoichiometric reagents such as SEDs or energy equivalents in

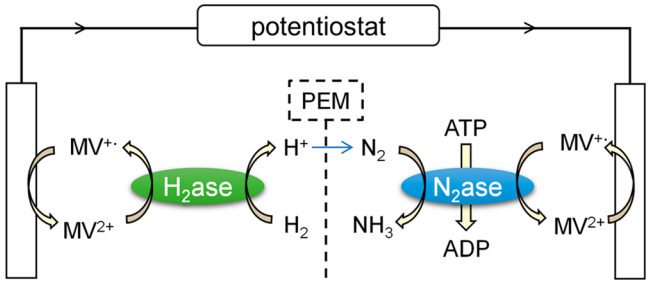

Figure 72. Enzymatic fuel cell for the reduction of N_2 to ammonia.

the form of ATP. Nevertheless, they provide a blueprint for transition metal-catalyzed systems once such suitable catalysts become available.

8.3.2. Reduction of N_2 Using Transition Metal Complexes. A family of low valent iron complexes with tripodal ligands have been used as model complexes for the N_2ase FeMo-co. A tetradentate ligand system with general formula P_3^R was used, in which three phosphine donors are bound through an *ortho*-phenylene linker to a central atom (Figure 73, Z = boron in **Fe38**, with Z = carbon or silicon also being reported). All three iron complexes afforded catalytic amounts of NH_3 at temperatures of −78 °C when using an excess of strong reductants and strong acids, such as KC_8 and $HBAr^F_4{\cdot}2Et_2O$, respectively.[1110−1112] Studies in which reactive intermediates have been isolated and characterized are consistent with a Chatt-type mechanism involving a single isolated metal center.[1113,1114] Moreover, DFT studies carried out on this model system have identified a variety of intermediates that have not been observed experimentally and support a mononuclear asymmetric pathway for the reduction of N_2.[1115] An improvement of this catalytic system has been achieved by using milder reductants (Cp^*_2Co) and weaker acids ($[Ph_2NH_2][OTf]$ or $[PhNH_3][OTf]$; Figure 73), which allowed a PCET pathway to proceed.[1110−1114] The highest TON_{NH3} was 84 per Fe atom.[1116]

A variety of mono- and polynuclear iron complexes with N_2ase and H_2ase inspired structures and various types of ligands have also been applied as N_2 reduction catalysts which operature through different mechanisms.[1117−1120] The reduction of N_2 to NH_3 with complex **$Fe_2$47** (Figure 74) as a catalyst has been achieved by using $HBAr^F_4$ as a proton source and KC_8 as a reductant under irradiation with a mercury lamp, leading to the

DOI: 10.1021/acs.chemrev.8b00392
Chem. Rev. 2019, 119, 2752−2875

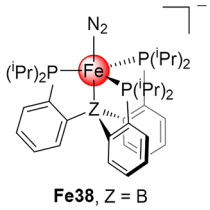

Fe38, Z = B

N_2 + [PhNH$_2$][OTf] + Cp*$_2$Co —**Fe38**, Et_2O, −196 → −78 °C→ NH_3

Figure 73. Structure of iron complex **Fe38** used as a N_2 reduction catalyst and general conditions used for the reduction of N_2 to ammonia catalyzed by this complex.

formation of up to 67 equivalents of NH_3 under optimized conditions (Scheme 9a).[1121] The iron PNP complex **Fe39** (Figure 74) can also catalytically reduce N_2 to ammonia and hydrazine. Since hydrazine is a known intermediate in the N_2ase-catalyzed biological nitrogen reduction process, such an analogous synthetic process could aid in understanding of the biological mechanism. When using almost 200 equivalents of both KC_8 as a reductant and $[H(OEt_2)_2][BAr^F{}_4]$ as a proton source, reduction of N_2 was achieved with up to 14.3 equivalents of ammonia and 1.8 equivalents of hydrazine produced per iron center (Scheme 9b).[1122]

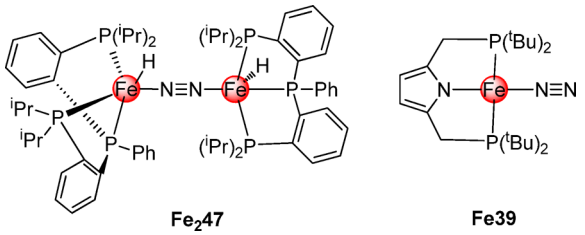

Fe$_2$47 **Fe39**

Figure 74. Iron complexes applied in the catalytic reduction of dinitrogen.

Scheme 9. Reaction Conditions Used for the Catalytic Reduction of N_2 with Iron Complexes

(a) N_2 + [H(OEt$_2$)$_2$][BAr$^F{}_4$] + KC_8 —**Fe$_2$47**, Et_2O, −78°C, 1 h, Hg lamp→ NH_3

(b) N_2 + [H(OEt$_2$)$_2$][BAr$^F{}_4$] + KC_8 —**Fe39**, Et_2O, −78°C, 1 h→ NH_3 + N_2H_4

The examples detailed above use an iron center for the reduction of N_2, which can be ascribed to the presence of iron in the active center of N_2ases, as well as in the solid-state catalyst used for the Haber−Bosch process. Despite the advantages of using iron catalysts, most of the compounds described are air and moisture sensitive and therefore have to be handled under the rigorous exclusion of O_2 and water. The use of these complexes requires special equipment which makes large-scale synthesis and storage challenging and limits their application to laboratory scale reactions.

Titanium-based molecular complexes have also been investigated as Earth-abundant molecular catalysts for N_2 reduction. Early reports date back over 50 years and suggested that organometallic titanium complexes such as titanocene derivatives show significant promise.[1123] Further studies have shown that the activity of titanocene dichloride (**Ti1**, section 2.2.1) can be improved by using a variety of alkali metals as reductants.[1124] Mechanistic studies have corroborated a reactive titanium dimer (**Ti$_2$1**, Scheme 10) as an intermediate in the nitrogen reduction process. This dimer is in equilibrium with the respective monomer, which can react with N_2 to give a Ti dinitrogen complex, thus promoting the reduction of the coordinated N_2 to ammonia.[1125,1126] Later studies reported an electrochemical system for the reduction of N_2 to ammonia, giving substoichiometric yields with **Ti1**. Optimized conditions included the use of a platinum WE operating at −2.2 V vs a Ag wire pseudoreference electrode, with **Ti1** in MeOH containing $LiClO_4$, catechol, and sodium methoxide ultimately giving a TON for NH_3 production of 0.015.[1127]

Molecular dinitrogen can be reduced to give ammonia, but it can also be reacted with a trimethylsilyl halide (Scheme 11) and an appropriate reductant to afford trimethylsilylamine N(Si(Me$_3$)$_3$), which is an alternative N_2 fixation route. Silylamine can either be hydrolyzed under acidic conditions to yield a quantitative amount of ammonia or used as a synthon in organic synthesis. An important application of silylamine is the fabrication of Si−N based polymers, which are applied in ceramic materials and SCs.[1128−1130] Thus, it would be of value to develop an industrial procedure for the synthesis of silylamine from N_2 under ambient conditions.

Scheme 11. Reaction Conditions Used for the Reduction of N_2 to Silyl Amine

(a) N_2 + 6 Na + 6 Me_3SiCl_3 —**Co$_2$3** + 2 eq bpy, DME, RT→ 2 N(SiMe$_3$)$_3$ + 6 NaCl, 49 eq

(b) N_2 + 6 Me_3SiCl_3 —**Co$_2$4**, KC_8, THF, RT→ 2 N(SiMe$_3$)$_3$ + 6 NaCl, 30 % yield

(c) N_2 + 6 Na + 6 Me_3SiCl_3 —**V$_2$1**, DME, RT→ 2 N(SiMe$_3$)$_3$ + 6 NaCl, 24 eq

The first catalytic formation of silylamine used Li^0 as a reductant, along with several transition metal salts as catalysts. However, this procedure yielded only small amounts of silylamine and the formation of lithium nitride intermediates (Li_3N) could not be ruled out.[1131] A variety of simple iron complexes and cobalt carbonyls were more recently applied as catalysts, with **Co$_2$3** yielding 49 equivalents of N(SiMe$_3$)$_3$ in the presence of bpy (Scheme 11a; Figure 75)[1132,1133] The binuclear cobalt complex **Co$_2$4** (Figure 75) has been reported as an active

Scheme 10. Proposed Mechanism for the Titanocene Mediated Reduction of Dinitrogen

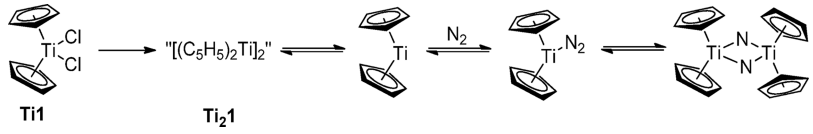

Ti1 **Ti$_2$1**

DOI: 10.1021/acs.chemrev.8b00392
Chem. Rev. 2019, 119, 2752−2875

catalyst for the formation of $N(SiMe_3)_3$ from N_2 when using 2000 equivalents of KC_8 as a reductant (Scheme 11b), displaying a final turnover rate of 200 min^{-1}. Mechanistic studies suggest that electronic stabilization of the catalytically active cobalt site by the adjacent cobalt center leads to an enhanced catalytic activity.[1134] The use of vanadium complex $\mathbf{V_21}$ (Figure 75) in the catalytic reduction of N_2 gave up to 24 equivalents of silylamine (Scheme 11c). This study is of importance for the N_2 reduction community, as no vanadium complex has previously been used to successfully promote the reduction of N_2, despite the existence of a vanadium-dependent N_2ase enzyme.[1135]

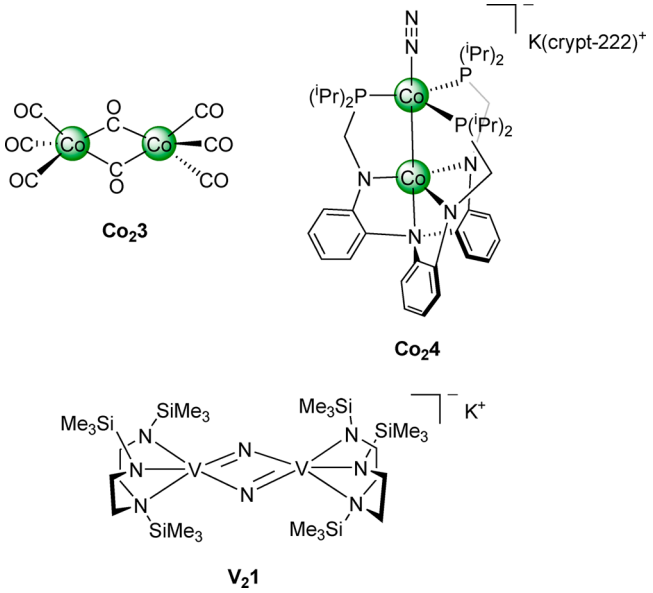

Figure 75. Structures of complexes applied for the catalytic reduction of N_2 to silyl amine.

Progress has been achieved in developing molecular first row transition metal catalysts for N_2 reduction, but the Haber–Bosch process remains the sole industrial route for NH_3 synthesis. The low yields of ammonia produced when using molecular catalysts in combination with the multistep syntheses and air- and moisture-sensitivity of such compounds currently makes their practical application very challenging. Nevertheless, using abundant sunlight as an energy source to drive N_2 fixation and alleviate global reliance on the Haber–Bosch process would be enormously beneficial, at the very least by diminishing fossil fuel usage and reducing CO_2 emissions. The combination of basic academic research with industrial expertise may allow for this milestone being achievable.

9. CONCLUSION

The development of molecular catalysts containing first row transition metals for electro- and solar fuel synthesis has experienced rapid progress during the past decade. Their immobilization onto electrodes, photoelectrodes, or SC-nanoparticle surfaces permits catalyst recycling and in-depth mechanistic studies by an ever-growing suite of techniques and, from a functional point of view, overcomes diffusional electron transfer kinetics; an important step toward efficient electrocatalysis and device integration. The selection of the catalyst, material, and anchoring strategy are critical to achieving the desired properties and performances in the resulting hybrid system.

The rational development of DuBois' Ni bis(diphosphine) catalyst stands out as a prototype H_2ase-inspired HEC and exemplifies what is achievable when the secondary coordination environment is successfully mimicked.[283,286] Immobilization of this 3d transition metal catalyst onto a CNT-based electrode displays reversible electrocatalysis (operation at the thermodynamic potential) that closely resembles the profile of Pt or immobilized H_2ase for H_2 evolution and oxidation.[726,732] Despite the recent progress in the development of synthetic CRCs and their immobilization onto electrodes,[23,25,1136] reversible electrocatalysis as observed with CO_2 reductases has yet to be achieved.[822,1137] The bioinspired design of CRCs may therefore focus on the integration of elaborated secondary proton relays and make use of multinuclear catalytic centers with suitable Lewis acids. Design principles of cooperative catalysis can also be adapted for heterogenized systems in future development, where "metal-material", instead of "metal–ligand"-assisted catalysis, can be envisioned.[1138,1139]

Immobilization of molecular catalysts onto SCs is an attractive approach to bridge the gap between fast photophysics and slow chemical catalysis. Thereby, a SC (or dye-sensitized SC) absorbs light and provides an efficient means to transfer multiple, low potential electrons to a coattached catalytic site on a suitable time scale. Since the demonstration of proton reduction with an immobilized cobaloxime on a dye-sensitized TiO_2 particle,[541] many examples have been reported for proton and CO_2 reduction in water.[538,870,910] Avoiding the use of SEDs in photodriven colloidal schemes remains a key objective, and a few demonstrations on coupling fuel synthesis with clean organic substrate oxidation have recently been reported.[843,847] Solar-driven H_2 production coupled to lignocellulose oxidation (valorization of "waste biomass") has also been accomplished with a carbon nitride photocatalyst in combination with a DuBois Ni catalyst.[1140]

Another approach is the integration of catalysts into PEC cells and coupling of the fuel-making photocathode with a suitable photoanode, thus segregating the two redox reactions of interest to two different surfaces and compartments.[757,952,1141,1142] Suitable attachment strategies allow for straightforward immobilization and the accurate determination of active sites and performance parameters, which is challenging in traditional heterogeneous catalysis. The lack of suitable photocathodes is a current challenge, with narrow-bandgap SCs often being prone to photocorrosion and wide-bandgap SCs such as NiO suffering from fast charge-recombination. A quickly expanding approach is the use of protection layers such as ALD-TiO_2 that encapsulate water-sensitive SCs. New approaches such as metallic encapsulation (shown for lead halide perovskites) or the deposition of single source precursors to protect fragile electrodes are in development.[560] As for wide-bandgap SC dye-sensitized photocathodes, alternatives to NiO such as $CuGaO_2$ and $CuCrO_2$ are being investigated.[926,969] Alternatively, new strategies involving molecular electrode design to enable the extraction of two-electrons[992] and donor–acceptor assemblies that allow the use of conductive scaffolds such as ITO as an electrode scaffold are being considered.[881,1143]

The fields of homogeneous and heterogeneous catalysis merge when studying immobilized molecular catalysts. Heterogenization of molecular catalysts ensures the grafting of "single-site" active centers that can be rigorously investigated and tuned. Nevertheless, anchoring of catalysts with an elaborate ligand

DOI: 10.1021/acs.chemrev.8b00392
Chem. Rev. 2019, 119, 2752–2875

scaffold also introduces fragility to the hybrid material and encouraging work is currently in progress to integrate defined catalyst scaffolds directly within the material structure.[1144] Promising examples of such single metal site catalysts involve graphite electrodes with porphyrin-like Fe-N_4 moieties and graphite-conjugated metal catalysts for CO_2 reduction.[1145−1147]

The lessons learned from the immobilization of molecular HECs and CRCs are valuable for a wide range of other photocatalytic reactions. The use of endothermic and multi-electron chemistry to achieve selective solar fuel synthesis is currently contrasted by the exothermic and single-electron chemistry of organic photoredox catalysis. We envision that solar fuel synthesis can effectively be coupled to solar-driven chemical oxidations, even if this would only produce a small amount of global fuel.[1148] In such a scenario, the main commercial value would most likely stem from the organic product and the fuel be considered as a byproduct. The solar-driven, direct hydrogenation of organic substrates from aqueous protons without intermediate H_2 generation is an emerging approach of artificial photosynthesis to drive organic reactions.[1058,1149] Another attractive prospect beyond reductive fuel synthesis is the production of ammonia from N_2. Although catalytically demanding, it is thermodynamically more facile than proton and most CO_2 reduction reactions, and could benefit from the high N_2 levels in the Earth's atmosphere. Using the above strategies of electro- and solar-driven chemistry based on first row transition metals has the potential to contribute in tackling the global challenges of the coming decades.

AUTHOR INFORMATION

Corresponding Author

*E-mail: reisner@ch.cam.ac.uk.

ORCID

Bertrand Reuillard: 0000-0002-9553-1773
Erwin Reisner: 0000-0002-7781-1616

Author Contributions

†K.E.D. and J.W. contributed equally.

Notes

The authors declare no competing financial interest.

Biographies

Kristian E. Dalle obtained a B.Sc. (Hon I) in chemistry at the University of Queensland, during which time he studied structural and catalytic models for phosphoesterases in the groups of Prof. Lawrence R. Gahan and Assoc. Prof. Ross P. McGeary. He then moved to Georg-August Universität Göttingen where he completed his Ph.D. in 2014 under the supervision of Prof. Franc Meyer, investigating activation of oxygen with pyrazole-supported binuclear copper complexes. Since 2015 he has been developing molecular catalysts for heterogeneous energy capture and storage applications in the group of Prof. Erwin Reisner at the University of Cambridge.

Julien Warnan studied organic chemistry at the Université de Nantes (France) where he obtained his Ph.D. in 2012 under the supervision of Dr. F. Odobel working on the synthesis of innovative dyes for applications in dye-sensitized solar cells. After developing semi-conducting polymers and organic solar cells as a postdoctoral researcher at King Abdullah University of Science and Technology (Saudi Arabia) he joined the group of Prof. Erwin Reisner at the University of Cambridge (U.K.) in 2014 as a postdoctoral associate. His current research is focused on the development of organic chromophores, polymeric systems, and hybrid photocathodes toward solar-driven fuel synthesis.

Jane J. Leung obtained her Bachelor of Science (Honours) degree in chemistry at the University of Auckland, New Zealand, under the supervision of Prof. David Williams, working on conducting polymer films with switchable surface properties. She joined the group of Prof. Erwin Reisner at the University of Cambridge as a Woolf Fisher Scholar in 2014 to conduct her Ph.D. studies. Her research focuses on the immobilization of molecular H_2 evolution and CO_2 reduction catalysts onto photoelectrodes towards hybrid systems active in aqueous solutions.

Bertrand Reuillard received his Ph.D. degree in 2014 from the Université de Grenoble Alpes, under the supervision of Dr. Alan Le Goff and Dr. Serge Cosnier, working on carbon nanotube based electrode surface modification for the efficient electronic wiring of redox enzymes. He then joined the group of Prof. Erwin Reisner in Cambridge in January 2015 for postdoctoral work with a focus on the immobilization of molecular or enzymatic electrocatalysts on electrode surfaces for energy conversion (solar fuels production). From February 2018, he has joined the group of Dr. Vincent Artero for the development of powerful noble metal-free, molecular based anodes for H_2-O_2 fuel cells.

Isabell S. Karmel graduated with her Ph.D. in 2015 from the Technion - Israel Institute of Technology. During her Ph.D. in the group of Prof. Moris S. Eisen she worked on the development of novel actinide coordination complexes and their application as catalysts for organic transformations. In 2015 she joined the group of Prof. Erwin Reisner as a postdoctoral researcher with a Blavatnik Fellowship. Her research in this period focused on the development of photo- and electrocatalysts for the reduction of dinitrogen to ammonia. Currently, Isabell works as a senior research scientist at Photocentric Ltd., where she leads the development of novel daylight resins for 3D printing.

Erwin Reisner received his education at the University of Vienna (Diploma in 2002, Ph.D. with Prof. Bernhard K. Keppler in 2005 and Habilitation in 2010). He worked as an Erwin Schrödinger postdoctoral fellow at the Massachusetts Institute of Technology with Prof. Stephen J. Lippard (2005−2007), followed by further postdoctoral research at the University of Oxford with Prof. Fraser A. Armstrong (2008−2009). He joined the University of Cambridge as a University Lecturer in the Department of Chemistry and as a Fellow of St. John's College in 2010. He became the head of the Christian Doppler Laboratory for Sustainable SynGas Chemistry in 2012, was appointed to Reader in 2015, and to his current position as Professor of Energy and Sustainability in 2017. His laboratory explores chemical biology, synthetic chemistry, materials science, and engineering relevant to the development of solar-driven chemistry for the sustainable synthesis of fuels and chemicals. As director of the UK Solar Fuels Network, he promotes and coordinates the national activities in artificial photosynthesis.

ACKNOWLEDGMENTS

The authors acknowledge the referees for helpful comments and the reviewing of this manuscript. Support by the Christian Doppler Research Association (Austrian Federal Ministry of Science, Research and Economy and National Foundation for Research, Technology and Development), the OMV Group, the Woolf Fisher Trust (New Zealand), the Cambridge Trust (University of Cambridge), the EPSRC (IAA Follow on Fund), the ERC Consolidator Grant "MatEnSAP" (682833), and a Blavatnik Fellowship is gratefully acknowledged.

DOI: 10.1021/acs.chemrev.8b00392
Chem. Rev. 2019, 119, 2752−2875

LIST OF ACRONYMS AND ABBREVIATIONS

A	geometrical electrode surface area (in cm^2)
AA	ascorbic acid
AcOH	acetic acid
ALD	atomic layer deposition
AM1.5G	air mass 1.5 global
ATP	adenosine triphosphate
β-CD	β-cyclodextrine
BHJ	bulk heterojunction
BIH	1,3-dimethyl-2-phenyl-2,3-dihydro-1*H*-benzo[*d*]-imidazole
BPG	basal-plane graphite
bdtc	3-carboxybenzene-1,2- dithiolate
bpy	2,2′-bipyridine
CB	conduction band
CNT	carbon nanotube
CODH	carbon monoxide dehydrogenase
COF	covalent organic framework
Cp*	1,2,3,4,5-pentamethylcyclopentadienyl
CPE	controlled potential electrolysis
CPPE	controlled potential photoelectrolysis
CRC	CO_2 reduction catalyst
CTAB	cetyltrimethylammonium bromide
CV	cyclic voltammetry
DCM	dichloromethane
DETA	diethylenetriamine
DFT	density functional theory
DHA	dehydroascorbic acid
DLS	dynamic light scattering
DMF	*N*,*N*-dimethylformamide
$dmgBF_2$	difluoroboryldimethylglyoximato anion
dmgH	dimethylglyoximato anion
$dmgH_2$	dimethylglyoxime
DMSO	dimethyl sulfoxide
DOPC	1,2-dioleoyl-*sn*-glycero-3-phosphocholine
DPP	diketopyrrolopyrrole
DSPC	dye-sensitized photocathode
DSP	dye-sensitized photocatalysis
DSSC	dye-sensitized solar cell
$E^{\circ\prime}$	formal potential under nonstandard conditions
E_{appl}	applied potential
E_{CB}	conduction band potential
E_{VB}	valence band potential
E_g	bandgap energy
E_{onset}	catalysis onset potential
EDTA	ethylenediaminetetraacetic acid
EDX	energy-dispersive X-ray
EPG	edge-plane graphite
EPR	electron paramagnetic resonance
ET	electron transfer
F	Faraday constant
Fc^+/Fc	ferrocenium/ferrocene
FccA	fumarate reductase
FE	Faradaic efficiency
Fe_d	distal iron center in [FeFe]-H_2ase
Fe_p	proximal iron center in [FeFe]-H_2ase
FDH	formate dehydrogenase
FT-IR	Fourier transform infrared
FTO	fluorine-doped tin oxide
Γ	surface loading of catalyst (in nmol cm^{-2})
GC	glassy carbon
GO	graphene oxide
η	overpotential
H_2ase	hydrogenase
HEC	hydrogen evolution catalyst
HOMO	highest occupied molecular orbital
ImDipp	1,3-bis(2,6-diisopropylphenyl)-imidazol-2-ylidene
IO	inverse opal
IPCE	incident photon-to-current conversion efficiency
IR	infrared
ITO	indium tin oxide
J_{ph}	photocurrent density
λ	wavelength
LAPC	light-absorbing photocathode
LED	light-emitting diode
LSV	linear sweep voltammetry
LUMO	lowest unoccupied molecular orbital
μ	bridging
MeCN	acetonitrile
MEDA	2-(dimethylamino)ethanethiol
MeOH	methanol
MES	2-(*N*-morpholino)ethanesulfonic acid
mesoITO	mesoporous ITO
$mesoTiO_2$	mesoporous TiO_2
MO_x	metal oxide
MOS	metal organic surface
MOF	metal organic framework
MPA	3-mercaptopropionic acid
MS	mass spectrometry
MV	methyl viologen
MWCNT	multiwalled carbon nanotube
n	oxidation state of catalyst
N_2ase	nitrogenase
n_{cat}	amount of catalyst (in mol)
n_{prod}	amount of product (in mol)
NAD^+	nicotinamide adenine dinucleotide
NADH	reduced nicotinamide adenine dinucleotide
NHC	N-heterocyclic carbene
NHE	normal hydrogen electrode
NMR	nuclear magnetic resonance
OEC	oxygen evolving complex
OTf	triflate anion ($CF_3SO_3^-$)
P3HT	poly(3-hexylthiophene)
Pc	phthalocyanine
PCET	proton coupled electron transfer
PEM	proton exchange membrane
PEC	photoelectrochemical
PEI	polyethylenimine
PFE	protein film electrochemistry
phen	1,10-phenanthroline
p-SC	p-type semiconductor
PS	photosensitizer
PVI	polyvinylimidazole
PVP	polyvinylpyridine
Q	charge (in C)
QD	quantum dot
QY	quantum yield
qtpy	2,2′:6′,2″:6″,2‴-quaterpyridine
RGO	reduced graphene oxide
RHE	reversible hydrogen electrode
RT	room temperature
SC	semiconductor
SCE	saturated calomel electrode
SDS	sodium dodecyl sulfate
SEC	spectroelectrochemical

DOI: 10.1021/acs.chemrev.8b00392
Chem. Rev. 2019, 119, 2752−2875

SED	sacrificial electron donor
SEM	scanning electron microscopy
t	time
TAS	transient absorption spectroscopy
TEA	triethylamine
TEOA	triethanolamine
TFA	trifluoroacetic acid
TFE	2,2,2-trifluoroethanol
TGA	thioglycolic acid
THF	tetrahydrofuran
TOF	turnover frequency
TON	turnover number
TPA	tris(2-pyridylmethyl)amine
TPP	*meso*-tetraphenylporphyrin
tpy	2,2′:6′,2″-terpyridine
TsOH	tosylic acid
UV−vis	ultraviolet−visible
VB	valence band
WE	working electrode
XANES	X-ray absorption near-edge structure
XPS	X-ray photoelectron spectroscopy
z	number of electrons

REFERENCES

(1) Appel, A. M.; Bercaw, J. E.; Bocarsly, A. B.; Dobbek, H.; DuBois, D. L.; Dupuis, M.; Ferry, J. G.; Fujita, E.; Hille, R.; Kenis, P. J.; et al. Frontiers, Opportunities, and Challenges in Biochemical and Chemical Catalysis of CO_2 fixation. *Chem. Rev.* **2013**, *113*, 6621−6658.

(2) Aresta, M.; Dibenedetto, A.; Angelini, A. Catalysis for the Valorization of Exhaust Carbon: from CO_2 to Chemicals, Materials, and Fuels. Technological Use of CO_2. *Chem. Rev.* **2014**, *114*, 1709−1742.

(3) Grice, K. A. Carbon dioxide reduction with homogenous early transition metal complexes: Opportunities and challenges for developing CO_2 catalysis. *Coord. Chem. Rev.* **2017**, *336*, 78−95.

(4) Parties to the United Nations Framework Convention on Climate Change, *Paris Agreement*, United Nations, 2015.

(5) *BP Statistical Review of World Energy 2017*, 2018, British Petroleum Company.

(6) *Global Energy and CO_2 Status Report 2017*, 2018, International Energy Agency.

(7) Mondal, B.; Song, J.; Neese, F.; Ye, S. Bio-inspired mechanistic insights into CO_2 reduction. *Curr. Opin. Chem. Biol.* **2015**, *25*, 103−109.

(8) Benson, E. E.; Kubiak, C. P.; Sathrum, A. J.; Smieja, J. M. Electrocatalytic and homogeneous approaches to conversion of CO_2 to liquid fuels. *Chem. Soc. Rev.* **2009**, *38*, 89−99.

(9) Barber, J. Photosynthetic energy conversion: natural and artificial. *Chem. Soc. Rev.* **2009**, *38*, 185−196.

(10) Crabtree, G. W.; Lewis, N. S. Solar energy conversion. *Phys. Today* **2007**, *60*, 37−42.

(11) Woolerton, T. W.; Sheard, S.; Chaudhary, Y. S.; Armstrong, F. A. Enzymes and bio-inspired electrocatalysts in solar fuel devices. *Energy Environ. Sci.* **2012**, *5*, 7470−7490.

(12) Beer, C.; Reichstein, M.; Tomelleri, E.; Ciais, P.; Jung, M.; Carvalhais, N.; Rödenbeck, C.; Arain, M. A.; Baldocchi, D.; Bonan, G. B.; et al. Terrestrial Gross Carbon Dioxide Uptake: Global Distribution and Covariation with Climate. *Science* **2010**, *329*, 834−838.

(13) Geider, R. J.; Delucia, E. H.; Falkowski, P. G.; Finzi, A. C.; Grime, J. P.; Grace, J.; Kana, T. M.; Roche, J. L.; Long, S. P.; Osborne, B. A.; et al. Primary productivity of planet earth: biological determinants and physical constraints in terrestrial and aquatic habitats. *Glob. Chang. Biol.* **2001**, *7*, 849−882.

(14) Barber, J. *Solar Fuels and Photosynthesis*; Royal Society of Chemistry: London, 2012.

(15) Hammarström, L.; Hammes-Schiffer, S. Artificial Photosynthesis and Solar Fuels. *Acc. Chem. Res.* **2009**, *42*, 1859−1860.

(16) Bachmeier, A.; Armstrong, F. Solar-driven proton and carbon dioxide reduction to fuels-lessons from metalloenzymes. *Curr. Opin. Chem. Biol.* **2015**, *25*, 141−151.

(17) Kaim, W. *Bioinorganic chemistry -- Inorganic Elements in the Chemistry of Life: An Introduction and Guide*, 2nd ed.; Wiley: Chichester, U.K., 2013.

(18) Woolerton, T. W.; Sheard, S.; Reisner, E.; Pierce, E.; Ragsdale, S. W.; Armstrong, F. A. Efficient and Clean Photoreduction of CO_2 to CO by Enzyme-Modified TiO_2 Nanoparticles Using Visible Light. *J. Am. Chem. Soc.* **2010**, *132*, 2132−2133.

(19) Wombwell, C.; Caputo, C. A.; Reisner, E. [NiFeSe]-Hydrogenase Chemistry. *Acc. Chem. Res.* **2015**, *48*, 2858−2865.

(20) Handoko, A. D.; Li, K.; Tang, J. Recent progress in artificial photosynthesis: CO_2 photoreduction to valuable chemicals in a heterogeneous system. *Curr. Opin. Chem. Eng.* **2013**, *2*, 200−206.

(21) White, J. L.; Baruch, M. F.; Pander, J. E., III; Hu, Y.; Fortmeyer, I. C.; Park, J. E.; Zhang, T.; Liao, K.; Gu, J.; Yan, Y.; et al. Light-Driven Heterogeneous Reduction of Carbon Dioxide: Photocatalysts and Photoelectrodes. *Chem. Rev.* **2015**, *115*, 12888−12935.

(22) Berardi, S.; Drouet, S.; Francàs, L.; Gimbert-Suriñach, C.; Guttentag, M.; Richmond, C.; Stoll, T.; Llobet, A. Molecular artificial photosynthesis. *Chem. Soc. Rev.* **2014**, *43*, 7501−7519.

(23) Francke, R.; Schille, B.; Roemelt, M. Homogeneously Catalyzed Electroreduction of Carbon Dioxide-Methods, Mechanisms, and Catalysts. *Chem. Rev.* **2018**, *118*, 4631−4701.

(24) Elgrishi, N.; Griveau, S.; Chambers, M. B.; Bedioui, F.; Fontecave, M. Versatile functionalization of carbon electrodes with a polypyridine ligand: metallation and electrocatalytic H^+ and CO_2 reduction. *Chem. Commun.* **2015**, *51*, 2995−2998.

(25) Windle, C. D.; Reisner, E. Heterogenised Molecular Catalysts for the Reduction of CO_2 to Fuels. *Chimia* **2015**, *69*, 435−441.

(26) Kraatz, H. B.; Metzler-Nolte, N. *Concepts and Models in Bioinorganic Chemistry*; Wiley: Weinheim, Germany, 2006.

(27) Reedijk, J. Metal-Ligand Exchange Kinetics in Platinum and Ruthenium Complexes. *Platinum Met. Rev.* **2008**, *52*, 2−11.

(28) Lide, D. R. *CRC handbook of chemistry and physics: a ready-reference book of chemical and physical data*; CRC: London, 2008.

(29) Lubitz, W.; Ogata, H.; Rudiger, O.; Reijerse, E. Hydrogenases. *Chem. Rev.* **2014**, *114*, 4081−4148.

(30) Peters, J. W.; Schut, G. J.; Boyd, E. S.; Mulder, D. W.; Shepard, E. M.; Broderick, J. B.; King, P. W.; Adams, M. W. W. [FeFe]- and [NiFe]-hydrogenase diversity, mechanism, and maturation. *Biochim. Biophys. Acta, Mol. Cell Res.* **2015**, *1853*, 1350−1369.

(31) Frey, M. Hydrogenases: Hydrogen-Activating Enzymes. *ChemBioChem* **2002**, *3*, 153−160.

(32) Jones, A. K.; Sillery, E.; Albracht, S. P. J.; Armstrong, F. A. Direct comparison of the electrocatalytic oxidation of hydrogen by an enzyme and a platinum catalyst. *Chem. Commun.* **2002**, 866−867.

(33) Madden, C.; Vaughn, M. D.; Díez-Pérez, I.; Brown, K. A.; King, P. W.; Gust, D.; Moore, A. L.; Moore, T. A. Catalytic Turnover of [FeFe]-Hydrogenase Based on Single-Molecule Imaging. *J. Am. Chem. Soc.* **2012**, *134*, 1577−1582.

(34) Evans, R. M.; Brooke, E. J.; Wehlin, S. A. M.; Nomerotskaia, E.; Sargent, F.; Carr, S. B.; Phillips, S. E. V.; Armstrong, F. A. Mechanism of hydrogen activation by [NiFe] hydrogenases. *Nat. Chem. Biol.* **2016**, *12*, 46−50.

(35) Berggren, G.; Adamska, A.; Lambertz, C.; Simmons, T. R.; Esselborn, J.; Atta, M.; Gambarelli, S.; Mouesca, J. M.; Reijerse, E.; Lubitz, W.; et al. Biomimetic assembly and activation of [FeFe]-hydrogenases. *Nature* **2013**, *499*, 66−69.

(36) Esselborn, J.; Lambertz, C.; Adamska-Venkatesh, A.; Simmons, T.; Berggren, G.; Noth, J.; Siebel, J.; Hemschemeier, A.; Artero, V.; Reijerse, E.; et al. Spontaneous activation of [FeFe]-hydrogenases by an inorganic [2Fe] active site mimic. *Nat. Chem. Biol.* **2013**, *9*, 607−609.

(37) Ensign, S. A. Reactivity of Carbon Monoxide Dehydrogenase from *Rhodospirillum rubrum* with Carbon Dioxide, Carbonyl Sulfide, and Carbon Disulfide. *Biochemistry* **1995**, *34*, 5372−5381.

(38) Majumdar, A. Bioinorganic modeling chemistry of carbon monoxide dehydrogenases: description of model complexes, current

DOI: 10.1021/acs.chemrev.8b00392
Chem. Rev. 2019, 119, 2752−2875

status and possible future scopes. *Dalton Trans.* **2014**, *43*, 12135−12145.
(39) Dobbek, H.; Svetlitchnyi, V.; Gremer, L.; Huber, R.; Meyer, O. Crystal Structure of a Carbon Monoxide Dehydrogenase Reveals a [Ni-4Fe-5S] Cluster. *Science* **2001**, *293*, 1281−1285.
(40) Jeoung, J. H.; Dobbek, H. Carbon Dioxide Activation at the Ni,Fe-Cluster of Anaerobic Carbon Monoxide Dehydrogenase. *Science* **2007**, *318*, 1461−1464.
(41) Volbeda, A.; Fontecilla-Camps, J. C. Structural bases for the catalytic mechanism of Ni-containing carbon monoxide dehydrogenases. *Dalton Trans.* **2005**, 3443−3450.
(42) Can, M.; Armstrong, F. A.; Ragsdale, S. W. Structure, Function, and Mechanism of the Nickel Metalloenzymes, CO Dehydrogenase, and Acetyl-CoA Synthase. *Chem. Rev.* **2014**, *114*, 4149−4174.
(43) Drennan, C. L.; Heo, J.; Sintchak, M. D.; Schreiter, E.; Ludden, P. W. Life on carbon monoxide: X-ray structure of *Rhodospirillum rubrum* Ni-Fe-S carbon monoxide dehydrogenase. *Proc. Natl. Acad. Sci. U. S. A.* **2001**, *98*, 11973−11978.
(44) Chen, J.; Huang, S.; Seravalli, J.; Gutzman, H.; Swartz, D. J.; Ragsdale, S. W.; Bagley, K. A. Infrared Studies of Carbon Monoxide Binding to Carbon Monoxide Dehydrogenase/Acetyl-CoA Synthase from *Moorella thermoacetica*. *Biochemistry* **2003**, *42*, 14822−14830.
(45) Kim, E. J.; Feng, J.; Bramlett, M. R.; Lindahl, P. A. Evidence for a Proton Transfer Network and a Required Persulfide-Bond-Forming Cysteine Residue in Ni-Containing Carbon Monoxide Dehydrogenases. *Biochemistry* **2004**, *43*, 5728−5734.
(46) Kaim, W.; Schwederski, B. Non-innocent ligands in bioinorganic chemistry−An overview. *Coord. Chem. Rev.* **2010**, *254*, 1580−1588.
(47) Rigby, S. E. J.; Muhiuddin, I. P.; Santabarbara, S.; Evans, M. C. W.; Heathcote, P. Proton ENDOR spectroscopy of the anion radicals of the chlorophyll primary electron acceptors in type I photosynthetic reaction centres. *Chem. Phys.* **2003**, *294*, 319−328.
(48) Chang, C. J.; Chang, M. C.; Damrauer, N. H.; Nocera, D. G. Proton-coupled electron transfer: a unifying mechanism for biological charge transport, amino acid radical initiation and propagation, and bond making/breaking reactions of water and oxygen. *Biochim. Biophys. Acta, Bioenerg.* **2004**, *1655*, 13−28.
(49) Siewert, I. Proton-Coupled Electron Transfer Reactions Catalysed by 3 d Metal Complexes. *Chem. - Eur. J.* **2015**, *21*, 15078−15091.
(50) Wang, L.-S.; Reutt, J. E.; Lee, Y. T.; Shirley, D. A. High resolution UV photoelectron spectroscopy of CO_2^+, COS^+ and CS_2^+ using supersonic molecular beams. *J. Electron Spectrosc. Relat. Phenom.* **1988**, *47*, 167−186.
(51) Mascetti, J. In *Carbon Dioxide as Chemical Feedstock*; Aresta, M., Ed.; Wiley: Weinheim, Germany, 2010.
(52) Mirica, L. M.; Ottenwaelder, X.; Stack, T. D. P. Structure and Spectroscopy of Copper−Dioxygen Complexes. *Chem. Rev.* **2004**, *104*, 1013−1046.
(53) Rosen, B. A.; Salehi-Khojin, A.; Thorson, M. R.; Zhu, W.; Whipple, D. T.; Kenis, P. J. A.; Masel, R. I. Ionic Liquid−Mediated Selective Conversion of CO_2 to CO at Low Overpotentials. *Science* **2011**, *334*, 643−644.
(54) Bassegoda, A.; Madden, C.; Wakerley, D. W.; Reisner, E.; Hirst, J. Reversible Interconversion of CO_2 and Formate by a Molybdenum-Containing Formate Dehydrogenase. *J. Am. Chem. Soc.* **2014**, *136*, 15473−15476.
(55) Li, K.; Peng, B.; Peng, T. Recent Advances in Heterogeneous Photocatalytic CO_2 Conversion to Solar Fuels. *ACS Catal.* **2016**, *6*, 7485−7527.
(56) Reda, T.; Plugge, C. M.; Abram, N. J.; Hirst, J. Reversible interconversion of carbon dioxide and formate by an electroactive enzyme. *Proc. Natl. Acad. Sci. U. S. A.* **2008**, *105*, 10654−10658.
(57) Kuehnel, M. F.; Orchard, K. L.; Dalle, K. E.; Reisner, E. Selective Photocatalytic CO_2 Reduction in Water through Anchoring of a Molecular Ni Catalyst on CdS Nanocrystals. *J. Am. Chem. Soc.* **2017**, *139*, 7217−7223.
(58) Wang, J.-W.; Liu, W.-J.; Zhong, D.-C.; Lu, T.-B. Nickel complexes as molecular catalysts for water splitting and CO_2 reduction. *Coord. Chem. Rev.* **2019**, *378*, 237−261.
(59) Schneider, J.; Jia, H.; Kobiro, K.; Cabelli, D. E.; Muckerman, J. T.; Fujita, E. Nickel(II) macrocycles: highly efficient electrocatalysts for the selective reduction of CO_2 to CO. *Energy Environ. Sci.* **2012**, *5*, 9502−9510.
(60) Walsh, J. J.; Neri, G.; Smith, C. L.; Cowan, A. J. Electrocatalytic CO_2 reduction with a membrane supported manganese catalyst in aqueous solution. *Chem. Commun.* **2014**, *50*, 12698−12701.
(61) Thoi, V. S.; Sun, Y.; Long, J. R.; Chang, C. J. Complexes of earth-abundant metals for catalytic electrochemical hydrogen generation under aqueous conditions. *Chem. Soc. Rev.* **2013**, *42*, 2388−2400.
(62) Eckenhoff, W. T.; Eisenberg, R. Molecular systems for light driven hydrogen production. *Dalton Trans.* **2012**, *41*, 13004−13021.
(63) Morris, R. H. Brønsted-Lowry Acid Strength of Metal Hydride and Dihydrogen Complexes. *Chem. Rev.* **2016**, *116*, 8588−8654.
(64) Reuillard, B.; Ly, K. H.; Rosser, T. E.; Kuehnel, M. F.; Zebger, I.; Reisner, E. Tuning Product Selectivity for Aqueous CO_2 Reduction with a Mn(bipyridine)-pyrene Catalyst Immobilized on a Carbon Nanotube Electrode. *J. Am. Chem. Soc.* **2017**, *139*, 14425−14435.
(65) Franco, F.; Cometto, C.; Nencini, L.; Barolo, C.; Sordello, F.; Minero, C.; Fiedler, J.; Robert, M.; Gobetto, R.; Nervi, C. Local Proton Source in Electrocatalytic CO_2 Reduction with $[Mn(bpy-R)(CO)_3Br]$ Complexes. *Chem. - Eur. J.* **2017**, *23*, 4782−4793.
(66) Darensbourg, D. J. Chemistry of Carbon Dioxide Relevant to Its Utilization: A Personal Perspective. *Inorg. Chem.* **2010**, *49*, 10765−10780.
(67) Jessop, P. G.; Ikariya, T.; Noyori, R. Homogeneous Hydrogenation of Carbon Dioxide. *Chem. Rev.* **1995**, *95*, 259−272.
(68) Göttle, A. J.; Koper, M. T. M. Determinant Role of Electrogenerated Reactive Nucleophilic Species on Selectivity during Reduction of CO_2 Catalyzed by Metalloporphyrins. *J. Am. Chem. Soc.* **2018**, *140*, 4826−4834.
(69) Chen, L.; Guo, Z.; Wei, X.-G.; Gallenkamp, C.; Bonin, J.; Anxolabéhère-Mallart, E.; Lau, K.-C.; Lau, T.-C.; Robert, M. Molecular Catalysis of the Electrochemical and Photochemical Reduction of CO_2 with Earth-Abundant Metal Complexes. Selective Production of CO vs HCOOH by Switching of the Metal Center. *J. Am. Chem. Soc.* **2015**, *137*, 10918−10921.
(70) Collin, J.-P.; Jouaiti, A.; Sauvage, J.-P. Electrocatalytic Properties of $Ni(cyclam)^{2+}$ and $Ni_2(biscyclam)^{4+}$ with Respect to CO_2 and H_2O Reduction. *Inorg. Chem.* **1988**, *27*, 1986−1990.
(71) Song, J.; Klein, E. L.; Neese, F.; Ye, S. The Mechanism of Homogeneous CO_2 Reduction by Ni(cyclam): Product Selectivity, Concerted Proton−Electron Transfer and C−O Bond Cleavage. *Inorg. Chem.* **2014**, *53*, 7500−7507.
(72) Appel, A. M.; Helm, M. L. Determining the Overpotential for a Molecular Electrocatalyst. *ACS Catal.* **2014**, *4*, 630−633.
(73) Artero, V.; Savéant, J.-M. Toward the rational benchmarking of homogeneous H_2-evolving catalysts. *Energy Environ. Sci.* **2014**, *7*, 3808−3814.
(74) Fourmond, V.; Jacques, P. A.; Fontecave, M.; Artero, V. H_2 Evolution and Molecular Electrocatalysts: Determination of Overpotentials and Effect of Homoconjugation. *Inorg. Chem.* **2010**, *49*, 10338−10347.
(75) Costentin, C.; Drouet, S.; Robert, M.; Savéant, J.-M. Turnover Numbers, Turnover Frequencies, and Overpotential in Molecular Catalysis of Electrochemical Reactions. Cyclic Voltammetry and Preparative-Scale Electrolysis. *J. Am. Chem. Soc.* **2012**, *134*, 11235−11242.
(76) Costentin, C.; Robert, M.; Savéant, J.-M. Catalysis of the electrochemical reduction of carbon dioxide. *Chem. Soc. Rev.* **2013**, *42*, 2423−2436.
(77) Pool, D. H.; DuBois, D. L. $[Ni(P^{Ph}_2N^{Ar}_2)_2(NCMe)][BF_4]_2$ as an electrocatalyst for H_2 production: $P^{Ph}_2N^{Ar}_2$=1,5-(di(4-(thiophene-3-yl)phenyl)-3,7-diphenyl-1,5-diaza-3,7-diphosphacyclooctane). *J. Organomet. Chem.* **2009**, *694*, 2858−2865.

DOI: 10.1021/acs.chemrev.8b00392
Chem. Rev. 2019, 119, 2752−2875

(78) Agarwal, J.; Shaw, T. W.; Stanton, C. J., III; Majetich, G. F.; Bocarsly, A. B.; Schaefer, H. F., III NHC-Containing Manganese(I) Electrocatalysts for the Two-Electron Reduction of CO_2. *Angew. Chem.* **2014**, *126*, 5252−5255.
(79) Yamazaki, Y.; Takeda, H.; Ishitani, O. Photocatalytic reduction of CO_2 using metal complexes. *J. Photochem. Photobiol., C* **2015**, *25*, 106−137.
(80) Morris, A. J.; Meyer, G. J.; Fujita, E. Molecular Approaches to the Photocatalytic Reduction of Carbon Dioxide for Solar Fuels. *Acc. Chem. Res.* **2009**, *42*, 1983−1994.
(81) IUPAC *Compendium of Chemical Terminology*, 2nd ed. (the "Gold Book"); McNaught, A. D., Wilkinson, A., Eds.; Blackwell Scientific Publications: Oxford, U.K., 1997.
(82) Chaudret, B.; Philippot, K. Organometallic Nanoparticles of Metals or Metal Oxides. *Oil Gas Sci. Technol.* **2007**, *62*, 799−817.
(83) Lassenberger, A.; Grünewald, T. A.; van Oostrum, P. D. J.; Rennhofer, H.; Amenitsch, H.; Zirbs, R.; Lichtenegger, H. C.; Reimhult, E. Monodisperse Iron Oxide Nanoparticles by Thermal Decomposition: Elucidating Particle Formation by Second-Resolved in Situ Small-Angle X-ray Scattering. *Chem. Mater.* **2017**, *29*, 4511−4522.
(84) Mir, N.; Heidari, A.; Salavati-Niasari, M.; Pourmolai, N. One-pot synthesis of cobalt nanoparticle-embedded lamellar sheets by using inorganic complex via thermal decomposition route. *J. Mater. Sci.: Mater. Electron.* **2016**, *27*, 10747−10753.
(85) Stuart, E. J. E.; Pumera, M. Electrochemistry of a Whole Group of Compounds Affected by Metallic Impurities within Carbon Nanotubes. *J. Phys. Chem. C* **2010**, *114*, 21296−21298.
(86) Artero, V.; Fontecave, M. Solar fuels generation and molecular systems: is it homogeneous or heterogeneous catalysis? *Chem. Soc. Rev.* **2013**, *42*, 2338−2356.
(87) Widegren, J. A.; Finke, R. G. A review of the problem of distinguishing true homogeneous catalysis from soluble or other metal-particle heterogeneous catalysis under reducing conditions. *J. Mol. Catal. A: Chem.* **2003**, *198*, 317−341.
(88) Beley, M.; Collin, J. P.; Ruppert, R.; Sauvage, J. P. Electrocatalytic Reduction of CO_2 by Nickel Cyclam^{2+} in Water: Study of the Factors Affecting the Efficiency and the Selectivity of the Process. *J. Am. Chem. Soc.* **1986**, *108*, 7461−7467.
(89) Lam, K.-M.; Wong, K.-Y.; Yang, S.-M.; Che, C.-M. Cobalt and nickel complexes of 2,2':6',2'':6'',2'''-quaterpyridine as catalysts for electrochemical reduction of carbon dioxide. *J. Chem. Soc., Dalton Trans.* **1995**, 1103−1107.
(90) Wu, Y.; Rudshteyn, B.; Zhanaidarova, A.; Froehlich, J. D.; Ding, W.; Kubiak, C. P.; Batista, V. S. Electrode-Ligand Interactions Dramatically Enhance CO_2 Conversion to CO by the [Ni(cyclam)]-$(PF_6)_2$ Catalyst. *ACS Catal.* **2017**, *7*, 5282−5288.
(91) Elgrishi, N.; McCarthy, B. D.; Rountree, E. S.; Dempsey, J. L. Reaction Pathways of Hydrogen-Evolving Electrocatalysts: Electrochemical and Spectroscopic Studies of Proton-Coupled Electron Transfer Processes. *ACS Catal.* **2016**, *6*, 3644−3659.
(92) Grice, K. A.; Saucedo, C.; Sovereign, M. A.; Cho, A. P. The Electrochemical Behavior of Early Metal Metallocene Cp_2MCl_2 Complexes under CO_2. *Electrochim. Acta* **2016**, *218*, 110−118.
(93) Kessler, M.; Hansen, S.; Hollmann, D.; Klahn, M.; Beweries, T.; Spannenberg, A.; Brückner, A.; Rosenthal, U. Synthesis of Cp^*_2Ti-(OTf) and Its Reaction with Water. *Eur. J. Inorg. Chem.* **2011**, *2011*, 627−631.
(94) Hollmann, D.; Grabow, K.; Jiao, H.; Kessler, M.; Spannenberg, A.; Beweries, T.; Bentrup, U.; Bruckner, A. Hydrogen generation by water reduction with [Cp*(2) Ti(OTf)]: identifying elemental mechanistic steps by combined in situ FTIR and in situ EPR spectroscopy supported by DFT calculations. *Chem. - Eur. J.* **2013**, *19*, 13705−13713.
(95) Bourrez, M.; Molton, F.; Chardon-Noblat, S.; Deronzier, A. [Mn(bipyridyl)$(CO)_3$Br]: An Abundant Metal Carbonyl Complex as Efficient Electrocatalyst for CO_2 Reduction. *Angew. Chem., Int. Ed.* **2011**, *50*, 9903−9906.
(96) Smieja, J. M.; Sampson, M. D.; Grice, K. A.; Benson, E. E.; Froehlich, J. D.; Kubiak, C. P. Manganese as a Substitute for Rhenium in CO_2 Reduction Catalysts: The Importance of Acids. *Inorg. Chem.* **2013**, *52*, 2484−2491.
(97) Valyaev, D. A.; Peterleitner, M. G.; Semeikin, O. V.; Utegenov, K. I.; Ustynyuk, N. A.; Sournia-Saquet, A.; Lugan, N.; Lavigne, G. Proton reduction catalysis by manganese vinylidene and allenylidene complexes. *J. Organomet. Chem.* **2007**, *692*, 3207−3211.
(98) Hou, K.; Lauw, S. J. L.; Webster, R. D.; Fan, W. Y. Electrochemical proton reduction catalysed by selenolato-manganese carbonyl complexes. *RSC Adv.* **2015**, *5*, 39303−39309.
(99) Hou, K.; Poh, H. T.; Fan, W. Y. Electrocatalytic hydrogen generation by a trithiolato-bridged dimanganese hexacarbonyl anion with a turnover frequency exceeding 40,000 s^{-1}. *Chem. Commun.* **2014**, *50*, 6630−6632.
(100) Agarwal, J.; Stanton, C. J., III; Shaw, T. W.; Vandezande, J. E.; Majetich, G. F.; Bocarsly, A. B.; Schaefer, H. F., III Exploring the effect of axial ligand substitution (X = Br, NCS, CN) on the photo-decomposition and electrochemical activity of [MnX(N−C)$(CO)_3$] complexes. *Dalton Trans.* **2015**, *44*, 2122−2131.
(101) Sampson, M. D.; Kubiak, C. P. Electrocatalytic Dihydrogen Production by an Earth-Abundant Manganese Bipyridine Catalyst. *Inorg. Chem.* **2015**, *54*, 6674−6676.
(102) Sampson, M. D.; Nguyen, A. D.; Grice, K. A.; Moore, C. E.; Rheingold, A. L.; Kubiak, C. P. Manganese Catalysts with Bulky Bipyridine Ligands for the Electrocatalytic Reduction of Carbon Dioxide: Eliminating Dimerization and Altering Catalysis. *J. Am. Chem. Soc.* **2014**, *136*, 5460−5471.
(103) Carrington, S. J.; Chakraborty, I.; Mascharak, P. K. Rapid CO release from a Mn(I) carbonyl complex derived from azopyridine upon exposure to visible light and its phototoxicity toward malignant cells. *Chem. Commun.* **2013**, *49*, 11254−11256.
(104) Gonzalez, M. A.; Carrington, S. J.; Fry, N. L.; Martinez, J. L.; Mascharak, P. K. Syntheses, Structures, and Properties of New Manganese Carbonyls as Photoactive CO-Releasing Molecules: Design Strategies That Lead to CO Photolability in the Visible Region. *Inorg. Chem.* **2012**, *51*, 11930−11940.
(105) Gonzalez, M. A.; Yim, M. A.; Cheng, S.; Moyes, A.; Hobbs, A. J.; Mascharak, P. K. Manganese Carbonyls Bearing Tripodal Polypyridine Ligands as Photoactive Carbon Monoxide-Releasing Molecules. *Inorg. Chem.* **2012**, *51*, 601−608.
(106) Govender, P.; Pai, S.; Schatzschneider, U.; Smith, G. S. Next Generation PhotoCORMs: Polynuclear Tricarbonylmanganese(I)-Functionalized Polypyridyl Metallodendrimers. *Inorg. Chem.* **2013**, *52*, 5470−5478.
(107) Ward, J. S.; Lynam, J. M.; Moir, J. W. B.; Sanin, D. E.; Mountford, A. P.; Fairlamb, I. J. S. A therapeutically viable photo-activated manganese-based CO-releasing molecule (photo-CO-RM). *Dalton Trans.* **2012**, *41*, 10514−10517.
(108) Yempally, V.; Kyran, S. J.; Raju, R. K.; Fan, W. Y.; Brothers, E. N.; Darensbourg, D. J.; Bengali, A. A. Thermal and Photochemical Reactivity of Manganese Tricarbonyl and Tetracarbonyl Complexes with a Bulky Diazabutadiene Ligand. *Inorg. Chem.* **2014**, *53*, 4081−4088.
(109) Capon, J.-F.; Gloaguen, F.; Pétillon, F. Y.; Schollhammer, P.; Talarmin, J. Electron and proton transfers at diiron dithiolate sites relevant to the catalysis of proton reduction by the [FeFe]-hydrogenases. *Coord. Chem. Rev.* **2009**, *253*, 1476−1494.
(110) Gloaguen, F.; Rauchfuss, T. B. Small molecule mimics of hydrogenases: hydrides and redox. *Chem. Soc. Rev.* **2009**, *38*, 100−108.
(111) Schilter, D.; Camara, J. M.; Huynh, M. T.; Hammes-Schiffer, S.; Rauchfuss, T. B. Hydrogenase Enzymes and Their Synthetic Models: The Role of Metal Hydrides. *Chem. Rev.* **2016**, *116*, 8693−8749.
(112) Tard, C.; Pickett, C. J. Structural and Functional Analogues of the Active Sites of the [Fe]-, [NiFe]-, and [FeFe]-Hydrogenases. *Chem. Rev.* **2009**, *109*, 2245−2274.
(113) Kaur-Ghumaan, S.; Schwartz, L.; Lomoth, R.; Stein, M.; Ott, S. Catalytic Hydrogen Evolution from Mononuclear Iron(II) Carbonyl Complexes as Minimal Functional Models of the [FeFe] Hydrogenase Active Site. *Angew. Chem., Int. Ed.* **2010**, *49*, 8033−8036.

DOI: 10.1021/acs.chemrev.8b00392
Chem. Rev. 2019, 119, 2752−2875

(114) Bitterwolf, T. E.; Ling, A. C. Metallocene basicity: III. Protonation of compounds containing two ferrocenyl moieties. *J. Organomet. Chem.* **1973**, *57*, C15−C18.
(115) Mueller-Westerhoff, U. T.; Nazzal, A. [1.1]Ferrocenophanes as effective catalysts in the photoelectrochemical hydrogen evolution from acidic aqueous media. *J. Am. Chem. Soc.* **1984**, *106*, 5381−5382.
(116) Gloaguen, F.; Lawrence, J. D.; Rauchfuss, T. B. Biomimetic Hydrogen Evolution Catalyzed by an Iron Carbonyl Thiolate. *J. Am. Chem. Soc.* **2001**, *123*, 9476−9477.
(117) Ott, S.; Kritikos, M.; Akermark, B.; Sun, L.; Lomoth, R. A Biomimetic Pathway for Hydrogen Evolution from a Model of the Iron Hydrogenase Active Site. *Angew. Chem., Int. Ed.* **2004**, *43*, 1006−1009.
(118) Duan, L.; Wang, M.; Li, P.; Na, Y.; Wang, N.; Sun, L. Carbene−pyridine chelating 2Fe2S hydrogenase model complexes as highly active catalysts for the electrochemical reduction of protons from weak acid (HOAc). *Dalton Trans.* **2007**, 1277−1283.
(119) Barton, B. E.; Rauchfuss, T. B. Terminal Hydride in [FeFe]-Hydrogenase Model Has Lower Potential for H_2 Production Than the Isomeric Bridging Hydride. *Inorg. Chem.* **2008**, *47*, 2261−2263.
(120) Carroll, M. E.; Barton, B. E.; Rauchfuss, T. B.; Carroll, P. J. Synthetic Models for the Active Site of the [FeFe]-Hydrogenase: Catalytic Proton Reduction and the Structure of the Doubly Protonated Intermediate. *J. Am. Chem. Soc.* **2012**, *134*, 18843−18852.
(121) Custelcean, R.; Jackson, J. E. Dihydrogen Bonding: Structures, Energetics, and Dynamics. *Chem. Rev.* **2001**, *101*, 1963−1980.
(122) Na, Y.; Wang, M.; Jin, K.; Zhang, R.; Sun, L. An approach to water-soluble hydrogenase active site models: Synthesis and electrochemistry of diiron dithiolate complexes with 3,7-diacetyl-1,3,7-triaza-5-phosphabicyclo[3.3.1]nonane ligand(s). *J. Organomet. Chem.* **2006**, *691*, 5045−5051.
(123) Apfel, U.-P.; Halpin, Y.; Gottschaldt, M.; Görls, H.; Vos, J. G.; Weigand, W. Functionalized Sugars as Ligands towards Water-Soluble [Fe-only] Hydrogenase Models. *Eur. J. Inorg. Chem.* **2008**, *2008*, 5112−5118.
(124) Song, L. C.; Wang, Y. X.; Xing, X. K.; Ding, S. D.; Zhang, L. D.; Wang, X. Y.; Zhang, H. T. Hydrophilic Quaternary Ammonium-Group-Containing [FeFe]-Hydrogenase Models: Synthesis, Structures, and Electrocatalytic Hydrogen Production. *Chem. - Eur. J.* **2016**, *22*, 16304−16314.
(125) Cao, W. N.; Wang, F.; Wang, H. Y.; Chen, B.; Feng, K.; Tung, C. H.; Wu, L. Z. Photocatalytic hydrogen production from a simple water-soluble [FeFe]-hydrogenase model system. *Chem. Commun.* **2012**, *48*, 8081−8083.
(126) Jian, J.-X.; Ye, C.; Wang, X.-Z.; Wen, M.; Li, Z.-J.; Li, X.-B.; Chen, B.; Tung, C.-H.; Wu, L.-Z. Comparison of H_2 photogeneration by [FeFe]-hydrogenase mimics with CdSe QDs and $Ru(bpy)_3Cl_2$ in aqueous solution. *Energy Environ. Sci.* **2016**, *9*, 2083−2089.
(127) Singleton, M. L.; Crouthers, D. J.; Duttweiler, R. P., III; Reibenspies, J. H.; Darensbourg, M. Y. Sulfonated Diiron Complexes as Water-Soluble Models of the [Fe−Fe]-Hydrogenase Enzyme Active Site. *Inorg. Chem.* **2011**, *50*, 5015−5026.
(128) Cheng, M.; Wang, M.; Zhang, S.; Liu, F.; Yang, Y.; Wan, B.; Sun, L. Photocatalytic H_2 production using a hybrid assembly of an [FeFe]-hydrogenase model and CdSe quantum dot linked through a thiolato-functionalized cyclodextrin. *Faraday Discuss.* **2017**, *198*, 197−209.
(129) Onoda, A.; Kihara, Y.; Fukumoto, K.; Sano, Y.; Hayashi, T. Photoinduced Hydrogen Evolution Catalyzed by a Synthetic Diiron Dithiolate Complex Embedded within a Protein Matrix. *ACS Catal.* **2014**, *4*, 2645−2648.
(130) Roy, A.; Madden, C.; Ghirlanda, G. Photo-induced hydrogen production in a helical peptide incorporating a [FeFe] hydrogenase active site mimic. *Chem. Commun.* **2012**, *48*, 9816−9818.
(131) Sano, Y.; Onoda, A.; Hayashi, T. A hydrogenase model system based on the sequence of cytochrome *c*: photochemical hydrogen evolution in aqueous media. *Chem. Commun.* **2011**, *47*, 8229−8231.
(132) Sano, Y.; Onoda, A.; Hayashi, T. Photocatalytic hydrogen evolution by a diiron hydrogenase model based on a peptide fragment of cytochrome c_{556} with an attached diiron carbonyl cluster and an attached ruthenium photosensitizer. *J. Inorg. Biochem.* **2012**, *108*, 159−162.
(133) Jian, J.-X.; Liu, Q.; Li, Z.-J.; Wang, F.; Li, X.-B.; Li, C.-B.; Liu, B.; Meng, Q.-Y.; Chen, B.; Feng, K.; et al. Chitosan confinement enhances hydrogen photogeneration from a mimic of the diiron subsite of [FeFe]-hydrogenase. *Nat. Commun.* **2013**, *4*, 2695.
(134) Orain, C.; Quentel, F.; Gloaguen, F. Photocatalytic Hydrogen Production Using Models of the Iron-Iron Hydrogenase Active Site Dispersed in Micellar Solution. *ChemSusChem* **2014**, *7*, 638−643.
(135) Quentel, F.; Passard, G.; Gloaguen, F. Electrochemical hydrogen production in aqueous micellar solution by a diiron benzenedithiolate complex relevant to [FeFe] hydrogenases. *Energy Environ. Sci.* **2012**, *5*, 7757−7761.
(136) Quentel, F.; Passard, G.; Gloaguen, F. A Binuclear Iron-Thiolate Catalyst for Electrochemical Hydrogen Production in Aqueous Micellar Solution. *Chem. - Eur. J.* **2012**, *18*, 13473−13479.
(137) Nguyen, A. D.; Rail, M. D.; Shanmugam, M.; Fettinger, J. C.; Berben, L. A. Electrocatalytic Hydrogen Evolution from Water by a Series of Iron Carbonyl Clusters. *Inorg. Chem.* **2013**, *52*, 12847−12854.
(138) Rail, M. D.; Berben, L. A. Directing the Reactivity of $[HFe_4N(CO)_{12}]^-$ toward H^+ or CO_2 Reduction by Understanding the Electrocatalytic Mechanism. *J. Am. Chem. Soc.* **2011**, *133*, 18577−18579.
(139) Loewen, N. D.; Thompson, E. J.; Kagan, M.; Banales, C. L.; Myers, T. W.; Fettinger, J. C.; Berben, L. A. A pendant proton shuttle on $[Fe_4N(CO)_{12}]^-$ alters product selectivity in formate vs. H_2 production via the hydride $[H{-}Fe_4N(CO)_{12}]$. *Chem. Sci.* **2016**, *7*, 2728−2735.
(140) Lv, H.; Ruberu, T. P. A.; Fleischauer, V. E.; Brennessel, W. W.; Neidig, M. L.; Eisenberg, R. Catalytic Light-Driven Generation of Hydrogen from Water by Iron Dithiolene Complexes. *J. Am. Chem. Soc.* **2016**, *138*, 11654−11663.
(141) Sproules, S.; Wieghardt, K. *o*-Dithiolene and *o*-aminothiolate chemistry of iron: Synthesis, structure and reactivity. *Coord. Chem. Rev.* **2010**, *254*, 1358−1382.
(142) Sellmann, D.; Geck, M.; Moll, M. Transition-Metal Complexes with Sulfur Ligands. 62. Hydrogen Evolution upon Reaction of Protons with Sulfur-Coordinated Fe(II) Complexes. Investigation of the H^+, H_2 and H^- Interactions with Iron 1,2-Benzenedithiolate Complexes. *J. Am. Chem. Soc.* **1991**, *113*, 5259−5264.
(143) Kang, B. S.; Weng, L. H.; Wu, D. X.; Wang, F.; Guo, Z.; Huang, L. R.; Huang, Z. Y.; Liu, H. Q. Pentacoordinate Iron-Sulfur Complexes. Structure and Spectroscopic and Electrochemical Properties of Phenoxy- and Thiophenoxy-Bridged Binuclear Complexes. *Inorg. Chem.* **1988**, *27*, 1128−1130.
(144) Ezzaher, S.; Gogoll, A.; Bruhn, C.; Ott, S. Directing protonation in [FeFe] hydrogenase active site models by modifications in their second coordination sphere. *Chem. Commun.* **2010**, *46*, 5775−5777.
(145) Begum, A.; Sarkar, S. An Iron(III) Dithiolene Complex as a Functional Model of Iron Hydrogenase. *Eur. J. Inorg. Chem.* **2012**, *2012*, 40−43.
(146) Yamazaki, S.-i. Metalloporphyrins and related metallomacrocycles as electrocatalysts for use in polymer electrolyte fuel cells and water electrolyzers. *Coord. Chem. Rev.* **2018**, *373*, 148−166.
(147) Zhang, W.; Lai, W.; Cao, R. Energy-Related Small Molecule Activation Reactions: Oxygen Reduction and Hydrogen and Oxygen Evolution Reactions Catalyzed by Porphyrin- and Corrole-Based Systems. *Chem. Rev.* **2017**, *117*, 3717−3797.
(148) Römelt, C.; Song, J.; Tarrago, M.; Rees, J. A.; van Gastel, M.; Weyhermüller, T.; DeBeer, S.; Bill, E.; Neese, F.; Ye, S. Electronic Structure of a Formal Iron(0) Porphyrin Complex Relevant to CO_2 Reduction. *Inorg. Chem.* **2017**, *56*, 4745−4750.
(149) Römelt, C.; Ye, S.; Bill, E.; Weyhermüller, T.; van Gastel, M.; Neese, F. Electronic Structure and Spin Multiplicity of Iron Tetraphenylporphyrins in Their Reduced States as Determined by a Combination of Resonance Raman Spectroscopy and Quantum Chemistry. *Inorg. Chem.* **2018**, *57*, 2141−2148.
(150) Hammouche, M.; Lexa, D.; Momenteau, M.; Savéant, J. M. Chemical Catalysis of Electrochemical Reactions. Homogeneous Catalysis of the Electrochemical Reduction of Carbon Dioxide by

DOI: 10.1021/acs.chemrev.8b00392
Chem. Rev. 2019, 119, 2752−2875

Iron(″0″) Porphyrins. Role of the Addition of Magnesium Cations. *J. Am. Chem. Soc.* **1991**, *113*, 8455−8466.
(151) Hammouche, M.; Lexa, D.; Savéant, J. M.; Momenteau, M. Catalysis of the electrochemical reduction of carbon dioxide by iron("0") porphyrins. *J. Electroanal. Chem. Interfacial Electrochem.* **1988**, *249*, 347−351.
(152) Bhugun, I.; Lexa, D.; Savéant, J.-M. Homogeneous Catalysis of Electrochemical Hydrogen Evolution by Iron(0) Porphyrins. *J. Am. Chem. Soc.* **1996**, *118*, 3982−3983.
(153) Graham, D. J.; Nocera, D. G. Electrocatalytic H_2 Evolution by Proton-Gated Hangman Iron Porphyrins. *Organometallics* **2014**, *33*, 4994−5001.
(154) Rana, A.; Mondal, B.; Sen, P.; Dey, S.; Dey, A. Activating Fe(I) Porphyrins for the Hydrogen Evolution Reaction Using Second-Sphere Proton Transfer Residues. *Inorg. Chem.* **2017**, *56*, 1783−1793.
(155) Cavell, A. C.; Hartley, C. L.; Liu, D.; Tribble, C. S.; McNamara, W. R. Sulfinato Iron(III) Complex for Electrocatalytic Proton Reduction. *Inorg. Chem.* **2015**, *54*, 3325−3330.
(156) Connor, G. P.; Mayer, K. J.; Tribble, C. S.; McNamara, W. R. Hydrogen Evolution Catalyzed by an Iron Polypyridyl Complex in Aqueous Solutions. *Inorg. Chem.* **2014**, *53*, 5408−5410.
(157) Hartley, C. L.; DiRisio, R. J.; Chang, T. Y.; Zhang, W.; McNamara, W. R. Electrocatalytic hydrogen evolution by an iron complex containing a nitro-functionalized polypyridyl ligand. *Polyhedron* **2016**, *114*, 133−137.
(158) Zhang, Y.-X.; Fu, L.-Z.; Zhou, L.-L.; Tang, L.-Z.; Zhan, S.-Z. Synthesis and catalytic properties of an iron(III) complex supported by amine-bis(phenolate) ligand. *J. Coord. Chem.* **2015**, *68*, 2286−2295.
(159) Zhou, L.-L.; Tang, L.-Z.; Zhang, Y.-X.; Zhan, S.-Z. Synthesis of a molecular electrocatalyst based on an iron(III) complex supported by amine-bis(phenolate) ligand for water reduction. *Polyhedron* **2015**, *92*, 124−129.
(160) Na, Y.; Wang, M.; Pan, J.; Zhang, P.; Åkermark, B.; Sun, L. Visible Light-Driven Electron Transfer and Hydrogen Generation Catalyzed by Bioinspired [2Fe2S] Complexes. *Inorg. Chem.* **2008**, *47*, 2805−2810.
(161) Zhang, P.; Wang, M.; Na, Y.; Li, X.; Jiang, Y.; Sun, L. Homogeneous photocatalytic production of hydrogen from water by a bioinspired $[Fe_2S_2]$ catalyst with high turnover numbers. *Dalton Trans.* **2010**, *39*, 1204−1206.
(162) Streich, D.; Astuti, Y.; Orlandi, M.; Schwartz, L.; Lomoth, R.; Hammarström, L.; Ott, S. High-Turnover Photochemical Hydrogen Production Catalyzed by a Model Complex of the [FeFe]-Hydrogenase Active Site. *Chem. - Eur. J.* **2010**, *16*, 60−63.
(163) Li, X.; Wang, M.; Chen, L.; Wang, X.; Dong, J.; Sun, L. Photocatalytic Water Reduction and Study of the Formation of Fe(I)Fe(0) Species in Diiron Catalyst Systems. *ChemSusChem* **2012**, *5*, 913−919.
(164) Wang, X.-B.; Zheng, H.-Q.; Rao, H.; Yao, H.-C.; Fan, Y.-T.; Hou, H.-W. Synthesis of a new iron−sulfur cluster compound and its photocatalytic H_2 evolution activity through visible light irradiation. *Appl. Organomet. Chem.* **2016**, *30*, 638−644.
(165) Yu, T.; Zeng, Y.; Chen, J.; Li, Y. Y.; Yang, G.; Li, Y. Exceptional Dendrimer-Based Mimics of Diiron Hydrogenase for the Photochemical Production of Hydrogen. *Angew. Chem., Int. Ed.* **2013**, *52*, 5631−5635.
(166) Eckenhoff, W. T. Molecular catalysts of Co, Ni, Fe, and Mo for hydrogen generation in artificial photosynthetic systems. *Coord. Chem. Rev.* **2018**, *373*, 295−316.
(167) Wang, F.; Wang, W.-G.; Wang, H.-Y.; Si, G.; Tung, C.-H.; Wu, L.-Z. Artificial Photosynthetic Systems Based on [FeFe]-Hydrogenase Mimics: the Road to High Efficiency for Light-Driven Hydrogen Evolution. *ACS Catal.* **2012**, *2*, 407−416.
(168) Wu, L. Z.; Chen, B.; Li, Z. J.; Tung, C. H. Enhancement of the Efficiency of Photocatalytic Reduction of Protons to Hydrogen via Molecular Assembly. *Acc. Chem. Res.* **2014**, *47*, 2177−2185.
(169) Gao, S.; Zhang, W.-Y.; Duan, Q.; Liang, Q.-C.; Jiang, D.-Y.; Zhao, J.-X.; Hou, J.-H. An artificial [FeFe]-hydrogenase mimic with organic chromophore-linked thiolate bridges for the photochemical production of hydrogen. *Chem. Pap.* **2017**, *71*, 617−625.
(170) Goy, R.; Apfel, U.-P.; Elleouet, C.; Escudero, D.; Elstner, M.; Görls, H.; Talarmin, J.; Schollhammer, P.; González, L.; Weigand, W. A Silicon-Heteroaromatic System as Photosensitizer for Light-Driven Hydrogen Production by Hydrogenase Mimics. *Eur. J. Inorg. Chem.* **2013**, *2013*, 4466−4472.
(171) Goy, R.; Bertini, L.; Rudolph, T.; Lin, S.; Schulz, M.; Zampella, G.; Dietzek, B.; Schacher, F. H.; De Gioia, L.; Sakai, K.; et al. Photocatalytic Hydrogen Evolution Driven by [FeFe] Hydrogenase Models Tethered to Fluorene and Silafluorene Sensitizers. *Chem. - Eur. J.* **2017**, *23*, 334−345.
(172) Gärtner, F.; Sundararaju, B.; Surkus, A. E.; Boddien, A.; Loges, B.; Junge, H.; Dixneuf, P. H.; Beller, M. Light-Driven Hydrogen Generation: Efficient Iron-Based Water Reduction Catalysts. *Angew. Chem., Int. Ed.* **2009**, *48*, 9962−9965.
(173) Gärtner, F.; Boddien, A.; Barsch, E.; Fumino, K.; Losse, S.; Junge, H.; Hollmann, D.; Brückner, A.; Ludwig, R.; Beller, M. Photocatalytic Hydrogen Generation from Water with Iron Carbonyl Phosphine Complexes: Improved Water Reduction Catalysts and Mechanistic Insights. *Chem. - Eur. J.* **2011**, *17*, 6425−6436.
(174) Gärtner, F.; Cozzula, D.; Losse, S.; Boddien, A.; Anilkumar, G.; Junge, H.; Schulz, T.; Marquet, N.; Spannenberg, A.; Gladiali, S.; et al. Synthesis, Characterisation and Application of Iridium(III) Photosensitisers for Catalytic Water Reduction. *Chem. - Eur. J.* **2011**, *17*, 6998−7006.
(175) Luo, S. P.; Mejía, E.; Friedrich, A.; Pazidis, A.; Junge, H.; Surkus, A. E.; Jackstell, R.; Denurra, S.; Gladiali, S.; Lochbrunner, S.; et al. Photocatalytic Water Reduction with Copper-Based Photosensitizers: A Noble-Metal-Free System. *Angew. Chem., Int. Ed.* **2013**, *52*, 419−423.
(176) Mejía, E.; Luo, S. P.; Karnahl, M.; Friedrich, A.; Tschierlei, S.; Surkus, A. E.; Junge, H.; Gladiali, S.; Lochbrunner, S.; Beller, M. A noble-metal-free system for photocatalytic hydrogen production from water. *Chem. - Eur. J.* **2013**, *19*, 15972−15978.
(177) Fischer, S.; Hollmann, D.; Tschierlei, S.; Karnahl, M.; Rockstroh, N.; Barsch, E.; Schwarzbach, P.; Luo, S.-P.; Junge, H.; Beller, M.; et al. Death and Rebirth: Photocatalytic Hydrogen Production by a Self-Organizing Copper−Iron System. *ACS Catal.* **2014**, *4*, 1845−1849.
(178) Sun, Y.-Y.; Wang, H.; Chen, N.-Y.; Lennox, A. J. J.; Friedrich, A.; Xia, L.-M.; Lochbrunner, S.; Junge, H.; Beller, M.; Zhou, S.; et al. Efficient Photocatalytic Water Reduction Using In Situ Generated Knölker's Iron Complexes. *ChemCatChem* **2016**, *8*, 2340−2344.
(179) Junge, H.; Rockstroh, N.; Fischer, S.; Brückner, A.; Ludwig, R.; Lochbrunner, S.; Kühn, O.; Beller, M. Light to Hydrogen: Photocatalytic Hydrogen Generation from Water with Molecularly-Defined Iron Complexes. *Inorganics* **2017**, *5*, 14.
(180) Hartley, C. L.; DiRisio, R. J.; Screen, M. E.; Mayer, K. J.; McNamara, W. R. Iron Polypyridyl Complexes for Photocatalytic Hydrogen Generation. *Inorg. Chem.* **2016**, *55*, 8865−8870.
(181) Queyriaux, N.; Jane, R. T.; Massin, J.; Artero, V.; Chavarot-Kerlidou, M. Recent developments in hydrogen evolving molecular cobalt(II)−polypyridyl catalysts. *Coord. Chem. Rev.* **2015**, *304−305*, 3−19.
(182) Thoi, V. S.; Kornienko, N.; Margarit, C. G.; Yang, P.; Chang, C. J. Visible-Light Photoredox Catalysis: Selective Reduction of Carbon Dioxide to Carbon Monoxide by a Nickel N-Heterocyclic Carbene−Isoquinoline Complex. *J. Am. Chem. Soc.* **2013**, *135*, 14413−14424.
(183) Artero, V.; Chavarot-Kerlidou, M.; Fontecave, M. Splitting Water with Cobalt. *Angew. Chem., Int. Ed.* **2011**, *50*, 7238−7266.
(184) Dempsey, J. L.; Brunschwig, B. S.; Winkler, J. R.; Gray, H. B. Hydrogen Evolution Catalyzed by Cobaloximes. *Acc. Chem. Res.* **2009**, *42*, 1995−2004.
(185) Schrauzer, G. N.; Holland, R. J. Hydridocobaloximes. *J. Am. Chem. Soc.* **1971**, *93*, 1505−1506.
(186) Fisher, B. J.; Eisenberg, R. Electrocatalytic reduction of carbon dioxide by using macrocycles of nickel and cobalt. *J. Am. Chem. Soc.* **1980**, *102*, 7361−7363.

DOI: 10.1021/acs.chemrev.8b00392
Chem. Rev. 2019, 119, 2752−2875

(187) Hawecker, J.; Lehn, J.-M.; Ziessel, R. Efficient Homogeneous Photochemical Hydrogen Generation and Water Reduction Mediated by Cobaloxime or Macrocyclic Cobalt Complexes. *Nouv. J. Chim.* **1983**, *7*, 271−277.
(188) Razavet, M.; Artero, V.; Fontecave, M. Proton Electroreduction Catalyzed by Cobaloximes: Functional Models for Hydrogenases. *Inorg. Chem.* **2005**, *44*, 4786−4795.
(189) Connolly, P.; Espenson, J. H. Cobalt-catalyzed evolution of molecular hydrogen. *Inorg. Chem.* **1986**, *25*, 2684−2688.
(190) Hu, X.; Cossairt, B. M.; Brunschwig, B. S.; Lewis, N. S.; Peters, J. C. Electrocatalytic hydrogen evolution by cobalt difluoroboryl-diglyoximate complexes. *Chem. Commun.* **2005**, *0*, 4723−4725.
(191) Lakadamyali, F.; Kato, M.; Muresan, N. M.; Reisner, E. Selective Reduction of Aqueous Protons to Hydrogen with a Synthetic Cobaloxime Catalyst in the Presence of Atmospheric Oxygen. *Angew. Chem., Int. Ed.* **2012**, *51*, 9381−9384.
(192) Wakerley, D. W.; Gross, M. A.; Reisner, E. Proton reduction by molecular catalysts in water under demanding atmospheres. *Chem. Commun.* **2014**, *50*, 15995−15998.
(193) Wakerley, D. W.; Reisner, E. Development and understanding of cobaloxime activity through electrochemical molecular catalyst screening. *Phys. Chem. Chem. Phys.* **2014**, *16*, 5739−5746.
(194) Willkomm, J.; Reisner, E. Photo- and electrocatalytic H_2 evolution with cobalt oxime complexes. *Bull. Jpn. Soc. Coord. Chem.* **2018**, *71*, 18−29.
(195) Wakerley, D. W.; Reisner, E. Oxygen-tolerant proton reduction catalysis: much O_2 about nothing? *Energy Environ. Sci.* **2015**, *8*, 2283−2295.
(196) Coutard, N.; Kaeffer, N.; Artero, V. Molecular engineered nanomaterials for catalytic hydrogen evolution and oxidation. *Chem. Commun.* **2016**, *52*, 13728−13748.
(197) Jacques, P.-A.; Artero, V.; Pécaut, J.; Fontecave, M. Cobalt and nickel diimine-dioxime complexes as molecular electrocatalysts for hydrogen evolution with low overvoltages. *Proc. Natl. Acad. Sci. U. S. A.* **2009**, *106*, 20627−20632.
(198) Kaeffer, N.; Chavarot-Kerlidou, M.; Artero, V. Hydrogen Evolution Catalyzed by Cobalt Diimine-Dioxime Complexes. *Acc. Chem. Res.* **2015**, *48*, 1286−1295.
(199) McCrory, C. C.; Uyeda, C.; Peters, J. C. Electrocatalytic Hydrogen Evolution in Acidic Water with Molecular Cobalt Tetraazamacrocycles. *J. Am. Chem. Soc.* **2012**, *134*, 3164−3170.
(200) Bhattacharjee, A.; Andreiadis, E. S.; Chavarot-Kerlidou, M.; Fontecave, M.; Field, M. J.; Artero, V. A Computational Study of the Mechanism of Hydrogen Evolution by Cobalt(Diimine-Dioxime) Catalysts. *Chem. - Eur. J.* **2013**, *19*, 15166−15174.
(201) Solis, B. H.; Yu, Y.; Hammes-Schiffer, S. Effects of Ligand Modification and Protonation on Metal Oxime Hydrogen Evolution Electrocatalysts. *Inorg. Chem.* **2013**, *52*, 6994−6999.
(202) Muckerman, J. T.; Fujita, E. Theoretical studies of the mechanism of catalytic hydrogen production by a cobaloxime. *Chem. Commun.* **2011**, *47*, 12456−12458.
(203) Anxolabéhère-Mallart, E.; Costentin, C.; Fournier, M.; Nowak, S.; Robert, M.; Savéant, J.-M. Boron-Capped Tris(glyoximato) Cobalt Clathrochelate as a Precursor for the Electrodeposition of Nanoparticles Catalyzing H_2 Evolution in Water. *J. Am. Chem. Soc.* **2012**, *134*, 6104−6107.
(204) Anxolabéhère-Mallart, E.; Costentin, C.; Fournier, M.; Robert, M. Cobalt-Bisglyoximato Diphenyl Complex as a Precatalyst for Electrocatalytic H_2 Evolution. *J. Phys. Chem. C* **2014**, *118*, 13377−13381.
(205) Cobo, S.; Heidkamp, J.; Jacques, P.-A.; Fize, J.; Fourmond, V.; Guetaz, L.; Jousselme, B.; Ivanova, V.; Dau, H.; Palacin, S.; et al. A Janus cobalt-based catalytic material for electro-splitting of water. *Nat. Mater.* **2012**, *11*, 802−807.
(206) Kaeffer, N.; Morozan, A.; Fize, J.; Martinez, E.; Guetaz, L.; Artero, V. The Dark Side of Molecular Catalysis: Diimine−Dioxime Cobalt Complexes Are Not the Actual Hydrogen Evolution Electrocatalyst in Acidic Aqueous Solutions. *ACS Catal.* **2016**, *6*, 3727−3737.
(207) Kellett, R. M.; Spiro, T. G. Cobalt(I) Porphyrin Catalysts of Hydrogen Production from Water. *Inorg. Chem.* **1985**, *24*, 2373−2377.
(208) Kleingardner, J. G.; Kandemir, B.; Bren, K. L. Hydrogen Evolution from Neutral Water under Aerobic Conditions Catalyzed by Cobalt Microperoxidase-11. *J. Am. Chem. Soc.* **2014**, *136*, 4−7.
(209) Beyene, B. B.; Mane, S. B.; Hung, C.-H. Highly efficient electrocatalytic hydrogen evolution from neutral aqueous solution by a water-soluble anionic cobalt(II) porphyrin. *Chem. Commun.* **2015**, *51*, 15067−15070.
(210) Liu, Y.; Fu, L.-Z.; Yang, L.-M.; Liu, X.-P.; Zhan, S.-Z.; Ni, C.-L. The impact of modifying the ligands on hydrogen production electrocatalyzed by *meso*-tetra-*p*-X-phenylporphin cobalt complexes, CoT(X)PP. *J. Mol. Catal. A: Chem.* **2016**, *417*, 101−106.
(211) Zhang, D.-X.; Yuan, H.-Q.; Wang, H.-H.; Ali, A.; Wen, W.-H.; Xie, A.-N.; Zhan, S.-Z.; Liu, H.-Y. Transition metal tetrapentafluorophenyl porphyrin catalyzed hydrogen evolution from acetic acid and water. *Transition Met. Chem.* **2017**, *42*, 773−782.
(212) Natali, M.; Luisa, A.; Iengo, E.; Scandola, F. Efficient photocatalytic hydrogen generation from water by a cationic cobalt(II) porphyrin. *Chem. Commun.* **2014**, *50*, 1842−1844.
(213) Lee, C. H.; Dogutan, D. K.; Nocera, D. G. Hydrogen Generation by Hangman Metalloporphyrins. *J. Am. Chem. Soc.* **2011**, *133*, 8775−8777.
(214) Bigi, J. P.; Hanna, T. E.; Harman, W. H.; Chang, A.; Chang, C. J. Electrocatalytic reduction of protons to hydrogen by a water-compatible cobalt polypyridyl platform. *Chem. Commun.* **2010**, *46*, 958−960.
(215) Khnayzer, R. S.; Thoi, V. S.; Nippe, M.; King, A. E.; Jurss, J. W.; El Roz, K. A.; Long, J. R.; Chang, C. J.; Castellano, F. N. Towards a comprehensive understanding of visible-light photogeneration of hydrogen from water using cobalt(II) polypyridyl catalysts. *Energy Environ. Sci.* **2014**, *7*, 1477−1488.
(216) Nippe, M.; Khnayzer, R. S.; Panetier, J. A.; Zee, D. Z.; Olaiya, B. S.; Head-Gordon, M.; Chang, C. J.; Castellano, F. N.; Long, J. R. Catalytic proton reduction with transition metal complexes of the redox-active ligand bpy2PYMe. *Chem. Sci.* **2013**, *4*, 3934−3945.
(217) Sun, Y.; Bigi, J. P.; Piro, N. A.; Tang, M. L.; Long, J. R.; Chang, C. J. Molecular Cobalt Pentapyridine Catalysts for Generating Hydrogen from Water. *J. Am. Chem. Soc.* **2011**, *133*, 9212−9215.
(218) Jurss, J. W.; Khnayzer, R. S.; Panetier, J. A.; El Roz, K. A.; Nichols, E. M.; Head-Gordon, M.; Long, J. R.; Castellano, F. N.; Chang, C. J. Bioinspired design of redox-active ligands for multielectron catalysis: effects of positioning pyrazine reservoirs on cobalt for electro- and photocatalytic generation of hydrogen from water. *Chem. Sci.* **2015**, *6*, 4954−4972.
(219) Stubbert, B. D.; Peters, J. C.; Gray, H. B. Rapid Water Reduction to H_2 Catalyzed by a Cobalt Bis(iminopyridine) Complex. *J. Am. Chem. Soc.* **2011**, *133*, 18070−18073.
(220) Leung, C.-F.; Chen, Y.-Z.; Yu, H.-Q.; Yiu, S.-M.; Ko, C.-C.; Lau, T.-C. Electro- and photocatalytic hydrogen generation in acetonitrile and aqueous solutions by a cobalt macrocyclic Schiff-base complex. *Int. J. Hydrogen Energy* **2011**, *36*, 11640−11645.
(221) McNamara, W. R.; Han, Z.; Yin, C.-J.; Brennessel, W. W.; Holland, P. L.; Eisenberg, R. Cobalt-dithiolene complexes for the photocatalytic and electrocatalytic reduction of protons in aqueous solutions. *Proc. Natl. Acad. Sci. U. S. A.* **2012**, *109*, 15594−15599.
(222) McNamara, W. R.; Han, Z.; Alperin, P. J.; Brennessel, W. W.; Holland, P. L.; Eisenberg, R. A Cobalt−Dithiolene Complex for the Photocatalytic and Electrocatalytic Reduction of Protons. *J. Am. Chem. Soc.* **2011**, *133*, 15368−15371.
(223) Solis, B. H.; Hammes-Schiffer, S. Computational Study of Anomalous Reduction Potentials for Hydrogen Evolution Catalyzed by Cobalt Dithiolene Complexes. *J. Am. Chem. Soc.* **2012**, *134*, 15253−15256.
(224) Utschig, L. M.; Silver, S. C.; Mulfort, K. L.; Tiede, D. M. Nature-Driven Photochemistry for Catalytic Solar Hydrogen Production: A Photosystem I−Transition Metal Catalyst Hybrid. *J. Am. Chem. Soc.* **2011**, *133*, 16334−16337.

DOI: 10.1021/acs.chemrev.8b00392
Chem. Rev. 2019, 119, 2752−2875

(225) Du, P.; Knowles, K.; Eisenberg, R. A Homogeneous System for the Photogeneration of Hydrogen from Water Based on a Platinum(II) Terpyridyl Acetylide Chromophore and a Molecular Cobalt Catalyst. *J. Am. Chem. Soc.* **2008**, *130*, 12576−12577.
(226) Du, P.; Schneider, J.; Luo, G.; Brennessel, W. W.; Eisenberg, R. Visible Light-Driven Hydrogen Production from Aqueous Protons Catalyzed by Molecular Cobaloxime Catalysts. *Inorg. Chem.* **2009**, *48*, 4952−4962.
(227) To, W. P.; Tong, G. S.; Lu, W.; Ma, C.; Liu, J.; Chow, A. L.; Che, C. M. Luminescent Organogold(III) Complexes with Long-Lived Triplet Excited States for Light-Induced Oxidative C−H Bond Functionalization and Hydrogen Production. *Angew. Chem., Int. Ed.* **2012**, *51*, 2654−2657.
(228) McCormick, T. M.; Han, Z.; Weinberg, D. J.; Brennessel, W. W.; Holland, P. L.; Eisenberg, R. Impact of ligand exchange in hydrogen production from cobaloxime-containing photocatalytic systems. *Inorg. Chem.* **2011**, *50*, 10660−10666.
(229) Lazarides, T.; McCormick, T.; Du, P.; Luo, G.; Lindley, B.; Eisenberg, R. Making Hydrogen from Water Using a Homogeneous System Without Noble Metals. *J. Am. Chem. Soc.* **2009**, *131*, 9192−9194.
(230) McCormick, T. M.; Calitree, B. D.; Orchard, A.; Kraut, N. D.; Bright, F. V.; Detty, M. R.; Eisenberg, R. Reductive Side of Water Splitting in Artificial Photosynthesis: New Homogeneous Photosystems of Great Activity and Mechanistic Insight. *J. Am. Chem. Soc.* **2010**, *132*, 15480−15483.
(231) Wang, J.; Li, C.; Zhou, Q.; Wang, W.; Hou, Y.; Zhang, B.; Wang, X. Enhanced photocatalytic hydrogen production by introducing the carboxylic acid group into cobaloxime catalysts. *Dalton Trans.* **2015**, *44*, 17704−17711.
(232) Zhang, P.; Wang, M.; Dong, J.; Li, X.; Wang, F.; Wu, L.; Sun, L. Photocatalytic Hydrogen Production from Water by Noble-Metal-Free Molecular Catalyst Systems Containing Rose Bengal and the Cobaloximes of BF_x-Bridged Oxime Ligands. *J. Phys. Chem. C* **2010**, *114*, 15868−15874.
(233) Zhang, P.; Jacques, P. A.; Chavarot-Kerlidou, M.; Wang, M.; Sun, L.; Fontecave, M.; Artero, V. Phosphine Coordination to a Cobalt Diimine-Dioxime Catalyst Increases Stability During Light-Driven H_2 Production. *Inorg. Chem.* **2012**, *51*, 2115−2120.
(234) Guttentag, M.; Rodenberg, A.; Kopelent, R.; Probst, B.; Buchwalder, C.; Brandstätter, M.; Hamm, P.; Alberto, R. Photocatalytic H_2 Production with a Rhenium/Cobalt System in Water under Acidic Conditions. *Eur. J. Inorg. Chem.* **2012**, *2012*, 59−64.
(235) Zhang, P.; Wang, M.; Li, C.; Li, X.; Dong, J.; Sun, L. Photochemical H_2 with noble-metal-free molecular devices comprising a porphyrin photosensitizer and a cobaloxime catalyst. *Chem. Commun.* **2009**, *46*, 8806−8808.
(236) Luo, G.-G.; Fang, K.; Wu, J.-H.; Dai, J.-C.; Zhao, Q.-H. Noble-metal-free BODIPY-cobaloxime photocatalysts for visible-light-driven hydrogen production. *Phys. Chem. Chem. Phys.* **2014**, *16*, 23884−23894.
(237) Luo, G.-G.; Fang, K.; Wu, J.-H.; Mo, J. Photocatalytic water reduction from a noble-metal-free molecular dyad based on a thienyl-expanded BODIPY photosensitizer. *Chem. Commun.* **2015**, *51*, 12361−12364.
(238) Xie, A.; Liu, X.-L.; Xiang, Y.-C.; Luo, G.-G. A homogeneous molecular system for the photogeneration of hydrogen from water based on a $[Ru^{II}(bpy)_3]^{2+}$ photosensitizer and a phthalycyanine cobalt catalyst. *J. Alloys Compd.* **2017**, *717*, 226−231.
(239) Luo, G. G.; Li, X. C.; Wang, J. H. Visible Light-Driven Hydrogen Evolution from Aqueous Solution in a Noble-Metal-Free System Catalyzed by a Cobalt Phthalocyanine. *ChemistrySelect* **2016**, *1*, 425−429.
(240) Yu, B.; Lever, A. B. P.; Swaddle, T. W. Electrochemistry of Metal Phthalocyanines in Organic Solvents at Variable Pressure. *Inorg. Chem.* **2004**, *43*, 4496−4504.
(241) Kirch, M.; Lehn, J. M.; Sauvage, J. P. Hydrogen Generation by Visible Light Irradiation of Aqueous Solutions of Metal Complexes. An approach to the photochemical conversion and storage of solar energy. *Helv. Chim. Acta* **1979**, *62*, 1345−1384.
(242) Krishnan, C. V.; Sutin, N. Homogeneous Catalysis of the Photoreduction of Water by Visible Light. 2. Mediation by a Tris(2,2'-bipyridine)ruthenium(II)-cobalt(II) Bipyridine System. *J. Am. Chem. Soc.* **1981**, *103*, 2141−2142.
(243) Goldsmith, J. I.; Hudson, W. R.; Lowry, M. S.; Anderson, T. H.; Bernhard, S. Discovery and High-Throughput Screening of Heteroleptic Iridium Complexes for Photoinduced Hydrogen Production. *J. Am. Chem. Soc.* **2005**, *127*, 7502−7510.
(244) Dong, J.; Wang, M.; Zhang, P.; Yang, S.; Liu, J.; Li, X.; Sun, L. Promoting Effect of Electrostatic Interaction between a Cobalt Catalyst and a Xanthene Dye on Visible-Light-Driven Electron Transfer and Hydrogen Production. *J. Phys. Chem. C* **2011**, *115*, 15089−15096.
(245) Leung, C.-F.; Ng, S.-M.; Ko, C.-C.; Man, W.-L.; Wu, J.; Chen, L.; Lau, T.-C. A cobalt(II) quaterpyridine complex as a visible light-driven catalyst for both water oxidation and reduction. *Energy Environ. Sci.* **2012**, *5*, 7903−7907.
(246) Tong, L.; Zong, R.; Thummel, R. P. Visible Light-Driven Hydrogen Evolution from Water Catalyzed by A Molecular Cobalt Complex. *J. Am. Chem. Soc.* **2014**, *136*, 4881−4884.
(247) Tong, L.; Kopecky, A.; Zong, R.; Gagnon, K. J.; Ahlquist, M. S.; Thummel, R. P. Light-Driven Proton Reduction in Aqueous Medium Catalyzed by a Family of Cobalt Complexes with Tetradentate Polypyridine-Type Ligands. *Inorg. Chem.* **2015**, *54*, 7873−7884.
(248) Guttentag, M.; Rodenberg, A.; Bachmann, C.; Senn, A.; Hamm, P.; Alberto, R. A highly stable polypyridyl-based cobalt catalyst for homo- and heterogeneous photocatalytic water reduction. *Dalton Trans.* **2013**, *42*, 334−337.
(249) Singh, W. M.; Baine, T.; Kudo, S.; Tian, S.; Ma, X. A.; Zhou, H.; DeYonker, N. J.; Pham, T. C.; Bollinger, J. C.; Baker, D. L.; et al. Electrocatalytic and Photocatalytic Hydrogen Production in Aqueous Solution by a Molecular Cobalt Complex. *Angew. Chem., Int. Ed.* **2012**, *51*, 5941−5944.
(250) Bachmann, C.; Guttentag, M.; Spingler, B.; Alberto, R. 3d Element Complexes of Pentadentate Bipyridine-Pyridine-Based Ligand Scaffolds: Structures and Photocatalytic Activities. *Inorg. Chem.* **2013**, *52*, 6055−6061.
(251) Bachmann, C.; Probst, B.; Guttentag, M.; Alberto, R. Ascorbate as an electron relay between an irreversible electron donor and Ru(II) or Re(I) photosensitizers. *Chem. Commun.* **2014**, *50*, 6737−6739.
(252) Lykkesfeldt, J. Determination of Ascorbic Acid and Dehydroascorbic Acid in Biological Samples by High-Performance Liquid Chromatography Using Subtraction Methods: Reliable Reduction with Tris[2-carboxyethyl]phosphine Hydrochloride. *Anal. Biochem.* **2000**, *282*, 89−93.
(253) Wechtersbach, L.; Cigić, B. Reduction of dehydroascorbic acid at low pH. *J. Biochem. Biophys. Methods* **2007**, *70*, 767−772.
(254) Joliat, E.; Schnidrig, S.; Probst, B.; Bachmann, C.; Spingler, B.; Baldridge, K. K.; von Rohr, F.; Schilling, A.; Alberto, R. Cobalt complexes of tetradentate, bipyridine-based macrocycles: their structures, properties and photocatalytic proton reduction. *Dalton Trans.* **2016**, *45*, 1737−1745.
(255) Tinnemans, A. H. A.; Koster, T. P. M.; Thewissen, D. H. M. W.; Mackor, A. Tetraaza-macrocyclic cobalt(II) and nickel(II) complexes as electron-transfer agents in the photo(electro)chemical and electrochemical reduction of carbon dioxide. *Recl. Trav. Chim. Pays-Bas* **1984**, *103*, 288−295.
(256) Gueret, R.; Poulard, L.; Oshinowo, M.; Chauvin, J.; Dahmane, M.; Dupeyre, G.; Lainé, P. P.; Fortage, J.; Collomb, M.-N. Challenging the $[Ru(bpy)_3]^{2+}$ Photosensitizer with a Triazatriangulenium Robust Organic Dye for Visible-Light-Driven Hydrogen Production in Water. *ACS Catal.* **2018**, *8*, 3792−3802.
(257) Rao, H.; Wang, Z.-Y.; Zheng, H.-Q.; Wang, X.-B.; Pan, C.-M.; Fan, Y.-T.; Hou, H.-W. Photocatalytic hydrogen evolution from a cobalt/nickel complex with dithiolene ligands under irradiation with visible light. *Catal. Sci. Technol.* **2015**, *5*, 2332−2339.
(258) Zhao, Y.; Wang, Y.; Wu, Q.; Lin, J.; Wu, S.; Hou, W.; Wu, R.; Luo, G. New tricks for an old dog: Visible light-driven hydrogen

DOI: 10.1021/acs.chemrev.8b00392
Chem. Rev. 2019, 119, 2752−2875

production from water catalyzed by *fac*- and *mer*- geometrical isomers of tris(thiosemicarbazide) cobalt(III). *Chin. J. Catal.* **2018**, *39*, 517−526.
(259) Das, A.; Han, Z.; Haghighi, M. G.; Eisenberg, R. Photogeneration of hydrogen from water using CdSe nanocrystals demonstrating the importance of surface exchange. *Proc. Natl. Acad. Sci. U. S. A.* **2013**, *110*, 16716−16723.
(260) Pantani, O.; Anxolabéhère-Mallart, E.; Aukauloo, A.; Millet, P. Electroactivity of cobalt and nickel glyoximes with regard to the electroreduction of protons into molecular hydrogen in acidic media. *Electrochem. Commun.* **2007**, *9*, 54−58.
(261) Efros, L. L.; Thorp, H. H.; Brudvig, G. W.; Crabtree, R. H. Towards a Functional Model of Hydrogenase: Electrocatalytic Reduction of Protons to Dihydrogen by a Nickel Macrocyclic Complex. *Inorg. Chem.* **1992**, *31*, 1722−1724.
(262) Lewis, J.; Schröder, M. Reduction of Schiff-base macrocyclic complexes. Stabilisation of nickel(I) conjugated macrocyclic complexes *via* a reversible ligand-to-metal electron-transfer process. *J. Chem. Soc., Dalton Trans.* **1982**, 1085−1089.
(263) Luca, O. R.; Konezny, S. J.; Blakemore, J. D.; Colosi, D. M.; Saha, S.; Brudvig, G. W.; Batista, V. S.; Crabtree, R. H. A tridentate Ni pincer for aqueous electrocatalytic hydrogen production. *New J. Chem.* **2012**, *36*, 1149−1152.
(264) Manuel, T. D.; Rohde, J.-U. Reaction of a Redox-Active Ligand Complex of Nickel with Dioxygen Probes Ligand-Radical Character. *J. Am. Chem. Soc.* **2009**, *131*, 15582−15583.
(265) Bediako, D. K.; Solis, B. H.; Dogutan, D. K.; Roubelakis, M. M.; Maher, A. G.; Lee, C. H.; Chambers, M. B.; Hammes-Schiffer, S.; Nocera, D. G. Role of pendant proton relays and proton-coupled electron transfer on the hydrogen evolution reaction by nickel hangman porphyrins. *Proc. Natl. Acad. Sci. U. S. A.* **2014**, *111*, 15001−15006.
(266) Solis, B. H.; Maher, A. G.; Dogutan, D. K.; Nocera, D. G.; Hammes-Schiffer, S. Nickel phlorin intermediate formed by proton-coupled electron transfer in hydrogen evolution mechanism. *Proc. Natl. Acad. Sci. U. S. A.* **2016**, *113*, 485−492.
(267) Han, Y.; Fang, H.; Jing, H.; Sun, H.; Lei, H.; Lai, W.; Cao, R. Singly versus Doubly Reduced Nickel Porphyrins for Proton Reduction: Experimental and Theoretical Evidence for a Homolytic Hydrogen-Evolution Reaction. *Angew. Chem., Int. Ed.* **2016**, *55*, 5457−5462.
(268) Wu, Z.-Y.; Wang, T.; Meng, Y.-S.; Rao, Y.; Wang, B.-W.; Zheng, J.; Gao, S.; Zhang, J.-L. Enhancing the reactivity of nickel(II) in hydrogen evolution reactions (HERs) by β-hydrogenation of porphyrinoid ligands. *Chem. Sci.* **2017**, *8*, 5953−5961.
(269) Zee, D. Z.; Chantarojsiri, T.; Long, J. R.; Chang, C. J. Metal−Polypyridyl Catalysts for Electro- and Photochemical Reduction of Water to Hydrogen. *Acc. Chem. Res.* **2015**, *48*, 2027−2036.
(270) Zhang, P.; Wang, M.; Yang, Y.; Zheng, D.; Han, K.; Sun, L. Highly efficient molecular nickel catalysts for electrochemical hydrogen production from neutral water. *Chem. Commun.* **2014**, *50*, 14153−14156.
(271) Kankanamalage, P. H. A.; Mazumder, S.; Tiwari, V.; Kpogo, K. K.; Schlegel, H. B.; Verani, C. N. Efficient electro/photocatalytic water reduction using a $[Ni^{II}(N_2Py_3)]^{2+}$ complex. *Chem. Commun.* **2016**, *52*, 13357−13360.
(272) Xue, D.; Peng, Q.-X.; Li, D.; Zhan, S.-Z. Synthesis, characterization and electro-catalytic properties of a water-soluble nickel(II) complex supported by picolinic acid ions. *Polyhedron* **2017**, *126*, 239−244.
(273) Xue, D.; Peng, Q.-X.; Zhan, S.-Z. Synthesis and electrochemical properties of a water soluble nickel(II) complex supported by *N*-phenylpyridin-2-ylmethanimine ligand. *Inorg. Chem. Commun.* **2017**, *82*, 11−15.
(274) Begum, A.; Moula, G.; Sarkar, S. A Nickel(II)−Sulfur-Based Radical-Ligand Complex as a Functional Model of Hydrogenase. *Chem. - Eur. J.* **2010**, *16*, 12324−12327.
(275) Zarkadoulas, A.; Field, M. J.; Papatriantafyllopoulou, C.; Fize, J.; Artero, V.; Mitsopoulou, C. A. Experimental and Theoretical Insight into Electrocatalytic Hydrogen Evolution with Nickel Bis(aryldithiolene) Complexes as Catalysts. *Inorg. Chem.* **2016**, *55*, 432−444.
(276) Bowmaker, G. A.; Boyd, P. D. W.; Campbell, G. K. Electrochemical and ESR Studies of the Redox Reactions of Nickel(II), Palladium(II), and Platinum(II) Complexes of 1,2-Diphenyl-1,2-ethenedithiolate(2−)-*S*,*S*′. *Inorg. Chem.* **1983**, *22*, 1208−1213.
(277) Koshiba, K.; Yamauchi, K.; Sakai, K. A Nickel Dithiolate Water Reduction Catalyst Providing Ligand-Based Proton-Coupled Electron-Transfer Pathways. *Angew. Chem.* **2017**, *129*, 4311−4315.
(278) Bachler, V.; Olbrich, G.; Neese, F.; Wieghardt, K. Theoretical Evidence for the Singlet Diradical Character of Square Planar Nickel Complexes Containing Two *o*-Semiquinonato Type Ligands. *Inorg. Chem.* **2002**, *41*, 4179−4193.
(279) Das, A.; Han, Z.; Brennessel, W. W.; Holland, P. L.; Eisenberg, R. Nickel Complexes for Robust Light-Driven and Electrocatalytic Hydrogen Production from Water. *ACS Catal.* **2015**, *5*, 1397−1406.
(280) Herebian, D.; Bothe, E.; Bill, E.; Weyhermüller, T.; Wieghardt, K. Experimental Evidence for the Noninnocence of *o*-Aminothiophenolates: Coordination Chemistry of *o*-Iminothionebenzosemiquinonate(1-) π-Radicals with Ni(II), Pd(II), Pt(II). *J. Am. Chem. Soc.* **2001**, *123*, 10012−10023.
(281) Bullock, R. M.; Appel, A. M.; Helm, M. L. Production of hydrogen by electrocatalysis: making the H−H bond by combining protons and hydrides. *Chem. Commun.* **2014**, *50*, 3125−3143.
(282) DuBois, D. L. Development of Molecular Electrocatalysts for Energy Storage. *Inorg. Chem.* **2014**, *53*, 3935−3960.
(283) Helm, M. L.; Stewart, M. P.; Bullock, R. M.; DuBois, D. L.; DuBois, M. R. A Synthetic Nickel Electrocatalyst with a Turnover Frequency Above 100,000 s^{-1} for H_2 Production. *Science* **2011**, *333*, 863−866.
(284) Hoffert, W. A.; Roberts, J. A.; Morris Bullock, R.; Helm, M. L. Production of H_2 at fast rates using a nickel electrocatalyst in water−acetonitrile solutions. *Chem. Commun.* **2013**, *49*, 7767−7769.
(285) Kilgore, U. J.; Roberts, J. A.; Pool, D. H.; Appel, A. M.; Stewart, M. P.; DuBois, M. R.; Dougherty, W. G.; Kassel, W. S.; Bullock, R. M.; DuBois, D. L. $[Ni(P^{Ph}_2N^{C6H4X}_2)_2]^{2+}$ Complexes as Electrocatalysts for H_2 Production: Effect of Substituents, Acids, and Water on Catalytic Rates. *J. Am. Chem. Soc.* **2011**, *133*, 5861−5872.
(286) Wilson, A. D.; Newell, R. H.; McNevin, M. J.; Muckerman, J. T.; Rakowski DuBois, M.; DuBois, D. L. Hydrogen Oxidation and Production Using Nickel-Based Molecular Catalysts with Positioned Proton Relays. *J. Am. Chem. Soc.* **2006**, *128*, 358−366.
(287) Smith, S. E.; Yang, J. Y.; DuBois, D. L.; Bullock, R. M. Reversible Electrocatalytic Production and Oxidation of Hydrogen at Low Overpotentials by a Functional Hydrogenase Mimic. *Angew. Chem., Int. Ed.* **2012**, *51*, 3152−3155.
(288) Rountree, E. S.; Dempsey, J. L. Potential-Dependent Electrocatalytic Pathways: Controlling Reactivity with pKa for Mechanistic Investigation of a Nickel-Based Hydrogen Evolution Catalyst. *J. Am. Chem. Soc.* **2015**, *137*, 13371−13380.
(289) Appel, A. M.; Pool, D. H.; O'Hagan, M.; Shaw, W. J.; Yang, J. Y.; Rakowski DuBois, M.; DuBois, D. L.; Bullock, R. M. $[Ni(P^{Ph}_2N^{Bn}_2)_2(CH_3CN)]^{2+}$ as an Electrocatalyst for H_2 Production: Dependence on Acid Strength and Isomer Distribution. *ACS Catal.* **2011**, *1*, 777−785.
(290) Horvath, S.; Fernandez, L. E.; Appel, A. M.; Hammes-Schiffer, S. pH-Dependent Reduction Potentials and Proton-Coupled Electron Transfer Mechanisms in Hydrogen-Producing Nickel Molecular Electrocatalysts. *Inorg. Chem.* **2013**, *52*, 3643−3652.
(291) O'Hagan, M.; Ho, M.-H.; Yang, J. Y.; Appel, A. M.; DuBois, M. R.; Raugei, S.; Shaw, W. J.; DuBois, D. L.; Bullock, R. M. Proton Delivery and Removal in $[Ni(P^{R}_2N^{R'}_2)_2]^{2+}$ Hydrogen Production and Oxidation Catalysts. *J. Am. Chem. Soc.* **2012**, *134*, 19409−19424.
(292) Wilson, A. D.; Shoemaker, R. K.; Miedaner, A.; Muckerman, J. T.; DuBois, D. L.; DuBois, M. R. Nature of hydrogen interactions with Ni(II) complexes containing cyclic phosphine ligands with pendant nitrogen bases. *Proc. Natl. Acad. Sci. U. S. A.* **2007**, *104*, 6951−6956.
(293) Wiese, S.; Kilgore, U. J.; Ho, M.-H.; Raugei, S.; DuBois, D. L.; Bullock, R. M.; Helm, M. L. Hydrogen Production Using Nickel

DOI: 10.1021/acs.chemrev.8b00392
Chem. Rev. 2019, 119, 2752−2875

Electrocatalysts with Pendant Amines: Ligand Effects on Rates and Overpotentials. *ACS Catal.* **2013**, *3*, 2527−2535.
(294) Stewart, M. P.; Ho, M. H.; Wiese, S.; Lindstrom, M. L.; Thogerson, C. E.; Raugei, S.; Bullock, R. M.; Helm, M. L. High Catalytic Rates for Hydrogen Production Using Nickel Electrocatalysts with Seven-Membered Cyclic Diphosphine Ligands Containing One Pendant Amine. *J. Am. Chem. Soc.* **2013**, *135*, 6033−6046.
(295) Gross, M. A.; Reynal, A.; Durrant, J. R.; Reisner, E. Versatile Photocatalytic Systems for H_2 Generation in Water Based on an Efficient DuBois-Type Nickel Catalyst. *J. Am. Chem. Soc.* **2014**, *136*, 356−366.
(296) Dutta, A.; DuBois, D. L.; Roberts, J. A. S.; Shaw, W. J. Amino acid modified Ni catalyst exhibits reversible H_2 oxidation/production over a broad pH range at elevated temperatures. *Proc. Natl. Acad. Sci. U. S. A.* **2014**, *111*, 16286−16291.
(297) Priyadarshani, N.; Dutta, A.; Ginovska, B.; Buchko, G. W.; O'Hagan, M.; Raugei, S.; Shaw, W. J. Achieving Reversible H_2/H^+ Interconversion at Room Temperature with Enzyme-Inspired Molecular Complexes: A Mechanistic Study. *ACS Catal.* **2016**, *6*, 6037−6049.
(298) Silver, S. C.; Niklas, J.; Du, P.; Poluektov, O. G.; Tiede, D. M.; Utschig, L. M. Protein Delivery of a Ni Catalyst to Photosystem I for Light-Driven Hydrogen Production. *J. Am. Chem. Soc.* **2013**, *135*, 13246−13249.
(299) Brown, H. J. S.; Wiese, S.; Roberts, J. A. S.; Bullock, R. M.; Helm, M. L. Electrocatalytic Hydrogen Production by $[Ni(7P^{Ph2}N^{H})_2]^{2+}$: Removing the Distinction Between Endo- and Exo-Protonation Sites. *ACS Catal.* **2015**, *5*, 2116−2123.
(300) Reback, M. L.; Buchko, G. W.; Kier, B. L.; Ginovska-Pangovska, B.; Xiong, Y.; Lense, S.; Hou, J.; Roberts, J. A.; Sorensen, C. M.; Raugei, S.; et al. Enzyme Design from the Bottom Up: An Active Nickel Electrocatalyst with a Structured Peptide Outer Coordination Sphere. *Chem. - Eur. J.* **2014**, *20*, 1510−1514.
(301) Reback, M. L.; Ginovska, B.; Buchko, G. W.; Dutta, A.; Priyadarshani, N.; Kier, B. L.; Helm, M. L.; Raugei, S.; Shaw, W. J. Investigating the role of chain and linker length on the catalytic activity of an H_2 production catalyst containing a β-hairpin peptide. *J. Coord. Chem.* **2016**, *69*, 1730−1747.
(302) Chen, L.; Chen, G.; Leung, C.-F.; Yiu, S.-M.; Ko, C.-C.; Anxolabéhère-Mallart, E.; Robert, M.; Lau, T.-C. Dual Homogeneous and Heterogeneous Pathways in Photo- and Electrocatalytic Hydrogen Evolution with Nickel(II) Catalysts Bearing Tetradentate Macrocyclic Ligands. *ACS Catal.* **2015**, *5*, 356−364.
(303) Luca, O. R.; Blakemore, J. D.; Konezny, S. J.; Praetorius, J. M.; Schmeier, T. J.; Hunsinger, G. B.; Batista, V. S.; Brudvig, G. W.; Hazari, N.; Crabtree, R. H. Organometallic Ni Pincer Complexes for the Electrocatalytic Production of Hydrogen. *Inorg. Chem.* **2012**, *51*, 8704−8709.
(304) Tatematsu, R.; Inomata, T.; Ozawa, T.; Masuda, H. Electrocatalytic Hydrogen Production by a Nickel(II) Complex with a Phosphinopyridyl Ligand. *Angew. Chem., Int. Ed.* **2016**, *55*, 5247−5250.
(305) Tsay, C.; Livesay, B. N.; Ruelas, S.; Yang, J. Y. Solvation Effects on Transition Metal Hydricity. *J. Am. Chem. Soc.* **2015**, *137*, 14114−14121.
(306) Tsay, C.; Yang, J. Y. Electrocatalytic Hydrogen Evolution under Acidic Aqueous Conditions and Mechanistic Studies of a Highly Stable Molecular Catalyst. *J. Am. Chem. Soc.* **2016**, *138*, 14174−14177.
(307) Henning, R.; Schlamann, W.; Kisch, H. Photolysis of Water Catalyzed by Transition Metal Dithiolenes. *Angew. Chem., Int. Ed. Engl.* **1980**, *19*, 645−646.
(308) Hontzopoulos, E.; Vrachnou-Astra, E.; Konstantatos, J.; Katakis, D. A new photosensitizer−catalyst for the photochemical cleavage of water. *J. Photochem.* **1985**, *30*, 117−120.
(309) McLaughlin, M. P.; McCormick, T. M.; Eisenberg, R.; Holland, P. L. A stable molecular nickel catalyst for the homogeneous photogeneration of hydrogen in aqueous solution. *Chem. Commun.* **2011**, *47*, 7989−7991.
(310) Inoue, S.; Mitsuhashi, M.; Ono, T.; Yan, Y. N.; Kataoka, Y.; Handa, M.; Kawamoto, T. Photo- and Electrocatalytic Hydrogen Production Using Valence Isomers of N_2S_2-Type Nickel Complexes. *Inorg. Chem.* **2017**, *56*, 12129−12138.
(311) Luo, G. G.; Wang, Y. H.; Wang, J. H.; Wu, J. H.; Wu, R. B. A square-planar nickel dithiolate complex as an efficient molecular catalyst for the electro- and photoreduction of protons. *Chem. Commun.* **2017**, *53*, 7007−7010.
(312) Wise, C. F.; Liu, D.; Mayer, K. J.; Crossland, P. M.; Hartley, C. L.; McNamara, W. R. A nickel complex of a conjugated bis-dithiocarbazate Schiff base for the photocatalytic production of hydrogen. *Dalton Trans.* **2015**, *44*, 14265−14271.
(313) Jing, X.; Wu, P.; Liu, X.; Yang, L.; He, C.; Duan, C. Light-driven hydrogen evolution with a nickel thiosemicarbazone redox catalyst featuring Ni···H interactions under basic conditions. *New J. Chem.* **2015**, *39*, 1051−1059.
(314) Han, Z.; McNamara, W. R.; Eum, M. S.; Holland, P. L.; Eisenberg, R. A Nickel Thiolate Catalyst for the Long-Lived Photocatalytic Production of Hydrogen in a Noble-Metal-Free System. *Angew. Chem., Int. Ed.* **2012**, *51*, 1667−1670.
(315) Han, Z.; Shen, L.; Brennessel, W. W.; Holland, P. L.; Eisenberg, R. Nickel Pyridinethiolate Complexes as Catalysts for the Light-Driven Production of Hydrogen from Aqueous Solutions in Noble-Metal-Free Systems. *J. Am. Chem. Soc.* **2013**, *135*, 14659−14669.
(316) Yuan, Y. J.; Lu, H. W.; Tu, J. R.; Fang, Y.; Yu, Z. T.; Fan, X. X.; Zou, Z. G. A Noble-Metal-Free Nickel(II) Polypyridyl Catalyst for Visible-Light-Driven Hydrogen Production from Water. *ChemPhysChem* **2015**, *16*, 2925−2930.
(317) Yang, Y.; Wang, M.; Xue, L.; Zhang, F.; Chen, L.; Ahlquist, M. S.; Sun, L. Nickel Complex with Internal Bases as Efficient Molecular Catalyst for Photochemical H_2 Production. *ChemSusChem* **2014**, *7*, 2889−2897.
(318) Campbell, R. H.; Heath, G. A.; Hefter, G. T.; McQueen, R. C. S. A.C. and D.C. voltammetry in liquid naphthalene solutions: stepwise electrode potentials for metal phthalocyanines and porphyrins in strictly non-co-ordinating media. *J. Chem. Soc., Chem. Commun.* **1983**, 1123−1125.
(319) Liao, M.-S.; Scheiner, S. Electronic structure and bonding in metal phthalocyanines, Metal = Fe, Co, Ni, Cu, Zn, Mg. *J. Chem. Phys.* **2001**, *114*, 9780−9791.
(320) Yuan, Y. J.; Tu, J. R.; Lu, H. W.; Yu, Z. T.; Fan, X. X.; Zou, Z. G. Neutral nickel(II) phthalocyanine as a stable catalyst for visible-light-driven hydrogen evolution from water. *Dalton Trans.* **2016**, *45*, 1359−1363.
(321) Cui, H. H.; Wang, J. Y.; Hu, M. Q.; Ma, C. B.; Wen, H. M.; Song, X. W.; Chen, C. N. Efficient photo-driven hydrogen evolution by binuclear nickel catalysts of different coordination in noble-metal-free systems. *Dalton Trans.* **2013**, *42*, 8684−8691.
(322) Zhang, W.; Hong, J.; Zheng, J.; Huang, Z.; Zhou, J. S.; Xu, R. Nickel−Thiolate Complex Catalyst Assembled in One Step in Water for Solar H_2 Production. *J. Am. Chem. Soc.* **2011**, *133*, 20680−20683.
(323) Kagalwala, H. N.; Gottlieb, E.; Li, G.; Li, T.; Jin, R.; Bernhard, S. Photocatalytic Hydrogen Generation System Using a Nickel-Thiolate Hexameric Cluster. *Inorg. Chem.* **2013**, *52*, 9094−9101.
(324) Kügler, M.; Scholz, J.; Kronz, A.; Siewert, I. Copper complexes as catalyst precursors in the electrochemical hydrogen evolution reaction. *Dalton Trans.* **2016**, *45*, 6974−6982.
(325) Liu, X.; Cui, S.; Sun, Z.; Du, P. Robust and highly active copper-based electrocatalyst for hydrogen production at low overpotential in neutral water. *Chem. Commun.* **2015**, *51*, 12954−12957.
(326) Liu, X.; Zheng, H.; Sun, Z.; Han, A.; Du, P. Earth-Abundant Copper-Based Bifunctional Electrocatalyst for Both Catalytic Hydrogen Production and Water Oxidation. *ACS Catal.* **2015**, *5*, 1530−1538.
(327) Nestke, S.; Kügler, M.; Scholz, J.; Wilken, M.; Jooss, C.; Siewert, I. A Copper Complex as Catalyst in Proton Reduction. *Eur. J. Inorg. Chem.* **2017**, *2017*, 3376−3382.
(328) Zhang, P.; Wang, M.; Chen, H.; Liang, Y.; Sun, J.; Sun, L. A Cu-Based Nanoparticulate Film as Super-Active and Robust Catalyst Surpasses Pt for Electrochemical H_2 Production from Neutral and Weak Acidic Aqueous Solutions. *Adv. Energy Mater.* **2016**, *6*, 1502319.

DOI: 10.1021/acs.chemrev.8b00392
Chem. Rev. 2019, 119, 2752−2875

(329) Atkins, P. W. *Shriver & Atkins' Inorganic Chemistry*; Oxford University Press: Oxford, U.K., 2010.
(330) Burg, A.; Maimon, E.; Cohen, H.; Meyerstein, D. Ligand Effects on the Chemical Activity of Copper(I) Complexes: Outer- and Inner-Sphere Oxidation of $Cu^{I}L$. *Eur. J. Inorg. Chem.* **2007**, 530−536.
(331) Zhang, P.; Wang, M.; Yang, Y.; Yao, T.; Sun, L. A Molecular Copper Catalyst for Electrochemical Water Reduction with a Large Hydrogen-Generation Rate Constant in Aqueous Solution. *Angew. Chem., Int. Ed.* **2014**, *53*, 13803−13807.
(332) Ekanayake, D. M.; Kulesa, K. M.; Singh, J.; Kpogo, K. K.; Mazumder, S.; Schlegel, H. B.; Verani, C. N. A pentadentate nitrogen-rich copper electrocatalyst for water reduction with pH-dependent molecular mechanisms. *Dalton Trans.* **2017**, *46*, 16812−16820.
(333) Xin, Z.-J.; Liu, S.; Li, C.-B.; Lei, Y.-J.; Xue, D.-X.; Gao, X.-W.; Wang, H.-Y. Hydrogen production in a neutral aqueous solution with a water-soluble copper complex. *Int. J. Hydrogen Energy* **2017**, *42*, 4202−4207.
(334) Cao, J.-P.; Fang, T.; Fu, L.-Z.; Zhou, L.-L.; Zhan, S.-Z. First mononuclear copper(II) electro-catalyst for catalyzing hydrogen evolution from acetic acid and water. *Int. J. Hydrogen Energy* **2014**, *39*, 13972−13978.
(335) Samide, M. J.; Peters, D. G. Electrochemical reduction of copper(II) salen at carbon cathodes in dimethylformamide. *J. Electroanal. Chem.* **1998**, *443*, 95−102.
(336) Fu, L.-Z.; Fang, T.; Zhou, L.-L.; Zhan, S.-Z. A mononuclear copper electrocatalyst for both water reduction and oxidation. *RSC Adv.* **2014**, *4*, 53674−53680.
(337) Cao, J.-P.; Fang, T.; Wang, Z.-Q.; Ren, Y.-W.; Zhan, S. A dinuclear triazenido−copper complex: A new molecular electro-catalyst for generating hydrogen from acetic acid or water. *J. Mol. Catal. A: Chem.* **2014**, *391*, 191−197.
(338) Fang, T.; Lu, H.-X.; Zhao, J.-X.; Zhan, S.-Z.; Lv, Q.-Y. A new copper(I)−triazenido electro-catalyst for catalyzing hydrogen evolution from acetic acid and water. *J. Mol. Catal. A: Chem.* **2015**, *396*, 304−309.
(339) Fang, T.; Zhou, L.-L.; Fu, L.-Z.; Zhan, S.-Z.; Lv, Q.-Y. Synthesis and studies of a molecular copper(I)-triazenido electrocatalyst for catalyzing hydrogen evolution from acetic acid and water. *Polyhedron* **2015**, *85*, 355−360.
(340) Wang, J.; Li, C.; Zhou, Q.; Wang, W.; Hou, Y.; Zhang, B.; Wang, X. Photocatalytic hydrogen evolution by Cu(II) complexes. *Dalton Trans.* **2016**, *45*, 5439−5443.
(341) Majee, K.; Patel, J.; Das, B.; Padhi, S. K. μ-Pyridine-bridged copper complex with robust proton-reducing ability. *Dalton Trans.* **2017**, *46*, 14869−14879.
(342) Perra, A.; Davies, E. S.; Hyde, J. R.; Wang, Q.; McMaster, J.; Schröder, M. Electrocatalytic production of hydrogen by a synthetic model of [NiFe] hydrogenases. *Chem. Commun.* **2006**, *0*, 1103−1105.
(343) Lauderbach, F.; Prakash, R.; Götz, A. W.; Munoz, M.; Heinemann, F. W.; Nickel, U.; Hess, B. A.; Sellmann, D. Alternative Synthesis, Density Functional Calculations and Proton Reactivity Study of a Trinuclear [NiFe] Hydrogenase Model Compound. *Eur. J. Inorg. Chem.* **2007**, *2007*, 3385−3393.
(344) Barton, B. E.; Whaley, C. M.; Rauchfuss, T. B.; Gray, D. L. Nickel−Iron Dithiolato Hydrides Relevant to the [NiFe]-Hydrogenase Active Site. *J. Am. Chem. Soc.* **2009**, *131*, 6942−6943.
(345) Barton, B. E.; Rauchfuss, T. B. Hydride-Containing Models for the Active Site of the Nickel−Iron Hydrogenases. *J. Am. Chem. Soc.* **2010**, *132*, 14877−14885.
(346) Canaguier, S.; Field, M.; Oudart, Y.; Pécaut, J.; Fontecave, M.; Artero, V. A structural and functional mimic of the active site of NiFe hydrogenases. *Chem. Commun.* **2010**, *46*, 5876−5878.
(347) Ding, S.; Ghosh, P.; Lunsford, A. M.; Wang, N.; Bhuvanesh, N.; Hall, M. B.; Darensbourg, M. Y. Hemilabile Bridging Thiolates as Proton Shuttles in Bioinspired H_2 Production Electrocatalysts. *J. Am. Chem. Soc.* **2016**, *138*, 12920−12927.
(348) Gan, L.; Groy, T. L.; Tarakeshwar, P.; Mazinani, S. K. S.; Shearer, J.; Mujica, V.; Jones, A. K. A Nickel Phosphine Complex as a Fast and Efficient Hydrogen Production Catalyst. *J. Am. Chem. Soc.* **2015**, *137*, 1109−1115.
(349) Brazzolotto, D.; Gennari, M.; Queyriaux, N.; Simmons, T. R.; Pécaut, J.; Demeshko, S.; Meyer, F.; Orio, M.; Artero, V.; Duboc, C. Nickel-centred proton reduction catalysis in a model of [NiFe] hydrogenase. *Nat. Chem.* **2016**, *8*, 1054−1060.
(350) Fourmond, V.; Canaguier, S.; Golly, B.; Field, M. J.; Fontecave, M.; Artero, V. A nickel−manganese catalyst as a biomimic of the active site of NiFe hydrogenases: a combined electrocatalytical and DFT mechanistic study. *Energy Environ. Sci.* **2011**, *4*, 2417−2427.
(351) Song, L.-C.; Li, J.-P.; Xie, Z.-J.; Song, H.-B. Synthesis, Structural Characterization, and Electrochemical Properties of Dinuclear Ni/Mn Model Complexes for the Active Site of [NiFe]-Hydrogenases. *Inorg. Chem.* **2013**, *52*, 11618−11626.
(352) Paparo, A.; Silvia, J. S.; Kefalidis, C. E.; Spaniol, T. P.; Maron, L.; Okuda, J.; Cummins, C. C. A Dimetalloxycarbene Bonding Mode and Reductive Coupling Mechanism for Oxalate Formation from CO_2. *Angew. Chem., Int. Ed.* **2015**, *54*, 9115−9119.
(353) Woen, D. H.; Chen, G. P.; Ziller, J. W.; Boyle, T. J.; Furche, F.; Evans, W. J. Solution Synthesis, Structure, and CO_2 Reduction Reactivity of a Scandium(II) Complex, $\{Sc[N(SiMe_3)_2]_3\}^-$. *Angew. Chem., Int. Ed.* **2017**, *56*, 2050−2053.
(354) Rebelein, J. G.; Hu, Y.; Ribbe, M. W. Differential Reduction of CO_2 by Molybdenum and Vanadium Nitrogenases. *Angew. Chem., Int. Ed.* **2014**, *53*, 11543−11546.
(355) Rebelein, J. G.; Hu, Y.; Ribbe, M. W. Widening the Product Profile of Carbon Dioxide Reduction by Vanadium Nitrogenase. *ChemBioChem* **2015**, *16*, 1993−1996.
(356) Sippel, D.; Einsle, O. The structure of vanadium nitrogenase reveals an unusual bridging ligand. *Nat. Chem. Biol.* **2017**, *13*, 956−960.
(357) Chinchen, G. C.; Logan, R. H.; Spencer, M. S. Water-gas shift reaction over an iron oxide/chromium oxide catalyst.: I: Mass transport effects. *Appl. Catal.* **1984**, *12*, 69−88.
(358) Darensbourg, D. J.; Rokicki, A.; Darensbourg, M. Y. Facile reduction of carbon dioxide by anionic Group 6b metal hydrides. Chemistry relevant to catalysis of the water-gas shift reaction. *J. Am. Chem. Soc.* **1981**, *103*, 3223−3224.
(359) Newsome, D. S. *Cat. Rev. − Sci. Eng.* **1980**, *21*, 275−318.
(360) Lee, G. R.; Maher, J. M.; Cooper, N. J. Reductive Disproportionation of Carbon Dioxide by Dianionic Carbonylmetalates of the Transition Metals. *J. Am. Chem. Soc.* **1987**, *109*, 2956−2962.
(361) Grice, K. A.; Saucedo, C. Electrocatalytic Reduction of CO_2 by Group 6 $M(CO)_6$ Species without "Non-Innocent" Ligands. *Inorg. Chem.* **2016**, *55*, 6240−6246.
(362) Hawecker, J.; Lehn, J.-M.; Ziessel, R. Electrocatalytic reduction of carbon dioxide mediated by $Re(bipy)(CO)_3Cl$ (bipy = 2,2'-bipyridine). *J. Chem. Soc., Chem. Commun.* **1984**, 328−330.
(363) Sinopoli, A.; La Porte, N. T.; Martinez, J. F.; Wasielewski, M. R.; Sohail, M. Manganese carbonyl complexes for CO_2 reduction. *Coord. Chem. Rev.* **2018**, *365*, 60−74.
(364) Stanbury, M.; Compain, J.-D.; Chardon-Noblat, S. Electro and photoreduction of CO_2 driven by manganese-carbonyl molecular catalysts. *Coord. Chem. Rev.* **2018**, *361*, 120−137.
(365) Stor, G. J.; Morrison, S. L.; Stufkens, D. J.; Oskam, A. The Remarkable Photochemistry of *fac*-$XMn(CO)_3(\alpha$-diimine) (X = Halide): Formation of $Mn_2(CO)_6(\alpha$-diimine)$_2$ via the *mer* Isomer and Photocatalytic Substitution of X^- in the Presence of PR_3. *Organometallics* **1994**, *13*, 2641−2650.
(366) van der Graaf, T.; Hofstra, R. M. J.; Schilder, P. G. M.; Rijkhoff, M.; Stufkens, D. J.; Van der Linden, J. G. M. Metal to Ligand Charge-Transfer Photochemistry of Metal−Metal-Bonded Complexes. 10. Photochemical and Electrochemical Study of the Electron-Transfer Reactions of $Mn(CO)_3(\alpha$-diimine)(L) (L = N-, P-donor) Radicals Formed by Irradiation of $(CO)_5MnMn(CO)_3(\alpha$-diimine) Complexes in the Presence of L. *Organometallics* **1991**, *10*, 3668−3679.
(367) Bourrez, M.; Orio, M.; Molton, F.; Vezin, H.; Duboc, C.; Deronzier, A.; Chardon-Noblat, S. Pulsed-EPR Evidence of a Manganese(II) Hydroxycarbonyl Intermediate in the Electrocatalytic

DOI: 10.1021/acs.chemrev.8b00392
Chem. Rev. 2019, 119, 2752−2875

Reduction of Carbon Dioxide by a Manganese Bipyridyl Derivative. *Angew. Chem., Int. Ed.* **2014**, *53*, 240−243.
(368) Riplinger, C.; Carter, E. A. Influence of Weak Brønsted Acids on Electrocatalytic CO_2 Reduction by Manganese and Rhenium Bipyridine Catalysts. *ACS Catal.* **2015**, *5*, 900−908.
(369) Riplinger, C.; Sampson, M. D.; Ritzmann, A. M.; Kubiak, C. P.; Carter, E. A. Mechanistic Contrasts between Manganese and Rhenium Bipyridine Electrocatalysts for the Reduction of Carbon Dioxide. *J. Am. Chem. Soc.* **2014**, *136*, 16285−16298.
(370) Machan, C. W.; Stanton, C. J., III; Vandezande, J. E.; Majetich, G. F.; Schaefer, H. F., III; Kubiak, C. P.; Agarwal, J. Electrocatalytic Reduction of Carbon Dioxide by $Mn(CN)(2,2'\text{-bipyridine})(CO)_3$: CN Coordination Alters Mechanism. *Inorg. Chem.* **2015**, *54*, 8849−8856.
(371) Sun, C.; Rotundo, L.; Garino, C.; Nencini, L.; Yoon, S. S.; Gobetto, R.; Nervi, C. Electrochemical CO_2 Reduction at Glassy Carbon Electrodes Functionalized by Mn^I and Re^I Organometallic Complexes. *ChemPhysChem* **2017**, *18*, 3219−3229.
(372) Hartl, F.; Rosa, P.; Ricard, L.; Le Floch, P.; Záliš, S. Electronic transitions and bonding properties in a series of five-coordinate "16-electron" complexes $[Mn(CO)_3(L_2)]^-$ (L_2=chelating redox-active π-donor ligand). *Coord. Chem. Rev.* **2007**, *251*, 557−576.
(373) Pickett, C. J.; Pletcher, D. Electrochemical oxidation and reduction of binary metal carbonyls in aprotic solvents. *J. Chem. Soc., Dalton Trans.* **1975**, 879−886.
(374) Vandezande, J. E.; Schaefer, H. F., III CO_2 Reduction Pathways on $MnBr(N\text{-}C)(CO)_3$ Electrocatalysts. *Organometallics* **2018**, *37*, 337−342.
(375) Franco, F.; Pinto, M. F.; Royo, B.; Lloret-Fillol, J. A Highly Active N-Heterocyclic Carbene Manganese(I) Complex for Selective Electrocatalytic CO_2 Reduction to CO. *Angew. Chem., Int. Ed.* **2018**, *57*, 4603−4606.
(376) Spall, S. J. P.; Keane, T.; Tory, J.; Cocker, D. C.; Adams, H.; Fowler, H.; Meijer, A. J. H. M.; Hartl, F.; Weinstein, J. A. Manganese Tricarbonyl Complexes with Asymmetric 2-Iminopyridine Ligands: Toward Decoupling Steric and Electronic Factors in Electrocatalytic CO_2 Reduction. *Inorg. Chem.* **2016**, *55*, 12568−12582.
(377) Vollmer, M. V.; Machan, C. W.; Clark, M. L.; Antholine, W. E.; Agarwal, J.; Schaefer, H. F., III; Kubiak, C. P.; Walensky, J. R. Synthesis, Spectroscopy, and Electrochemistry of $(\alpha\text{-Diimine})M(CO)_3Br$, M = Mn, Re, Complexes: Ligands Isoelectronic to Bipyridyl Show Differences in CO_2 Reduction. *Organometallics* **2015**, *34*, 3−12.
(378) Sampson, M. D.; Kubiak, C. P. Manganese Electrocatalysts with Bulky Bipyridine Ligands: Utilizing Lewis Acids To Promote Carbon Dioxide Reduction at Low Overpotentials. *J. Am. Chem. Soc.* **2016**, *138*, 1386−1393.
(379) Franco, F.; Cometto, C.; Ferrero Vallana, F.; Sordello, F.; Priola, E.; Minero, C.; Nervi, C.; Gobetto, R. A local proton source in a $[Mn(bpy\text{-}R)(CO)_3Br]$-type redox catalyst enables CO_2 reduction even in the absence of Brønsted acids. *Chem. Commun.* **2014**, *50*, 14670−14673.
(380) Ngo, K. T.; McKinnon, M.; Mahanti, B.; Narayanan, R.; Grills, D. C.; Ertem, M. Z.; Rochford, J. Turning on the Protonation-First Pathway for Electrocatalytic CO_2 Reduction by Manganese Bipyridyl Tricarbonyl Complexes. *J. Am. Chem. Soc.* **2017**, *139*, 2604−2618.
(381) Machan, C. W.; Kubiak, C. P. Electrocatalytic reduction of carbon dioxide with Mn(terpyridine) carbonyl complexes. *Dalton Trans.* **2016**, *45*, 17179−17186.
(382) Mukhopadhyay, T. K.; MacLean, N. L.; Gan, L.; Ashley, D. C.; Groy, T. L.; Baik, M. H.; Jones, A. K.; Trovitch, R. J. Carbon Dioxide Promoted H^+ Reduction Using a Bis(imino)pyridine Manganese Electrocatalyst. *Inorg. Chem.* **2015**, *54*, 4475−4482.
(383) Rao, G. K.; Pell, W.; Korobkov, I.; Richeson, D. Electrocatalytic reduction of CO_2 using Mn complexes with unconventional coordination environments. *Chem. Commun.* **2016**, *52*, 8010−8013.
(384) Stor, G. J.; Stufkens, D. J.; Vernooijs, P.; Baerends, E. J.; Fraanje, J.; Goubitz, K. X-ray Structure of *fac*-$IMn(CO)_3(bpy)$ and Electronic Structures and Transitions of the Complexes *fac*-$XMn(CO)_3(bpy)$ (X = Cl, I) and *mer*-$ClMn(CO)_3(bpy)$. *Inorg. Chem.* **1995**, *34*, 1588−1594.
(385) Grills, D. C.; Farrington, J. A.; Layne, B. H.; Lymar, S. V.; Mello, B. A.; Preses, J. M.; Wishart, J. F. Mechanism of the Formation of a Mn-Based CO_2 Reduction Catalyst Revealed by Pulse Radiolysis with Time-Resolved Infrared Detection. *J. Am. Chem. Soc.* **2014**, *136*, 5563−5566.
(386) Allen, D. M.; Cox, A.; Kemp, T. J.; Sultana, Q.; Pitts, R. B. Photochemistry of some binuclear carbonyl compounds of manganese, rhenium, molybdenum, and tungsten, and of some related pentacarbonylmetal halides in *n*-donor solvents. *J. Chem. Soc., Dalton Trans.* **1976**, 1189−1193.
(387) Kokkes, M. W.; De Lange, W. G. J.; Stufkens, D. J.; Oskam, A. Photochemistry of metal−metal bonded complexes complexes: III. MLCT photolysis of $(CO)_5MM'(CO)_3(\text{a-diimine})$ (M, M' = Mn, Re) in 2-Me-THF and THF at 293 K; Evidence of photocatalytic formation of $[(Mn(CO)_3(\alpha\text{-diimine})(P(n\text{-}Bu)_3)]^+$ $[M(CO)_5]^-$ upon photolysis in the presence of $P(n\text{-}Bu)_3$. *J. Organomet. Chem.* **1985**, *294*, 59−73.
(388) Takeda, H.; Koizumi, H.; Okamoto, K.; Ishitani, O. Photocatalytic CO_2 reduction using a Mn complex as a catalyst. *Chem. Commun.* **2014**, *50*, 1491−1493.
(389) Cheung, P. L.; Machan, C. W.; Malkhasian, A. Y. S.; Agarwal, J.; Kubiak, C. P. Photocatalytic Reduction of Carbon Dioxide to CO and HCO_2H Using *fac*-$Mn(CN)(bpy)(CO)_3$. *Inorg. Chem.* **2016**, *55*, 3192−3198.
(390) Zhang, J.-X.; Hu, C.-Y.; Wang, W.; Wang, H.; Bian, Z.-Y. Visible light driven reduction of CO_2 catalyzed by an abundant manganese catalyst with zinc porphyrin photosensitizer. *Appl. Catal., A* **2016**, *522*, 145−151.
(391) Bhugun, I.; Lexa, D.; Savéant, J.-M. Ultraefficient Selective Homogeneous Catalysis of the Electrochemical Reduction of Carbon Dioxide by an Iron(0) Porphyrin Associated with a Weak Brönsted Acid Cocatalyst. *J. Am. Chem. Soc.* **1994**, *116*, 5015−5016.
(392) Bhugun, I.; Lexa, D.; Savéant, J.-M. Catalysis of the Electrochemical Reduction of Carbon Dioxide by Iron(0) Porphyrins: Synergystic Effect of Weak Brönsted Acids. *J. Am. Chem. Soc.* **1996**, *118*, 1769−1776.
(393) Bhugun, I.; Lexa, D.; Savéant, J.-M. Catalysis of the Electrochemical Reduction of Carbon Dioxide by Iron(0) Porphyrins. Synergistic Effect of Lewis Acid Cations. *J. Phys. Chem.* **1996**, *100*, 19981−19985.
(394) Costentin, C.; Drouet, S.; Robert, M.; Savéant, J.-M. A Local Proton Source Enhances CO_2 Electroreduction to CO by a Molecular Fe Catalyst. *Science* **2012**, *338*, 90−94.
(395) Costentin, C.; Drouet, S.; Passard, G.; Robert, M.; Savéant, J.-M. Proton-Coupled Electron Transfer Cleavage of Heavy-Atom Bonds in Electrocatalytic Processes. Cleavage of a C−O Bond in the Catalyzed Electrochemical Reduction of CO_2. *J. Am. Chem. Soc.* **2013**, *135*, 9023−9031.
(396) Costentin, C.; Passard, G.; Robert, M.; Savéant, J.-M. Pendant Acid−Base Groups in Molecular Catalysts: H-Bond Promoters or Proton Relays? Mechanisms of the Conversion of CO_2 to CO by Electrogenerated Iron(0)Porphyrins Bearing Prepositioned Phenol Functionalities. *J. Am. Chem. Soc.* **2014**, *136*, 11821−11829.
(397) Costentin, C.; Robert, M.; Savéant, J.-M. Current Issues in Molecular Catalysis Illustrated by Iron Porphyrins as Catalysts of the CO_2-to-CO Electrochemical Conversion. *Acc. Chem. Res.* **2015**, *48*, 2996−3006.
(398) Mondal, B.; Rana, A.; Sen, P.; Dey, A. Intermediates Involved in the $2e^-/2H^+$ Reduction of CO_2 to CO by Iron(0) Porphyrin. *J. Am. Chem. Soc.* **2015**, *137*, 11214−11217.
(399) Costentin, C.; Passard, G.; Robert, M.; Savéant, J.-M. Ultraefficient homogeneous catalyst for the CO_2-to-CO electrochemical conversion. *Proc. Natl. Acad. Sci. U. S. A.* **2014**, *111*, 14990−14994.
(400) Costentin, C.; Robert, M.; Savéant, J.-M.; Tatin, A. Efficient and selective molecular catalyst for the CO_2-to-CO electrochemical conversion in water. *Proc. Natl. Acad. Sci. U. S. A.* **2015**, *112*, 6882−6886.
(401) Azcarate, I.; Costentin, C.; Robert, M.; Savéant, J.-M. Through-Space Charge Interaction Substituent Effects in Molecular Catalysis

DOI: 10.1021/acs.chemrev.8b00392
Chem. Rev. 2019, 119, 2752−2875

Leading to the Design of the Most Efficient Catalyst of CO_2-to-CO Electrochemical Conversion. *J. Am. Chem. Soc.* **2016**, *138*, 16639−16644.
(402) Nichols, E. M.; Derrick, J. S.; Nistanaki, S. K.; Smith, P. T.; Chang, C. J. Positional effects of second-sphere amide pendants on electrochemical CO_2 reduction catalyzed by iron porphyrins. *Chem. Sci.* **2018**, *9*, 2952−2960.
(403) Mohamed, E. A.; Zahran, Z. N.; Naruta, Y. Efficient electrocatalytic CO_2 reduction with a molecular cofacial iron porphyrin dimer. *Chem. Commun.* **2015**, *51*, 16900−16903.
(404) Zahran, Z. N.; Mohamed, E. A.; Naruta, Y. Bio-inspired cofacial Fe porphyrin dimers for efficient electrocatalytic CO_2 to CO conversion: Overpotential tuning by substituents at the porphyrin rings. *Sci. Rep.* **2016**, *6*, 24533.
(405) Guo, Z.; Cheng, S.; Cometto, C.; Anxolabéhère-Mallart, E.; Ng, S.-M.; Ko, C.-C.; Liu, G.; Chen, L.; Robert, M.; Lau, T.-C. Highly Efficient and Selective Photocatalytic CO_2 Reduction by Iron and Cobalt Quaterpyridine Complexes. *J. Am. Chem. Soc.* **2016**, *138*, 9413−9416.
(406) Cometto, C.; Chen, L.; Lo, P.-K.; Guo, Z.; Lau, K.-C.; Anxolabéhère-Mallart, E.; Fave, C.; Lau, T.-C.; Robert, M. Highly Selective Molecular Catalysts for the CO_2-to-CO Electrochemical Conversion at Very Low Overpotential. Contrasting Fe vs Co Quaterpyridine Complexes upon Mechanistic Studies. *ACS Catal.* **2018**, *8*, 3411−3417.
(407) Pun, S.-N.; Chung, W.-H.; Lam, K.-M.; Guo, P.; Chan, P.-H.; Wong, K.-Y.; Che, C.-M.; Chen, T.-Y.; Peng, S.-M. Iron(I) complexes of 2,9-bis(2-hydroxyphenyl)-1,10-phenanthroline (H_2dophen) as electrocatalysts for carbon dioxide reduction. X-Ray crystal structures of $[Fe(dophen)Cl]_2{\cdot}2HCON(CH_3)_2$ and $[Fe(dophen)(N\text{-}MeIm)_2]\text{-}ClO_4$ (N-MeIm = 1-methylimidazole). *J. Chem. Soc., Dalton Trans.* **2002**, 575−583.
(408) Taheri, A.; Thompson, E. J.; Fettinger, J. C.; Berben, L. A. An Iron Electrocatalyst for Selective Reduction of CO_2 to Formate in Water: Including Thermochemical Insights. *ACS Catal.* **2015**, *5*, 7140−7151.
(409) Grodkowski, J.; Dhanasekaran, T.; Neta, P.; Hambright, P.; Brunschwig, B. S.; Shinozaki, K.; Fujita, E. Reduction of Cobalt and Iron Phthalocyanines and the Role of the Reduced Species in Catalyzed Photoreduction of CO_2. *J. Phys. Chem. A* **2000**, *104*, 11332−11339.
(410) Grodkowski, J.; Neta, P.; Fujita, E.; Mahammed, A.; Simkhovich, L.; Gross, Z. Reduction of Cobalt and Iron Corroles and Catalyzed Reduction of CO_2. *J. Phys. Chem. A* **2002**, *106*, 4772−4778.
(411) Bonin, J.; Chaussemier, M.; Robert, M.; Routier, M. Homogeneous Photocatalytic Reduction of CO_2 to CO Using Iron(0) Porphyrin Catalysts: Mechanism and Intrinsic Limitations. *ChemCatChem* **2014**, *6*, 3200−3207.
(412) Grodkowski, J.; Behar, D.; Neta, P.; Hambright, P. Iron Porphyrin-Catalyzed Reduction of CO_2. Photochemical and Radiation Chemical Studies. *J. Phys. Chem. A* **1997**, *101*, 248−254.
(413) Dhanasekaran, T.; Grodkowski, J.; Neta, P.; Hambright, P.; Fujita, E. *p*-Terphenyl-Sensitized Photoreduction of CO_2 with Cobalt and Iron Porphyrins. Interaction between CO and Reduced Metalloporphyrins. *J. Phys. Chem. A* **1999**, *103*, 7742−7748.
(414) Bonin, J.; Robert, M.; Routier, M. Selective and Efficient Photocatalytic CO_2 Reduction to CO Using Visible Light and an Iron-Based Homogeneous Catalyst. *J. Am. Chem. Soc.* **2014**, *136*, 16768−16771.
(415) Rao, H.; Bonin, J.; Robert, M. Visible-light Homogeneous Photocatalytic Conversion of CO_2 into CO in Aqueous Solutions with an Iron Catalyst. *ChemSusChem* **2017**, *10*, 4447−4450.
(416) Rao, H.; Bonin, J.; Robert, M. Non-sensitized selective photochemical reduction of CO_2 to CO under visible light with an iron molecular catalyst. *Chem. Commun.* **2017**, *53*, 2830−2833.
(417) Alsabeh, P. G.; Rosas-Hernández, A.; Barsch, E.; Junge, H.; Ludwig, R.; Beller, M. Iron-catalyzed photoreduction of carbon dioxide to synthesis gas. *Catal. Sci. Technol.* **2016**, *6*, 3623−3630.
(418) Rosas-Hernandez, A.; Alsabeh, P. G.; Barsch, E.; Junge, H.; Ludwig, R.; Beller, M. Highly active and selective photochemical reduction of CO_2 to CO using molecular-defined cyclopentadienone iron complexes. *Chem. Commun.* **2016**, *52*, 8393−8396.
(419) Takeda, H.; Ohashi, K.; Sekine, A.; Ishitani, O. Photocatalytic CO_2 Reduction Using Cu(I) Photosensitizers with a Fe(II) Catalyst. *J. Am. Chem. Soc.* **2016**, *138*, 4354−4357.
(420) Rao, H.; Schmidt, L. C.; Bonin, J.; Robert, M. Visible-light-driven methane formation from CO_2 with a molecular iron catalyst. *Nature* **2017**, *548*, 74−77.
(421) Rao, H.; Bonin, J.; Robert, M. Toward Visible-Light Photochemical CO_2-to-CH_4 Conversion in Aqueous Solutions Using Sensitized Molecular Catalysis. *J. Phys. Chem. C* **2018**, *122*, 13834−13839.
(422) Hiratsuka, K.; Takahashi, K.; Sasaki, H.; Toshima, S. Electrocatalytic Behavior of Tetrasulfonated Metal Phthalocyanines in the Reduction of Carbon Dioxide. *Chem. Lett.* **1977**, *6*, 1137−1140.
(423) Takahashi, K.; Hiratsuka, K.; Sasaki, H.; Toshima, S. Electrocatalytic Behavior of Metal Porphyrins in the Reduction of Carbon Dioxide. *Chem. Lett.* **1979**, *8*, 305−308.
(424) Enoki, O.; Imaoka, T.; Yamamoto, K. Electrochemical reduction of carbon dioxide catalyzed by cofacial dinuclear metalloporphyrin. *Macromol. Symp.* **2003**, *204*, 151−158.
(425) Behar, D.; Dhanasekaran, T.; Neta, P.; Hosten, C. M.; Ejeh, D.; Hambright, P.; Fujita, E. Cobalt Porphyrin Catalyzed Reduction of CO_2. Radiation Chemical, Photochemical, and Electrochemical Studies. *J. Phys. Chem. A* **1998**, *102*, 2870−2877.
(426) Creutz, C.; Schwarz, H. A.; Wishart, J. F.; Fujita, E.; Sutin, N. A Dissociative Pathway for Equilibration of a Hydrido $CoL(H)^{2+}$ Complex with CO_2 and CO: Ligand-Binding Constants in the Macrocyclic [14]Dienecobalt(I) System. *J. Am. Chem. Soc.* **1989**, *111*, 1153−1154.
(427) Fujita, E.; Creutz, C.; Sutin, N.; Szalda, D. J. Carbon Dioxide Activation by Cobalt(I) Macrocycles: Factors Affecting CO_2 and CO Binding. *J. Am. Chem. Soc.* **1991**, *113*, 343−353.
(428) Fujita, E.; Szalda, D. J.; Creutz, C.; Sutin, N. Carbon Dioxide Activation: Thermodynamics of CO_2 Binding and the Involvement of Two Cobalt Centers in the Reduction of CO_2 by a Cobalt(I) Macrocycle. *J. Am. Chem. Soc.* **1988**, *110*, 4870−4871.
(429) Fujita, E.; Creutz, C.; Sutin, N.; Brunschwig, B. S. Carbon Dioxide Activation by Cobalt Macrocycles: Evidence of Hydrogen Bonding between Bound CO_2 and the Macrocycle in Solution. *Inorg. Chem.* **1993**, *32*, 2657−2662.
(430) Fujita, E.; Furenlid, L. R.; Renner, M. W. Direct XANES Evidence for Charge Transfer in Co−CO_2 Complexes. *J. Am. Chem. Soc.* **1997**, *119*, 4549−4550.
(431) Ogata, T.; Yanagida, S.; Brunschwig, B. S.; Fujita, E. Mechanistic and kinetic studies of cobalt macrocycles in a photochemical CO_2 reduction system. *Energy Convers. Manage.* **1995**, *36*, 669−672.
(432) Che, C.-M.; Mak, S.-T.; Lee, W.-O.; Fung, K.-W.; Mak, T. C. W. Electrochemical studies of nickel(II) and cobalt(II) complexes of tetraazamacrocycles bearing a pyridine functional group and *X*-ray structures of $[Ni^{II}(L^3)Cl]ClO_4$ and $[Ni^{II}(L^3)][ClO_4]_2{\cdot}H_2O$ (L^3=*meso*-2,3,7,11,12-pentamethyl-3,7,11,17-tetra-azabicyclo[11.3.1]-heptadeca-1(17),13,15-triene. *J. Chem. Soc., Dalton Trans.* **1988**, 2153−2159.
(433) Lacy, D. C.; McCrory, C. C. L.; Peters, J. C. Studies of Cobalt-Mediated Electrocatalytic CO_2 Reduction Using a Redox-Active Ligand. *Inorg. Chem.* **2014**, *53*, 4980−4988.
(434) Zhang, M.; El-Roz, M.; Frei, H.; Mendoza-Cortes, J. L.; Head-Gordon, M.; Lacy, D. C.; Peters, J. C. Visible Light Sensitized CO_2 Activation by the Tetraaza $[Co^{II}N_4H(MeCN)]^{2+}$ Complex Investigated by FT-IR Spectroscopy and DFT Calculations. *J. Phys. Chem. C* **2015**, *119*, 4645−4654.
(435) Nie, W.; McCrory, C. C. L. Electrocatalytic CO_2 reduction by a cobalt bis(pyridylmonoimine) complex: effect of acid concentration on catalyst activity and stability. *Chem. Commun.* **2018**, *54*, 1579−1582.
(436) Elgrishi, N.; Chambers, M. B.; Artero, V.; Fontecave, M. Terpyridine complexes of first row transition metals and electro-

DOI: 10.1021/acs.chemrev.8b00392
Chem. Rev. 2019, 119, 2752−2875

chemical reduction of CO_2 to CO. *Phys. Chem. Chem. Phys.* **2014**, *16*, 13635−13644.
(437) Chapovetsky, A.; Do, T. H.; Haiges, R.; Takase, M. K.; Marinescu, S. C. Proton-Assisted Reduction of CO_2 by Cobalt Aminopyridine Macrocycles. *J. Am. Chem. Soc.* **2016**, *138*, 5765−5768.
(438) Chapovetsky, A.; Welborn, M.; Luna, J. M.; Haiges, R.; Miller, T. F., III; Marinescu, S. C. Pendant Hydrogen-Bond Donors in Cobalt Catalysts Independently Enhance CO_2 Reduction. *ACS Cent. Sci.* **2018**, *4*, 397−404.
(439) Wang, F.; Cao, B.; To, W.-P.; Tse, C.-W.; Li, K.; Chang, X.-Y.; Zang, C.; Chan, S. L.-F.; Che, C.-M. The effects of chelating N_4 ligand coordination on Co(II)-catalysed photochemical conversion of CO_2 to CO: reaction mechanism and DFT calculations. *Catal. Sci. Technol.* **2016**, *6*, 7408−7420.
(440) Roy, S.; Sharma, B.; Pécaut, J.; Simon, P.; Fontecave, M.; Tran, P. D.; Derat, E.; Artero, V. Molecular Cobalt Complexes with Pendant Amines for Selective Electrocatalytic Reduction of Carbon Dioxide to Formic Acid. *J. Am. Chem. Soc.* **2017**, *139*, 3685−3696.
(441) Fang, M.; Wiedner, E. S.; Dougherty, W. G.; Kassel, W. S.; Liu, T.; DuBois, D. L.; Bullock, R. M. Cobalt Complexes Containing Pendant Amines in the Second Coordination Sphere as Electrocatalysts for H_2 Production. *Organometallics* **2014**, *33*, 5820−5833.
(442) Lehn, J.-M.; Ziessel, R. Photochemical generation of carbon monoxide and hydrogen by reduction of carbon dioxide and water under visible light irradiation. *Proc. Natl. Acad. Sci. U. S. A.* **1982**, *79*, 701−704.
(443) Ziessel, R.; Hawecker, J.; Lehn, J.-M. Photogeneration of Carbon Monoxide and of Hydrogen via Simultaneous Photochemical Reduction of Carbon Dioxide and Water by Visible-Light Irradiation of Organic Solutions Containing Tris(2,2′-bipyridine)ruthenium(II) and Cobalt(II) Species as Homogeneous Catalysts. *Helv. Chim. Acta* **1986**, *69*, 1065−1084.
(444) Matsuoka, S.; Yamamoto, K.; Ogata, T.; Kusaba, M.; Nakashima, N.; Fujita, E.; Yanagida, S. Efficient and Selective Electron Mediation of Cobalt Complexes with Cyclam and Related Macrocycles in the *p*-Terphenyl-Catalyzed Photoreduction of CO_2. *J. Am. Chem. Soc.* **1993**, *115*, 601−609.
(445) Matsuoka, S.; Yamamoto, K.; Pac, C.; Yanagida, S. Enhanced *p*-Terphenyl-Catalyzed Photoreduction of CO_2 to CO through the Mediation of Co(III)−Cyclam Complex. *Chem. Lett.* **1991**, *20*, 2099−2100.
(446) Creutz, C.; Schwarz, H. A.; Wishart, J. F.; Fujita, E.; Sutin, N. Thermodynamics and Kinetics of Carbon Dioxide Binding to Two Stereoisomers of a Cobalt(I) Macrocycle in Aqueous Solution. *J. Am. Chem. Soc.* **1991**, *113*, 3361−3371.
(447) Ogata, T.; Yamamoto, Y.; Wada, Y.; Murakoshi, K.; Kusaba, M.; Nakashima, N.; Ishida, A.; Takamuku, S.; Yanagida, S. Phenazine-Photosensitized Reduction of CO_2 Mediated by a Cobalt-Cyclam Complex through Electron and Hydrogen Transfer. *J. Phys. Chem.* **1995**, *99*, 11916−11922.
(448) Grodkowski, J.; Neta, P. Cobalt Corrin Catalyzed Photoreduction of CO_2. *J. Phys. Chem. A* **2000**, *104*, 1848−1853.
(449) Sheng, H.; Frei, H. Direct Observation by Rapid-Scan FT-IR Spectroscopy of Two-Electron-Reduced Intermediate of Tetraaza Catalyst $[Co^{II}N_4H(MeCN)]^{2+}$ Converting CO_2 to CO. *J. Am. Chem. Soc.* **2016**, *138*, 9959−9967.
(450) Chan, S. L.-F.; Lam, T. L.; Yang, C.; Yan, S.-C.; Cheng, N. M. A robust and efficient cobalt molecular catalyst for CO_2 reduction. *Chem. Commun.* **2015**, *51*, 7799−7801.
(451) Yang, C.; Mehmood, F.; Lam, T. L.; Chan, S. L.-F.; Wu, Y.; Yeung, C.-S.; Guan, X.; Li, K.; Chung, C. Y.-S.; Zhou, C.-Y.; et al. Stable luminescent iridium(III) complexes with bis(N-heterocyclic carbene) ligands: photo-stability, excited state properties, visible-light-driven radical cyclization and CO_2 reduction, and cellular imaging. *Chem. Sci.* **2016**, *7*, 3123−3136.
(452) Chan, S. L.-F.; Lam, T. L.; Yang, C.; Lai, J.; Cao, B.; Zhou, Z.; Zhu, Q. Cobalt(II) tris(2-pyridylmethyl)amine complexes $[Co(TPA)X]^+$ bearing coordinating anion (X = Cl^-, Br^-, I^- and NCS^-): synthesis and application for carbon dioxide reduction. *Polyhedron* **2017**, *125*, 156−163.
(453) Zhu, C.-Y.; Huang, Y.-C.; Hu, J.-C.; Li, Q.-K.; Tan, H.; Gui, M.-X.; Deng, S.-F.; Wang, F. *Cis*-$[Co^{II}(MPCA)X_2]$ (X = Cl or Br) complexes as catalyst exhibiting different activity for visible light induced photocatalytic CO_2-to-CO conversion. *J. Photochem. Photobiol., A* **2018**, *355*, 175−179.
(454) Ouyang, T.; Hou, C.; Wang, J.-W.; Liu, W.-J.; Zhong, D.-C.; Ke, Z.-F.; Lu, T.-B. A Highly Selective and Robust Co(II)-Based Homogeneous Catalyst for Reduction of CO_2 to CO in CH_3CN/H_2O Solution Driven by Visible Light. *Inorg. Chem.* **2017**, *56*, 7307−7311.
(455) Hirose, T.; Maeno, Y.; Himeda, Y. Photocatalytic carbon dioxide photoreduction by $Co(bpy)_3^{2+}$ sensitized by $Ru(bpy)_3^{2+}$ fixed to cation exchange polymer. *J. Mol. Catal. A: Chem.* **2003**, *193*, 27−32.
(456) Komatsuzaki, N.; Himeda, Y.; Hirose, T.; Sugihara, H.; Kasuga, K. Synthesis and Photochemical Properties of Ruthenium−Cobalt and Ruthenium−Nickel Dinuclear Complexes. *Bull. Chem. Soc. Jpn.* **1999**, *72*, 725−731.
(457) Wang, X.; Goudy, V.; Genesio, G.; Maynadie, J.; Meyer, D.; Fontecave, M. Ruthenium-cobalt dinuclear complexes as photocatalysts for CO_2 reduction. *Chem. Commun.* **2017**, *53*, 5040−5043.
(458) Ouyang, T.; Huang, H.-H.; Wang, J.-W.; Zhong, D.-C.; Lu, T.-B. A Dinuclear Cobalt Cryptate as a Homogeneous Photocatalyst for Highly Selective and Efficient Visible-Light Driven CO_2 Reduction to CO in CH_3CN/H_2O Solution. *Angew. Chem., Int. Ed.* **2017**, *56*, 738−743.
(459) Beley, M.; Collin, J.-P.; Ruppert, R.; Sauvage, J.-P. Nickel(II)-cyclam: an extremely selective electrocatalyst for reduction of CO_2 in water. *J. Chem. Soc., Chem. Commun.* **1984**, 1315−1316.
(460) Neri, G.; Aldous, I. M.; Walsh, J. J.; Hardwick, L. J.; Cowan, A. J. A highly active nickel electrocatalyst shows excellent selectivity for CO_2 reduction in acidic media. *Chem. Sci.* **2016**, *7*, 1521−1526.
(461) Schneider, J.; Jia, H.; Muckerman, J. T.; Fujita, E. Thermodynamics and kinetics of CO_2, CO, and H^+ binding to the metal centre of CO_2 reduction catalysts. *Chem. Soc. Rev.* **2012**, *41*, 2036−2051.
(462) Froehlich, J. D.; Kubiak, C. P. Homogeneous CO_2 Reduction by Ni(cyclam) at a Glassy Carbon Electrode. *Inorg. Chem.* **2012**, *51*, 3932−3934.
(463) Kelly, C. A.; Mulazzani, Q. G.; Venturi, M.; Blinn, E. L.; Rodgers, M. A. J. The Thermodynamics and Kinetics of CO_2 and H^+ Binding to $Ni(cyclam)^+$ in Aqueous Solution. *J. Am. Chem. Soc.* **1995**, *117*, 4911−4919.
(464) Froehlich, J. D.; Kubiak, C. P. The Homogeneous Reduction of CO_2 by $[Ni(cyclam)]^+$: Increased Catalytic Rates with the Addition of a CO Scavenger. *J. Am. Chem. Soc.* **2015**, *137*, 3565−3573.
(465) Balazs, G. B.; Anson, F. C. The adsorption of $Ni(cyclam)^+$ at mercury electrodes and its relation to the electrocatalytic reduction of CO_2. *J. Electroanal. Chem.* **1992**, *322*, 325−345.
(466) Fujihira, M.; Hirata, Y.; Suga, K. Electrocatalytic reduction of CO_2 by nickel(II) cyclam: Study of the reduction mechanism on mercury by cyclic voltammetry, polarography and electrocapillarity. *J. Electroanal. Chem. Interfacial Electrochem.* **1990**, *292*, 199−215.
(467) Sakaki, S. Can CO_2 Coordinate to a Ni(I) Complex? An ab initio MO/SD-CI Study. *J. Am. Chem. Soc.* **1990**, *112*, 7813−7814.
(468) Sakaki, S. An ab Initio MO/SD-CI Study of Model Complexes of Intermediates in Electrochemical Reduction of CO_2 Catalyzed by $NiCl_2$(cyclam). *J. Am. Chem. Soc.* **1992**, *114*, 2055−2062.
(469) Bujno, K.; Bilewicz, R.; Siegfried, L.; Kaden, T. A. Effects of ligand structure on the adsorption of nickel tetraazamacrocyclic complexes and electrocatalytic CO_2 reduction. *J. Electroanal. Chem.* **1998**, *445*, 47−53.
(470) Connolly, P. J.; Billo, E. J. ^1H NMR Evidence for the *R,S,R,S* Isomer of the (1,4,8,11-tetraazacyclotetradecane)nickel(II) Ion. *Inorg. Chem.* **1987**, *26*, 3224−3226.
(471) Balazs, G. B.; Anson, F. C. Effects of CO on the electrocatalytic activity of Ni $(cyclam)^{2+}$ toward the reduction of CO_2. *J. Electroanal. Chem.* **1993**, *361*, 149−157.

DOI: 10.1021/acs.chemrev.8b00392
Chem. Rev. 2019, 119, 2752−2875

(472) Fujita, E.; Haff, J.; Sanzenbacher, R.; Elias, H. High Electrocatalytic Activity of *RRSS*-[Ni^{II}HTIM]$(ClO_4)_2$ and [Ni^{II}DMC]$(ClO_4)_2$ for Carbon Dioxide Reduction (HTIM = 2,3,9,10-Tetramethyl-1,4,8,11-tetraazacyclotetradecane, DMC = C-*meso*-5,12-Dimethyl-1,4,8,11-tetraazacyclotetradecane). *Inorg. Chem.* **1994**, *33*, 4627−4628.
(473) Cook, T. D.; Tyler, S. F.; McGuire, C. M.; Zeller, M.; Fanwick, P. E.; Evans, D. H.; Peters, D. G.; Ren, T. Nickel Complexes of C-Substituted Cyclams and Their Activity for CO_2 and H^+ Reduction. *ACS Omega* **2017**, *2*, 3966−3976.
(474) Rudolph, M.; Dautz, S.; Jäger, E.-G. Macrocyclic [N_4^{2-}] Coordinated Nickel Complexes as Catalysts for the Formation of Oxalate by Electrochemical Reduction of Carbon Dioxide. *J. Am. Chem. Soc.* **2000**, *122*, 10821−10830.
(475) Cope, J. D.; Liyanage, N. P.; Kelley, P. J.; Denny, J. A.; Valente, E. J.; Webster, C. E.; Delcamp, J. H.; Hollis, T. K. Electrocatalytic reduction of CO_2 with CCC-NHC pincer nickel complexes. *Chem. Commun.* **2017**, *53*, 9442−9445.
(476) Sheng, M.; Jiang, N.; Gustafson, S.; You, B.; Ess, D. H.; Sun, Y. A nickel complex with a biscarbene pincer-type ligand shows high electrocatalytic reduction of CO_2 over H_2O. *Dalton Trans.* **2015**, *44*, 16247−16250.
(477) Thoi, V. S.; Chang, C. J. Nickel N-heterocyclic carbene-pyridine complexes that exhibit selectivity for electrocatalytic reduction of carbon dioxide over water. *Chem. Commun.* **2011**, *47*, 6578−6580.
(478) Therrien, J. A.; Wolf, M. O.; Patrick, B. O. Synthesis and comparison of nickel, palladium, and platinum bis(N-heterocyclic carbene) pincer complexes for electrocatalytic CO_2 reduction. *Dalton Trans.* **2018**, *47*, 1827−1840.
(479) Ratliff, K. S.; Lentz, R. E.; Kubiak, C. P. Carbon Dioxide Chemistry of the Trinuclear Complex [$Ni_3(\mu_3$-CNMe$)(\mu_3$-I$)$-$(dppm)_3$][PF_6]. Electrocatalytic Reduction of Carbon Dioxide. *Organometallics* **1992**, *11*, 1986−1988.
(480) Simón-Manso, E.; Kubiak, C. P. Dinuclear Nickel Complexes as Catalysts for Electrochemical Reduction of Carbon Dioxide. *Organometallics* **2005**, *24*, 96−102.
(481) Grant, J. L.; Goswami, K.; Spreer, L. O.; Otvos, J. W.; Calvin, M. Photochemical reduction of carbon dioxide to carbon monoxide in water using a nickel(II) tetra-azamacrocycle complex as catalyst. *J. Chem. Soc., Dalton Trans.* **1987**, 2105−2109.
(482) Craig, C. A.; Spreer, L. O.; Otvos, J. W.; Calvin, M. Photochemical Reduction of Carbon Dioxide Using Nickel Tetraaza-macrocycles. *J. Phys. Chem.* **1990**, *94*, 7957−7960.
(483) Kimura, E.; Bu, X.; Shionoya, M.; Wada, S.; Maruyama, S. A New Nickel(II) Cyclam (Cyclam = 1,4,8,11-tetraazacyclotetradecane) Complex Covalently Attached to $Ru(Phen)_3^{2+}$ (Phen = 1,10-phenanthroline). A New Candidate for the Catalytic Photoreduction of Carbon Dioxide. *Inorg. Chem.* **1992**, *31*, 4542−4546.
(484) Kimura, E.; Wada, S.; Shionoya, M.; Takahashi, T.; Iitaka, Y. A novel cyclam−nickel(II) complex appended with a tris-(2,2'-bipyridine) ruthenium(II) complex (cyclam = 1,4,8,11-tetra-azacyclo-tetradecane). *J. Chem. Soc., Chem. Commun.* **1990**, 397−398.
(485) Kimura, E.; Wada, S.; Shionoya, M.; Okazaki, Y. New Series of Multifunctionalized Nickel(II)-Cyclam (Cyclam = 1,4,8,11-Tetraaza-cyclotetradecane) Complexes. Application to the Photoreduction of Carbon Dioxide. *Inorg. Chem.* **1994**, *33*, 770−778.
(486) Mochizuki, K.; Manaka, S.; Takeda, I.; Kondo, T. Synthesis and Structure of [6,6'-Bi(5,7-dimethyl-1,4,8,11-tetraazacyclotetradecane)]-dinickel(II) Triflate and Its Catalytic Activity for Photochemical CO_2 Reduction. *Inorg. Chem.* **1996**, *35*, 5132−5136.
(487) Hong, D.; Tsukakoshi, Y.; Kotani, H.; Ishizuka, T.; Kojima, T. Visible-Light-Driven Photocatalytic CO_2 Reduction by a Ni(II) Complex Bearing a Bioinspired Tetradentate Ligand for Selective CO Production. *J. Am. Chem. Soc.* **2017**, *139*, 6538−6541.
(488) Fujiwara, H.; Nonaka, T. Cyclic voltammetric study on carbon dioxide reduction using Cu complexes as electrocatalysts. *J. Electroanal. Chem.* **1992**, *332*, 303−307.
(489) Kang, S.-J.; Dale, A.; Sarkar, S.; Yoo, J.; Lee, H. Electrocatalytic Reduction of CO_2 by Copper (II) Cyclam Derivatives. *J. Electrochem. Sci. Technol.* **2015**, *6*, 106−110.
(490) Fabbrizzi, L.; Poggi, A.; Zanello, P. Oxidation and reduction of copper(II) complexes with saturated poly-aza macrocycles of varying size and denticity. *J. Chem. Soc., Dalton Trans.* **1983**, 2191−2195.
(491) Zanello, P.; Seeber, R.; Cinquantini, A.; Mazzocchin, G.-A.; Fabbrizzi, L. Electrochemical behaviour of complexes of copper(II) with 14-membered saturated tetra-aza macrocycles. *J. Chem. Soc., Dalton Trans.* **1982**, 893−897.
(492) Ríos-Escudero, A.; Villagrán, M.; Caruso, F.; Muena, J. P.; Spodine, E.; Venegas-Yazigi, D.; Massa, L.; Todaro, L. J.; Zagal, J. H.; Cárdenas-Jirón, G. I.; et al. Electrocatalytic reduction of carbon dioxide induced by bis(*N*-R-2-hydroxy-1-naphthaldiminato)-copper(II) (R = *n*-octyl, *n*-dodecyl): Magnetic and theoretical studies and the X-ray structure of bis(*N*-*n*-octyl-2-hydroxy-1-naphthaldiminato)-copper(II). *Inorg. Chim. Acta* **2006**, *359*, 3947−3953.
(493) Haines, R. J.; Wittrig, R. E.; Kubiak, C. P. Electrocatalytic Reduction of Carbon Dioxide by the Binuclear Copper Complex. *Inorg. Chem.* **1994**, *33*, 4723−4728.
(494) Lilio, A. M.; Grice, K. A.; Kubiak, C. P. A Series of Dinuclear Copper Complexes Bridged by Phosphanylbipyridine Ligands: Synthesis, Structural Characterization and Electrochemistry. *Eur. J. Inorg. Chem.* **2013**, 4016−4023.
(495) Angamuthu, R.; Byers, P.; Lutz, M.; Spek, A. L.; Bouwman, E. Electrocatalytic CO_2 Conversion to Oxalate by a Copper Complex. *Science* **2010**, *327*, 313−315.
(496) Pokharel, U. R.; Fronczek, F. R.; Maverick, A. W. Reduction of carbon dioxide to oxalate by a binuclear copper complex. *Nat. Commun.* **2014**, *5*, 5883.
(497) Kunkely, H.; Vogler, A. Photoreduction of carbonate in a copper(I) complex. *Inorg. Chem. Commun.* **2010**, *13*, 137−138.
(498) Guo, Z.; Yu, F.; Yang, Y.; Leung, C.-F.; Ng, S.-M.; Ko, C.-C.; Cometto, C.; Lau, T.-C.; Robert, M. Photocatalytic Conversion of CO_2 to CO by a Copper(II) Quaterpyridine Complex. *ChemSusChem* **2017**, *10*, 4009−4013.
(499) Potts, K. T.; Keshavarz-K, M.; Tham, F. S.; Abruña, H. D.; Arana, C. R. Metal ion-induced self-assembly of functionalized 2,6-oligopyridines. 2. Copper-containing double-stranded helicates derived from functionalized quaterpyridine and quinquepyridine: redox state-induced transformations and electron communication in mixed-valence systems. *Inorg. Chem.* **1993**, *32*, 4422−4435.
(500) Donovan, E. S.; Barry, B. M.; Larsen, C. A.; Wirtz, M. N.; Geiger, W. E.; Kemp, R. A. Facilitated carbon dioxide reduction using a Zn(II) complex. *Chem. Commun.* **2016**, *52*, 1685−1688.
(501) Wu, Y.; Jiang, J.; Weng, Z.; Wang, M.; Broere, D. L. J.; Zhong, Y.; Brudvig, G. W.; Feng, Z.; Wang, H. Electroreduction of CO_2 Catalyzed by a Heterogenized Zn−Porphyrin Complex with a Redox-Innocent Metal Center. *ACS Cent. Sci.* **2017**, *3*, 847−852.
(502) Liu, X.; Inagaki, S.; Gong, J. Heterogeneous Molecular Systems for Photocatalytic CO_2 Reduction with Water Oxidation. *Angew. Chem., Int. Ed.* **2016**, *55*, 14924−14950.
(503) Bullock, R. M.; Das, A. K.; Appel, A. M. Surface Immobilization of Molecular Electrocatalysts for Energy Conversion. *Chem. - Eur. J.* **2017**, *23*, 7626−7641.
(504) Mills, A.; Le Hunte, S. An overview of semiconductor photocatalysis. *J. Photochem. Photobiol., A* **1997**, *108*, 1−35.
(505) O'Regan, B.; Grätzel, M. A low-cost, high-efficiency solar cell based on dye-sensitized colloidal TiO_2 films. *Nature* **1991**, *353*, 737−740.
(506) Shehzad, K.; Xu, Y.; Gao, C.; Duan, X. Three-dimensional macro-structures of two-dimensional nanomaterials. *Chem. Soc. Rev.* **2016**, *45*, 5541−5588.
(507) Kato, M.; Cardona, T.; Rutherford, A. W.; Reisner, E. Covalent Immobilization of Oriented Photosystem II on a Nanostructured Electrode for Solar Water Oxidation. *J. Am. Chem. Soc.* **2013**, *135*, 10610−10613.
(508) Sokol, K. P.; Mersch, D.; Hartmann, V.; Zhang, J. Z.; Nowaczyk, M. M.; Rogner, M.; Ruff, A.; Schuhmann, W.; Plumeré, N.; Reisner, E.

DOI: 10.1021/acs.chemrev.8b00392
Chem. Rev. 2019, 119, 2752−2875

Rational wiring of photosystem II to hierarchical indium tin oxide electrodes using redox polymers. *Energy Environ. Sci.* **2016**, *9*, 3698−3709.
(509) Materna, K. L.; Crabtree, R. H.; Brudvig, G. W. Anchoring groups for photocatalytic water oxidation on metal oxide surfaces. *Chem. Soc. Rev.* **2017**, *46*, 6099−6110.
(510) Clegg, R. S.; Hutchison, J. E. *Electron Transfer in Chemistry*; Balzani, V., Ed.; Wiley-VCH Verlag GmbH: Weinheim, Germany, 2008.
(511) Ambrosi, A.; Chua, C. K.; Bonanni, A.; Pumera, M. Electrochemistry of Graphene and Related Materials. *Chem. Rev.* **2014**, *114*, 7150−7188.
(512) McCreery, R. L. Advanced carbon electrode materials for molecular electrochemistry. *Chem. Rev.* **2008**, *108*, 2646−2687.
(513) Dai, L.; Chang, D. W.; Baek, J. B.; Lu, W. Carbon nanomaterials for advanced energy conversion and storage. *Small* **2012**, *8*, 1130−1166.
(514) Asefa, T. Metal-Free and Noble Metal-Free Heteroatom-Doped Nanostructured Carbons as Prospective Sustainable Electrocatalysts. *Acc. Chem. Res.* **2016**, *49*, 1873−1883.
(515) Duan, X.; Xu, J.; Wei, Z.; Ma, J.; Guo, S.; Wang, S.; Liu, H.; Dou, S. Metal-Free Carbon Materials for CO_2 Electrochemical Reduction. *Adv. Mater.* **2017**, *29*, 1701784.
(516) Kong, X.-K.; Chen, C.-L.; Chen, Q.-W. Doped graphene for metal-free catalysis. *Chem. Soc. Rev.* **2014**, *43*, 2841−2857.
(517) Zhang, L.; Zhao, Z.-J.; Gong, J. Nanostructured Materials for Heterogeneous Electrocatalytic CO_2 Reduction and Related Reaction Mechanisms. *Angew. Chem., Int. Ed.* **2017**, *56*, 11326−11353.
(518) Laursen, A. B.; Varela, A. S.; Dionigi, F.; Fanchiu, H.; Miller, C.; Trinhammer, O. L.; Rossmeisl, J.; Dahl, S. Electrochemical hydrogen evolution: Sabatier's principle and the volcano plot. *J. Chem. Educ.* **2012**, *89*, 1595−1599.
(519) Sheng, W.; Myint, M.; Chen, J. G.; Yan, Y. Correlating the hydrogen evolution reaction activity in alkaline electrolytes with the hydrogen binding energy on monometallic surfaces. *Energy Environ. Sci.* **2013**, *6*, 1509−1512.
(520) Zhu, D. D.; Liu, J. L.; Qiao, S. Z. Recent Advances in Inorganic Heterogeneous Electrocatalysts for Reduction of Carbon Dioxide. *Adv. Mater.* **2016**, *28*, 3423−3452.
(521) Ramesha, G. K.; Brennecke, J. F.; Kamat, P. V. Origin of Catalytic Effect in the Reduction of CO_2 at Nanostructured TiO_2 Films. *ACS Catal.* **2014**, *4*, 3249−3254.
(522) Zhang, S.; Kang, P.; Meyer, T. J. Nanostructured Tin Catalysts for Selective Electrochemical Reduction of Carbon Dioxide to Formate. *J. Am. Chem. Soc.* **2014**, *136*, 1734−1737.
(523) Baruch, M. F.; Pander, J. E., III; White, J. L.; Bocarsly, A. B. Mechanistic Insights into the Reduction of CO_2 on Tin Electrodes using in Situ ATR-IR Spectroscopy. *ACS Catal.* **2015**, *5*, 3148−3156.
(524) Rosser, T. E.; Reisner, E. Understanding Immobilized Molecular Catalysts for Fuel-Forming Reactions through UV/Vis Spectroelectrochemistry. *ACS Catal.* **2017**, *7*, 3131−3141.
(525) Leung, J. J.; Warnan, J.; Nam, D. H.; Zhang, J. Z.; Willkomm, J.; Reisner, E. Photoelectrocatalytic H_2 evolution in water with molecular catalysts immobilised on p-Si via a stabilising mesoporous TiO_2 interlayer. *Chem. Sci.* **2017**, *8*, 5172−5180.
(526) Wang, M.; Han, K.; Zhang, S.; Sun, L. Integration of organometallic complexes with semiconductors and other nanomaterials for photocatalytic H_2 production. *Coord. Chem. Rev.* **2015**, *287*, 1−14.
(527) Willkomm, J.; Orchard, K. L.; Reynal, A.; Pastor, E.; Durrant, J. R.; Reisner, E. Dye-sensitised semiconductors modified with molecular catalysts for light-driven H_2 production. *Chem. Soc. Rev.* **2016**, *45*, 9−23.
(528) Harris, R. D.; Bettis Homan, S.; Kodaimati, M.; He, C.; Nepomnyashchii, A. B.; Swenson, N. K.; Lian, S.; Calzada, R.; Weiss, E. A. Electronic Processes within Quantum Dot-Molecule Complexes. *Chem. Rev.* **2016**, *116*, 12865−12919.
(529) Osterloh, F. E. Inorganic nanostructures for photoelectrochemical and photocatalytic water splitting. *Chem. Soc. Rev.* **2013**, *42*, 2294−2320.
(530) Kessler, F. K.; Zheng, Y.; Schwarz, D.; Merschjann, C.; Schnick, W.; Wang, X.; Bojdys, M. J. Functional carbon nitride materials − design strategies for electrochemical devices. *Nat. Rev. Mater.* **2017**, *2*, 17030.
(531) Hutton, G. A. M.; Martindale, B. C. M.; Reisner, E. Carbon dots as photosensitisers for solar-driven catalysis. *Chem. Soc. Rev.* **2017**, *46*, 6111−6123.
(532) Sprick, R. S.; Bonillo, B.; Sachs, M.; Clowes, R.; Durrant, J. R.; Adams, D. J.; Cooper, A. I. Extended conjugated microporous polymers for photocatalytic hydrogen evolution from water. *Chem. Commun.* **2016**, *52*, 10008−10011.
(533) Sprick, R. S.; Bonillo, B.; Clowes, R.; Guiglion, P.; Brownbill, N. J.; Slater, B. J.; Blanc, F.; Zwijnenburg, M. A.; Adams, D. J.; Cooper, A. I. Visible-Light-Driven Hydrogen Evolution Using Planarized Conjugated Polymer Photocatalysts. *Angew. Chem., Int. Ed.* **2016**, *55*, 1792−1796.
(534) Li, R.-X.; Ren, X.-T.; Tang, M.-Y.; Chen, M.-X.; Huang, G.-B.; Fang, C.-H.; Liu, T.; Feng, Z.-H.; Yin, Y.-B.; Guo, Y.-M.; et al. Fabrication of covalently linked graphene-mediated [FeFe]-hydrogenases biomimetic photocatalytic hydrogen evolution system in aqueous solution. *Appl. Catal., B* **2018**, *224*, 772−782.
(535) Aoi, S.; Mase, K.; Ohkubo, K.; Fukuzumi, S. Photocatalytic reduction of CO_2 and H_2O to CO and H_2 with a cobalt chlorin complex adsorbed on multi-walled carbon nanotubes. *Catal. Sci. Technol.* **2016**, *6*, 4077−4080.
(536) Weiss, E. A. Designing the Surfaces of Semiconductor Quantum Dots for Colloidal Photocatalysis. *ACS Energy Lett.* **2017**, *2*, 1005−1013.
(537) Wen, F.; Yang, J.; Zong, X.; Ma, B.; Wang, D.; Li, C. Photocatalytic H_2 production on hybrid catalyst system composed of inorganic semiconductor and cobaloximes catalysts. *J. Catal.* **2011**, *281*, 318−324.
(538) Han, K.; Wang, M.; Zhang, S.; Wu, S.; Yang, Y.; Sun, L. Photochemical hydrogen production from water catalyzed by CdTe quantum dots/molecular cobalt catalyst hybrid systems. *Chem. Commun.* **2015**, *51*, 7008−7011.
(539) Wang, F.; Liang, W.-J.; Jian, J.-X.; Li, C.-B.; Chen, B.; Tung, C.-H.; Wu, L.-Z. Exceptional Poly(acrylic acid)-Based Artificial [FeFe]-Hydrogenases for Photocatalytic H_2 Production in Water. *Angew. Chem., Int. Ed.* **2013**, *52*, 8134−8138.
(540) Hagfeldt, A.; Boschloo, G.; Sun, L.; Kloo, L.; Pettersson, H. Dye-Sensitized Solar Cells. *Chem. Rev.* **2010**, *110*, 6595−6663.
(541) Lakadamyali, F.; Reisner, E. Photocatalytic H_2 evolution from neutral water with a molecular cobalt catalyst on a dye-sensitised TiO_2 nanoparticle. *Chem. Commun.* **2011**, *47*, 1695−1697.
(542) Bachmann, C.; Probst, B.; Oberholzer, M.; Fox, T.; Alberto, R. Photocatalytic proton reduction with ruthenium and cobalt complexes immobilized on fumed reversed-phase silica. *Chem. Sci.* **2016**, *7*, 436−445.
(543) Willkomm, J.; Muresan, N. M.; Reisner, E. Enhancing H_2 evolution performance of an immobilised cobalt catalyst by rational ligand design. *Chem. Sci.* **2015**, *6*, 2727−2736.
(544) Grimaldi, J. J.; Boileau, S.; Lehn, J.-M. Light-driven, carrier-mediated electron transfer across artificial membranes. *Nature* **1977**, *265*, 229−230.
(545) Watanabe, K.; Takizawa, S.-y.; Murata, S. Hydrogen Generation Using a Photoinduced Electron-transport System with a Molecular Catalyst in Vesicles. *Chem. Lett.* **2011**, *40*, 345−347.
(546) Hansen, M.; Troppmann, S.; König, B. Artificial Photosynthesis at Dynamic Self-Assembled Interfaces in Water. *Chem. - Eur. J.* **2016**, *22*, 58−72.
(547) Wang, H.-Y.; Wang, W.-G.; Si, G.; Wang, F.; Tung, C.-H.; Wu, L.-Z. Photocatalytic Hydrogen Evolution from Rhenium(I) Complexes to [FeFe] Hydrogenase Mimics in Aqueous SDS Micellar Systems: A Biomimetic Pathway. *Langmuir* **2010**, *26*, 9766−9771.

DOI: 10.1021/acs.chemrev.8b00392
Chem. Rev. 2019, 119, 2752−2875

(548) He, L.; Luo, C.; Hou, Y.; Li, C.; Zhou, Q.; Sun, Y.; Wang, W.; Zhang, B.; Wang, X. The effects of micellar media on the photocatalytic H_2 production from water. *Int. J. Hydrogen Energy* **2011**, *36*, 10593−10599.
(549) Troppmann, S.; König, B. Functionalized Vesicles with Co-Embedded CdSe Quantum Dots and [FeFe]-Hydrogenase Mimic for Light-Driven Hydrogen Production. *ChemistrySelect* **2016**, *1*, 1405−1409.
(550) Queyriaux, N.; Kaeffer, N.; Morozan, A.; Chavarot-Kerlidou, M.; Artero, V. Molecular cathode and photocathode materials for hydrogen evolution in photoelectrochemical devices. *J. Photochem. Photobiol., C* **2015**, *25*, 90−105.
(551) Wang, M.; Yang, Y.; Shen, J.; Jiang, J.; Sun, L. Visible-light-absorbing semiconductor/molecular catalyst hybrid photoelectrodes for H_2 or O_2 evolution: recent advances and challenges. *Sustainable Energy & Fuels* **2017**, *1*, 1641−1663.
(552) Tian, H. Molecular Catalyst Immobilized Photocathodes for Water/Proton and Carbon Dioxide Reduction. *ChemSusChem* **2015**, *8*, 3746−3759.
(553) Jiang, C.; Moniz, S. J. A.; Wang, A.; Zhang, T.; Tang, J. Photoelectrochemical devices for solar water splitting - materials and challenges. *Chem. Soc. Rev.* **2017**, *46*, 4645−4660.
(554) Dini, D.; Halpin, Y.; Vos, J. G.; Gibson, E. A. The influence of the preparation method of NiO_x photocathodes on the efficiency of p-type dye-sensitized solar cells. *Coord. Chem. Rev.* **2015**, *304−305*, 179−201.
(555) Yu, M.; Draskovic, T. I.; Wu, Y. Cu(I)-based delafossite compounds as photocathodes in p-type dye-sensitized solar cells. *Phys. Chem. Chem. Phys.* **2014**, *16*, 5026−5033.
(556) Gibson, E. A. Dye-sensitized photocathodes for H_2 evolution. *Chem. Soc. Rev.* **2017**, *46*, 6194−6209.
(557) Sahara, G.; Kumagai, H.; Maeda, K.; Kaeffer, N.; Artero, V.; Higashi, M.; Abe, R.; Ishitani, O. Photoelectrochemical Reduction of CO_2 Coupled to Water Oxidation Using a Photocathode With a Ru(II)-Re(I) Complex Photocatalyst and a CoO_x/TaON Photoanode. *J. Am. Chem. Soc.* **2016**, *138*, 14152−14158.
(558) Xu, P.; McCool, N. S.; Mallouk, T. E. Water splitting dye-sensitized solar cells. *Nano Today* **2017**, *14*, 42−58.
(559) D'Amario, L.; Föhlinger, J.; Boschloo, G.; Hammarström, L. Unveiling hole trapping and surface dynamics of NiO nanoparticles. *Chem. Sci.* **2018**, *9*, 223−230.
(560) Crespo-Quesada, M.; Reisner, E. Emerging approaches to stabilise photocorrodible electrodes and catalysts for solar fuel applications. *Energy Environ. Sci.* **2017**, *10*, 1116−1127.
(561) Downard, A. J. Electrochemically Assisted Covalent Modification of Carbon Electrodes. *Electroanalysis* **2000**, *12*, 1085−1096.
(562) Pinson, J.; Podvorica, F. Attachment of organic layers to conductive or semiconductive surfaces by reduction of diazonium salts. *Chem. Soc. Rev.* **2005**, *34*, 429−439.
(563) Axet, M. R.; Dechy-Cabaret, O.; Durand, J.; Gouygou, M.; Serp, P. Coordination chemistry on carbon surfaces. *Coord. Chem. Rev.* **2016**, *308*, 236−345.
(564) Tasis, D.; Tagmatarchis, N.; Bianco, A.; Prato, M. Chemistry of Carbon Nanotubes. *Chem. Rev.* **2006**, *106*, 1105−1136.
(565) Singh, P.; Campidelli, S.; Giordani, S.; Bonifazi, D.; Bianco, A.; Prato, M. Organic functionalisation and characterisation of single-walled carbon nanotubes. *Chem. Soc. Rev.* **2009**, *38*, 2214−2230.
(566) Karousis, N.; Tagmatarchis, N.; Tasis, D. Current Progress on the Chemical Modification of Carbon Nanotubes. *Chem. Rev.* **2010**, *110*, 5366−5397.
(567) Bahr, J. L.; Tour, J. M. Covalent chemistry of single-wall carbon nanotubes. *J. Mater. Chem.* **2002**, *12*, 1952−1958.
(568) De Volder, M. F. L.; Tawfick, S. H.; Baughman, R. H.; Hart, A. J. Carbon Nanotubes: Present and Future Commercial Applications. *Science* **2013**, *339*, 535−539.
(569) Georgakilas, V.; Otyepka, M.; Bourlinos, A. B.; Chandra, V.; Kim, N.; Kemp, K. C.; Hobza, P.; Zboril, R.; Kim, K. S. Functionalization of Graphene: Covalent and Non-Covalent Approaches, Derivatives and Applications. *Chem. Rev.* **2012**, *112*, 6156−6214.
(570) Bowers, M. L.; Yenser, B. A. Electrochemical behavior of glassy carbon electrodes modified by electrochemical oxidation. *Anal. Chim. Acta* **1991**, *243*, 43−53.
(571) Jannakoudakis, A. D.; Jannakoudakis, P. D.; Theodoridou, E.; Besenhard, J. O. Electrochemical oxidation of carbon fibres in aqueous solutions and analysis of the surface oxides. *J. Appl. Electrochem.* **1990**, *20*, 619−624.
(572) Xing, Y.; Li, L.; Chusuei, C. C.; Hull, R. V. Sonochemical Oxidation of Multiwalled Carbon Nanotubes. *Langmuir* **2005**, *21*, 4185−4190.
(573) Ziegler, K. J.; Gu, Z.; Peng, H.; Flor, E. L.; Hauge, R. H.; Smalley, R. E. Controlled Oxidative Cutting of Single-Walled Carbon Nanotubes. *J. Am. Chem. Soc.* **2005**, *127*, 1541−1547.
(574) Andersson, C.-H.; Grennberg, H. Reproducibility and Efficiency of Carbon Nanotube End-Group Generation and Functionalization. *Eur. J. Org. Chem.* **2009**, *2009*, 4421−4428.
(575) Gromov, A.; Dittmer, S.; Svensson, J.; Nerushev, O. A.; Perez-García, S. A.; Licea-Jiménez, L.; Rychwalski, R.; Campbell, E. E. B. Covalent amino-functionalisation of single-wall carbon nanotubes. *J. Mater. Chem.* **2005**, *15*, 3334−3339.
(576) Song, S.; Xue, Y.; Feng, L.; Elbatal, H.; Wang, P.; Moorefield, C. N.; Newkome, G. R.; Dai, L. Reversible Self-Assembly of Terpyridine-Functionalized Graphene Oxide for Energy Conversion. *Angew. Chem., Int. Ed.* **2014**, *53*, 1415−1419.
(577) Hutton, G. A. M.; Reuillard, B.; Martindale, B. C. M.; Caputo, C. A.; Lockwood, C. W. J.; Butt, J. N.; Reisner, E. Carbon Dots as Versatile Photosensitizers for Solar-Driven Catalysis with Redox Enzymes. *J. Am. Chem. Soc.* **2016**, *138*, 16722−16730.
(578) Delamar, M.; Hitmi, R.; Pinson, J.; Savéant, J. M. Covalent modification of carbon surfaces by grafting of functionalized aryl radicals produced from electrochemical reduction of diazonium salts. *J. Am. Chem. Soc.* **1992**, *114*, 5883−5884.
(579) Allongue, P.; Delamar, M.; Desbat, B.; Fagebaume, O.; Hitmi, R.; Pinson, J.; Savéant, J.-M. Covalent Modification of Carbon Surfaces by Aryl Radicals Generated from the Electrochemical Reduction of Diazonium Salts. *J. Am. Chem. Soc.* **1997**, *119*, 201−207.
(580) Mahouche-Chergui, S.; Gam-Derouich, S.; Mangeney, C.; Chehimi, M. M. Aryl diazonium salts: a new class of coupling agents for bonding polymers, biomacromolecules and nanoparticles to surfaces. *Chem. Soc. Rev.* **2011**, *40*, 4143−4166.
(581) Sandmeyer, T. Über die Ersetzung der Amidgruppe durch Chlor in den aromatischen Substanzen. *Ber. Dtsch. Chem. Ges.* **1884**, *17*, 1633−1635.
(582) Bahr, J. L.; Tour, J. M. Highly Functionalized Carbon Nanotubes Using in Situ Generated Diazonium Compounds. *Chem. Mater.* **2001**, *13*, 3823−3824.
(583) Baranton, S.; Bélanger, D. Electrochemical Derivatization of Carbon Surface by Reduction of in Situ Generated Diazonium Cations. *J. Phys. Chem. B* **2005**, *109*, 24401−24410.
(584) Breton, T.; Bélanger, D. Modification of Carbon Electrode with Aryl Groups Having an Aliphatic Amine by Electrochemical Reduction of In Situ Generated Diazonium Cations. *Langmuir* **2008**, *24*, 8711−8718.
(585) Evrard, D.; Lambert, F.; Policar, C.; Balland, V.; Limoges, B. Electrochemical Functionalization of Carbon Surfaces by Aromatic Azide or Alkyne Molecules: A Versatile Platform for Click Chemistry. *Chem. - Eur. J.* **2008**, *14*, 9286−9291.
(586) Campidelli, S.; Ballesteros, B.; Filoramo, A.; Díaz, D. D.; de la Torre, G.; Torres, T.; Rahman, G. M. A.; Ehli, C.; Kiessling, D.; Werner, F.; et al. Facile Decoration of Functionalized Single-Wall Carbon Nanotubes with Phthalocyanines via "Click Chemistry". *J. Am. Chem. Soc.* **2008**, *130*, 11503−11509.
(587) Georgakilas, V.; Kordatos, K.; Prato, M.; Guldi, D. M.; Holzinger, M.; Hirsch, A. Organic Functionalization of Carbon Nanotubes. *J. Am. Chem. Soc.* **2002**, *124*, 760−761.

DOI: 10.1021/acs.chemrev.8b00392
Chem. Rev. 2019, 119, 2752−2875

(588) Tagmatarchis, N.; Prato, M. Functionalization of carbon nanotubes via 1,3-dipolar cycloadditions. *J. Mater. Chem.* **2004**, *14*, 437−439.
(589) Cioffi, C.; Campidelli, S.; Brunetti, F. G.; Meneghetti, M.; Prato, M. Functionalisation of carbon nanohorns. *Chem. Commun.* **2006**, 2129−2131.
(590) Wang, X.; Jiang, D.-e.; Dai, S. Surface Modification of Ordered Mesoporous Carbons via 1,3-Dipolar Cycloaddition of Azomethine Ylides. *Chem. Mater.* **2008**, *20*, 4800−4802.
(591) Hassner, A.; Marinescu, L.; Bols, M. *Encyclopedia of Reagents for Organic Synthesis*; John Wiley & Sons, Ltd.: Hoboken, NJ, 2001.
(592) Devadoss, A.; Chidsey, C. E. D. Azide-Modified Graphitic Surfaces for Covalent Attachment of Alkyne-Terminated Molecules by "Click" Chemistry. *J. Am. Chem. Soc.* **2007**, *129*, 5370−5371.
(593) McCrory, C. C. L.; Devadoss, A.; Ottenwaelder, X.; Lowe, R. D.; Stack, T. D. P.; Chidsey, C. E. D. Electrocatalytic O_2 Reduction by Covalently Immobilized Mononuclear Copper(I) Complexes: Evidence for a Binuclear Cu_2O_2 Intermediate. *J. Am. Chem. Soc.* **2011**, *133*, 3696−3699.
(594) Das, A. K.; Engelhard, M. H.; Liu, F.; Bullock, R. M.; Roberts, J. A. S. The Electrode as Organolithium Reagent: Catalyst-Free Covalent Attachment of Electrochemically Active Species to an Azide-Terminated Glassy Carbon Electrode Surface. *Inorg. Chem.* **2013**, *52*, 13674−13684.
(595) Holzinger, M.; Vostrowsky, O.; Hirsch, A.; Hennrich, F.; Kappes, M.; Weiss, R.; Jellen, F. Sidewall Functionalization of Carbon Nanotubes. *Angew. Chem., Int. Ed.* **2001**, *40*, 4002−4005.
(596) Hu, H.; Zhao, B.; Hamon, M. A.; Kamaras, K.; Itkis, M. E.; Haddon, R. C. Sidewall Functionalization of Single-Walled Carbon Nanotubes by Addition of Dichlorocarbene. *J. Am. Chem. Soc.* **2003**, *125*, 14893−14900.
(597) Holzinger, M.; Abraham, J.; Whelan, P.; Graupner, R.; Ley, L.; Hennrich, F.; Kappes, M.; Hirsch, A. Functionalization of Single-Walled Carbon Nanotubes with (R-)Oxycarbonyl Nitrenes. *J. Am. Chem. Soc.* **2003**, *125*, 8566−8580.
(598) Coleman, K. S.; Bailey, S. R.; Fogden, S.; Green, M. L. H. Functionalization of Single-Walled Carbon Nanotubes via the Bingel Reaction. *J. Am. Chem. Soc.* **2003**, *125*, 8722−8723.
(599) Delgado, J. L.; de la Cruz, P.; Langa, F.; Urbina, A.; Casado, J.; Lopez Navarrete, J. T. Microwave-assisted sidewall functionalization of single-wall carbon nanotubes by Diels-Alder cycloaddition. *Chem. Commun.* **2004**, 1734−1735.
(600) Zhao, Y.-L.; Stoddart, J. F. Noncovalent Functionalization of Single-Walled Carbon Nanotubes. *Acc. Chem. Res.* **2009**, *42*, 1161−1171.
(601) Pérez, E. M.; Martín, N. π-π interactions in carbon nanostructures. *Chem. Soc. Rev.* **2015**, *44*, 6425−6433.
(602) de Groot, M. T.; Koper, M. T. M. Redox transitions of chromium, manganese, iron, cobalt and nickel protoporphyrins in aqueous solution. *Phys. Chem. Chem. Phys.* **2008**, *10*, 1023−1031.
(603) Smith, H. L.; Usala, R. L.; McQueen, E. W.; Goldsmith, J. I. Novel Polyaromatic-Terminated Transition Metal Complexes for the Functionalization of Carbon Surfaces. *Langmuir* **2010**, *26*, 3342−3349.
(604) Mann, J. A.; Dichtel, W. R. Improving the Binding Characteristics of Tripodal Compounds on Single Layer Graphene. *ACS Nano* **2013**, *7*, 7193−7199.
(605) Zhao, Y.-L.; Hu, L.; Stoddart, J. F.; Grüner, G. Pyrenecyclodextrin-Decorated Single-Walled Carbon Nanotube Field-Effect Transistors as Chemical Sensors. *Adv. Mater.* **2008**, *20*, 1910−1915.
(606) Tran, P. D.; Le Goff, A.; Heidkamp, J.; Jousselme, B.; Guillet, N.; Palacin, S.; Dau, H.; Fontecave, M.; Artero, V. Noncovalent Modification of Carbon Nanotubes with Pyrene-Functionalized Nickel Complexes: Carbon Monoxide Tolerant Catalysts for Hydrogen Evolution and Uptake. *Angew. Chem., Int. Ed.* **2011**, *50*, 1371−1374.
(607) Blakemore, J. D.; Gupta, A.; Warren, J. J.; Brunschwig, B. S.; Gray, H. B. Noncovalent Immobilization of Electrocatalysts on Carbon Electrodes for Fuel Production. *J. Am. Chem. Soc.* **2013**, *135*, 18288−18291.
(608) Reuillard, B.; Le Goff, A.; Cosnier, S. Non-covalent double functionalization of carbon nanotubes with a NADH oxidation Ru(II)-based molecular catalyst and a NAD-dependent glucose dehydrogenase. *Chem. Commun.* **2014**, *50*, 11731−11734.
(609) Li, F.; Zhang, B.; Li, X.; Jiang, Y.; Chen, L.; Li, Y.; Sun, L. Highly Efficient Oxidation of Water by a Molecular Catalyst Immobilized on Carbon Nanotubes. *Angew. Chem., Int. Ed.* **2011**, *50*, 12276−12279.
(610) Kang, P.; Zhang, S.; Meyer, T. J.; Brookhart, M. Rapid Selective Electrocatalytic Reduction of Carbon Dioxide to Formate by an Iridium Pincer Catalyst Immobilized on Carbon Nanotube Electrodes. *Angew. Chem., Int. Ed.* **2014**, *53*, 8709−8713.
(611) Das, A.; Stahl, S. S. Noncovalent Immobilization of Molecular Electrocatalysts for Chemical Synthesis: Efficient Electrochemical Alcohol Oxidation with a Pyrene−TEMPO Conjugate. *Angew. Chem., Int. Ed.* **2017**, *56*, 8892−8897.
(612) Song, X.-W.; Wen, H.-M.; Ma, C.-B.; Cui, H.-H.; Chen, H.; Chen, C.-N. Efficient photocatalytic hydrogen evolution with end-group-functionalized cobaloxime catalysts in combination with graphite-like C_3N_4. *RSC Adv.* **2014**, *4*, 18853−18861.
(613) Kar, T.; Bettinger, H. F.; Scheiner, S.; Roy, A. K. Noncovalent π−π Stacking and CH—π Interactions of Aromatics on the Surface of Single-Wall Carbon Nanotubes: An MP2 Study. *J. Phys. Chem. C* **2008**, *112*, 20070−20075.
(614) Mann, J. A.; Rodríguez-López, J.; Abruña, H. D.; Dichtel, W. R. Multivalent Binding Motifs for the Noncovalent Functionalization of Graphene. *J. Am. Chem. Soc.* **2011**, *133*, 17614−17617.
(615) McQueen, E. W.; Goldsmith, J. I. Electrochemical Analysis of Single-Walled Carbon Nanotubes Functionalized with Pyrene-Pendant Transition Metal Complexes. *J. Am. Chem. Soc.* **2009**, *131*, 17554−17556.
(616) Le Goff, A.; Moggia, F.; Debou, N.; Jegou, P.; Artero, V.; Fontecave, M.; Jousselme, B.; Palacin, S. Facile and tunable functionalization of carbon nanotube electrodes with ferrocene by covalent coupling and π-stacking interactions and their relevance to glucose bio-sensing. *J. Electroanal. Chem.* **2010**, *641*, 57−63.
(617) Le Goff, A.; Reuillard, B.; Cosnier, S. A Pyrene-Substituted Tris(bipyridine)osmium(II) Complex as a Versatile Redox Probe for Characterizing and Functionalizing Carbon Nanotube- and Graphene-Based Electrodes. *Langmuir* **2013**, *29*, 8736−8742.
(618) Chen, R. J.; Zhang, Y.; Wang, D.; Dai, H. Noncovalent Sidewall Functionalization of Single-Walled Carbon Nanotubes for Protein Immobilization. *J. Am. Chem. Soc.* **2001**, *123*, 3838−3839.
(619) Krishnan, S.; Armstrong, F. A. Order-of-magnitude enhancement of an enzymatic hydrogen-air fuel cell based on pyrenyl carbon nanostructures. *Chem. Sci.* **2012**, *3*, 1015−1023.
(620) Reuillard, B.; Le Goff, A.; Holzinger, M.; Cosnier, S. Non-covalent functionalization of carbon nanotubes with boronic acids for the wiring of glycosylated redox enzymes in oxygen-reducing biocathodes. *J. Mater. Chem. B* **2014**, *2*, 2228−2232.
(621) Lalaoui, N.; Rousselot-Pailley, P.; Robert, V.; Mekmouche, Y.; Villalonga, R.; Holzinger, M.; Cosnier, S.; Tron, T.; Le Goff, A. Direct Electron Transfer between a Site-Specific Pyrene-Modified Laccase and Carbon Nanotube/Gold Nanoparticle Supramolecular Assemblies for Bioelectrocatalytic Dioxygen Reduction. *ACS Catal.* **2016**, *6*, 1894−1900.
(622) Bosch-Navarro, C.; Matt, B.; Izzet, G.; Romero-Nieto, C.; Dirian, K.; Raya, A.; Molina, S. I.; Proust, A.; Guldi, D. M.; Martí-Gastaldo, C.; et al. Charge transfer interactions in self-assembled single walled carbon nanotubes/Dawson-Wells polyoxometalate hybrids. *Chem. Sci.* **2014**, *5*, 4346−4354.
(623) Ma, D.; Liang, L.; Chen, W.; Liu, H.; Song, Y.-F. Covalently Tethered Polyoxometalate−Pyrene Hybrids for Noncovalent Sidewall Functionalization of Single-Walled Carbon Nanotubes as High-Performance Anode Material. *Adv. Funct. Mater.* **2013**, *23*, 6100−6105.
(624) Modugno, G.; Syrgiannis, Z.; Bonasera, A.; Carraro, M.; Giancane, G.; Valli, L.; Bonchio, M.; Prato, M. The supramolecular design of low-dimensional carbon nano-hybrids encoding a polyoxometalate-bis-pyrene tweezer. *Chem. Commun.* **2014**, *50*, 4881−4883.

DOI: 10.1021/acs.chemrev.8b00392
Chem. Rev. 2019, 119, 2752−2875

(625) Sun, X.; Sun, H.; Li, H.; Peng, H. Developing Polymer Composite Materials: Carbon Nanotubes or Graphene? *Adv. Mater.* **2013**, *25*, 5153−5176.
(626) Zhou, Q.; Shi, G. Conducting Polymer-Based Catalysts. *J. Am. Chem. Soc.* **2016**, *138*, 2868−2876.
(627) Cosnier, S. Affinity Biosensors Based on Electropolymerized Films. *Electroanalysis* **2005**, *17*, 1701−1715.
(628) Cosnier, S.; Holzinger, M. Electrosynthesized polymers for biosensing. *Chem. Soc. Rev.* **2011**, *40*, 2146−2156.
(629) Zhong, Y.-W.; Yao, C.-J.; Nie, H.-J. Electropolymerized films of vinyl-substituted polypyridine complexes: Synthesis, characterization, and applications. *Coord. Chem. Rev.* **2013**, *257*, 1357−1372.
(630) Abe, T.; Yoshida, T.; Tokita, S.; Taguchi, F.; Imaya, H.; Kaneko, M. Factors affecting selective electrocatalytic CO_2 reduction with cobalt phthalocyanine incorporated in a polyvinylpyridine membrane coated on a graphite electrode. *J. Electroanal. Chem.* **1996**, *412*, 125−132.
(631) Ibrahim, S. K.; Liu, X.; Tard, C.; Pickett, C. J. Electropolymeric materials incorporating subsite structures related to iron-only hydrogenase: active ester functionalised poly(pyrroles) for covalent binding of {2Fe3S}-carbonyl/cyanide assemblies. *Chem. Commun.* **2007**, 1535−1537.
(632) Reuillard, B.; Le Goff, A.; Cosnier, S. Polypyrrolic Bipyridine Bis(phenantrolinequinone) Ru(II) Complex/Carbon Nanotube Composites for NAD-Dependent Enzyme Immobilization and Wiring. *Anal. Chem.* **2014**, *86*, 4409−4415.
(633) Hickey, D. P.; Milton, R. D.; Chen, D.; Sigman, M. S.; Minteer, S. D. TEMPO-Modified Linear Poly(ethylenimine) for Immobilization-Enhanced Electrocatalytic Oxidation of Alcohols. *ACS Catal.* **2015**, *5*, 5519−5524.
(634) Heller, A. Electron-conducting redox hydrogels: design, characteristics and synthesis. *Curr. Opin. Chem. Biol.* **2006**, *10*, 664−672.
(635) Mao, F.; Mano, N.; Heller, A. Long Tethers Binding Redox Centers to Polymer Backbones Enhance Electron Transport in Enzyme "Wiring" Hydrogels. *J. Am. Chem. Soc.* **2003**, *125*, 4951−4957.
(636) MacAodha, D.; Ferrer, M. L.; Conghaile, P. O.; Kavanagh, P.; Leech, D. Crosslinked redox polymer enzyme electrodes containing carbon nanotubes for high and stable glucose oxidation current. *Phys. Chem. Chem. Phys.* **2012**, *14*, 14667−14672.
(637) Plumeré, N.; Rüdiger, O.; Oughli, A. A.; Williams, R.; Vivekananthan, J.; Pöller, S.; Schuhmann, W.; Lubitz, W. A redox hydrogel protects hydrogenase from high-potential deactivation and oxygen damage. *Nat. Chem.* **2014**, *6*, 822−827.
(638) Kramer, W. W.; McCrory, C. C. L. Polymer coordination promotes selective CO_2 reduction by cobalt phthalocyanine. *Chem. Sci.* **2016**, *7*, 2506−2515.
(639) Pander, J. E., III; Fogg, A.; Bocarsly, A. B. Utilization of Electropolymerized Films of Cobalt Porphyrin for the Reduction of Carbon Dioxide in Aqueous Media. *ChemCatChem* **2016**, *8*, 3536−3545.
(640) Reuillard, B.; Warnan, J.; Leung, J. J.; Wakerley, D. W.; Reisner, E. A Poly(cobaloxime)/Carbon Nanotube Electrode: Freestanding Buckypaper with Polymer-Enhanced H_2-Evolution Performance. *Angew. Chem., Int. Ed.* **2016**, *55*, 3952−3957.
(641) Zhang, L.; Cole, J. M. Anchoring Groups for Dye-Sensitized Solar Cells. *ACS Appl. Mater. Interfaces* **2015**, *7*, 3427−3455.
(642) Barteau, M. A. Organic Reactions at Well-Defined Oxide Surfaces. *Chem. Rev.* **1996**, *96*, 1413−1430.
(643) Vohs, J. M. Site Requirements for the Adsorption and Reaction of Oxygenates on Metal Oxide Surfaces. *Chem. Rev.* **2013**, *113*, 4136−4163.
(644) Pujari, S. P.; Scheres, L.; Marcelis, A. T. M.; Zuilhof, H. Covalent Surface Modification of Oxide Surfaces. *Angew. Chem., Int. Ed.* **2014**, *53*, 6322−6356.
(645) Brennan, B. J.; Llansola Portolés, M. J.; Liddell, P. A.; Moore, T. A.; Moore, A. L.; Gust, D. Comparison of silatrane, phosphonic acid, and carboxylic acid functional groups for attachment of porphyrin sensitizers to TiO_2 in photoelectrochemical cells. *Phys. Chem. Chem. Phys.* **2013**, *15*, 16605−16614.
(646) Brewster, T. P.; Konezny, S. J.; Sheehan, S. W.; Martini, L. A.; Schmuttenmaer, C. A.; Batista, V. S.; Crabtree, R. H. Hydroxamate Anchors for Improved Photoconversion in Dye-Sensitized Solar Cells. *Inorg. Chem.* **2013**, *52*, 6752−6764.
(647) Martini, L. A.; Moore, G. F.; Milot, R. L.; Cai, L. Z.; Sheehan, S. W.; Schmuttenmaer, C. A.; Brudvig, G. W.; Crabtree, R. H. Modular Assembly of High-Potential Zinc Porphyrin Photosensitizers Attached to TiO_2 with a Series of Anchoring Groups. *J. Phys. Chem. C* **2013**, *117*, 14526−14533.
(648) Paniagua, S. A.; Giordano, A. J.; Smith, O. N. L.; Barlow, S.; Li, H.; Armstrong, N. R.; Pemberton, J. E.; Brédas, J.-L.; Ginger, D.; Marder, S. R. Phosphonic Acids for Interfacial Engineering of Transparent Conductive Oxides. *Chem. Rev.* **2016**, *116*, 7117−7158.
(649) Bae, E.; Choi, W.; Park, J.; Shin, H. S.; Kim, S. B.; Lee, J. S. Effects of Surface Anchoring Groups (Carboxylate vs Phosphonate) in Ruthenium-Complex-Sensitized TiO_2 on Visible Light Reactivity in Aqueous Suspensions. *J. Phys. Chem. B* **2004**, *108*, 14093−14101.
(650) Nazeeruddin, M. K.; Humphry-Baker, R.; Officer, D. L.; Campbell, W. M.; Burrell, A. K.; Grätzel, M. Application of Metalloporphyrins in Nanocrystalline Dye-Sensitized Solar Cells for Conversion of Sunlight into Electricity. *Langmuir* **2004**, *20*, 6514−6517.
(651) Lim, M. S.; Feng, K.; Chen, X.; Wu, N.; Raman, A.; Nightingale, J.; Gawalt, E. S.; Korakakis, D.; Hornak, L. A.; Timperman, A. T. Adsorption and Desorption of Stearic Acid Self-Assembled Monolayers on Aluminum Oxide. *Langmuir* **2007**, *23*, 2444−2452.
(652) Reisner, E.; Powell, D. J.; Cavazza, C.; Fontecilla-Camps, J. C.; Armstrong, F. A. Visible Light-Driven H_2 Production by Hydrogenases Attached to Dye-Sensitized TiO_2 Nanoparticles. *J. Am. Chem. Soc.* **2009**, *131*, 18457−18466.
(653) Reisner, E. Solar Hydrogen Evolution with Hydrogenases: From Natural to Hybrid Systems. *Eur. J. Inorg. Chem.* **2011**, 1005−1016.
(654) Caputo, C. A.; Wang, L.; Beranek, R.; Reisner, E. Carbon nitride−TiO_2 hybrid modified with hydrogenase for visible light driven hydrogen production. *Chem. Sci.* **2015**, *6*, 5690−5694.
(655) Queffélec, C.; Petit, M.; Janvier, P.; Knight, D. A.; Bujoli, B. Surface Modification Using Phosphonic Acids and Esters. *Chem. Rev.* **2012**, *112*, 3777−3807.
(656) Boissezon, R.; Muller, J.; Beaugeard, V.; Monge, S.; Robin, J.-J. Organophosphonates as anchoring agents onto metal oxide-based materials: synthesis and applications. *RSC Adv.* **2014**, *4*, 35690−35707.
(657) Mutin, P. H.; Guerrero, G.; Vioux, A. Hybrid materials from organophosphorus coupling molecules. *J. Mater. Chem.* **2005**, *15*, 3761−3768.
(658) Brodard-Severac, F.; Guerrero, G.; Maquet, J.; Florian, P.; Gervais, C.; Mutin, P. H. High-Field ^{17}O MAS NMR Investigation of Phosphonic Acid Monolayers on Titania. *Chem. Mater.* **2008**, *20*, 5191−5196.
(659) Norris, M. R.; Concepcion, J. J.; Glasson, C. R. K.; Fang, Z.; Lapides, A. M.; Ashford, D. L.; Templeton, J. L.; Meyer, T. J. Synthesis of Phosphonic Acid Derivatized Bipyridine Ligands and Their Ruthenium Complexes. *Inorg. Chem.* **2013**, *52*, 12492−12501.
(660) Jiang, J.; Swierk, J. R.; Hedstrom, S.; Matula, A. J.; Crabtree, R. H.; Batista, V. S.; Schmuttenmaer, C. A.; Brudvig, G. W. Molecular design of light-harvesting photosensitizers: effect of varied linker conjugation on interfacial electron transfer. *Phys. Chem. Chem. Phys.* **2016**, *18*, 18678−18682.
(661) Hirao, T.; Masunaga, T.; Ohshiro, Y.; Agawa, T. A Novel Synthesis of Dialkyl Arenephosphonates. *Synthesis* **1981**, 56−57.
(662) Ghosh, P.; Spiro, T. G. Photoelectrochemistry of tris-(bipyridyl)ruthenium(II) covalently attached to n-type tin(IV) oxide. *J. Am. Chem. Soc.* **1980**, *102*, 5543−5549.
(663) Fung, A. K. M.; Chiu, B. K. W.; Lam, M. H. W. Surface modification of TiO_2 by a ruthenium(II) polypyridyl complex via silyl-linkage for the sensitized photocatalytic degradation of carbon tetrachloride by visible irradiation. *Water Res.* **2003**, *37*, 1939−1947.

DOI: 10.1021/acs.chemrev.8b00392
Chem. Rev. 2019, 119, 2752−2875

(664) Herzer, N.; Hoeppener, S.; Schubert, U. S. Fabrication of patterned silane based self-assembled monolayers by photolithography and surface reactions on silicon-oxide substrates. *Chem. Commun.* **2010**, *46*, 5634−5652.
(665) Shambayati, S.; Schreiber, S. L.; Blake, J. F.; Wierschke, S. G.; Jorgensen, W. L. Structure and Basicity of Silyl Ethers: A Crystallographic and ab Initio Inquiry into the Nature of Silicon-Oxygen Interactions. *J. Am. Chem. Soc.* **1990**, *112*, 697−703.
(666) Brennan, B. J.; Keirstead, A. E.; Liddell, P. A.; Vail, S. A.; Moore, T. A.; Moore, A. L.; Gust, D. 1-(3′-amino)propylsilatrane derivatives as covalent surface linkers to nanoparticulate metal oxide films for use in photoelectrochemical cells. *Nanotechnology* **2009**, *20*, 505203.
(667) Gao, Y.; Ding, X.; Liu, J.; Wang, L.; Lu, Z.; Li, L.; Sun, L. Visible Light Driven Water Splitting in a Molecular Device with Unprecedentedly High Photocurrent Density. *J. Am. Chem. Soc.* **2013**, *135*, 4219−4222.
(668) Brennan, B. J.; Gust, D.; Brudvig, G. W. Organosilatrane building blocks. *Tetrahedron Lett.* **2014**, *55*, 1062−1064.
(669) Materna, K. L.; Rudshteyn, B.; Brennan, B. J.; Kane, M. H.; Bloomfield, A. J.; Huang, D. L.; Shopov, D. Y.; Batista, V. S.; Crabtree, R. H.; Brudvig, G. W. Heterogenized Iridium Water-Oxidation Catalyst from a Silatrane Precursor. *ACS Catal.* **2016**, *6*, 5371−5377.
(670) Brennan, B. J.; Chen, J.; Rudshteyn, B.; Chaudhuri, S.; Mercado, B. Q.; Batista, V. S.; Crabtree, R. H.; Brudvig, G. W. Molecular titanium-hydroxamate complexes as models for TiO_2 surface binding. *Chem. Commun.* **2016**, *52*, 2972−2975.
(671) Brennan, B. J.; Koenigsmann, C.; Materna, K. L.; Kim, P. M.; Koepf, M.; Crabtree, R. H.; Schmuttenmaer, C. A.; Brudvig, G. W. Surface-Induced Deprotection of THP-Protected Hydroxamic Acids on Titanium Dioxide. *J. Phys. Chem. C* **2016**, *120*, 12495−12502.
(672) McNamara, W. R.; Snoeberger, R. C., III; Li, G.; Richter, C.; Allen, L. J.; Milot, R. L.; Schmuttenmaer, C. A.; Crabtree, R. H.; Brudvig, G. W.; Batista, V. S. Hydroxamate anchors for water-stable attachment to TiO_2 nanoparticles. *Energy Environ. Sci.* **2009**, *2*, 1173−1175.
(673) McNamara, W. R.; Milot, R. L.; Song, H.-e.; Snoeberger, R. C., III; Batista, V. S.; Schmuttenmaer, C. A.; Brudvig, G. W.; Crabtree, R. H. Water-stable, hydroxamate anchors for functionalization of TiO_2 surfaces with ultrafast interfacial electron transfer. *Energy Environ. Sci.* **2010**, *3*, 917−923.
(674) Heimer, T. A.; D'Arcangelis, S. T.; Farzad, F.; Stipkala, J. M.; Meyer, G. J. An Acetylacetonate-Based Semiconductor−Sensitizer Linkage. *Inorg. Chem.* **1996**, *35*, 5319−5324.
(675) McNamara, W. R.; Snoeberger, R. C., III; Li, G.; Schleicher, J. M.; Cady, C. W.; Poyatos, M.; Schmuttenmaer, C. A.; Crabtree, R. H.; Brudvig, G. W.; Batista, V. S. Acetylacetonate Anchors for Robust Functionalization of TiO_2 Nanoparticles with Mn(II)−Terpyridine Complexes. *J. Am. Chem. Soc.* **2008**, *130*, 14329−14338.
(676) Xiao, D.; Martini, L. A.; Snoeberger, R. C.; Crabtree, R. H.; Batista, V. S. Inverse Design and Synthesis of acac-Coumarin Anchors for Robust TiO_2 Sensitization. *J. Am. Chem. Soc.* **2011**, *133*, 9014−9022.
(677) Warnan, J.; Pellegrin, Y.; Blart, E.; Zhang, L.; Brown, A.; Hammarström, L.; Jacquemin, D.; Odobel, F. Acetylacetone anchoring group for NiO-based dye-sensitized solar cell. *Dyes Pigm.* **2014**, *105*, 174−179.
(678) Kessler, V. G.; Gohil, S.; Parola, S. Interaction of some divalent metal acetylacetonates with Al, Ti, Nb and Ta isopropoxides. Factors influencing the formation and stability of heterometallic alkoxide complexes. *Dalton Trans.* **2003**, 544−550.
(679) Bahers, T. L.; Pauporté, T.; Labat, F.; Lefèvre, G.; Ciofini, I. Acetylacetone, an Interesting Anchoring Group for ZnO-Based Organic−Inorganic Hybrid Materials: A Combined Experimental and Theoretical Study. *Langmuir* **2011**, *27*, 3442−3450.
(680) Jiang, Y.; Wu, N.; Wu, H.; He, M. An Efficient and Mild CuI/*L*-Proline-Catalyzed Arylation of Acetylacetone or Ethyl Cyanoacetate. *Synlett* **2005**, *2005*, 2731−2734.
(681) Nitta, M.; Kobayashi, T. Reductive ring opening of isoxazoles with $Mo(CO)_6$ and water. *J. Chem. Soc., Chem. Commun.* **1982**, 877−878.
(682) Warnan, J.; Guerin, V.-M.; Anne, F. B.; Pellegrin, Y.; Blart, E.; Jacquemin, D.; Pauporté, T.; Odobel, F. Ruthenium Sensitizer Functionalized by Acetylacetone Anchoring Groups for Dye-Sensitized Solar Cells. *J. Phys. Chem. C* **2013**, *117*, 8652−8660.
(683) Moss, J. A.; Yang, J. C.; Stipkala, J. M.; Wen, X.; Bignozzi, C. A.; Meyer, G. J.; Meyer, T. J. Sensitization and Stabilization of TiO_2 Photoanodes with Electropolymerized Overlayer Films of Ruthenium and Zinc Polypyridyl Complexes: A Stable Aqueous Photoelectrochemical Cell. *Inorg. Chem.* **2004**, *43*, 1784−1792.
(684) Cecchet, F.; Alebbi, M.; Bignozzi, C. A.; Paolucci, F. Efficiency enhancement of the electrocatalytic reduction of CO_2: *fac*-[Re(v-bpy)$(CO)_3$Cl] electropolymerized onto mesoporous TiO_2 electrodes. *Inorg. Chim. Acta* **2006**, *359*, 3871−3874.
(685) Lapides, A. M.; Ashford, D. L.; Hanson, K.; Torelli, D. A.; Templeton, J. L.; Meyer, T. J. Stabilization of a Ruthenium(II) Polypyridyl Dye on Nanocrystalline TiO_2 by an Electropolymerized Overlayer. *J. Am. Chem. Soc.* **2013**, *135*, 15450−15458.
(686) Ashford, D. L.; Lapides, A. M.; Vannucci, A. K.; Hanson, K.; Torelli, D. A.; Harrison, D. P.; Templeton, J. L.; Meyer, T. J. Water Oxidation by an Electropolymerized Catalyst on Derivatized Mesoporous Metal Oxide Electrodes. *J. Am. Chem. Soc.* **2014**, *136*, 6578−6581.
(687) Li, M.; Zhang, J.; Nie, H.-J.; Liao, M.; Sang, L.; Qiao, W.; Wang, Z. Y.; Ma, Y.; Zhong, Y.-W.; Ariga, K. *In situ* switching layer-by-layer assembly: one-pot rapid layer assembly *via* alternation of reductive and oxidative electropolymerization. *Chem. Commun.* **2013**, *49*, 6879−6881.
(688) Brown, K. A.; Dayal, S.; Ai, X.; Rumbles, G.; King, P. W. Controlled Assembly of Hydrogenase-CdTe Nanocrystal Hybrids for Solar Hydrogen Production. *J. Am. Chem. Soc.* **2010**, *132*, 9672−9680.
(689) Wang, F.; Wang, W.-G.; Wang, X.-J.; Wang, H.-Y.; Tung, C.-H.; Wu, L.-Z. A Highly Efficient Photocatalytic System for Hydrogen Production by a Robust Hydrogenase Mimic in an Aqueous Solution. *Angew. Chem., Int. Ed.* **2011**, *50*, 3193−3197.
(690) Han, Z.; Qiu, F.; Eisenberg, R.; Holland, P. L.; Krauss, T. D. Robust Photogeneration of H_2 in Water Using Semiconductor Nanocrystals and a Nickel Catalyst. *Science* **2012**, *338*, 1321−1324.
(691) Brown, K. A.; Wilker, M. B.; Boehm, M.; Dukovic, G.; King, P. W. Characterization of Photochemical Processes for H_2 Production by CdS Nanorod−[FeFe] Hydrogenase Complexes. *J. Am. Chem. Soc.* **2012**, *134*, 5627−5636.
(692) Aldana, J.; Wang, Y. A.; Peng, X. Photochemical Instability of CdSe Nanocrystals Coated by Hydrophilic Thiols. *J. Am. Chem. Soc.* **2001**, *123*, 8844−8850.
(693) Soreni-Harari, M.; Yaacobi-Gross, N.; Steiner, D.; Aharoni, A.; Banin, U.; Millo, O.; Tessler, N. Tuning Energetic Levels in Nanocrystal Quantum Dots through Surface Manipulations. *Nano Lett.* **2008**, *8*, 678−684.
(694) Peterson, M. D.; Jensen, S. C.; Weinberg, D. J.; Weiss, E. A. Mechanisms for Adsorption of Methyl Viologen on CdS Quantum Dots. *ACS Nano* **2014**, *8*, 2826−2837.
(695) Anderson, N. C.; Hendricks, M. P.; Choi, J. J.; Owen, J. S. Ligand Exchange and the Stoichiometry of Metal Chalcogenide Nanocrystals: Spectroscopic Observation of Facile Metal-Carboxylate Displacement and Binding. *J. Am. Chem. Soc.* **2013**, *135*, 18536−18548.
(696) Aldeek, F.; Hawkins, D.; Palomo, V.; Safi, M.; Palui, G.; Dawson, P. E.; Alabugin, I.; Mattoussi, H. UV and Sunlight Driven Photoligation of Quantum Dots: Understanding the Photochemical Transformation of the Ligands. *J. Am. Chem. Soc.* **2015**, *137*, 2704−2714.
(697) Bloom, B. P.; Zhao, L.-B.; Wang, Y.; Waldeck, D. H.; Liu, R.; Zhang, P.; Beratan, D. N. Ligand-Induced Changes in the Characteristic Size-Dependent Electronic Energies of CdSe Nanocrystals. *J. Phys. Chem. C* **2013**, *117*, 22401−22411.
(698) Brown, P. R.; Kim, D.; Lunt, R. R.; Zhao, N.; Bawendi, M. G.; Grossman, J. C.; Bulović, V. Energy Level Modification in Lead Sulfide

DOI: 10.1021/acs.chemrev.8b00392
Chem. Rev. 2019, 119, 2752−2875

Quantum Dot Thin Films through Ligand Exchange. *ACS Nano* **2014**, *8*, 5863−5872.
(699) Huang, J.; Mulfort, K. L.; Du, P.; Chen, L. X. Photodriven Charge Separation Dynamics in CdSe/ZnS Core/Shell Quantum Dot/Cobaloxime Hybrid for Efficient Hydrogen Production. *J. Am. Chem. Soc.* **2012**, *134*, 16472−16475.
(700) Butler, M. A.; Ginley, D. S. P-Type GaP as a Semiconducting Photoelectrode. *J. Electrochem. Soc.* **1980**, *127*, 1273−1278.
(701) Sun, K.; Shen, S.; Liang, Y.; Burrows, P. E.; Mao, S. S.; Wang, D. Enabling Silicon for Solar-Fuel Production. *Chem. Rev.* **2014**, *114*, 8662−8719.
(702) Hu, S.; Lewis, N. S.; Ager, J. W.; Yang, J.; McKone, J. R.; Strandwitz, N. C. Thin-Film Materials for the Protection of Semiconducting Photoelectrodes in Solar-Fuel Generators. *J. Phys. Chem. C* **2015**, *119*, 24201−24228.
(703) Beiler, A. M.; Khusnutdinova, D.; Jacob, S. I.; Moore, G. F. Solar Hydrogen Production Using Molecular Catalysts Immobilized on Gallium Phosphide (111)A and (111)B Polymer-Modified Photocathodes. *ACS Appl. Mater. Interfaces* **2016**, *8*, 10038−10047.
(704) Stewart, M. P.; Maya, F.; Kosynkin, D. V.; Dirk, S. M.; Stapleton, J. J.; McGuiness, C. L.; Allara, D. L.; Tour, J. M. Direct Covalent Grafting of Conjugated Molecules onto Si, GaAs, and Pd Surfaces from Aryldiazonium Salts. *J. Am. Chem. Soc.* **2004**, *126*, 370−378.
(705) Richards, D.; Zemlyanov, D.; Ivanisevic, A. Assessment of the Passivation Capabilities of Two Different Covalent Chemical Modifications on GaP(100). *Langmuir* **2010**, *26*, 8141−8146.
(706) Wang, X.; Ruther, R. E.; Streifer, J. A.; Hamers, R. J. UV-Induced Grafting of Alkenes to Silicon Surfaces: Photoemission versus Excitons. *J. Am. Chem. Soc.* **2010**, *132*, 4048−4049.
(707) Peczonczyk, S. L.; Mukherjee, J.; Carim, A. I.; Maldonado, S. Wet Chemical Functionalization of III−V Semiconductor Surfaces: Alkylation of Gallium Arsenide and Gallium Nitride by a Grignard Reaction Sequence. *Langmuir* **2012**, *28*, 4672−4682.
(708) Moore, G. F.; Sharp, I. D. A Noble-Metal-Free Hydrogen Evolution Catalyst Grafted to Visible Light-Absorbing Semiconductors. *J. Phys. Chem. Lett.* **2013**, *4*, 568−572.
(709) Krawicz, A.; Yang, J.; Anzenberg, E.; Yano, J.; Sharp, I. D.; Moore, G. F. Photofunctional construct that interfaces molecular cobalt-based catalysts for H_2 production to a visible-light-absorbing semiconductor. *J. Am. Chem. Soc.* **2013**, *135*, 11861−11868.
(710) Khusnutdinova, D.; Beiler, A. M.; Wadsworth, B. L.; Jacob, S. I.; Moore, G. F. Metalloporphyrin-modified semiconductors for solar fuel production. *Chem. Sci.* **2017**, *8*, 253−259.
(711) Seger, B.; Pedersen, T.; Laursen, A. B.; Vesborg, P. C. K.; Hansen, O.; Chorkendorff, I. Using TiO_2 as a Conductive Protective Layer for Photocathodic H_2 Evolution. *J. Am. Chem. Soc.* **2013**, *135*, 1057−1064.
(712) Hu, S.; Shaner, M. R.; Beardslee, J. A.; Lichterman, M.; Brunschwig, B. S.; Lewis, N. S. Amorphous TiO_2 coatings stabilize Si, GaAs, and GaP photoanodes for efficient water oxidation. *Science* **2014**, *344*, 1005−1009.
(713) Lee, C.-Y.; Park, H. S.; Fontecilla-Camps, J. C.; Reisner, E. Photoelectrochemical H_2 Evolution with a Hydrogenase Immobilized on a TiO_2-Protected Silicon Electrode. *Angew. Chem., Int. Ed.* **2016**, *55*, 5971−5974.
(714) Nam, D. H.; Zhang, J.; Andrei, V.; Kornienko, N.; Heidary, N.; Wagner, A.; Nakanishi, K.; Sokol, K.; Slater, B.; Zebger, I.; et al. Solar Water Splitting with a Hydrogenase Integrated in Photoelectrochemical Tandem Cells. *Angew. Chem., Int. Ed.* **2018**, *57*, 10595−10599.
(715) Cheng, Y.-J.; Yang, S.-H.; Hsu, C.-S. Synthesis of Conjugated Polymers for Organic Solar Cell Applications. *Chem. Rev.* **2009**, *109*, 5868−5923.
(716) Bourgeteau, T.; Tondelier, D.; Geffroy, B.; Brisse, R.; Cornut, R.; Artero, V.; Jousselme, B. Enhancing the Performances of P3HT:PCBM-MoS_3-Based H_2-Evolving Photocathodes with Interfacial Layers. *ACS Appl. Mater. Interfaces* **2015**, *7*, 16395−16403.
(717) Bourgeteau, T.; Tondelier, D.; Geffroy, B.; Brisse, R.; Laberty-Robert, C.; Campidelli, S.; de Bettignies, R.; Artero, V.; Palacin, S.; Jousselme, B. A H_2-evolving photocathode based on direct sensitization of MoS_3 with an organic photovoltaic cell. *Energy Environ. Sci.* **2013**, *6*, 2706−2713.
(718) Abe, T.; Tobinai, S.; Taira, N.; Chiba, J.; Itoh, T.; Nagai, K. Molecular Hydrogen Evolution by Organic p/n Bilayer Film of Phthalocyanine/Fullerene in the Entire Visible-Light Energy Region. *J. Phys. Chem. C* **2011**, *115*, 7701−7705.
(719) Lattach, Y.; Fortage, J.; Deronzier, A.; Moutet, J.-C. Polypyrrole-Ru(2,2′-bipyridine)$_3^{2+}$/MoS_x Structured Composite Film As a Photocathode for the Hydrogen Evolution Reaction. *ACS Appl. Mater. Interfaces* **2015**, *7*, 4476−4480.
(720) Chen, Y.; Chen, H.; Tian, H. Immobilization of a cobalt catalyst on fullerene in molecular devices for water reduction. *Chem. Commun.* **2015**, *51*, 11508−11511.
(721) Fumagalli, F.; Bellani, S.; Schreier, M.; Leonardi, S.; Rojas, H. C.; Ghadirzadeh, A.; Tullii, G.; Savoini, A.; Marra, G.; Meda, L.; et al. Hybrid organic−inorganic H_2-evolving photocathodes: understanding the route towards high performance organic photoelectrochemical water splitting. *J. Mater. Chem. A* **2016**, *4*, 2178−2187.
(722) Vijaikanth, V.; Capon, J.-F.; Gloaguen, F.; Schollhammer, P.; Talarmin, J. Chemically modified electrode based on an organometallic model of the [FeFe] hydrogenase active center. *Electrochem. Commun.* **2005**, *7*, 427−430.
(723) Thomas, C. M.; Rüdiger, O.; Liu, T.; Carson, C. E.; Hall, M. B.; Darensbourg, M. Y. Synthesis of Carboxylic Acid-Modified [FeFe]-Hydrogenase Model Complexes Amenable to Surface Immobilization. *Organometallics* **2007**, *26*, 3976−3984.
(724) Le Goff, A.; Artero, V.; Metayé, R.; Moggia, F.; Jousselme, B.; Razavet, M.; Tran, P. D.; Palacin, S.; Fontecave, M. Immobilization of FeFe hydrogenase mimics onto carbon and gold electrodes by controlled aryldiazonium salt reduction: an electrochemical, XPS and ATR-IR study. *Int. J. Hydrogen Energy* **2010**, *35*, 10790−10796.
(725) Ahmed, M. E.; Dey, S.; Mondal, B.; Dey, A. H_2 evolution catalyzed by a FeFe-hydrogenase synthetic model covalently attached to graphite surfaces. *Chem. Commun.* **2017**, *53*, 8188−8191.
(726) Le Goff, A.; Artero, V.; Jousselme, B.; Tran, P. D.; Guillet, N.; Métayé, R.; Fihri, A.; Palacin, S.; Fontecave, M. From Hydrogenases to Noble Metal−Free Catalytic Nanomaterials for H_2 Production and Uptake. *Science* **2009**, *326*, 1384−1387.
(727) Das, A. K.; Engelhard, M. H.; Bullock, R. M.; Roberts, J. A. S. A Hydrogen-Evolving Ni(P_2N_2)$_2$ Electrocatalyst Covalently Attached to a Glassy Carbon Electrode: Preparation, Characterization, and Catalysis. Comparisons with the Homogeneous Analogue. *Inorg. Chem.* **2014**, *53*, 6875−6885.
(728) Andreiadis, E. S.; Jacques, P.-A.; Tran, P. D.; Leyris, A.; Chavarot-Kerlidou, M.; Jousselme, B.; Matheron, M.; Pécaut, J.; Palacin, S.; Fontecave, M.; et al. Molecular engineering of a cobalt-based electrocatalytic nanomaterial for H_2 evolution under fully aqueous conditions. *Nat. Chem.* **2013**, *5*, 48−53.
(729) Rodriguez-Maciá, P.; Dutta, A.; Lubitz, W.; Shaw, W. J.; Rüdiger, O. Direct Comparison of the Performance of a Bio-inspired Synthetic Nickel Catalyst and a [NiFe]-Hydrogenase, Both Covalently Attached to Electrodes. *Angew. Chem., Int. Ed.* **2015**, *54*, 12303−12307.
(730) Huan, T. N.; Jane, R. T.; Benayad, A.; Guetaz, L.; Tran, P. D.; Artero, V. Bio-inspired noble metal-free nanomaterials approaching platinum performances for H_2 evolution and uptake. *Energy Environ. Sci.* **2016**, *9*, 940−947.
(731) Rodríguez-Maciá, P.; Priyadarshani, N.; Dutta, A.; Weidenthaler, C.; Lubitz, W.; Shaw, W. J.; Rüdiger, O. Covalent Attachment of the Water-insoluble Ni($P^{Cy}_2N^{Phe}_2$)$_2$ Electrocatalyst to Electrodes Showing Reversible Catalysis in Aqueous Solution. *Electroanalysis* **2016**, *28*, 2452−2458.
(732) Gentil, S.; Lalaoui, N.; Dutta, A.; Nedellec, Y.; Cosnier, S.; Shaw, W. J.; Artero, V.; Le Goff, A. Carbon-Nanotube-Supported Bio-Inspired Nickel Catalyst and Its Integration in Hybrid Hydrogen/Air Fuel Cells. *Angew. Chem., Int. Ed.* **2017**, *56*, 1845−1849.
(733) Das, A. K.; Engelhard, M. H.; Lense, S.; Roberts, J. A. S.; Bullock, R. M. Covalent attachment of diphosphine ligands to glassy

DOI: 10.1021/acs.chemrev.8b00392
Chem. Rev. 2019, 119, 2752−2875

carbon electrodes via Cu-catalyzed alkyne-azide cycloaddition. Metallation with Ni(II). *Dalton Trans.* **2015**, *44*, 12225−12233.
(734) El Ghachtouli, S.; Fournier, M.; Cherdo, S.; Guillot, R.; Charlot, M.-F.; Anxolabéhère-Mallart, E.; Robert, M.; Aukauloo, A. Monometallic Cobalt−Trisglyoximato Complexes as Precatalysts for Catalytic H_2 Evolution in Water. *J. Phys. Chem. C* **2013**, *117*, 17073−17077.
(735) Baxter, L. A. M.; Bobrowski, A.; Bond, A. M.; Heath, G. A.; Paul, R. L.; Mrzljak, R.; Zarebski, J. Electrochemical and Spectroscopic Investigation of the Reduction of Dimethylglyoxime at Mercury Electrodes in the Presence of Cobalt and Nickel. *Anal. Chem.* **1998**, *70*, 1312−1323.
(736) Kaeffer, N.; Morozan, A.; Artero, V. Oxygen Tolerance of a Molecular Engineered Cathode for Hydrogen Evolution Based on a Cobalt Diimine−Dioxime Catalyst. *J. Phys. Chem. B* **2015**, *119*, 13707−13713.
(737) Kellett, R. M.; Spiro, T. G. Cobalt porphyrin electrode films as hydrogen catalysts. *Inorg. Chem.* **1985**, *24*, 2378−2382.
(738) Abe, T.; Taguchi, F.; Imaya, H.; Zhao, F.; Zhang, J.; Kaneko, M. Highly active electrocatalysis by cobalt tetraphenylporphyrin incorporated in a Nafion membrane for proton reduction. *Polym. Adv. Technol.* **1998**, *9*, 559−562.
(739) Zhao, F.; Zhang, J.; Abe, T.; Wöhrle, D.; Kaneko, M. Electrocatalytic proton reduction by phthalocyanine cobalt derivatives incorporated in poly(4-vinylpyridine-co-styrene) film. *J. Mol. Catal. A: Chem.* **1999**, *145*, 245−256.
(740) Rioual, S.; Lescop, B.; Quentel, F.; Gloaguen, F. A molecular material based on electropolymerized cobalt macrocycles for electrocatalytic hydrogen evolution. *Phys. Chem. Chem. Phys.* **2015**, *17*, 13374−13379.
(741) Queyriaux, N.; Andreiadis, E. S.; Torelli, S.; Pecaut, J.; Veldkamp, B. S.; Margulies, E. A.; Wasielewski, M. R.; Chavarot-Kerlidou, M.; Artero, V. CuAAC-based assembly and characterization of a ruthenium-copper dyad containing a diimine-dioxime ligand framework. *Faraday Discuss.* **2017**, *198*, 251−261.
(742) Eady, S. C.; Peczonczyk, S. L.; Maldonado, S.; Lehnert, N. Facile heterogenization of a cobalt catalyst via graphene adsorption: robust and versatile dihydrogen production systems. *Chem. Commun.* **2014**, *50*, 8065−8068.
(743) Eady, S. C.; MacInnes, M. M.; Lehnert, N. Immobilized Cobalt Bis(benzenedithiolate) Complexes: Exceptionally Active Heterogeneous Electrocatalysts for Dihydrogen Production from Mildly Acidic Aqueous Solutions. *Inorg. Chem.* **2017**, *56*, 11654−11667.
(744) Eady, S. C.; MacInnes, M. M.; Lehnert, N. A Smorgasbord of Carbon: Electrochemical Analysis of Cobalt−Bis(benzenedithiolate) Complex Adsorption and Electrocatalytic Activity on Diverse Graphitic Supports. *ACS Appl. Mater. Interfaces* **2016**, *8*, 23624−23634.
(745) Clough, A. J.; Yoo, J. W.; Mecklenburg, M. H.; Marinescu, S. C. Two-Dimensional Metal−Organic Surfaces for Efficient Hydrogen Evolution from Water. *J. Am. Chem. Soc.* **2015**, *137*, 118−121.
(746) Downes, C. A.; Marinescu, S. C. Bioinspired Metal Selenolate Polymers with Tunable Mechanistic Pathways for Efficient H_2 Evolution. *ACS Catal.* **2017**, *7*, 848−854.
(747) Dong, R.; Pfeffermann, M.; Liang, H.; Zheng, Z.; Zhu, X.; Zhang, J.; Feng, X. Large-Area, Free-Standing, Two-Dimensional Supramolecular Polymer Single-Layer Sheets for Highly Efficient Electrocatalytic Hydrogen Evolution. *Angew. Chem., Int. Ed.* **2015**, *54*, 12058−12063.
(748) Downes, C. A.; Marinescu, S. C. One dimensional metal dithiolene (M = Ni, Fe, Zn) coordination polymers for the hydrogen evolution reaction. *Dalton Trans.* **2016**, *45*, 19311−19321.
(749) Downes, C. A.; Marinescu, S. C. Efficient Electrochemical and Photoelectrochemical H_2 Production from Water by a Cobalt Dithiolene One-Dimensional Metal-Organic Surface. *J. Am. Chem. Soc.* **2015**, *137*, 13740−13743.
(750) Fang, M.; Engelhard, M. H.; Zhu, Z.; Helm, M. L.; Roberts, J. A. S. Electrodeposition from Acidic Solutions of Nickel Bis(benzenedithiolate) Produces a Hydrogen-Evolving Ni−S Film on Glassy Carbon. *ACS Catal.* **2014**, *4*, 90−98.
(751) Wombwell, C.; Reisner, E. Synthesis, structure and reactivity of Ni site models of [NiFeSe] hydrogenases. *Dalton Trans.* **2014**, *43*, 4483−4493.
(752) Wombwell, C.; Reisner, E. Synthetic Active Site Model of the [NiFeSe] Hydrogenase. *Chem. - Eur. J.* **2015**, *21*, 8096−8104.
(753) Downes, C. A.; Marinescu, S. C. Understanding Variability in the Hydrogen Evolution Activity of a Cobalt Anthracenetetrathiolate Coordination Polymer. *ACS Catal.* **2017**, *7*, 8605−8612.
(754) Muresan, N. M.; Willkomm, J.; Mersch, D.; Vaynzof, Y.; Reisner, E. Immobilization of a Molecular Cobaloxime Catalyst for Hydrogen Evolution on a Mesoporous Metal Oxide Electrode. *Angew. Chem., Int. Ed.* **2012**, *51*, 12749−12753.
(755) Scherer, M. R. J.; Muresan, N. M.; Steiner, U.; Reisner, E. RYB tri-colour electrochromism based on a molecular cobaloxime. *Chem. Commun.* **2013**, *49*, 10453−10455.
(756) Wadsworth, B. L.; Beiler, A. M.; Khusnutdinova, D.; Jacob, S. I.; Moore, G. F. Electrocatalytic and Optical Properties of Cobaloxime Catalysts Immobilized at a Surface-Grafted Polymer Interface. *ACS Catal.* **2016**, *6*, 8048−8057.
(757) Rosser, T. E.; Gross, M. A.; Lai, Y.-H.; Reisner, E. Precious-metal free photoelectrochemical water splitting with immobilised molecular Ni and Fe redox catalysts. *Chem. Sci.* **2016**, *7*, 4024−4035.
(758) Vincent, K. A.; Parkin, A.; Armstrong, F. A. Investigating and Exploiting the Electrocatalytic Properties of Hydrogenases. *Chem. Rev.* **2007**, *107*, 4366−4413.
(759) del Barrio, M.; Sensi, M.; Orain, C.; Baffert, C.; Dementin, S.; Fourmond, V.; Léger, C. Electrochemical Investigations of Hydrogenases and Other Enzymes That Produce and Use Solar Fuels. *Acc. Chem. Res.* **2018**, *51*, 769−777.
(760) Armstrong, F. A.; Belsey, N. A.; Cracknell, J. A.; Goldet, G.; Parkin, A.; Reisner, E.; Vincent, K. A.; Wait, A. F. Dynamic electrochemical investigations of hydrogen oxidation and production by enzymes and implications for future technology. *Chem. Soc. Rev.* **2009**, *38*, 36−51.
(761) Armstrong, F. A.; Evans, R. M.; Hexter, S. V.; Murphy, B. J.; Roessler, M. M.; Wulff, P. Guiding Principles of Hydrogenase Catalysis Instigated and Clarified by Protein Film Electrochemistry. *Acc. Chem. Res.* **2016**, *49*, 884−892.
(762) Bianco, P.; Haladjian, J. Electrocatalytic Hydrogen-Evolution at the Pyrolytic Graphite Electrode in the Presence of Hydrogenase. *J. Electrochem. Soc.* **1992**, *139*, 2428−2432.
(763) Varfolomeyev, S. D.; Yaropolov, A. I.; Karyakin, A. A. Bioelectrocatalysis: the electrochemical kinetics of hydrogenase action. *J. Biotechnol.* **1993**, *27*, 331−339.
(764) Butt, J. N.; Filipiak, M.; Hagen, W. R. Direct Electrochemistry of *Megasphaera Elsdenii* Iron Hydrogenase. *Eur. J. Biochem.* **1997**, *245*, 116−122.
(765) Pershad, H. R.; Duff, J. L. C.; Heering, H. A.; Duin, E. C.; Albracht, S. P. J.; Armstrong, F. A. Catalytic Electron Transport in *Chromatium vinosum* [NiFe]-Hydrogenase: Application of Voltammetry in Detecting Redox-Active Centers and Establishing That Hydrogen Oxidation Is Very Fast Even at Potentials Close to the Reversible H^+/H_2 Value. *Biochemistry* **1999**, *38*, 8992−8999.
(766) Morozov, S. V.; Vignais, P. M.; Cournac, L.; Zorin, N. A.; Karyakina, E. E.; Karyakin, A. A.; Cosnier, S. Bioelectrocatalytic hydrogen production by hydrogenase electrodes. *Int. J. Hydrogen Energy* **2002**, *27*, 1501−1505.
(767) Morozov, S. V.; Voronin, O. G.; Karyakina, E. E.; Zorin, N. A.; Cosnier, S.; Karyakin, A. A. Tolerance to oxygen of hydrogen enzyme electrodes. *Electrochem. Commun.* **2006**, *8*, 851−854.
(768) Ciaccafava, A.; Infossi, P.; Ilbert, M.; Guiral, M.; Lecomte, S.; Giudici-Orticoni, M. T.; Lojou, E. Electrochemistry, AFM, and PM-IRRA Spectroscopy of Immobilized Hydrogenase: Role of a Hydrophobic Helix in Enzyme Orientation for Efficient H_2 Oxidation. *Angew. Chem., Int. Ed.* **2012**, *51*, 953−956.
(769) Ciaccafava, A.; De Poulpiquet, A.; Techer, V.; Giudici-Orticoni, M. T.; Tingry, S.; Innocent, C.; Lojou, E. An innovative powerful and mediatorless H_2/O_2 biofuel cell based on an outstanding bioanode. *Electrochem. Commun.* **2012**, *23*, 25−28.

DOI: 10.1021/acs.chemrev.8b00392
Chem. Rev. 2019, 119, 2752−2875

(770) Rüdiger, O.; Abad, J. M.; Hatchikian, E. C.; Fernandez, V. M.; De Lacey, A. L. Oriented Immobilization of *Desulfovibrio gigas* Hydrogenase onto Carbon Electrodes by Covalent Bonds for Nonmediated Oxidation of H_2. *J. Am. Chem. Soc.* **2005**, *127*, 16008−16009.
(771) Baffert, C.; Sybirna, K.; Ezanno, P.; Lautier, T.; Hajj, V.; Meynial-Salles, I.; Soucaille, P.; Bottin, H.; Léger, C. Covalent Attachment of FeFe Hydrogenases to Carbon Electrodes for Direct Electron Transfer. *Anal. Chem.* **2012**, *84*, 7999−8005.
(772) Gentil, S.; Che Mansor, S. M.; Jamet, H.; Cosnier, S.; Cavazza, C.; Le Goff, A. Oriented Immobilization of [NiFeSe] Hydrogenases on Covalently and Noncovalently Functionalized Carbon Nanotubes for H_2/Air Enzymatic Fuel Cells. *ACS Catal.* **2018**, *8*, 3957−3964.
(773) Alonso-Lomillo, M. A.; Rüdiger, O.; Maroto-Valiente, A.; Velez, M.; Rodríguez-Ramos, I.; Muñoz, F. J.; Fernández, V. M.; De Lacey, A. L. Hydrogenase-Coated Carbon Nanotubes for Efficient H_2 Oxidation. *Nano Lett.* **2007**, *7*, 1603−1608.
(774) Lalaoui, N.; de Poulpiquet, A.; Haddad, R.; Le Goff, A.; Holzinger, M.; Gounel, S.; Mermoux, M.; Infossi, P.; Mano, N.; Lojou, E.; et al. A membraneless air-breathing hydrogen biofuel cell based on direct wiring of thermostable enzymes on carbon nanotube electrodes. *Chem. Commun.* **2015**, *51*, 7447−7450.
(775) Hambourger, M.; Gervaldo, M.; Svedruzic, D.; King, P. W.; Gust, D.; Ghirardi, M.; Moore, A. L.; Moore, T. A. [FeFe]-Hydrogenase-Catalyzed H_2 Production in a Photoelectrochemical Biofuel Cell. *J. Am. Chem. Soc.* **2008**, *130*, 2015−2022.
(776) Svedružić, D.; Blackburn, J. L.; Tenent, R. C.; Rocha, J.-D. R.; Vinzant, T. B.; Heben, M. J.; King, P. W. High-Performance Hydrogen Production and Oxidation Electrodes with Hydrogenase Supported on Metallic Single-Wall CarbonNanotube Networks. *J. Am. Chem. Soc.* **2011**, *133*, 4299−4306.
(777) Renault, C.; Andrieux, C. P.; Tucker, R. T.; Brett, M. J.; Balland, V.; Limoges, B. Unraveling the Mechanism of Catalytic Reduction of O_2 by Microperoxidase-11 Adsorbed within a Transparent 3D-Nanoporous ITO Film. *J. Am. Chem. Soc.* **2012**, *134*, 6834−6845.
(778) Reuillard, B.; Ly, K. H.; Hildebrandt, P.; Jeuken, L. J. C.; Butt, J. N.; Reisner, E. High Performance Reduction of H_2O_2 with an Electron Transport Decaheme Cytochrome on a Porous ITO Electrode. *J. Am. Chem. Soc.* **2017**, *139*, 3324−3327.
(779) Bae, S.; Shim, E.; Yoon, J.; Joo, H. Photoanodic and cathodic role of anodized tubular titania in light-sensitized enzymatic hydrogen production. *J. Power Sources* **2008**, *185*, 439−444.
(780) Yoon, J.; Bae, S.; Shim, E.; Joo, H. *Pyrococcus furiosus*-immobilized anodized tubular titania cathode in a hydrogen production system. *J. Power Sources* **2009**, *189*, 1296−1301.
(781) Reisner, E.; Fontecilla-Camps, J. C.; Armstrong, F. A. Catalytic electrochemistry of a [NiFeSe]-hydrogenase on TiO_2 and demonstration of its suitability for visible-light driven H_2 production. *Chem. Commun.* **2009**, 550−552.
(782) Mersch, D.; Lee, C.-Y.; Zhang, J. Z.; Brinkert, K.; Fontecilla-Camps, J. C.; Rutherford, A. W.; Reisner, E. Wiring of Photosystem II to Hydrogenase for Photoelectrochemical Water Splitting. *J. Am. Chem. Soc.* **2015**, *137*, 8541−8549.
(783) Meshitsuka, S.; Ichikawa, M.; Tamaru, K. Electrocatalysis by metal phthalocyanines in the reduction of carbon dioxide. *J. Chem. Soc., Chem. Commun.* **1974**, 158−159.
(784) Lieber, C. M.; Lewis, N. S. Catalytic reduction of carbon dioxide at carbon electrodes modified with cobalt phthalocyanine. *J. Am. Chem. Soc.* **1984**, *106*, 5033−5034.
(785) Kapusta, S.; Hackerman, N. Carbon Dioxide Reduction at a Metal Phthalocyanine Catalyzed Carbon Electrode. *J. Electrochem. Soc.* **1984**, *131*, 1511−1514.
(786) Aga, H.; Aramata, A.; Hisaeda, Y. The electroreduction of carbon dioxide by macrocyclic cobalt complexes chemically modified on a glassy carbon electrode. *J. Electroanal. Chem.* **1997**, *437*, 111−118.
(787) Isaacs, M.; Armijo, F.; Ramírez, G.; Trollund, E.; Biaggio, S. R.; Costamagna, J.; Aguirre, M. J. Electrochemical reduction of CO_2 mediated by poly-M-aminophthalocyanines (M = Co, Ni, Fe): poly-Co-tetraaminophthalocyanine, a selective catalyst. *J. Mol. Catal. A: Chem.* **2005**, *229*, 249−257.
(788) Furuya, N.; Matsui, K. Electroreduction of carbon dioxide on gas-diffusion electrodes modified by metal phthalocyanines. *J. Electroanal. Chem. Interfacial Electrochem.* **1989**, *271*, 181−191.
(789) Mahmood, M. N.; Masheder, D.; Harty, C. J. Use of gas-diffusion electrodes for high-rate electrochemical reduction of carbon dioxide. II. Reduction at metal phthalocyanine-impregnated electrodes. *J. Appl. Electrochem.* **1987**, *17*, 1223−1227.
(790) Shen, J.; Kortlever, R.; Kas, R.; Birdja, Y. Y.; Diaz-Morales, O.; Kwon, Y.; Ledezma-Yanez, I.; Schouten, K. J. P.; Mul, G.; Koper, M. T. M. Electrocatalytic reduction of carbon dioxide to carbon monoxide and methane at an immobilized cobalt protoporphyrin. *Nat. Commun.* **2015**, *6*, 8177.
(791) Atoguchi, T.; Aramata, A.; Kazusaka, A.; Enyo, M. Electrocatalytic activity of Co^{II} TPP-pyridine complex modified carbon electrode for CO_2 reduction. *J. Electroanal. Chem. Interfacial Electrochem.* **1991**, *318*, 309−320.
(792) Yoshida, T.; Kamato, K.; Tsukamoto, M.; Iida, T.; Schlettwein, D.; Wöhrle, D.; Kaneko, M. Selective electroacatalysis for CO_2 reduction in the aqueous phase using cobalt phthalocyanine/poly-4-vinylpyridine modified electrodes. *J. Electroanal. Chem.* **1995**, *385*, 209−225.
(793) Yoshida, T.; Iida, T.; Shirasagi, T.; Lin, R.-J.; Kaneko, M. Electrocatalytic reduction of carbon dioxide in aqueous medium by bis(2,2′: 6′,2″-terpyridine)cobalt(II) complex incorporated into a coated polymer membrane. *J. Electroanal. Chem.* **1993**, *344*, 355−362.
(794) Hurrell, H. C.; Mogstad, A. L.; Usifer, D. A.; Potts, K. T.; Abruña, H. D. Electrocatalytic activity of electropolymerized films of bis(vinylterpyridine)cobalt(2+) for the reduction of carbon dioxide and oxygen. *Inorg. Chem.* **1989**, *28*, 1080−1084.
(795) Arana, C.; Keshavarz, M.; Potts, K. T.; Abruña, H. D. Electrocatalytic reduction of CO_2 and O_2 with electropolymerized films of vinyl-terpyridine complexes of Fe, Ni and Co. *Inorg. Chim. Acta* **1994**, *225*, 285−295.
(796) Ramos Sende, J. A.; Arana, C. R.; Hernandez, L.; Potts, K. T.; Keshevarz-K, M.; Abruña, H. D. Electrocatalysis of CO_2 Reduction in Aqueous Media at Electrodes Modified with Electropolymerized Films of Vinylterpyridine Complexes of Transition Metals. *Inorg. Chem.* **1995**, *34*, 3339−3348.
(797) Aoi, S.; Mase, K.; Ohkubo, K.; Fukuzumi, S. Selective electrochemical reduction of CO_2 to CO with a cobalt chlorin complex adsorbed on multi-walled carbon nanotubes in water. *Chem. Commun.* **2015**, *51*, 10226−10228.
(798) Aoi, S.; Mase, K.; Ohkubo, K.; Suenobu, T.; Fukuzumi, S. Selective CO Production in Photoelectrochemical Reduction of CO_2 with a Cobalt Chlorin Complex Adsorbed on Multiwalled Carbon Nanotubes in Water. *ACS Energy Lett.* **2017**, *2*, 532−536.
(799) Wang, M.; Chen, L.; Lau, T. C.; Robert, M. A Hybrid Co Quaterpyridine Complex/Carbon Nanotube Catalytic Material for CO_2 Reduction in Water. *Angew. Chem., Int. Ed.* **2018**, *57*, 7769−7773.
(800) Walsh, J. J.; Smith, C. L.; Neri, G.; Whitehead, G. F. S.; Robertson, C. M.; Cowan, A. J. Improving the efficiency of electrochemical CO_2 reduction using immobilized manganese complexes. *Faraday Discuss.* **2015**, *183*, 147−160.
(801) Macor, K. A.; Spiro, T. G. Oxidative electrochemistry of electropolymerized metalloprotoporphyrin films. *J. Electroanal. Chem. Interf. Electrochem.* **1984**, *163*, 223−236.
(802) Hu, X.-M.; Salmi, Z.; Lillethorup, M.; Pedersen, E. B.; Robert, M.; Pedersen, S. U.; Skrydstrup, T.; Daasbjerg, K. Controlled electropolymerisation of a carbazole-functionalised iron porphyrin electrocatalyst for CO_2 reduction. *Chem. Commun.* **2016**, *52*, 5864−5867.
(803) Kornienko, N.; Zhao, Y.; Kley, C. S.; Zhu, C.; Kim, D.; Lin, S.; Chang, C. J.; Yaghi, O. M.; Yang, P. Metal−Organic Frameworks for Electrocatalytic Reduction of Carbon Dioxide. *J. Am. Chem. Soc.* **2015**, *137*, 14129−14135.
(804) Lin, S.; Diercks, C. S.; Zhang, Y.-B.; Kornienko, N.; Nichols, E. M.; Zhao, Y.; Paris, A. R.; Kim, D.; Yang, P.; Yaghi, O. M.; et al.

DOI: 10.1021/acs.chemrev.8b00392
Chem. Rev. 2019, 119, 2752−2875

Covalent organic frameworks comprising cobalt porphyrins for catalytic CO_2 reduction in water. *Science* **2015**, *349*, 1208−1213.
(805) Diercks, C. S.; Lin, S.; Kornienko, N.; Kapustin, E. A.; Nichols, E. M.; Zhu, C.; Zhao, Y.; Chang, C. J.; Yaghi, O. M. Reticular Electronic Tuning of Porphyrin Active Sites in Covalent Organic Frameworks for Electrocatalytic Carbon Dioxide Reduction. *J. Am. Chem. Soc.* **2018**, *140*, 1116−1122.
(806) Smith, P. T.; Benke, B. P.; Cao, Z.; Kim, Y.; Nichols, E. M.; Kim, K.; Chang, C. J. Iron Porphyrins Embedded into a Supramolecular Porous Organic Cage for Electrochemical CO_2 Reduction in Water. *Angew. Chem., Int. Ed.* **2018**, *57*, 9684−9688.
(807) Zhang, X.; Wu, Z.; Zhang, X.; Li, L.; Li, Y.; Xu, H.; Li, X.; Yu, X.; Zhang, Z.; Liang, Y.; et al. Highly selective and active CO_2 reduction electrocatalysts based on cobalt phthalocyanine/carbon nanotube hybrid structures. *Nat. Commun.* **2017**, *8*, 14675.
(808) Han, N.; Wang, Y.; Ma, L.; Wen, J.; Li, J.; Zheng, H.; Nie, K.; Wang, X.; Zhao, F.; Li, Y.; et al. Supported Cobalt Polyphthalocyanine for High-Performance Electrocatalytic CO_2 Reduction. *Chem* **2017**, *3*, 652−664.
(809) Zhu, M.; Ye, R.; Jin, K.; Lazouski, N.; Manthiram, K. Elucidating the Reactivity and Mechanism of CO_2 Electroreduction at Highly Dispersed Cobalt Phthalocyanine. *ACS Energy Lett.* **2018**, *3*, 1381−1386.
(810) Morlanés, N.; Takanabe, K.; Rodionov, V. Simultaneous Reduction of CO_2 and Splitting of H_2O by a Single Immobilized Cobalt Phthalocyanine Electrocatalyst. *ACS Catal.* **2016**, *6*, 3092−3095.
(811) Hu, X.-M.; Rønne, M. H.; Pedersen, S. U.; Skrydstrup, T.; Daasbjerg, K. Enhanced Catalytic Activity of Cobalt Porphyrin in CO_2 Electroreduction upon Immobilization on Carbon Materials. *Angew. Chem., Int. Ed.* **2017**, *56*, 6468−6472.
(812) Maurin, A.; Robert, M. Noncovalent Immobilization of a Molecular Iron-Based Electrocatalyst on Carbon Electrodes for Selective, Efficient CO_2-to-CO Conversion in Water. *J. Am. Chem. Soc.* **2016**, *138*, 2492−2495.
(813) Sato, S.; Saita, K.; Sekizawa, K.; Maeda, S.; Morikawa, T. Low-Energy Electrocatalytic CO_2 Reduction in Water over Mn-Complex Catalyst Electrode Aided by a Nanocarbon Support and K^+ Cations. *ACS Catal.* **2018**, *8*, 4452−4458.
(814) Yao, S. A.; Ruther, R. E.; Zhang, L.; Franking, R. A.; Hamers, R. J.; Berry, J. F. Covalent Attachment of Catalyst Molecules to Conductive Diamond: CO_2 Reduction Using "Smart" Electrodes. *J. Am. Chem. Soc.* **2012**, *134*, 15632−15635.
(815) Maurin, A.; Robert, M. Catalytic CO_2-to-CO conversion in water by covalently functionalized carbon nanotubes with a molecular iron catalyst. *Chem. Commun.* **2016**, *52*, 12084−12087.
(816) Hod, I.; Sampson, M. D.; Deria, P.; Kubiak, C. P.; Farha, O. K.; Hupp, J. T. Fe-Porphyrin-Based Metal−Organic Framework Films as High-Surface Concentration, Heterogeneous Catalysts for Electrochemical Reduction of CO_2. *ACS Catal.* **2015**, *5*, 6302−6309.
(817) Mohamed, E. A.; Zahran, Z. N.; Naruta, Y. Efficient Heterogeneous CO_2 to CO Conversion with a Phosphonic Acid Fabricated Cofacial Iron Porphyrin Dimer. *Chem. Mater.* **2017**, *29*, 7140−7150.
(818) Rosser, T. E.; Windle, C. D.; Reisner, E. Electrocatalytic and Solar-Driven CO_2 Reduction to CO with a Molecular Manganese Catalyst Immobilized on Mesoporous TiO_2. *Angew. Chem., Int. Ed.* **2016**, *55*, 7388−7392.
(819) Walsh, J. J.; Forster, M.; Smith, C. L.; Neri, G.; Potter, R. J.; Cowan, A. J. Directing the mechanism of CO_2 reduction by a Mn catalyst through surface immobilization. *Phys. Chem. Chem. Phys.* **2018**, *20*, 6811−6816.
(820) Neri, G.; Walsh, J. J.; Wilson, C.; Reynal, A.; Lim, J. Y. C.; Li, X.; White, A. J. P.; Long, N. J.; Durrant, J. R.; Cowan, A. J. A functionalised nickel cyclam catalyst for CO_2 reduction: electrocatalysis, semiconductor surface immobilisation and light-driven electron transfer. *Phys. Chem. Chem. Phys.* **2015**, *17*, 1562−1566.
(821) Wang, V. C. C.; Can, M.; Pierce, E.; Ragsdale, S. W.; Armstrong, F. A. A Unified Electrocatalytic Description of the Action of Inhibitors of Nickel Carbon Monoxide Dehydrogenase. *J. Am. Chem. Soc.* **2013**, *135*, 2198−2206.
(822) Parkin, A.; Seravalli, J.; Vincent, K. A.; Ragsdale, S. W.; Armstrong, F. A. Rapid and Efficient Electrocatalytic CO_2/CO Interconversions by *Carboxydothermus hydrogenoformans* CO Dehydrogenase I on an Electrode. *J. Am. Chem. Soc.* **2007**, *129*, 10328−10329.
(823) Sakai, K.; Hsieh, B.-C.; Maruyama, A.; Kitazumi, Y.; Shirai, O.; Kano, K. Interconversion between formate and hydrogen carbonate by tungsten-containing formate dehydrogenase-catalyzed mediated bioelectrocatalysis. *Sens. Biosensing Res.* **2015**, *5*, 90−96.
(824) Robinson, W. E.; Bassegoda, A.; Reisner, E.; Hirst, J. Oxidation-State-Dependent Binding Properties of the Active Site in a Mo-Containing Formate Dehydrogenase. *J. Am. Chem. Soc.* **2017**, *139*, 9927−9936.
(825) Yadav, R. K.; Baeg, J.-O.; Oh, G. H.; Park, N.-J.; Kong, K.-j.; Kim, J.; Hwang, D. W.; Biswas, S. K. A Photocatalyst−Enzyme Coupled Artificial Photosynthesis System for Solar Energy in Production of Formic Acid from CO_2. *J. Am. Chem. Soc.* **2012**, *134*, 11455−11461.
(826) Yadav, R. K.; Oh, G. H.; Park, N.-J.; Kumar, A.; Kong, K.-j.; Baeg, J.-O. Highly Selective Solar-Driven Methanol from CO_2 by a Photocatalyst/Biocatalyst Integrated System. *J. Am. Chem. Soc.* **2014**, *136*, 16728−16731.
(827) Kuk, S. K.; Singh, R. K.; Nam, D. H.; Singh, R.; Lee, J. K.; Park, C. B. Photoelectrochemical Reduction of Carbon Dioxide to Methanol through a Highly Efficient Enzyme Cascade. *Angew. Chem., Int. Ed.* **2017**, *56*, 3827−3832.
(828) Domnik, L.; Merrouch, M.; Goetzl, S.; Jeoung, J.-H.; Léger, C.; Dementin, S.; Fourmond, V.; Dobbek, H. CODH-IV: A High-Efficiency CO-Scavenging CO Dehydrogenase with Resistance to O_2. *Angew. Chem., Int. Ed.* **2017**, *56*, 15466−15469.
(829) Fabian, D. M.; Hu, S.; Singh, N.; Houle, F. A.; Hisatomi, T.; Domen, K.; Osterloh, F. E.; Ardo, S. Particle suspension reactors and materials for solar-driven water splitting. *Energy Environ. Sci.* **2015**, *8*, 2825−2850.
(830) Zhang, X.; Peng, T.; Song, S. Recent advances in dye-sensitized semiconductor systems for photocatalytic hydrogen production. *J. Mater. Chem. A* **2016**, *4*, 2365−2402.
(831) Cao, S.; Yu, J. g-C_3N_4-Based Photocatalysts for Hydrogen Generation. *J. Phys. Chem. Lett.* **2014**, *5*, 2101−2107.
(832) Li, X.; Ward, A. J.; Masters, A. F.; Maschmeyer, T. Solar Hydrogen from an Aqueous, Noble-Metal-Free Hybrid System in a Continuous-Flow Sampling Reaction System. *Chem. - Eur. J.* **2014**, *20*, 7345−7350.
(833) Wang, X.; Maeda, K.; Thomas, A.; Takanabe, K.; Xin, G.; Carlsson, J. M.; Domen, K.; Antonietti, M. A metal-free polymeric photocatalyst for hydrogen production from water under visible light. *Nat. Mater.* **2009**, *8*, 76−80.
(834) Ong, W.-J.; Tan, L.-L.; Ng, Y. H.; Yong, S.-T.; Chai, S.-P. Graphitic Carbon Nitride ($g\text{-}C_3N_4$)-Based Photocatalysts for Artificial Photosynthesis and Environmental Remediation: Are We a Step Closer To Achieving Sustainability? *Chem. Rev.* **2016**, *116*, 7159−7329.
(835) Lotsch, B. V.; Döblinger, M.; Sehnert, J.; Seyfarth, L.; Senker, J.; Oeckler, O.; Schnick, W. Unmasking Melon by a Complementary Approach Employing Electron Diffraction, Solid-State NMR Spectroscopy, and Theoretical Calculations−Structural Characterization of a Carbon Nitride Polymer. *Chem. - Eur. J.* **2007**, *13*, 4969−4980.
(836) Maeda, K.; Wang, X.; Nishihara, Y.; Lu, D.; Antonietti, M.; Domen, K. Photocatalytic Activities of Graphitic Carbon Nitride Powder for Water Reduction and Oxidation under Visible Light. *J. Phys. Chem. C* **2009**, *113*, 4940−4947.
(837) Hong, J.; Wang, Y.; Wang, Y.; Zhang, W.; Xu, R. Noble-Metal-Free NiS/C_3N_4 for Efficient Photocatalytic Hydrogen Evolution from Water. *ChemSusChem* **2013**, *6*, 2263−2268.
(838) Hou, Y.; Laursen, A. B.; Zhang, J.; Zhang, G.; Zhu, Y.; Wang, X.; Dahl, S.; Chorkendorff, I. Layered Nanojunctions for Hydrogen-Evolution Catalysis. *Angew. Chem., Int. Ed.* **2013**, *52*, 3621−3625.
(839) Dong, J.; Wang, M.; Li, X.; Chen, L.; He, Y.; Sun, L. Simple Nickel-Based Catalyst Systems Combined With Graphitic Carbon

DOI: 10.1021/acs.chemrev.8b00392
Chem. Rev. 2019, 119, 2752−2875

Nitride for Stable Photocatalytic Hydrogen Production in Water. *ChemSusChem* **2012**, *5*, 2133−2138.
(840) Wang, D.; Zhang, Y.; Chen, W. A novel nickel-thiourea-triethylamine complex adsorbed on graphitic C_3N_4 for low-cost solar hydrogen production. *Chem. Commun.* **2014**, *50*, 1754−1756.
(841) Cao, S.-W.; Liu, X.-F.; Yuan, Y.-P.; Zhang, Z.-Y.; Fang, J.; Loo, S. C. J.; Barber, J.; Sum, T. C.; Xue, C. Artificial photosynthetic hydrogen evolution over g-C_3N_4 nanosheets coupled with cobaloxime. *Phys. Chem. Chem. Phys.* **2013**, *15*, 18363−18366.
(842) Caputo, C. A.; Gross, M. A.; Lau, V. W.; Cavazza, C.; Lotsch, B. V.; Reisner, E. Photocatalytic Hydrogen Production using Polymeric Carbon Nitride with a Hydrogenase and a Bioinspired Synthetic Ni Catalyst. *Angew. Chem., Int. Ed.* **2014**, *53*, 11538−11542.
(843) Kasap, H.; Caputo, C. A.; Martindale, B. C. M.; Godin, R.; Lau, V. W.-h.; Lotsch, B. V.; Durrant, J. R.; Reisner, E. Solar-Driven Reduction of Aqueous Protons Coupled to Selective Alcohol Oxidation with a Carbon Nitride−Molecular Ni Catalyst System. *J. Am. Chem. Soc.* **2016**, *138*, 9183−9192.
(844) Kasap, H.; Godin, R.; Jeay Bizot, C.; Achilleos, D. S.; Fang, X.; Durrant, J. R.; Reisner, E. Interfacial Engineering of a Carbon Nitride−Graphene Oxide−Molecular Ni Catalyst Hybrid for Enhanced Photocatalytic Activity. *ACS Catal.* **2018**, *8*, 6914−6926.
(845) Camara, J. M.; Rauchfuss, T. B. Combining acid−base, redox and substrate binding functionalities to give a complete model for the [FeFe]-hydrogenase. *Nat. Chem.* **2012**, *4*, 26−30.
(846) Cao, L.; Sahu, S.; Anilkumar, P.; Bunker, C. E.; Xu, J.; Fernando, K. A. S.; Wang, P.; Guliants, E. A.; Tackett, K. N.; Sun, Y.-P. Carbon Nanoparticles as Visible-Light Photocatalysts for Efficient CO_2 Conversion and Beyond. *J. Am. Chem. Soc.* **2011**, *133*, 4754−4757.
(847) Martindale, B. C. M.; Joliat, E.; Bachmann, C.; Alberto, R.; Reisner, E. Clean Donor Oxidation Enhances the H_2 Evolution Activity of a Carbon Quantum Dot−Molecular Catalyst Photosystem. *Angew. Chem., Int. Ed.* **2016**, *55*, 9402−9406.
(848) Martindale, B. C. M.; Hutton, G. A. M.; Caputo, C. A.; Reisner, E. Solar Hydrogen Production Using Carbon Quantum Dots and a Molecular Nickel Catalyst. *J. Am. Chem. Soc.* **2015**, *137*, 6018−6025.
(849) Liu, C.; Qiu, F.; Peterson, J. J.; Krauss, T. D. Aqueous Photogeneration of H_2 with CdSe Nanocrystals and Nickel Catalysts: Electron Transfer Dynamics. *J. Phys. Chem. B* **2015**, *119*, 7349−7357.
(850) Huang, Y.; Xu, Y.; Zhang, J.; Yin, X.; Guo, Y.; Zhang, B. Hierarchical ultrathin-branched CdS nanowire arrays with enhanced photocatalytic performance. *J. Mater. Chem. A* **2015**, *3*, 19507−19516.
(851) Wen, F.; Wang, X.; Huang, L.; Ma, G.; Yang, J.; Li, C. A Hybrid Photocatalytic System Comprising ZnS as Light Harvester and an $[Fe_2S_2]$ Hydrogenase Mimic as Hydrogen Evolution Catalyst. *ChemSusChem* **2012**, *5*, 849−853.
(852) Xu, Y.; Yin, X.; Huang, Y.; Du, P.; Zhang, B. Hydrogen Production on a Hybrid Photocatalytic System Composed of Ultrathin CdS Nanosheets and a Molecular Nickel Complex. *Chem. - Eur. J.* **2015**, *21*, 4571−4575.
(853) Zhou, Y.; Yang, S.; Huang, J. Light-driven hydrogen production from aqueous solutions based on a new Dubois-type nickel catalyst. *Phys. Chem. Chem. Phys.* **2017**, *19*, 7471−7475.
(854) Ye, Y.; Xu, Y.; Huang, L.; Fan, D.; Feng, Z.; Wang, X.; Li, C. Roles of adsorption sites in electron transfer from CdS quantum dots to molecular catalyst cobaloxime studied by time-resolved spectroscopy. *Phys. Chem. Chem. Phys.* **2016**, *18*, 17389−17397.
(855) Xu, Y.; Chen, R.; Li, Z.; Li, A.; Han, H.; Li, C. Influence of the Electrostatic Interaction between a Molecular Catalyst and Semiconductor on Photocatalytic Hydrogen Evolution Activity in Cobaloxime/CdS Hybrid Systems. *ACS Appl. Mater. Interfaces* **2017**, *9*, 23230−23237.
(856) Xu, Y.; Ye, Y.; Liu, T.; Wang, X.; Zhang, B.; Wang, M.; Han, H.; Li, C. Unraveling a Single-Step Simultaneous Two-Electron Transfer Process from Semiconductor to Molecular Catalyst in a CoPy/CdS Hybrid System for Photocatalytic H_2 Evolution under Strong Alkaline Conditions. *J. Am. Chem. Soc.* **2016**, *138*, 10726−10729.
(857) Rajh, T.; Micic, O. I.; Nozik, A. J. Synthesis and characterization of surface-modified colloidal cadmium telluride quantum dots. *J. Phys. Chem.* **1993**, *97*, 11999−12003.
(858) Wilker, M. B.; Utterback, J. K.; Greene, S.; Brown, K. A.; Mulder, D. W.; King, P. W.; Dukovic, G. Role of Surface-Capping Ligands in Photoexcited Electron Transfer between CdS Nanorods and [FeFe] Hydrogenase and the Subsequent H_2 Generation. *J. Phys. Chem. C* **2018**, *122*, 741−750.
(859) Li, C.-B.; Li, Z.-J.; Yu, S.; Wang, G.-X.; Wang, F.; Meng, Q.-Y.; Chen, B.; Feng, K.; Tung, C.-H.; Wu, L.-Z. Interface-directed assembly of a simple precursor of [FeFe]-H_2ase mimics on CdSe QDs for photosynthetic hydrogen evolution in water. *Energy Environ. Sci.* **2013**, *6*, 2597−2602.
(860) Song, X.-W.; Wen, H.-M.; Ma, C.-B.; Hu, M.-Q.; Chen, H.; Cui, H.-H.; Chen, C.-N. Photocatalytic hydrogen evolution by two comparable [FeFe]-hydrogenase mimics assembled to the surface of ZnS. *Appl. Organomet. Chem.* **2014**, *28*, 267−273.
(861) Wen, M.; Li, X.-B.; Jian, J.-X.; Wang, X.-Z.; Wu, H.-L.; Chen, B.; Tung, C.-H.; Wu, L.-Z. Secondary coordination sphere accelerates hole transfer for enhanced hydrogen photogeneration from [FeFe]-hydrogenase mimic and CdSe QDs in water. *Sci. Rep.* **2016**, *6*, 29851.
(862) Wang, C. J.; Cao, S.; Qin, B.; Zhang, C.; Li, T. T.; Fu, W. F. Photoreduction of Iron(III) to Iron(0) Nanoparticles for Simultaneous Hydrogen Evolution in Aqueous Solution. *ChemSusChem* **2014**, *7*, 1924−1933.
(863) Yamada, Y.; Miyahigashi, T.; Kotani, H.; Ohkubo, K.; Fukuzumi, S. Photocatalytic hydrogen evolution with Ni nanoparticles by using 2-phenyl-4-(1-naphthyl)quinolinium ion as a photocatalyst. *Energy Environ. Sci.* **2012**, *5*, 6111−6118.
(864) Ekström, J.; Abrahamsson, M.; Olson, C.; Bergquist, J.; Kaynak, F. B.; Eriksson, L.; Sun, L.; Becker, H.-C.; Akermark, B.; Hammarström, L.; et al. Bio-inspired, side-on attachment of a ruthenium photosensitizer to an iron hydrogenase active site model. *Dalton Trans.* **2006**, 4599−4606.
(865) Lomoth, R.; Ott, S. Introducing a dark reaction to photochemistry: photocatalytic hydrogen from [FeFe] hydrogenase active site model complexes. *Dalton Trans.* **2009**, 9952−9959.
(866) Reber, J. F.; Meier, K. Photochemical production of hydrogen with zinc sulfide suspensions. *J. Phys. Chem.* **1984**, *88*, 5903−5913.
(867) Benegas, J. C.; Cleven, R. F. M. J.; van den Hoop, M. A. G. T. Potentiometric titration of poly(acrylic acid) in mixed counterion systems: Chemical binding of Cd ions. *Anal. Chim. Acta* **1998**, *369*, 109−114.
(868) Zhang, H.; Zhou, Z.; Yang, B.; Gao, M. The Influence of Carboxyl Groups on the Photoluminescence of Mercaptocarboxylic Acid-Stabilized CdTe Nanoparticles. *J. Phys. Chem. B* **2003**, *107*, 8−13.
(869) Liang, W.-J.; Wang, F.; Wen, M.; Jian, J.-X.; Wang, X.-Z.; Chen, B.; Tung, C.-H.; Wu, L.-Z. Branched Polyethylenimine Improves Hydrogen Photoproduction from a CdSe Quantum Dot/[FeFe]-Hydrogenase Mimic System in Neutral Aqueous Solutions. *Chem. - Eur. J.* **2015**, *21*, 3187−3192.
(870) Zhao, W.; Huang, Y.; Liu, Y.; Cao, L.; Zhang, F.; Guo, Y.; Zhang, B. A Heterogeneous Photocatalytic Hydrogen Evolution Dyad: $[(tpy^{**}\text{-}CHO)_2Ni]Cl_2$ Covalently Anchored to CdS−Amine Inorganic−Organic Hybrid Nanosheets. *Chem. - Eur. J.* **2016**, *22*, 15049−15057.
(871) Carneiro, J. T.; Savenije, T. J.; Moulijn, J. A.; Mul, G. How Phase Composition Influences Optoelectronic and Photocatalytic Properties of TiO_2. *J. Phys. Chem. C* **2011**, *115*, 2211−2217.
(872) Park, Y.; Kim, W.; Monllor-Satoca, D.; Tachikawa, T.; Majima, T.; Choi, W. Role of Interparticle Charge Transfers in Agglomerated Photocatalyst Nanoparticles: Demonstration in Aqueous Suspension of Dye-Sensitized TiO_2. *J. Phys. Chem. Lett.* **2013**, *4*, 189−194.
(873) Lakadamyali, F.; Reynal, A.; Kato, M.; Durrant, J. R.; Reisner, E. Electron Transfer in Dye-Sensitised Semiconductors Modified with Molecular Cobalt Catalysts: Photoreduction of Aqueous Protons. *Chem. - Eur. J.* **2012**, *18*, 15464−15475.

DOI: 10.1021/acs.chemrev.8b00392
Chem. Rev. 2019, 119, 2752−2875

(874) Lakadamyali, F.; Kato, M.; Reisner, E. Colloidal metal oxide particles loaded with synthetic catalysts for solar H_2 production. *Faraday Discuss.* **2012**, *155*, 191−205.
(875) Reynal, A.; Lakadamyali, F.; Gross, M. A.; Reisner, E.; Durrant, J. R. Parameters affecting electron transfer dynamics from semiconductors to molecular catalysts for the photochemical reduction of protons. *Energy Environ. Sci.* **2013**, *6*, 3291−3300.
(876) Lee, J.-S.; Won, D.-I.; Jung, W.-J.; Son, H.-J.; Pac, C.; Kang, S. O. Widely Controllable Syngas Production by a Dye-Sensitized TiO_2 Hybrid System with Re^{I} and Co^{III} Catalysts under Visible-Light Irradiation. *Angew. Chem., Int. Ed.* **2017**, *56*, 976−980.
(877) Warnan, J.; Willkomm, J.; Ng, J. N.; Godin, R.; Prantl, S.; Durrant, J. R.; Reisner, E. Solar H_2 evolution in water with modified diketopyrrolopyrrole dyes immobilised on molecular Co and Ni catalyst-TiO_2 hybrids. *Chem. Sci.* **2017**, *8*, 3070−3079.
(878) Veldkamp, B. S.; Han, W.-S.; Dyar, S. M.; Eaton, S. W.; Ratner, M. A.; Wasielewski, M. R. Photoinitiated multi-step charge separation and ultrafast charge transfer induced dissociation in a pyridyl-linked photosensitizer−cobaloxime assembly. *Energy Environ. Sci.* **2013**, *6*, 1917−1928.
(879) Reynal, A.; Willkomm, J.; Muresan, N. M.; Lakadamyali, F.; Planells, M.; Reisner, E.; Durrant, J. R. Distance dependent charge separation and recombination in semiconductor/molecular catalyst systems for water splitting. *Chem. Commun.* **2014**, *50*, 12768−12771.
(880) Yin, M.; Ma, S.; Wu, C.; Fan, Y. A noble-metal-free photocatalytic hydrogen production system based on cobalt(III) complex and eosin Y-sensitized TiO_2. *RSC Adv.* **2015**, *5*, 1852−1858.
(881) Orchard, K. L.; Hojo, D.; Sokol, K. P.; Chan, M.-J.; Asao, N.; Adschiri, T.; Reisner, E. Catechol-TiO_2 hybrids for photocatalytic H_2 production and photocathode assembly. *Chem. Commun.* **2017**, *53*, 12638−12641.
(882) Ooyama, Y.; Harima, Y. Photophysical and electrochemical properties, and molecular structures of organic dyes for dye-sensitized solar cells. *ChemPhysChem* **2012**, *13*, 4032−4080.
(883) Tsvetkov, I. M.; Buyanova, E. R.; Lymar, S. V.; Parmon, V. N. Photocatalytic evolution of dihydrogen from aqueous solutions of lipid vesicles. *React. Kinet. Catal. Lett.* **1983**, *22*, 159−163.
(884) Menzel, K.; Apfel, U.-P.; Wolter, N.; Rüger, R.; Alpermann, T.; Steiniger, F.; Gabel, D.; Förster, S.; Weigand, W.; Fahr, A. [FeFe]-Hydrogenase models assembled into vesicular structures. *J. Liposome Res.* **2014**, *24*, 59−68.
(885) Troppmann, S.; König, B. Functionalized Membranes for Photocatalytic Hydrogen Production. *Chem. - Eur. J.* **2014**, *20*, 14570−14574.
(886) Wang, F.; Wen, M.; Feng, K.; Liang, W.-J.; Li, X.-B.; Chen, B.; Tung, C.-H.; Wu, L.-Z. Amphiphilic polymeric micelles as microreactors: improving the photocatalytic hydrogen production of the [FeFe]-hydrogenase mimic in water. *Chem. Commun.* **2016**, *52*, 457−460.
(887) Watanabe, M.; Honda, Y.; Hagiwara, H.; Ishihara, T. [FeFe]-Hydrogenase and its organic molecule mimics−Artificial and bioengineering application for hydrogen production. *J. Photochem. Photobiol., C* **2017**, *33*, 1−26.
(888) Di, Y.; Wang, X.; Thomas, A.; Antonietti, M. Making Metal−Carbon Nitride Heterojunctions for Improved Photocatalytic Hydrogen Evolution with Visible Light. *ChemCatChem* **2010**, *2*, 834−838.
(889) Ishida, Y.; Chabanne, L.; Antonietti, M.; Shalom, M. Morphology Control and Photocatalysis Enhancement by the One-Pot Synthesis of Carbon Nitride from Preorganized Hydrogen-Bonded Supramolecular Precursors. *Langmuir* **2014**, *30*, 447−451.
(890) Cuendet, P.; Graetzel, M.; Rao, K. K.; Hall, D. O. Immobilized enzymes on semiconducting powder: Photogeneration of hydrogen by titanium dioxide and cadmium sulfide bound hydrogenases. *Photobiochem. Photobiophys.* **1984**, *7*, 331−340.
(891) Wilker, M. B.; Shinopoulos, K. E.; Brown, K. A.; Mulder, D. W.; King, P. W.; Dukovic, G. Electron Transfer Kinetics in CdS Nanorod−[FeFe]-Hydrogenase Complexes and Implications for Photochemical H_2 Generation. *J. Am. Chem. Soc.* **2014**, *136*, 4316−4324.
(892) Utterback, J. K.; Wilker, M. B.; Brown, K. A.; King, P. W.; Eaves, J. D.; Dukovic, G. Competition between electron transfer, trapping, and recombination in CdS nanorod-hydrogenase complexes. *Phys. Chem. Chem. Phys.* **2015**, *17*, 5538−5542.
(893) Brown, K. A.; Song, Q.; Mulder, D. W.; King, P. W. Diameter Dependent Electron Transfer Kinetics in Semiconductor−Enzyme Complexes. *ACS Nano* **2014**, *8*, 10790−10798.
(894) Cuendet, P.; Grätzel, M.; Pélaprat, M. L. Viologen-derivatization of TiO_2 particles and light-induced H_2 evolution by immobilized hydrogenase. *J. Electroanal. Chem. Interfacial Electrochem.* **1984**, *181*, 173−185.
(895) Cuendet, P.; Rao, K. K.; Grätzel, M.; Hall, D. O. Light induced H_2 evolution in a hydrogenase-TiO_2 particle system by direct electron transfer or via Rhodium complexes. *Biochimie* **1986**, *68*, 217−221.
(896) Kuriki, R.; Sekizawa, K.; Ishitani, O.; Maeda, K. Visible-Light-Driven CO_2 Reduction with Carbon Nitride: Enhancing the Activity of Ruthenium Catalysts. *Angew. Chem., Int. Ed.* **2015**, *54*, 2406−2409.
(897) Kuriki, R.; Matsunaga, H.; Nakashima, T.; Wada, K.; Yamakata, A.; Ishitani, O.; Maeda, K. Nature-Inspired, Highly Durable CO_2 Reduction System Consisting of a Binuclear Ruthenium(II) Complex and an Organic Semiconductor Using Visible Light. *J. Am. Chem. Soc.* **2016**, *138*, 5159−5170.
(898) Kuriki, R.; Yamamoto, M.; Higuchi, K.; Yamamoto, Y.; Akatsuka, M.; Lu, D.; Yagi, S.; Yoshida, T.; Ishitani, O.; Maeda, K. Robust Binding between Carbon Nitride Nanosheets and a Binuclear Ruthenium(II) Complex Enabling Durable, Selective CO_2 Reduction under Visible Light in Aqueous Solution. *Angew. Chem., Int. Ed.* **2017**, *56*, 4867−4871.
(899) Sato, S.; Morikawa, T.; Saeki, S.; Kajino, T.; Motohiro, T. Visible-Light-Induced Selective CO_2 Reduction Utilizing a Ruthenium Complex Electrocatalyst Linked to a p-Type Nitrogen-Doped Ta_2O_5 Semiconductor. *Angew. Chem., Int. Ed.* **2010**, *49*, 5101−5105.
(900) Jin, T.; Liu, C.; Li, G. Photocatalytic CO_2 reduction using a molecular cobalt complex deposited on TiO_2 nanoparticles. *Chem. Commun.* **2014**, *50*, 6221−6224.
(901) Nakada, A.; Nakashima, T.; Sekizawa, K.; Maeda, K.; Ishitani, O. Visible-light-driven CO_2 reduction on a hybrid photocatalyst consisting of a Ru(II) binuclear complex and a Ag-loaded TaON in aqueous solutions. *Chem. Sci.* **2016**, *7*, 4364−4371.
(902) Sekizawa, K.; Maeda, K.; Domen, K.; Koike, K.; Ishitani, O. Artificial Z-Scheme Constructed with a Supramolecular Metal Complex and Semiconductor for the Photocatalytic Reduction of CO_2. *J. Am. Chem. Soc.* **2013**, *135*, 4596−4599.
(903) Won, D.-I.; Lee, J.-S.; Ba, Q.; Cho, Y.-J.; Cheong, H.-Y.; Choi, S.; Kim, C. H.; Son, H.-J.; Pac, C.; Kang, S. O. Development of a Lower Energy Photosensitizer for Photocatalytic CO_2 Reduction: Modification of Porphyrin Dye in Hybrid Catalyst System. *ACS Catal.* **2018**, *8*, 1018−1030.
(904) Won, D.-I.; Lee, J.-S.; Ji, J.-M.; Jung, W.-J.; Son, H.-J.; Pac, C.; Kang, S. O. Highly Robust Hybrid Photocatalyst for Carbon Dioxide Reduction: Tuning and Optimization of Catalytic Activities of Dye/TiO_2/Re(I) Organic−Inorganic Ternary Systems. *J. Am. Chem. Soc.* **2015**, *137*, 13679−13690.
(905) Windle, C. D.; Pastor, E.; Reynal, A.; Whitwood, A. C.; Vaynzof, Y.; Durrant, J. R.; Perutz, R. N.; Reisner, E. Improving the Photocatalytic Reduction of CO_2 to CO through Immobilisation of a Molecular Re Catalyst on TiO_2. *Chem. - Eur. J.* **2015**, *21*, 3746−3754.
(906) Lin, L.; Hou, C.; Zhang, X.; Wang, Y.; Chen, Y.; He, T. Highly efficient visible-light driven photocatalytic reduction of CO_2 over g-C_3N_4 nanosheets/tetra(4-carboxyphenyl)porphyrin iron(III) chloride heterogeneous catalysts. *Appl. Catal., B* **2018**, *221*, 312−319.
(907) Kuehnel, M. F.; Sahm, C. D.; Neri, G.; Lee, J. R.; Orchard, K.; Cowan, A. J.; Reisner, E. ZnSe quantum dots modified with a Ni(cyclam) catalyst for efficient visible-light driven CO_2 reduction in water. *Chem. Sci.* **2018**, *9*, 2501−2509.
(908) Yang, X.; Xu, C.; Giles, N. C. Intrinsic electron mobilities in CdSe, CdS, ZnO, and ZnS and their use in analysis of temperature-dependent Hall measurements. *J. Appl. Phys.* **2008**, *104*, 073727.

DOI: 10.1021/acs.chemrev.8b00392
Chem. Rev. 2019, 119, 2752−2875

(909) Chang, C. M.; Orchard, K.; Martindale, B. C. M.; Reisner, E. Ligand removal from CdS quantum dots for enhanced photocatalytic H_2 generation in pH neutral water. *J. Mater. Chem. A* **2016**, *4*, 2856−2862.
(910) Lian, S.; Kodaimati, M. S.; Weiss, E. A. Photocatalytically Active Superstructures of Quantum Dots and Iron Porphyrins for Reduction of CO_2 to CO in Water. *ACS Nano* **2018**, *12*, 568−575.
(911) Neri, G.; Forster, M.; Walsh, J. J.; Robertson, C. M.; Whittles, T. J.; Farras, P.; Cowan, A. J. Photochemical CO_2 reduction in water using a co-immobilised nickel catalyst and a visible light sensitiser. *Chem. Commun.* **2016**, *52*, 14200−14203.
(912) Buncel, E.; Symons, E. A. The inherent instability of dimethylformamide-water systems containing hydroxide ion. *J. Chem. Soc. D* **1970**, *0*, 164−165.
(913) Feng, X.; Li, Z. Photocatalytic promoting dimethylformamide (DMF) decomposition to in-situ generation of self-supplied CO for carbonylative Suzuki reaction. *J. Photochem. Photobiol., A* **2017**, *337*, 19−24.
(914) Sakimoto, K. K.; Zhang, S. J.; Yang, P. Cysteine−Cystine Photoregeneration for Oxygenic Photosynthesis of Acetic Acid from CO_2 by a Tandem Inorganic−Biological Hybrid System. *Nano Lett.* **2016**, *16*, 5883−5887.
(915) Sakimoto, K. K.; Wong, A. B.; Yang, P. Self-photosensitization of nonphotosynthetic bacteria for solar-to-chemical production. *Science* **2016**, *351*, 74−77.
(916) Woolerton, T. W.; Sheard, S.; Pierce, E.; Ragsdale, S. W.; Armstrong, F. A. CO_2 photoreduction at enzyme-modified metal oxide nanoparticles. *Energy Environ. Sci.* **2011**, *4*, 2393−2399.
(917) Chaudhary, Y. S.; Woolerton, T. W.; Allen, C. S.; Warner, J. H.; Pierce, E.; Ragsdale, S. W.; Armstrong, F. A. Visible light-driven CO_2 reduction by enzyme coupled CdS nanocrystals. *Chem. Commun.* **2012**, *48*, 58−60.
(918) Zhang, L.; Can, M.; Ragsdale, S. W.; Armstrong, F. A. Fast and Selective Photoreduction of CO_2 to CO Catalyzed by a Complex of Carbon Monoxide Dehydrogenase, TiO_2, and Ag Nanoclusters. *ACS Catal.* **2018**, *8*, 2789−2795.
(919) Wakerley, D. W.; Kuehnel, M. F.; Orchard, K. L.; Ly, K. H.; Rosser, T. E.; Reisner, E. Solar-driven reforming of lignocellulose to H_2 with a CdS/CdO_x photocatalyst. *Nat. Energy.* **2017**, *2*, 17021.
(920) Wu, H. L.; Li, X. B.; Tung, C. H.; Wu, L. Z. Recent Advances in Sensitized Photocathodes: From Molecular Dyes to Semiconducting Quantum Dots. *Adv. Sci.* **2018**, *5*, 1700684.
(921) Concepcion, J. J.; Jurss, J. W.; Brennaman, M. K.; Hoertz, P. G.; Patrocinio, A. O. T.; Murakami Iha, N. Y.; Templeton, J. L.; Meyer, T. J. Making Oxygen with Ruthenium Complexes. *Acc. Chem. Res.* **2009**, *42*, 1954−1965.
(922) Gust, D.; Moore, T. A.; Moore, A. L. Solar Fuels via Artificial Photosynthesis. *Acc. Chem. Res.* **2009**, *42*, 1890−1898.
(923) Youngblood, W. J.; Lee, S.-H. A.; Maeda, K.; Mallouk, T. E. Visible Light Water Splitting Using Dye-Sensitized Oxide Semiconductors. *Acc. Chem. Res.* **2009**, *42*, 1966−1973.
(924) Brennaman, M. K.; Dillon, R. J.; Alibabaei, L.; Gish, M. K.; Dares, C. J.; Ashford, D. L.; House, R. L.; Meyer, G. J.; Papanikolas, J. M.; Meyer, T. J. Finding the Way to Solar Fuels with Dye-Sensitized Photoelectrosynthesis Cells. *J. Am. Chem. Soc.* **2016**, *138*, 13085−13102.
(925) Kou, Y.; Nakatani, S.; Sunagawa, G.; Tachikawa, Y.; Masui, D.; Shimada, T.; Takagi, S.; Tryk, D. A.; Nabetani, Y.; Tachibana, H.; et al. Visible light-induced reduction of carbon dioxide sensitized by a porphyrin−rhenium dyad metal complex on p-type semiconducting NiO as the reduction terminal end of an artificial photosynthetic system. *J. Catal.* **2014**, *310*, 57−66.
(926) Kumagai, H.; Sahara, G.; Maeda, K.; Higashi, M.; Abe, R.; Ishitani, O. Hybrid photocathode consisting of a $CuGaO_2$ p-type semiconductor and a Ru(II)-Re(I) supramolecular photocatalyst: non-biased visible-light-driven CO_2 reduction with water oxidation. *Chem. Sci.* **2017**, *8*, 4242−4249.
(927) Sahara, G.; Abe, R.; Higashi, M.; Morikawa, T.; Maeda, K.; Ueda, Y.; Ishitani, O. Photoelectrochemical CO_2 reduction using a Ru(II)-Re(I) multinuclear metal complex on a p-type semiconducting NiO electrode. *Chem. Commun.* **2015**, *51*, 10722−10725.
(928) Dare-Edwards, M. P.; Goodenough, J. B.; Hamnett, A.; Nicholson, N. D. Photoelectrochemistry of nickel(II) oxide. *J. Chem. Soc., Faraday Trans. 2* **1981**, *77*, 643−661.
(929) Nandy, S.; Saha, B.; Mitra, M. K.; Chattopadhyay, K. K. Effect of oxygen partial pressure on the electrical and optical properties of highly (200) oriented p-type $Ni_{1-x}O$ films by DC sputtering. *J. Mater. Sci.* **2007**, *42*, 5766−5772.
(930) Gross, M. A.; Creissen, C. E.; Orchard, K. L.; Reisner, E. Photoelectrochemical hydrogen production in water using a layer-by-layer assembly of a Ru dye and Ni catalyst on NiO. *Chem. Sci.* **2016**, *7*, 5537−5546.
(931) Chan, X.-H.; Jennings, J. R.; Hossain, M. A.; Koh Zhen Yu, K.; Wang, Q. Characteristics of p-NiO Thin Films Prepared by Spray Pyrolysis and Their Application in CdS-sensitized Photocathodes. *J. Electrochem. Soc.* **2011**, *158*, H733−H740.
(932) Natu, G.; Hasin, P.; Huang, Z.; Ji, Z.; He, M.; Wu, Y. Valence Band-Edge Engineering of Nickel Oxide Nanoparticles via Cobalt Doping for Application in p-Type Dye-Sensitized Solar Cells. *ACS Appl. Mater. Interfaces* **2012**, *4*, 5922−5929.
(933) Warnan, J.; Gardner, J.; Le Pleux, L.; Petersson, J.; Pellegrin, Y.; Blart, E.; Hammarström, L.; Odobel, F. Multichromophoric Sensitizers Based on Squaraine for NiO Based Dye-Sensitized Solar Cells. *J. Phys. Chem. C* **2014**, *118*, 103−113.
(934) Vera, F.; Schrebler, R.; Muñoz, E.; Suarez, C.; Cury, P.; Gómez, H.; Córdova, R.; Marotti, R. E.; Dalchiele, E. A. Preparation and characterization of Eosin B- and Erythrosin J-sensitized nanostructured NiO thin film photocathodes. *Thin Solid Films* **2005**, *490*, 182−188.
(935) Zhu, H.; Hagfeldt, A.; Boschloo, G. Photoelectrochemistry of Mesoporous NiO Electrodes in Iodide/Triiodide Electrolytes. *J. Phys. Chem. C* **2007**, *111*, 17455−17458.
(936) Qin, P.; Zhu, H.; Edvinsson, T.; Boschloo, G.; Hagfeldt, A.; Sun, L. Design of an Organic Chromophore for P-Type Dye-Sensitized Solar Cells. *J. Am. Chem. Soc.* **2008**, *130*, 8570−8571.
(937) Kuang, D.-B.; Lei, B.-X.; Pan, Y.-P.; Yu, X.-Y.; Su, C.-Y. Fabrication of Novel Hierarchical β-$Ni(OH)_2$ and NiO Microspheres via an Easy Hydrothermal Process. *J. Phys. Chem. C* **2009**, *113*, 5508−5513.
(938) Lepleux, L.; Chavillon, B.; Pellegrin, Y.; Blart, E.; Cario, L.; Jobic, S.; Odobel, F. Simple and reproducible procedure to prepare self-nanostructured NiO films for the fabrication of P-type dye-sensitized solar cells. *Inorg. Chem.* **2009**, *48*, 8245−8250.
(939) Li, L.; Gibson, E. A.; Qin, P.; Boschloo, G.; Gorlov, M.; Hagfeldt, A.; Sun, L. Double-layered NiO photocathodes for p-type DSSCs with record IPCE. *Adv. Mater.* **2010**, *22*, 1759−1762.
(940) Sumikura, S.; Mori, S.; Shimizu, S.; Usami, H.; Suzuki, E. Syntheses of NiO nanoporous films using nonionic triblock co-polymer templates and their application to photo-cathodes of p-type dye-sensitized solar cells. *J. Photochem. Photobiol., A* **2008**, *199*, 1−7.
(941) Wood, C. J.; Summers, G. H.; Clark, C. A.; Kaeffer, N.; Braeutigam, M.; Carbone, L. R.; D'Amario, L.; Fan, K.; Farre, Y.; Narbey, S.; et al. A comprehensive comparison of dye-sensitized NiO photocathodes for solar energy conversion. *Phys. Chem. Chem. Phys.* **2016**, *18*, 10727−10738.
(942) Nakade, S.; Kanzaki, T.; Wada, Y.; Yanagida, S. Stepped Light-Induced Transient Measurements of Photocurrent and Voltage in Dye-Sensitized Solar Cells: Application for Highly Viscous Electrolyte Systems. *Langmuir* **2005**, *21*, 10803−10807.
(943) Mori, S.; Fukuda, S.; Sumikura, S.; Takeda, Y.; Tamaki, Y.; Suzuki, E.; Abe, T. Charge-Transfer Processes in Dye-Sensitized NiO Solar Cells. *J. Phys. Chem. C* **2008**, *112*, 16134−16139.
(944) Mishra, A.; Fischer, M. K.; Bauerle, P. Metal-free organic dyes for dye-sensitized solar cells: from structure: property relationships to design rules. *Angew. Chem., Int. Ed.* **2009**, *48*, 2474−2499.
(945) Kaeffer, N.; Massin, J.; Lebrun, C.; Renault, O.; Chavarot-Kerlidou, M.; Artero, V. Covalent Design for Dye-Sensitized H_2-Evolving Photocathodes Based on a Cobalt Diimine-Dioxime Catalyst. *J. Am. Chem. Soc.* **2016**, *138*, 12308−12311.

DOI: 10.1021/acs.chemrev.8b00392
Chem. Rev. 2019, 119, 2752−2875

(946) Pati, P. B.; Zhang, L.; Philippe, B.; Fernández-Terán, R.; Ahmadi, S.; Tian, L.; Rensmo, H.; Hammarström, L.; Tian, H. Insights into the Mechanism of a Covalently Linked Organic Dye−Cobaloxime Catalyst System for Dye-Sensitized Solar Fuel Devices. *ChemSusChem* **2017**, *10*, 2480−2495.
(947) Bolton, J. R.; Strickler, S. J.; Connolly, J. S. Limiting and realizable efficiencies of solar photolysis of water. *Nature* **1985**, *316*, 495−500.
(948) Pinaud, B. A.; Benck, J. D.; Seitz, L. C.; Forman, A. J.; Chen, Z.; Deutsch, T. G.; James, B. D.; Baum, K. N.; Baum, G. N.; Ardo, S.; et al. Technical and economic feasibility of centralized facilities for solar hydrogen production via photocatalysis and photoelectrochemistry. *Energy Environ. Sci.* **2013**, *6*, 1983−2002.
(949) Fountaine, K. T.; Lewerenz, H. J.; Atwater, H. A. Efficiency limits for photoelectrochemical water-splitting. *Nat. Commun.* **2016**, *7*, 13706.
(950) Li, L.; Duan, L.; Wen, F.; Li, C.; Wang, M.; Hagfeldt, A.; Sun, L. Visible light driven hydrogen production from a photo-active cathode based on a molecular catalyst and organic dye-sensitized p-type nanostructured NiO. *Chem. Commun.* **2012**, *48*, 988−990.
(951) Fan, K.; Li, F.; Wang, L.; Daniel, Q.; Gabrielsson, E.; Sun, L. Pt-free tandem molecular photoelectrochemical cells for water splitting driven by visible light. *Phys. Chem. Chem. Phys.* **2014**, *16*, 25234−25240.
(952) Li, F.; Fan, K.; Xu, B.; Gabrielsson, E.; Daniel, Q.; Li, L.; Sun, L. Organic Dye-Sensitized Tandem Photoelectrochemical Cell for Light Driven Total Water Splitting. *J. Am. Chem. Soc.* **2015**, *137*, 9153−9159.
(953) Gardner, J. M.; Beyler, M.; Karnahl, M.; Tschierlei, S.; Ott, S.; Hammarström, L. Light-driven electron transfer between a photosensitizer and a proton-reducing catalyst co-adsorbed to NiO. *J. Am. Chem. Soc.* **2012**, *134*, 19322−19325.
(954) Brown, A. M.; Antila, L. J.; Mirmohades, M.; Pullen, S.; Ott, S.; Hammarström, L. Ultrafast Electron Transfer Between Dye and Catalyst on a Mesoporous NiO Surface. *J. Am. Chem. Soc.* **2016**, *138*, 8060−8063.
(955) Antila, L. J.; Ghamgosar, P.; Maji, S.; Tian, H.; Ott, S.; Hammarström, L. Dynamics and Photochemical H_2 Evolution of Dye−NiO Photocathodes with a Biomimetic FeFe-Catalyst. *ACS Energy Lett.* **2016**, *1*, 1106−1111.
(956) Gatty, M. G.; Pullen, S.; Sheibani, E.; Tian, H.; Ott, S.; Hammarström, L. Direct evidence of catalyst reduction on dye and catalyst co-sensitized NiO photocathodes by mid-infrared transient absorption spectroscopy. *Chem. Sci.* **2018**, *9*, 4983−4991.
(957) Meng, P.; Wang, M.; Yang, Y.; Zhang, S.; Sun, L. CdSe quantum dots/molecular cobalt catalyst co-grafted open porous NiO film as a photocathode for visible light driven H_2 evolution from neutral water. *J. Mater. Chem. A* **2015**, *3*, 18852−18859.
(958) Barceló, I.; Guillén, E.; Lana-Villarreal, T.; Gómez, R. Preparation and Characterization of Nickel Oxide Photocathodes Sensitized with Colloidal Cadmium Selenide Quantum Dots. *J. Phys. Chem. C* **2013**, *117*, 22509−22517.
(959) Kang, S. H.; Zhu, K.; Neale, N. R.; Frank, A. J. Hole transport in sensitized CdS-NiO nanoparticle photocathodes. *Chem. Commun.* **2011**, *47*, 10419−10421.
(960) Ran, J.; Zhang, J.; Yu, J.; Jaroniec, M.; Qiao, S. Z. Earth-abundant cocatalysts for semiconductor-based photocatalytic water splitting. *Chem. Soc. Rev.* **2014**, *43*, 7787−7812.
(961) Tran, P. D.; Wong, L. H.; Barber, J.; Loo, J. S. C. Recent advances in hybrid photocatalysts for solar fuel production. *Energy Environ. Sci.* **2012**, *5*, 5902−5918.
(962) Wen, F.; Li, C. Hybrid Artificial Photosynthetic Systems Comprising Semiconductors as Light Harvesters and Biomimetic Complexes as Molecular Cocatalysts. *Acc. Chem. Res.* **2013**, *46*, 2355−2364.
(963) Das, B. C.; Batabyal, S. K.; Pal, A. J. A Bit per Particle: Electrostatic Assembly of CdSe Quantum Dots as Memory Elements. *Adv. Mater.* **2007**, *19*, 4172−4176.
(964) Huang, J.; Stockwell, D.; Huang, Z.; Mohler, D. L.; Lian, T. Photoinduced Ultrafast Electron Transfer from CdSe Quantum Dots to Re-bipyridyl Complexes. *J. Am. Chem. Soc.* **2008**, *130*, 5632−5633.
(965) Na, Y.; Hu, B.; Yang, Q.-L.; Liu, J.; Zhou, L.; Fan, R.-Q.; Yang, Y.-L. CdS quantum dot sensitized p-type NiO as photocathode with integrated cobaloxime in photoelectrochemical cell for water splitting. *Chin. Chem. Lett.* **2015**, *26*, 141−144.
(966) Abdellah, M.; Zhang, S.; Wang, M.; Hammarström, L. Competitive Hole Transfer from CdSe Quantum Dots to Thiol Ligands in CdSe-Cobaloxime Sensitized NiO Films Used as Photocathodes for H_2 Evolution. *ACS Energy Lett.* **2017**, *2*, 2576−2580.
(967) Horvath, S.; Fernandez, L. E.; Soudackov, A. V.; Hammes-Schiffer, S. Insights into proton-coupled electron transfer mechanisms of electrocatalytic H_2 oxidation and production. *Proc. Natl. Acad. Sci. U. S. A.* **2012**, *109*, 15663−15668.
(968) van den Bosch, B.; Rombouts, J. A.; Orru, R. V. A.; Reek, J. N. H.; Detz, R. J. Nickel-Based Dye-Sensitized Photocathode: Towards Proton Reduction Using a Molecular Nickel Catalyst and an Organic Dye. *ChemCatChem* **2016**, *8*, 1392−1398.
(969) Creissen, C. E.; Warnan, J.; Reisner, E. Solar H_2 generation in water with a $CuCrO_2$ photocathode modified with an organic dye and molecular Ni catalyst. *Chem. Sci.* **2018**, *9*, 1439−1447.
(970) Gu, J.; Yan, Y.; Krizan, J. W.; Gibson, Q. D.; Detweiler, Z. M.; Cava, R. J.; Bocarsly, A. B. p-type $CuRhO_2$ as a self-healing photoelectrode for water reduction under visible light. *J. Am. Chem. Soc.* **2014**, *136*, 830−833.
(971) Prévot, M. S.; Guijarro, N.; Sivula, K. Enhancing the Performance of a robust sol-gel-processed p-type delafossite $CuFeO_2$ photocathode for solar water reduction. *ChemSusChem* **2015**, *8*, 1359−1367.
(972) Prévot, M. S.; Jeanbourquin, X. A.; Bourée, W. S.; Abdi, F.; Friedrich, D.; van de Krol, R.; Guijarro, N.; Le Formal, F.; Sivula, K. Evaluating Charge Carrier Transport and Surface States in $CuFeO_2$ Photocathodes. *Chem. Mater.* **2017**, *29*, 4952−4962.
(973) Jiang, T.; Li, X.; Bujoli-Doeuff, M.; Gautron, E.; Cario, L.; Jobic, S.; Gautier, R. Modulation of Defects in Semiconductors by Facile and Controllable Reduction: The Case of p-type $CuCrO_2$ Nanoparticles. *Inorg. Chem.* **2016**, *55*, 7729−7733.
(974) Scanlon, D. O.; Watson, G. W. Understanding the p-type defect chemistry of $CuCrO_2$. *J. Mater. Chem.* **2011**, *21*, 3655−3663.
(975) Xiong, D.; Xu, Z.; Zeng, X.; Zhang, W.; Chen, W.; Xu, X.; Wang, M.; Cheng, Y.-B. Hydrothermal synthesis of ultrasmall $CuCrO_2$ nanocrystal alternatives to NiO nanoparticles in efficient p-type dye-sensitized solar cells. *J. Mater. Chem.* **2012**, *22*, 24760−24768.
(976) Ketir, W.; Bouguelia, A.; Trari, M. NO_3^- removal with a new delafossite $CuCrO_2$ photocatalyst. *Desalination* **2009**, *244*, 144−152.
(977) Ding, X.; Gao, Y.; Zhang, L.; Yu, Z.; Liu, J.; Sun, L. Visible Light-Driven Water Splitting in Photoelectrochemical Cells with Supramolecular Catalysts on Photoanodes. *ACS Catal.* **2014**, *4*, 2347−2350.
(978) Hanson, K.; Torelli, D. A.; Vannucci, A. K.; Brennaman, M. K.; Luo, H.; Alibabaei, L.; Song, W.; Ashford, D. L.; Norris, M. R.; Glasson, C. R. K.; et al. Self-Assembled Bilayer Films of Ruthenium(II)/Polypyridyl Complexes through Layer-by-Layer Deposition on Nanostructured Metal Oxides. *Angew. Chem., Int. Ed.* **2012**, *51*, 12782−12785.
(979) Kanaizuka, K.; Kato, S.; Moriyama, H.; Pac, C. Photophysical and electrochemical behavior of thin solid films based on a three-dimensional ruthenium complex network. *Res. Chem. Intermed.* **2007**, *33*, 91−100.
(980) Shan, B.; Das, A. K.; Marquard, S.; Farnum, B. H.; Wang, D.; Bullock, R. M.; Meyer, T. J. Photogeneration of hydrogen from water by a robust dye-sensitized photocathode. *Energy Environ. Sci.* **2016**, *9*, 3693−3697.
(981) Shan, B.; Sherman, B. D.; Klug, C. M.; Nayak, A.; Marquard, S. L.; Liu, Q.; Bullock, R. M.; Meyer, T. J. Modulating Hole Transport in Multilayered Photocathodes with Derivatized p-Type Nickel Oxide and Molecular Assemblies for Solar-Driven Water Splitting. *J. Phys. Chem. Lett.* **2017**, *8*, 4374−4379.
(982) Ji, Z.; He, M.; Huang, Z.; Ozkan, U.; Wu, Y. Photostable p-type dye-sensitized photoelectrochemical cells for water reduction. *J. Am. Chem. Soc.* **2013**, *135*, 11696−11699.

DOI: 10.1021/acs.chemrev.8b00392
Chem. Rev. 2019, 119, 2752−2875

(983) Fihri, A.; Artero, V.; Pereira, A.; Fontecave, M. Efficient H_2-producing photocatalytic systems based on cyclometalated iridium- and tricarbonylrhenium-diimine photosensitizers and cobaloxime catalysts. *Dalton Trans.* **2008**, *0*, 5567−5569.
(984) Flynn, C. J.; McCullough, S. M.; Oh, E.; Li, L.; Mercado, C. C.; Farnum, B. H.; Li, W.; Donley, C. L.; You, W.; Nozik, A. J.; et al. Site-Selective Passivation of Defects in NiO Solar Photocathodes by Targeted Atomic Deposition. *ACS Appl. Mater. Interfaces* **2016**, *8*, 4754−4761.
(985) Natu, G.; Huang, Z.; Ji, Z.; Wu, Y. The effect of an atomically deposited layer of alumina on NiO in P-type dye-sensitized solar cells. *Langmuir* **2012**, *28*, 950−956.
(986) Uehara, S.; Sumikura, S.; Suzuki, E.; Mori, S. Retardation of electron injection at NiO/dye/electrolyte interface by aluminium alkoxide treatment. *Energy Environ. Sci.* **2010**, *3*, 641−644.
(987) Kamire, R. J.; Majewski, M. B.; Hoffeditz, W. L.; Phelan, B. T.; Farha, O. K.; Hupp, J. T.; Wasielewski, M. R. Photodriven hydrogen evolution by molecular catalysts using Al_2O_3-protected perylene-3,4-dicarboximide on NiO electrodes. *Chem. Sci.* **2017**, *8*, 541−549.
(988) Favereau, L.; Warnan, J.; Pellegrin, Y.; Blart, E.; Boujtita, M.; Jacquemin, D.; Odobel, F. Diketopyrrolopyrrole derivatives for efficient NiO-based dye-sensitized solar cells. *Chem. Commun.* **2013**, *49*, 8018−8020.
(989) Ito, S.; Miura, H.; Uchida, S.; Takata, M.; Sumioka, K.; Liska, P.; Comte, P.; Pechy, P.; Grätzel, M. High-conversion-efficiency organic dye-sensitized solar cells with a novel indoline dye. *Chem. Commun.* **2008**, *0*, 5194−5196.
(990) Windle, C. D.; Massin, J.; Chavarot-Kerlidou, M.; Artero, V. A protocol for quantifying hydrogen evolution by dye-sensitized molecular photocathodes and its implementation for evaluating a new covalent architecture based on an optimized dye-catalyst dyad. *Dalton Trans.* **2018**, *47*, 10509−10516.
(991) Wen, M.; Wu, H.-L.; Jian, J.-X.; Wang, X.-Z.; Li, X.-B.; Chen, B.; Tung, C.-H.; Wu, L.-Z. Integrating CdSe Quantum Dots with a [FeFe]-Hydrogenase Mimic into a Photocathode for Hydrogen Evolution at a Low Bias Voltage. *ChemPhotoChem* **2017**, *1*, 260−264.
(992) Lefebvre, J.-F.; Schindler, J.; Traber, P.; Zhang, Y.; Kupfer, S.; Grafe, S.; Baussanne, I.; Demeunynck, M.; Mouesca, J.-M.; Gambarelli, S.; et al. An artificial photosynthetic system for photoaccumulation of two electrons on a fused dipyridophenazine (dppz)−pyridoquinolinone ligand. *Chem. Sci.* **2018**, *9*, 4152−4159.
(993) Bachmeier, A.; Hall, S.; Ragsdale, S. W.; Armstrong, F. A. Selective visible-light-driven CO_2 reduction on a p-type dye-sensitized NiO photocathode. *J. Am. Chem. Soc.* **2014**, *136*, 13518−13521.
(994) Gibson, E. A.; Awais, M.; Dini, D.; Dowling, D. P.; Pryce, M. T.; Vos, J. G.; Boschloo, G.; Hagfeldt, A. Dye sensitised solar cells with nickel oxide photocathodes prepared via scalable microwave sintering. *Phys. Chem. Chem. Phys.* **2013**, *15*, 2411−2420.
(995) Zhang, X. L.; Zhang, Z.; Chen, D.; Bauerle, P.; Bach, U.; Cheng, Y. B. Sensitization of nickel oxide: improved carrier lifetime and charge collection by tuning nanoscale crystallinity. *Chem. Commun.* **2012**, *48*, 9885−9887.
(996) Hu, S.; Xiang, C.; Haussener, S.; Berger, A. D.; Lewis, N. S. An analysis of the optimal band gaps of light absorbers in integrated tandem photoelectrochemical water-splitting systems. *Energy Environ. Sci.* **2013**, *6*, 2984−2993.
(997) Prévot, M. S.; Sivula, K. Photoelectrochemical Tandem Cells for Solar Water Splitting. *J. Phys. Chem. C* **2013**, *117*, 17879−17893.
(998) Paracchino, A.; Brauer, J. C.; Moser, J.-E.; Thimsen, E.; Graetzel, M. Synthesis and Characterization of High-Photoactivity Electrodeposited Cu_2O Solar Absorber by Photoelectrochemistry and Ultrafast Spectroscopy. *J. Phys. Chem. C* **2012**, *116*, 7341−7350.
(999) Lee, M. H.; Takei, K.; Zhang, J.; Kapadia, R.; Zheng, M.; Chen, Y. Z.; Nah, J.; Matthews, T. S.; Chueh, Y. L.; Ager, J. W.; et al. p-Type InP nanopillar photocathodes for efficient solar-driven hydrogen production. *Angew. Chem., Int. Ed.* **2012**, *51*, 10760−10764.
(1000) Hettick, M.; Zheng, M.; Lin, Y.; Sutter-Fella, C. M.; Ager, J. W.; Javey, A. Nonepitaxial Thin-Film InP for Scalable and Efficient Photocathodes. *J. Phys. Chem. Lett.* **2015**, *6*, 2177−2182.
(1001) Cedeno, D.; Krawicz, A.; Moore, G. F. Hybrid photocathodes for solar fuel production: coupling molecular fuel-production catalysts with solid-state light harvesting and conversion technologies. *Interface Focus* **2015**, *5*, 20140085.
(1002) Bansal, A.; Turner, J. A. Suppression of Band Edge Migration at the p-$GaInP_2$/H_2O Interface under Illumination via Catalysis. *J. Phys. Chem. B* **2000**, *104*, 6591−6598.
(1003) MacLeod, B. A.; Steirer, K. X.; Young, J. L.; Koldemir, U.; Sellinger, A.; Turner, J. A.; Deutsch, T. G.; Olson, D. C. Phosphonic Acid Modification of $GaInP_2$ Photocathodes Toward Unbiased Photoelectrochemical Water Splitting. *ACS Appl. Mater. Interfaces* **2015**, *7*, 11346−11350.
(1004) Seger, B.; Laursen, A. B.; Vesborg, P. C.; Pedersen, T.; Hansen, O.; Dahl, S.; Chorkendorff, I. Hydrogen production using a molybdenum sulfide catalyst on a titanium-protected n^+p-silicon photocathode. *Angew. Chem., Int. Ed.* **2012**, *51*, 9128−9131.
(1005) Lin, Y.; Battaglia, C.; Boccard, M.; Hettick, M.; Yu, Z.; Ballif, C.; Ager, J. W.; Javey, A. Amorphous Si thin film based photocathodes with high photovoltage for efficient hydrogen production. *Nano Lett.* **2013**, *13*, 5615−5618.
(1006) Morales-Guio, C. G.; Thorwarth, K.; Niesen, B.; Liardet, L.; Patscheider, J.; Ballif, C.; Hu, X. Solar Hydrogen Production by Amorphous Silicon Photocathodes Coated with a Magnetron Sputter Deposited Mo_2C Catalyst. *J. Am. Chem. Soc.* **2015**, *137*, 7035−7038.
(1007) Schreier, M.; Luo, J.; Gao, P.; Moehl, T.; Mayer, M. T.; Grätzel, M. Covalent Immobilization of a Molecular Catalyst on Cu_2O Photocathodes for CO_2 Reduction. *J. Am. Chem. Soc.* **2016**, *138*, 1938−1946.
(1008) Bae, D.; Seger, B.; Vesborg, P. C.; Hansen, O.; Chorkendorff, I. Strategies for stable water splitting via protected photoelectrodes. *Chem. Soc. Rev.* **2017**, *46*, 1933−1954.
(1009) Gu, J.; Yan, Y.; Young, J. L.; Steirer, K. X.; Neale, N. R.; Turner, J. A. Water reduction by a p-$GaInP_2$ photoelectrode stabilized by an amorphous TiO_2 coating and a molecular cobalt catalyst. *Nat. Mater.* **2016**, *15*, 456−460.
(1010) Hong, D.; Mandal, S.; Yamada, Y.; Lee, Y. M.; Nam, W.; Llobet, A.; Fukuzumi, S. Water oxidation catalysis with nonheme iron complexes under acidic and basic conditions: homogeneous or heterogeneous? *Inorg. Chem.* **2013**, *52*, 9522−9531.
(1011) Lai, Y.-H.; Palm, D. W.; Reisner, E. Multifunctional Coatings from Scalable Single Source Precursor Chemistry in Tandem Photoelectrochemical Water Splitting. *Adv. Energy Mater.* **2015**, *5*, 1501668.
(1012) Pfrommer, J.; Lublow, M.; Azarpira, A.; Gobel, C.; Lucke, M.; Steigert, A.; Pogrzeba, M.; Menezes, P. W.; Fischer, A.; Schedel-Niedrig, T.; et al. A molecular approach to self-supported cobalt-substituted ZnO materials as remarkably stable electrocatalysts for water oxidation. *Angew. Chem., Int. Ed.* **2014**, *53*, 5183−5187.
(1013) Nann, T.; Ibrahim, S. K.; Woi, P. M.; Xu, S.; Ziegler, J.; Pickett, C. J. Water splitting by visible light: a nanophotocathode for hydrogen production. *Angew. Chem., Int. Ed.* **2010**, *49*, 1574−1577.
(1014) Buriak, J. M. Organometallic Chemistry on Silicon and Germanium Surfaces. *Chem. Rev.* **2002**, *102*, 1271−1308.
(1015) Krawicz, A.; Cedeno, D.; Moore, G. F. Energetics and efficiency analysis of a cobaloxime-modified semiconductor under simulated air mass 1.5 illumination. *Phys. Chem. Chem. Phys.* **2014**, *16*, 15818−15824.
(1016) Solis, B. H.; Hammes-Schiffer, S. Theoretical analysis of mechanistic pathways for hydrogen evolution catalyzed by cobaloximes. *Inorg. Chem.* **2011**, *50*, 11252−11262.
(1017) Price, M. J.; Maldonado, S. Macroporous n-GaP in Nonaqueous Regenerative Photoelectrochemical Cells. *J. Phys. Chem. C* **2009**, *113*, 11988−11994.
(1018) Sun, J.; Liu, C.; Yang, P. Surfactant-free, large-scale, solution-liquid-solid growth of gallium phosphide nanowires and their use for visible-light-driven hydrogen production from water reduction. *J. Am. Chem. Soc.* **2011**, *133*, 19306−19309.
(1019) Kaiser, B.; Fertig, D.; Ziegler, J.; Klett, J.; Hoch, S.; Jaegermann, W. Solar hydrogen generation with wide-band-gap

DOI: 10.1021/acs.chemrev.8b00392
Chem. Rev. 2019, 119, 2752−2875

semiconductors: GaP(100) photoelectrodes and surface modification. *ChemPhysChem* **2012**, *13*, 3053−3060.
(1020) Cedeno, D.; Krawicz, A.; Doak, P.; Yu, M.; Neaton, J. B.; Moore, G. F. Using Molecular Design to Control the Performance of Hydrogen-Producing Polymer-Brush-Modified Photocathodes. *J. Phys. Chem. Lett.* **2014**, *5*, 3222−3226.
(1021) Beiler, A. M.; Khusnutdinova, D.; Jacob, S. I.; Moore, G. F. Chemistry at the Interface: Polymer-Functionalized GaP Semiconductors for Solar Hydrogen Production. *Ind. Eng. Chem. Res.* **2016**, *55*, 5306−5314.
(1022) Yang, G. H.; Kang, E. T.; Neoh, K. G.; Zhang, Y.; Tan, K. L. Electroless deposition of copper on polyimide films modified by surface graft copolymerization with nitrogen-containing vinyl monomers. *Colloid Polym. Sci.* **2001**, *279*, 745−753.
(1023) Shin, K.; Kramer, S. K.; Goff, H. M. Base-promoted autoreduction of iron(III) porphyrins in dimethyl sulfoxide solution: magnetic resonance spectroscopy of hydroxoiron(II) porphyrin complexes. *Inorg. Chem.* **1987**, *26*, 4103−4106.
(1024) Balch, A. L.; Noll, B. C.; Olmstead, M. M.; Phillips, S. L. Structural and Spectroscopic Characterization of Iron(III) Dioxoporphodimethene Complexes and Their Autoreduction to an Iron(II) Complex in Pyridine. *Inorg. Chem.* **1996**, *35*, 6495−6506.
(1025) St Claire, T. N.; Balch, A. L. In Situ Monitoring of the Degradation of Iron Porphyrins by Dioxygen with Hydrazine as Sacrificial Reductant. Detection of Paramagnetic Intermediates in the Coupled Oxidation Process by ^{1}H NMR Spectroscopy. *Inorg. Chem.* **1999**, *38*, 684−691.
(1026) Beiler, A. M.; Khusnutdinova, D.; Wadsworth, B. L.; Moore, G. F. Cobalt Porphyrin-Polypyridyl Surface Coatings for Photoelectrosynthetic Hydrogen Production. *Inorg. Chem.* **2017**, *56*, 12178−12185.
(1027) Walter, M. G.; Warren, E. L.; McKone, J. R.; Boettcher, S. W.; Mi, Q.; Santori, E. A.; Lewis, N. S. Solar Water Splitting Cells. *Chem. Rev.* **2010**, *110*, 6446−6473.
(1028) Khaselev, O.; Turner, J. A. Electrochemical Stability of *p*-$GaInP_2$ in Aqueous Electrolytes Toward Photoelectrochemical Water Splitting. *J. Electrochem. Soc.* **1998**, *145*, 3335−3339.
(1029) Chandrasekaran, S.; Macdonald, T. J.; Mange, Y. J.; Voelcker, N. H.; Nann, T. A quantum dot sensitized catalytic porous silicon photocathode. *J. Mater. Chem. A* **2014**, *2*, 9478−9481.
(1030) Seo, J.; Pekarek, R. T.; Rose, M. J. Photoelectrochemical operation of a surface-bound, nickel-phosphine H_2 evolution catalyst on p-Si(111): a molecular semiconductor|catalyst construct. *Chem. Commun.* **2015**, *51*, 13264−13267.
(1031) Kim, H. J.; Seo, J.; Rose, M. J. H_2 Photogeneration Using a Phosphonate-Anchored Ni-PNP Catalyst on a Band-Edge-Modified *p*-Si(111)|AZO Construct. *ACS Appl. Mater. Interfaces* **2016**, *8*, 1061−1066.
(1032) Beaujuge, P. M.; Fréchet, J. M. Molecular design and ordering effects in π-functional materials for transistor and solar cell applications. *J. Am. Chem. Soc.* **2011**, *133*, 20009−20029.
(1033) Forrest, S. R. The path to ubiquitous and low-cost organic electronic appliances on plastic. *Nature* **2004**, *428*, 911−918.
(1034) Bourgeteau, T.; Tondelier, D.; Geffroy, B.; Brisse, R.; Campidelli, S.; Cornut, R.; Jousselme, B. All solution-processed organic photocathodes with increased efficiency and stability via the tuning of the hole-extracting layer. *J. Mater. Chem. A* **2016**, *4*, 4831−4839.
(1035) Haro, M.; Solis, C.; Molina, G.; Otero, L.; Bisquert, J.; Gimenez, S.; Guerrero, A. Toward Stable Solar Hydrogen Generation Using Organic Photoelectrochemical Cells. *J. Phys. Chem. C* **2015**, *119*, 6488−6494.
(1036) Rojas, H. C.; Bellani, S.; Fumagalli, F.; Tullii, G.; Leonardi, S.; Mayer, M. T.; Schreier, M.; Grätzel, M.; Lanzani, G.; Di Fonzo, F.; et al. Polymer-based photocathodes with a solution-processable cuprous iodide anode layer and a polyethyleneimine protective coating. *Energy Environ. Sci.* **2016**, *9*, 3710−3723.
(1037) Zhao, Y.; Anderson, N. C.; Ratzloff, M. W.; Mulder, D. W.; Zhu, K.; Turner, J. A.; Neale, N. R.; King, P. W.; Branz, H. M. Proton Reduction Using a Hydrogenase-Modified Nanoporous Black Silicon Photoelectrode. *ACS Appl. Mater. Interfaces* **2016**, *8*, 14481−14487.
(1038) Arai, T.; Sato, S.; Uemura, K.; Morikawa, T.; Kajino, T.; Motohiro, T. Photoelectrochemical reduction of CO_2 in water under visible-light irradiation by a p-type InP photocathode modified with an electropolymerized ruthenium complex. *Chem. Commun.* **2010**, *46*, 6944−6946.
(1039) Arai, T.; Tajima, S.; Sato, S.; Uemura, K.; Morikawa, T.; Kajino, T. Selective CO_2 conversion to formate in water using a CZTS photocathode modified with a ruthenium complex polymer. *Chem. Commun.* **2011**, *47*, 12664−12666.
(1040) Sato, S.; Arai, T.; Morikawa, T.; Uemura, K.; Suzuki, T. M.; Tanaka, H.; Kajino, T. Selective CO_2 conversion to formate conjugated with H_2O oxidation utilizing semiconductor/complex hybrid photocatalysts. *J. Am. Chem. Soc.* **2011**, *133*, 15240−15243.
(1041) Arai, T.; Sato, S.; Kajino, T.; Morikawa, T. Solar CO_2 reduction using H_2O by a semiconductor/metal-complex hybrid photocatalyst: enhanced efficiency and demonstration of a wireless system using $SrTiO_3$ photoanodes. *Energy Environ. Sci.* **2013**, *6*, 1274−1282.
(1042) Arai, T.; Sato, S.; Morikawa, T. A monolithic device for CO_2 photoreduction to generate liquid organic substances in a single-compartment reactor. *Energy Environ. Sci.* **2015**, *8*, 1998−2002.
(1043) Torralba-Peñalver, E.; Luo, Y.; Compain, J.-D.; Chardon-Noblat, S.; Fabre, B. Selective Catalytic Electroreduction of CO_2 at Silicon Nanowires (SiNWs) Photocathodes Using Non- Noble Metal-Based Manganese Carbonyl Bipyridyl Molecular Catalysts in Solution and Grafted onto SiNWs. *ACS Catal.* **2015**, *5*, 6138−6147.
(1044) Alenezi, K.; Ibrahim, S. K.; Li, P.; Pickett, C. J. Solar fuels: photoelectrosynthesis of CO from CO_2 at p-type Si using Fe porphyrin electrocatalysts. *Chem. - Eur. J.* **2013**, *19*, 13522−13527.
(1045) He, D.; Jin, T.; Li, W.; Pantovich, S.; Wang, D.; Li, G. Photoelectrochemical CO_2 Reduction by a Molecular Cobalt(II) Catalyst on Planar and Nanostructured Si Surfaces. *Chem. - Eur. J.* **2016**, *22*, 13064−13067.
(1046) Crespo-Quesada, M.; Pazos-Outón, L. M.; Warnan, J.; Kuehnel, M. F.; Friend, R. H.; Reisner, E. Metal-encapsulated organolead halide perovskite photocathode for solar-driven hydrogen evolution in water. *Nat. Commun.* **2016**, *7*, 12555.
(1047) Andrei, V.; Hoye, R. L. Z.; Crespo-Quesada, M.; Bajada, M.; Ahmad, S.; De Volder, M.; Friend, R.; Reisner, E. Scalable Triple Cation Mixed Halide Perovskite−$BiVO_4$ Tandems for Bias-Free Water Splitting. *Adv. Energy Mater.* **2018**, *8*, 1801403.
(1048) Andersor, W. T. Photosensitization in Chlorination. *Ind. Eng. Chem.* **1947**, *39*, 844−846.
(1049) Pape, M. *Pure Appl. Chem.* **1975**, *41*, 535.
(1050) Fischer, M. Industrial Applications of Photochemical Syntheses. *Angew. Chem., Int. Ed. Engl.* **1978**, *17*, 16−26.
(1051) Chiron, S.; Fernandez-Alba, A.; Rodriguez, A.; Garcia-Calvo, E. Pesticide chemical oxidation: state-of-the-art. *Water Res.* **2000**, *34*, 366−377.
(1052) Fouassier, J. P.; Allonas, X.; Burget, D. Photopolymerization reactions under visible lights: principle, mechanisms and examples of applications. *Prog. Org. Coat.* **2003**, *47*, 16−36.
(1053) Roy, S. C.; Varghese, O. K.; Paulose, M.; Grimes, C. A. Toward Solar Fuels: Photocatalytic Conversion of Carbon Dioxide to Hydrocarbons. *ACS Nano* **2010**, *4*, 1259−1278.
(1054) Wu, T.; Zou, L.; Han, D.; Li, F.; Zhang, Q.; Niu, L. A carbon-based photocatalyst efficiently converts CO_2 to CH_4 and C_2H_2 under visible light. *Green Chem.* **2014**, *16*, 2142−2146.
(1055) Weng, Z.; Jiang, J.; Wu, Y.; Wu, Z.; Guo, X.; Materna, K. L.; Liu, W.; Batista, V. S.; Brudvig, G. W.; Wang, H. Electrochemical CO_2 Reduction to Hydrocarbons on a Heterogeneous Molecular Cu Catalyst in Aqueous Solution. *J. Am. Chem. Soc.* **2016**, *138*, 8076−8079.
(1056) El-Khouly, M. E.; El-Mohsnawy, E.; Fukuzumi, S. Solar energy conversion: From natural to artificial photosynthesis. *J. Photochem. Photobiol., C* **2017**, *31*, 36−83.
(1057) Alstrum-Acevedo, J. H.; Brennaman, M. K.; Meyer, T. J. Chemical Approaches to Artificial Photosynthesis. *Inorg. Chem.* **2005**, *44*, 6802−6827.

DOI: 10.1021/acs.chemrev.8b00392
Chem. Rev. 2019, 119, 2752−2875

(1058) Call, A.; Casadevall, C.; Acuña-Parés, F.; Casitas, A.; Lloret-Fillol, J. Dual cobalt−copper light-driven catalytic reduction of aldehydes and aromatic ketones in aqueous media. *Chem. Sci.* **2017**, *8*, 4739−4749.
(1059) Bachmeier, A.; Murphy, B. J.; Armstrong, F. A. A Multi-Heme Flavoenzyme as a Solar Conversion Catalyst. *J. Am. Chem. Soc.* **2014**, *136*, 12876−12879.
(1060) Gerhartz, W. *Enzymes in industry: production and applications/ edited by Wolfgang Gerhartz*; VCH Verlagsgesellschaft mbH: Weinheim, F.R.D., 1990.
(1061) Roth, L. E.; Nguyen, J. C.; Tezcan, F. A. ATP- and Iron−Protein-Independent Activation of Nitrogenase Catalysis by Light. *J. Am. Chem. Soc.* **2010**, *132*, 13672−13674.
(1062) Shimakoshi, H.; Hisaeda, Y. B_{12}-TiO_2 Hybrid Catalyst for Light-Driven Hydrogen Production and Hydrogenation of C−C Multiple Bonds. *ChemPlusChem* **2014**, *79*, 1250−1253.
(1063) Hu, M.; Liu, Y.; Yao, Z.; Ma, L.; Wang, X. Catalytic reduction for water treatment. *Front. Environ. Sci. Eng.* **2018**, *12*, 3.
(1064) Peters, D. G.; McGuire, C. M.; Pasciak, E. M.; Peverly, A. A.; Strawsine, L. M.; Wagoner, E. R.; Tyler Barnes, J. Electrochemical Dehalogenation of Organic Pollutants. *J. Mex. Chem. Soc.* **2017**, *58*, 287−302.
(1065) Shimakoshi, H.; Hisaeda, Y. A Hybrid Catalyst for Light-Driven Green Molecular Transformations. *ChemPlusChem* **2017**, *82*, 18−29.
(1066) Shimakoshi, H.; Nagami, Y.; Hisaeda, Y. Crystal Structure Dependence for Reactivities of B_{12}-TiO_2 Hybrid Catalysts with Anatase and Rutile Forms. *Rapid Communication in Photoscience* **2015**, *4*, 9−11.
(1067) Hisashi, S.; Makoto, A.; Keita, K.; Nobuo, K.; Midori, W.; Yoshio, H. Preparation and Reactivity of Vitamin B_{12}−TiO_2 Hybrid Catalyst Immobilized on a Glass Plate. *Bull. Chem. Soc. Jpn.* **2010**, *83*, 170−172.
(1068) Obare, S. O.; Ito, T.; Meyer, G. J. Controlling Reduction Potentials of Semiconductor-Supported Molecular Catalysts for Environmental Remediation of Organohalide Pollutants. *Environ. Sci. Technol.* **2005**, *39*, 6266−6272.
(1069) Blaser, H.-U.; Malan, C.; Pugin, B.; Spindler, F.; Steiner, H.; Studer, M. Selective Hydrogenation for Fine Chemicals: Recent Trends and New Developments. *Adv. Synth. Catal.* **2003**, *345*, 103−151.
(1070) Ager, D. J.; de Vries, A. H. M.; de Vries, J. G. Asymmetric homogeneous hydrogenations at scale. *Chem. Soc. Rev.* **2012**, *41*, 3340−3380.
(1071) Filonenko, G. A.; van Putten, R.; Hensen, E. J. M.; Pidko, E. A. Catalytic (de)hydrogenation promoted by non-precious metals − Co, Fe and Mn: recent advances in an emerging field. *Chem. Soc. Rev.* **2018**, *47*, 1459−1483.
(1072) Werkmeister, S.; Neumann, J.; Junge, K.; Beller, M. Pincer-Type Complexes for Catalytic (De)Hydrogenation and Transfer (De)Hydrogenation Reactions: Recent Progress. *Chem. - Eur. J.* **2015**, *21*, 12226−12250.
(1073) Cabrero-Antonino, J. R.; Alberico, E.; Junge, K.; Junge, H.; Beller, M. Towards a general ruthenium-catalyzed hydrogenation of secondary and tertiary amides to amines. *Chem. Sci.* **2016**, *7*, 3432−3442.
(1074) Garg, J. A.; Chakraborty, S.; Ben-David, Y.; Milstein, D. Unprecedented iron-catalyzed selective hydrogenation of activated amides to amines and alcohols. *Chem. Commun.* **2016**, *52*, 5285−5288.
(1075) Rezayee, N. M.; Samblanet, D. C.; Sanford, M. S. Iron-Catalyzed Hydrogenation of Amides to Alcohols and Amines. *ACS Catal.* **2016**, *6*, 6377−6383.
(1076) Schneck, F.; Assmann, M.; Balmer, M.; Harms, K.; Langer, R. Selective Hydrogenation of Amides to Amines and Alcohols Catalyzed by Improved Iron Pincer Complexes. *Organometallics* **2016**, *35*, 1931−1943.
(1077) Papa, V.; Cabrero-Antonino, J. R.; Alberico, E.; Spanneberg, A.; Junge, K.; Junge, H.; Beller, M. Efficient and selective hydrogenation of amides to alcohols and amines using a well-defined manganese-PNN pincer complex. *Chem. Sci.* **2017**, *8*, 3576−3585.
(1078) Jochmann, P.; Stephan, D. W. H_2 Cleavage, Hydride Formation, and Catalytic Hydrogenation of Imines with Zinc Complexes of C_5Me_5 and N-Heterocyclic Carbenes. *Angew. Chem., Int. Ed.* **2013**, *52*, 9831−9835.
(1079) Zhang, G.; Scott, B. L.; Hanson, S. K. Mild and Homogeneous Cobalt-Catalyzed Hydrogenation of C=C, C=O, and C=N Bonds. *Angew. Chem., Int. Ed.* **2012**, *51*, 12102−12106.
(1080) Lagaditis, P. O.; Sues, P. E.; Sonnenberg, J. F.; Wan, K. Y.; Lough, A. J.; Morris, R. H. Iron(II) Complexes Containing Unsymmetrical P−N−P′ Pincer Ligands for the Catalytic Asymmetric Hydrogenation of Ketones and Imines. *J. Am. Chem. Soc.* **2014**, *136*, 1367−1380.
(1081) Zell, T.; Ben-David, Y.; Milstein, D. Unprecedented Iron-Catalyzed Ester Hydrogenation. Mild, Selective, and Efficient Hydrogenation of Trifluoroacetic Esters to Alcohols Catalyzed by an Iron Pincer Complex. *Angew. Chem., Int. Ed.* **2014**, *53*, 4685−4689.
(1082) Elangovan, S.; Garbe, M.; Jiao, H.; Spannenberg, A.; Junge, K.; Beller, M. Hydrogenation of Esters to Alcohols Catalyzed by Defined Manganese Pincer Complexes. *Angew. Chem., Int. Ed.* **2016**, *55*, 15364−15368.
(1083) Espinosa-Jalapa, N. A.; Nerush, A.; Shimon, L. J. W.; Leitus, G.; Avram, L.; Ben-David, Y.; Milstein, D. Manganese-Catalyzed Hydrogenation of Esters to Alcohols. *Chem. - Eur. J.* **2017**, *23*, 5934−5938.
(1084) Chakraborty, S.; Dai, H.; Bhattacharya, P.; Fairweather, N. T.; Gibson, M. S.; Krause, J. A.; Guan, H. Iron-Based Catalysts for the Hydrogenation of Esters to Alcohols. *J. Am. Chem. Soc.* **2014**, *136*, 7869−7872.
(1085) Elangovan, S.; Wendt, B.; Topf, C.; Bachmann, S.; Scalone, M.; Spannenberg, A.; Jiao, H.; Baumann, W.; Junge, K.; Beller, M. Improved Second Generation Iron Pincer Complexes for Effective Ester Hydrogenation. *Adv. Synth. Catal.* **2016**, *358*, 820−825.
(1086) Srimani, D.; Mukherjee, A.; Goldberg, A. F. G.; Leitus, G.; Diskin-Posner, Y.; Shimon, L. J. W.; Ben David, Y.; Milstein, D. Cobalt-Catalyzed Hydrogenation of Esters to Alcohols: Unexpected Reactivity Trend Indicates Ester Enolate Intermediacy. *Angew. Chem., Int. Ed.* **2015**, *54*, 12357−12360.
(1087) Junge, K.; Wendt, B.; Cingolani, A.; Spannenberg, A.; Wei, Z.; Jiao, H.; Beller, M. Cobalt Pincer Complexes for Catalytic Reduction of Carboxylic Acid Esters. *Chem. - Eur. J.* **2018**, *24*, 1046−1052.
(1088) Elangovan, S.; Topf, C.; Fischer, S.; Jiao, H.; Spannenberg, A.; Baumann, W.; Ludwig, R.; Junge, K.; Beller, M. Selective Catalytic Hydrogenations of Nitriles, Ketones, and Aldehydes by Well-Defined Manganese Pincer Complexes. *J. Am. Chem. Soc.* **2016**, *138*, 8809−8814.
(1089) Langer, R.; Leitus, G.; Ben-David, Y.; Milstein, D. Efficient Hydrogenation of Ketones Catalyzed by an Iron Pincer Complex. *Angew. Chem., Int. Ed.* **2011**, *50*, 2120−2124.
(1090) Wienhöfer, G.; Westerhaus, F. A.; Junge, K.; Ludwig, R.; Beller, M. A Molecularly Defined Iron-Catalyst for the Selective Hydrogenation of α,β-Unsaturated Aldehydes. *Chem. - Eur. J.* **2013**, *19*, 7701−7707.
(1091) Gorgas, N.; Stöger, B.; Veiros, L. F.; Kirchner, K. Highly Efficient and Selective Hydrogenation of Aldehydes: A Well-Defined Fe(II) Catalyst Exhibits Noble-Metal Activity. *ACS Catal.* **2016**, *6*, 2664−2672.
(1092) Zell, T.; Ben-David, Y.; Milstein, D. Highly efficient, general hydrogenation of aldehydes catalyzed by PNP iron pincer complexes. *Catal. Sci. Technol.* **2015**, *5*, 822−826.
(1093) Yoshimura, M.; Tanaka, S.; Kitamura, M. Recent topics in catalytic asymmetric hydrogenation of ketones. *Tetrahedron Lett.* **2014**, *55*, 3635−3640.
(1094) Monti, D.; Ottolina, G.; Carrea, G.; Riva, S. Redox Reactions Catalyzed by Isolated Enzymes. *Chem. Rev.* **2011**, *111*, 4111−4140.
(1095) Reeve, H. A.; Lauterbach, L.; Lenz, O.; Vincent, K. A. Enzyme-Modified Particles for Selective Biocatalytic Hydrogenation by Hydrogen-Driven NADH Recycling. *ChemCatChem* **2015**, *7*, 3480−3487.

DOI: 10.1021/acs.chemrev.8b00392
Chem. Rev. 2019, 119, 2752−2875

(1096) Reeve, H. A.; Lauterbach, L.; Ash, P. A.; Lenz, O.; Vincent, K. A. A modular system for regeneration of NAD cofactors using graphite particles modified with hydrogenase and diaphorase moieties. *Chem. Commun.* **2012**, *48*, 1589−1591.
(1097) Lee, S. H.; Nam, D. H.; Kim, J. H.; Baeg, J. O.; Park, C. B. Eosin Y-Sensitized Artificial Photosynthesis by Highly Efficient Visible-Light-Driven Regeneration of Nicotinamide Cofactor. *ChemBioChem* **2009**, *10*, 1621−1624.
(1098) Hoffman, B. M.; Lukoyanov, D.; Yang, Z.-Y.; Dean, D. R.; Seefeldt, L. C. Mechanism of Nitrogen Fixation by Nitrogenase: The Next Stage. *Chem. Rev.* **2014**, *114*, 4041−4062.
(1099) Smith, B. E. Nitrogenase Reveals Its Inner Secrets. *Science* **2002**, *297*, 1654−1655.
(1100) Haber, F.; Le Rossignol, R. Über die technische Darstellung von Ammoniak aus den Elementen. *Zeitschrift für Elektrochemie und angewandte physikalische Chemie* **1913**, *19*, 53−72.
(1101) Berl, E. Fritz Haber zum 60. Geburtstag. *Zeitschrift für Elektrochemie und angewandte physikalische Chemie* **1928**, *34*, 797−803.
(1102) van der Ham, C. J. M.; Koper, M. T. M.; Hetterscheid, D. G. H. Challenges in reduction of dinitrogen by proton and electron transfer. *Chem. Soc. Rev.* **2014**, *43*, 5183−5191.
(1103) Spatzal, T. The Center of Biological Nitrogen Fixation: FeMo-Cofactor. *Z. Anorg. Allg. Chem.* **2015**, *641*, 10−17.
(1104) Chen, X.; Li, N.; Kong, Z.; Ong, W.-J.; Zhao, X. Photocatalytic fixation of nitrogen to ammonia: state-of-the-art advancements and future prospects. *Mater. Horiz.* **2018**, *5*, 9−27.
(1105) Milton, R. D.; Abdellaoui, S.; Khadka, N.; Dean, D. R.; Leech, D.; Seefeldt, L. C.; Minteer, S. D. Nitrogenase bioelectrocatalysis: heterogeneous ammonia and hydrogen production by MoFe protein. *Energy Environ. Sci.* **2016**, *9*, 2550−2554.
(1106) Milton, R. D.; Minteer, S. D. Enzymatic Bioelectrosynthetic Ammonia Production: Recent Electrochemistry of Nitrogenase, Nitrate Reductase, and Nitrite Reductase. *ChemPlusChem* **2017**, *82*, 513−521.
(1107) Brown, K. A.; Harris, D. F.; Wilker, M. B.; Rasmussen, A.; Khadka, N.; Hamby, H.; Keable, S.; Dukovic, G.; Peters, J. W.; Seefeldt, L. C.; et al. Light-driven dinitrogen reduction catalyzed by a CdS:nitrogenase MoFe protein biohybrid. *Science* **2016**, *352*, 448−450.
(1108) Milton, R. D.; Cai, R.; Abdellaoui, S.; Leech, D.; De Lacey, A. L.; Pita, M.; Minteer, S. D. Bioelectrochemical Haber−Bosch Process: An Ammonia-Producing H_2/N_2 Fuel Cell. *Angew. Chem., Int. Ed.* **2017**, *56*, 2680−2683.
(1109) Fourmond, V.; Léger, C. Dinitrogen Reduction: Interfacing the Enzyme Nitrogenase with Electrodes. *Angew. Chem., Int. Ed.* **2017**, *56*, 4388−4390.
(1110) Anderson, J. S.; Rittle, J.; Peters, J. C. Catalytic conversion of nitrogen to ammonia by an iron model complex. *Nature* **2013**, *501*, 84−87.
(1111) Del Castillo, T. J.; Thompson, N. B.; Peters, J. C. A Synthetic Single-Site Fe Nitrogenase: High Turnover, Freeze-Quench ^{57}Fe Mössbauer Data, and a Hydride Resting State. *J. Am. Chem. Soc.* **2016**, *138*, 5341−5350.
(1112) Creutz, S. E.; Peters, J. C. Catalytic Reduction of N_2 to NH_3 by an Fe−N_2 Complex Featuring a C-Atom Anchor. *J. Am. Chem. Soc.* **2014**, *136*, 1105−1115.
(1113) Anderson, J. S.; Cutsail, G. E.; Rittle, J.; Connor, B. A.; Gunderson, W. A.; Zhang, L.; Hoffman, B. M.; Peters, J. C. Characterization of an Fe≡N−NH_2 Intermediate Relevant to Catalytic N_2 Reduction to NH_3. *J. Am. Chem. Soc.* **2015**, *137*, 7803−7809.
(1114) Rittle, J.; Peters, J. C. An Fe-N_2 Complex That Generates Hydrazine and Ammonia via Fe═NNH_2: Demonstrating a Hybrid Distal-to-Alternating Pathway for N_2 Reduction. *J. Am. Chem. Soc.* **2016**, *138*, 4243−4248.
(1115) Gogoi, U.; Guha, A. K.; Phukan, A. K. Tracing the Route to Ammonia: A Theoretical Study on the Possible Pathways for Dinitrogen Reduction with Tripodal Iron Complexes. *Chem. - Eur. J.* **2013**, *19*, 11077−11089.
(1116) Chalkley, M. J.; Del Castillo, T. J.; Matson, B. D.; Roddy, J. P.; Peters, J. C. Catalytic N_2-to-NH_3 Conversion by Fe at Lower Driving Force: A Proposed Role for Metallocene-Mediated PCET. *ACS Cent. Sci.* **2017**, *3*, 217−223.
(1117) Creutz, S. E.; Peters, J. C. Diiron Bridged-Thiolate Complexes That Bind N_2 at the $Fe^{II}Fe^{II}$, $Fe^{II}Fe^{I}$, and $Fe^{I}Fe^{I}$ Redox States. *J. Am. Chem. Soc.* **2015**, *137*, 7310−7313.
(1118) Lee, Y.; Sloane, F. T.; Blondin, G.; Abboud, K. A.; García-Serres, R.; Murray, L. J. Dinitrogen Activation Upon Reduction of a Triiron(II) Complex. *Angew. Chem., Int. Ed.* **2015**, *54*, 1499−1503.
(1119) Ung, G.; Peters, J. C. Low-Temperature N_2 Binding to Two-Coordinate L_2Fe^0 Enables Reductive Trapping of $L_2FeN_2^-$ and NH_3 Generation. *Angew. Chem., Int. Ed.* **2015**, *54*, 532−535.
(1120) Gilbertson, J. D.; Szymczak, N. K.; Tyler, D. R. Reduction of N_2 to Ammonia and Hydrazine Utilizing H_2 as the Reductant. *J. Am. Chem. Soc.* **2005**, *127*, 10184−10185.
(1121) Buscagan, T. M.; Oyala, P. H.; Peters, J. C. N_2-to-NH_3 Conversion by a triphos−Iron Catalyst and Enhanced Turnover under Photolysis. *Angew. Chem., Int. Ed.* **2017**, *56*, 6921−6926.
(1122) Kuriyama, S.; Arashiba, K.; Nakajima, K.; Matsuo, Y.; Tanaka, H.; Ishii, K.; Yoshizawa, K.; Nishibayashi, Y. Catalytic transformation of dinitrogen into ammonia and hydrazine by iron-dinitrogen complexes bearing pincer ligand. *Nat. Commun.* **2016**, *7*, 12181.
(1123) Vol'Pin, M. E.; Shur, V. B. Nitrogen Fixation by Transition Metal Complexes. *Nature* **1966**, *209*, 1236−1236.
(1124) Bayer, E.; Schurig, V. Stickstoff-Fixierung und Reduktion zu Ammoniak mit metallorganischen Katalysatoren. *Chem. Ber.* **1969**, *102*, 3378−3390.
(1125) van Tamelen, E. E.; Fechter, R. B.; Schneller, S. W.; Boche, G.; Greeley, R. H.; Akermark, B. Titanium(II) in the fixation-reduction of molecular nitrogen under mild conditions. *J. Am. Chem. Soc.* **1969**, *91*, 1551−1552.
(1126) van Tamelen, E. E.; Seeley, D. A. Catalytic fixation of molecular nitrogen by electrolytic and chemical reduction. *J. Am. Chem. Soc.* **1969**, *91*, 5194−5194.
(1127) Becker, J. Y.; Avraham, S.; Posin, B. Nitrogen fixation: Part I. Electrochemical reduction of titanium compounds in the presence of catechol and N_2 in MeOH or THF. *J. Electroanal. Chem. Interfacial Electrochem.* **1987**, *230*, 143−153.
(1128) Riley, F. L. Silicon Nitride and Related Materials. *J. Am. Ceram. Soc.* **2000**, *83*, 245−265.
(1129) Nishibayashi, Y. Recent Progress in Transition-Metal-Catalyzed Reduction of Molecular Dinitrogen under Ambient Reaction Conditions. *Inorg. Chem.* **2015**, *54*, 9234−9247.
(1130) Tanabe, Y.; Nishibayashi, Y. Developing more sustainable processes for ammonia synthesis. *Coord. Chem. Rev.* **2013**, *257*, 2551−2564.
(1131) Shiina, K. Reductive silylation of molecular nitrogen via fixation to tris(trialkylsilyl)amine. *J. Am. Chem. Soc.* **1972**, *94*, 9266−9267.
(1132) Yuki, M.; Tanaka, H.; Sasaki, K.; Miyake, Y.; Yoshizawa, K.; Nishibayashi, Y. Iron-catalysed transformation of molecular dinitrogen into silylamine under ambient conditions. *Nat. Commun.* **2012**, *3*, 1254.
(1133) Imayoshi, R.; Tanaka, H.; Matsuo, Y.; Yuki, M.; Nakajima, K.; Yoshizawa, K.; Nishibayashi, Y. Cobalt-Catalyzed Transformation of Molecular Dinitrogen into Silylamine under Ambient Reaction Conditions. *Chem. - Eur. J.* **2015**, *21*, 8905−8909.
(1134) Siedschlag, R. B.; Bernales, V.; Vogiatzis, K. D.; Planas, N.; Clouston, L. J.; Bill, E.; Gagliardi, L.; Lu, C. C. Catalytic Silylation of Dinitrogen with a Dicobalt Complex. *J. Am. Chem. Soc.* **2015**, *137*, 4638−4641.
(1135) Imayoshi, R.; Nakajima, K.; Nishibayashi, Y. Vanadium-catalyzed Reduction of Molecular Dinitrogen into Silylamine under Ambient Reaction Conditions. *Chem. Lett.* **2017**, *46*, 466−468.
(1136) Louis, M. E.; Fenton, T. G.; Rondeau, J.; Jin, T.; Li, G. Solar CO_2 Reduction Using Surface-Immobilized Molecular Catalysts. *Comments Inorg. Chem.* **2016**, *36*, 38−60.
(1137) Armstrong, F. A.; Hirst, J. Reversibility and efficiency in electrocatalytic energy conversion and lessons from enzymes. *Proc. Natl. Acad. Sci. U. S. A.* **2011**, *108*, 14049−14054.

DOI: 10.1021/acs.chemrev.8b00392
Chem. Rev. 2019, 119, 2752−2875

(1138) Fiorio, J. L.; López, N.; Rossi, L. M. Gold−Ligand-Catalyzed Selective Hydrogenation of Alkynes into cis-Alkenes via H_2 Heterolytic Activation by Frustrated Lewis Pairs. *ACS Catal.* **2017**, *7*, 2973−2980.
(1139) Gong, M.; Cao, Z.; Liu, W.; Nichols, E. M.; Smith, P. T.; Derrick, J. S.; Liu, Y.-S.; Liu, J.; Wen, X.; Chang, C. J. Supramolecular Porphyrin Cages Assembled at Molecular−Materials Interfaces for Electrocatalytic CO Reduction. *ACS Cent. Sci.* **2017**, *3*, 1032−1040.
(1140) Kasap, H.; Achilleos, D. S.; Huang, A.; Reisner, E. Photoreforming of Lignocellulose into H_2 Using Nanoengineered Carbon Nitride under Benign Conditions. *J. Am. Chem. Soc.* **2018**, *140*, 11604−11607.
(1141) Alibabaei, L.; Brennaman, M. K.; Norris, M. R.; Kalanyan, B.; Song, W.; Losego, M. D.; Concepcion, J. J.; Binstead, R. A.; Parsons, G. N.; Meyer, T. J. Solar water splitting in a molecular photoelectrochemical cell. *Proc. Natl. Acad. Sci. U. S. A.* **2013**, *110*, 20008.
(1142) Yu, Z.; Li, F.; Sun, L. Recent advances in dye-sensitized photoelectrochemical cells for solar hydrogen production based on molecular components. *Energy Environ. Sci.* **2015**, *8*, 760−775.
(1143) Farnum, B. H.; Wee, K.-R.; Meyer, T. J. Self-assembled molecular p/n junctions for applications in dye-sensitized solar energy conversion. *Nat. Chem.* **2016**, *8*, 845−852.
(1144) Cui, X.; Li, W.; Ryabchuk, P.; Junge, K.; Beller, M. Bridging homogeneous and heterogeneous catalysis by heterogeneous single-metal-site catalysts. *Nat. Catal.* **2018**, *1*, 385−397.
(1145) Leonard, N.; Ju, W.; Sinev, I.; Steinberg, J.; Luo, F.; Varela, A. S.; Roldan Cuenya, B.; Strasser, P. The chemical identity, state and structure of catalytically active centers during the electrochemical CO_2 reduction on porous Fe−nitrogen−carbon (Fe−N−C) materials. *Chem. Sci.* **2018**, *9*, 5064−5073.
(1146) Oh, S.; Gallagher, J. R.; Miller, J. T.; Surendranath, Y. Graphite-Conjugated Rhenium Catalysts for Carbon Dioxide Reduction. *J. Am. Chem. Soc.* **2016**, *138*, 1820−1823.
(1147) Copéret, C.; Comas-Vives, A.; Conley, M. P.; Estes, D. P.; Fedorov, A.; Mougel, V.; Nagae, H.; Núñez-Zarur, F.; Zhizhko, P. A. Surface Organometallic and Coordination Chemistry toward Single-Site Heterogeneous Catalysts: Strategies, Methods, Structures, and Activities. *Chem. Rev.* **2016**, *116*, 323−421.
(1148) Hennessey, S.; Farràs, P. Production of solar chemicals: gaining selectivity with hybrid molecule/semiconductor assemblies. *Chem. Commun.* **2018**, *54*, 6662−6680.
(1149) Pinto, M.; Friães, S.; Franco, F.; Lloret-Fillol, J.; Royo, B. Manganese N-Heterocyclic Carbene Complexes for Catalytic Reduction of Ketones with Silanes. *ChemCatChem* **2018**, *10*, 2734−2740.

DOI: 10.1021/acs.chemrev.8b00392
Chem. Rev. 2019, 119, 2752−2875